technische universität
dortmund

Supramolecular Coordination Cages Based on Light-Switchable Diarylethene Ligands

Fakultät für Chemie und Chemische Biologie der Technischen Universität Dortmund

Rujin Li

From Hubei, China

Dortmund, 2019

Ever tried. Ever failed. No matter. Try again. Fail again.
Fail better.

Samuel Beckett

Principal advisor:	Prof. Dr. Guido Clever
Secondary surveyor:	Prof. Dr. Andreas Steffen
Filed on:	July 9, 2019

Publications and conferences

Publications:

"Mechanistic Interplay between Light-Switching and Guest-Binding in Photochromic [Pd_2Dithienylethene$_4$] Coordination Cages", **R.-J. Li**, J. J. Holstein, W. G. Hiller, J. Andréasson, G. H. Clever, *J. Am. Chem. Soc.* **2019**, *141*, 2097.

"Successive Photoswitching and Derivatization Effects in Photochromic DTE-based Coordination Cages", **R.-J. Li**, M. Han, J. Tessarolo, J. J. Holstein, J. Lübben, B. Dittrich, C. Volkmann, M. Finze, C. Jenne, and G. H. Clever, *ChemPhotoChem* **2019**, *3*, 378.

Conferences:

Poster, 14th International Symposium on Macrocyclic and Supramolecular Chemistry (ISMSC), **2019**, *Lecce*, Italy

Poster, Tag der Chemie, **2018**, *Dortmund*, Germany

Poster, 13th International Symposium on Macrocyclic and Supramolecular Chemistry (ISMSC), **2018**, *Quebec City*, Canada

Poster, Münster Symposium on Cooperative Effects in Chemistry, **2018**, *Münster*, Germany

Poster, Suprachem, **2017**, *Aachen*, Germany

Abstract

Supramolecular coordination cages, assembled from square-planer cations (Pd^{II} or Pt^{II}) and banana-shaped ligands, have been widely studied in the past decades. Interests in this field gradually shifted from structure to function. This thesis explores the self-assembly of light-switchable homo- and hetero-leptic cages formed from Diarylethene (DAE) ligands which enable a fast photo-responsive interconversion between a flexible open form and rigid closed form of the chromophore backbone. In addition, the host-guest chemistry, their application in photo-controlled chirality transfer and singlet oxygen generation are investigated.

First, in chapter 2, preparation and characterization of a new lantern like cage (*o*-**C^{a}**) in its open-form and a bowl like complex (*c*-**B**) in its closed-form are presented. Both are composed of Pd^{II} cations and ligand **L^{a}** (DAE unit modified with bulky group). *o*-**C^{a}** and *c*-**B** could reversibly be interconverted by irradiation with UV (313 nm) and red light (617 nm). Since the Pd^{II} atoms in *c*-**B** were coordinately unsaturated with pyridyl ligands (carrying solvents molecule as fourth ligands), mixing *c*-**B** with pre-designed ligand (with similar N-N distance as **L^{a}**) allowed to synthesize a series of heteroleptic cages of the type $Pd_2L^A{}_3L^B$. Moreover, the internal cavity of the heteroleptic cages could be enlarged by introducing longer ligand arms, which are investigated with guests varying in size (**G1**, **G2**, **G3**). In addition, by titrating Br^-/Ag^+ in presence or absence of guest, the heteroleptic cage (*c*-**B**+**L^{e}**) was partially decomposed and re-assembled by removing and re-coordinating of **L^{e}**, resulting in guest release and capture. Further, by mixing the bowl complex with ligand **L^{g}** instead, *o*/*c*-**B**-**L^{g}** was assembled (Chapter 4). However, the thermally unstable *o*/*c*-**B**-**L^{g}** gradually transform to the thermodynamically favored cage [Pd_2**L^{a}**$_2$**L^{g}**$_2$].

In Chapter 3, the combination of *c*-**B** with the chiral helicene-based ligand **L^{1}** to obtain *c*-**B**-**L^{1}** was presented. Chirality transfer was first achieved in a lantern cage from **L^{1P}**/**L^{1M}** to **L^{a}**. Irradiation at 617 nm leads to the opening of the previously closed ligands. After switching back to the closed form under UV light (313 nm), the induced chiral information was locked. Following cage decomposition allowed to analyze the degree of induced chirality through chiral HPLC.

Moreover, in Chapter 5, by linking di, tri and tetratopic carboxylate ligands with *c*-**B**, a series of di, tri and tetramer supramolecular ferris-wheels were constructed. Due to the different triplet energy gaps between open and closed state DAE ligand, $^1O_2$ generation

in a tetramer utilizing a zinc-tetra(4-carboxylatophenyl)porphyrin photosensitizer could be reversibly switched on and off with light.

Finally, Chapter 6 describes that less-bulky $\mathbf{L^b}$ assembles to coordination cages in both photoisomeric forms (*o*/*c*-$\mathbf{C^b}$) were assembled, which allowed to trigger guest uptake and release by irradiation with light of different wavelengths. With the intrinsic chirality of the DAE backbones as reporter, it was possible to monitor the interplay between photoisomerization steps and guest location inside/outside the cavity. In its open form, the C_2-symmetric DAE chromophore quickly converts between energetically degenerate *P* and *M* helical conformations. After binding homochiral camphor sulfonate (*R*-CSA or *S*-CSA), a guest-to-host chirality transfer was observed by circular dichroism (CD) spectroscopy. Irradiating the *R/S*-CSA@*o*-$\mathbf{C^b}$ host-guest complexes at 313 nm produced closed photo-isomers, thus locking the induced chirality with an enantiomeric excess close to 25%. This value (corresponding to chiral induction for one out of four ligands) together with DOSY NMR, ion mobility mass spectrometry and X-ray structure results, shows, that closure of the first photo-switch is sufficient to expel the guest from the cavity.

Zusammenfassung

In den letzten Jahrzehnten wurden supramolekulare Koordinationskäfige, welche aus quadratisch planar koordinierten Kationen (Pd^{II} oder Pt^{II}) und bananenförmigen Liganden assembliert sind, ausgiebig untersucht. Allmählich wurden die Interessen in diesem Feld von Strukturen zu Funktionen verschoben. Diese Arbeit beleuchtet die Selbstassemblierung von durch Licht schaltbaren homo- und heteroleptischen Käfigen mit Diarylethen-Liganden (DAE), die eine schnelle photoresponsive Umwandlung von einer flexiblen, offenen Form zu einer starren, geschlossenen Form des chromophoren Rückgrats ermöglichen. Zusätzlich wurde die Wirt-Gast-Chemie, die Anwendung in lichtkontrolliertem Chiralitätstransfer und die Erzeugung von Singulett-Sauerstoff untersucht.

In Kapitel **2** wird zunächst die Synthese und Charakterisierung eines neuen, laternenförmigen Käfigs (*o*-**C**^{a}) in seiner offenen Form und eines schüsselartigen Komplexes (*c*-**B**) in seiner geschlossenen Form präsentiert. Beide Strukturen sind aus Pd^{II} Kationen und dem Liganden **L**^{a} (DAE-Einheit mit sterisch anspruchsvollen Resten) aufgebaut. Sowohl *o*-**C**^{a} als auch *c*-**B** können reversibel durch Bestrahlung mit UV- (313 nm) und rotem (617 nm) Licht geschaltet werden. Da die Pd^{II} Atome des *c*-**B** Komplexes bezüglich der Pyridylliganden koordinativ ungesättigt sind (die vierte Koordinationsstelle besetzt ein Lösemittelmolekül), war es möglich aus einer Mischung von *c*-**B** und einem weiteren Liganden (mit ähnlichem N-N-Abstand wie **L**^{a}) eine Serie von heteroleptischen Käfigen des Typs $Pd_2L^{A}{}_3L^{B}$ zu synthetisieren. Darüber hinaus konnten die internen Kavitäten der heteroleptischen Käfige durch Einführung längerer Ligandenarme vergrößert werden, welche mit Hilfe verschieden großer Gastmoleküle (**G1**, **G2**, **G3**) untersucht wurden. Zusätzlich konnte gezeigt werden, dass durch Titration von Br^{-}/Ag^{+} in An- oder Abwesenheit des Gastes der heteroleptische Käfig (*c*-**B**+**L**^{e}) durch Entfernen oder Koordination des Liganden **L**^{e} partiell zerstört beziehungsweise reassembliert wurde, was zu einer Gastabgabe beziehungsweise -aufnahme führte. Des Weiteren wurde durch Mischen des schüsselförmigen Komplexes mit dem Liganden L^{g} die Assemblierung von *o/c*-**B**-**L**^{g} erhalten (vgl. Kapitel 4). Außerdem wurde gezeigt, dass der thermodynamisch instabile Komplex *o*/*c*-**B**-**L**^{g} graduell zum thermodynamisch stabilen Käfig [Pd_2**L**$^{a}{}_2$**L**$^{g}{}_2$] reagiert.

In Kapitel **3** wird präsentiert, wie die Kombination aus *c*-**B** mit dem chiralen, helicenbasierten Liganden **L**^{1} zu *c*-**B**-**L**^{1} führt. Hier wurde erstmals ein Chiralitätstransfer in einem laternenförmigen Käfig von **L**^{1P}**/L**^{1M} auf **L**^{a} erreicht. Die Bestrahlung bei 617 nm führte zu einer Öffnung der vorher geschlossenen Liganden. Nach Rückschaltung zur

geschlossenen Form mit UV-Licht (313 nm) war auch die induzierte chirale Information fixiert. Nach einer darauffolgenden Zersetzung des Käfigs konnte der Grad der induzierten Chiralitätsinformation mittels chiraler HPLC bestimmt werden.

In Kapitel **5** wurde ferner gezeigt, wie mit Hilfe der Kombination von di-, tri- und tetrameren Carboxylatliganden mit *c*-**B** eine Serie von di-, tri- und tetrameren, supramolekularen, riesenradähnlichen Strukturen konstruiert wurden. Aufgrund der verschieden großen Triplettenergielücken zwischen den offenen und geschlossenen Zuständen des DAE-Liganden konnte die $^1O_2$-Erzeugung in einem Tetramer unter Benutzung von Zinktetra(4-carboxylatophenyl)porphyrin als Photosensibilisator reversibel mit Lichtschaltung gesteuert werden.

Zuletzt wird in Kapitel **6** beschrieben, wie Koordinationskäfige in beiden photoisomeren Formen (*o/c*-$\mathbf{C^b}$) mit dem sterisch weniger anspruchsvollen Liganden $\mathbf{L^b}$ assembliert wurden und eine schaltbare Gastaufnahme bzw. –abgabe durch Bestrahlung mit Licht verschiedener Wellenlängen aufzeigen. Mit Hilfe der intrinsischen Chiralität des DEA-Rückgrates als Reporter war es möglich, das Zusammenspiel von Photoisomerisierungszuständen und Lokalisierung des Gastes inner- bzw. außerhalb der Kavität zu verfolgen. In seiner offenen Form wechselt das C_2-symmetrische DAE-Rückgrat schnell zwischen den energetisch entarteten helikalen Konformeren *P* und *M* umher. Nach der Bindung eines homochiralen Camphersulfonats (*R*-CSA oder *S*-CSA) konnte ein Chiralitätstransfer von Gast zu Wirt mittels Zirkulardichroismus Spektroskopie (CD) beobachtet werden. Die Bestrahlung des *R*/*S*-CSA@*o*-$\mathbf{C^b}$ Wirt-Gast-Komplexes bei 313 nm produzierte geschlossene Photoisomere, welche folglich die induzierte Chiralität mit einem Enatiomerenüberschuss von 25% beibehalten. Dieser Wert (passend zur vollständigen chiralen Induktion in einem der vier Liganden) zeigt zusammen mit DOSY NMR Spektroskopie, Ionenmobiltätsmassenspektrometrie und Einkristallröntgenstrukturanalyse, dass das Schließen des ersten Photoschalters ausreicht, um den Gast aus der Kavität zu vertreiben.

Table of Content

1 Introduction

1.1 Photoswitches

The long history of photochromic compounds, which undergo reversible transformation between two isomers by light-irradiation, wittiness their promising application in optical materials, biological systems, molecular memory devices, logic gates *etc*.[1] However, the basic photochromic palette have not too much expanded regardless of the upraise interest during the past decades. Typical examples of photoswitches are stilbenes,[2] azobenzenes,[3] spiropyrans & spirooxazines,[4] and diarylethenes[5] (Figure 1.1). Upon UV light irradiation, transformation of the *trans* isomer of azobenzene to *cis* isomer leads to change of color from yellow to orange. However, the color of thermally unstable *cis* isomer turns back to pale yellow upon thermal excitation (Figure 1.1a). Unlike X=X (X = CH, N) double bond isomerization, the reversible photoswitching of spiropyrans were achieved through cleavage and reformation of the spiro C-O bond. Apart from the photo-induced reverse ring-closing reaction, the colorless thermally stable closed form spiropyrans can be obtained under heating as well (Figure 1.1b). Thermally reversible properties of both azobenzenes and spiropyrans, however, limited their application in optical memories, switches and molecular machines. Therefore, a new family of photochromic molecules diarylethenes (DAEs), showing thermal stability in both isomeric forms, is being developed to fulfill such requirements.

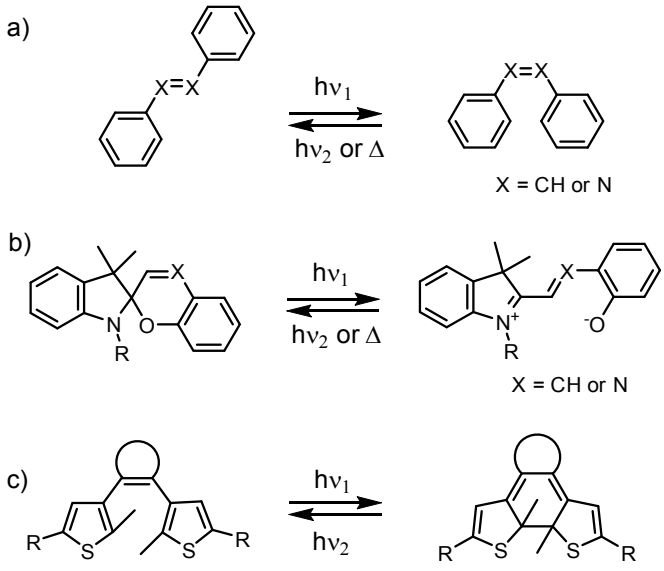

Figure 1.1 Photochromism of (a) stilbenes and azobenzenes, (b) spiropyrans and spirooxazines, and (c) diarylethenes.

Diaryethenes, with high fatigue-resistance, fast photo-response and thermally irreversible properties, have been extensively studied in the past decades. It was first discovered as side reaction during photochromic reversibility study on the isomerization of *trans-cis* stilbenes.[6] Since the first paper on DAEs published in 1988,[7] the reports in the field have shown growing dramatically: 2782 publications until Jan. 20th, 2019 (Figure 1.2). Under UV or visible light irradiation, the cyclization and cycloreversion of DAEs are reversibly switched (Figure 1.1c), resulting in their geometrical structure difference, on the other hand, changing their electronic structures as well. In this chapter, geometrical and electronic switches of DAEs are briefly described as below.

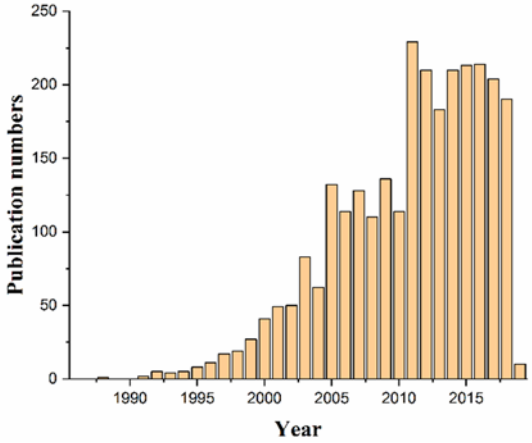

Figure 1.2 Distribution of the number of publications based on key words of diarylethene or dithienylethene. (Until Jan. 20th, 2019 from Web of Science)

1.2 Geometrical structure switching

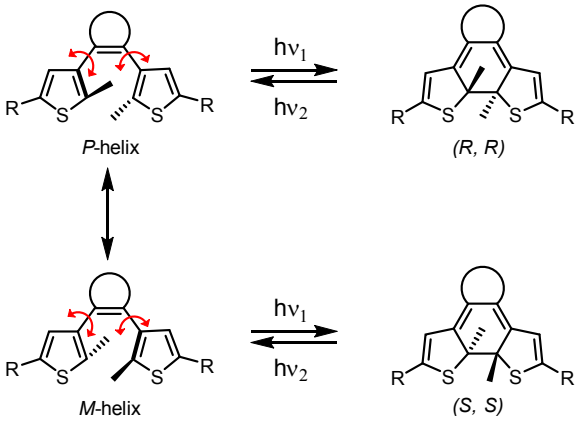

Figure 1.3 Photoisomerization of a diarylethene (DAE). The photocyclization reactions from *P*- and *M*-helical conformers of the open-ring isomer produce (*R, R*) and (*S, S*) enantiomers of the closed-ring isomer, respectively.

As mentioned above, the ring-closing and ring-opening reaction of DAEs are reversibly switched with light irradiation. In open form DAEs, thiophene group can be freely rotated along the joint single bond with cyclic ethene backbone, therefore, behaving much more

flexible (Figure 1.3). However, after cyclization reaction under UV light irradiation, the two thiophene rings are locked together, resulting in a rigid closed form molecule (Figure 1.3). Furthermore, due to the fast conversion of *P*-helical and *M*-helical conformers of DAEs, the photochemical cyclization reaction produced two enantiomers in equal amounts (Figure 1.3).

1.2.1 Structure switch

Because of structural differences, DAEs in their open and closed isomers behave completely different in supramolecular coordination assembles. Clever and co-workers prepared a photochromic cage $Pd_2\mathbf{L}_4$ by coordinating functionalized DAE ligands to Pd^{II} ion[8] (Figure 1.4a). They explored photo-controlled guest uptake and release through the reversible interconversion between the cage isomers. The flexible ligands in the open form cage make it stronger affinity with anionic cargo $[B_{12}F_{12}]^{2-}$, After switching by UV light, the closed isomer showed a lower binding constant owing to its more rigid and protracted structure, thus releasing the guest.

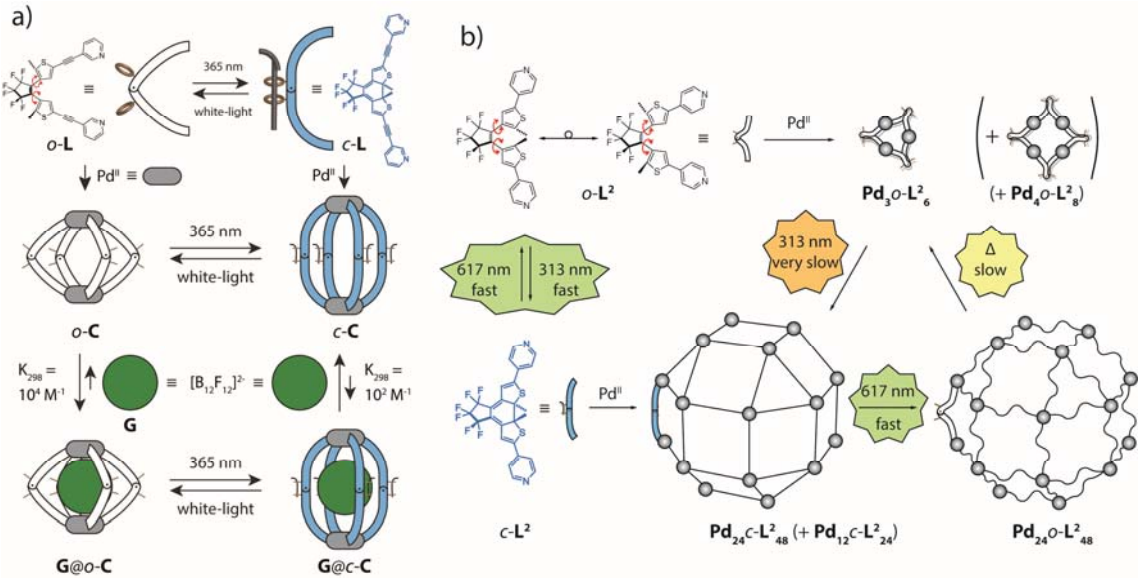

Figure 1.4 (a) Diarylethene coordination cage for guest uptake and release; (b) light-controlled interconversion between diarylethene based rings and rhombicuboctahedral sphere. Copyright © 2013 and 2016 Wiley-VCH Verlag GmbH & Co.

Using same DAE backbone but pyridyl modified ligand, Clever *et al.* constructed small triangle $Pd_3o\text{-}\mathbf{L^2}_6$ and tetramer $Pd_4o\text{-}\mathbf{L^2}_8$ ring mixtures via complexing Pd^{II} ion with the open-form ligands. While it assembled into a large rhombicuboctahedral sphere with the formula of $Pd_{24}c\text{-}\mathbf{L^2}_{48}$ when switched the $o\text{-}\mathbf{L^2}$ to more rigid $c\text{-}\mathbf{L^2}$ with a large coordination angle (Figure 1.4b). Under light irradiation, the triangle and rhombicuboctahedral sphere can be reversible interconverted.[9]

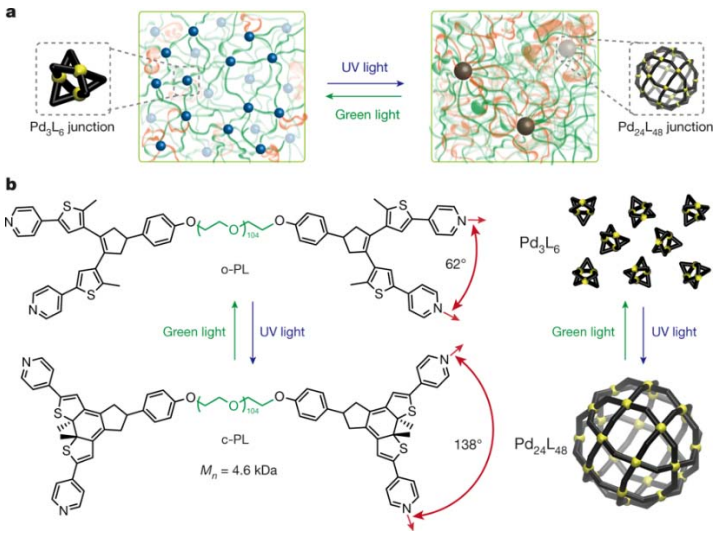

Figure 1.5 Polymer metal-organic cage (PolyMOC) with photoswitchable topology. Copyright © 2018 Nature Publishing Group.

Based on Clever's work, Johnson *et al.* modified polymer chains with DAE motif, giving a photochromic polymer ligand. Open form polymer ligand (*o*-PL) and closed ligand isomer (*c*-PL) can be freely switched. When mixed with Pd^{II}, two different polymer network: a dark brown *o*-gel (Pd_3*o*-L_6 & Pd_4*o*-L_8) and deep blue *c*-gel (Pd_{24}*c*-L_{48}) were obtained separately, showing different network topologies. Similarly, the interconversion between these two gels with different network topologies can be controlled by light as well[10] (Figure 1.5).

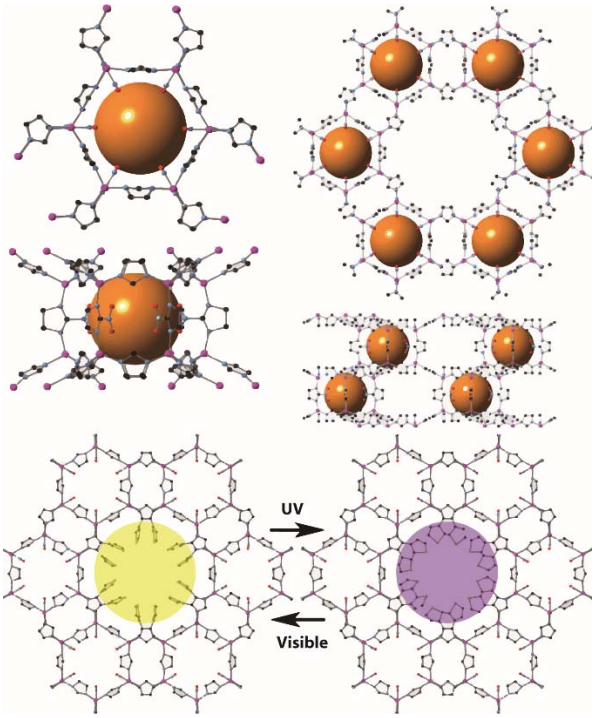

Figure 1.6 DAE contained metal-organic frameworks (MOFs) with photoswitchable pore properties. Copyright © 2017 American Chemical Society.

Metal-Organic Frameworks (MOFs), as one of the most popular materials, have been well developed in the past decades.[11] Katz and coworkers fabricated a DAE doped MOF derived from ZIF-70.[12] Under post synthesis of solvent assisted linker exchange (SALE), part of the ligands pointed to the large pore in ZIF-70 are replaced by DAE ligands, resulting in new class of MOF materials: PSZ-1. With UV or visible light irradiation, the property of the large pore is changed due to the structural difference between the isomers, showing reversibly switched chemical separation abilities (Figure 1.6).

1.2.2 Chiral control

In general, the C_2 symmetric open form DAEs do not show any chirality since their fast rotation features. Upon photocyclization, however, their chirality are locked as a pair of racemic in most cases which is possible to be resolved through chiral HPLC. Therefore, to date, many efforts such as asymmetric synthesis,[13] chiral induction[14] and crystallization[15] etc. have been done to make open-form DAEs preferably to one of the helical-forms, thus resolving DAEs enantiomers after ring-closure reaction.

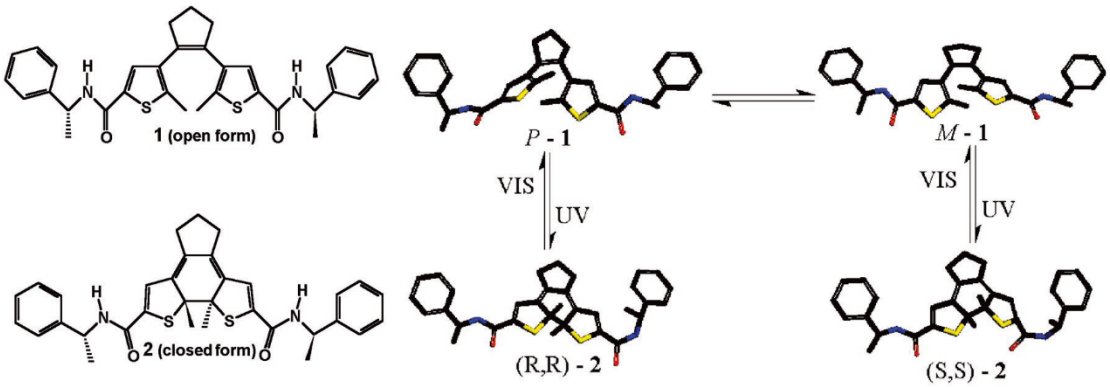

Figure 1.7 Chiral switch with diarylethene gelator. Copyright © 2004 American Association for the Advancement of Science.

Feringa *et al.* synthesized an amide functionalized diarylethene gelator and reported reversible optical transcription of supramolecular chirality into molecular chirality[16] (Figure 1.7). With the help of the interaction of intermolecular hydrogen bonding, the small gelator aggregated into *P*- or *M*-helical supramolecular gels. After photochemical ring closure of the gelator in the chiral gels, its molecular stereoisomers were locked. Later, Feringa and coworkers use the similar supramolecular and molecular chirality communication together with sergeant-solider strategy to amplify the inherent chirality of diarylethene.[17] Doping small amount of pre-resolved enantiopure closed DAE (S, S-closed) into an open isomer solution with 1 : 1 of *P*- and *M*- racemic gelator mixtures, the open isomers would be induced to major *M*-form during gelation. Moreover, the

induced and amplified chirality are fixed to DAE molecule as well under UV light (Figure 1.8).

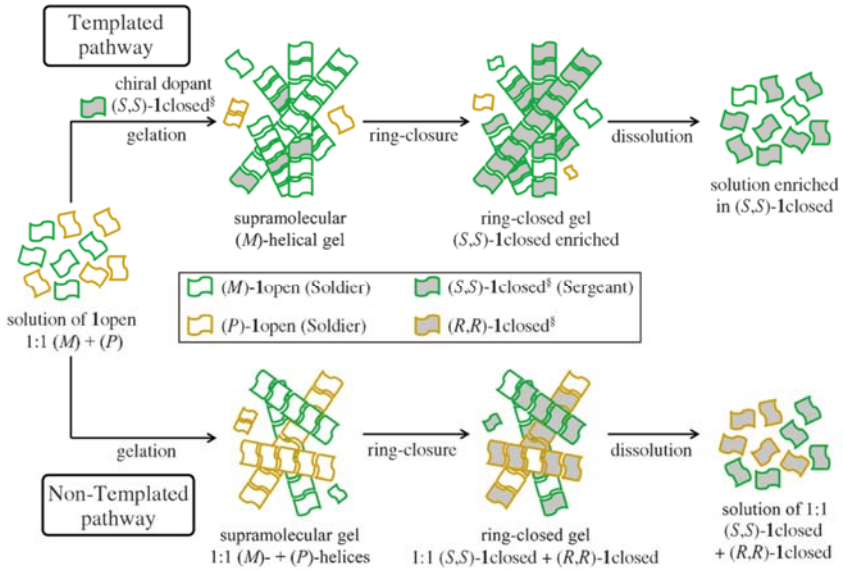

Figure 1.8 Sergeant-solider strategy for chirality auto-amplification with DAE gels. Copyright © 2014 Wiley-VCH Verlag GmbH & Co.

Another example showing chirality amplification was reported by Zhu *et al*.[18] they linked an α-chiral amino acid modified naphthalimide to the DAE core as chiral gelator. Self-assemble of open form isomer through hydrogen bonding, a helix gel is formed. When transformed flexible open isomers to rigid closed ones, however, the self-assembled helical nanostructures are broken, dissociated into an amorphous state (Figure 1.9).

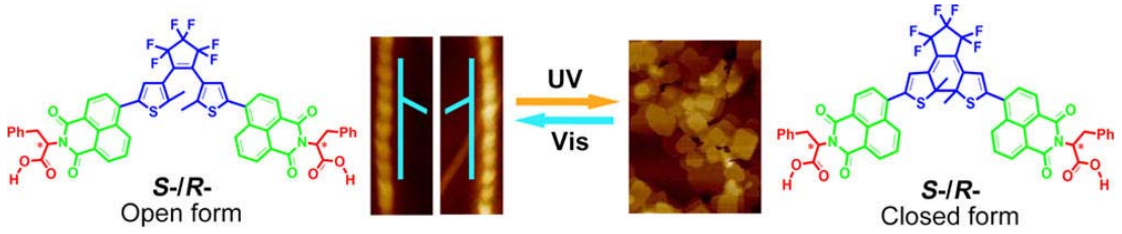

Figure 1.9 The reversible morphological switch of the chiral DAE assemblies induced by light and hydrogen-bonding self-assembly. Copyright © 2016 American Chemical Society.

As discussed before, the interconversion between *P*- and *M*-helix is very fast. As a result, it is difficult to enrich one of the enantiomers especially in solution. However, if the DAE molecule is crystallized in chiral, where their thiophene rings rotation were restricted, the chiral resolution becomes easier. Pioneer work has been developed by Irie etc. In a seminal contribution, Irie and coworkers synthesized a naphthyl groups modified DAE molecule which crystallized in chiral when co-crystallized with octafluoronaphthalene (Np^F).[15c] Therefore, the molecule underwent highly enantioselective photocyclization

owing to the conformational confinement in the crystal although both molecules are achiral (Figure 1.10).

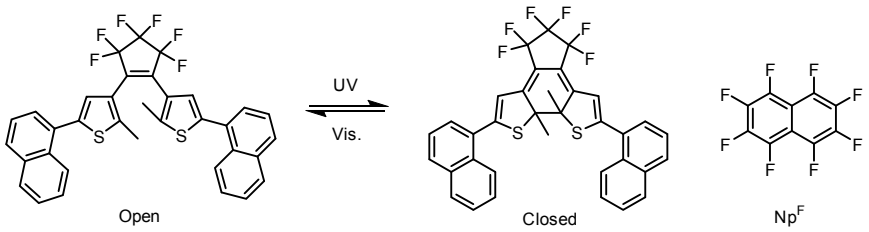

Figure 1.10 The reversible switch of DAE containing two naphthyl groups and octafluoronaphthalene (Np^F).

1.3 Electron and energy transfer

During the ring-closing reaction, not only the structures of DAEs were switched from flexible open form to their rigid closed form isomers. Meanwhile, the π-conjugation are also extended, thus, resulting in switchable properties related to their electronic structures such as absorbance, fluorescence, magnetic and *etc.*[19] (Figure 1.11).

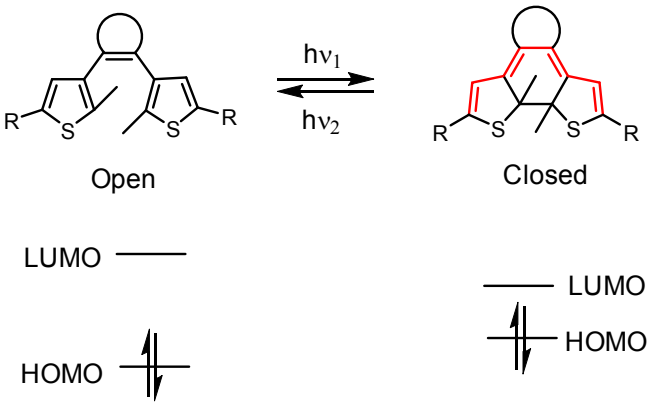

Figure 1.11 Reversible electronic changes on DAE molecules.

1.3.1 Color change

The first sight and promising phenomenon is a color change, which can be observed with naked eyes directly. In the open isomer, π-conjugation is mainly located in each of the thiophene rings, therefore, UV-vis spectrum is similar to that of thiophene in UV area, which makes the open isomer colorless. However, the π-conjugation is expanded and distributed throughout the molecule in their closed form. As a consequence, a new absorbance in long wavelength of the spectrum comes out due to the smaller HOMO-LUMO gap after photo-cyclization (Figure 1.11). The color of DAE compounds are switched from colorless to colored in their closed from. On the contrary, the deep colored DAEs fade back to colorless through ring-opening reaction with visible light irradiation (Figure 1.12).

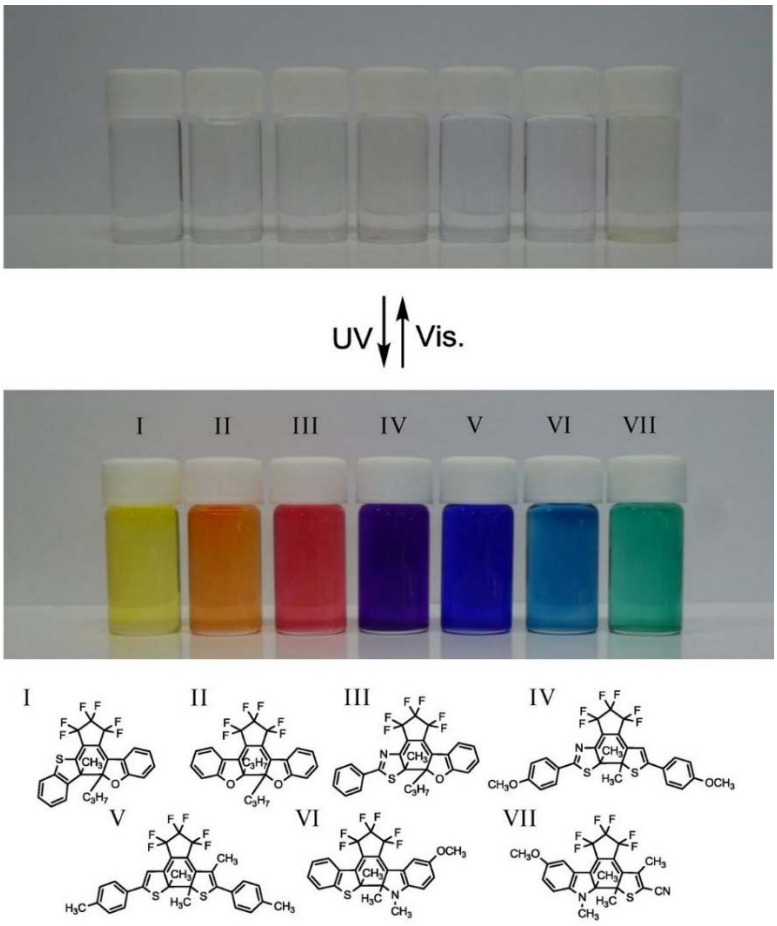

Figure 1.12 Color change of DAE compounds. Copyright © 2016 American Chemical Society.

1.3.2 Fluorescence

As described above that ring-opening and closing reaction of diarylethenes will result in a color change. Similarly, the electronic change will influence their fluorescence properties as well. Since most diarylethenes are non-fluorescent for both isomers, combining photochromic DAEs and fluorescent chromophores in a molecule or expanding π-conjugation of DAEs makes photoswitchable fluorescent dyes possible, which shows potential application as optical memory materials.

Irie *et al*. designed a series of sulfone derived DAEs molecules, exhibiting “turn-on” fluorescence switches[20] (Figure 1.13). In general, most of the DAE derivatives are fluorescent in their open isomer. Upon UV irradiation, the fluorescence quenches. However, in this case, sulfone derived DAEs initially exhibits non-luminescence in open form. Under UV light irradiation, they were activated to luminescence isomers. Both isomers exhibit brilliant and fatigue resistant fluorescence upon irradiation with 488 or 532 nm light, showing potential application in PALM (photoactivated localization microscopy) or STORM (stochastic optical reconstruction microscopy), as well as

RESOLFT (reversible saturable optical fluorescence transition), superresolution bioimaging.

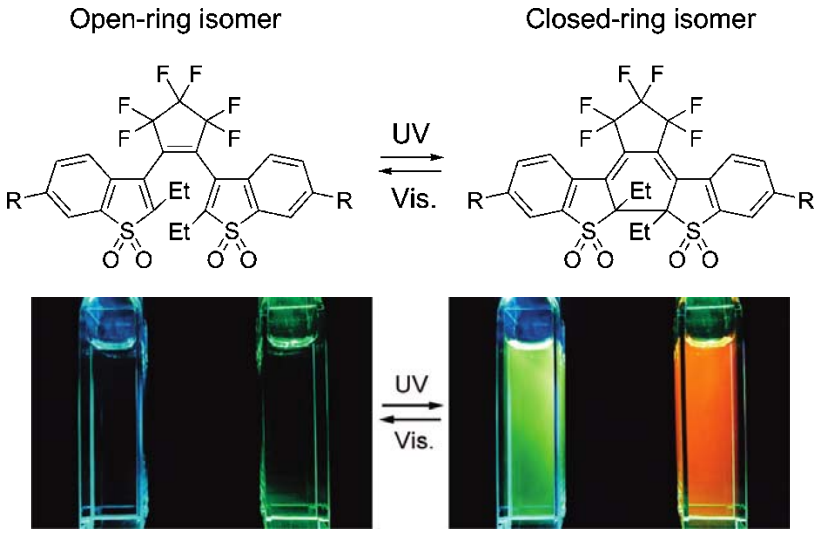

Figure 1.13 Photoactivatable fluorescent of DAE compounds. Copyright © 2011 American Chemical Society.

Besides the fluorescence "on-off" of the DAEs molecules themselves, they also affected luminescence behavior of other molecule through disturbing their energy transfer pathway due to the different HOMO-LUMO gap of DAEs. Shustova and coworkers synthesized a 3D metal-organic framework (MOF) Zn(ZnTCPP)-DAE combining a 2D sheet Zn(ZnTCPP) and pyridyl modified DAE pillar spacer ligand together[21] (Figure 1.14). Zn(ZnTCPP)-DAE in its open form shows promising emission at λ_{max} = 590 nm based on Zn(ZnTCPP). After irradiation of the Zn(ZnTCPP)-DAE under UV light, however, the fluorescence was quenched, showing "turn-off" state. That is because the energy of exited [Zn(ZnTCPP)]* could not be transfered to open DAE but to closed isomer due to its lower energy barrier (Figure 1.14).

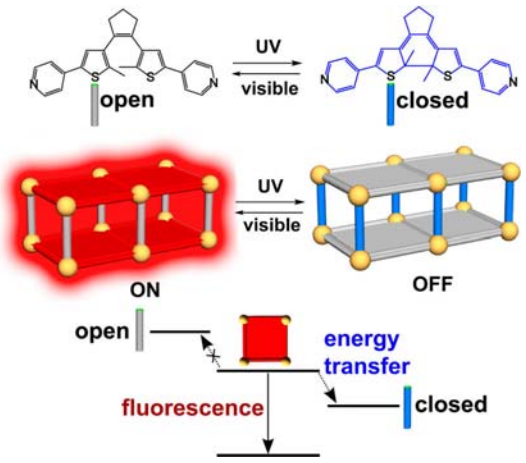

Figure 1.14 Diaryethene-porphyrin based MOF showing on-off fluorescence. Copyright © 2014 American Chemical Society.

Similarly, Zhou *et al*. constructed a 3D MOF from Zn(ZnTCPP) and DAE as well[22] (Figure 1.15). Using same energy transfer scheme, the energy passed to closed DAE when ZnTCPP was activated to [Zn(ZnTCPP)]*. However, the pathway to open form are forbidden but transferred to $^3O_2$, producing singlet $^1O_2$. Benefited from the properties of photochromic DAEs, the MOF showed reversible control of $^1O_2$ generation, meanwhile, showed photo-catalytic activity.

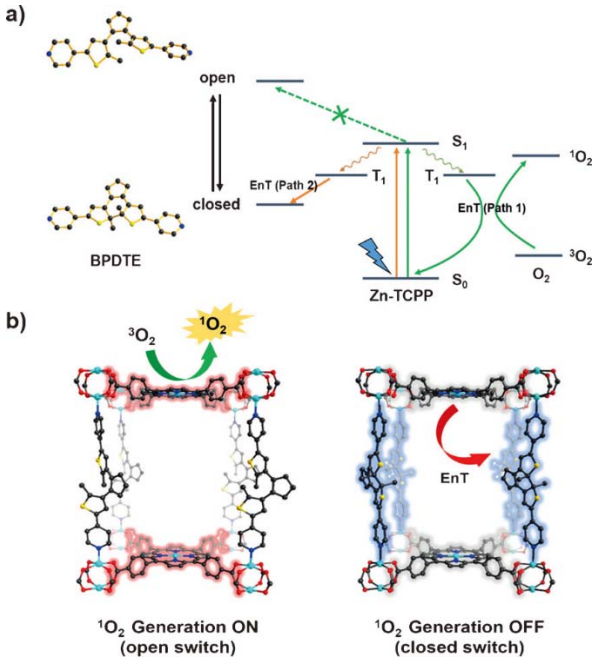

Figure 1.15 (a) Mechanism for photo-regulation of $^1O_2$ production by diarylethene-porphyrin; (b) diaryethene-porphyrin based MOF for photoswitchable $^1O_2$ production. Copyright © 2015 Wiley-VCH Verlag GmbH & Co.

1.3.3 **Magnetic switch**

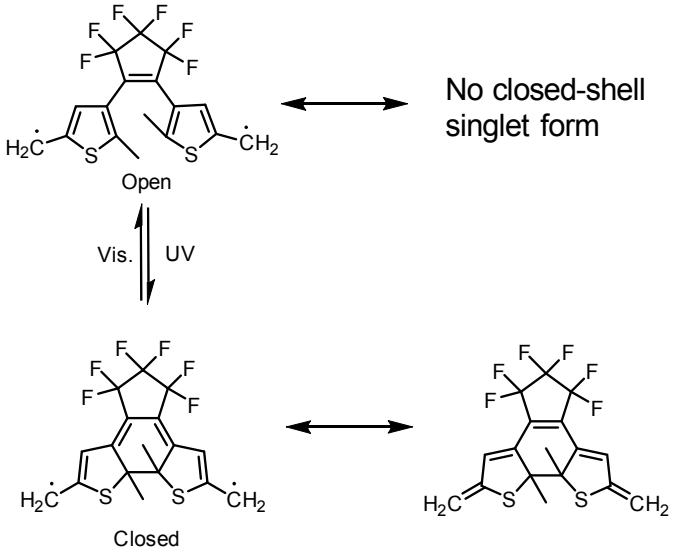

Figure 1.16 Resonance structure of the open- and closed-ring isomers of a DAE diradical. Copyright © 2000 American Chemical Society.

Figure 1.16 shows the electronic structure changes related to photoswitching of the intramolecule magnetic interaction.[23] In the open form DAE, electron was disconnected but distributed on thiophene rings. There have two unpaired electrons, showing no closed-shell singlet form. While, in closed form DAE, the resonant quinoid-type (Figure 1.16, right) exhibited closed-shell structure for closed DAE. In other word, the ring-open was expected small even no antiferromagnetic interaction, while ring-closed isomer would be strong.

On the basis of this principle, Irie and coworkers demonstrated a series photoswitching of magnetic interaction DAE compounds. For example, they synthesized DAEs with 2,5-bis(arylethynyl)-4-methyl-3-thienyl side group[24] (Figure 1.17). In ESR spectrum (originating from the change of the magnetic interaction between two unpaired the open DAE showed stronger exchange interaction than that of closed isomer, showing switchable magnetic interaction due to the change of the hybrid orbital and electronic structures.

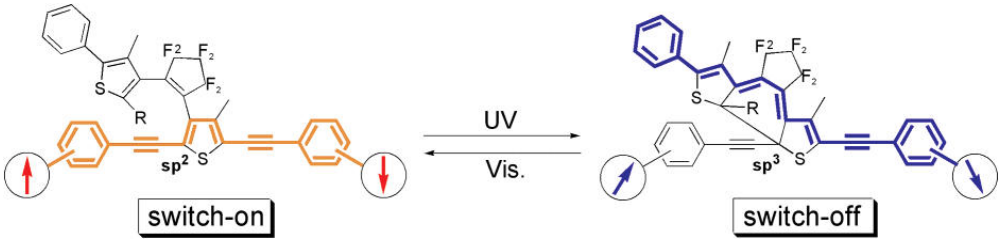

Figure 1.17 Photoswitching of the intramolecule magnetic interaction of diarylethene. Copyright © 2005 American Chemical Society.

Miyasaka *et al*. achieved reversible photoswitching of magnetic properties by connecting a single molecule magnet (SMM) of mixed valence tetranuclear $[Mn^{II}_2Mn^{III}_2]$ complex with DAE linker.[25] In its open form, the complex showed a drastic change in magnetic properties compared with $[Mn^{II}_2Mn^{III}_2]$, however, there is no significant change from closed isomer. Further, Yamashita and coworker bridged two manganese salen complexes using a DAE linker[26] (Figure 1.18). With visible light irradiation, a prominent changing was caused, therefore, activated their magnetic properties. On the other hand, the magnetic properties were switched off when irradiated under UV light. Which showed potential application as molecule memory devices composed of SMM.

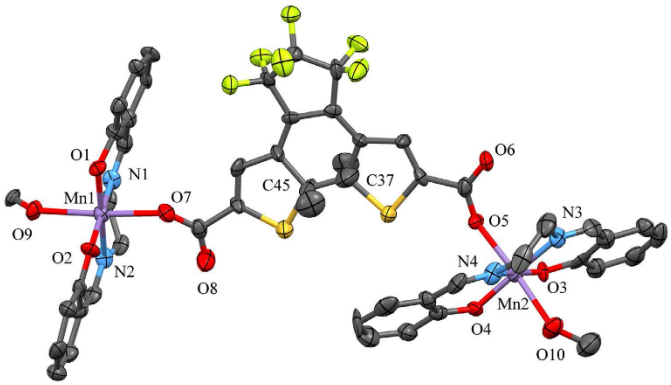

Figure 1.18 Photoschromic diarylethene ligand linked two manganese salen complexes. Copyright © 2016 Nature Publishing Group.

1.4 References

[1] (a) J. C. Crano, R. Guglielmetti, *Organic Photochromic and Thermochromic Compounds*, *Vol. 2*: Plenum Press, New York, **1999**; (b) J. C. Crano, R. Guglielmetti, *Organic Photochromic and Thermochromic Compounds*, *Vol. 1*: Plenum Press, New York, **1999**; (c) H. Tian, J. Zhang, Wiley-VCH: Weinheim, Germany, **2016**.

[2] D. H. Waldeck, *Chem. Rev*. **1991**, *91*, 415−436.

[3] H. Rau, R. Lvddecke, *J. Am.Chem. Soc*. **1982**, *6*, 1616−1620.

[4] N. Y. C. Chu, *Can. J. Chem*. **1983**, *61*, 300−305.

[5] M. Irie, T. Fukaminato, K. Matsuda, S. Kobatake, *Chem Rev* **2014**, *114*, 12174−12277.

[6] R. M. Kellogg, M. B. Groen, *J. Org. Chem*. **1967**, *32*, 3093−3100.

[7] M. Irie, M. Mohri, *J. Org. Chem*. **1988**, *53*, 803−808.

[8] M. X. Han, R. Michel, B. He, Y. S. Chen, D. Stalke, M. John, G. H. Clever, *Angew. Chem. Int. Ed.* **2013**, *52*, 1319−1323.

[9] M. X. Han, Y. S. Luo, B. Damaschke, L. Gomez, X. Ribas, A. Jose, P. Peretzki, M. Seibt, G. H. Clever, *Angew. Chem. Int. Ed.* **2016**, *55*, 445−449.

[10] Y. Gu, E. A. Alt, H. Wang, X. Li, A. P. Willard, J. A. Johnson, *Nature* **2018**, *560*, 65−69

[11] (a) Themed issue: Metal-organic frameworks, *Chem. Soc. Rev.*, ed. J. R. Long and O. M. Yaghi, **2009**, *vol. 38*, pp. 1201−1508; (b) Special Issue: 2012 Metal-Organic Frameworks, *Chem. Rev.*, ed. H.-C. Zhou, J. R. Long and O. M. Yaghi, **2012**, *vol. 112*, pp. 673−1268; (c) H. Furukawa, K. E.Cordova, M. O'Keeffe and O. M. Yaghi, Science, 2013, 341, 1230444; (d) Special Issue: 2014 Metal-Organic Frameworks, *Chem. Soc. Rev.*, ed. H.-C. Zhou, S. Kitagawa, **2014**, *vol. 43*, pp. 5415−6172;. (e) Special Issue: 2017 Metal-Organic Frameworks and

Porous Polymer-current and future chanllenges, *Chem. Soc. Rev.*, ed. G. Maurin, C. Serre, A. Cooper and G. Férey, **2017**, *vol. 46*, pp. 3104−3480;

[12] B. J. Furlong, M. J. Katz, *J. Am. Chem. Soc.* **2017**, *139*,.13280−13283.

[13] (a) T. Yamaguchi, K. Uchida and M. Irie, *J. Am. Chem. Soc*. **1997**, *119*, 6066−6071; (b) T. Shiozawa, M. K. Hossain, T. Ubukata, Y. Yokoyama, *Chem Commun* **2010**, *46*, 4785−4787.

[14] (a) E. Murguly, T. B. Norsten and N. R. Branda, *Angew.Chem. Int. Ed*. **2001**, *40*, 1752−1755; (b) T. C. Pace, V. Muller, S. Li, P. Lincoln, J. Andreasson, *Angew Chem Int Ed.* **2013**, *52*, 4393−4396; (c) M. Fukagawa, I. Kawamura, T. Ubukata, Y. Yokoyama, *Chem. Eur. J.* **2013**, *19*, 9434−9437; (d) K. Kawamura, K. Osawa, Y. Watanobe, Y. Saeki, N. Maruyama, Y. Yokoyama, *Chem. Commun.* **2017**, *53*, 3181−3184.

[15] (a) T. Kodani, K. Matsuda, T. Yamada, S. Kobatake and M. Irie, *J. Am. Chem. Soc.* **2000**, *122*, 9631−9637; (b) S. Yamamoto, K. Matsuda, M. Irie, *Angew. Chem. Int. Ed.* **2003**, *42*, 1636−1639; (c) M. Morimoto, S. Kobatake, M. Irie, *Chem. Commun.* **2008**, 335−337.

[16] J. J. D. de Jong, L. N. Lucas, R. M. Kellogg, J. H. van Esch, B. L. Feringa, *Science* **2004**, *304*, 278−281.

[17] D. J. van Dijken, J. M. Beierle, M. C. Stuart, W. Szymanski, W. R. Browne, B. L. Feringa, *Angew. Chem. Int. Ed.* **2014**, *53*, 5073−5077.

[18] Y. Cai, Z. Guo, J. Chen, W. Li, L. Zhong, Y. Gao, L. Jiang, L. Chi, H. Tian, W. H. Zhu, *J Am Chem Soc* **2016**, *138*, 2219−2224.

[19] K. Matsuda, M. Irie, *J. Photochem. Photobiol. C,* **2004**, *5*, 169−182; (b) C. Yun, J. You, J. Kim, J. Huh, E. Kim, *J. Photochem. Photobiol. C,* **2009**, *10*, 111−129; (c) T. Tsujioka, M. Irie, *J. Photochem. Photobiol. C,* **2010**, *11*, 1−14; (d) T. Fukaminato, *J. Photochem. Photobiol. C,* **2011**, *12*, 177−208; (e) M. M. Russew, S. Hecht, *Adv. Mater.* **2010**, *22*, 3348−3360; (f) A. Fihey, A. Perrier, W. R. Browne, D. Jacquemin, *Chem. Soc. Rev.* **2015**, *44*, 3719−3759; (g) H. Tian, S. Yang, *Chem. Soc. Rev.* **2004**, *33*, 85−97; (h) F. M. Raymo, M. Tomasulo, *Chem. Soc. Rev.* **2005**, *34*, 327−336; (i) D. Bleger, S. Hecht, *Angew. Chem. Int. Ed.* **2015**, *54*, 11338−11349; (j) M. Irie, *Chem. Rev*. **2000**, *100*, 1685-1716; (k) J. Zhang, Q. Zou, H. Tian, *Adv. Mater.* **2013**, *25*, 378−399.

[20] K. Uno, H. Niikura, M. Morimoto, Y. Ishibashi, H. Miyasaka, M. Irie, *J. Am. Chem. Soc.* **2011**, *133*, 13558−13564.

[21] D. E. Williams, J. A. Rietman, J. M. Maier, R. Tan, A. B. Greytak, M. D. Smith, J. A. Krause, N. B. Shustova, *J. Am. Chem. Soc.* **2014**, *136*, 11886−11889.

[22] J. Park, D. Feng, S. Yuan, H. C. Zhou, *Angew. Chem. Int. Ed.* **2015**, *54*, 430-435.

[23] K. Matsuda, M. Irie, *J. Am. Chem. Soc*. **2000**, *122*, 7195−7201.

[24] N. Tanifuji, M. Irie. and K. Matsuda, *J. Am. Chem. Soc*. **2005**, *127*, 13344−13353.

[25] M. Morimoto, H. Miyasaka, M. Yamashita, and M. Irie, *J. Am. Chem. Soc*. **2009**, *131*, 9823−9835.

[26] A. Fetoh, G. Cosquer, M. Morimoto, M. Irie, O. El-Gammal, G. Abu El-Reash, B. K. Breedlove, M. Yamashita, *Sci. Rep.* **2016**, *6*, 23785.

2 Objectives

In supramolecular chemistry, the self-assembly of banana-shaped bis-monodentate ligands and square-planar Pd^{II} and Pt^{II} cations has proven to be a very effective method to form discrete coordination cages.[1] Over the past decades, the pool of supramolecular coordination architectures has been rapidly growing through rational ligand design.[2] Recent studies show that the field of nano-sized cages tends to move away from monotonous structures towards functions.[3] Most of the examples, however, only one type of ligand is contained, each as the key component of their overall function, which limits them in multifunctional applications. Therefore, controlled formation of heteroleptic cages, assembled from more than one ligand, provides a platform for expanding the degree of functionalities. Diarylethenes (DAEs), as an elegant light-switchable group,[4] show efficiently photo-controlled switching both in structural and electronic properties (Chapter 1) and can be used as backbone to synthesize banana-shaped ligands.[5] In this thesis, the aim was to focus on the evolution of supramolecular photochromic homo- and hetero-leptic cages based on DAE ligands, investigation of host-guest chemistry as well as light-controlled application in chirality transfer and singlet oxygen generation.

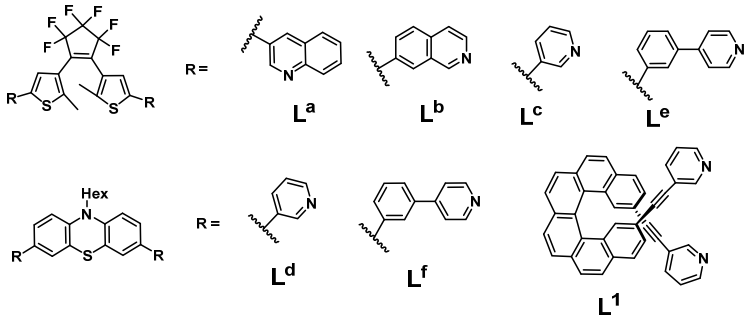

Figure 2.1 Aimed ligand structures.

Integrative self-sorting of $Pd_2L^A{}_2L^B{}_2$ heteroleptic cages based on 'naked' Pd^{II} cation and two different banana-shaped bispyridyl ligands has been achieved by the research groups of Clever,[6] Yoshizawa[7] and Crowley[8]. However, the selective formation of $Pd_2L^A{}_3L^B$ assemblies remains a challenge. Up to date, only one example, consisting in a 3:1 mixture of $Pd_2L^A{}_3L^B$ and $Pd_2L^A{}_4$, is reported by Hooley and coworkers, obtained by means of ligand interaction approach[9]. Another strategy relies on the introduction of steric hindrance in the donor site of the ligand, allowing to assemble bowl-shaped $Pd_2L^A{}_3$ compounds with two 'active' coordination sites. This opens the possibility to introduce a second less-sterically demonstrating ligand L^B leading to the formation of $Pd_2L^A{}_3L^B$ heteroleptic cages.

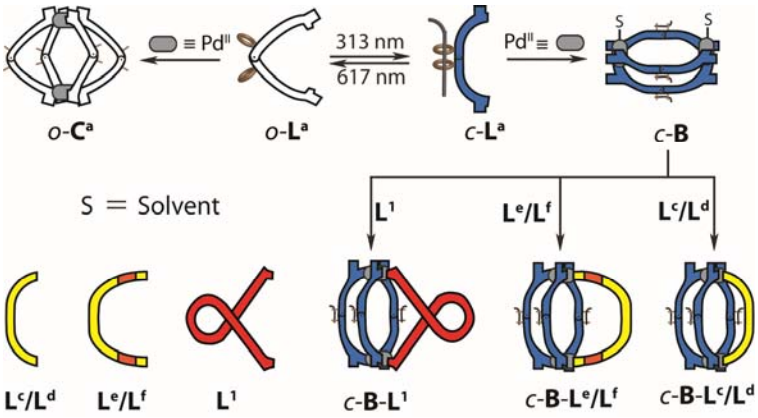

Figure 2.2 Schematic model of target $Pd_2L^A{}_3L^B$ heteroleptic cages.

Inspired by the successful formation of bowl compounds by the research groups of Clever[6d] and Gowda[10], the synthesis of a DAE-based ligand **L^a** with two quinolinyl donor groups is here reported (Figure 2.1). The important issues regarding to the target is, whether this approach will lead to the successfully assembly of $Pd_2L^A{}_3L^B$ heteroleptic cages (Figure 2.2). Besides, a series of ligands **L$^{c\text{-}f}$** (Figure 2.1) having a similar N-N distance as **L^a,** but different arm lenghts, are synthesized. These new ligands can be used to tune the cavity volume of the resulting heteroleptic assemblies. Host-guest titrations with a series of guests that differs in size and shape, give further evidence of the cavity expansion (Chapter 3). Moreover, by combining the bowl compound with an helicene-derivative ligand **L^1** (Figure 2.1), light-controlled chirality transfer in a heteroleptic cage is investigated (Chapter 4). In Chapter 5, the conversion from $Pd_2L^A{}_3L^B$ to $Pd_2L^A{}_2L^B{}_2$ cages is reported, showing that the self-assembly of a binary 1 : 1 mixture of ligands tend to give the thermodynamic product $Pd_2L^A{}_2L^B{}_2$.

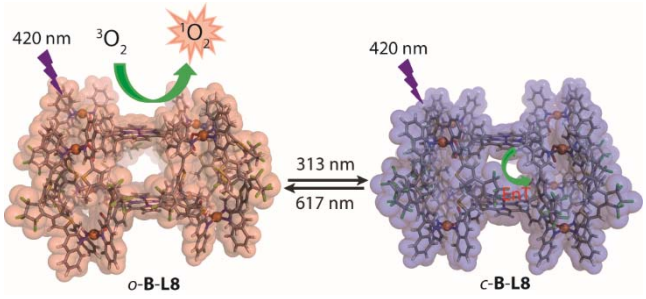

Figure 2.3 Light switchable supramolecular prism and controlled singlet oxygen generation.

In addition to that, is it possible to take advantage of the active coordination sites of the bowl compound and combine them with different linkers? Getting inspired by the design and construction of three dimension prisms reported by Stang,[11] Ribas[12] and *etc.*, another goal of this thesis is to build up Ferris-wheel like prism combining pre-assembled bowl-shaped compounds with di-, tri- and tetra-topic carboxylate linkers. Beside the structural role, when incorporate functional properties in the linkers, such as a

photosensitizer (zinc-tetra(4-carboxylatephenyl)porphyrin) (Figure 2.3), light-controlled singlet oxygen generation will be expected due to the triplet energy difference between the open and closed state of the DAE moiety (Chapter 6).

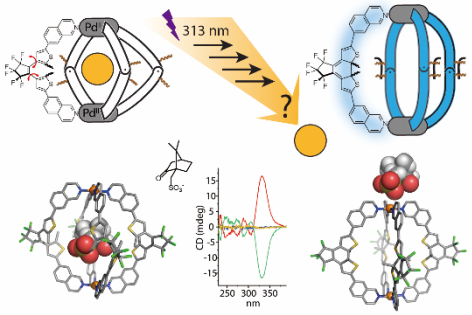

Figure 2.4 Proposed mechanistic of photoswitch and guest release. Copyright © 2019 The American Chemical Society.

Finally, the simultaneous presence of more DAE photoswitches in the same supramolecular compound, left some open mechanistic questions. Previously, the research group of Clever has reported DAE-based coordination cages and demonstrated the light-trigged guest uptake and release.[5b] We found the entropy was the key driven force. However, the process involves four consecutive photocyclization reactions to convert all ligands between their open and closed photoisomeric forms, the mechanistic details concerning the intermediate steps was still unclear. In order to clarify this, a chiral guest was used instead. Using intrinsic chirality of DAE backbones as a reporter (Figure 2.4), in the last chapter (Chapter 7), the relationship between photoisomerization steps and guest inside/outside the cavity by guest-to-host chirality transfer is investigated.

References

[1] (a) M. Frank, M. D. Johnstone, G. H. Clever, *Chem. Eur. J.* **2016**, *22*, 14104-14125; (b) M. Han, D. M. Engelhard, G. H. Clever, *Chem. Soc. Rev.* **2014**, *43*, 1848-1860; (c) S. Saha, I. Regeni, G. H. Clever, *Coord. Chem. Rev.* **2018**, *374*, 1-14.

[2] (a) R. Chakrabarty, P. S. Mukherjee, P. J. Stang, *Chem. Rev.* **2011**, *111*, 6810-6918; (b) T. R. Cook, P. J. Stang, *Chem. Rev.* **2015**, *115*, 7001-7045.

[3] Theme issure: Supramolecular and dynamic covalent reactivity, Ed. J. Nitschke, *Chem. Soc. Rev.* **2014**, *38*, 1788-1996; (b) Theme collection: Molecular containers, Ed. P. Ballester, M. Fujita and J. Rebek, *Chem. Soc. Rev.* **2015**, *44*, 392; (c) Special issure: Supramolecular chemistry in confined space and organized assemblies, Ed. V. Yam, M. Fujita and D. Toste, *Acc. Chem. Res. 51*, 1324; (d) L. J. Chen, H. B. Yang, M. Shionoya, *Chem. Soc. Rev.* **2017**, *46*,

2555-2576; (e) D. A. Roberts, B. S. Pilgrim, J. R. Nitschke, *Chem. Soc. Rev. 47*, 626-644; (f) M. M. Smulders, I. A. Riddell, C. Browne, J. R. Nitschke, *Chem. Soc. Rev.* **2013**, *42*, 1728-1754; (g) S. Zarra, D. M. Wood, D. A. Roberts, J. R. Nitschke, *Chem. Soc. Rev.* **2015**, *44*, 419-432.

[4] M. Irie, T. Fukaminato, K. Matsuda, S. Kobatake, *Chem. Rev.* **2014**, *114*, 12174-12277.

[5] (a) M. Han, Y. Luo, B. Damaschke, L. Gomez, X. Ribas, A. Jose, P. Peretzki, M. Seibt, G. H. Clever, *Angew. Chem. Int. Ed.* **2016**, *55*, 445-449; (b) M. Han, R. Michel, B. He, Y. S. Chen, D. Stalke, M. John, G. H. Clever, *Angew. Chem. Int. Ed.* **2013**, *52*, 1319-1323.

[6] (a) W. M. Bloch, Y. Abe, J. J. Holstein, C. M. Wandtke, B. Dittrich, G. H. Clever, *J. Am. Chem. Soc.* **2016**, *138*, 13750-13755; (b) W. M. Bloch, J. J. Holstein, H. Wolf, G. H. Clever, *Angew. Chem. Int. Ed.* **2017**, *56*, 8285-8289; (c) S. Saha, B. Holzapfel, Y. T. Chen, K. Terlinden, P. Lill, C. Gatsogiannis, H. Rehage, G. H. Clever, *J. Am. Chem. Soc.* **2018**; (d) R. Zhu, W. M. Bloch, J. J. Holstein, S. Mandal, L. V. Schafer, G. H. Clever, *Chem. Eur. J.* **2018**, *24*, 12976-12982.

[7] M. Yamashina, T. Yuki, Y. Sei, M. Akita, M. Yoshizawa, *Chem. Eur. J.* **2015**, *21*, 4200-4204.

[8] D. Preston, J. E. Barnsley, K. C. Gordon, J. D. Crowley, *J. Am. Chem. Soc.* **2016**, *138*, 10578-10585.

[9] A. M. Johnson, R. J. Hooley, *Inorg. Chem.* **2011**, *50*, 4671-4673.

[10] Shivakumaraiah, N. M. N. Gowda, *J. Chem. Res.* **2005**, *2005*, 505-507.

[11] (a) X. Yan, T. R. Cook, P. Wang, F. Huang, P. J. Stang, *Nat. Chem.* **2015**, *7*, 342-348; (b) X. Yan, M. Wang, T. R. Cook, M. Zhang, M. L. Saha, Z. Zhou, X. Li, F. Huang, P. J. Stang, *J. Am. Chem. Soc.* **2016**, *138*, 4580-4588; (c) Y. Ye, T. R. Cook, S. P. Wang, J. Wu, S. Li, P. J. Stang, *J. Am. Chem. Soc.* **2015**, *137*, 11896-11899; (d) Z. Zhou, X. Yan, M. L. Saha, M. Zhang, M. Wang, X. Li, P. J. Stang, *J. Am. Chem. Soc.* **2016**, *138*, 13131-13134; (e) X. Chang, Z. Zhou, C. Shang, G. Wang, Z. Wang, Y. Qi, Z. Y. Li, H. Wang, L. Cao, X. Li, Y. Fang, P. J. Stang, *J. Am. Chem. Soc.* **2019**, *141*, 1757-1765.

[12] (a) C. Colomban, C. Fuertes-Espinosa, S. Goeb, M. Salle, M. Costas, L. Blancafort, X. Ribas, *Chem. Eur. J.* **2018**, *24*, 4371-4381; (b) C. Garcia-Simon, M. Garcia-Borras, L. Gomez, T. Parella, S. Osuna, J. Juanhuix, I. Imaz, D. Maspoch, M. Costas, X. Ribas, *Nat. Commun.* **2014**, *5*, 5557.

3 Multi-Stimuli Gating Between Supramolecular Cage and Basket

3.1 Introduction

Since Cram pioneered the synthesis of container molecules in 1980s,[1] supramolecular container as an important hosts have received tremendous attention[2] due to its application in host-guest chemistry,[3] molecule recognition,[4] and drug delivery[5] as well as confined space catalysis.[6] According to the type of their cavities, supramolecular containers could be divided into enfold and unfold. Enfold containers with isolated discrete cavities (e.g. cages, capsules) could take up suitable guests matching well with the size of the cavity of the host, thus protecting the guest and resulting in stronger binding affinity. To encapsulate larger guests, the general approach requires an expansion of the building unit such as prolonging ligand length (Figure 3.1).[7] While unfold containers (such as bowls or barrels) are expected to bind guest molecules of various sizes, even binding larger guest molecules which sizes exceeding the host capacities.

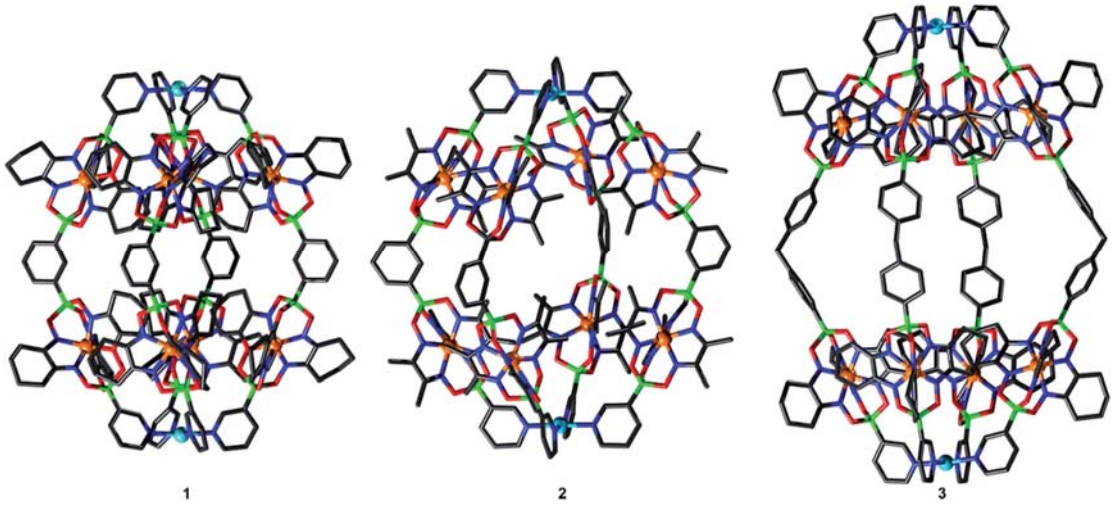

Figure 3.1 Molecule structures of cages 1 (left), 2 (middle), and 3 (right), as determined by single crystal X-ray diffraction. Hydrogen atoms, solvent molecules and anions are omitted for clarity. Gray: C; dark blue: N; green: B; red: O; light blue: Pd and orange: Fe. Copyright © 2017 Royal Society of Chemistry.

Up to now, attention has been paid to stimuli-response supramolecular gated containers.[8] Reversible switching between enfold and unfold containers triggered by external stimuli (e.g. light, heat, pH) controls the uptake and release of molecule cargo[8e] (Figure 3.2) with potential application in drug delivery and catalysis. Coordination-driven self-assembled containers,[8c] with their robust structures, would easily undergo gating (here disassembly/reassembled) under external stimuli due to their weaker coordination bonds and coordination diversities. Recently, Severin and co-worker used light with a metastable-state photoacid (PAH) guest to reverse the disassembled supramolecular

containers.[9] By adding/removing competing ligands, Crowley and co-worker controlled the release of the anticancer drug *cis*-platin. However, both of the examples showed the complete disassembly of the coordination containers to release their cargo.[10] Previously, we reported a light controlled interconversion between a self-assembled triangle and a rhombicuboctahedral sphere based on dithienylethene (DTE) ligands.[11] Also, using a similar DTE backbone with longer pyridin-3-ylethynyl donors, we presented light-switchable $[Pd_2\mathbf{L}_4]$ coordination cage isomers with different inner cavities resulting in the reversible uptake and release of $[B_{12}F_{12}]^{2-}$ guest owing to the nature of photochromic DTE ligands.[12]

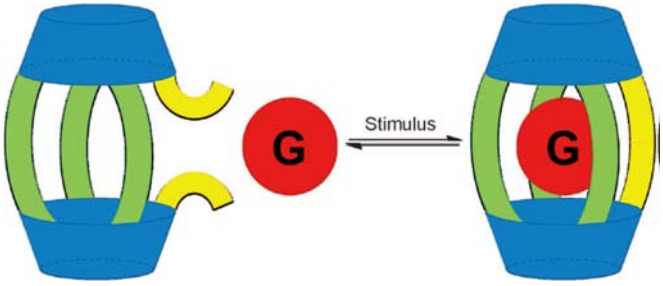

Figure 3.2 Gating in container molecules converts a hemicarcerand (left) into a carcerand (right) through stimulus. Copyright © 2013 Wiley-VCH Verlag GmbH & Co.

In this chapter, new bulky quinolin-3-yl donors were introduced to the DTE backbone. Thus, we synthesized $[Pd_2(o\text{-}\mathbf{L}^{\mathbf{a}})_4](BF_4)_4$ cage and concave bowl $[Pd_2(c\text{-}\mathbf{L}^{\mathbf{a}})_3](BF_4)_4$ from unprotected Pd^{II} cations and open and closed ligands, respectively (Figure 3.3). The bowl compound with two 'active' metal sites is stable in CD_3CN solution due to the sterically demanding quinoline group, the rigid DTE conformation as well as solution environment. The reversible photochemical gating is demonstrated between the cage and bowl with or without guests. Moreover, combining the bowl $[Pd_2(c\text{-}\mathbf{L}^{\mathbf{a}})_3](BF_4)_4$ with additional ligands, firstly result in the formation of pure $Pd_2L^A{}_3L^B$ type heteroleptic cages with different inner cavity sizes. The ligand L^B can be removed/re-coordinated upon adding/removing Br^- anion, which shows reversible release/re-encapsulation of guest.

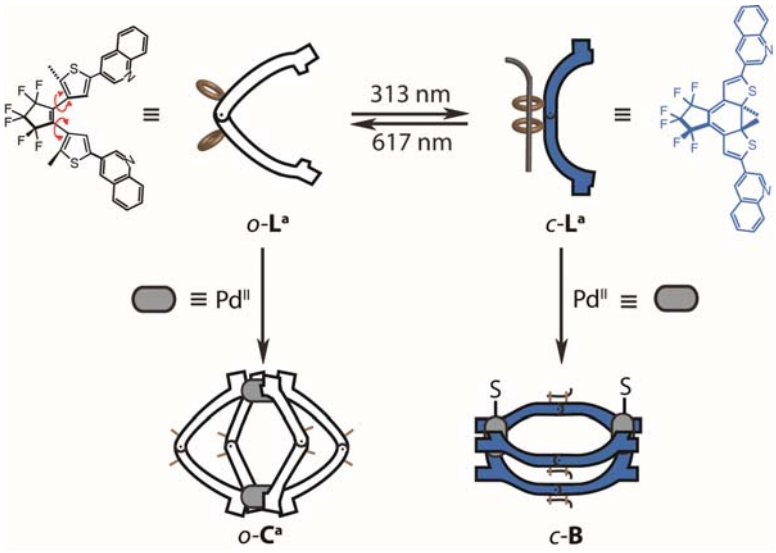

Figure 3.3 (Top) the conformationally flexible open-form ligand *o*-**L**^{a} based on a dithienylethene (DTE) photo switch is converted into its rigid closed-ring isomer *c*-**L**^{a} upon irradiation at 313 nm. The process can be fully reversed by irradiation with 617 nm light. (Down) Addition of stoichiometric amounts of Pd^{II} leads to quantitative formation of coordination cages *o*-**C**^{a} and bowl *c*-**B**.

3.2 Ligand synthesis and cage assembly

Following our previously reported protocols,[11] ligand *o*-**L**^{a} was synthesized by a Suzuki cross-coupling reaction of perfluoro-1,2-bis(2-iodo-5-methylthien-4-yl)cyclopentene and 2 eq. of quinolin-3-ylboronic acid. The cage compounds $[Pd_2(o\text{-}\mathbf{L}^{a})_4](BF_4)_4$ (*o*-**C**^{a}) were formed by combining 2:1 mixture of *o*-**L**^{a} with $[Pd(CH_3CN)_4](BF_4)_2$ in CD_3CN at 70 °C. The formation of the supramolecular compounds were confirmed by NMR spectroscopy, high-resolution ESI mass spectrometry (Figure 3.4a & c, Chapter 3.9.2.2.1) as well as single crystal X-ray diffraction (SCXRD) analysis (Figure 3.5a). Slow vapor diffusion of Et_2O into a CD_3CN solution of *o*-**C**^{a} resulted in the expected lantern cage structures, which crystallized in the tetragonal space group $P4_2$. Unlike our reported DTE-based cages,[12] the ligands in *o*-**C**^{a} are twisted in the same direction, released the crowded effect. As a result, *o*-**C**^{a} features a pair of *PPPP/MMMM* enantiomers arrangement of the DTE backbone in a crystal.

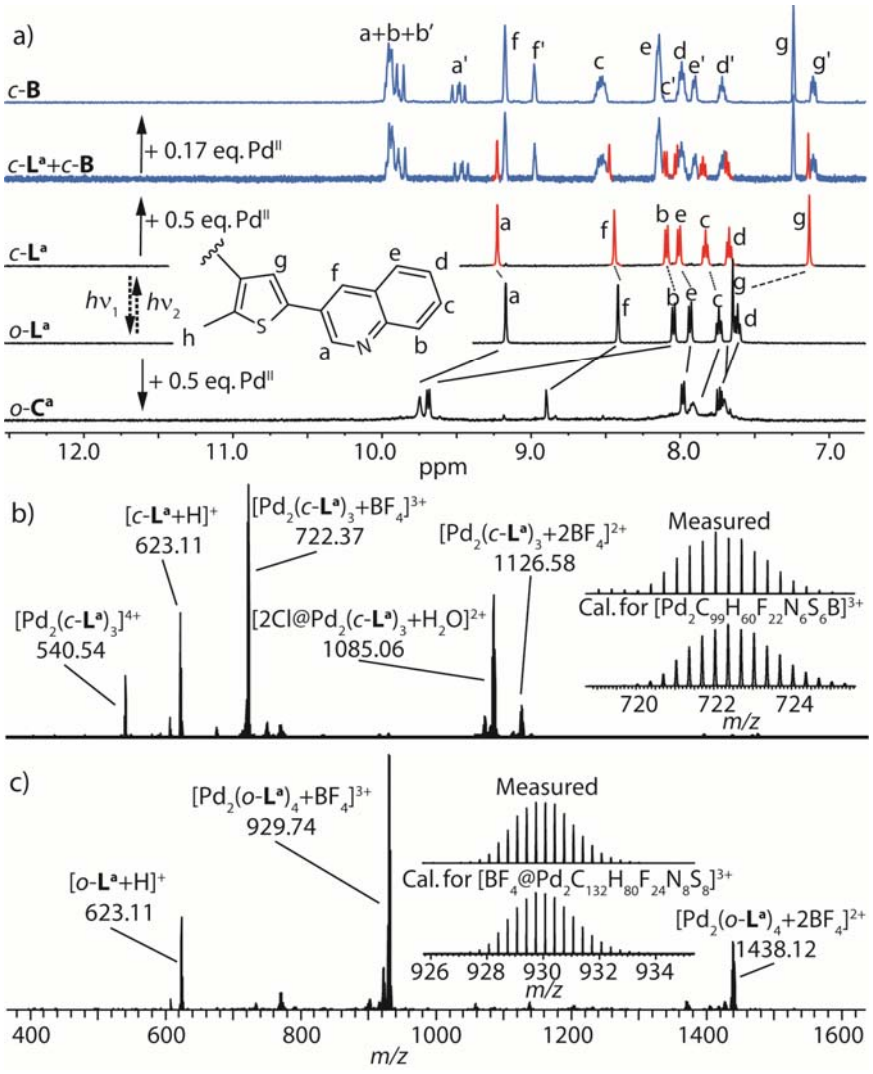

Figure 3.4 a) ^{1}H NMR spectra (500 MHz, CD_3CN, 298 K) of ligands *o*-**L^a**, *c*-**L^a**, open form cage *o*-**C^a** and closed form bowl *c*-**B**; ESI-MS spectra of c) *c*-**B** with isotope pattern of $[Pd_2(c\text{-}L^a)_3+BF_4]^{3+}$ shown in the inset and c) *o*-**C^a** with isotope pattern of $[Pd_2(o\text{-}L^a)_4+BF_4]^{3+}$ shown in the inset.

Next, the self-assembly properties of the photo-isomeric closed form ligand *c*-**L^a** was explored. Switching from *o*-**L^a** into *c*-**L^a** in CD_3CN solution proceeded with > 99% yield using 313 nm light of a 500 W mercury lamp. Subsequently, ligand *c*-**L^a** was heated in presence of 0.5 eq. $[Pd(CH_3CN)_4](BF_4)_2$ in CD_3CN for 2 h at 70 °C under exclusion of light. ^{1}H NMR spectroscopy showed that there was still 1/3 free ligands left even though prolonged heating time. After addition of 0.17 eq. $Pd^{II,}$ the free ligand was completely consumed, giving rather broad and complicated proton NMR signals (Figure 3.4a).

The ^{1}H NMR spectrum clearly gave two sets of clean signals in 2:1 ratio. ^{1}H DOSY NMR (298 K) spectrum showed that the two sets of ^{1}H NMR signals belongs to a single species (Figure 3.34). We cannot distinguish the proton signals of H_a, H_b and $H_{b'}$ due to the signal broadening and overlapping, however, their downfield shifting proved Pd^{II} complexation. ESI mass spectrum displayed a series of prominent peaks with a variable number of BF_4^- counter ions ($[Pd_2(c\text{-}L^a)_3]^{4+}$, $[Pd_2(c\text{-}L^a)_3+BF_4]^{3+}$ and $[Pd_2(c\text{-}L^a)_3+2BF_4]^{2+}$).

In all cases, experimental isotope patterns were found to be in agreement with the calculated distributions. Furthermore, the high intensity ESI mass peak of $[Pd_2(c\text{-}\mathbf{L^a})_3{+}2Cl{+}H_2O]^{2+}$ at 1085 m/z is presumably due to the contamination of Cl^- anions from the mass spectrometer, which occupy the two 'free' Pd^{II} coordination sites (Figure 3.4b). Therefore, the formation of bowl-shaped structure of $[Pd_2(c\text{-}\mathbf{L^a})_3(Solvent)_2](BF_4)_4$ (*c*-**B**) was unambiguously confirmed. Where the two ligands outside in the bowl have similar chemical environment, while the middle ligand is different. Which is consistent with the NMR spectrum showing signals in a 2:1 ratio. Since ligand *c*-$\mathbf{L^a}$ is racemic with C_2-symmetry, *c*-**B** would consist of all 6 diastereomers with four pairs of same chemical environments (Chapter 3.9.3). This could be clearly confirmed by the quadruple splitting, especially for protons $H_{a'}$ and $H_{g'}$ of the central ligand in *c*-**B** (Figure 3.4a). After resoluting of racemic ligands *c*-$\mathbf{L^a}$ by chiral HPLC, clearer and sharper ^{1}H NMR spectrum of optically assembly compound indeed confirmed the signal splitting of *c*-**B**. Afterward, each proton signal of the bowl could be clearly assigned with the help of ^{1}H-^{1}H COSY and ^{1}H-^{1}H NOESY NMR spectra (Figure 3.67 & Figure 3.68), further confirming the *c*-**B** formation in CD_3CN solution. Similarly, diffusion of Et_2O into *c*-**B** CD_3CN solution under strict exclusion of light gave a suitable crystal for SCXRD. However, the crystal structure showed the presence of the cage $[Pd_2(c\text{-}\mathbf{L^a})_4](BF_4)_4$ (*c*-$\mathbf{C^a}$) and not the expected *c*-**B** structure. Interestingly, all ligands *c*-$\mathbf{L^a}$ are straightly arranged without any twisting in the cage (Figure 3.5b).

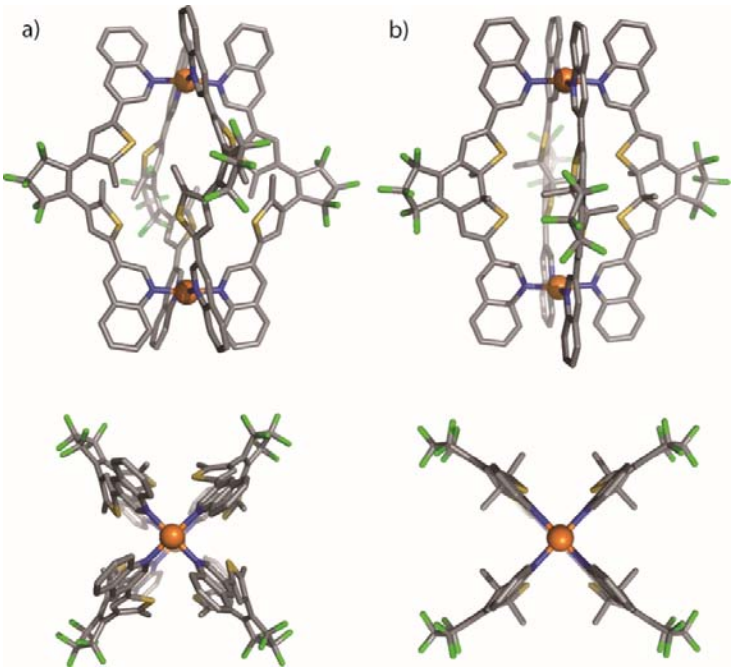

Figure 3.5 X-ray structures of a) cage *o*-$\mathbf{C^a}$ and b) *c*-$\mathbf{C^a}$ (side and top view). All hydrogen atoms, solvent molecules, counter anions and minor disordered components have been omitted. In *c*-$\mathbf{C^a}$, all backbone methyl groups are disordered over both possible positions with approximately 50% occupancy (here only one diastereomer is shown; C gray, N blue, F green, S yellow, Pd orange).

3.3 Bowl or cage

Besides conformational differences between the photo isomers, the steric crowding of the quinoline group might play an important role in the formation of the bowl-shaped structures in solution. Another DTE based ligand **L^{b}** (Figure 3.11, containing an isoquinoline group, in Chapter 7) and the ligand **L^{c}** (with pyridine group, reported by Su's group[13]) shows less steric hindrance around the coordinating nitrogen atoms. Thus, both ligands **L^{b}** and **L^{c}** favor cage formation in solution, either in their open or closed form. For the open cage *o*-**C^{a}** in this work, the twisted arrangement of the conformational flexible ligand in the cage would relieve the steric crowding from the large quinoline group around Pd^{II}. While in closed bowl-shaped complex *c*-**B**, the 'locked' rigid ligands did not allow to change their conformations. As a result, the fourth ligand was reluctant to adapt to the steric bulk, especially in solution.

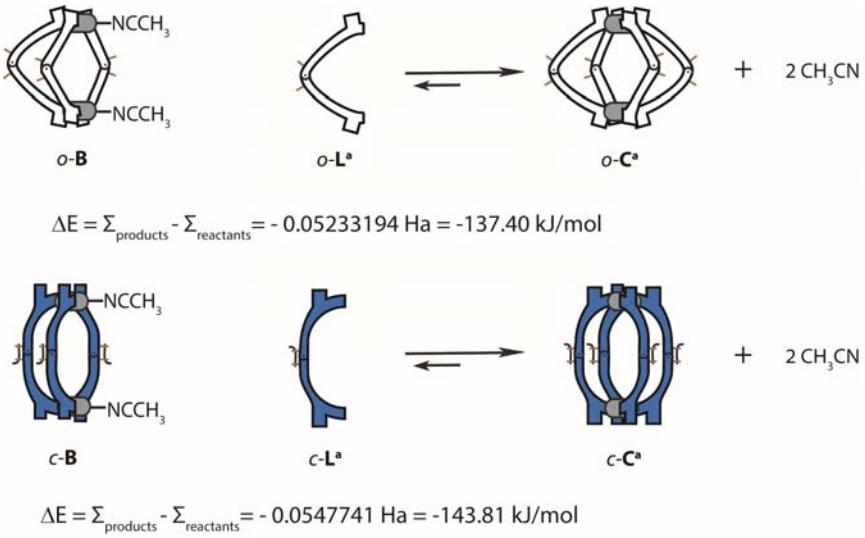

Figure 3.6 Cartoon scheme showing reaction equation between cage and bowl and their reaction energies as obtained from DFT (ωB97XD/LanL2DZ) minimized structures.

To obtain further energy information on the preference of cage or bowl compound, density functional theory (DFT)[14] calculation (gas phase, ωB97XD/LanL2DZ) was carried out (Chapter 3.9.5). The calculations showed that both cage compounds had lower formation energy compared with their corresponding bowl compounds. The open cage *o*-**C^{a}** is −137.40 kJ mol^{-1} lower than the open bowl isomer $[Pd_2(o\text{-}\mathbf{L^a})_3(CH_3CN)_2](BF_4)_4$ (*o*-**B**), which is consistent with the experimental result. For closed-form cage $[Pd_2(c\text{-}\mathbf{L^a})_4](BF_4)_4$ (*c*-**C^{a}**), it is −143.81 kJ mol^{-1} lower than *c*-**B** (here solvent = CH_3CN), indicating the formation of *c*-**C^{a}** is significantly more energetically favorable, agreed with SCXRD but not supported by the solution experimental result. Energy profile of DFT calculations and SCXRD suggested that the bowl compounds could be kinetic product but not thermodynamic product. Heating 1.0 mM of *c*-**B** solution for 3 days or even up to

10 days at 70 °C, showed no significant changes in the ^{1}H NMR spectra (Figure 3.7), indicating a high stabilization of *c*-**B** in CD_3CN. In other words, the steric effect of the quinoline group and conformational rigid as well as the CD_3CN solution environment might help to stabilize *c*-**B**, slowing down *c*-**B** to *c*-**C**^{a} transformation.

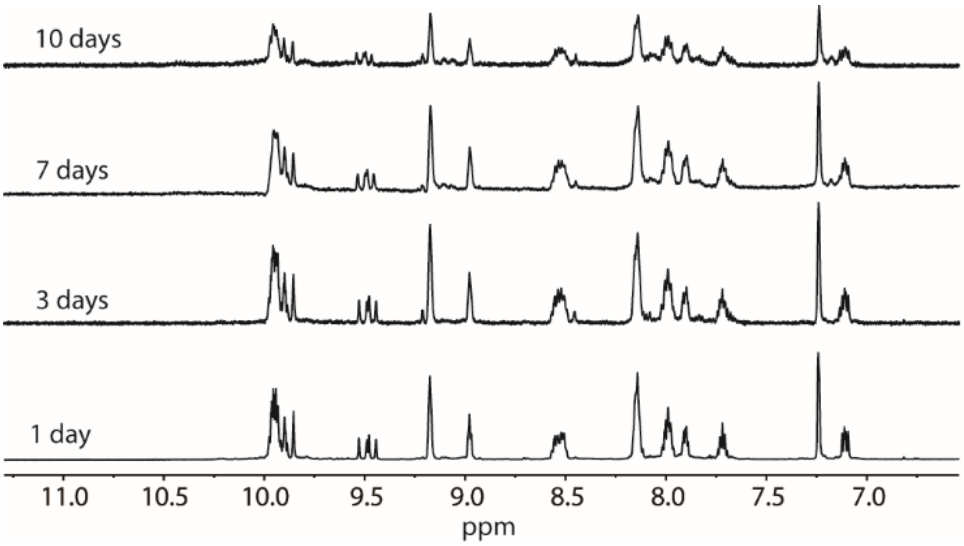

Figure 3.7 ^{1}H NMR spectra (500 MHz, 298 K, CD_3CN) of *c*-**B** after 1, 3, 7 and 10 days after heating at 70 ºC under exclusion of light.

3.4 Light-controlled gating

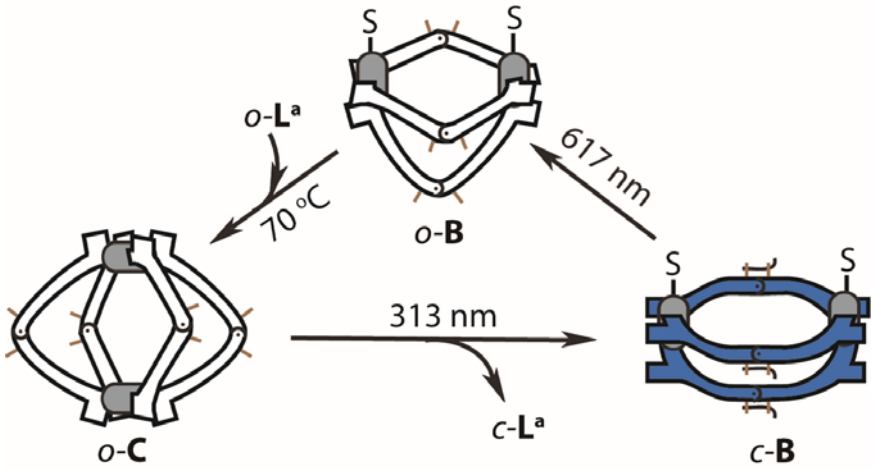

Figure 3.8 Scheme shows the interconversion process between cages *o*-**C**^{a} and bowl *c*-**B**.

Irradiated *o*-**C**^{a} under UV light (313 nm), the signals of bowl (*c*-**B**) and free ligands (*c*-**L**^{a}) were observed in a convoluted ^{1}H NMR spectrum (Figure 3.9). Moreover, addition of an excess of Pd^{II} cations (0.17 eq.) to the solution and heating for 1 h at 70 °C resulted in the disappearance of ^{1}H NMR signals corresponding to free ligand *c*-**L**^{a} and an increase in intensity of signals of *c*-**B** (Figure 3.9). In contrast, after irradiating closed bowl *c*-**B** at 617 nm, the ^{1}H NMR spectrum after immediate measurement showed broad and

complicated signals (Figure 3.9). However, we even could not find any signals of *o*-**B** through CSI mass spectrum (–30 °C). Extra *o*-$\mathbf{L^a}$ was added and the sample was heated at 70 °C for 1 h. The mixture completely transformed to open cage *o*-$\mathbf{C^a}$. Luckily, we could determine *o*-**B** indirectly through **G2**@*o*-**B** owing to **G2** (benzene-1,4-disulfonate) stabilizing *o*-**B** structure. After adding 1.0 eq. of **G2** into the fresh prepared *o*-**B**, we found that the broad signals turned clearer and sharper, which could be perfectly analyzed by NMR spectroscopy (Figure 3.104). High resolution ESI mass spectrum showed only single peak of [**G2**@Pd_2(*o*-$\mathbf{L^a}$)$_3$]$^{2+}$ and unambiguously confirmed the formation of the host-guest complex **G2**@*o*-**B** (Figure 3.105). Moreover, **G2**@*o*-**B** could be reversibly transformed into **G2**@*c*-**B**. Irradiation of **G2**@*o*-**B** under UV light (313 nm) transformed the sample fluently into **G2**@*c*-**B**. Irradiation at 617 nm reversed this progress, which was verified by ^{1}H NMR spectroscopy (Figure 3.106).

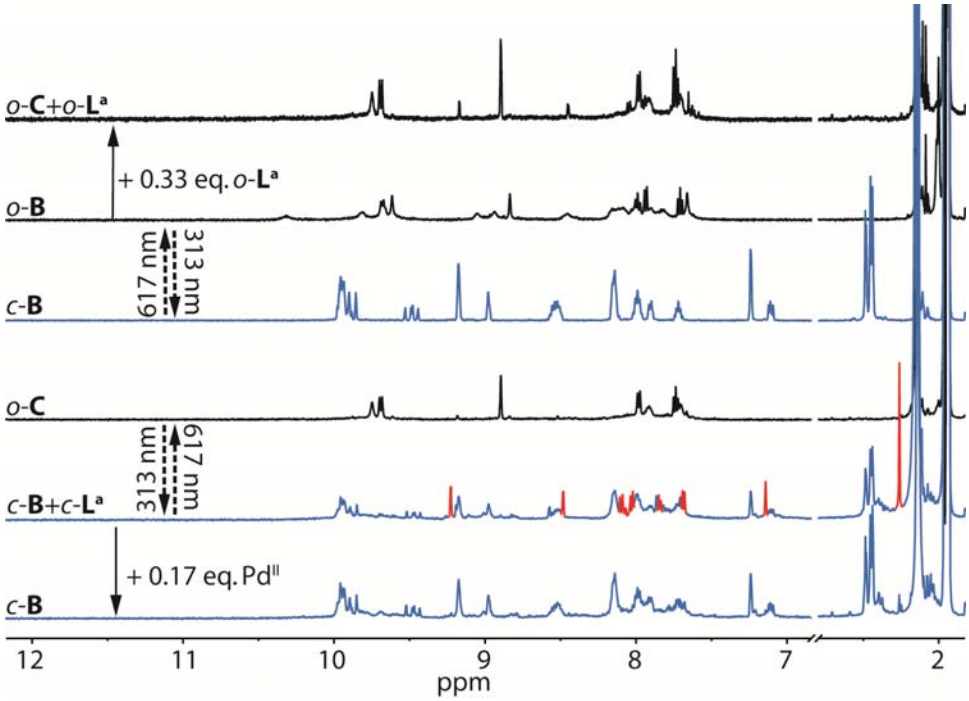

Figure 3.9 a) ^{1}H NMR spectra (500 MHz, CD_3CN, 298 K) of the interconversion between cages *o*-$\mathbf{C^a}$ and bowl *c*-**B**. Red color highlights the signals of uncoordinated 'free' ligand *c*-$\mathbf{L^a}$, and blue indicates the closed bowl structure *c*-**B**.

In order to further understand the light-controlled structure transformation, the UV-irradiation kinetics of photo-conversion experiments were introduced (Figure 3.10). $\mathbf{L^b}$ was used as a reference (Chapter 7). Free ligands of both $\mathbf{L^a}$ and $\mathbf{L^b}$ solutions could be switched from open to closed-form very quickly (reversible process). While the interconversion in the cage [Pd_2($\mathbf{L^b}$)$_4$](BF_4)$_4$ photoisomers is slightly slower after coordinated with Pd^{II} cations. Interconversion between open cage *o*-$\mathbf{C^a}$ and closed bowl *c*-**B**, however, is drastically slowed down. This might be due to the structural change occurring during the interconversion between *o*-$\mathbf{C^a}$ and *c*-**B**, which decreased the

switching rate. In contrast, the $[Pd_2(\mathbf{L^b})_4](BF_4)_4$ photoisomers switch between to open and the closed form in the cage structure, without structural rearrangement occurring, resulting in a higher switching rate.

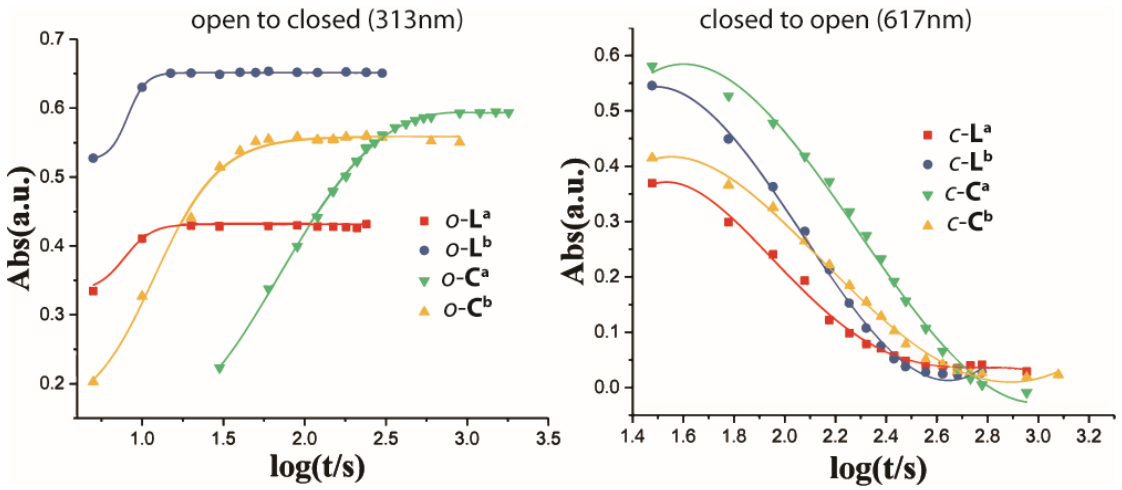

Figure 3.10 Time-course UV-Vis kinetics of the photo-conversions of open-form ligands and cages (left) irradiated with 313 nm light, and closed-form ligands and cages (right) upon irradiation with 617 nm light based on absorption around 600 nm.

3.5 $Pd_2L^A{}_3L^B$ type heteroleptic cage synthesis

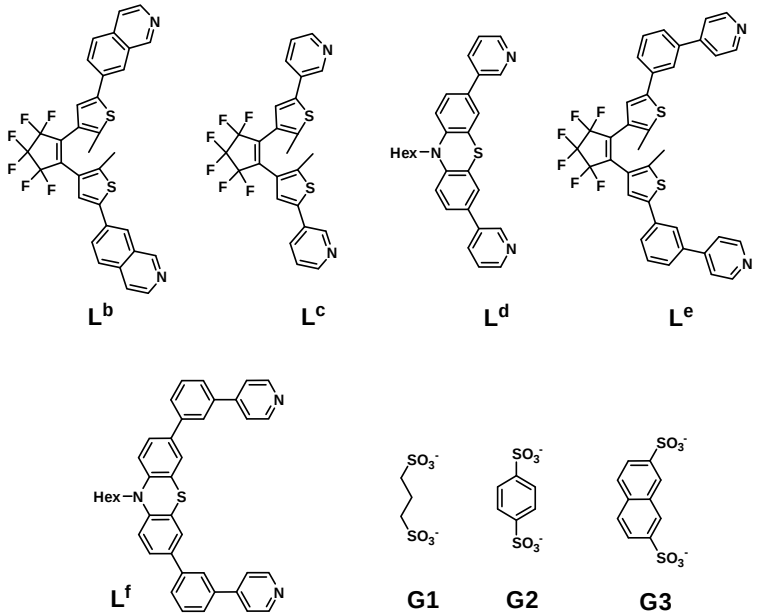

Figure 3.11 Overview of ligands **L^b**, **L^c**, **L^d**, **L^e**, **L^f**, and guests **G1**, **G2** and **G3**. The guest molecules are presented in their anionic form and their counter cation are tetrabutylammonium.

As discussed above, the DTE-based ligand **L^a** forms a lantern like cage in its open form and bowl-shaped complex in its closed photo-isomer in the presence of Pd^{II} cations. In the cage compound *o*-**C^a**, both Pd^{II} centers are fully coordinated by four ligands. In contrast, the bowl structure has two 'free' Pd^{II} coordination sites (occupied by solvent molecules), which encouraged us to introduce a new coordination ligand to form

$Pd_2L^A{}_3L^B$ type of heteroleptic cages. Thus, a 1 : 1 mixture of *c*-**B** (1 mM) and $\mathbf{L^c}$ (Figure 3.11) was stirred in CD_3CN at room temperature for 1 h, which resulted in quantitative formation of $[Pd_2(c\text{-}\mathbf{L^a})_3(\mathbf{L^c})](BF_4)_4$ (*c*-**B**-$\mathbf{L^c}$). The heteroleptic cage formation could unambiguously be confirmed by NMR spectroscopy and high resolution ESI mass spectrometry (Chapter 3.9.2.3.1).

To the best of our knowledge, there is only one reported non-statistic $Pd_2L^A{}_3L^B$ type of cage in a mixture together with cage $Pd_2L^A{}_4$.[15] Here, it is the first example to synthesize a clean $Pd_2L^A{}_3L^B$ type heteroleptic cage. This intriguing result and easy syntheses enticed us to design similar coordination ligands, with having the same length as $\mathbf{L^a}$ (similar N-N distance), but a different arm length (different handles length), expecting to tune the volume of the central cavity. Thus, ligands $\mathbf{L^c}$ and $\mathbf{L^e}$ based on a DTE backbone and $\mathbf{L^d}$ and $\mathbf{L^f}$ based on phenothiozine ligands were chosen (Figure 3.11). $\mathbf{L^c}$ and $\mathbf{L^d}$ were synthesized as previously described,[13, 16] while the longer arm ligands $\mathbf{L^e}$ and $\mathbf{L^f}$ were synthesized through a Suzuki cross-coupling reaction (Chapter 3.9.2.1). After mixing *c*-**B** (1 mM) with $\mathbf{L^d}$, $\mathbf{L^e}$ or $\mathbf{L^f}$ respectively as the same method as synthesizing *c*-**B**-$\mathbf{L^c}$, the heteroleptic cages $[Pd_2(c\text{-}\mathbf{L^a})_3(\mathbf{L^d})](BF_4)_4$ (*c*-**B**-$\mathbf{L^d}$), $[Pd_2(c\text{-}\mathbf{L^a})_3(\mathbf{L^e})](BF_4)_4$ (*c*-**B**-$\mathbf{L^e}$) and $[Pd_2(c\text{-}\mathbf{L^a})_3(\mathbf{L^f})](BF_4)_4$ (*c*-**B**-$\mathbf{L^f}$) were successfully synthesized. The formation was confirmed by NMR spectroscopy and high resolution ESI mass spectrometry (Chapter 3.9.2.3).

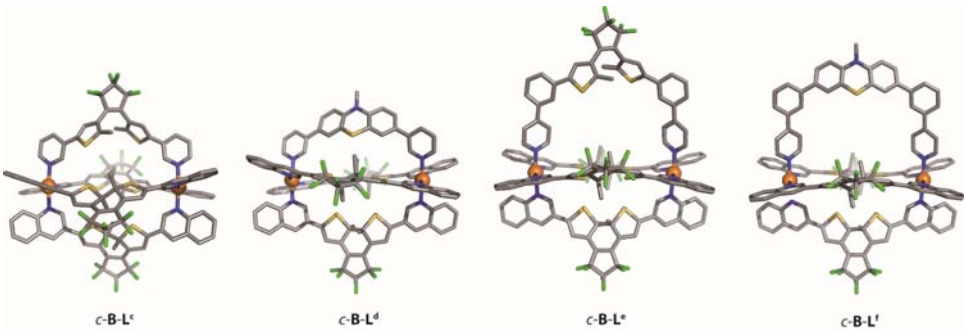

Figure 3.12 DFT optimized heteroleptic cages of *c*-**B**-$\mathbf{L^c}$, *c*-**B**-$\mathbf{L^d}$, *c*-**B**-$\mathbf{L^e}$ and *c*-**B**-$\mathbf{L^f}$.

3.6 Chemical-controlled gating

Interestingly, the heteroleptic cage and the bowl *c*-**B** could be reversibly converted. *c*-**B**-$\mathbf{L^e}$ as an example, after adding 2.0 eq. of Br^- (or Cl^-, NBu_4^+ as counter cation) into 1.0 mM *c*-**B**-$\mathbf{L^e}$ solution, the heteroleptic cage was partially decomposed, which was clearly seen from ^{1}H NMR spectra (Figure 3.13), giving a bowl compound $[Pd_2(c\text{-}\mathbf{L^a})3{+}2Br](BF_4)_2$ (*c*-**B**-**Br**) whose two reactive coordinated sites were occupied by Br^-, and releasing free $\mathbf{L^e}$ at the same time. Later, addition of 2.0 eq. Ag^+ (BF_4^- as counter anion) into the solution to reactive the coordination sites of the bowl, however, ^{1}H NMR

spectra did not show any change. After adding more Ag^+ (up to 20 eq.) into the mixture and stirring at room temperature for 3h, the heteroleptic cage *c*-**B**-**L**^{e} was reassembled (Figure 3.13).

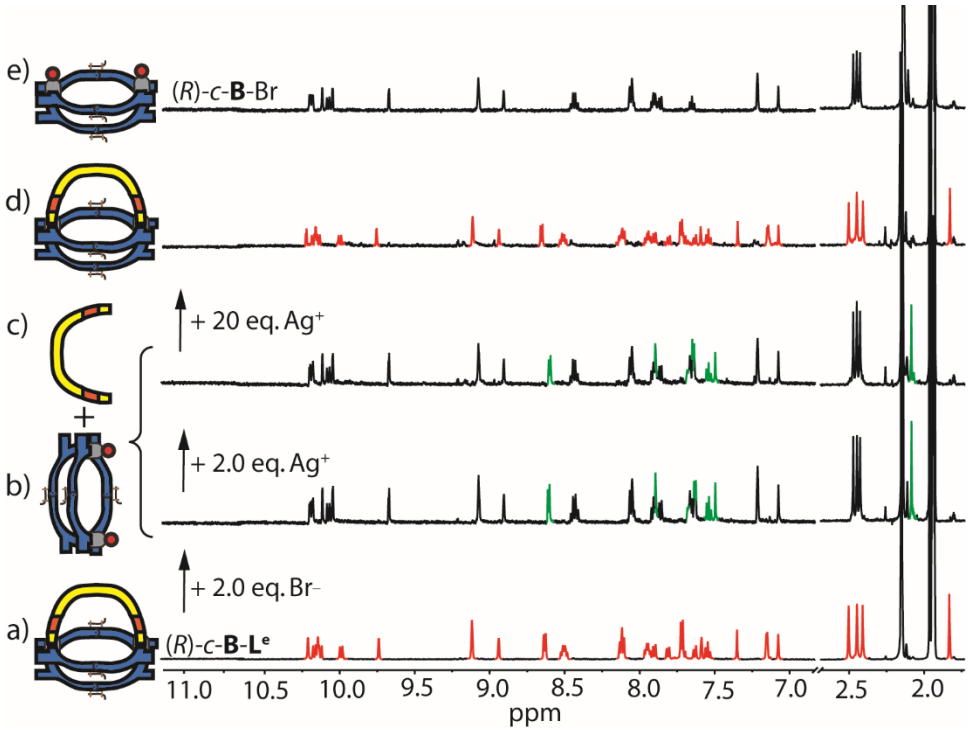

Figure 3.13 ^{1}H NMR spectra (500 MHz, CD_3CN, 298 K) of disassembly and reassembly of heteroleptic cage triggered by chemical stimuli. The ^{1}H NMR spectrum of (a) (*R*)-*c*-**B**-**L**^{e}; Stacking up one by one shown the ^{1}H NMR spectra of the mixture of (b) adding 2.0 eq. of Br^- to release **L**^{e}; later, (c) titrating of 2.0 eq. or even (d) 20 eq. Ag^+ into the same sample. The decomposed sample recovered back to (*R*)-*c*-**B**-**L**^{e}. (e) The ^{1}H NMR spectrum on the top setting for reference is (*R*)-*c*-**B**-**Br**. Red color marked as the signals of (*R*)-*c*-**B**-**L**^{e}, and green color marked as uncoordinated 'free' **L**^{e}.

3.7 Gating in presence of guest

In general, it is difficult for a large guest to be encapsulated by a cage over its sealed cavity size. In contrast, a bowl can capture a bigger guest regardless of the bowl slot size due to its open side/gate. Photo-controlled reversible interconversion between cage and bowl encouraged us to study size-dependent guest encapsulation of *o*-**C**^{a} and *c*-**B**. Therefore, we performed ^{1}H NMR titrations with three different bis-sulfonate anions guests **G1-G3** (Figure 3.11). First of all, stepwise addition of thin guest **G1** (propane-1,3-disulfonate) into open cage leads to the appearance of a new set of sharp ^{1}H NMR signals and significant downfield shift of the inward pointing protons (H_a, $\Delta\delta$ = 0.67), indicated encapsulation and slow exchange between the open cage and guest **G1** (Figure 3.72). High resolution ESI mass spectra showed signals assigned to host-guest complex [**G1**@*o*-**C**^{a}]$^{2+}$ (Figure 3.73), further confirming the guest encapsulation by *o*-**C**^{a}. Afterward, we chose slightly larger guests **G2** (benzene-1,4-disulfonate) and **G3**

(naphthalene-2,7-disulfonate), whose sizes were exceeding the volume of the cage cavity. As expected, the inward pointing proton H_a did not show any shift, instead a shifting of the outward pointing proton H_b of *o*-**C**[a] for both **G2** and **G3** (Figure 3.74 & Figure 3.75) was observed. This suggests an interaction with the cage from the outside, acting as a counter anion rather than being encapsulated.

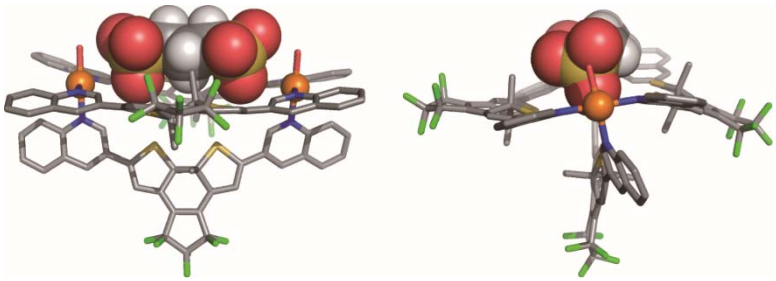

Figure 3.14 X-ray structure of **G1**@*c*-**B** showing the encapsulation of **G1**. All hydrogen atoms in *c*-**B**, solvent molecules, counter anions (except the encapsulated **G1**) and minor disordered components have been omitted for clarity (here only one diastereomer is shown; Color Scheme: C gray, H white, N blue, O red, F green, S yellow, Pd orange).

Next, we tested the formation of host-guest complexes with closed bowl *c*-**B**. For better evaluation of ^{1}H NMR signal shifting, enantiopure *S*-*c*-**B** was used for titration. Similarly, **G1** could be easily captured by *c*-**B**, which was confirmed by ^{1}H NMR titration and high-resolution ESI mass spectra (Figure 3.76 & Figure 3.77). X-Ray structure of **G1**@*c*-**B** further proved the guest encapsulation (Figure 3.14). For **G2**, titration of the guest into the *S*-*c*-**B** solution, resulted in the onset of new ^{1}H NMR signals and the downfield shifting of signals corresponding to encapsulated guest **G2** (Figure 3.78). Additional peaks in the high-resolution ESI mass spectrum assigned to [**G2**@*c*-**B**]$^{2+}$ (Figure 3.79), clearly determined the 1 : 1 encapsulation of **G2**. The new set of ^{1}H NMR signals turned particularly sharp and clear until adding 1.0 eq. of **G2** to the pure chiral bowl (Figure 3.78), indicating strong binding, slow exchange and good cavity fit of **G2** within the bowl. In contrast, addition of the largest guest **G3** to a solution of the bowl, resulted in the broadening of the ^{1}H NMR signals, which made an interpretation difficult. Nevertheless, a clear shifting of signals corresponding to protons $H_{a'}$ and the methyl group of the DTE backbone was overserved, indicating host-guest complexation (Figure 3.80). This could be further confirmed by ESI mass spectrum (Figure 3.81). Unluckily, a determination of association constants of all these host-guest complex from ^{1}H NMR titration data were not possible due to an onset of precipitations during the titration.

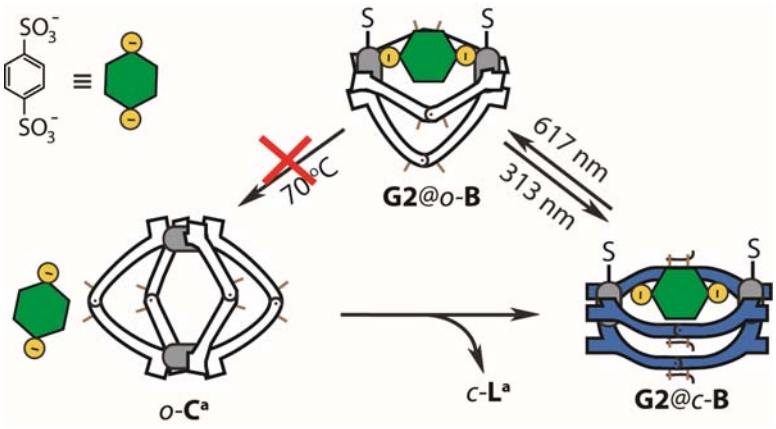

Figure 3.15 Cartoon scheme showing the light-gating process between cages *o*-**C**^{a} and bowl *c*-**B** in presence of **G2**.

Similar to the switching process without guest, irradiation of *o*-**C**^{a} in presence of 1.0 eq. of **G2** under 313 nm resulted in **G2**@*c*-**B** formation. After removing one of the four ligands in the cage during the photo-closing, the limited confined cavity is opened to an unfold bowl. Therefore, **G2** was encapsulated, which could be seen from the rising ^{1}H NMR signals of **G2**@*c*-**B** after photo-switching (Figure 3.106). However, the reversed switching of **G2**@*c*-**B** under 617 nm could not release the guest, instead the host-complex **G2**@*o*-**B** is formed (Figure 3.106). Both **G2**@*c*-**B** and **G2**@*o*-**B** are stable even under heating at 70 °C. To remove the guest, 2.0 eq. of Br^{-} was added to the **G2**@*c*-**B** solution and *c*-**B**-**Br** was formed. After titrated Ag^{+} to the solution, **G2** was recaptured again, showing reversible recovery of **G2**@*c*-**B** (Figure 3.109).

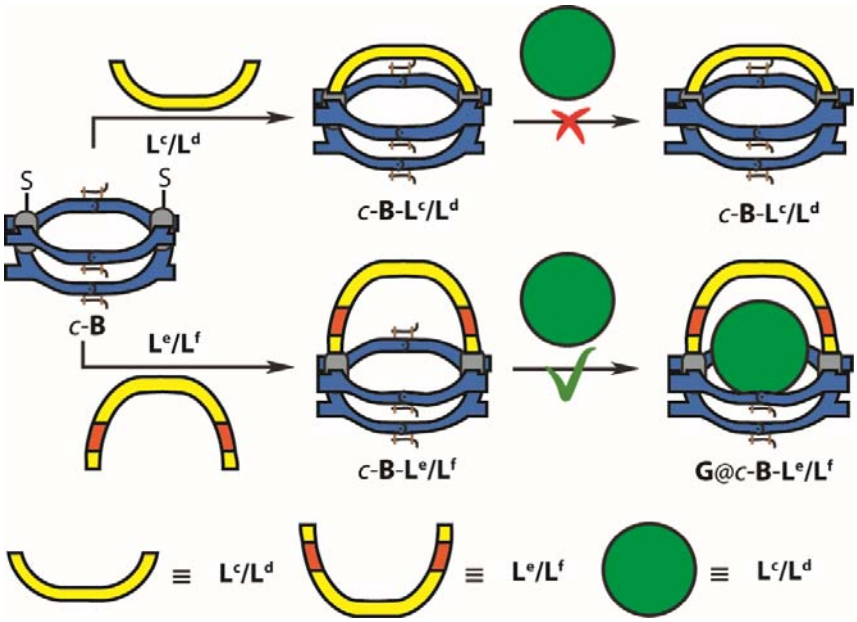

Figure 3.16 The formation of $Pd_2L^{A}{}_3L^{B}$ type of heteroleptic cage. Combining *c*-**B** with 1.0 eq. of shorter armed ligand **L**^{c}**/L**^{d} (top) or longer armed ligands **L**^{e}**/L**^{f} (down), forms heteroleptic cages *c*-**B**-**L**^{c}**/L**^{d} with smaller cavity and *c*-**B**-**L**^{e}**/L**^{f} with larger cavity. *c*-**B**-**L**^{c}**/L**^{d} could not be used for guest **G1**/**G2**/**G3** encapsulation. In contrast, *c*-**B**-**L**^{e}**/L**^{f} encapsulates all these guest due to enlarged cavity size.

As mentioned above, the combination of ligands of different arm length with preassembled bowl complex enables the design of coordination cages with different cavity sizes. The capability to encapsulate bis-anionic guest molecules (**G1-G3**) into the different cages were investigated by ^{1}H NMR titration in CD_3CN. First, we investigated *c*-**B**-**L**$^{\mathbf{c}}$ to form host-guest complexes with guest **G1-G3**. No proton signals shifting in the ^{1}H NMR spectra were observed for all **G1**, **G2** and **G3** even for the thinnest guest **G1** due to narrow window and small inner cavity with the short arm of **L**$^{\mathbf{c}}$ (Figure 3.85, Figure 3.86 & Figure 3.87). After adding a spacer (benzene) between the backbone and the coordinating pyridine moiety, the ligand was extended and referred to as ligand **L**$^{\mathbf{e}}$. Now, not only **G1**, but also the larger guest **G2** and **G3** were encapsulated into the coordination cage *c*-**B**-**L**$^{\mathbf{e}}$, which was verified by ^{1}H NMR titration and high resolution ESI mass spectra (Figure 3.91 to Figure 3.96). Thus, we successfully enlarged the cavity of heteroleptic cages by expanding the ligand arm, similar to prolonging the handle of a basket to extend its capacity limit (Figure 3.16). Furthermore, the encapsulated guest in the heteroleptic cage could be reversibly captured and released. By adding 2.0 eq of Br^- to a **G1**@*c*-**B**-**L**$^{\mathbf{e}}$ solution, the ^{1}H NMR spectra proofed the complete release of **G1** and the decomplexation of ligand **L**$^{\mathbf{e}}$ under formation of *c*-**B**-**Br** (Figure 3.17). Subsequently, by adding 20 eq. of Ag^+, the mixture of the disassembled species reformed the host guest complex **G1**@*c*-**B**-**L**$^{\mathbf{e}}$ (Figure 3.17).

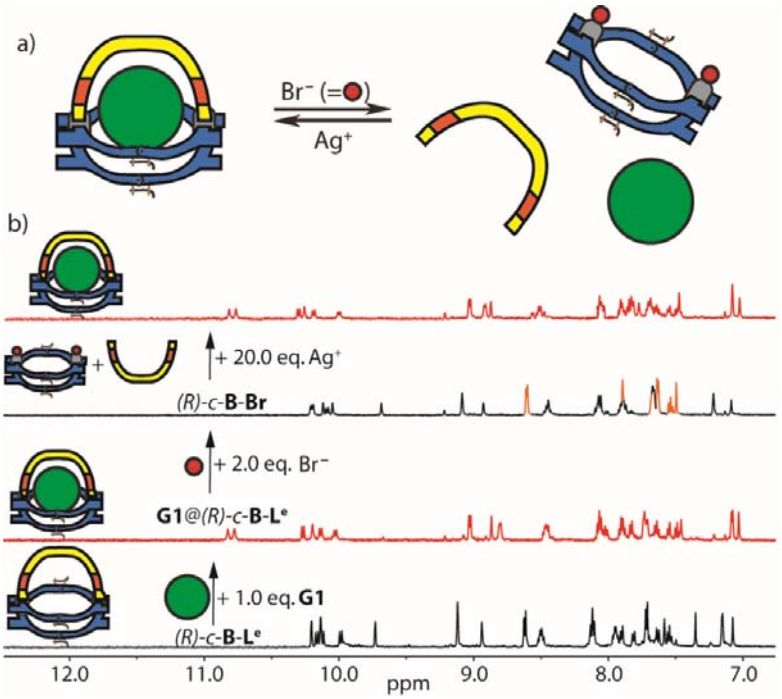

Figure 3.17 a) scheme and b) ^{1}H NMR spectra (500 MHz, CD_3CN, 298 K) showed reversible release and uptake of **G1** for a heteroleptic cage with Br^-/Ag^+. The bottom ^{1}H NMR spectrum shows (*R*)-*c*-**B**-**L**$^{\mathbf{e}}$. After encapsulating of 1.0 eq. of **G1**, the host-guest complex **G1**@(*R*)-*c*-**B**-**L**$^{\mathbf{e}}$ is formed (highlighted in red). Addition of 2.0 eq. of Br^- to **G1**@(*R*)-*c*-**B**-**L**$^{\mathbf{e}}$ leads to decomposition to 'free' ligand **L**$^{\mathbf{e}}$ and bowl (*R*)-*c*-**B**-**Br**, releasing the guest **G1** simultaneously. Addition of 20 eq. of Ag^+, leads to the formation of the host-guest complex **G1**@(*R*)-*c*-**B**-**L**$^{\mathbf{e}}$.

3.8 Conclusion

In summary, photochromic coordination cage *o*-**C^{a}** and bowl-shaped *c*-**B** compound based on a novel DTE ligand **L^{a}** were assembled. Furthermore, influencing factors of the assembly bowl *c*-**B** rather than *c*-**C^{a}** were examined. The formation and stabilization of *c*-**B** was mainly controlled by the conformational of rigid DTE backbone, the steric hindrance of quinoline groups. Open cage *o*-**C^{a}** and closed bowl *c*-**B** can be reversibly interconverted by irradiation with UV light (313 nm) or white light (617 nm). Compared with the confined capsule of *o*-**C^{a}**, *c*-**B** enables a higher tolerance for guest uptake. Indeed, the bowl compound *c*-**B** can encapsulate all guests **G1**, **G2** and **G3**, while for *o*-**C^{a}** only the smallest guest **G1** can be incorporated, due to its narrow internal apertures. This provided potential application as a light-controlled supramolecular sieve. Besides changing the cavity size by light, we furthermore firstly synthesized a series of pure $Pd_2L^A{}_3L^B$ type heteroleptic cages by modifying the arm length of ligand **L^{B}** to tune the cavity size. By adding Br^-/Ag^+, in addition, we could reversible control guest release and uptake, which shows potential application in controllable drug delivery. Moreover, the easily attached ligand L^B in $Pd_2L^A{}_3L^B$ made it a convenient platform to build a multi-functional heteroleptic cage.

3.9 Experimental section

3.9.1 General procedures

All chemicals, except otherwise specified, were obtained from commercial sources and used without further purification. Perfluoro-1,2-bis(2-iodo-5-methylthien-4-yl)cyclopentene[17], **L^{c}**,[13] **L^{d}**,[16] were prepared according to a literature procedure. The tetrabutylammonium salts of the guests (**G1**, **G2** and **G3**) were obtained according to a previously reported procedure.[18] Corresponding starting materials were obtained commercially as sodium salt or free sulfonic acids in the highest available purity. Recycling gel permeation chromatography was performed on a JAI LC-9210 II NEXT GPC system equipped with Jaigel 1H and 2H columns in series using chloroform as the eluent (HPLC grade). NMR measurements were all conducted at 298 K on Avance-500, Avance-600 and Avance-700 instruments from Bruker and INOVA 500 MHz machine from Varian. High-resolution ESI mass spectrometry measurements were carried out on maXis ESI-TOF MS and ESI-tims TOF machines from Bruker. The irradiations were performed with a 500 W Hg Arc lamp from LOT-Quantum Design. Chiral HPLC was performed on an Agilent Technologies 1260 infinity HPLC system equipped with Daicel

CHIRALPAK IC columns (250 x 4.6 mm and 250 x 10 mm) using a dichloromethane/hexane/methanol (39%/60%/1%) mixture as eluent for the separation of *c*-**L**[a]. UV-Vis spectra were recorded on an Agilent 8453 UV-Vis spectrophotometer. CD spectra were measured on an Applied Photophysics Chirascan circular dichroism spectrometer. All heteroleptic cages and *c*-**B** models were constructed using SPARTAN[19] and were first optimized on a PM6 level of theory (no counter ions were included) without constrains. The resulting structures were then further refined by DFT calculations (B3LYP/LANL2DZ) using the Gaussain 09 software.[14]

3.9.2 Synthesis

3.9.2.1 Ligand synthesis

*3.9.2.1.1 Synthesis of 3,3'-((perfluorocyclopent-1-ene-1,2-diyl)bis(5-methylthiophene-4,2-diyl))diquinoline (o-**L**[a])*

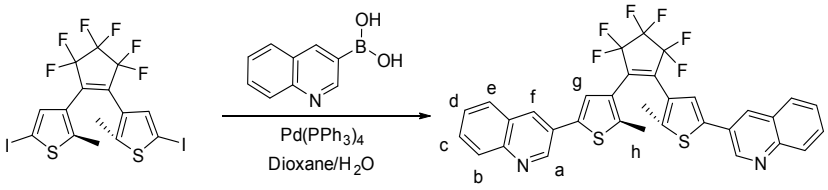

Scheme 2.1 Synthesis of *o*-**L**[a].

A mixture of perfluoro-1,2-bis(2-iodo-5-methylthien-4-yl)cyclopentene[17] (310 mg, 0.5 mmol), quinolin-3-ylboronic acid (259.6 mg, 1.5 mmol), $Pd(PPh_3)_4$ (34.7 mg, 0.03 mmol), K_3PO_4 (1.73 g, 7.5 mmol) and degassed Dioxane/H_2O (30 mL V/V = 1:1) were combined in an oven-dried Schlenk tube and stirred at 90 °C overnight. After cooling down to room temperature, CH_2Cl_2 was added, and the solution was washed with water and brine, dried over anhydrous $MgSO_4$ and concentrated *in vacuo*. The crude product was separated through column chromatography (silica) using CH_2Cl_2/MeOH (50:1) as eluents and further purified by GPC using $CHCl_3$ as eluents to give pure *o*-**L**[a] (199.3 mg, 0.32 mmol) as a bluish solid in 64% yield. ^{1}H NMR (500 MHz, CD_3CN) δ 9.17 (d, *J* = 2.4 Hz, 2H), 8.42 (d, *J* = 2.4 Hz, 2H), 8.04 (d, *J* = 8.5 Hz, 2H), 7.93 (d, *J* = 8.0 Hz, 2H), 7.74 (ddd, *J* = 8.4, 6.9, 1.5 Hz, 2H), 7.65 (s, 2H), 7.64 – 7.59 (m, 2H), 2.11 (s, 6H). ^{13}C NMR (151 MHz, CD_3CN) δ 149.05, 148.37, 144.13, 140.02, 132.21, 130.65, 130.04, 129.11, 128.73, 128.42, 127.33, 126.71, 125.25, 14.88. ^{19}F NMR (471 MHz, CD_3CN) δ –110.75 (t, *J* = 5.2 Hz), –132.49 (q, *J* = 5.1 Hz). ESI-HRMS calculated for $C_{33}H_{21}F_6N_2S_2$ $[M+H]^+$ *m/z* = 623.1050, found *m/z* = 623.1025.

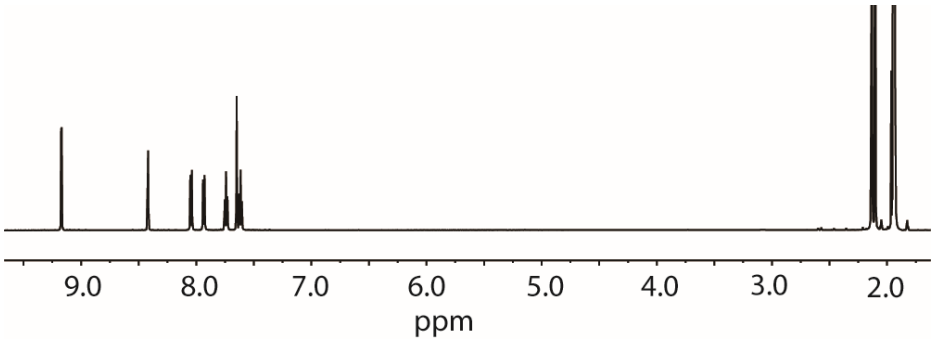

Figure 3.18 ^{1}H NMR spectrum (500 MHz, CD_3CN) of *o*-**L**^{a}.

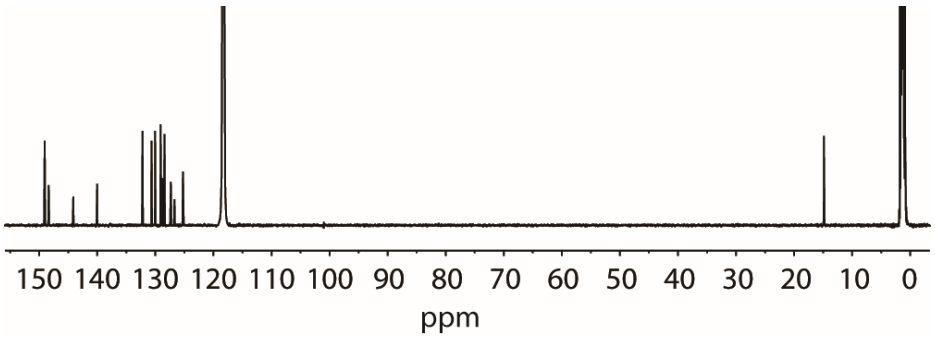

Figure 3.19 ^{13}C NMR spectrum (151 MHz, CD_3CN) of *o*-**L**^{a}.

*3.9.2.1.2 Synthesis of 4,4'-(((perfluorocyclopent-1-ene-1,2-diyl)bis(5-methylthiophene-4,2-diyl))bis(3,1-phenylene))dipyridine (o-**L**^{e})*

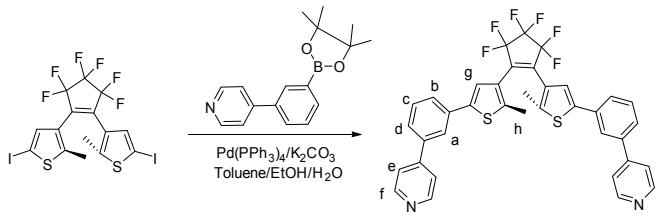

Scheme 2.2 Synthesis of *o*-**L**^{e}.

A mixture of perfluoro-1,2-bis(2-iodo-5-methylthien-4-yl)cyclopentene (310 mg, 0.5 mmol), 4-(3-(4,4,5,5-tetramethyl-1,3,2-dioxaborolan-2-yl)phenyl)pyridine (421.7 mg, 1.5 mmol), $Pd(PPh_3)_4$ (34.7 mg, 0.03 mmol), K_2CO_3 (1.1 g, 8.0 mmol) and degassed toluene/EtOH/H_2O (30 mL V/V/V = 2:1:1) were combined in an oven-dried Schlenk tube and stirred at 90 °C overnight. After cooling down to room temperature, CH_2Cl_2 was added, and the solution was washed with water and brine, dried over anhydrous $MgSO_4$ and concentrated *in vacuo*. The crude product was separated through column chromatography (silica) using CH_2Cl_2/MeOH (40:1) and further purified by GPC ($CHCl_3$ as eluents) to give pure *o*-**L**^{e} (124.3 mg, 0.2 mmol) as a bluish solid in 36.8% yield. ^{1}H NMR (500 MHz, CD_3CN) δ 8.63 – 8.59 (m, 4H), 7.90 (t, *J* = 1.8 Hz, 2H), 7.68 (p, *J* = 1.1 Hz, 2H), 7.66 (t, *J* = 2.0 Hz, 2H), 7.65 – 7.62 (m, 4H), 7.54 (t, *J* = 7.7 Hz, 2H), 7.50 (s, 2H), 2.07 (s, 6H). ^{13}C NMR (151 MHz, CD_3CN) δ 151.26, 148.12, 143.27, 142.47, 139.88, 134.93, 130.97, 127.62, 127.17, 126.51, 124.96, 124.61, 122.54, 14.76.

^{19}F NMR (471 MHz, $CDCl_3$) δ –109.94 (d, *J* = 5.6 Hz), –131.85. ESI-HRMS calculated for $C_{37}H_{25}F_6N_2S_2$ $[M+H]^+$ *m/z* = 675.1358, found *m/z* = 675.1368.

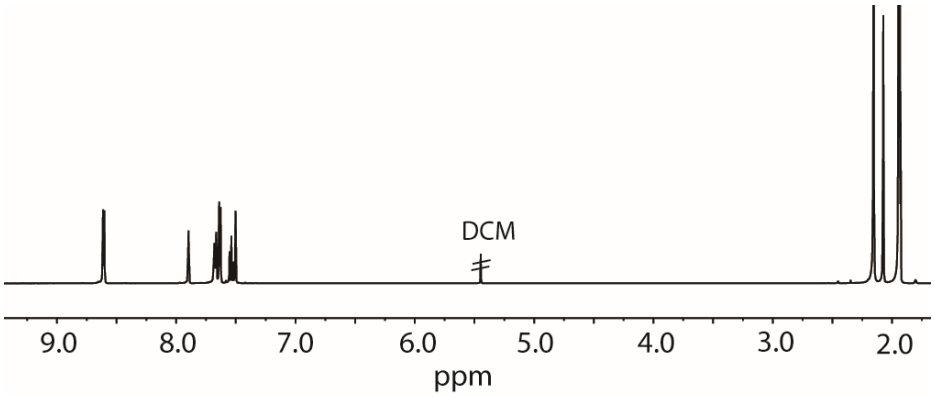

Figure 3.20 ^{1}H NMR spectrum (500 MHz, CD_3CN) of *o*-**L**^{e}.

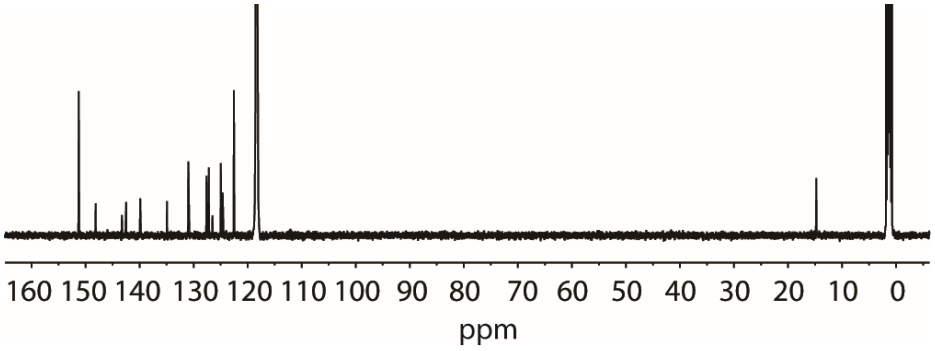

Figure 3.21 ^{13}C NMR spectrum (151 MHz, CD_3CN) of *o*-**L**^{e}.

*3.9.2.1.3 Synthesis of 4,4'-(((perfluorocyclopent-1-ene-1,2-diyl)bis(5-methylthiophene-4,2-diyl))bis(3,1-phenylene))dipyridine (**L**^{f})*

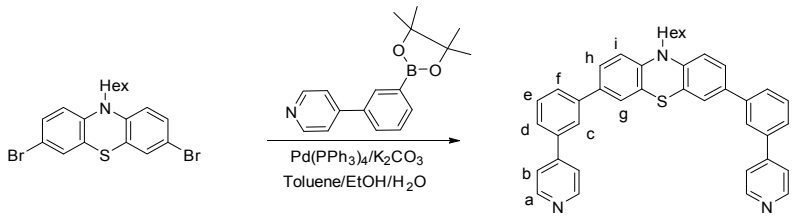

Scheme 2.3 Synthesis of **L**^{f}.

A mixture of 3,7-dibromo-10-hexyl-10*H*-phenothiazine (220.6 mg, 0.5 mmol), 4-(3-(4,4,5,5-tetramethyl-1,3,2-dioxaborolan-2-yl)phenyl)pyridine (421.7 mg, 1.5 mmol), $Pd(PPh_3)_4$ (34.7 mg, 0.03 mmol), K_2CO_3 (1.1 g, 8.0 mmol) and degassed toluene/EtOH/H_2O (30 mL V/V/V = 2:1:1) were combined in an oven-dried Schlenk tube and stirred at 90 °C overnight. After cooling down to room temperature, CH_2Cl_2 was added, and the solution was washed with water and brine, dried over anhydrous $MgSO_4$ and concentrated *in vacuo*. The crude product was separated by column chromatography (silica) using CH_2Cl_2/MeOH (40:1) as eluents and further purified through GPC to give pure **L**^{f} (253.7 mg, 0.4 mmol) as a yellow solid in 86% yield. ^{1}H NMR

(500 MHz, $CDCl_3$): δ = 8.79 – 8.64 (m, 4H), 7.80 (t, J = 1.8 Hz, 2H), 7.65 (ddd, J = 6.1, 3.5, 1.6 Hz, 6H), 7.61 (dt, J = 7.7, 1.5 Hz, 2H), 7.57 (t, J = 7.6 Hz, 2H), 7.47 (d, J = 2.2 Hz, 2H), 7.44 (d, J = 2.3 Hz, 2H), 6.99 (d, J = 8.2 Hz, 2H), 3.94 (t, J = 7.2 Hz, 2H), 1.96 – 1.83 (m, 2H), 1.57 – 1.46 (m, 2H), 1.36 (tt, J = 6.3, 2.9 Hz, 4H), 0.96 – 0.86 (m, 3H). ^{13}C NMR (126 MHz, $CDCl_3$): δ = 149.42, 149.21, 144.61, 141.06, 138.34, 134.82, 129.73, 127.54, 126.15, 125.90, 125.71, 125.29, 124.84, 122.07, 115.65, 47.68, 31.50, 26.84, 26.69, 22.65, 14.06. ESI-HRMS calculated for $C_{40}H_{36}N_3S$ $[M+H]^+$ m/z = 590.2624, found m/z = 590.2599.

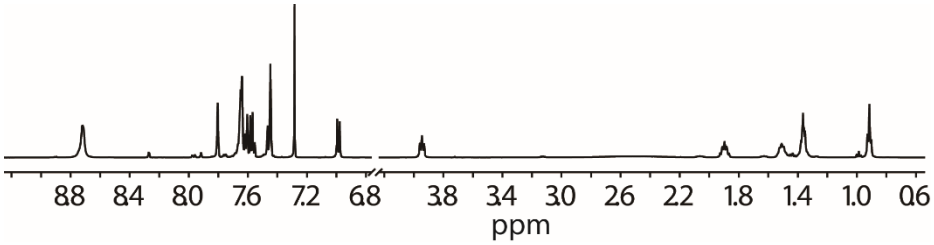

Figure 3.22 ^{1}H NMR spectrum (500 MHz, $CDCl_3$) of *o*-**L**$^{\mathbf{f}}$.

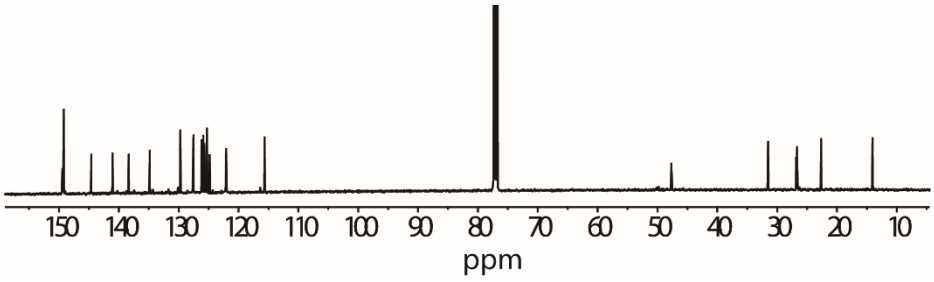

Figure 3.23 ^{13}C NMR spectrum (151 MHz, $CDCl_3$) of *o*-**L**$^{\mathbf{f}}$.

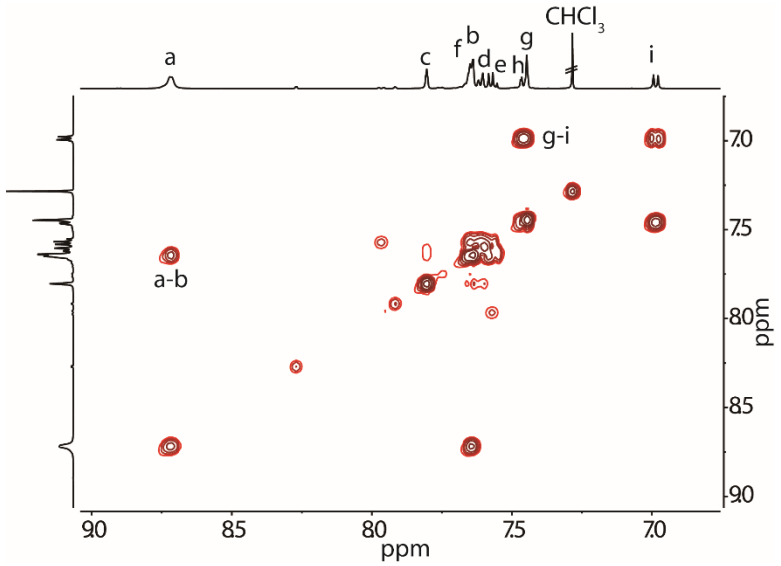

Figure 3.24 ^{1}H–^{1}H COSY spectrum (500 MHz, $CDCl_3$) of *o*-**L**$^{\mathbf{f}}$ (only showing aromatic region).

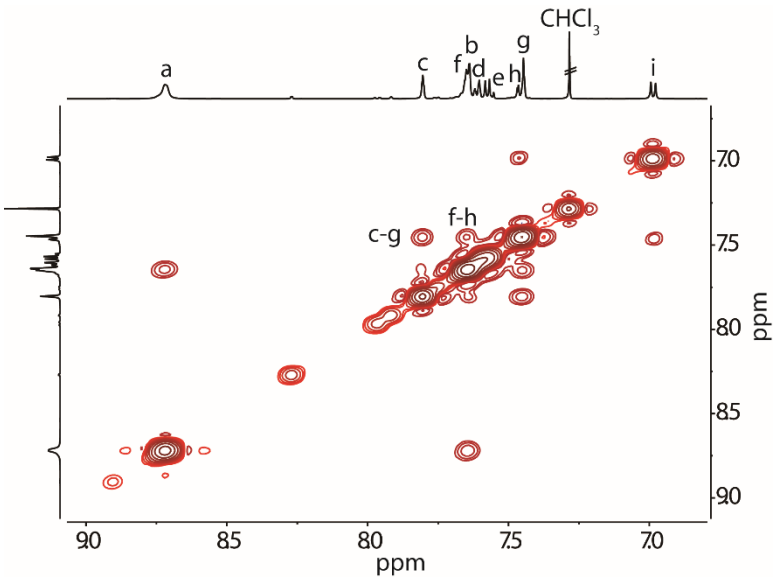

Figure 3.25 ^{1}H–^{1}H NOESY spectrum (500 MHz, $CDCl_3$) of *o*-**L**^{f} (only showing aromatic region).

3.9.2.2 Cage synthesis

3.9.2.2.1 Synthesis of [Pd$_2$(o-L^a)$_4$](BF$_4$)$_4$ (o-C^a)

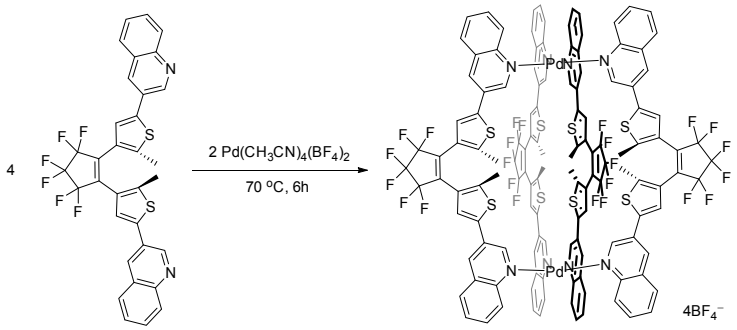

Scheme 2.4 Synthesis of *o*-**C**^{a}.

The open cage compound [Pd$_2$(*o*-**L**^{a})$_4$](BF$_4$)$_4$ (*o*-**C**^{a}) was synthesized in quantitative yield by heating a mixture of the ligand *o*-**L**^{a} in CD_3CN (4 µmol, 2.5 mg, 866.7 µL) and Pd(CH$_3$CN)$_4$(BF$_4$)$_2$ (2 µmol, 133.3 µL of a 15 mM stock solution in CD_3CN) at 70 °C for 6 h to give 1000 µl of a 1 mM solution of *o*-**C**^{a}. ^{1}H NMR (500 MHz, CD_3CN): δ = 9.75 (s, 8H), 9.69 (d, *J* = 8.7 Hz, 8H), 8.90 (s, 8H), 7.98 (d, *J* = 8.2 Hz, 8H), 7.92 (m, 8H), 7.74 (t, *J* = 7.6 Hz, 8H), 7.70 (s, 8H), 2.00 (s, 24H). ESI-HRMS calculated for [Pd$_2$(*o*-**L**^{3})$_4$+BF$_4$]$^{3+}$ *m/z* = 929.7325, found *m/z* = 929.7429.

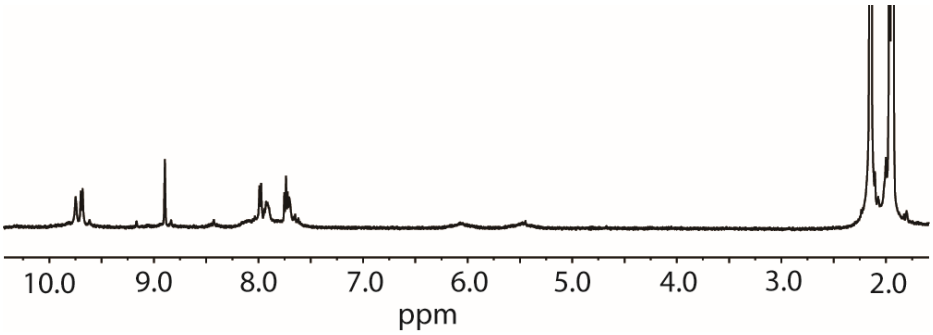

Figure 3.26 ^{1}H NMR spectrum (500 MHz, CD_3CN) of *o*-**C^{a}**.

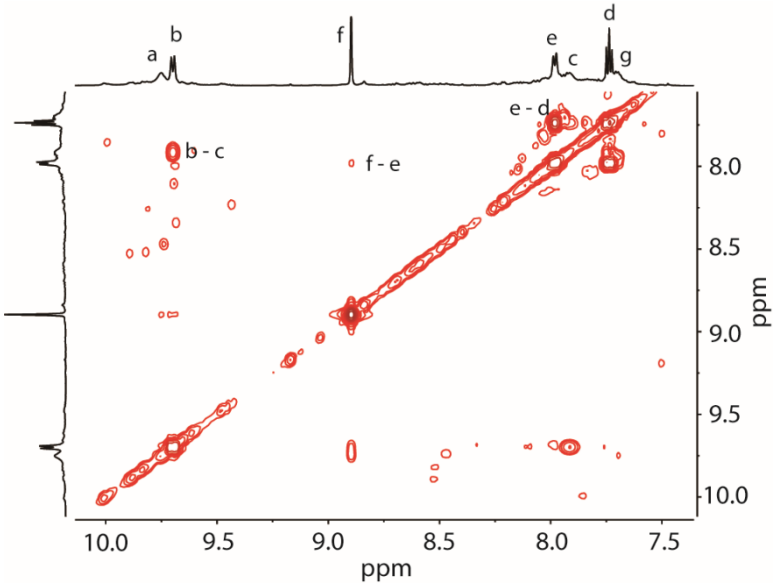

Figure 3.27 ^{1}H–^{1}H COSY spectrum (600 MHz, CD_3CN) of *o*-**C^{a}** (only showing aromatic region)**.**

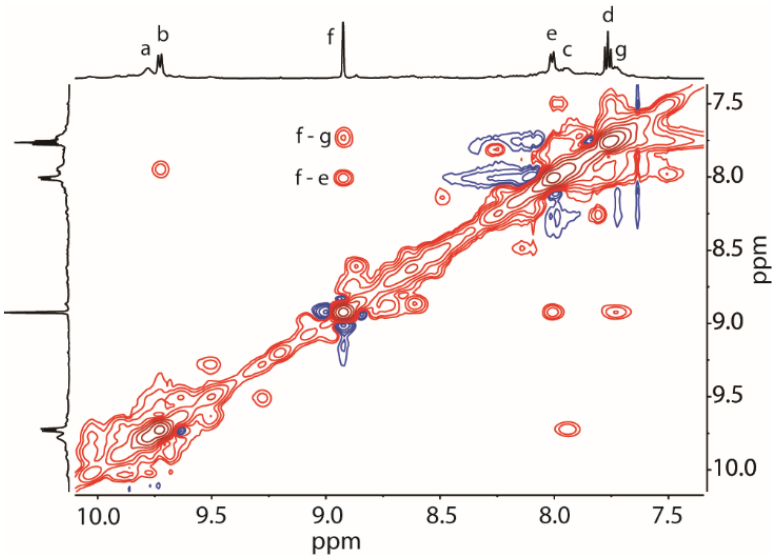

Figure 3.28 ^{1}H–^{1}H NOESY spectrum (600 MHz, CD_3CN) of *o*-**C^{a}** (only showing aromatic region).

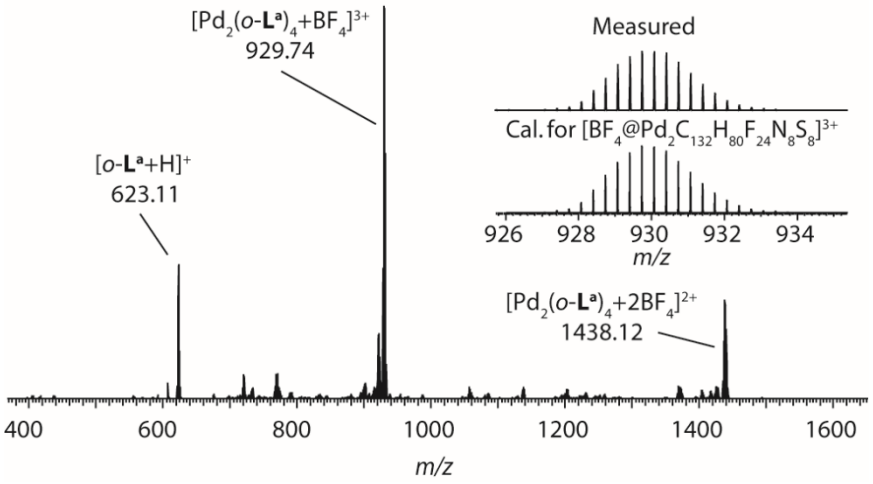

Figure 3.29 ESI-HRMS spectrum of *o*-**C^{a}.**

3.9.2.2.2 Synthesis of [Pd$_2$(c-L^{a})$_3$(Slovent)$_2$](BF$_4$)$_4$ (c-B)

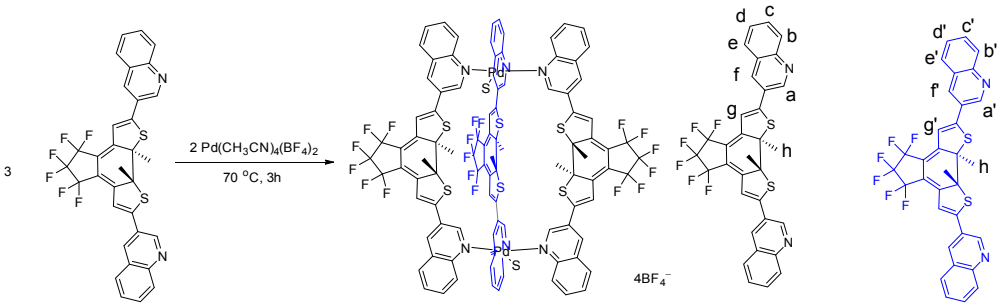

Scheme 2.5 Synthesis of *c*-**B**, S means coordinated solvents on Pd^{II}.

The closed bowl compound [Pd$_2$(*c*-**L^{a}**)$_3$(S)$_2$](BF$_4$)$_4$ (*c*-**B**) was synthesized in quantitative yield by heating a mixture of the ligand *c*-**L^{a}** in CD_3CN (3 µmol, 1.9 mg, 866.7 µL) and Pd(CH_3CN)$_4$(BF$_4$)$_2$ (2 µmol, 133.3 µL of a 15 mM stock solution in CD_3CN) at 70 °C for 6 h to give 1000 µl of a 1.0 mM solution of the cage compound *c*-**B**. ^{1}H NMR (600 MHz, CD_3CN): δ = 10.02 – 9.83 (10H), 9.55 – 9.41 (2H), 9.18 (4H), 8.98 (2H), 8.60 – 8.47 (4H), 8.20 – 8.09 (6H), 7.99 (4H), 7.94 – 7.87 (2H), 7.76 – 7.68 (2H), 7.27 – 7.22 (4H), 7.11 (2H), 2.51 – 2.46 (6H), 2.46 – 2.42 (12H). ESI-HRMS calculated for [Pd$_2$(*c*-**L^{a}**)$_3$+BF$_4$]$^{3+}$ *m/z* = 722.3668, found *m/z* = 722.3737.

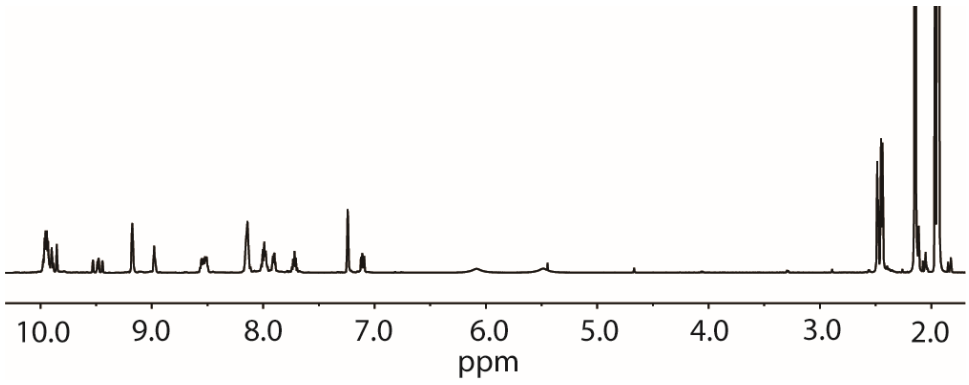

Figure 3.30 ^{1}H NMR spectrum (600 MHz, CD_3CN) of *c*-**B.**

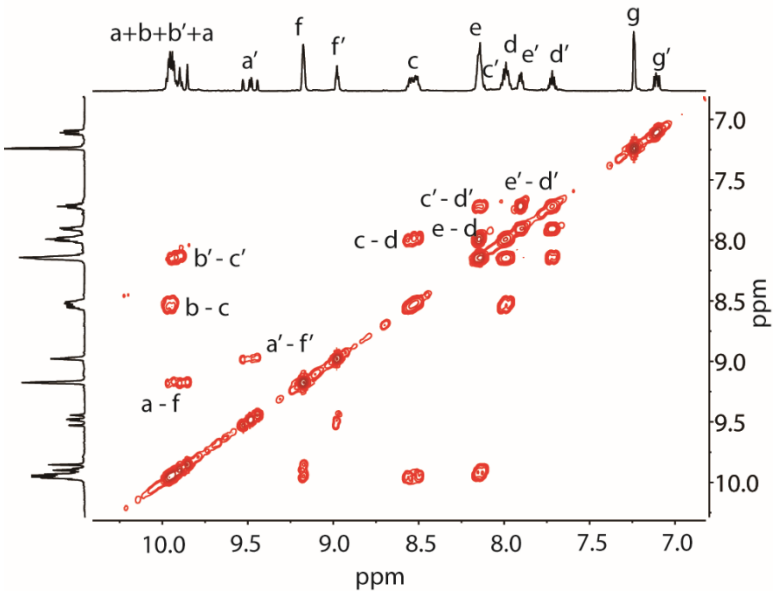

Figure 3.31 ^{1}H–^{1}H COSY spectrum (600 MHz, CD_3CN) of *c*-**B** (only showing aromatic region).

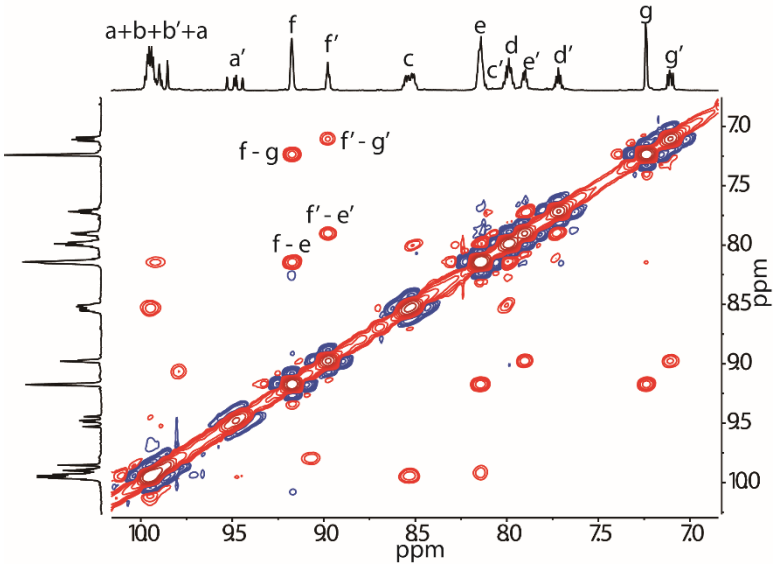

Figure 3.32 ^{1}H–^{1}H NOESY spectrum (600 MHz, CD_3CN) of *c*-**B** (only showing aromatic region).

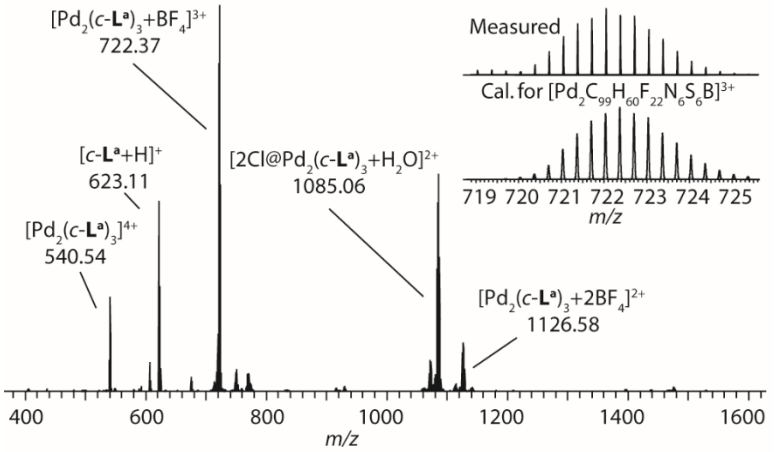

Figure 3.33 ESI-HRMS spectrum of *c*-**B**.

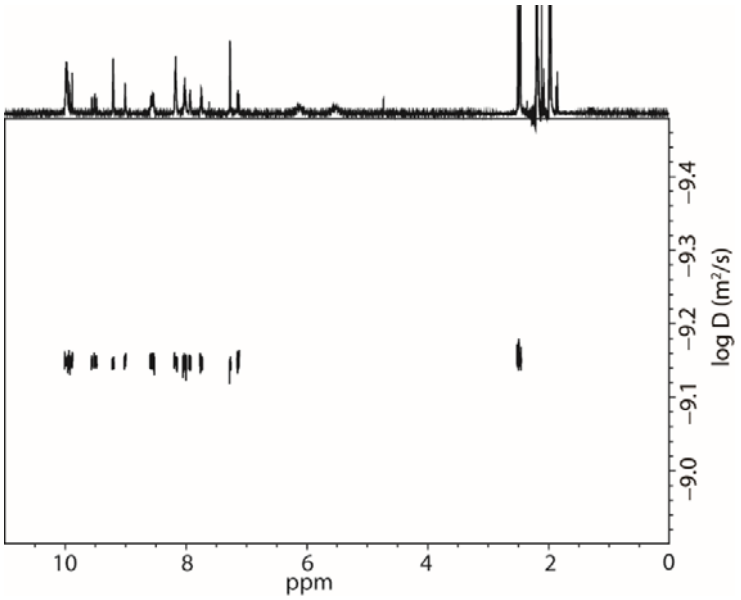

Figure 3.34 DOSY NMR spectrum of *o*-**B.**

3.9.2.2.3 Synthesis of [2Cl@Pd₂(c-L[a])₃](BF₄)₂ (c-B-Cl)

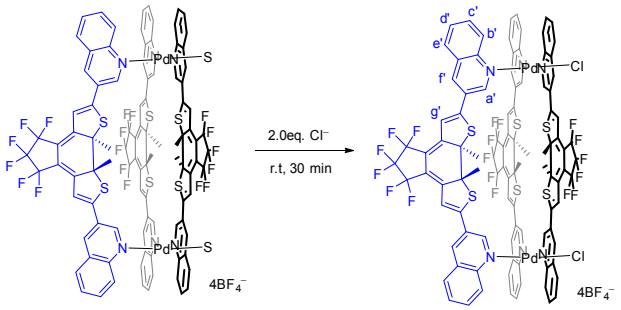

Scheme 2.6 Synthesis of *c*-**B**-**Cl**.

The closed bowl compound [2Cl@Pd_2(*c*-$\mathbf{L^a}$)$_3$](BF_4)$_2$ (*c*-**B**-**Cl**) was synthesized in quantitative yield by stirring a mixture of *c*-**B** in CD_3CN (0.7 µmol, 906.7 µL) and NBu_4Cl (1.4 µmol, 99.3 µL of a 15 mM stock solution in CD_3CN) at room temperature for 30 min. in a closed vial to yield 1000 µl of a 0.7 mM solution of *c*-**B**-**Cl**. For better analysis, only one enantiomer pure ((R)-*c*-**B**-**Cl**) NMR spectra here is given. ^{1}H NMR (600 MHz, CD_3CN): δ = 10.21 (dd, *J* = 8.6 Hz, 4.3 Hz, 4H), 10.13 (d, *J* = 8.7 Hz, 2H), 10.10 (s, 2H), 10.02 (s, 2H), 9.71 (s, 2H), 9.09 (s, 4H), 8.91 (s, 2H), 8.44 (dddd, *J* = 10.2, 8.5, 7.0, 1.4 Hz, 4H), 8.10 (m, 4H), 8.06 (m, 2H), 7.91 (m, 4H), 7.87 (m, 2H), 7.66 (m, 2H), 7.20 (s, 4H), 7.08 (s, 2H), 2.48 (s, 6H), 2.44 (s, 6H), 2.43 (s, 6H). ESI-HRMS calculated for [2Cl@Pd_2(*c*-$\mathbf{L^a}$)$_3$]$^{2+}$ *m/z* = 1075.8412, found *m/z* = 1075.5370.

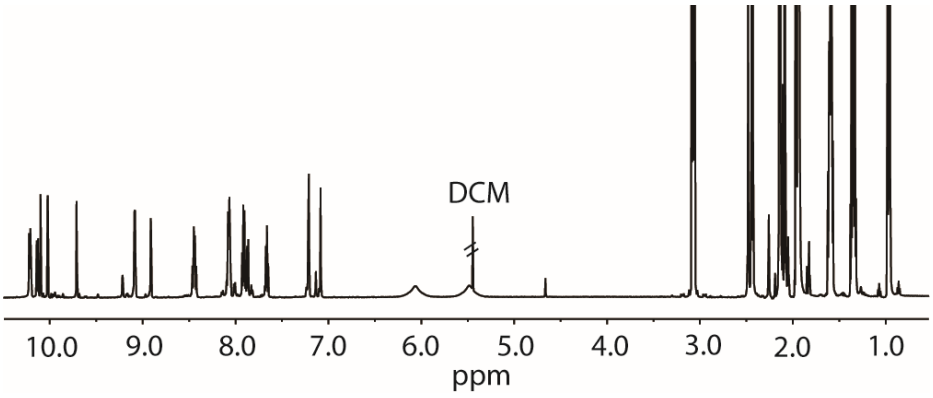

Figure 3.35 ^{1}H NMR spectrum (600 MHz, CD_3CN**)** of (*R*)-*c*-**B**-**Cl**.

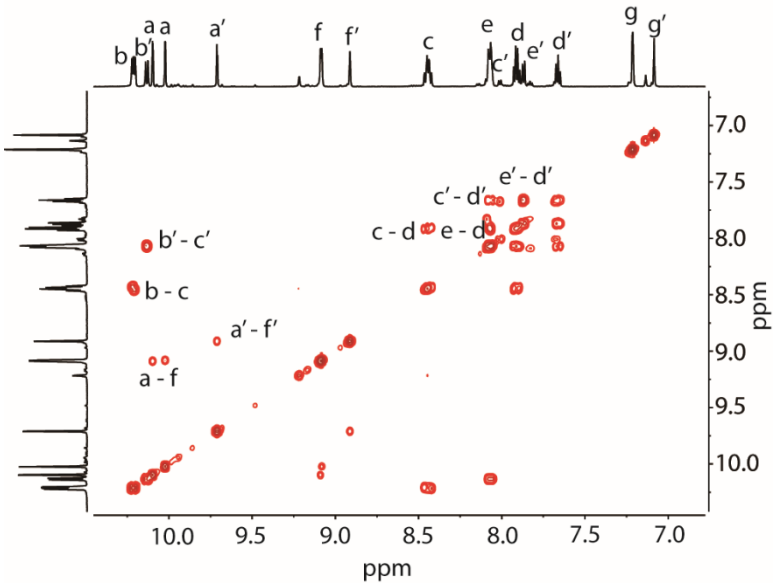

Figure 3.36 ^{1}H–^{1}H COSY spectrum (600 MHz, CD_3CN) of (*R*)-*c*-**B**-**Cl** (only showing aromatic region).

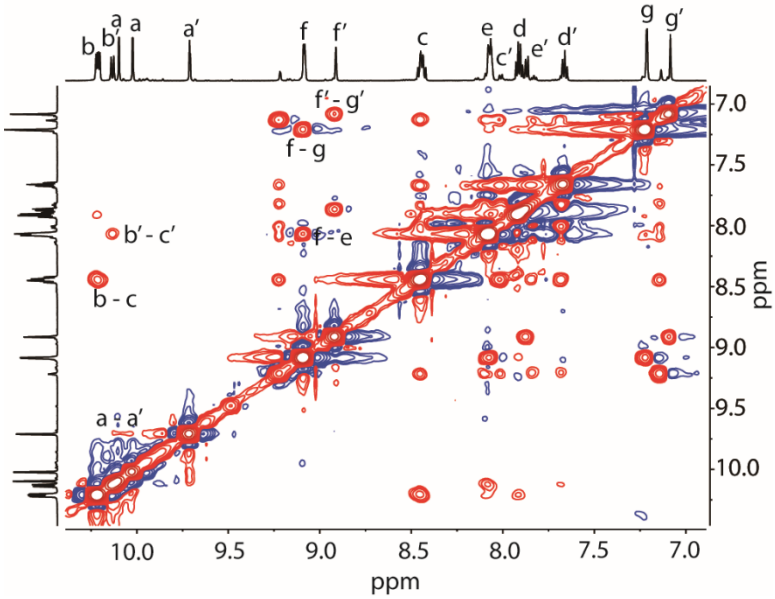

Figure 3.37 ^{1}H–^{1}H NOESY spectrum (600 MHz, CD_3CN) of (*R*)-*c*-**B**-**Cl** (only showing aromatic region).

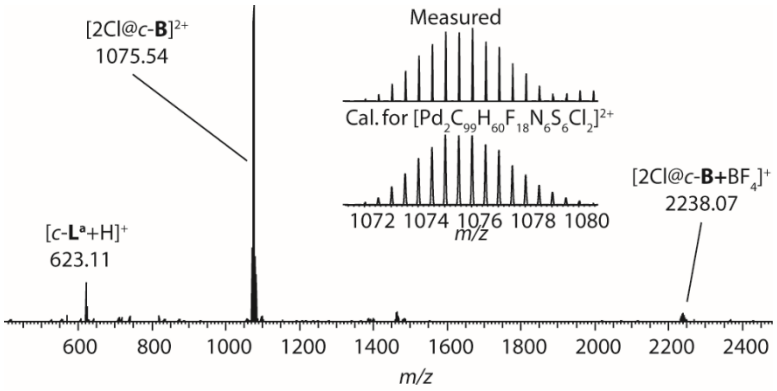

Figure 3.38 ESI-HRMS spectrum of *c*-**B**-**Cl**.

3.9.2.2.4 Synthesis of [2Br@Pd₂(c-L^a)₃](BF₄)₂ (c-B-Br)

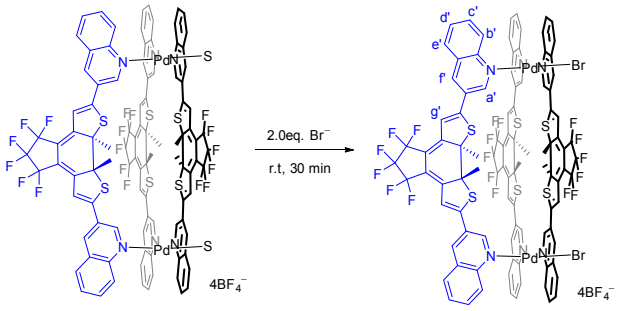

Scheme 2.7 Synthesis of *c*-**B**-**Br**.

The closed bowl compound [2Br@Pd_2(*c*-$\mathbf{L^a}$)$_3$](BF_4)$_2$ (*c*-**B**-**Br**) was synthesized in quantitative yield by stirring a mixture of the *c*-**B** in CD_3CN (0.7 µmol, 906.7 µL) and NBu_4Br (1.4 µmol, 99.3 µL of a 15 mM stock solution in CD_3CN) at room temperature for 30 min. in a closed vial to yield 1000 µl of a 0.7 mM solution of *c*-**B**-**Br**. For better analysis, only one enantiomer pure ((*R*)-*c*-**B**-**Br**) NMR spectra here are given. ^{1}H NMR (600 MHz, CD_3CN): δ = 10.19 (m, 4H), 10.12 (s, 2H), 10.10 (d, *J* = 8.5 Hz, 2H), 10.05 (s, 2H), 9.67 (s, 2H), 9.08 (s, 4H), 8.91 (s, 2H), 8.44 (dddd, *J* = 10.2, 8.5, 7.0, 1.4 Hz, 4H), 8.06 (m, 4H), 8.03 (m, 2H), 7.91 (m, 4H), 7.86 (m, 2H), 7.65 (ddd, *J* = 8.1, 7.2, 1.0 Hz, 2H), 7.22 (s, 4H), 7.08 (s, 2H), 2.47 (s, 6H), 2.45 (s, 6H), 2.43 (s, 6H). ESI-HRMS calculated for [2Br@Pd_2(*c*-$\mathbf{L^a}$)$_3$]$^{2+}$ *m/z* = 1119.9663, found *m/z* = 1119.9854.

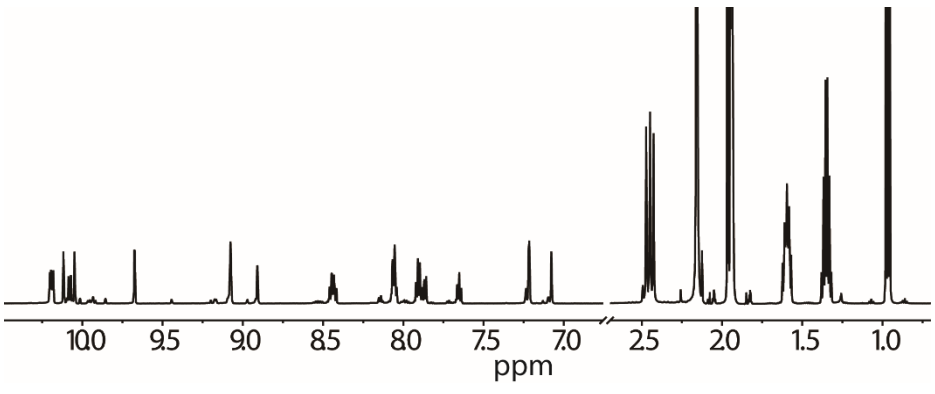

Figure 3.39 ^{1}H NMR spectrum (600 MHz, CD_3CN) of (*R*)-*c*-**B**-**Br**.

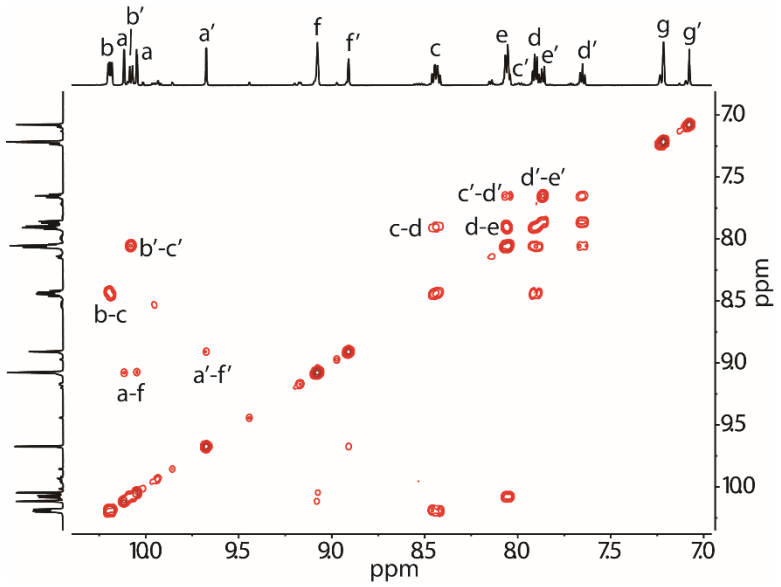

Figure 3.40 ^{1}H–^{1}H COSY spectrum (600 MHz, CD_3CN) of (*R*)-*c*-**B**-**Br** (only showing aromatic region).

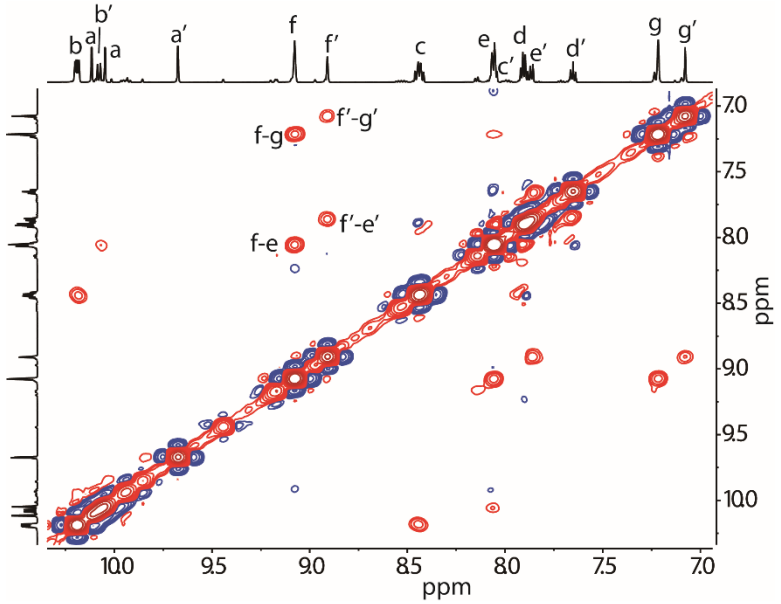

Figure 3.41 ^{1}H–^{1}H NOESY spectrum (600 MHz, CD_3CN) of (*R*)-c-**B**-**Br** (only showing aromatic region).

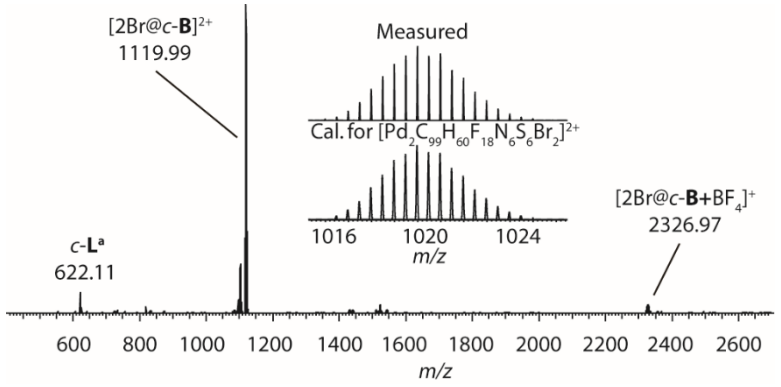

Figure 3.42 ESI-HRMS spectrum of *c*-**B**-**Br**.

3.9.2.3 Heterolotic cage synthesis

3.9.2.3.1 Synthesis *of* [Pd_2(*c*-**L**^{a})$_3$(*o*-**L**^{c})$_3$](BF$_4$)$_4$ (*c*-**B**-**L**^{c})

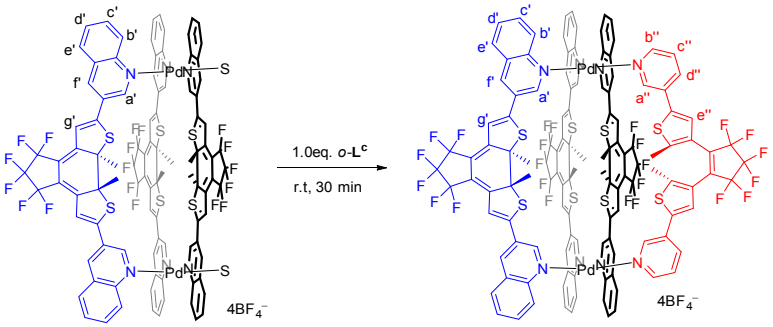

Scheme 2.8 Synthesis of *c*-**B**-**L**^{c}.

The heteroleptic cage compound [Pd_2(*c*-**L**^{a})$_3$(*o*-**L**^{c})](BF$_4$)$_4$ (*c*-**B**-**L**^{c}) was synthesized in quantitative yield by stirring a mixture of the *c*-**B** in CD_3CN (0.7 µmol, 976.67 µL) and *o*-**L**^{c} (0.7 µmol, 23.33 µL of a 30 mM stock solution in CD_3CN) at room temperature for 30 min. in a closed vial to yield 1000 µl of a 0.7 mM solution of *c*-**B**-**L**^{c}. For better analysis, only one enantiomer pure ((*R*)-*c*-**B**-**L**^{c}) NMR spectra here are given. ^{1}H NMR (600 MHz, CD_3CN) δ = 10.38 (b, 2H), 10.12 (b, 2H), 9.92 – 9.75 (m, 10H), δ 9.13 (s, 2H), 9.11 (s, 2H), 8.99 (s, 2H), 8.86 (b, 2H), 8.65 – 8.54 (m, 4H), 8.19 (dt, *J* = 8.3, 1.5 Hz, 2H), 8.16 – 8.11 (m, 4H), 8.08 (d, *J* = 7.8 Hz, 2H), 8.00 – 7.93 (m, 4H), 7.92 (dd, *J* = 8.2, 1.4 Hz, 2H), 7.72 (ddd, *J* = 8.1, 7.2, 0.9 Hz, 2H), 7.50 (s, 2H), 7.47 (dd, *J* = 8.0, 5.9 Hz, 2H), 7.20 (s, 2H), 7.14 (s, 4H), 2.49 (s, 6H), 2.43 (s, 6H), 2.39 (s, 6H), 1.87 (s, 6H). ESI-HRMS calculated for [Pd_2(*c*-**L**^{a})$_3$(*o*-**L**^{c})+BF$_4$]$^{3+}$ *m/z* = 896.3899, found *m/z* = 629.3913.

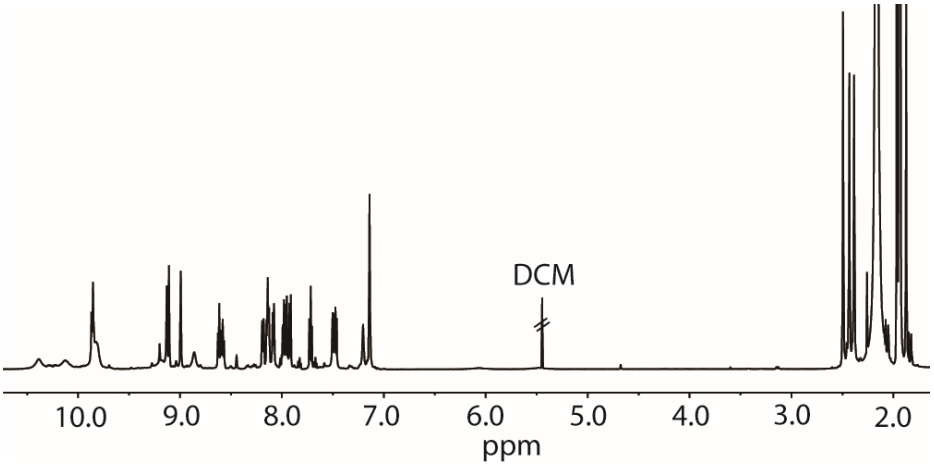

Figure 3.43 ^{1}H NMR spectrum (600 MHz, CD_3CN) of (*R*)-*c*-**B**-**L**^{c}.

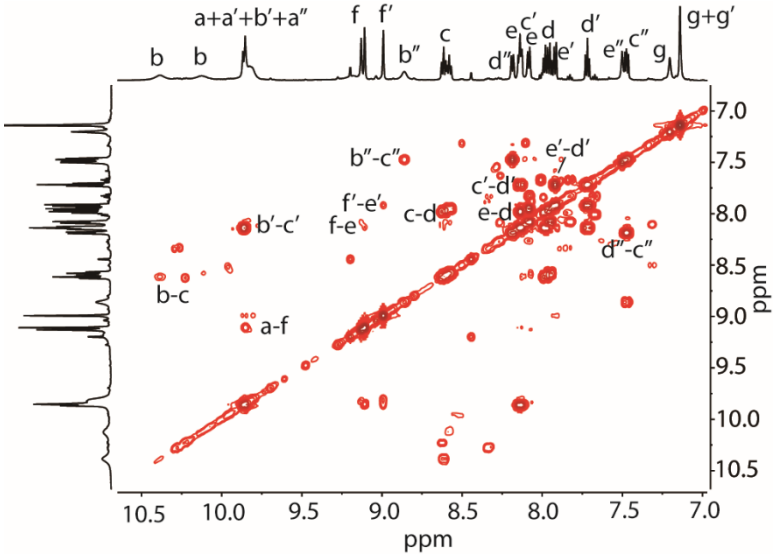

Figure 3.44 ^{1}H–^{1}H COSY spectrum (600 MHz, CD_3CN) of (*R*)-*c*-**B**-**L**^{c} (only showing aromatic region).

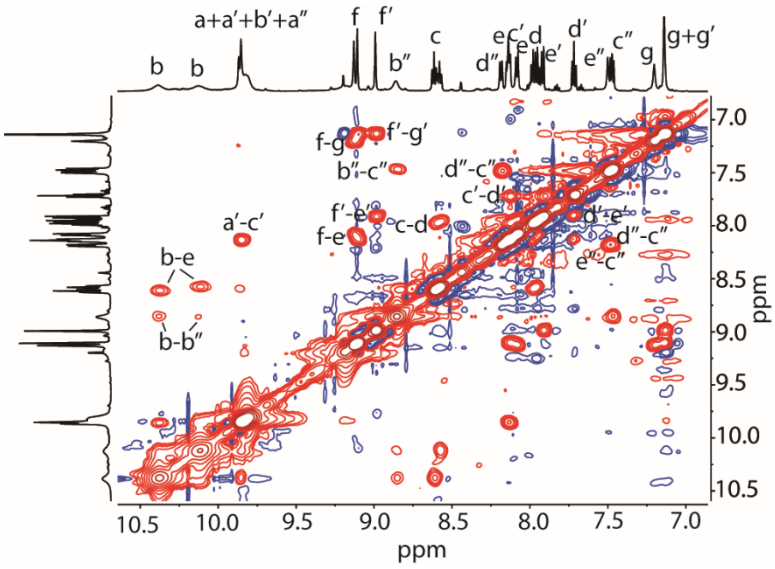

Figure 3.45 ^{1}H–^{1}H NOESY spectrum (600 MHz, CD_3CN) of (*R*)-*c*-**B**-**L**^{c} (only showing aromatic region).

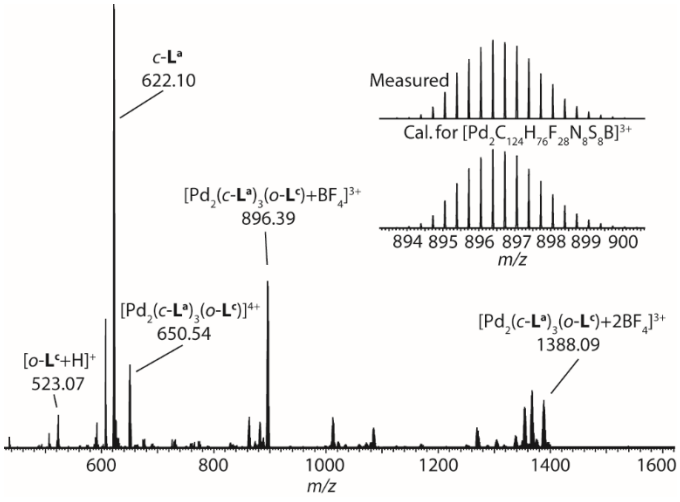

Figure 3.46 ESI-HRMS spectrum of *c*-**B**-**L**^{c}.

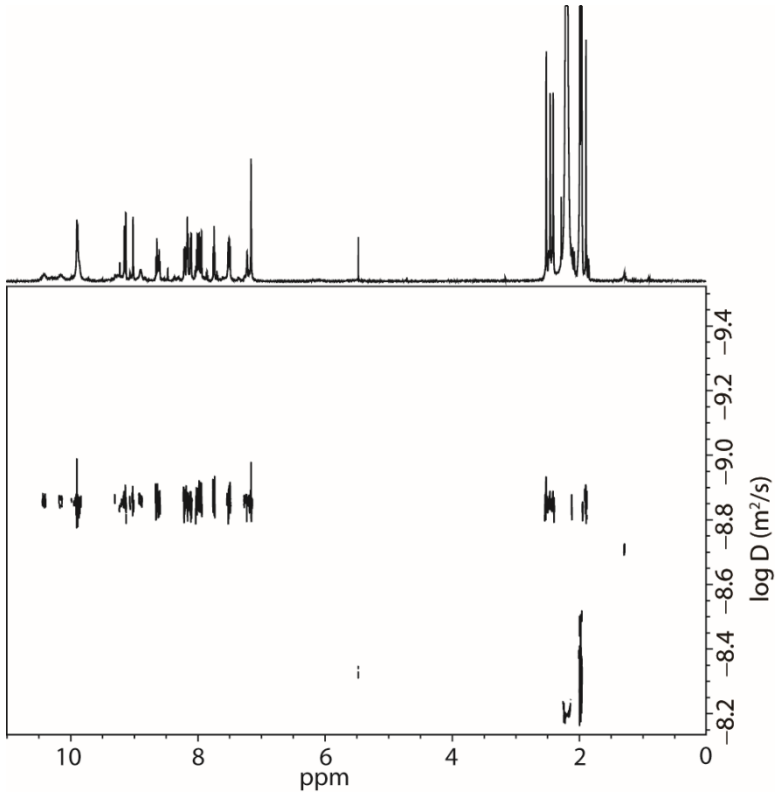

Figure 3.47 DOSY NMR spectrum of *c*-**B**-**L**^{c}.

3.9.2.3.2 Synthesis of [Pd$_2$(c-L^a)$_3$L^d](BF$_4$)$_4$ (c-B-L^d)

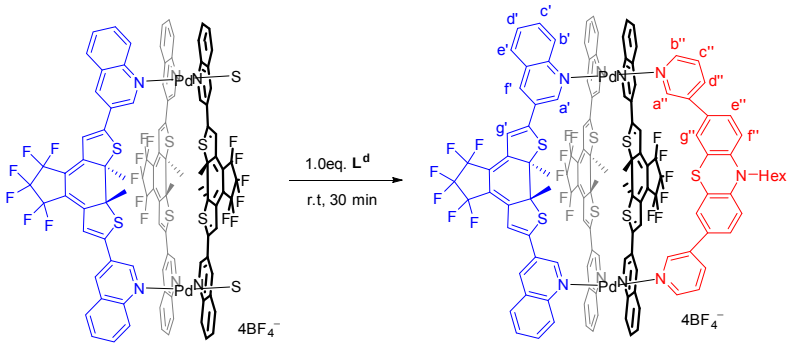

Scheme 2.9 Synthesis of *c*-**B**-**L**^{d}.

The heteroleptic cage compound [Pd$_2$(*c*-**L**^{a})$_3$**L**^{d}](BF$_4$)$_4$ (*c*-**B**-**L**^{d}) was synthesized in quantitative yield by stirring a mixture of *c*-**B** in CD$_3$CN (0.7 µmol, 976.7 µL) and **L**^{d} (0.7 µmol, 23.3 µL of a 4 mM stock solution in CD$_3$CN) at room temperature for 30 min. in a closed vial to yield 1000 µl of a 0.7 mM solution of *c*-**B**-**L**^{d}. For better analysis, only one enantiomer pure ((*R*)-*c*-**B**-**L**^{d}) NMR spectra here are given. ^{1}H NMR (600 MHz, CD$_3$CN): δ = 10.20 (d, *J* = 8.6 Hz, 2H), 10.14 (d, *J* = 8.6 Hz, 2H), 9.99 (d, *J* = 8.7 Hz, 2H), 9.79 (s, 2H), 9.76 (s, 2H), 9.55 (s, 2H), 9.28 (s, 2H), 9.09 (d, *J* = 5.9 Hz, 2H), 9.08 (s, 2H), 9.06 (s, 2H), 9.00 (s,2H), 8.53 (m, *J* = 8.6, 7.1, 1.4 Hz, 4H), 8.16 (d, 2H), 8.14 (d, 2H), 8.10 (d, *J* = 8.4 Hz, 4H), 8.08 (d, *J* = 8.7 Hz, 2H), 7.96 (m, 4H), 7.94 (m, 2H),7.5 (m, 2H), 7.64 (s, 2H), 7.51 (dd, *J* = 8.1, 5.9 Hz, 2H), 7.48 (dd, *J* = 8.6, 2.3 Hz, 2H), 7.14 (s,

2H), 7.13 (s, 4H), 7.06 (d, *J* = 8.5 Hz, 2H), 3.91 (t, *J* = 6.9 Hz, 2H), 2.50 (s, 6H), 2.46 (s, 6H), 2.43 (s, 6H), 1.68 (p, *J* = 7.2 Hz, 2H), 1.35 (t, *J* = 7.4 Hz, 2H), 1.23 – 1.16 (m, 4H), 0.82 – 0.73 (m, 3H). ESI-HRMS calculated for $[Pd_2(c\text{-}\mathbf{L}^{a})_3\mathbf{L}^{d}]^{4+}$ *m/z* = 629.5732, found *m/z* = 629.5746.

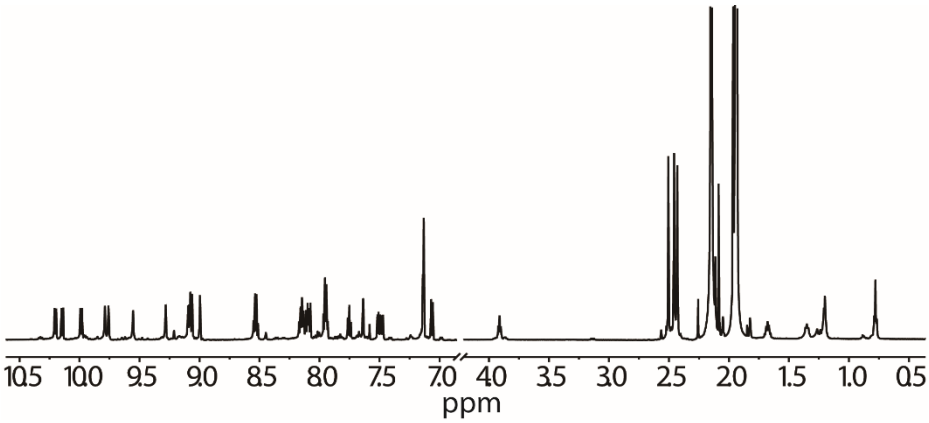

Figure 3.48 ^{1}H NMR spectrum (600 MHz, CD_3CN) of (*R*)-*c*-**B**-$\mathbf{L}^{d}$.

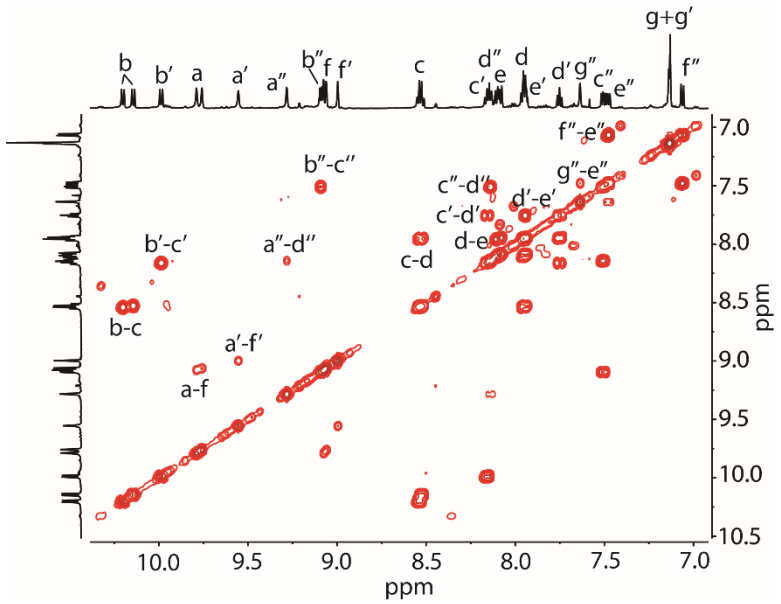

Figure 3.49 ^{1}H-^{1}H COSY spectrum (600 MHz, CD_3CN) of (*R*)-*c*-**B**-$\mathbf{L}^{d}$ (only showing aromatic region).

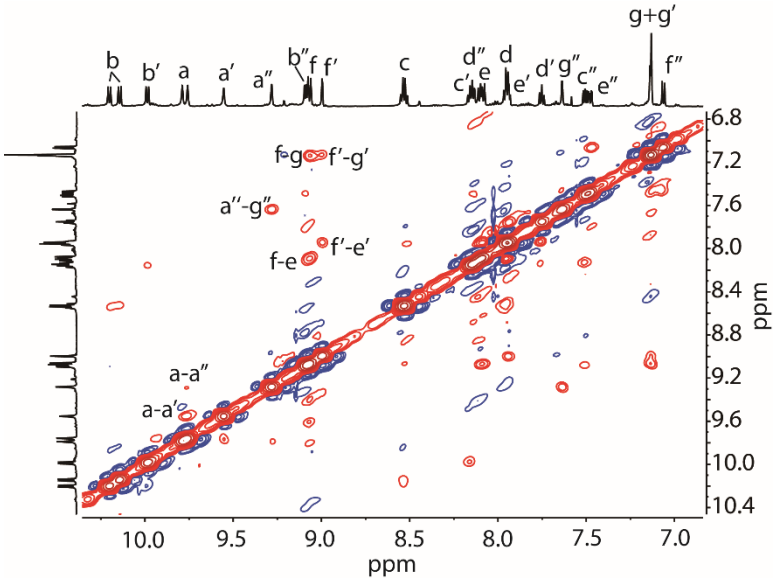

Figure 3.50 ^{1}H-^{1}H NOESY spectrum (600 MHz, CD_3CN) of (*R*)-*c*-**B**-$\mathbf{L^d}$ (only showing aromatic region).

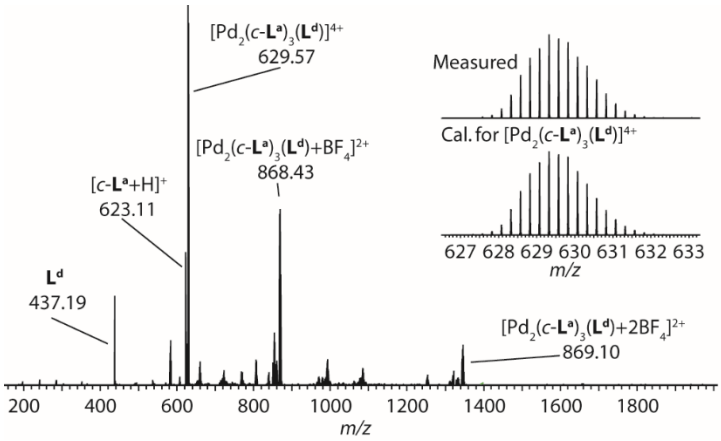

Figure 3.51 ESI-HRMS spectrum of (*R*)-*c*-**B**-$\mathbf{L^d}$.

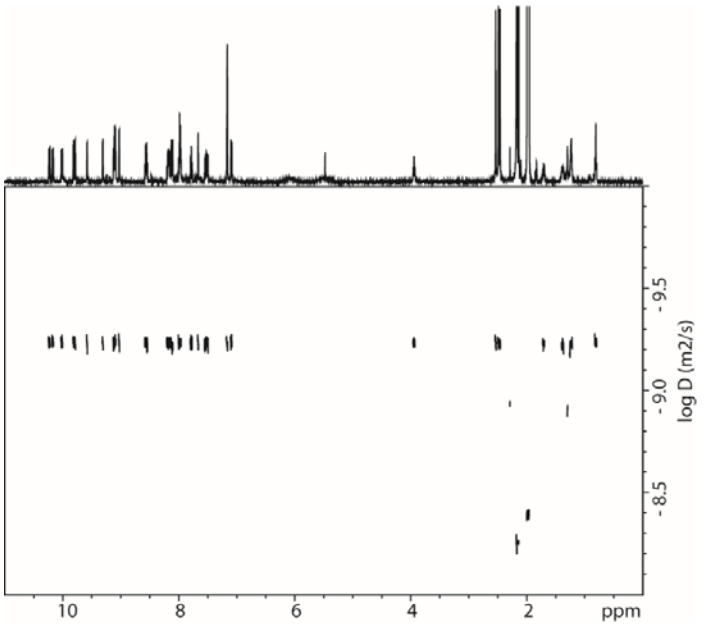

Figure 3.52 DOSY NMR spectrum (600 MHz, CD_3CN**)** of (*R*)-*c*-**B**-$\mathbf{L^d}$**.**

*3.9.2.3.3 Synthesis of [Pd$_2$(c-**L**^{a})$_3$(o-**L**^{e})](BF$_4$)$_4$ (c-**B**-**L**^{e})*

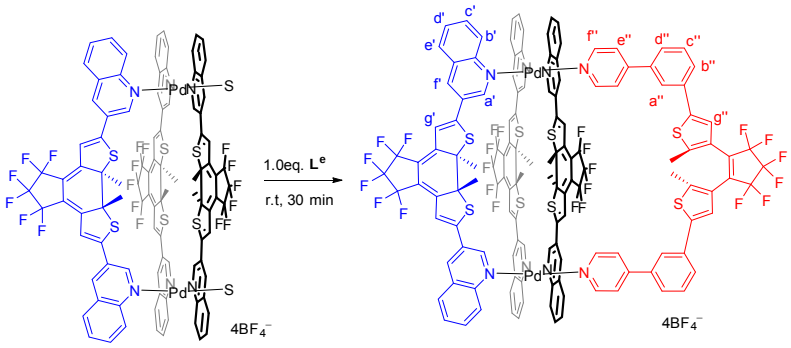

Scheme 2.10 Synthesis of *c*-**B**-**L**^{e}.

The heteroleptic cage compound [Pd$_2$(*c*-**L**^{a})$_3$(*o*-**L**^{e})](BF$_4$)$_4$ (*c*-**B**-**L**^{e}) was synthesized in quantitative yield by stirring a mixture of the *c*-**B** in CD$_3$CN (0.7 µmol, 976.7 µL) and *o*-**L**^{e} (0.7 µmol, 23.3 µL of a 4 mM stock solution in CD$_3$CN) at room temperature for 30 min. in a closed vial to yield 1000 µl of a 0.7 mM solution of *c*-**B**-**L**^{e}. For better analysis, only one enantiomer pure ((*R*)-*c*-**B**-**L**^{e}) NMR spectra here are given. ^{1}H NMR (600 MHz, CD$_3$CN): δ = 10.21 (s, 2H), 10.16 (d, *J* = 8.6 Hz, 2H), 10.14 (s, 2H), 10.12 (d, *J* = 8.7 Hz, 2H), 9.99 (d, *J* = 8.9 Hz, 1H), 9.73 (s, 2H), 9.12 (s, 4H), 8.94 (s, 2H), 8.61 (dd, 4H), 8.50 (dddd, *J* = 8.6, 7.2, 5.9, 1.4 Hz, 4H), 8.13 (m, 4H), 8.11 (m, 2H), 7.95 (dddd, *J* = 8.1, 7.1, 5.0, 0.9 Hz, 4H), 7.90 (m, 2H), 7.81 (ddd, *J* = 7.6, 1.8, 1.0 Hz, 2H), 7.72 (dd, *J* = 5.0, 3.4 Hz, 4H), 7.70 (d, *J* = 6.1 Hz, 2H), 7.63 (ddd, *J* = 8.0, 1.8, 1.0 Hz, 2H), 7.58 (s, 2H), 7.55 (t, *J* = 7.8 Hz, 2H), 7.35 (s, 2H), 7.16 (s, 2H), 7.14 (s, 2H),7.08 (s, 2H), 2.50 (s, 6H), 2.45 (s, 6H), 2.41 (s, 6H), 1.83 (s, 6H). ESI-HRMS calculated for [Pd$_2$(*c*-**L**^{a})$_3$(*o*-**L**^{e})+BF$_4$]$^{3+}$ *m/z* = 947.0763, found *m/z* = 947.0816.

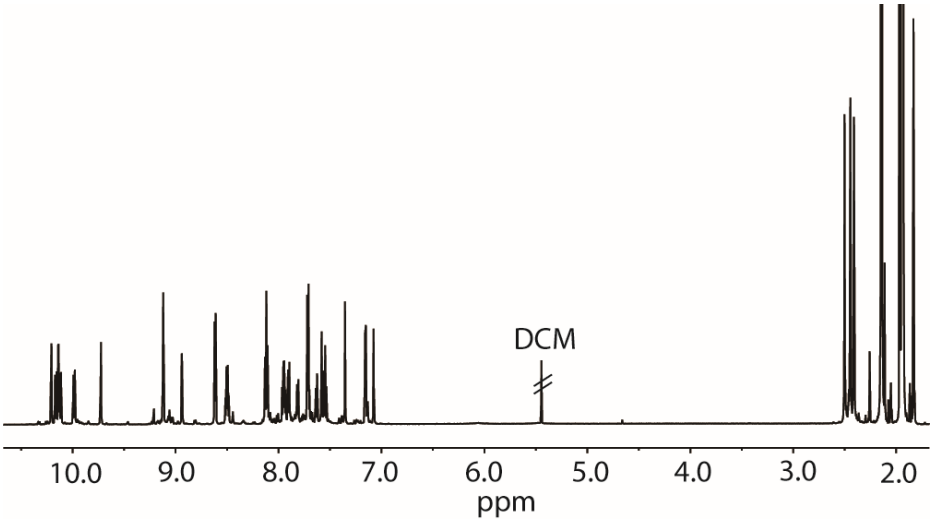

Figure 3.53 ^{1}H NMR spectrum (600 MHz, CD$_3$CN) of (*R*)-*c*-**B**-**L**^{e}.

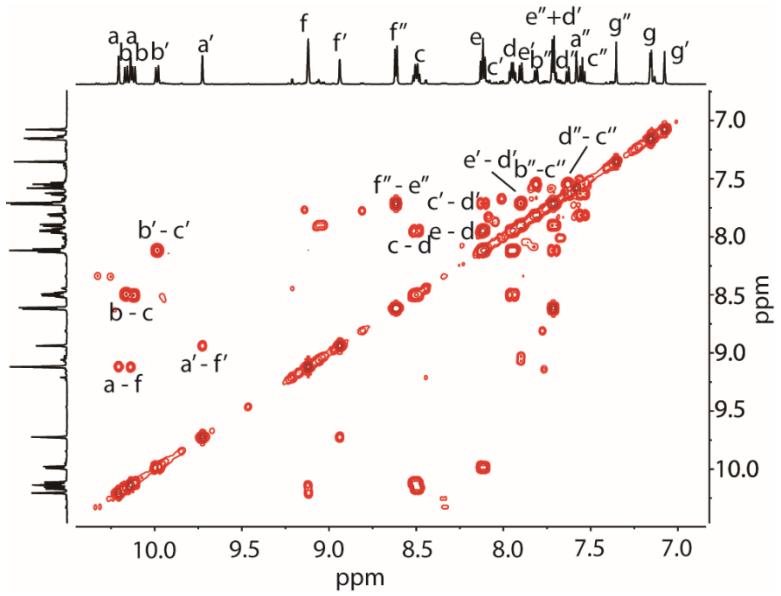

Figure 3.54 ^{1}H-^{1}H COSY spectrum (600 MHz, CD_3CN) of (*R*)-*c*-**B**-**L**^{e} (only showing aromatic region).

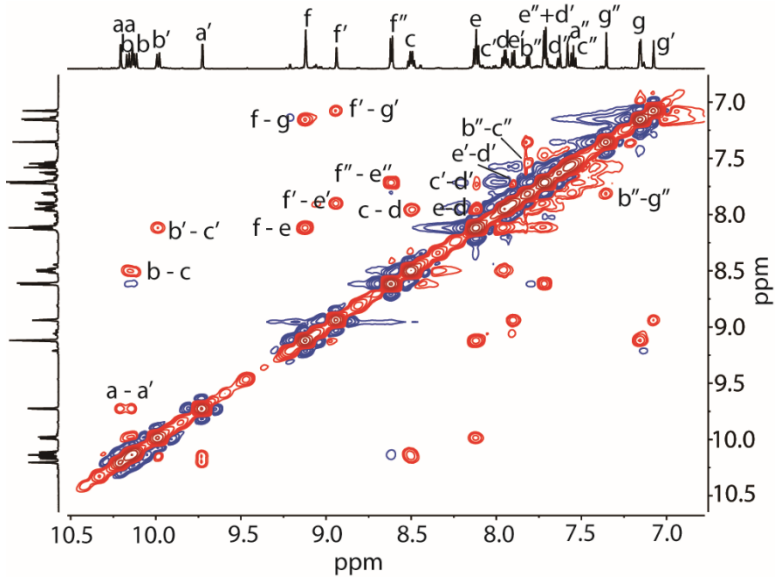

Figure 3.55 ^{1}H-^{1}H NOESY spectrum (600 MHz, CD_3CN) of (*R*)-*c*-**B**-**L**^{e} (only showing aromatic region).

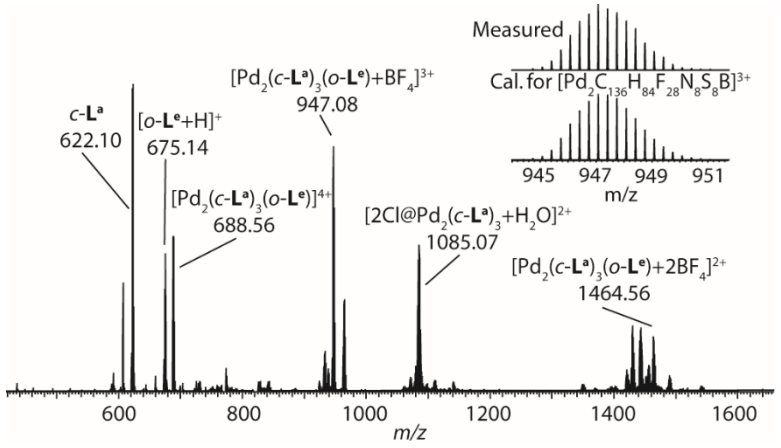

Figure 3.56 ESI-HRMS spectrum of (*R*)-*c*-**B**-**L**^{e}.

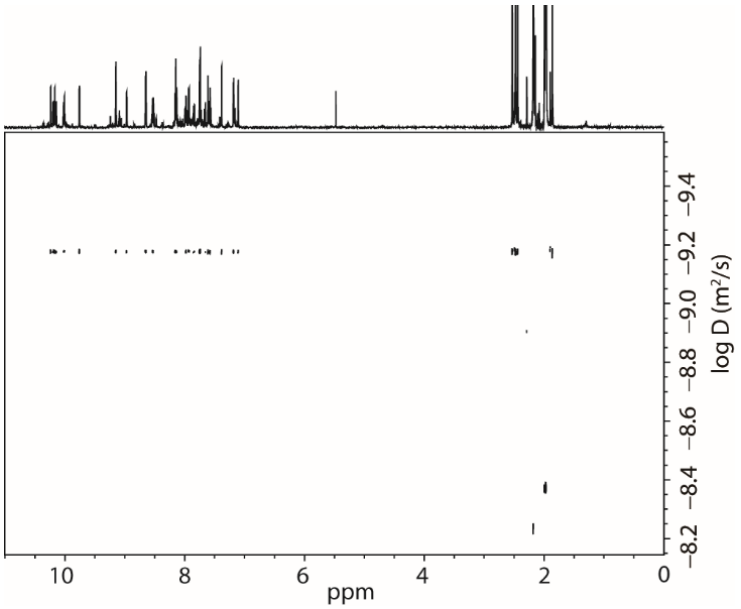

Figure 3.57 DOSY NMR spectrum of (*R*)-*c*-**B**-**L**^{e}.

*3.9.2.3.4 Synthesis of [Pd$_2$(c-**L**^{a})$_3$**L**^{f}](BF$_4$)$_4$ (c-**B**-**L**^{f})*

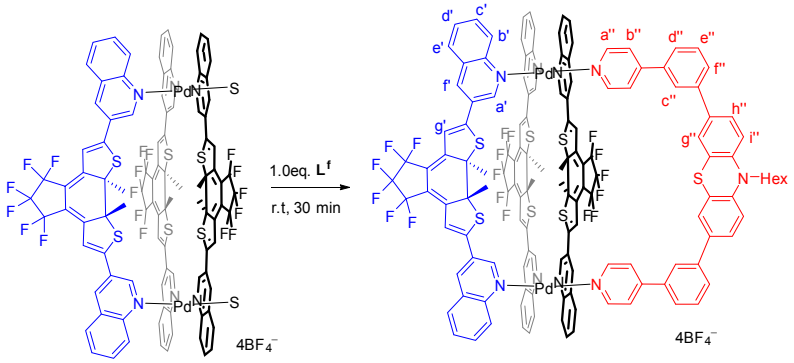

Scheme 2.11 Synthesis of *c*-**B**-**L**^{f}.

The heteroleptic cage compound [Pd$_2$(*c*-**L**^{a})$_3$(*o*-**L**^{f})](BF$_4$)$_4$ (*c*-**B**-**L**^{f}) was synthesized in quantitative yield by stirring a mixture of the *c*-**B** in CD$_3$CN (0.7 µmol, 976.7 µL) and **L**^{f} (0.7 µmol, 23.3 µL of a 4 mM stock solution in CD$_3$CN) at room temperature for 30 min. in a closed vial to yield 1000 µl of a 0.7 mM solution of *c*-**B**-**L**^{f}. For better analysis, only one enantiomer pure ((*R*)-*c*-**B**-**L**^{f}) NMR spectra here are given. ^{1}H NMR (600 MHz, CD$_3$CN): δ = 10.23 (s, 2H), 10.16 (s, 2H), 10.10 (d, *J* = 8.6 Hz, 2H), 10.05 (d, *J* = 8.6 Hz, 2H), 9.94 (d, *J* = 8.6 Hz, 2H), 9.72 (s, 2H), 9.12 (s, 4H), 8.94 (s, 2H), 8.57 (dd, 4H), 8.46 (tdd, *J* = 8.8, 7.1, 1.4 Hz, 4H), 8.11 (m, 4H), 8.09 (dd, *J* = 8.7, 1.4 Hz, 2H), 7.94 (m, 4H), 7.91 (m, 2H), 7.89 (m, 2H), 7.77 (dd, 4H), 7.73 (m, 2H), 7.71 (m, 2H), 7.63 (ddd, *J* = 8.0, 1.9, 1.0 Hz, 2H), 7.55 (t, *J* = 7.8 Hz, 2H), 7.49 (d, *J* = 2.2 Hz, 2H), 7.47 (dd, *J* = 8.4, 2.3 Hz, 2H), 7.16 (s, 2H), 7.14 (s, 2H), 7.08 (s, 2H), 7.03 (d, *J* = 8.3 Hz, 2H), 3.92 (t, *J* = 7.1 Hz, 2H), 2.50 (s, 6H), 2.45 (s, 6H), 2.41 (s, 6H), 1.75 (p, *J* = 7.3 Hz, 2H), 1.41 (q, *J* =

7.2 Hz, 2H), 1.27 (dt, *J* = 7.2, 3.7 Hz, 4H), 0.83 (td, *J* = 5.8, 4.6, 3.1 Hz, 3H). ESI-HRMS calculated for $[Pd_2(c\text{-}\mathbf{L}^{\mathbf{a}})_3\mathbf{L}^{\mathbf{f}}+BF_4]^{3+}$ *m/z* = 918.7851, found *m/z* = 918.7906.

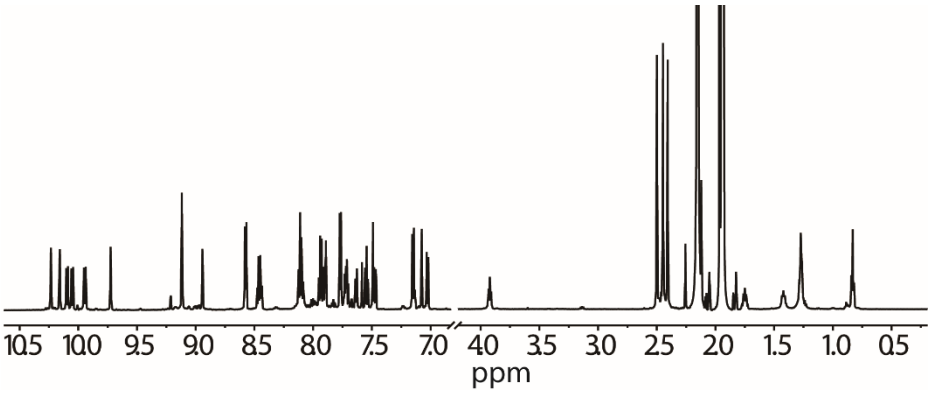

Figure 3.58 ^{1}H NMR spectrum (600 MHz, CD_3CN) of (*R*)-*c*-**B**-$\mathbf{L}^{\mathbf{f}}$.

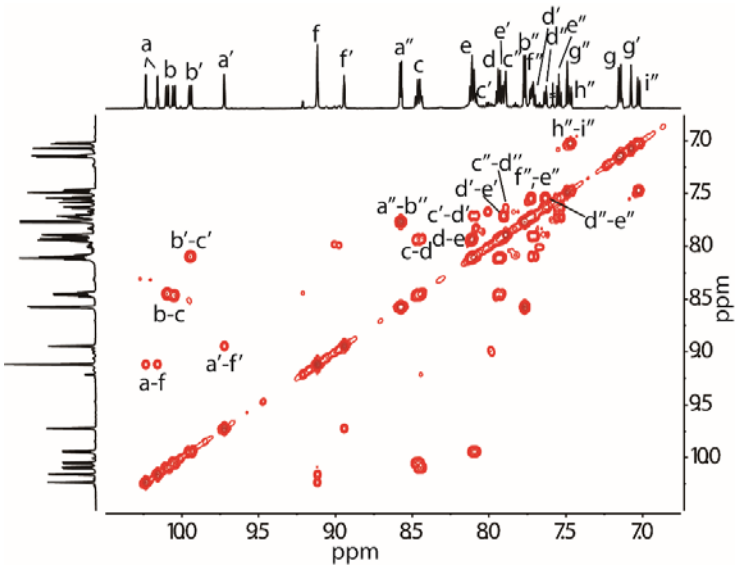

Figure 3.59 ^{1}H-^{1}H COSY spectrum (600 MHz, CD_3CN) of (*R*)-*c*-**B**-$\mathbf{L}^{\mathbf{f}}$ (only showing aromatic region).

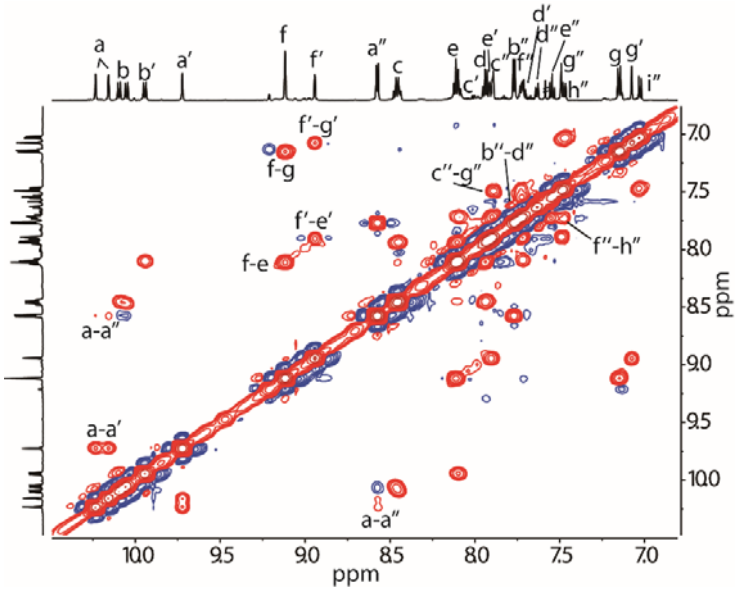

Figure 3.60 ^{1}H-^{1}H NOESY spectrum (600 MHz, CD_3CN) of (*R*)-*c*-**B**-$\mathbf{L}^{\mathbf{f}}$ (only showing aromatic region).

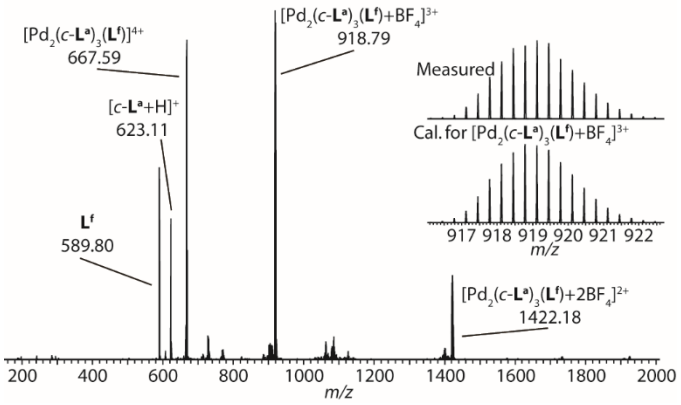

Figure 3.61 ESI-HRMS spectrum of (*R*)-*c*-**B**-**L^{f}.**

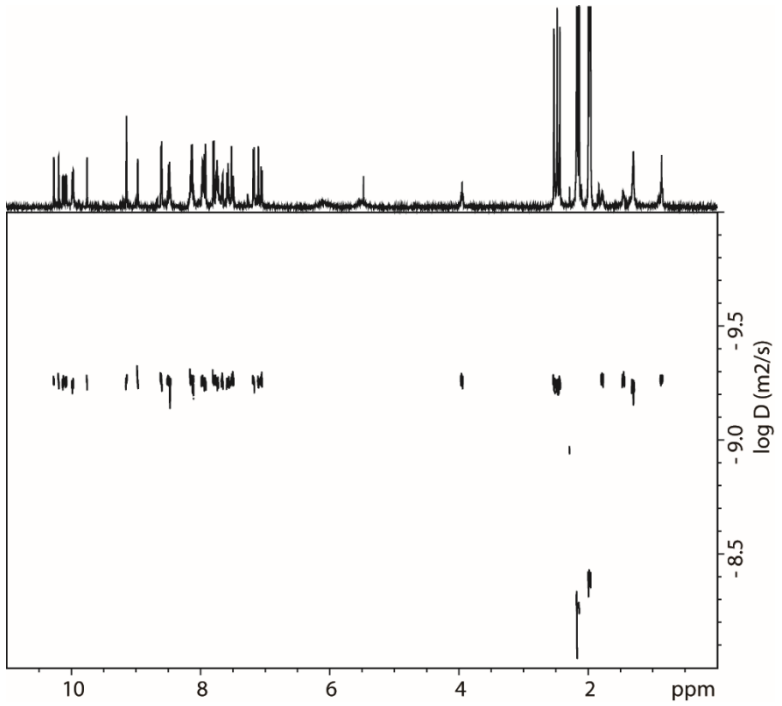

Figure 3.62 DOSY NMR spectrum of (*R*)-*c*-**B**-**L^{f}**.

3.9.3 Symmetry considerations

As similar analytical method as our previous reported cage,[13] there are 6 possible stereoisomers of the bowl like complex *c*-**B**: three pairs of enantiomers *PPP*/*MMM* (I), *PMM*/*MPP* (II) and *PMP/MPM* (III) that differ in the chirality (*P* or *M*) of the *C*2-symmetric ligands *c*-**L^{a}** occupying the three positions around the two metal centers. According to a statistical analysis based on the assumption that all isomers are energetically equal, their ratio (I) : (II) : (III) is (1+1) : (2+2) : (1+1) (Σ=8). However, for each enantiomer *PMM*/*MPP* (II), there have two different top views (two half different chemical environment). Therefore, there would have four different chemical environments of *c*-**B** with 2 : 2 : 2 : 2 ratio (see the following figure). Which was consistent with the

experimental ^{1}H NMR spectrum of *c*-**B**. We can clearly see the four sets NMR splitting, especially the signals of $H_{a'}$ and $H_{g'}$ from ^{1}H NMR spectrum, giving 1 : 1 : 1 : 1 ratio.

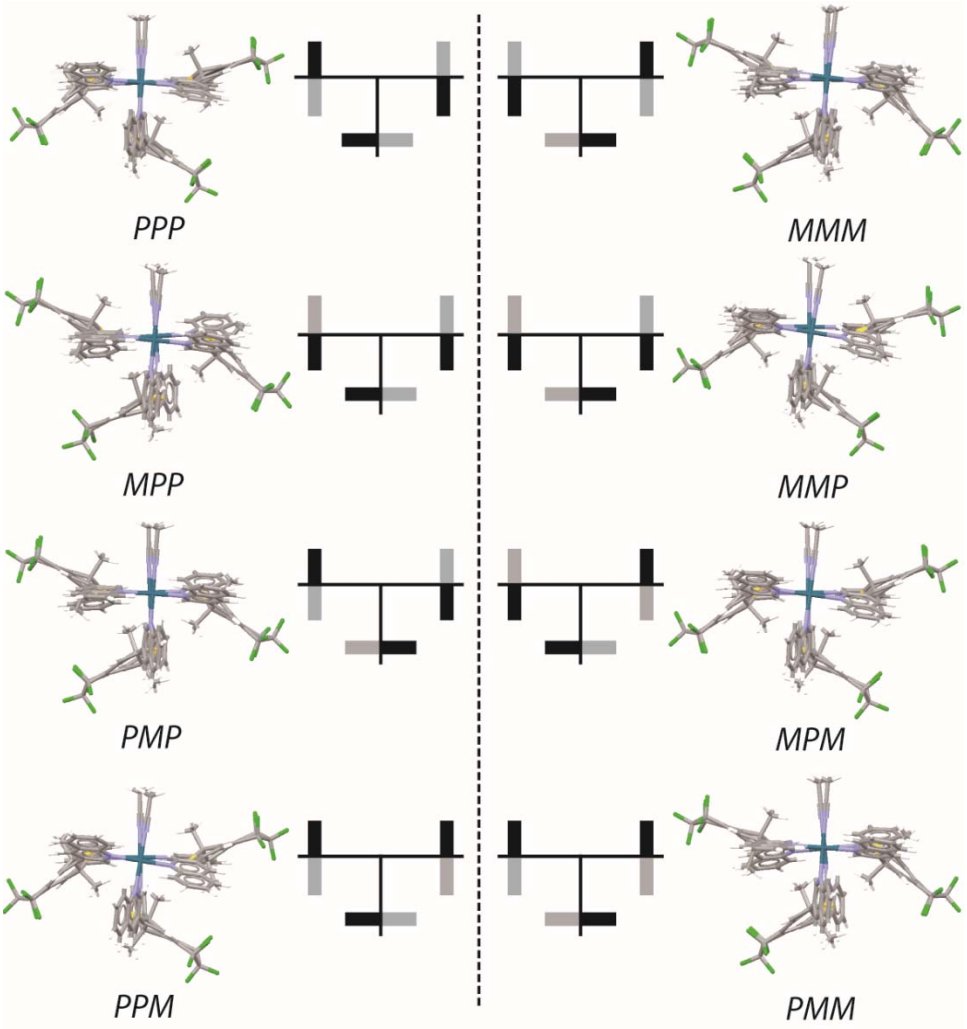

Figure 3.63 All possible bowl isomeric structures (built using the software Spartan) and their corresponding stereo-chemical relationships between the three ligands viewed from the top (black/gray bars: close/remote methyl groups).

3.9.4 Determination of absolute configuration

The open-form ligand *o*-**L^a** (10 mg) was dissolved in CD_2Cl_2 (1 mL) and then irradiated with 313 nm UV light. The pure (*R, R*) and (*S, S*) ligand enantiomers were separated by preparative chiral HPLC using a Daicel IC column (250 x 10 mm) under strict exclusion of daylight. The purity of separated **1** (the first fraction of HPLC) and **2** (the second fraction of HPLC) enantiomers were checked using analytical HPLC using a Daicel IA column (250 x 4.6 mm). In order to determine the absolute stereochemistry of the enantiomers, CD spectra were measured and compared to those calculated by TD-DFT methods at the B3LYP/6-31G(d) level of theory in the Gaussian 09 software[14] (using keyword iop(9/40=2)).

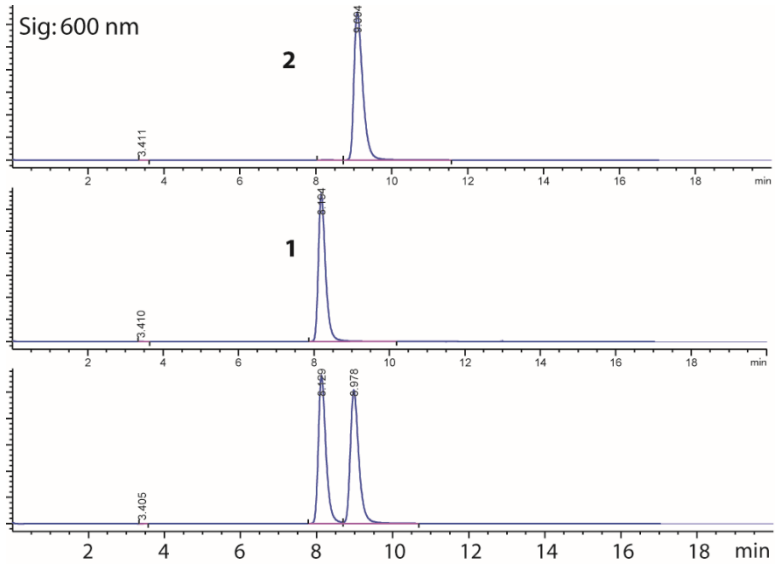

Figure 3.64 Chiral HPLC chromatograms of racemic *c*-**L**[a]. (Chromatographic column: Daicel IC. Mobile phase: Hexane/ CH_2Cl_2/Methanol = 60 : 39.1 : 0.9. Run time: 20 min. Flow rate: 1.0 mL/min).

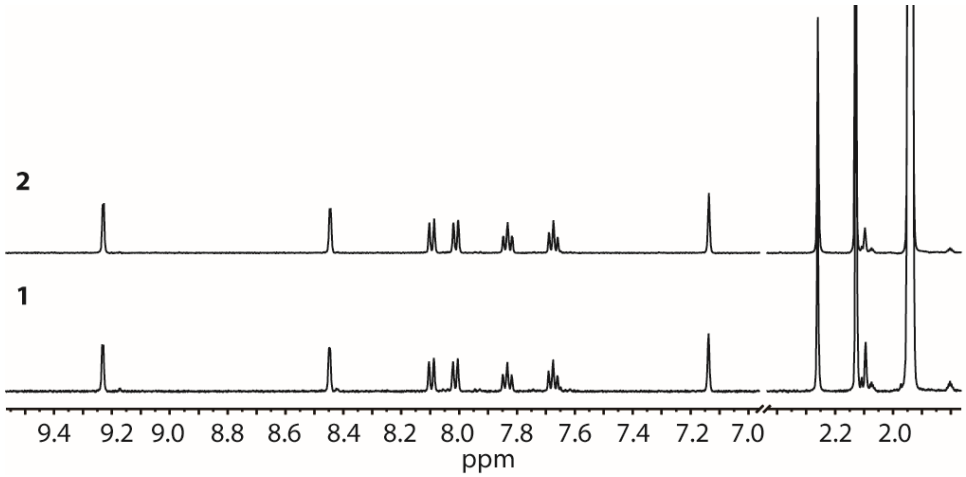

Figure 3.65 ^{1}H NMR spectra of enantiomeric pure fraction **1** and fraction **2**.

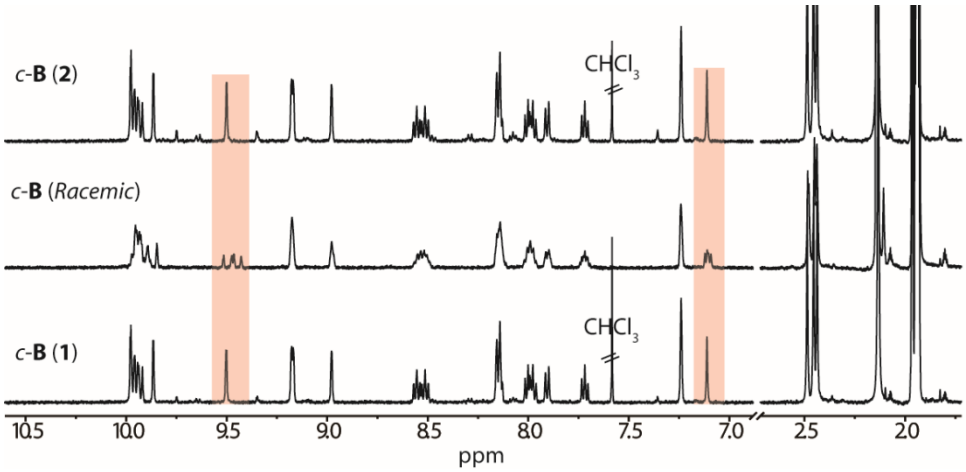

Figure 3.66 ^{1}H NMR spectra of racemic *c*-**B** and enantiomeric pure *c*-**B** (**1**) and *c*-**B** (**2**) made from enantiomerically pure ligands **1** and **2**, respectively. As can be seen, the signals of the enantiomeric pure cages *c*-**B** are much clearer and sharper than those of the racemic mixture of all possible *c*-**B** diastereomers. And from the red marked signals, there are four times ^{1}H NMR diastereomeric splitting, which was consistence with symmetry analysis above.

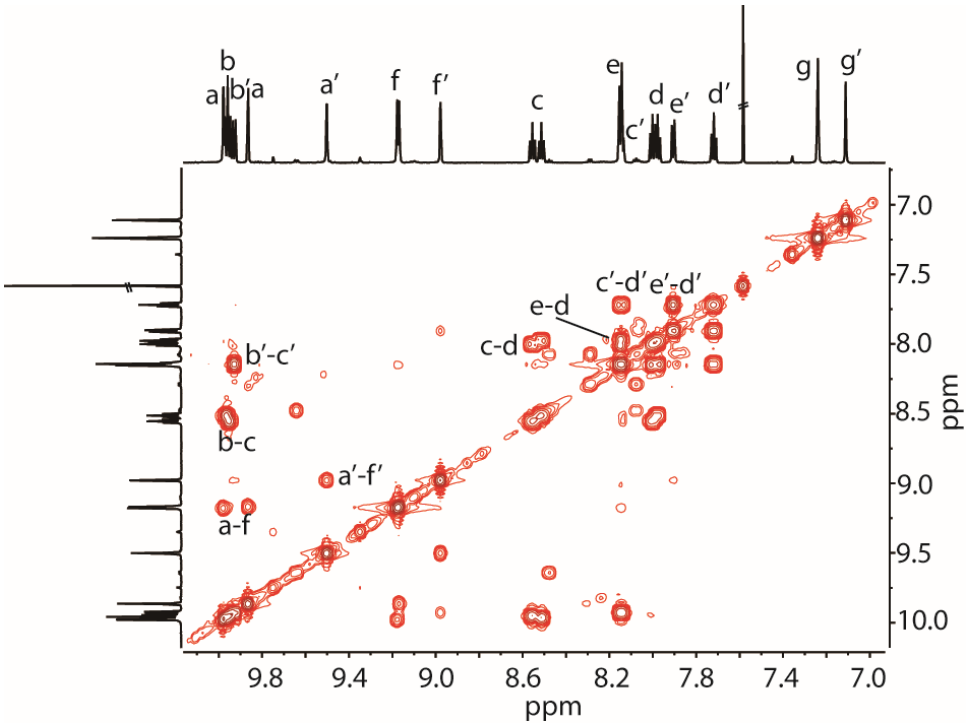

Figure 3.67 ^{1}H–^{1}H COSY spectrum (600 MHz, CD_3CD) of *c*-**B** (**1**) (only showing aromatic region).

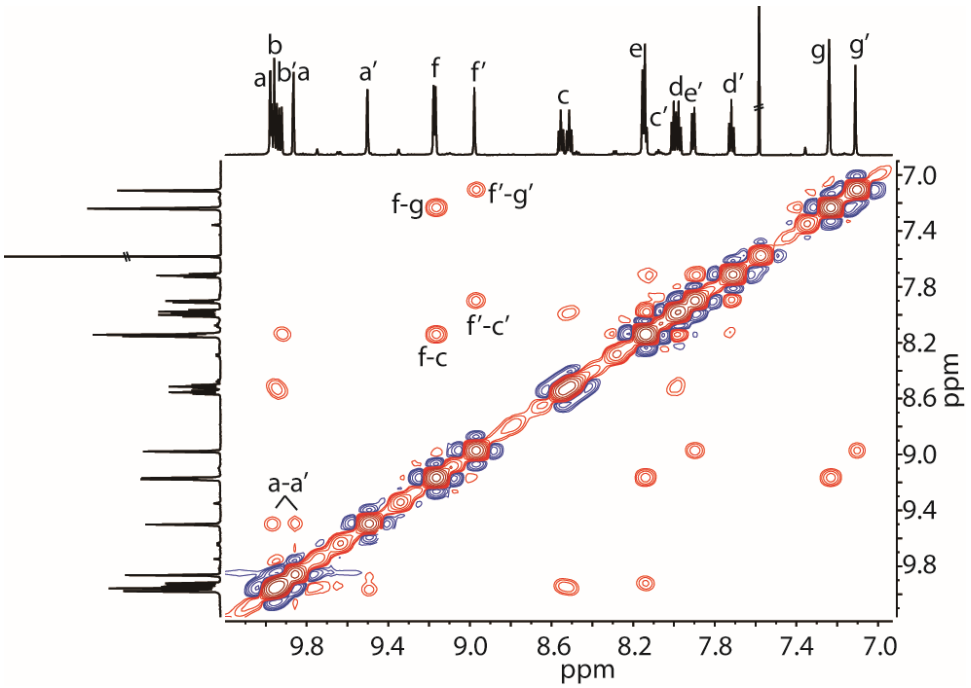

Figure 3.68 ^{1}H–^{1}H NOESY spectrum (600 MHz, CD_3CD) of *c*-**B** (**1**) (only showing aromatic region).

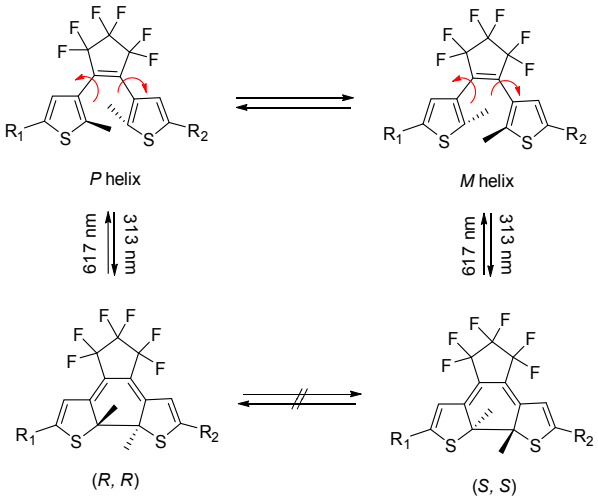

Scheme 2.12. Photoisomerization of a diarylethene (DTE). The photocyclization reactions from *P*- and *M*-helical conformers of the open-ring isomer produce (*R, R*) and (*S, S*) enantiomers of the closed-ring isomer, respectively.

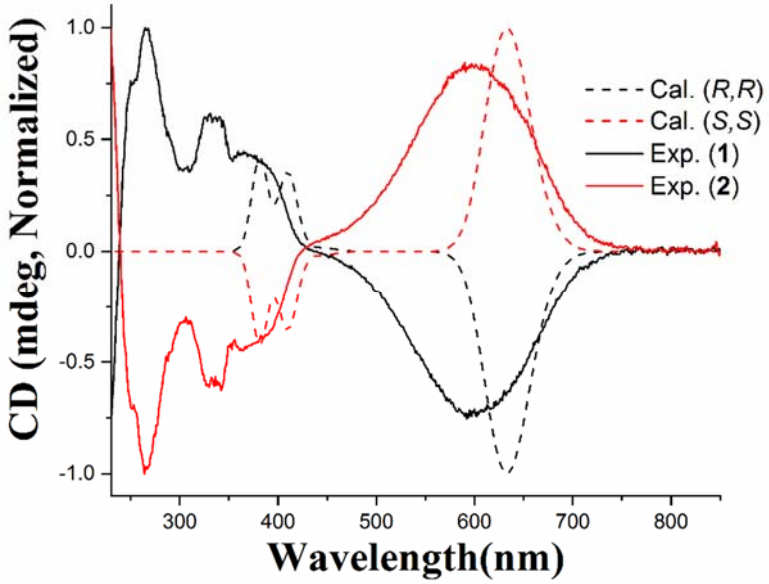

Figure 3.69 a) Calculated CD spectra of (*R, R*) and (*S, S*) closed form ligand enantiomers and measured CD spectra of closed ligand enantiomers from chiral HPLC resolved fraction **1** and **2** (0.1 mM, CH_3CN). Both of the calculated CD spectrum of *c*-**L**[a] (*R, R*) and fraction **1** give negative cotton effect from 500 nm to 800 nm (this area shows the characteristic peak of closed form DTE derives), which means fraction **1** has *R, R* configuration, in contrast, fraction **2** is *S, S* configuration.

3.9.5 Computational studies

All models were constructed using SPARTAN[19] and were first optimized on a PM6 level of theory (no counter ions were included) without constrains. The resulting structures were than further refined by DFT calculations (B3LYP/LANL2DZ) using Gaussain 09 software.[14]

3.9.5.1 Optimized structure of heteroleptic cage

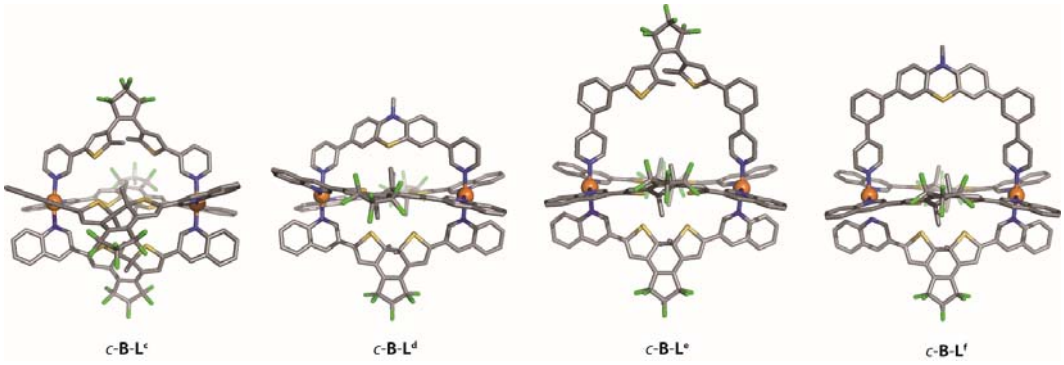

Figure 3.70 DFT energy minimized structures of *c*-**B**-**L**^{c}, *c*-**B**-**L**^{d}, *c*-**B**-**L**^{e} and *c*-**B**-**L**^{f}.

3.9.5.2 Comparison of the energy between cage and bowl structures

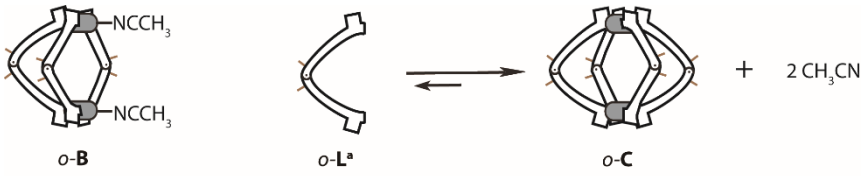

$\Delta E = \Sigma_{products} - \Sigma_{reactants} = -0.05233194$ Ha $= -137.40$ kJ/mol

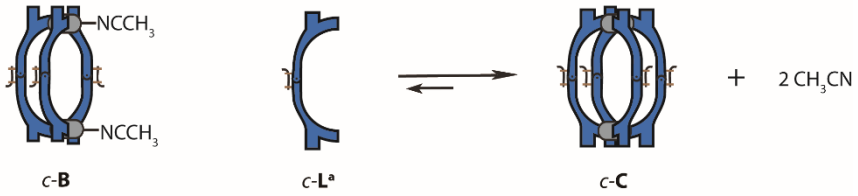

$\Delta E = \Sigma_{products} - \Sigma_{reactants} = -0.0547741$ Ha $= -143.81$ kJ/mol

Figure 3.71 Scheme showing reaction equation between cage & bowl and their reaction energies as obtained from respective DFT minimized structures.

3.9.6 Titration

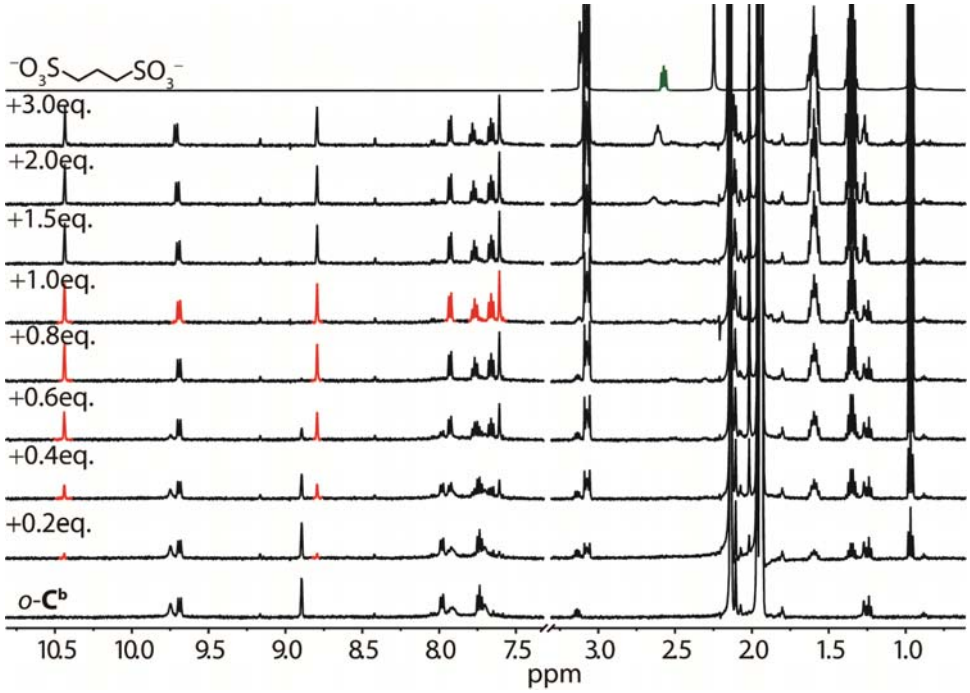

Figure 3.72 ^{1}H NMR titration (500 MHz, 298 K, CD_3CN) of ***o*-C^{a}** with $(NBu_4)_2$**G1**. Upon addition of one equivalent of guest **G1**, the ***o*-C^{a}** cage transforms into [**G1**@***o*-C^{a}**]. Excess addition of **G1** leads to precipitation. New set of NMR signals are highlighted in red.

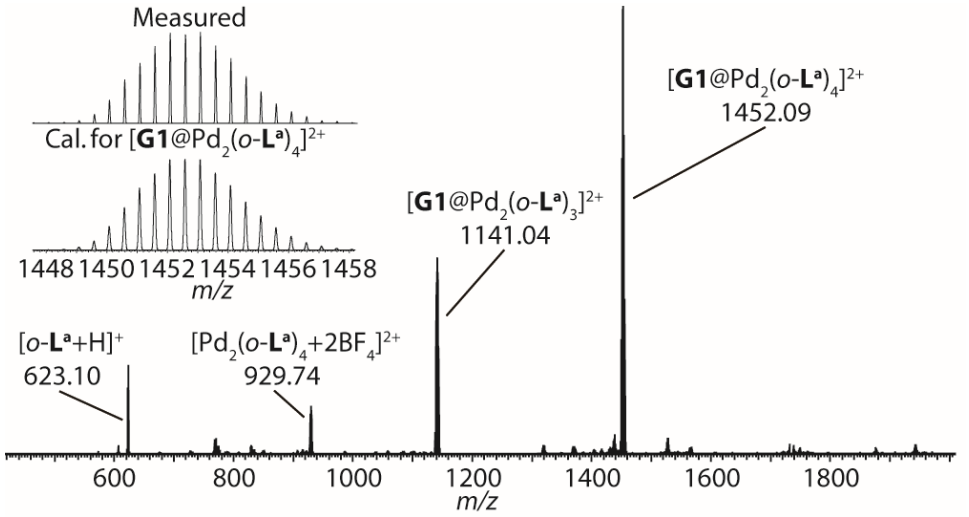

Figure 3.73 ESI-HRMS spectrum **of [G1@*o*-C^{a}].**

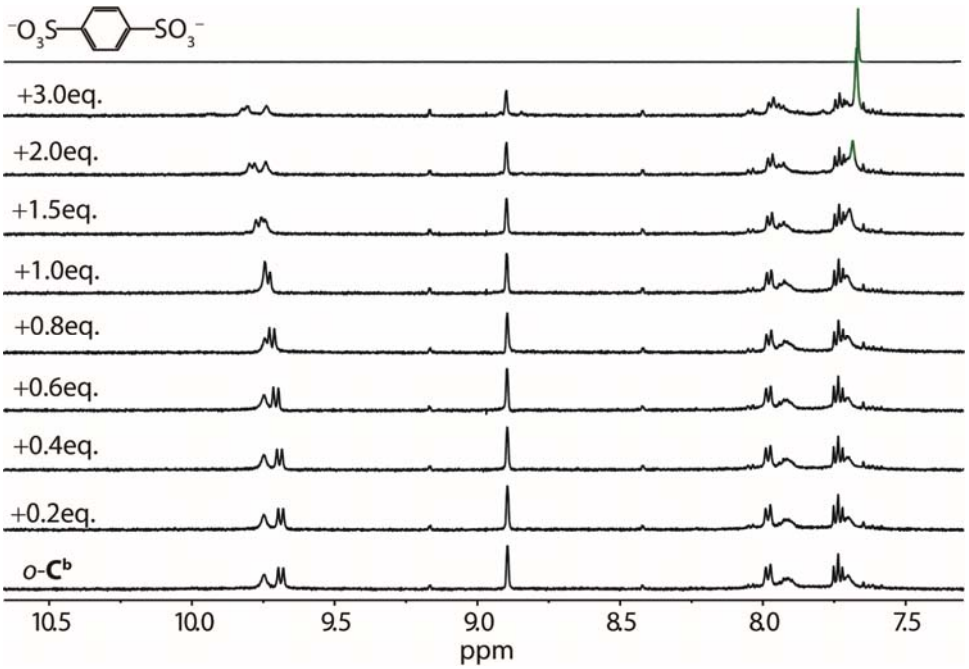

Figure 3.74 ^{1}H NMR titration (500 MHz, 298 K, CD_3CN) of *o*-**C**[a] with $(NBu_4)_2$**G2**. Upon addition of guest **G2**, inward pointing proton H_a did not show any shifting, while outward pointing proton H_a shows low field shifting, indicating that the larger size guest **G2** cannot be encapsulated inside the central cavity of the cage complex. Excess addition of **G2** leads to precipitation.

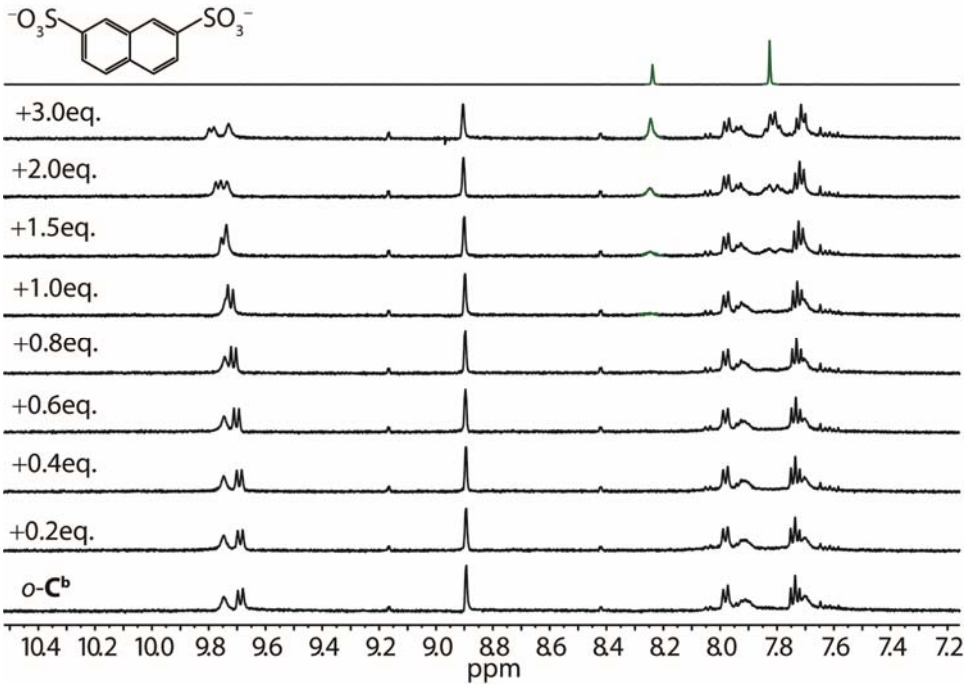

Figure 3.75 ^{1}H NMR titration (500 MHz, 298 K, CD_3CN) of *o*-**C**[a] with $(NBu_4)_2$**G3**. Similar to $(NBu_4)_2$**G2**, upon addition of guest **G3**, only outward proton H_a shows low field shifting, indicating that the larger size guest **G3** cannot be encapsulated. Excess addition of **G3** leads to precipitation.

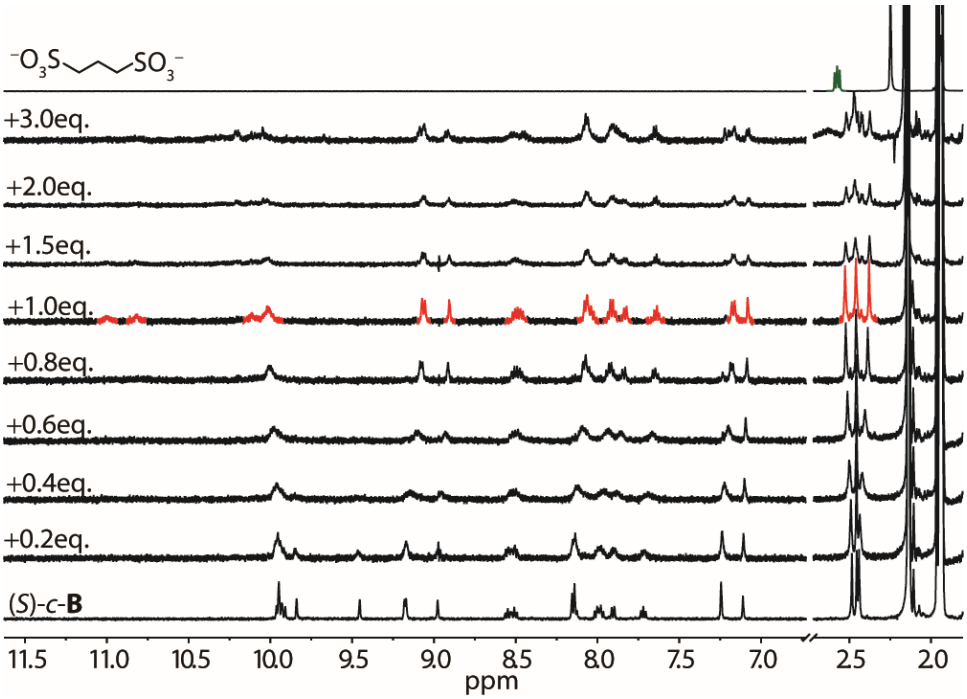

Figure 3.76 ^{1}H NMR titration (500 MHz, 298 K, CD_3CN) of (*S*)-*c*-**B** with $(NBu_4)_2$**G1**. Upon addition of one equivalent of guest **G1**, the (*S*)-*c*-**B** cage transforms into [**G1**@(*S*)-*c*-**B**]. Excess addition of **G1** leads to precipitation. New sets of NMR signals are highlighted in red.

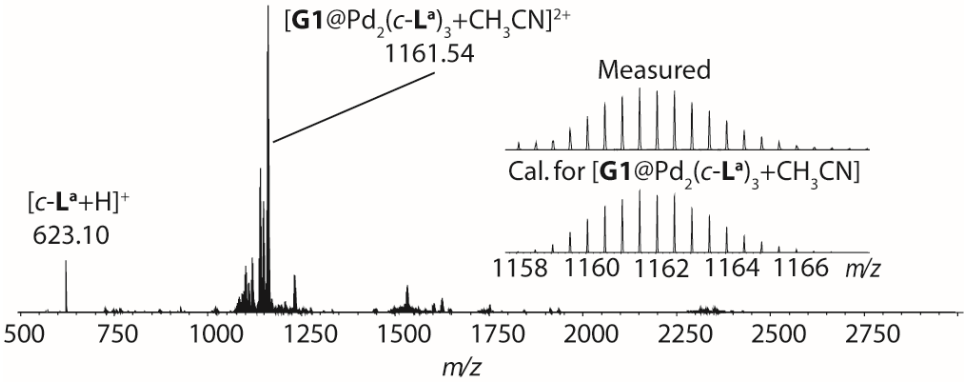

Figure 3.77 ESI-HRMS spectrum of [**G1**@*c*-**B**].

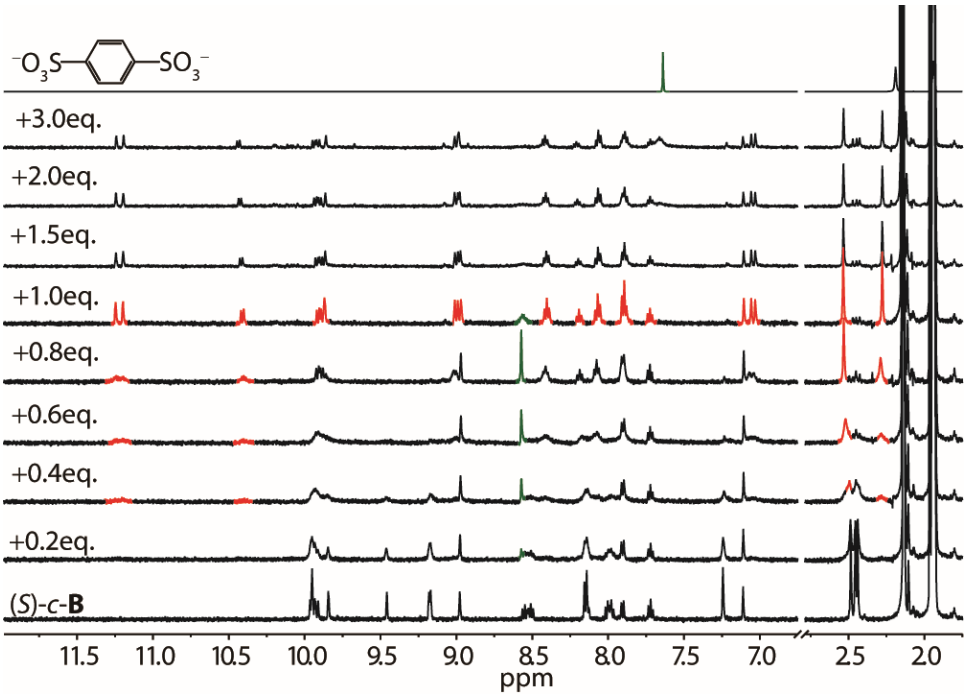

Figure 3.78 ^{1}H NMR titration (500 MHz, 298 K, CD_3CN) of (*S*)-*c*-**B** with $(NBu_4)_2$**G2**. Upon addition of one equivalent of guest **G2**, the (*S*)-*c*-**B** cage transforms into [**G2**@(*S*)-*c*-**B**]. New set of NMR signals are highlighted in red. Signals of encapsulated **G2** are highlighted in green.

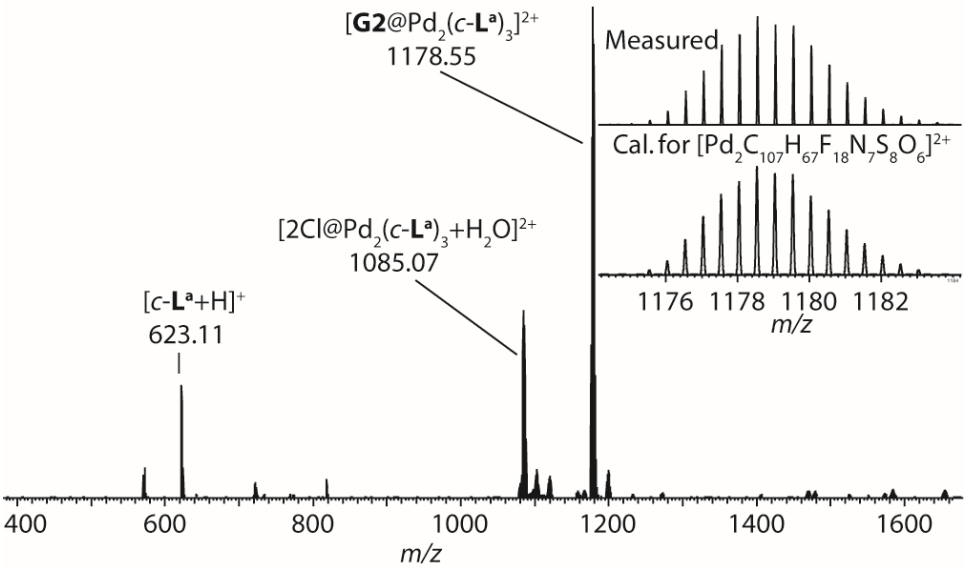

Figure 3.79 ESI-HRMS spectrum of [**G2**@*c*-**B**].

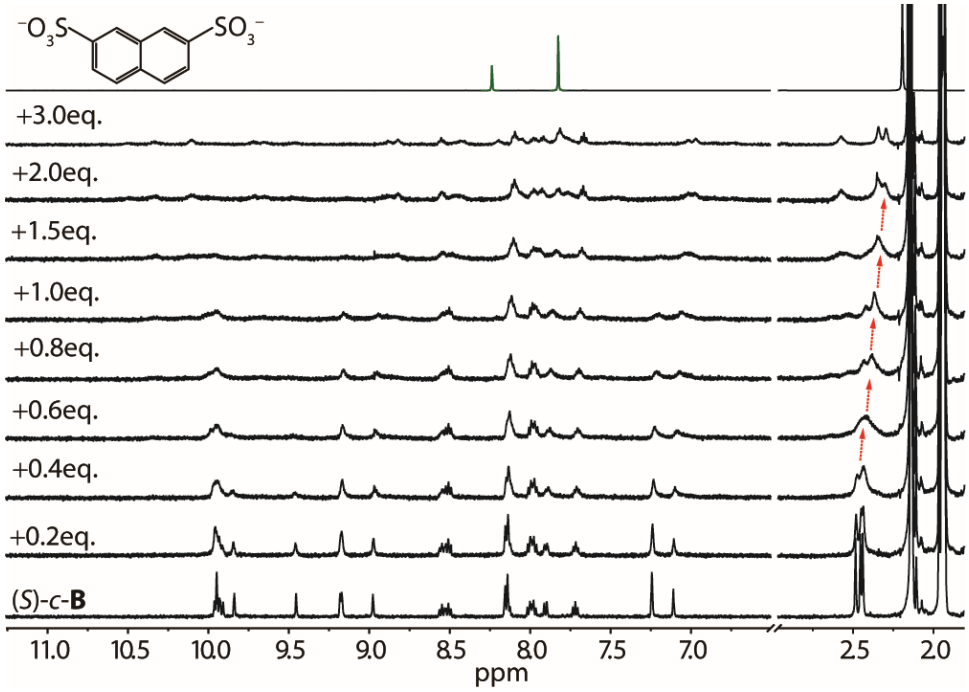

Figure 3.80 ^{1}H NMR titration (500 MHz, 298 K, CD_3CN) of (*S*)-*c*-**B** with $(NBu_4)_2$**G3**. Upon addition of one equivalent of guest **G3**, the (*S*)-*c*-**B** cage transforms into [**G3**@(*S*)-*c*-**B**]. Excess addition of **G3** leads to precipitation.

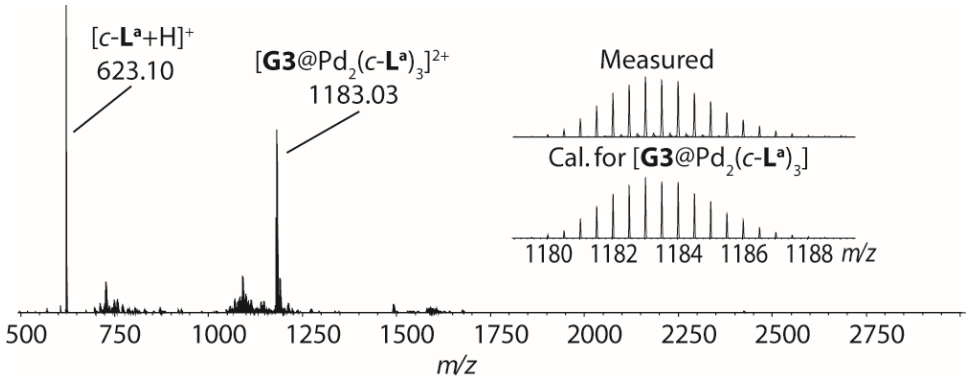

Figure 3.81 ESI-HRMS spectrum of [**G3**@*c*-**B**].

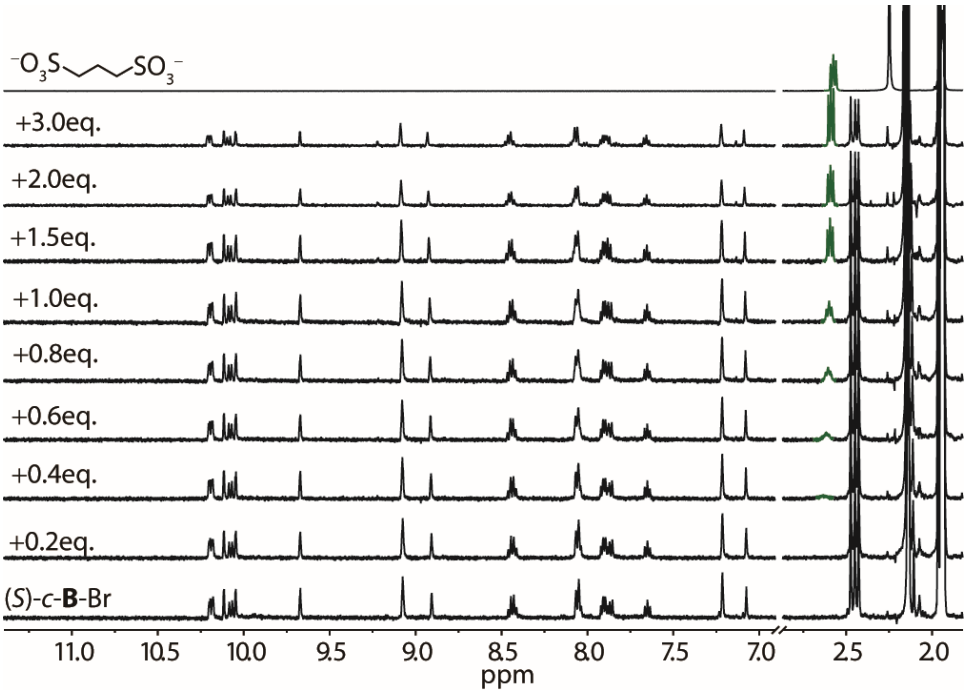

Figure 3.82 ^{1}H NMR titration (500 MHz, 298 K, CD_3CN) of (*S*)-*c*-**B**-**Br** with $(NBu_4)_2$**G1**. Upon addition of guest **G1**, both inward and outward proton did not show any shifting, indicating that there is no encapsulation of **G1**. Excess addition of **G1** leads to precipitation.

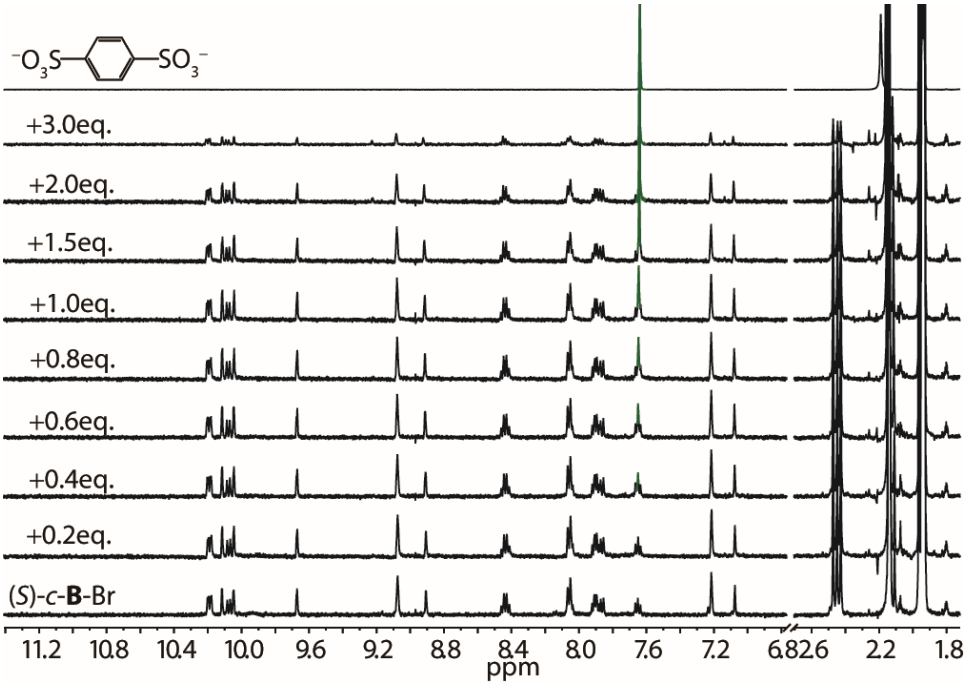

Figure 3.83 ^{1}H NMR titration (500 MHz, 298 K, CD_3CN) of (*S*)-*c*-**B**-**Br** with $(NBu_4)_2$**G2**. Upon addition of guest **G2**, both inward and outward proton did not show any shifting, indicating that there is no interaction of **G2** with the bowl complex. Excess addition of **G2** leads to precipitation.

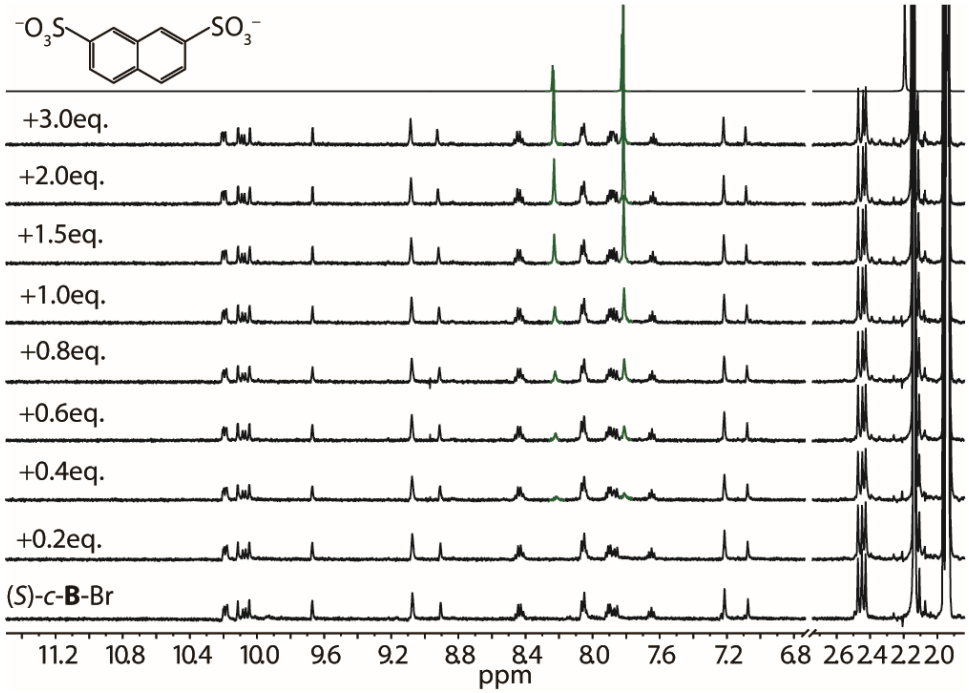

Figure 3.84 ^{1}H NMR titration (500 MHz, 298 K, CD_3CN) of (*S*)-*c*-**B**-**Br** with $(NBu_4)_2$**G3**. Upon addition of guest **G3**, both inward and outward proton did not show any shifting, indicating that there is no encapsulation or interaction of **G3**. Excess addition of **G3** leads to precipitation.

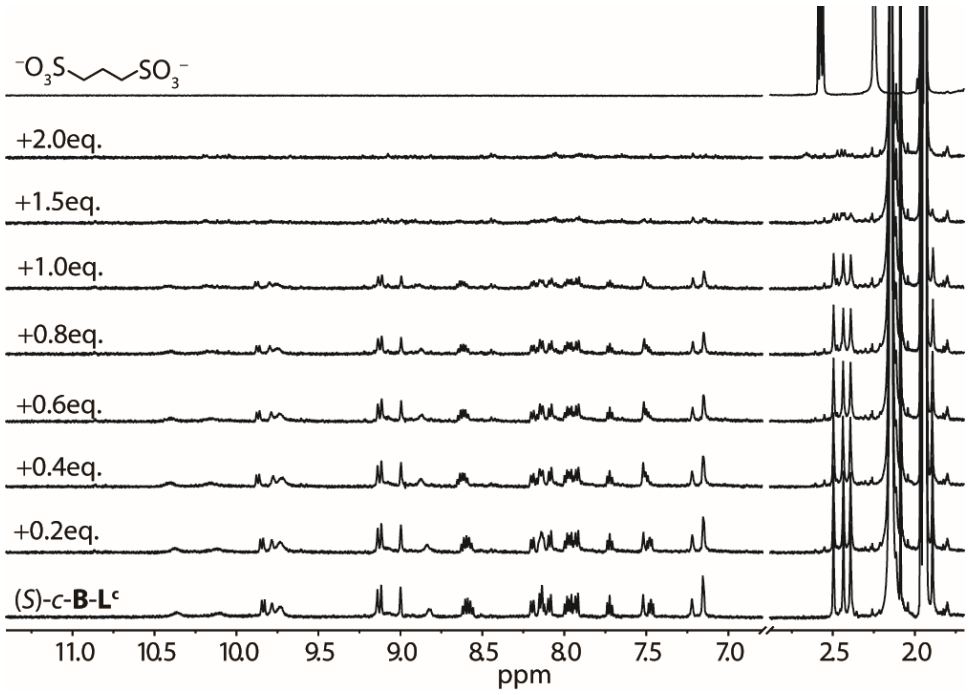

Figure 3.85 ^{1}H NMR titration (500 MHz, 298 K, CD_3CN) of (*S*)-*c*-**B**-**L**^{c} with $(NBu_4)_2$**G1**. Upon addition of guest **G1**, only outward proton H_b and $H_{b'}$ show low field shifting, indicating that the guest **G1** cannot be encapsulated. Excess addition of **G1** leads to precipitation.

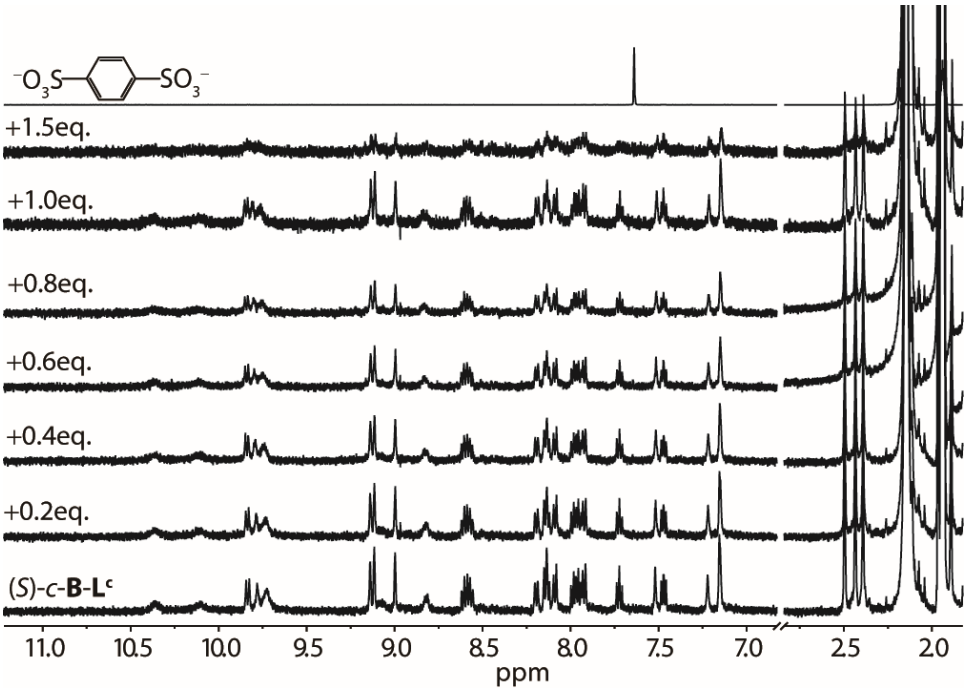

Figure 3.86 ^{1}H NMR titration (500 MHz, 298 K, CD_3CN) of (*S*)-*c*-**B**-**L**^{c} with $(NBu_4)_2$**G2**. Upon addition of guest **G2**, precipitation is formed immediately. Only outward proton H_b and $H_{b'}$ shows low field shifting, indicating that the guest **G2** cannot be encapsulated.

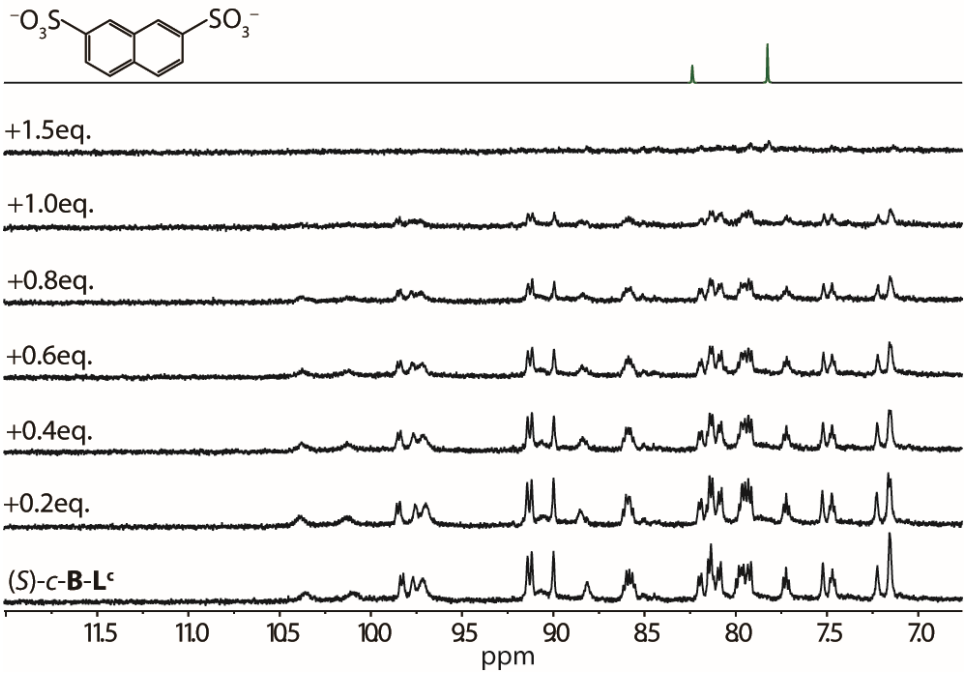

Figure 3.87 ^{1}H NMR titration (500 MHz, 298 K, CD_3CN) of (*S*)-*c*-**B**-**L**^{c} with $(NBu_4)_2$**G3**. Similar to **G2**, upon addition of guest **G3**, precipitation is formed immediately. Only outward proton H_b and $H_{b'}$ shows low field shifting, indicating that the guest **G3** cannot be encapsulated.

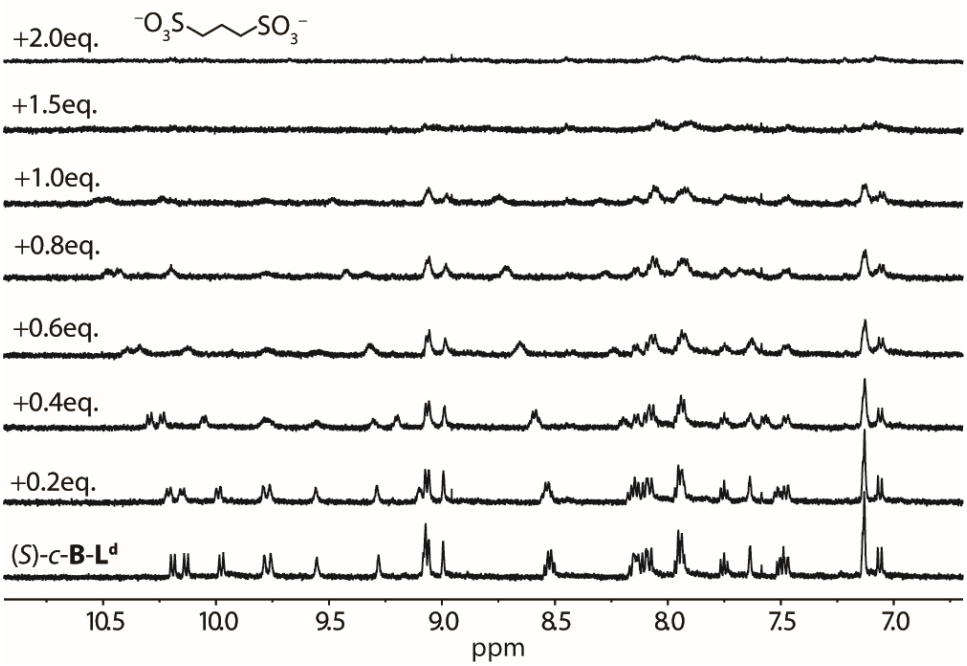

Figure 3.88 ^{1}H NMR titration (500 MHz, 298 K, CD_3CN) of (*S*)-*c*-**B**-**L**^{d} with $(NBu_4)_2$**G1**. Upon addition of guest **G1**, only outward proton H_b and $H_{b'}$ show low field shifting, indicating that the guest **G1** cannot be encapsulated. Excess addition of **G1** leads to precipitation.

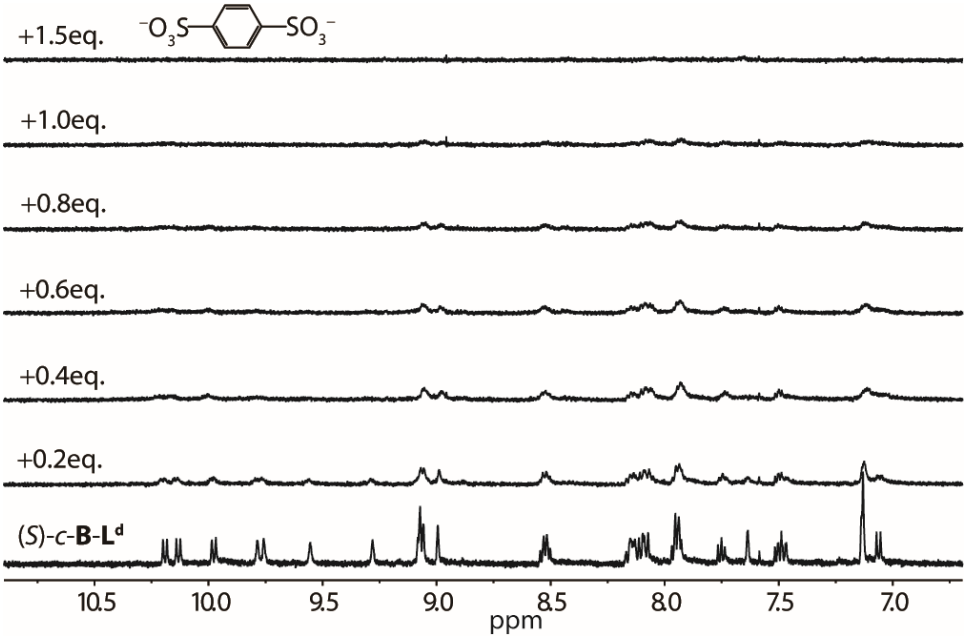

Figure 3.89 ^{1}H NMR titration (500 MHz, 298 K, CD_3CN) of (*S*)-*c*-**B**-**L**^{d} with $(NBu_4)_2$**G2**. Upon addition of guest **G2**, precipitation is formed immediately. Only outward proton H_b and $H_{b'}$ shows low field shifting, indicating that the guest **G2** cannot be encapsulated.

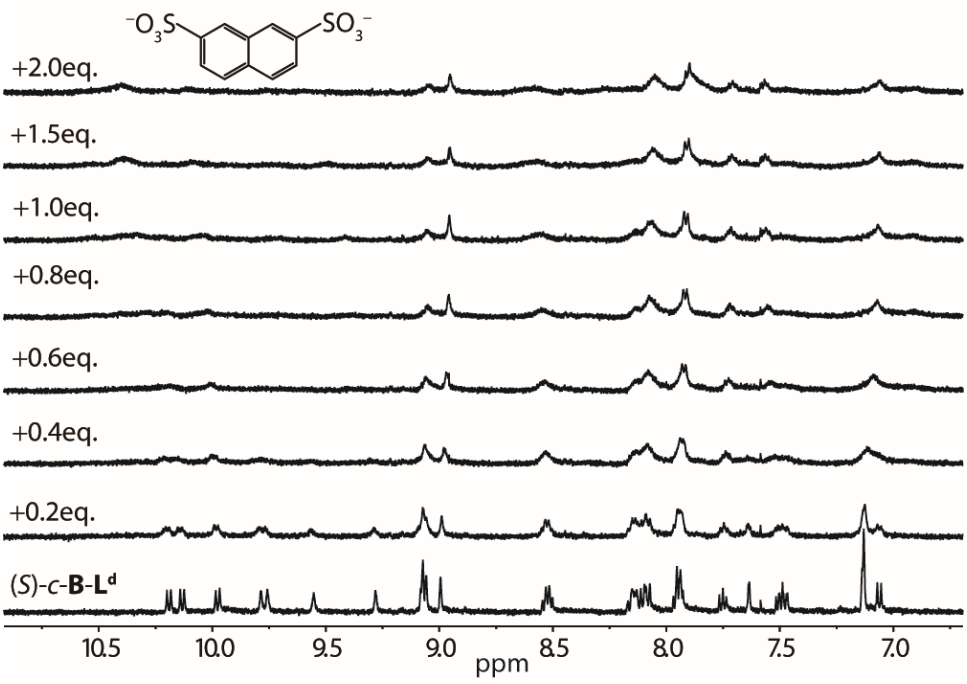

Figure 3.90 ^{1}H NMR titration (500 MHz, 298 K, CD_3CN) of (*S*)-*c*-**B**-**L**^{d} with $(NBu_4)_2$**G3**. Similar to **G2**, upon addition of guest **G3**, precipitation is formed immediately. Only outward proton H_b and $H_{b'}$ shows low field shifting, indicating that the guest **G3** cannot be encapsulated.

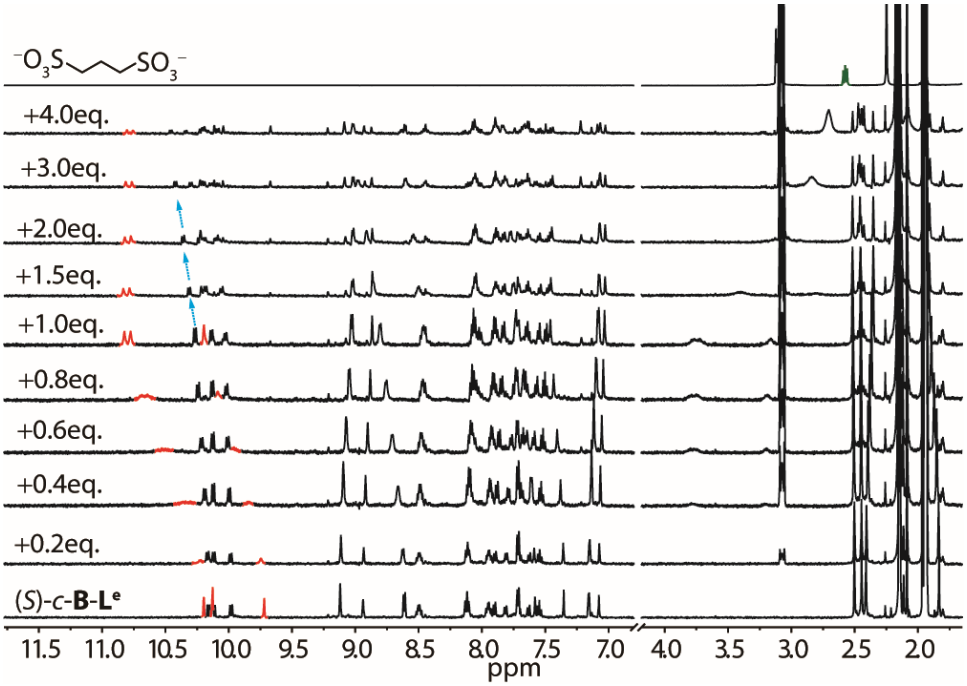

Figure 3.91 ^{1}H NMR titration (500 MHz, 298 K, CD_3CN) of (*S*)-*c*-**B**-**L**^{e} with $(NBu_4)_2$**G1**. Upon addition of guest **G1**, the inward proton H_a and $H_{a'}$ shows low field shifting (highlighted in red), while outward signals did not show any shifting, indicating the encapsulation of **G1** into (*S*)-*c*-**B**-**L**^{e}. Excess addition of **G1** leads to precipitation.

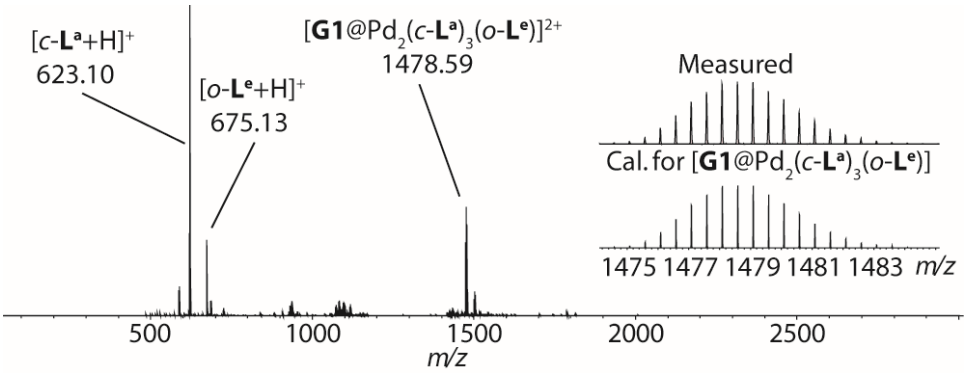

Figure 3.92 ESI-HRMS spectrum of [**G1**@*c*-**B**-**L**^{e}].

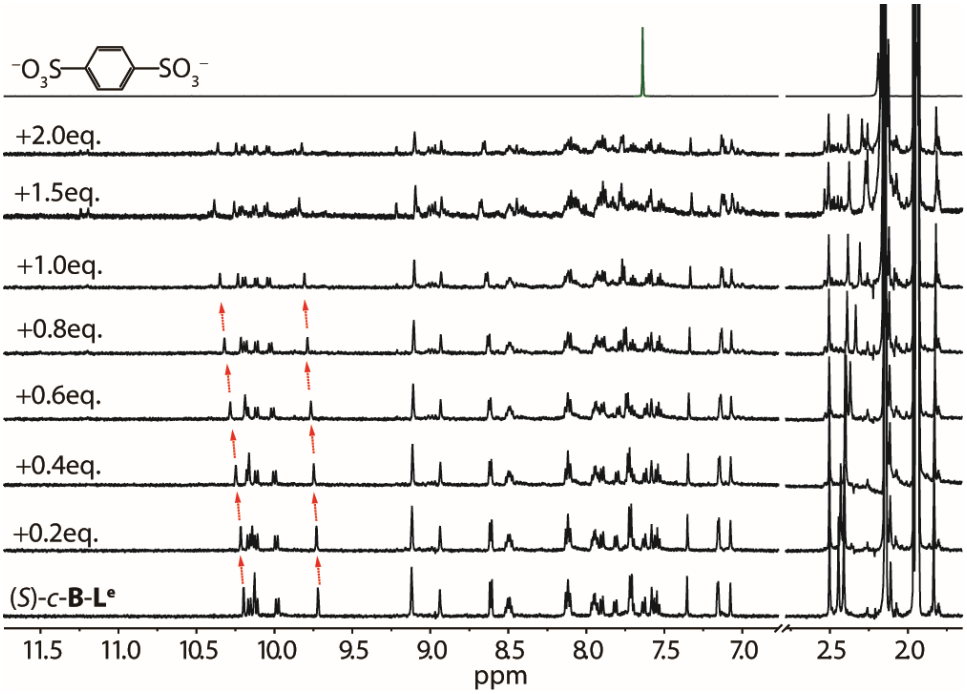

Figure 3.93 ^{1}H NMR titration (500 MHz, 298 K, CD_3CN) of (*S*)-*c*-**B**-**L**^{e} with $(NBu_4)_2$**G2**. Upon addition of guest **G2**, the inward proton H_a and $H_{a'}$ shows low field shifting (highlighted in red arrows), while outward signals did not show any shifting, indicating the encapsulation of **G2** into (*S*)-*c*-**B**-**L**^{e}. Excess addition of **G2** leads to precipitation.

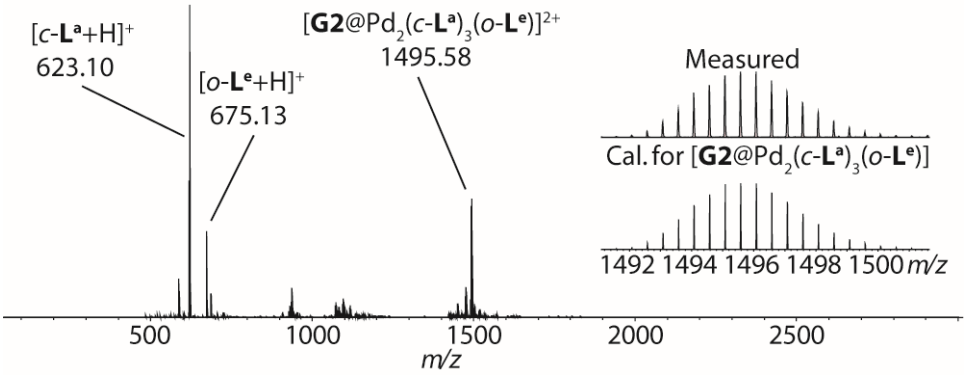

Figure 3.94 ESI-HRMS spectrum of [**G2**@*c*-**B**-**L**^{e}].

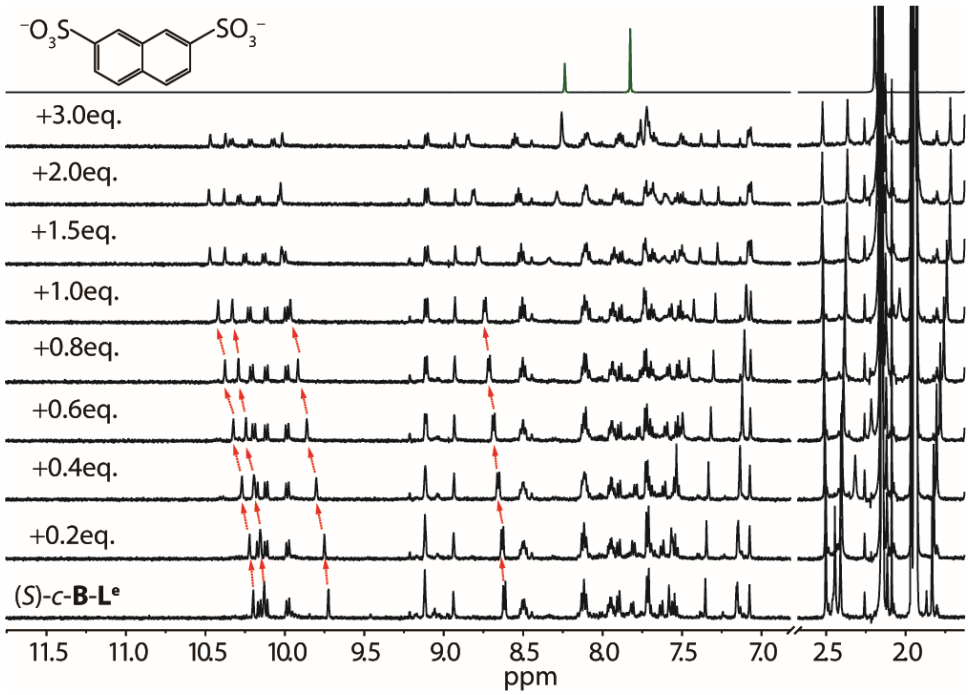

Figure 3.95 ^{1}H NMR titration (500 MHz, 298 K, CD_3CN) of (*S*)-*c*-**B**-**L**^{e} with $(NBu_4)_2$**G3**. Upon addition of guest **G3**, the inward proton H_a and $H_{a'}$ shows low field shifting (highlighted with red arrows), while outward pointing hydrogens did not show any shifting, indicating the encapsulation of **G3** into (*S*)-*c*-**B**-**L**^{e}. Excess addition of **G3** leads to precipitation.

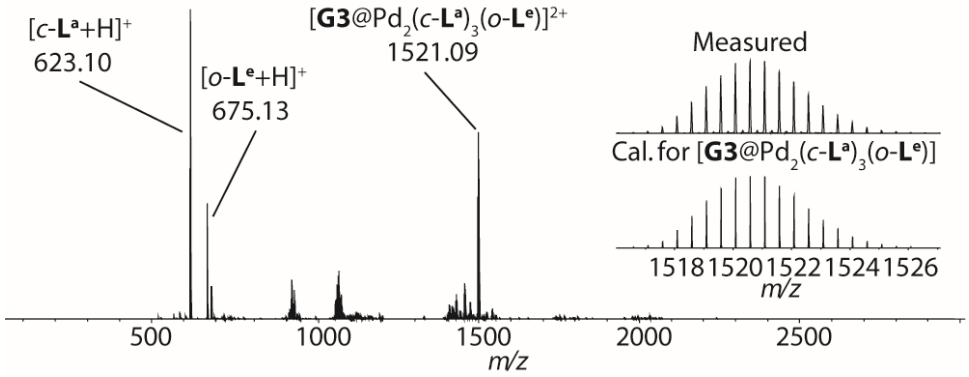

Figure 3.96 ESI-HRMS spectrum of [G3@*c*-**B**-**L**^{e}]**.**

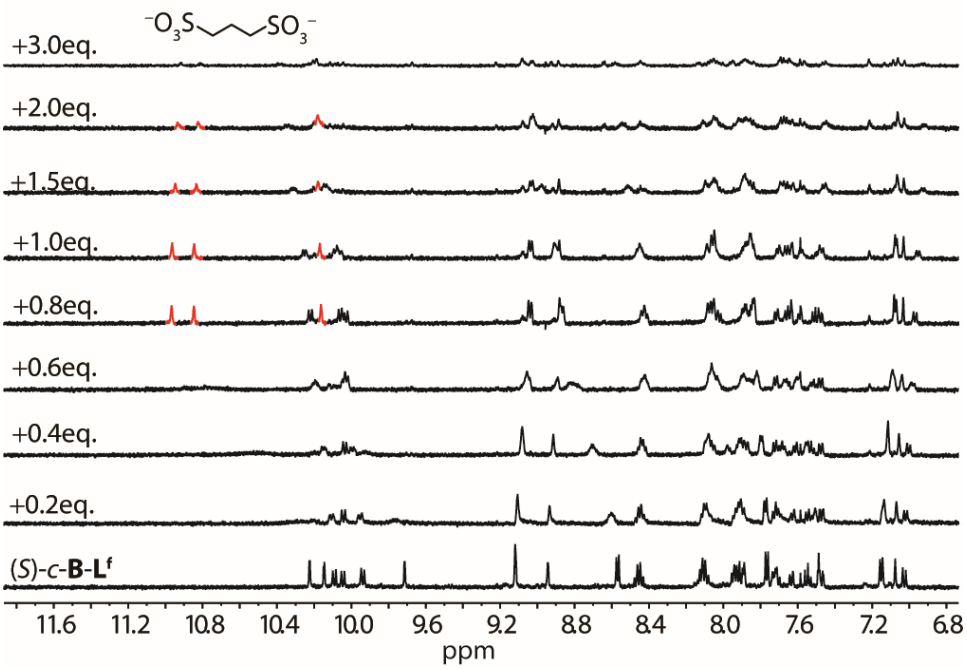

Figure 3.97 ^{1}H NMR titration (500 MHz, 298 K, CD_3CN) of (*S*)-*c*-**B**-**L**^{f} with $(NBu_4)_2$**G1**. Upon addition of 1.0 eq. of guest **G1**, the (*S*)-*c*-**B**-**L**^{f} cage transforms into [**G1**@(*S*)-*c*-**B**-**L**^{f}]. New set of NMR signals are highlighted in red. Excess addition of **G1** leads to precipitation.

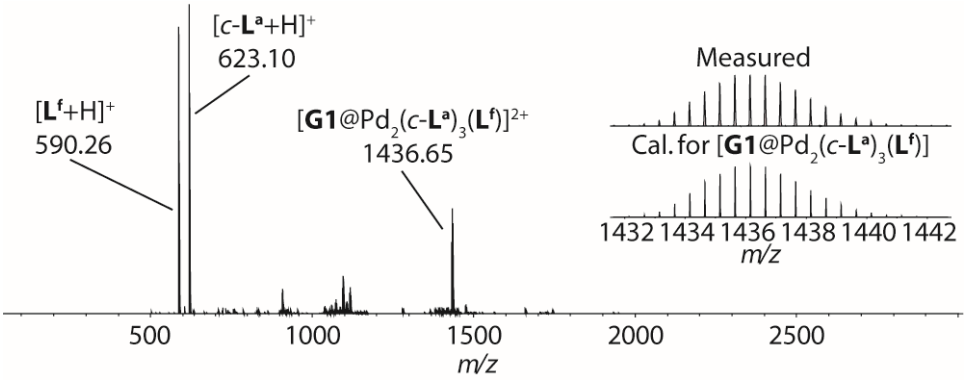

Figure 3.98 ESI-HRMS spectrum of [**G1**@*c*-**B**-**L**^{f}].

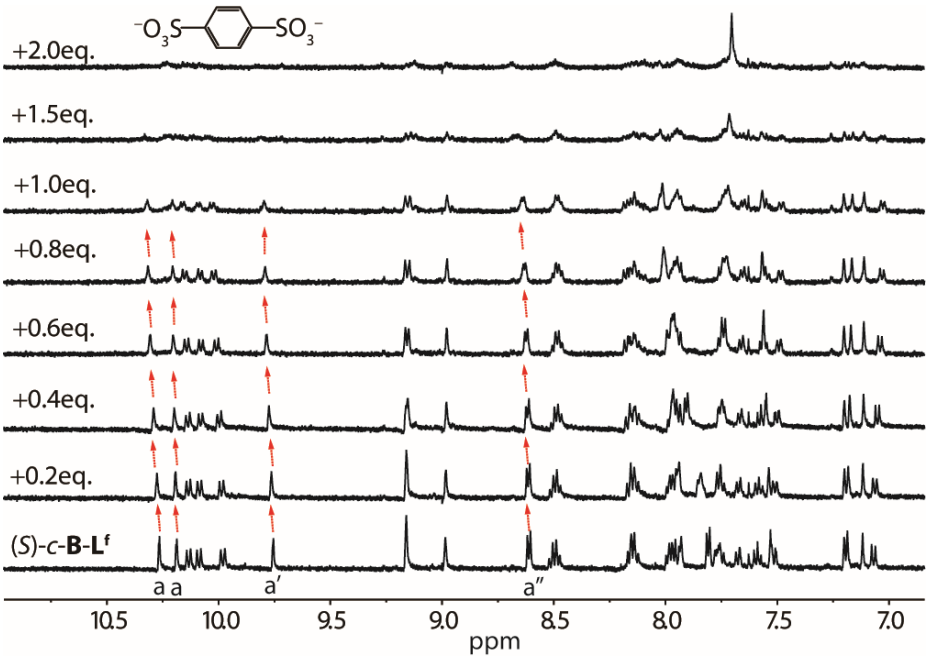

Figure 3.99 ^{1}H NMR titration (500 MHz, 298 K, CD_3CN) of (*S*)-*c*-**B**-$\mathbf{L^f}$ with $(NBu_4)_2$**G2**. Upon addition of guest **G2**, the inward pointing protons H_a and $H_{a'}$ show low field shifting (highlighted by red arrows), while outward signals did not show any shifting. (*S*)-*c*-**B**-$\mathbf{L^f}$ cage transforms into [**G2**@(*S*)-*c*-**B**-$\mathbf{L^f}$]. Excess addition of **G2** leads to precipitation.

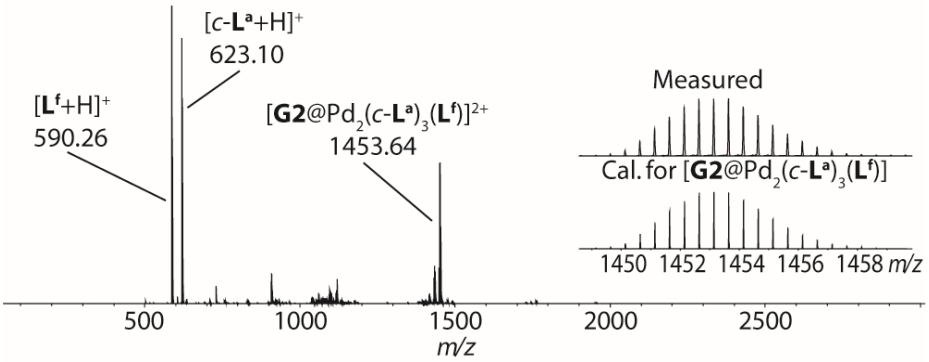

Figure 3.100 ESI-HRMS spectrum of [**G2**@*c*-**B**-$\mathbf{L^f}$].

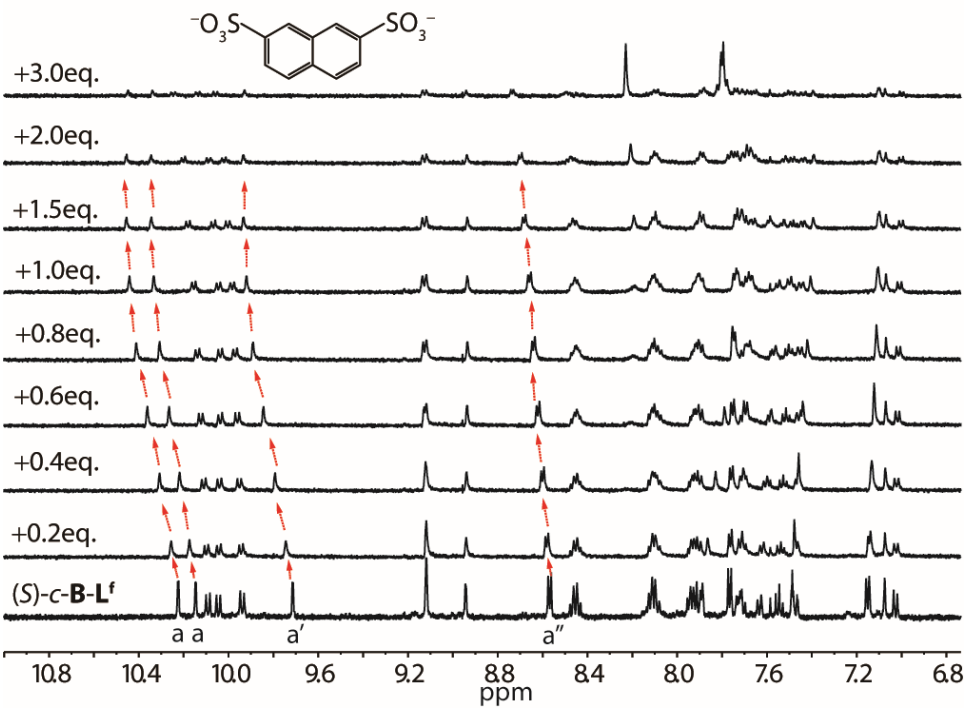

Figure 3.101 ^{1}H NMR titration (500 MHz, 298 K, CD_3CN) of (*S*)-*c*-**B**-L^f with $(NBu_4)_2$**G3**. Upon addition of guest **G3**, the inward proton H_a and $H_{a'}$ show low field shifting (highlighted by red arrows), while outward signals did not show any shifting. (*S*)-*c*-**B**-L^f cage transforms into [**G3**@(*S*)-*c*-**B**-L^f]. Excess addition of **G3** leads to precipitation.

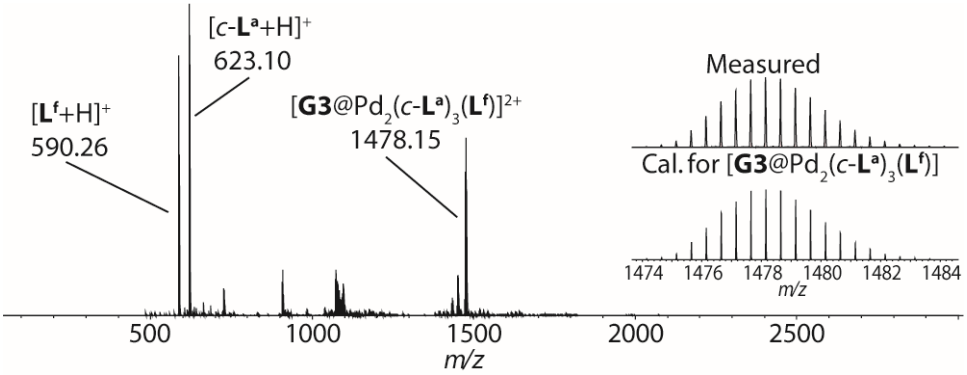

Figure 3.102 ESI-HRMS spectrum of [G3@*c*-**B**-L^f].

3.9.7 **Photoswitching between cage and bowl**

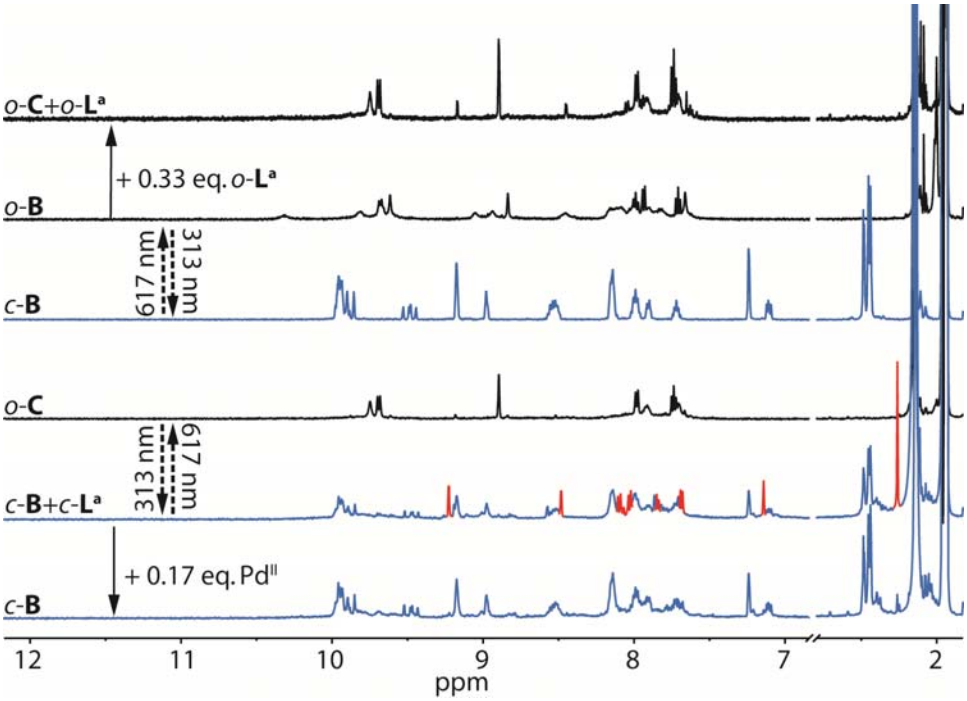

Figure 3.103 ^{1}H NMR spectra (500 MHz, CD_3CN, 298 K) of ***o*-C^{a}** and ***c*-B**, indicating the changes upon assembly and photoswitching of the cage and bowl.

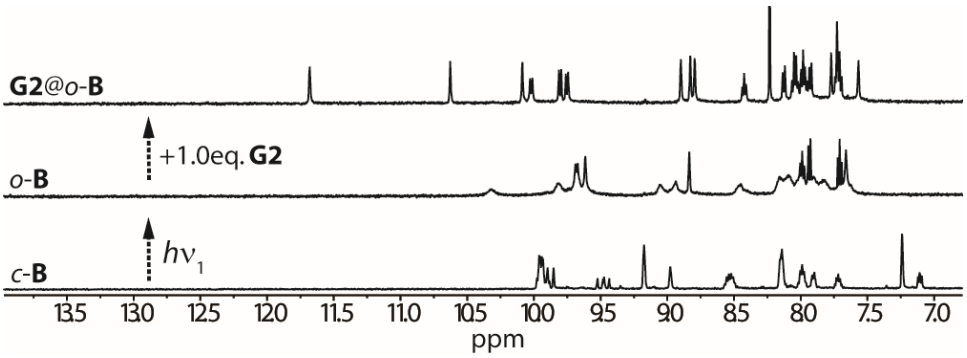

Figure 3.104 ^{1}H NMR spectra (500 MHz, 298 K, CD_3CN) of ***c*-B**, ***o*-B** and **G2@*o*-B**, proving the formation of the intermediate open bowl ***o*-B** after 617 nm irradiation.

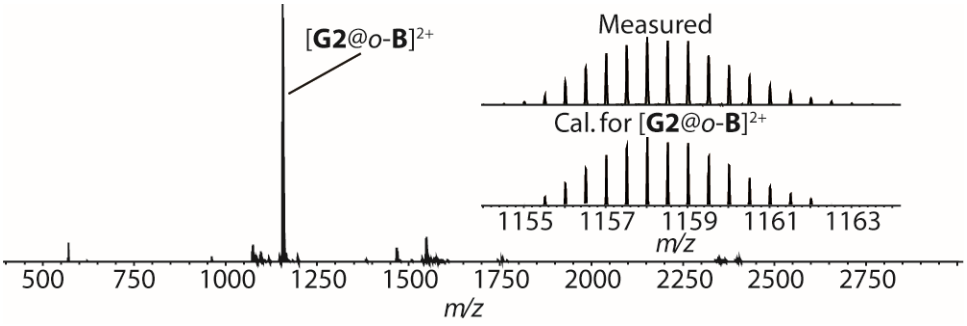

Figure 3.105 ESI-HRMS spectrum of **G2@*o*-B**.

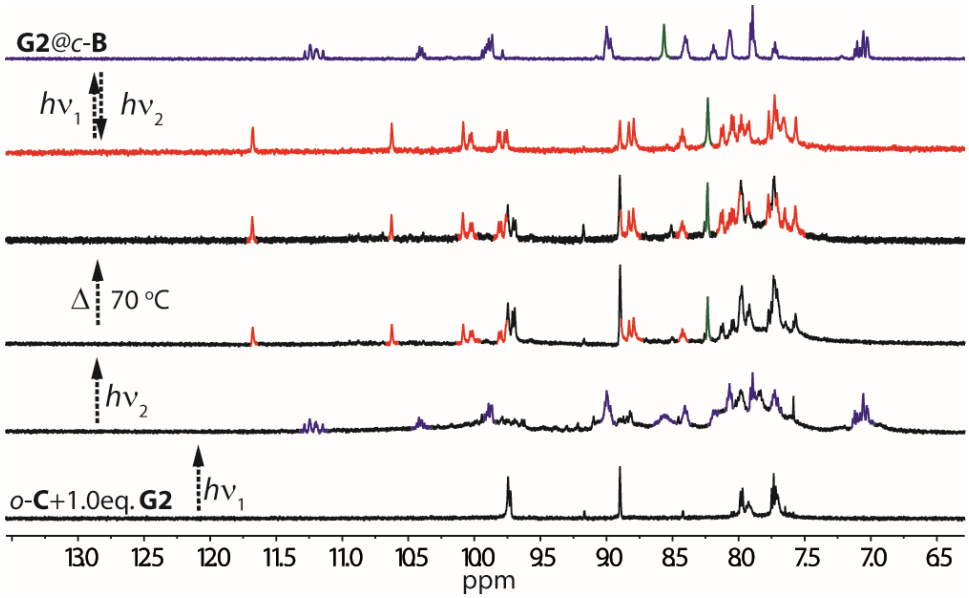

Figure 3.106 ^{1}H NMR spectra (500 MHz, 298 K, CD_3CN) shows photoswitching between cage and bowl in presence of **G2**.

3.9.8 UV-Vis monitored kinetics of photoconversions

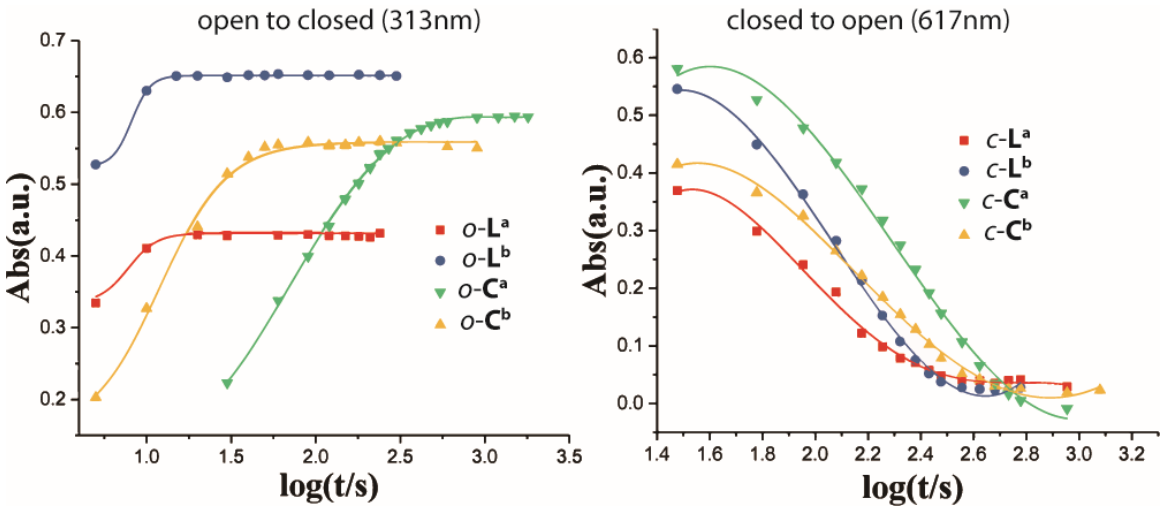

Figure 3.107 Time-course UV-Vis kinetics of the photoconversions of open-form ligands and cages (left) irradiated with 313 nm light, and closed-form ligands and cages (right) upon irradiation with 617 nm light based on absorption around 600 nm.

3.9.9 **Stability of *c*-B**

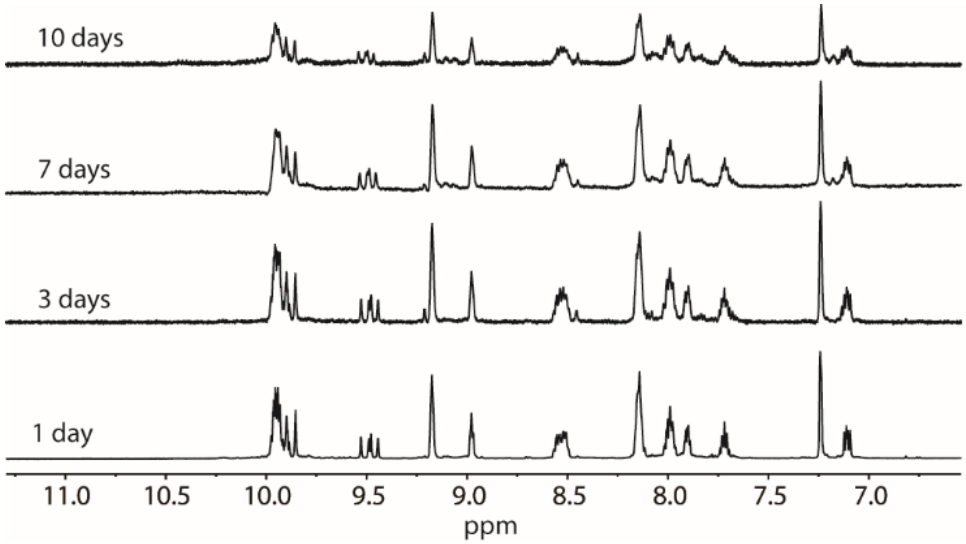

Figure 3.108 ^{1}H NMR spectra (500 MHz, 298 K, CD_3CN) of ***c*-B** in 10 days heating under 70 ºC.

3.9.10 **Reversible release/capture G2**

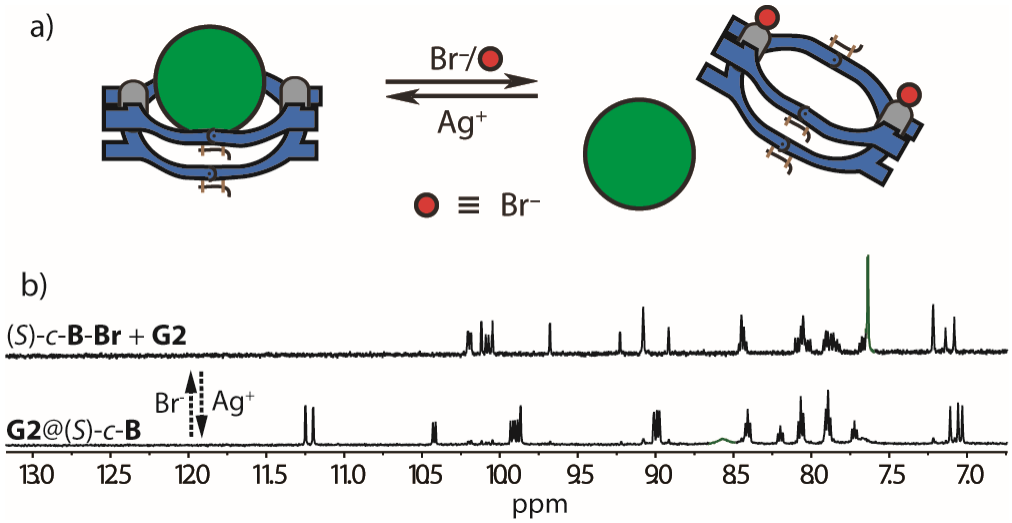

Figure 3.109 ^{1}H NMR spectra (500 MHz, 298 K, CD_3CN) of **G2**@(*S*)-*c*-**B** and (*S*)-*c*-**B**-**Br** with **G2**, showing the reversible uptake/release of **G2** upon adding Ag^+/Br^-.

3.9.11 **X-Ray data**

Crystals of *o*-**C^a**, *c*-**C^a** of were obtained after 10 days by slow vapor diffusion of diethyl ether into 1.0 mM *o*-**C^a** or *c*-**B** solution in CD_3CN in the dark separately. **G1**@*c*-**B** crystals were found to grow in the NMR tube after several days in the dark after titrating around 3.0 eq. of **G1** solution (15mM, CD_3CN) to *c*-**B** (0.5 mM, CD_3CN).

Suitable single crystals for X–ray structural analysis of *o*-**C^a**, *c*-**C^a** and **G1**@*c*-**B** were mounted at room temperature in NVH oil. Crystals were stored at cryogenic temperature

in dry shippers, in which they were safely transported to macromolecular beamline P11[20] at the Petra III synchrotron, DESY, Germany. X-ray diffraction data was collected at 80(2) K on a single axis goniometer, equipped with an Oxford Cryostream 800 low temperature device and a Pilatus 6M fast detector. The data integration and reduction were taken with XDS[21]. The structure was solved by direct methods[21]. The structure model was refined against all data by full-matrix least-squares methods on F^2 with the program SHELXL2014[22]. The SQUEEZE[23] method provided by the program Platon[24] was used to improve the contrast of the electron density map the structure.

Table S1. Crystallographic data of *o*-**C**[a], *c*-**C**[a] and **G1**@*c*-**B**.

CCDC number	*o*-**C**[a]	*c*-**C**[a]	**G1**@*c*-**B**
Empirical formula	$C_{140}H_{96}B_3F_{40}N_{10}OPd_2S_8$	$C_{132}H_{80}F_{20}N_8Pd_2S_8$	$C_{109}H_{82}F_{18}N_8O_{14}Pd_2S_{10}$
Formula weight	3195.98	2627.32	2603.23
Temperature	80(2) K	80(2) K	80(2) K
Wavelength	0.5636 Å	0.68880 Å	0.5636 Å
Crystal system	Triclinic	Tetragonal	Triclinic
Space group	*P* 42/n	*P*42/mcm	*P*-1
Unit cell dimensions	a = 23.508(3) Å b = 23.508(3) Å c = 25.231(5) Å α = 90° β = 90° γ = 90°	a = 16.324(2) Å b = 16.324(2) Å c = 25.539(5) Å α = 90° β = 90° γ = 90°	a = 14.951(3) Å b = 20.918(4) Å c = 22.075(4) Å α = 105.03(3)° β = 91.07(3)° γ = 90.59(3)°
Volume	13943(5) Å^3	6805(2) Å^3	6666(2) Å^3
Z	4	2	2
Density (calculated)	1.523 mg/m^3	1.282 mg/m^3	1.297 mg/m^3
Absorption coefficient	0.262 mm^{-1}	0.213 mm^{-1}	0.270 mm^{-1}
F(000)	6436	2656	2636
Crystal size	0.20 x 0.01 x 0.05 mm^3	0.15 x 0.15 x 0.15 mm^3	0.1 x 0.1 x 0.1 mm^3

Theta range for data collection	0.971 to 17.638°.	1.209 to 26.972°.	0.973 to 19.847°.
Index ranges	-25<=h<=25 -25<=k<=25 -27<=l<=27	-21<=h<=21 -21<=k<=21 -33<=l<=33	-18<=h<=18 -25<=k<=25 -26<=l<=26
Reflections collected	4549	3773	24405
Independent reflections	3035 [R(int) = 0.0997]	4375 [R(int) = 0.1614]	19289 [R(int) = 0.1973]
Completeness to theta = 18.161°	99.9 %	99.8 %	93.9 %
Refinement method	Full-matrix least-squares on F^2	Full-matrix least-squares on F^2	Full-matrix least-squares on F^2
Data / restraints / parameters	4549 / 642 / 822	4375 / 295 / 726	22919 / 1751 / 3179
Goodness-of-fit on F2	1.326	2.394	2.458
Final R indices [I>2sigma(I)]	R1 = 0.0997 wR2 = 0.2987	R1 = 0.1614 wR2 = 0.4694	R1 = 0.1973 wR2 = 0.5235
R indices (all data)	R1 = 0.1274 wR2 = 0.3270	R1 = 0.1657 wR2 = 0.4778	R1 = 0.2091 wR2 = 0.5290
Largest diff. peak and hole	2.195 and -0.632 e.Å^{-3}	2.195 and -0.632 e.Å^{-3}	2.195 and -0.632 e.Å^{-3}

Crystals of *o*-**L**^{e} were obtained after evaporing *o*-**L**^{e} solution (5 mM, CH_3CN) in several days in the dark. Suitable single crystals of *o*-**L**^{e} were mounted in NVH oil on a nylon loop. X-ray diffraction data were collected on Bruker d8 venture systems based on a kappa goniometers with Incoatec microfocus X-ray sources (IμS 2.0), Incoatec QUAZAR mirror optics and a Photon 100 detector. The data was collected at 100 K crystal temperature (Oxford Cryosystems CRYOSTREAM 700), 50 kV and 600 μA and an appropriate 0.5° omega scan strategy. Data reduction was performed with SAINT v8.30C

(Bruker, 2009a) out of the APEX II v2.2012.2 0 (Bruker, 2009b) program package. SADABS[26] (version 2014/4) was employed for the incident beam scaling, determination of the spherical harmonic coefficients, outlier rejection and determination of the error model parameters. All the structures were solved by direct methods with SHELXT[27]. They were refined by full-matrix least-squares against F^2 using SHELXL2014[22] with the help of the SHELXle[28] graphical user interface.

Table S2. Crystallographic data of *o*- **L^e**

CCDC number	*o*-**L^e**
Empirical formula	$C_{37}H_{30}F_6N_4S_2$
Formula weight	756.81
Temperature	100(2) K
Wavelength	0.71073 Å
Crystal system	Triclinic
Space group	*P* -1
Unit cell dimensions	a = 9.7291(5) Å b = 13.2496(7) Å c = 15.2727(8) Å α = 76.829(3)° β = 88.449(3)° γ = 69.950(3)°
Volume	1797.98(17) $Å^3$
Z	2
Density (calculated)	1.398 mg/m^3
Absorption coefficient	0.216 mm^{-1}
F(000)	780.0
Crystal size	0.40 x 0.1 x 0.1 mm^3
Theta range for data collection	0.917 to 34.971°.
Index ranges	-15<=h<=15 -21<=k<=21 -24<=l<=24

Reflections collected	15816
Independent reflections	10894 [R(int) = 0.0579]
Completeness to theta = 18.161°	100 %
Refinement method	Full-matrix least-squares on F^2
Data / restraints / parameters	15811 / 686 / 791
Goodness-of-fit on F2	1.293
Final R indices [I>2sigma(I)]	R1 = 0.0579 wR2 = 0.1820
R indices (all data)	R1 = 0.0969 wR2 = 0.2095
Largest diff. peak and hole	2.195 and -0.632 e.$Å^{-3}$

3.10 References

[1] (a) D. J. Cram, S. Karbach, Y. H. Kim, L. Baczynskyj, G. W. Kalleymeyn, *J. Am. Chem. Soc*. **1985**, *107*, 2575–2576; (b) D. J. Cram, J. M. Cram in *Container Molecules and Their Guests* (Ed. : J. F. Stoddard), The Royal Society of Chemistry, Cambridge, **1994**, pp. 131–216.

[2] Themed issue: Molecular containers, Ed. : P. Ballester, M. Fujita, J. Rebek, Jr., *Chem. Soc. Rev.* **2015**, *44*, 392–602.

[3] (a) L. Isaacs, *Acc. Chem. Res.* **2014**, *47*, 2052–2062; (b) D. H. Qu, Q. C. Wang, Q. W. Zhang, X. Ma, H. Tian, *Chem. Rev.* **2015**, *115*, 7543–7588; (c) B. Schmidt, C. Barner-Kowollik, *Angew. Chem. Int. Ed.* **2017**, *56*, 8350–8369; (d) H. J. Schneider, *Angew. Chem. Int. Ed.* **2009**, *48*, 3924–3977; (e) S. Zarra, D. M. Wood, D. A. Roberts, J. R. Nitschke, *Chem. Soc. Rev.* **2015**, *44*, 419–432; (f) X. Zhang, C. Wang, *Chem. Soc. Rev.* **2011**, *40*, 94–101; (g) M. Xue, Y. Yang, X. Chi, Z. Zhang, F. Huang, *Acc. Chem. Res.* **2012**, *45*, 1294–1308.

[4] (a) S. J. Barrow, S. Kasera, M. J. Rowland, J. del Barrio, O. A. Scherman, *Chem. Rev.* **2015**, *115*, 12320–12406; (b) D. S. Kim, J. L. Sessler, *Chem. Soc. Rev.* **2015**,

44, 532–546; (c) G. Yu, K. Jie, F. Huang, *Chem. Rev.* **2015**, *115*, 7240–7303; (d) M. Zhang, X. Yan, F. Huang, Z. Niu, H. W. Gibson, *Acc. Chem. Res.* **2014**, *47*, 1995–2005.

[5] (a) Q. D. Hu, G. P. Tang, P. K. Chu, *Acc. Chem. Res.* **2014**, *47*, 2017–2025; (b) X. Ma, Y. Zhao, *Chem. Rev.* **2015**, *115*, 7794-7839; (c) M. J. Webber, R. Langer, *Chem. Soc. Rev.* **2017**, *46*, 6600–6620.

[6] (a) M. Yoshizawa, J. K. Klosterman, M. Fujita, *Angew. Chem. Int. Ed.* **2009**, *48*, 3418–3438; (b) S. Wang, T. Sawada, M. Fujita, *Chem. Commun.* **2016**, *52*, 11653–11656. (c) M. D. Pluth, R. G. Bergman, K. N. Raymond, *Acc. Chem. Res.* **2009**, *42*, 1650–1659.

[7] S. M. Jansze, M. D. Wise, A. V. Vologzhanina, R. Scopelliti, K. Severin, *Chem. Sci.* **2017**, *8*, 1901–1908.

[8] (a) K. Hermann, Y. Ruan, A. M. Hardin, C. M. Hadad, J. D. Badjic, *Chem. Soc. Rev.* **2015**, *44*, 500–514; (b) F. Liu, R. C. Helgeson, K. N. Houk, *Acc. Chem. Res.* **2014**, *47*, 2168–2176; (c) A. Diaz-Moscoso, P. Ballester, *Chem. Commun.* **2017**, *53*, 4635–4652; (d) S. Rieth, K. Hermann, B. Y. Wang, J. D. Badjic, *Chem. Soc. Rev.* **2011**, *40*, 1609–1622; (e) H. Wang, F. Liu, R. C. Helgeson, K. N. Houk, *Angew. Chem. Int. Ed.* **2013**, *52*, 655–659.

[9] S. M. Jansze, G. Cecot, K. Severin, *Chem. Sci.* **2018**, *9*, 4253–4257.

[10] J. E. M. Lewis, E. L. Gavey, S. A. Cameron, J. D. Crowley, *Chem. Sci.* **2012**, *3*, 778–784; (b) T. Y. Kim, R. A. S. Vasdev, D. Preston, J. D. Crowley, *Chem. Eur. J.* **2018**, *24*, 14878–14890.

[11] M. Han, Y. Luo, B. Damaschke, L. Gomez, X. Ribas, A. Jose, P. Peretzki, M. Seibt, G. H. Clever, *Angew. Chem. Int. Ed.* **2016**, *55*, 445–449.

[12] M. Han, R. Michel, B. He, Y. S. Chen, D. Stalke, M. John, G. H. Clever, *Angew. Chem. Int. Ed.* **2013**, *52*, 1319–1323.

[13] S. C. Wei, M. Pan, Y. Z. Fan, H. Liu, J. Zhang, C. Y. Su, *Chem. Eur. J.* **2015**, *21*, 7418–7427.

[14] Gaussian 09, M. J. Frisch, G. W. Trucks, H. B. Schlegel, G. E. Scuseria, M. A. Robb, J. R. Cheeseman, G. Scalmani, V. Barone, B. Mennucci, G. A. Petersson, H. Nakatsuji, M. Caricato, X. Li, H. P. Hratchian, A. F. Izmaylov, J. Bloino, G. Zheng, J. L. Sonnenberg, M. Hada, M. Ehara, K. Toyota, R. Fukuda, J. Hasegawa, M. Ishida, T. Nakajima, Y. Honda, O. Kitao, H. Nakai, T. Vreven, J. A. Montgomery, Jr., J. E. Peralta, F. Ogliaro, M. Bearpark, J. J. Heyd, E. Brothers, K. N. Kudin, V. N. Staroverov, R. Kobayashi, J. Normand, K. Raghavachari, A. Rendell, J. C. Burant, S. S. Iyengar, J. Tomasi, M. Cossi, N. Rega, J. M. Millam, M. Klene, J. E. Knox, J. B. Cross, V. Bakken, C. Adamo, J. Jaramillo, R. Gomperts, R. E. Stratmann, O.

Yazyev, A. J. Austin, R. Cammi, C. Pomelli, J. W. Ochterski, R. L. Martin, K. Morokuma, V. G. Zakrzewski, G. A. Voth, P. Salvador, J. J. Dannenberg, S. Dapprich, A. D. Daniels, O. Farkas, J. B. Foresman, J. V. Ortiz, J. Cioslowski and D. J. Fox, Gaussian, Inc., Wallingford CT, **2009**.

[15] A. M. Johnson, R. J. Hooley, *Inorg. Chem.* **2011**, *50*, 4671–4673.

[16] M. Frank, J. Hey, I. Balcioglu, Y. S. Chen, D. Stalke, T. Suenobu, S. Fukuzumi, H. Frauendorf, G. H. Clever, *Angew. Chem. Int. Ed.* **2013**, *52*, 10102–10106.

[17] (a) S. Fraysse, C. Coudret, J. P. Launay, *Eur. J. Inorg. Chem.* **2000**, 1581–1590; b) B. He, O. S. Wenger, *J. Am. Chem. Soc.* **2011**, *133*, 17027.

[18] S. Loffler, J. Lubben, A. Wuttke, R. A. Mata, M. John, B. Dittrich, G. H. Clever, *Chem. Sci.* **2016**, *7*, 4676–4684.

[19] Spartan 08 Software, Wavefunction Inc., Irvine CA, **2008**.

[20] A. Burkhardt; T. Pakendorf; B. Reime; J. Meyer; P. Fischer; N. Stübe; S. Panneerselvam; O. Lorbeer; K. Stachnik; M. Warmer; P. Rödig; D. Göries; A. Meents, *Eur. Phys. J. Plus.*, **2016**, *131*, 56.

[21] W. Kabsch, *Acta Crystallogr. Sect. D*, **2010**, *66*, 125.

[22] T. R. Schneider; G. M. Sheldrick, *Acta Cryst*. **2002**, *D58*, 1772.

[23] G. M. Sheldrick, *Acta Crystallogr. Sect. A*, **2008**, *64*, 112.

[24] A. Spek, *Acta Crystallogr. Sect. C*, **2015**, *71*, 9.

[25] A. Spek, *Acta Crystallogr. Sect. D*, **2009**, *65*, 148.

[26] G. M. Sheldrick, *SADABS*, Universität Göttingen, Germany, **2000**.

[27] G. M. Sheldrick, *Acta Crystallogr. Sect. A*, **2015**, *71*, 3.

[28] C. B. Hubschle; G. M. Sheldrick; B. J. Dittrich, *Appl. Crystallogr.*, **2011**, *44*, 1281.

4 Light-Controlled Chirality Transfer in A $Pd_2L^A{}_3L^B$ Heteroleptic Cage

4.1 Introduction

Chirality, as a fundamental feature in nature, plays an import role both in biosynthesis of natural products as well as in man-made homogeneous catalysis and recent developments in polymer sciences.[1] In supramolecular chemistry, chirality has been introduced into self-assembled discrete entities *via* homochiral backbones, metal centers, covalently bound chiral moieties, host-guest induction and emerging from topological effects.[2]

Over the past years, multi-component heteroleptic assemblies, carrying more than one functionality, have been explored in metallo-supramolecular chemistry[3] (Figure 4.1). In most cases, however, the self-assembly of precursors produced statistic mixtures.[4] Examples of high level integrative self-sorting of discrete heteroleptic cages having been reported in which make use of a specific control via steric, template or shape complement effects etc.[5]

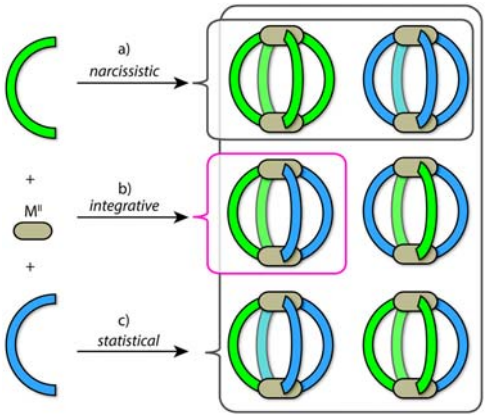

Figure 4.1 The three different self-sorting outcomes in coordination-driven self-assembly; a) a narcissistic self-sorted mixture; b) integrative self-sorting that gives rise to a single heteroleptic product of choice (here the *cis*-$Pd_2L^A{}_2L^B{}_2$ species); c) statistical mixture according to a Boltzmann distribution.[3] Copyright © 2017 The Royal Society of Chemistry.

Recently, chiral dithienyl ethene (DTE) chromophores,[6] being an attractive and elegant group, offered fascinating opportunities for the quantification of chirality transfer.[7] Because its chirality might be tunable by light in a fully reversible manner. For example, van Esch and Feringa used DTE-based gels to demonstrate optical transcription of supramolecular into molecule chirality.[8] Andréasson achieved non-covalent binding of cationic DTE derivatives to DNA, followed by enantioselective photoswitching.[9]

In this chapter, A $Pd_2L^A{}_3L^B$ type heteroleptic cage, combining a helicene ligand **L^1** and preassembled bowl-like compound *c*-**B**, was reported. Like our recently reported family

of photochromic DTE cages[10] with a stimuli-responsive chemistry,[11,12] the heteroleptic cage *c*-**B**-**L**^{1} could be reversible switched between its open and closed conformational form under UV (313 nm) and visible (617 nm) light. Using a homochiral ligand, either **L**^{1P} or **L**^{1M} instead, chirality transfer from helicene ligand to DTE ligands in the heteroleptic cage could be observed during light irradiation (Figure 4.2). The absolute configuration of ligand-to-ligand induction could be related through chiral HPLC, CD spectra and DFT-calculated Cotton effects. Thus, further allowed a better understanding of the ligand interactions in confined cages.

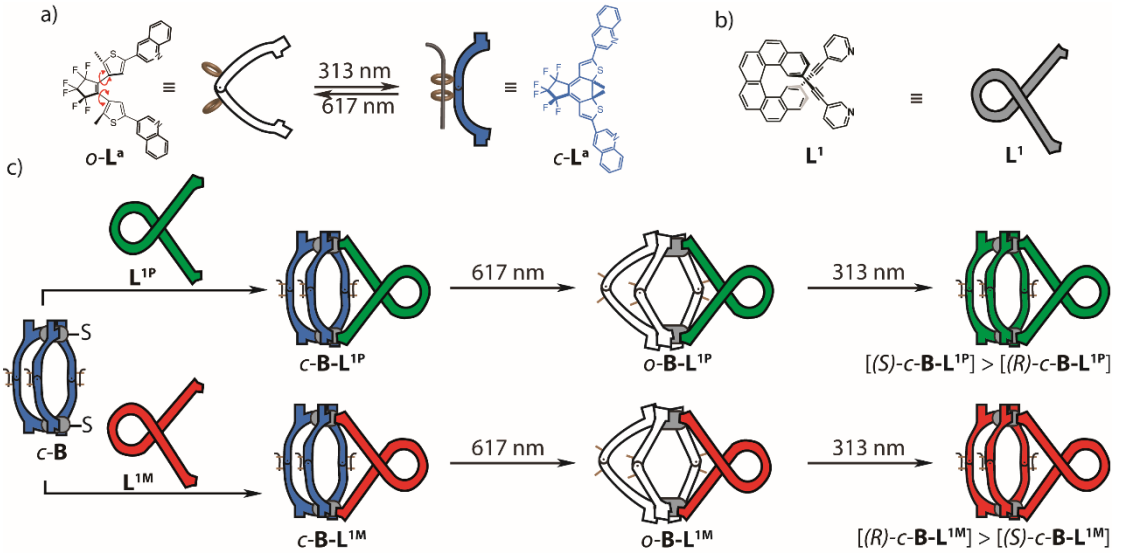

Figure 4.2 a) Reversible photo-switching of DTE based ligand between their conformational open form *o*-**L**^{a} and closed form *c*-**L**^{a}; b) Helicene based ligand **L**^{1}; c) Formation of heteroleptic cages with homochiral **L**^{1M} (up) and **L**^{1P} (down) and their chiral-transfer from **L**^{1P}/**L**^{1M} to **L**^{a} during light irradiation.

4.2 Synthesis of *c*-B-L^{1}

Following the protocols in Chapter 2, *c*-**B** was synthesized by heating a mixture of 3 eq. *c*-**L**^{a} and 2.0 eq. of $[Pd(CH_3CN)_4](BF_4)_2$ in CD_3CN at 70 °C for 2 h. Subsequently, stirring a 1 : 1 mixture of *c*-**B** solution with **L**^{1} (d_6-DMSO stock soluton) in CD_3CN at room temperature for 1 h, the heteroleptic cage $[Pd_2(c\text{-}\mathbf{L}^{a})_3\mathbf{L}^{1}](BF_4)_4$ (*c*-**B**-**L**^{1}) was formed quantitatively, as unambiguously confirmed by ^{1}H NMR spectroscopy, high-resolution ESI mass spectrometry (Figure 4.3b). Upon titration of **L**^{1} into a racemic *c*-**B** solution, the broad but clear ^{1}H NMR spectrum split up into several set of signals with signals broadening even with enantiopure **L**^{1P} due to the number of stereoisomers (Figure 4.3a). However, the ESI mass spectrum displayed a series of species supporting the expected heteroleptic cage *c*-**B**-**L**^{1} composition with a variable number of BF_4^- counter ions ($[Pd_2(c\text{-}\mathbf{L}^{a})_3\mathbf{L}^{1}]^{4+}$, $[Pd_2(c\text{-}\mathbf{L}^{a})_3\mathbf{L}^{1}+BF_4]^{3+}$ and $[Pd_2(c\text{-}\mathbf{L}^{a})_3\mathbf{L}^{1}+2BF_4]^{2+}$). In all cases, experimental isotope patterns were found to be in very good agreement with the calculated distributions (Figure 4.3b), indicating the formation of heteroleptic cage

c-**B**-**L**^{1}. Next, enantiopure (*R*)-*c*-**B** and **L**^{1P} were used instead in the synthesis. Fortunately, the signals in the ^{1}H NMR spectrum were much distinguishable, and could be fully analyzed though COSY, NOESY and DOSY NMR spectra (Figure 4.9, Figure 4.10 & Figure 4.12). The cross signals of $H_{a\text{-}a''}$ and $H_{b\text{-}b''}$ in the NOESY spectrum confidently provided evidence of combing **L**^{1} and *c*-**B** (Figure 4.10). Additionally, DOSY NMR analysis confirmed that all the signals belong to a single species, further revealing that *c*-**B**-**L**^{1} was successfully assembled (Figure 4.12).

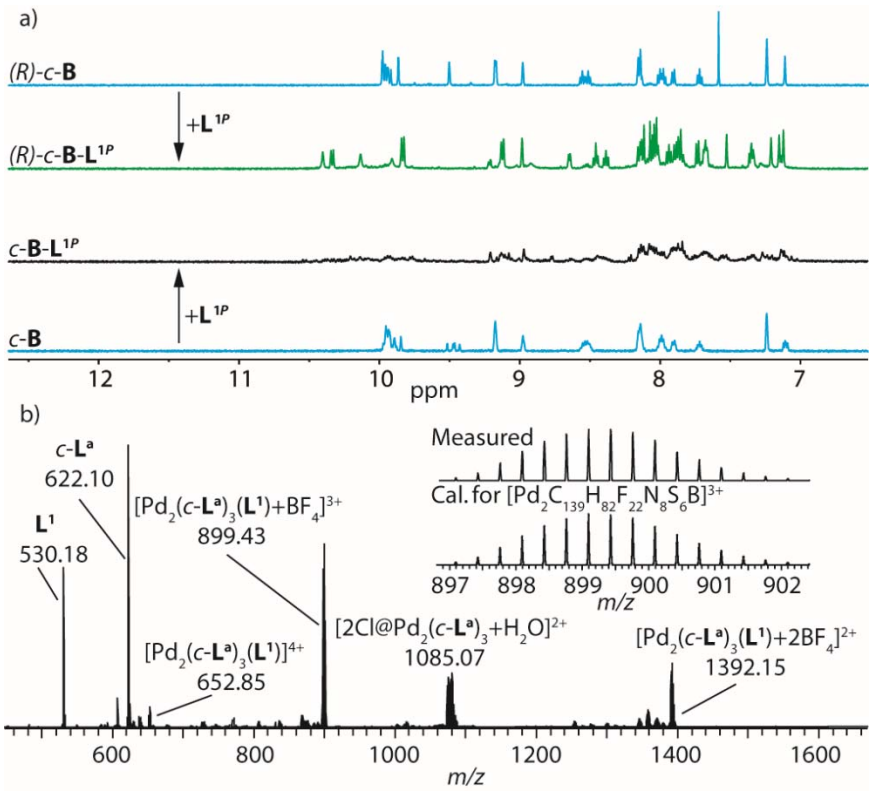

Figure 4.3 a) ^{1}H NMR spectra (500 MHz, CD_3CN, 298 K) of bowl *c*-**B**, (*R*)-*c*-**B** and heteroleptic cages *c*-**B**-**L**^{1}, (*R*)-*c*-**B**-**L**^{1}; b) ESI-MS spectrum of *c*-**B**-**L**^{1} with the measured and calculated isotope pattern of [*c*-**B**-**L**^{1}+BF_4]$^{3+}$ shown in the inset.

Despite numerous attempts, unfortunately, we could not obtain a single crystal suitable for X-ray analysis. The heteroleptic cage (*R*)-*c*-**B**-**L**^{1P} was modeled using SPARTAN and optimized on a PM6 level of theory without constrains. The obtained resulting structure was further refined by DFT calculations (B3LYP/LANL2DZ) using GAUSSAIN[15] (Figure 4.4).

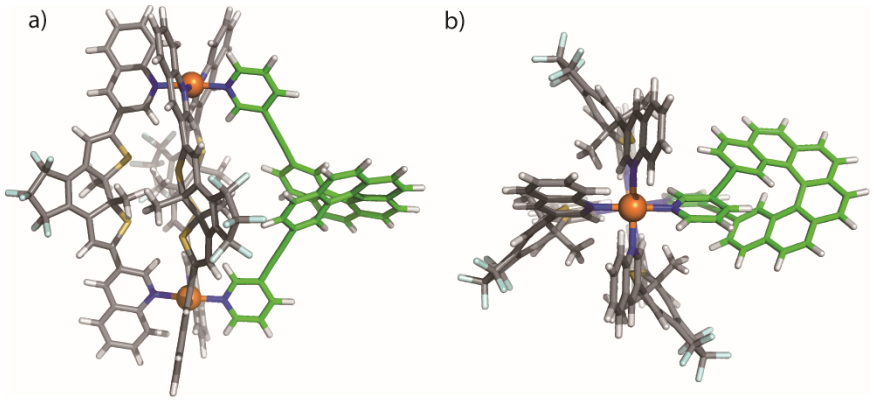

Figure 4.4 a) DFT optimized structure of a heteroleptic cage (*R*)-*c*-**B**-**L**^{1P} in its a) side and b) top view. Here the ligand **L**^{1P} was marked as green. (C gray except for **L**^{1P}, H white, N blue, F cyan, S yellow, Pd orange).

4.3 Chiral induction

With heteroleptic cage in hand, we set up to test whether chiral ligand can induce a transfer of chiral information onto the surrounding ligand in the cage structure with light. Firstly, the stability under light irradiation of heteroleptic cages *c*-**B**-**L**^{1P}/*c*-**B**-**L**^{1M} which assembled from racemic *c*-**B** and enantiopure **L**^{1P} or **L**^{1M} were checked via NMR spectroscopy and high resolution ESI mass spectrometry. Exposure of a CD_3CN solution of *c*-**B**-**L**^{1P}/*c*-**B**-**L**^{1M} with visible light (617 nm), the deep blue solution turned colorless and the strong characteristic UV-Vis absorbance band center at 600 nm decreased (Figure 4.5a). ^{1}H NMR shows that the broad and convoluted spectrum became recognizable (Figure 4.14 & Figure 4.15). Additionally, high resolution ESI mass was introduced to further determine if the heteroleptic cage was still intact after photo-reaction. With 617 nm irradiation, the signals in the ESI spectrum representing to heteroleptic cage (here *o*-**B**-**L**^{1M}(*c*-*o*)) are promising (Figure 4.16). Subsequently, the color of the solution changed back to deep blue and the absorbance band at 600 nm recovered again when irradiated under UV light (313 nm) at 298 K for the colorless sample (Figure 4.5a). Moreover, ^{1}H NMR spectrum was getting obscured again (Figure 4.14). At the same time, ESI mass signals of heteroleptic cage (here *c*-**B**-**L**^{1M}(*c*-*o*-*c*)) remained (Figure 4.17), which ambiguously confirmed that the light switching reaction could not decompose the heteroleptic cage.

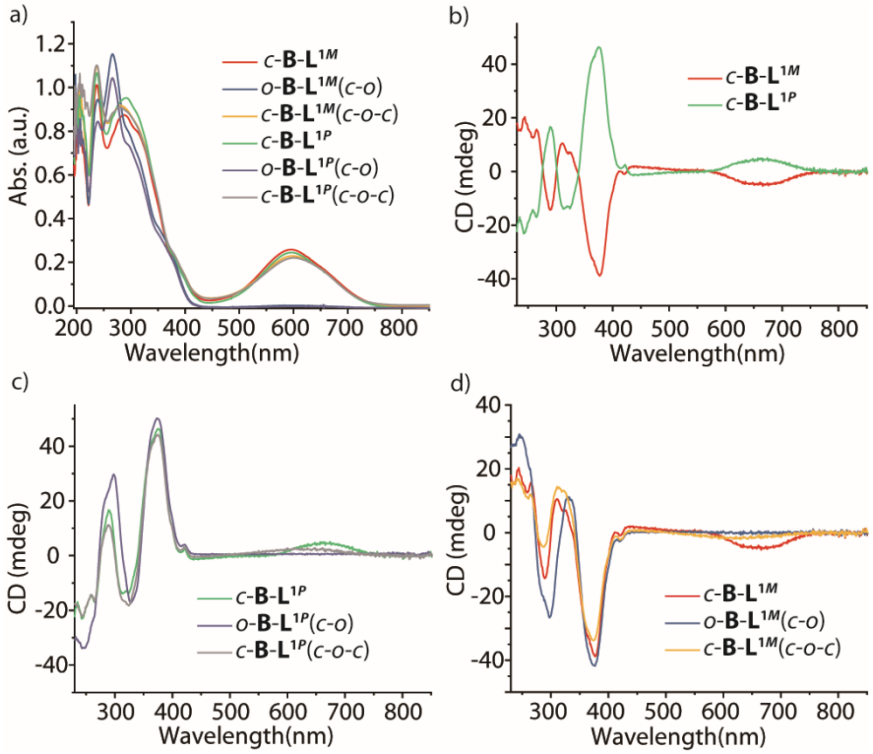

Figure 4.5 a) UV-vis spectra of *c*-**B**-**L**^{1P}/*c*-**B**-**L**^{1M} (0.05 mM, CH_3CN, 298 K), their corresponding photo-switched (617 nm) samples *o*-**B**-**L**^{1P}(*c*-*o*)/*o*-**B**-**L**^{1M}(*c*-*o*) (0.05 mM, CH_3CN, 298 K) and irradiated back (313 nm) samples *c*-**B**-**L**^{1P}(*c*-*o*-*c*)/*c*-**B**-**L**^{1M}(*c*-*o*-*c*) (0.05 mM, CH_3CN, 298 K); b) CD spectra of *c*-**B**-**L**^{1P}/*c*-**B**-**L**^{1M} (0.05 mM, CH_3CN, 298 K); c) CD spectra of *c*-**B**-**L**^{1P}, *o*-**B**-**L**^{1P}(*c*-*o*) and *c*-**B**-**L**^{1P}(*c*-*o*-*c*) (0.05 mM, CH_3CN, 298 K), irradiation under 298 K; d) CD spectra of *c*-**B**-**L**^{1M}, *o*-**B**-**L**^{1M}(*c*-*o*) and *c*-**B**-**L**^{1M}(*c*-*o*-*c*) (0.05 mM, CH_3CN, 298 K), irradiation under 298 K.

Next, circular dichroism (CD) spectra were measured to track the chirality transfer in the heteroleptic cage. Surprisingly, the spectra of *c*-**B**-**L**^{1P}/*c*-**B**-**L**^{1M} showed a Cotton effect assigned to the DTE ligand chromophore center at 660 nm, which would be expected to show no CD signals due to their deriving from racemic *c*-**B** (Figure 4.5b). That might be because the chiral ligand **L**^{1P}/**L**^{1M} induced overall chirality of the heteroleptic cage. After opening reaction to *o*-**B**-**L**^{1P}(*c*-*o*)/ *o*-**B**-**L**^{1M}(*c*-*o*), however, the induced CD bands at 660 nm completely disappeared and showed increasing intensity of CD bands at 296 nm and 373 nm (Figure 4.5c & d). Upon switching back under 313 nm at 298 K to *c*-**B**-**L**^{1P}(*c*-*o*-*c*)/ *c*-**B**-**L**^{1M}(*c*-*o*-*c*), the CD band at λ_{max} = 630 nm appeared, showing a slightly lower intensity with 30 nm blue shift compared with that of the as-synthesized *c*-**B**-**L**^{1P}/*c*-**B**-**L**^{1M} (Figure 4.5c & d). We explain this observation with a photochemical fixation of an opposite chirality locking of the DTE ligand to the overall cage structure derived chirality induced by the presence of **L**^{1P}/**L**^{1M}. And the slight decrease of the bands at 296 nm and 373 nm would be attributed to the part of degradation, which could be approved by UV-vis spectrum.

4.4 Degree of induction

To check the degree of chirality transfer from **L**^{1P}/**L**^{1M} to *o*-**L**^{a} in the cage, the closed form cages *c*-**B-L**^{1P}(*c*-*o*-*c*)/ *c*-**B-L**^{1M}(*c*-*o*-*c*), which were re-cyclized at 298 K, were disassembled. By adding aqueous EDTA-2Na, followed by extraction with DCM under strict exclusion of light, the disassembled solution was examined for enantiomeric excess (*ee*) by chiral HPLC. Compared with racemic *c*-**L**^{a} (Figure 4.6c), the enriched ligands *R*, *R*-*c*-**L**^{a} or *S*, *S*-*c*-**L**^{a}, giving 31.4% and 34.2% *ee* value separately for *c*-**B-L**^{1P}(*c*-*o*-*c*) and *c*-**B-L**^{1M}(*c*-*o*-*c*) were obviously observed (Figure 4.6). To determine the absolute configuration of the enrichment, TD-DFT calculation for CD spectrum was performed, which shows that the left HPLC signal represent *R*, *R*-*c*-**L**^{a} and the right trace is *S*, *S*-*c*-**L**^{a} (Chapter 4.6.4). The results indicate, that **L**^{2P} induced *S*, *S*-*c*-**L**^{a} photo-cyclization, while **L**^{1M} induced *R*, *R*-*c*-**L**^{a} enrichment in the heteroleptic cage.

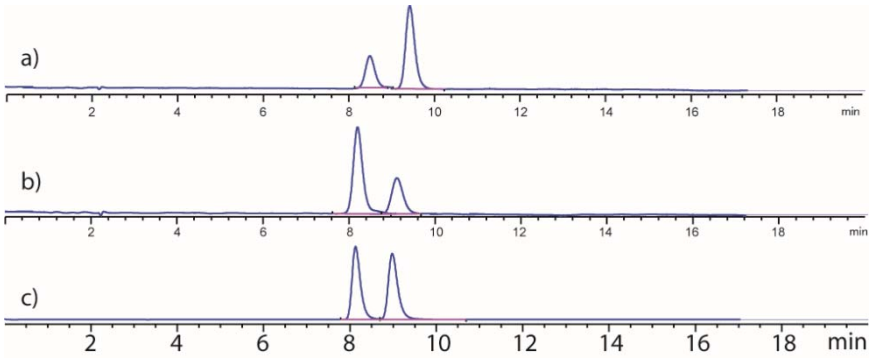

Figure 4.6 Chiral HPLC traces of the breakdown of a) *c*-**B**-**L**^{1P}(*c*-*o*-*c*) and b) *c*-**B**-**L**^{1M}(*c*-*o*-*c*) after irradiation with visible (617 nm) and UV (313 nm) light under 298 K; c) Chiral HPLC trace of racemic of *c*-**L**^{a}. (Chromatography column: Daicel IC. Mobile phase: Hexane/ CH_2Cl_2/ Methanol = 60:39:1. Run time: 20 min. Flow rate: 1.0 mL/min)

Since we reported that temperature would affect the degree of guest to host chirality transfer degree.[13] Thus, the same procedure at several lower temperatures down till to 77 K was used to test their chirality transfer degree. A quartz NMR tube containing the acetonitrile solution of *o*-**B-L**^{1P}(*c*-*o*)/ *o*-**B-L**^{1M}(*c*-*o*) was immersed in different cooling baths in a transparent quartz Dewar and irradiated with light at 313 nm. The CD spectra showed slightly increasing signal intensities with decreasing bath temperatures until 231 K, indicating enrichment of one ligand enantiomer over the other (Figure 4.21). Continuing cooling down the bath temperature to 195 K and 77 K to freeze the sample solution, however, there is no significant change with CD spectra (Figure 4.21). Later, the samples of *c*-**B-L**^{1P}(*c*-*o*-*c*) and *c*-**B-L**^{1M}(*c*-*o*-*c*) were disassembled and extracted corresponding ligands as the same procedure above to check the exact amount of chiral induction by chiral HPLC. **Table 1** summarizes the results, showing that the enrichment obviously improves at lower temperatures. Maximum obtained *ee* values were around 52 % for both enantiomers ligands. But they did not further increase after 231 K.

Table 3.1 Enantiomeric excess (*ee*) of ligands *R*, *R*-*c*-**L**[a] and *S*, *S*-*c*-**L**[a] after irradiation of [*o*-**B**-**L**^{1P}(c-o)/*o*-**B**-**L**^{1M}(c-o)] with 617 nm and 313 nm light at various temperatures

ee (%)[a]	298 K	273 K[b]	231 K[c]	195 K[d]	77 K[e]
c-**B**-**L**^{1P}(*c*-*o*-*c*)	31.4	39.9	49.6	51.1	51.6
c-**B**-**L**^{1M}(*c*-*o*-*c*)	34.2	42.2	50.0	52.0	52.7

[a] values determined by HPLC (monitored at 600 nm) with a Chiralpak IC column; [b] ice-water; [c] dry ice-acetonitrile; [d] dry ice-acetone; [e] liquid nitrogen.

4.5 Conclusion

In conclusion, a $Pd_2L^A{}_3L^B$ type heteroleptic cage *c*-**B**-**L**^{1} combined from DTE-based bowl *c*-**B** and ligand **L**^{1} was reported. The significantly chirality transfer of **L**^{1P}/**L**^{1M} to the DTE ligands in the cage were observed in the DTE closing reaction. The enantiomeric enhancement, to the best of our knowledge, is the first time observed in a $Pd_2L^A{}_3L^B$ type heteroleptic cage *c*-**B**-**L**^{1} which was controlled through light irradiation.

4.6 Experimental section

4.6.1 General procedures

All chemicals, except otherwise specified, were obtained from commercial sources and used without further purification. Perfluoro-1,2-bis(2-iodo-5-methylthien-4-yl)cyclopentene[14], **L**^{1} were prepared according to a literature procedure.[15] Recycling gel permeation chromatography was performed on a JAI LC-9210 II NEXT GPC system equipped with Jaigel 1H and 2H columns in series using chloroform as the eluent (HPLC grade). NMR measurements were all conducted at 298 K on Avance-500 and Avance-600 instruments from Bruker and INOVA 500 MHz machine from Varian. High-resolution ESI mass spectrometric measurements were carried out on maXis ESI-TOF MS and ESI-tims TOF machines from Bruker. The irradiations were performed with a 500 W Hg Arc lamp from LOT-Quantum Design. Chiral HPLC was performed on an Agilent Technologies 1260 infinity HPLC system equipped with Daicel CHIRALPAK IC columns (250 x 4.6 mm and 250 x 10 mm) using a dichloromethane/hexane/methanol (39%/60%/1%) mixture as eluent for the separation of *c*-**L**[a]. UV-vis spectra were recorded on an Agilent 8453 UV-Vis spectrophotometer. CD spectra were measured on an Applied Photophysics Chirascan circular dichroism spectrometer. Heteroleptic cage

(*R*)-*c*-**B**-**L**^{1P} model was constructed using SPARTAN[16] and were first optimized on a PM6 level of theory (no counter ions were included) without constrains. The resulting structures were than further refined by DFT calculations (B3LYP/LANL2DZ) using Gaussain 09.[17]

4.6.2 Synthesis

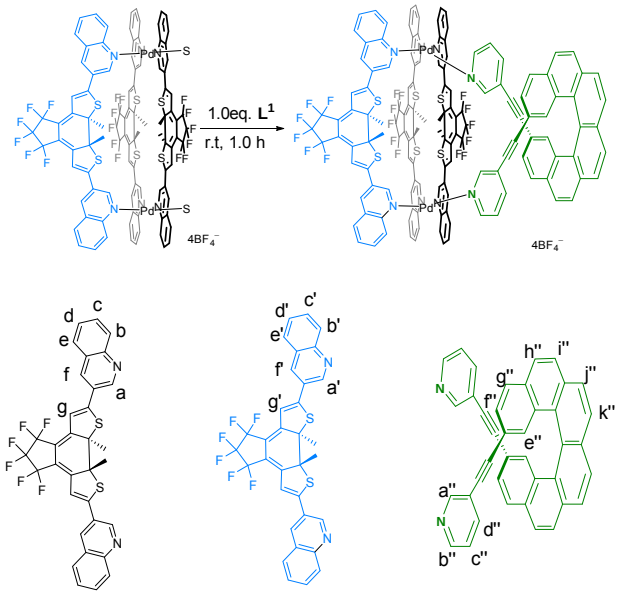

Scheme 3.1 Synthesis route of heteroleptic cage *c*-**B**-**L**^{1}.

The heteroleptic cage compound $[Pd_2(c\text{-}\mathbf{L}^{a})_3\mathbf{L}^{1}](BF_4)_4$ (*c*-**B**-**L**^{1}) was synthesized in quantitative yield by stiring a mixture of $[Pd_2(c\text{-}\mathbf{L}^{a})_3](BF_4)_4$ (*c*-**B**)(1.0 µmol, 666.67 µL of a 1.5 mM stock solution in CD_3CN), **L**^{1} (1.0 µmol, 33.33 µL of a 30 mM stock solution in d_6-DMSO) and 300 µL CD_3CN at room temperature for 30 minutes in a closed vial to yield 1000 µl of a 1.0 mM solution of *c*-**B**-**L**^{1}. Because of undistinguishable ^{1}H NMR spectrum (lots of diastereomers), the enantiopure data here ((R)-*c*-**B**-**L**^{1P}) was given for clarity. ^{1}H NMR (700 MHz, CD_3CD) δ 10.45 (s, 2H), 10.30 (d, *J* = 8.4 Hz, 2H), 10.14 (s, 2H), 9.93 (s, 2H), 9.87 (d, *J* = 8.7 Hz, 2H), 9.84 (d, *J* = 8.7 Hz, 2H), 9.14 (s, 2H), 9.12 (s, 1H), 9.11 (s, 3H), 8.97 (s, 2H), 8.81 (d, *J* = 6.0 Hz, 2H), 8.42 (dt, *J* = 20.9, 8.1 Hz, 4H), 8.14 – 8.01 (m, 14H), 7.92 (t, *J* = 7.6 Hz, 2H), 7.88 (t, *J* = 8.1 Hz, 2H), 7.85 (t, *J* = 9.1 Hz, 2H), 7.75 (d, *J* = 8.1 Hz, 2H), 7.68 (t, *J* = 7.7 Hz, 2H), 7.66 (t, 2H), 7.56 (s, 2H), 7.36 (t, *J* = 7.0 Hz, 2H), 7.33 (d, *J* = 8.0 Hz, 2H), 7.16 (s, 2H), 7.15 (s, 2H), 7.07 (s, 2H), 2.67 (s, 6H), 2.52 (s, 6H), 2.42 (s, 6H). ESI-HRMS calculated for $[Pd_2C_{139}H_{82}F_{22}N_8S_6B]^{3+}$ ($[Pd_2(c\text{-}\mathbf{L}^{a})_3\mathbf{L}^{1}+BF_4]^{3+}$) *m/z* = 899.4273, found *m/z* = 899.4300.

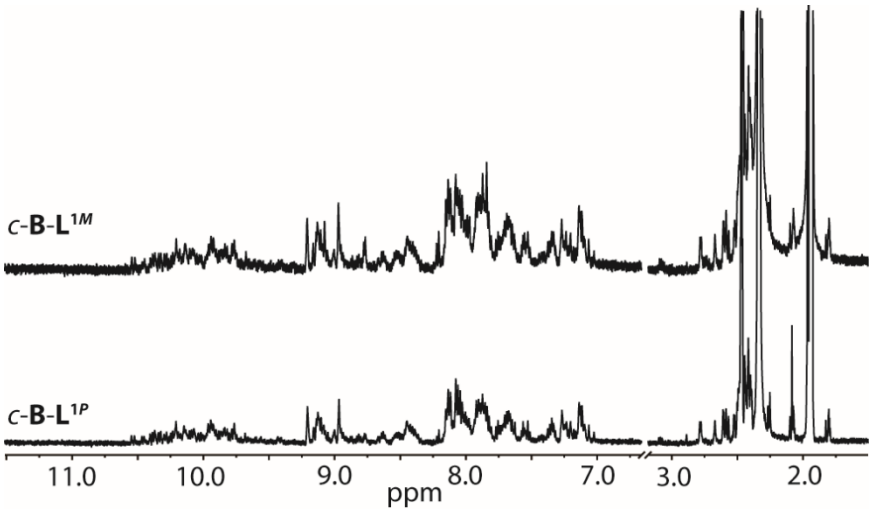

Figure 4.7 ^{1}H NMR spectra (600 MHz, CD_3CN, 298 K) of *c*-**B**-**L**$^{\mathbf{1P/1M}}$, started from a racemic *c*-**B**.

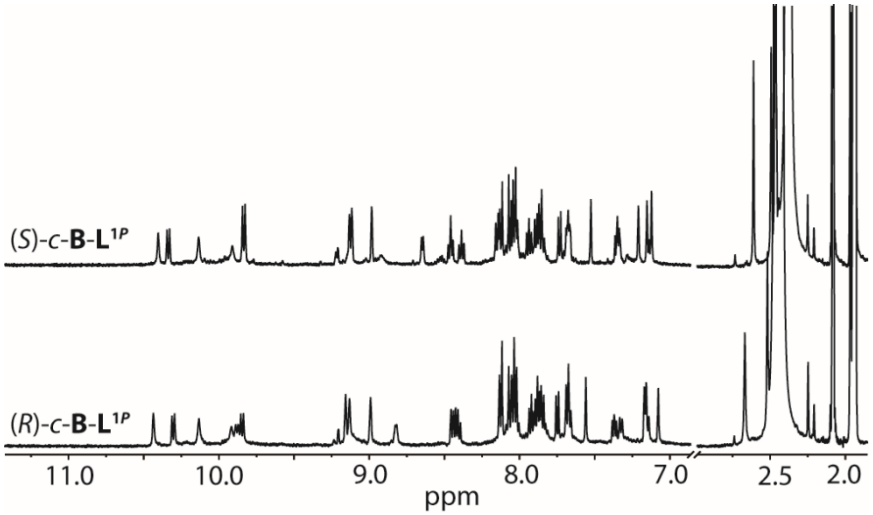

Figure 4.8 ^{1}H NMR spectra (700 MHz, CD_3CN, 298 K) of (*R/S*)-*c*-**B**-**L**$^{\mathbf{1P}}$, started from an enantiopure (*R/S*)-*c*-**B**.

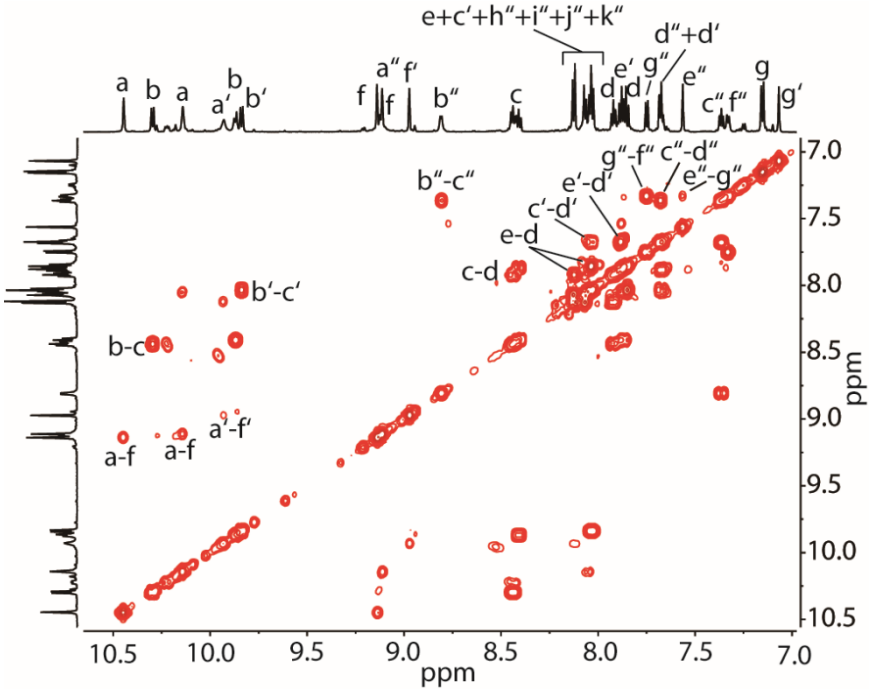

Figure 4.9 ^{1}H–^{1}H COSY spectrum (700 MHz, CD_3CN, 298 K) of (*R*)-*c*-**B**-**L**^{1P} (only showing aromatic region).

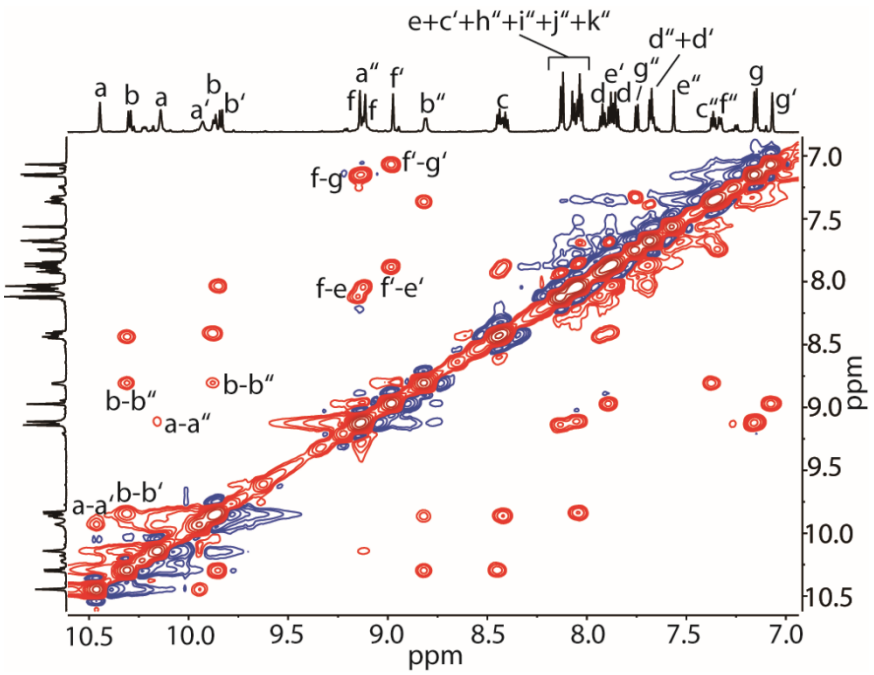

Figure 4.10 ^{1}H–^{1}H NOESY spectrum (700 MHz, CD_3CN, 298 K) of (*R*)-*c*-**B**-**L**^{1P} (only showing aromatic region).

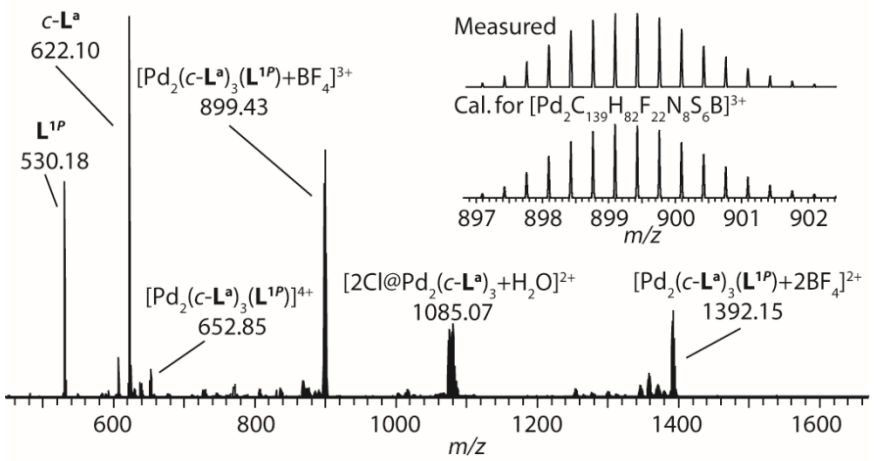

Figure 4.11 ESI-HRMS of *c*-**B**-**L**^{1P}.

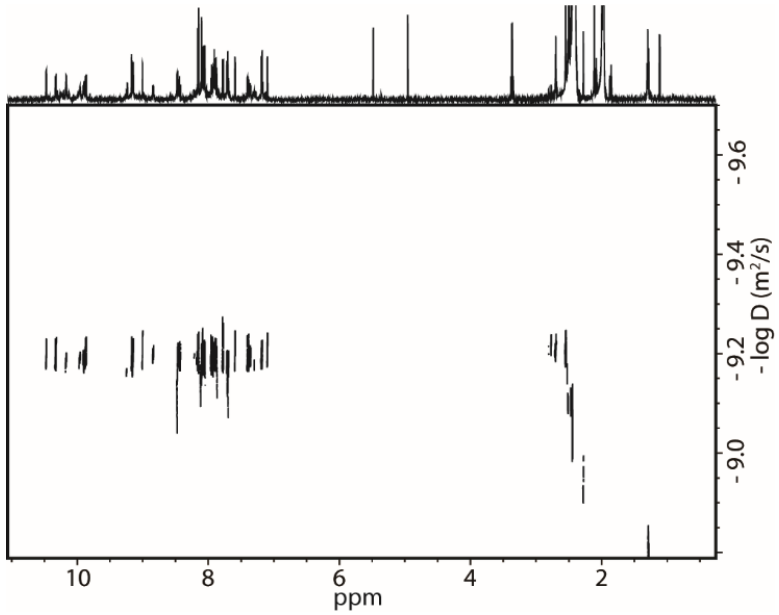

Figure 4.12 DOSY NMR spectrum (600 MHz, CD_3CD, 298 K) of (*R*)-*c*-**B**-**L**^{1P}**.**

4.6.3 Photo-switch between *c*-B-L^1 and *o*-B-L^1 photoisomers

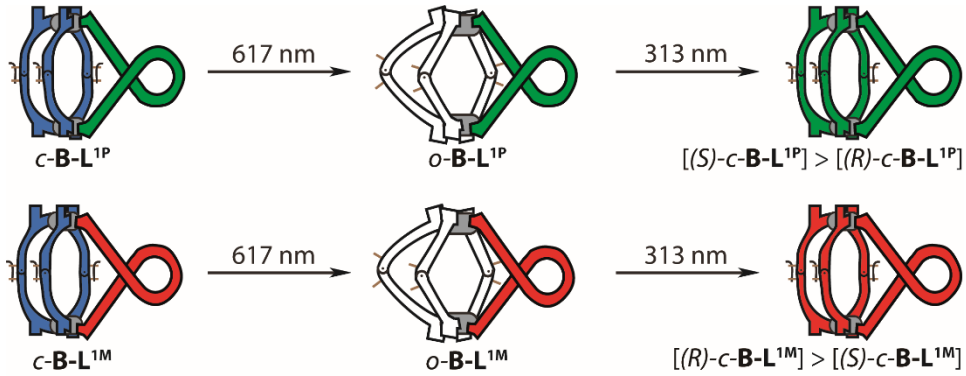

Figure 4.13 Scheme showing the photoswitching from *c*-**B**-**L**^{1} to *o*-**B**-**L**^{1}(c-o) under 617 nm, and switching back to their conformational closed form *c*-**B**-**L**^{1}(c-o-c) under UV light 313 nm.

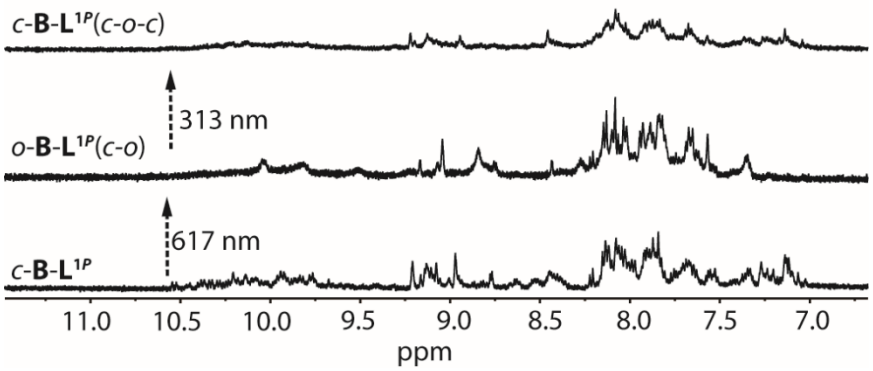

Figure 4.14 ^{1}H NMR spectra (500 MHz, CD_3CD, 298 K) of (*R/S*)-*c*-**B**-**L**^{1P}.

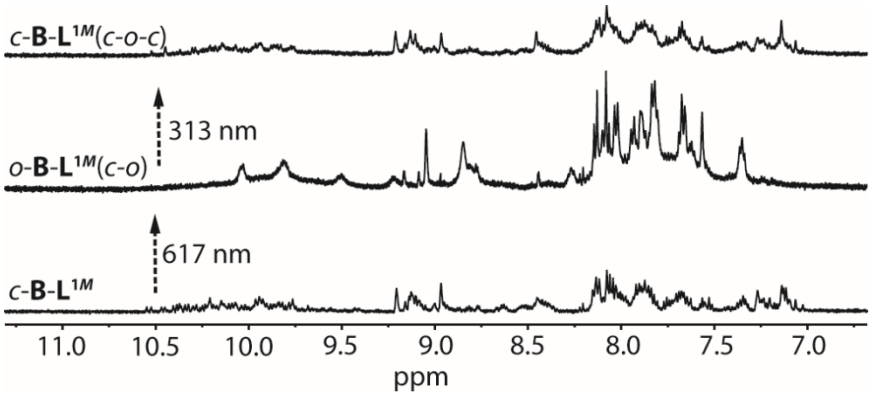

Figure 4.15 ^{1}H NMR spectra (500 MHz, CD_3CD, 298 K) of (*R/S*)-c-**B**-**L**^{1M}.

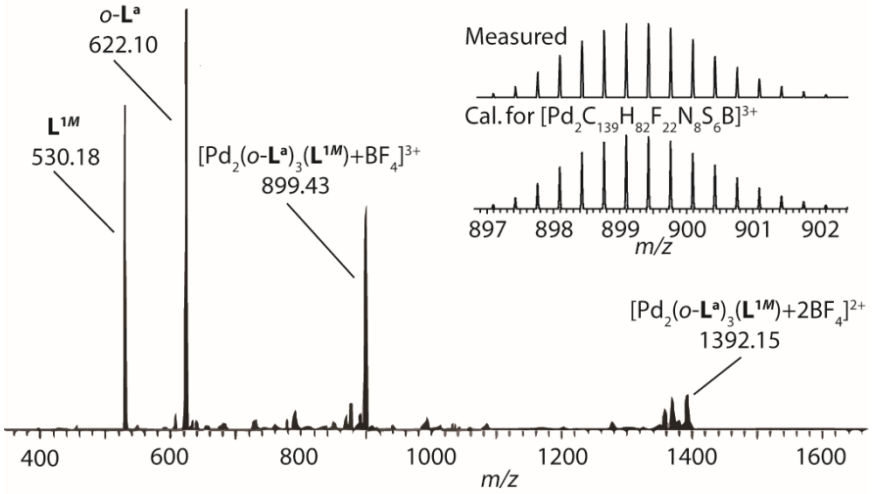

Figure 4.16 ESI-HRMS of *o*-**B**-**L**^{1M}(c-o). Calculated for $[Pd_2C_{139}H_{82}F_{22}N_8S_6B]^{3+}$ ($[Pd_2(c\text{-}L^a)_3L^{1M}+BF_4]^{3+}$) *m/z* = 899.4273, found *m/z* = 899.4300.

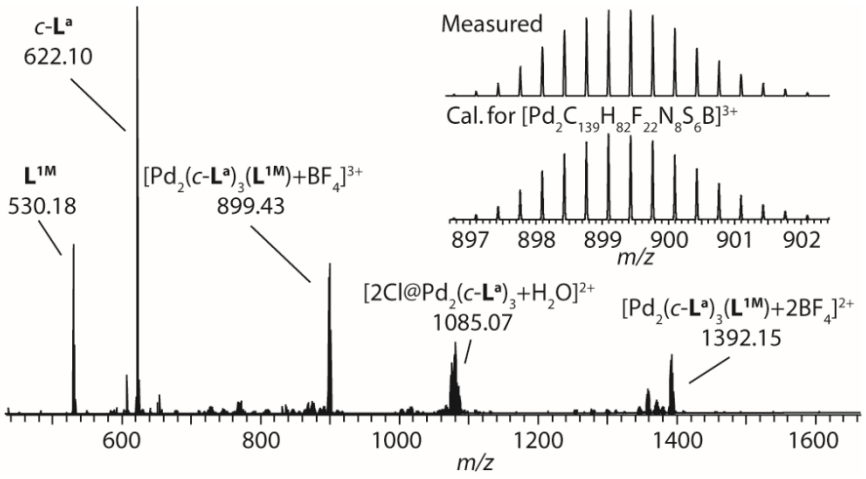

Figure 4.17 ESI-HRMS of *o*-**B-L^{1M}**(c-o-c). Calculated for $[Pd_2C_{139}H_{82}F_{22}N_8S_6B]^{3+}$ ($[Pd_2(c\text{-}L^a)_3L^{1M}+BF_4]^{3+}$) *m/z* = 899.4273, found *m/z* = 899.4300.

4.6.4 Absolute configuration

The open-form ligand *o*-**L^a** (10 mg) was dissolved in CD_2Cl_2 (1 mL) and then irradiated with 313 nm UV light. The pure (*R, R*) and (*S, S*) ligand enantiomers were separated by preparative chiral HPLC using a Daicel IC column (250 x 10 mm) under strict exclusion of daylight. The purity of separated **1** (the first fraction of HPLC) and **2** (the second fraction of HPLC) enantiomers were checked using analytical HPLC using a Daicel IA column (250 x 4.6 mm). In order to determine the absolute stereochemistry of the enantiomers, CD spectra were calculated by TD-DFT methods at the B3LYP/6-31G(d) level of theory in the Gaussian 09 software[15] (using keyword iop(9/40=2)).

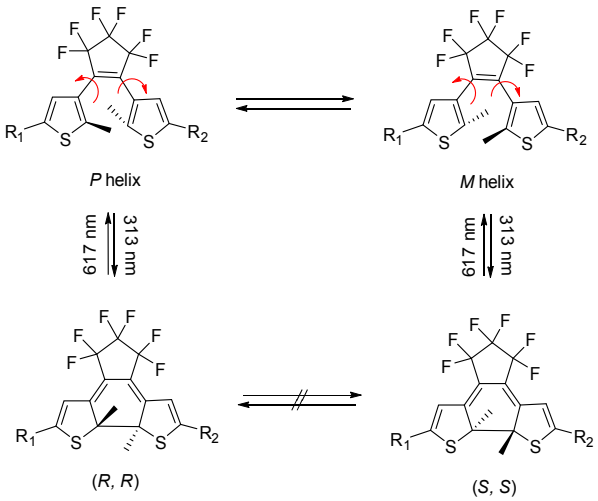

Scheme 3.2 Photoisomerization of a diarylethene (DTE). The photocyclization reactions from *P*- and *M*-helical conformers of the open-ring isomer produce (*R, R*) and (*S, S*) enantiomers of the closed-ring isomer, respectively.

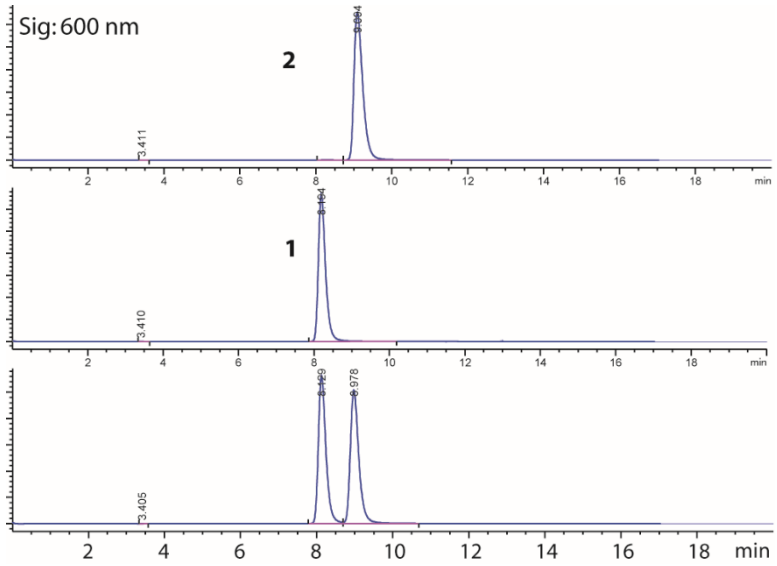

Figure 4.18 Chiral HPLC chromatograms of racemic *c*-**L**[a]. (Chromatographic column: Daicel IC. Mobile phase: Hexane/ CH_2Cl_2/Methanol = 60 : 39.1 : 0.9. Run time: 20 min. Flow rate: 1.0 mL/min).

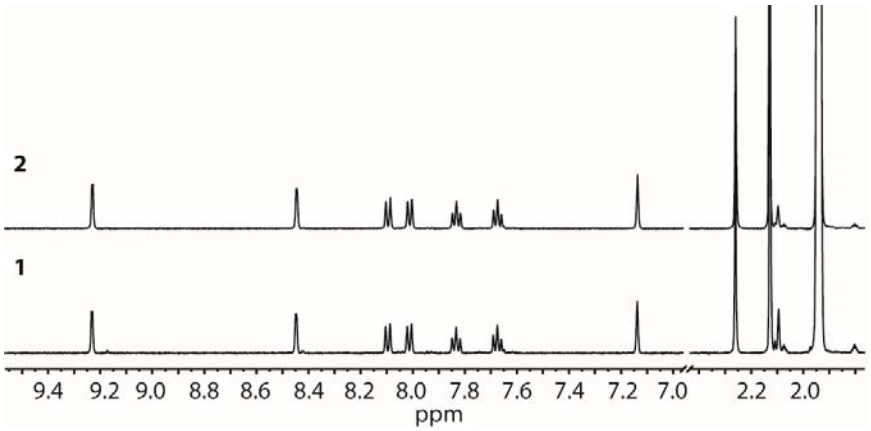

Figure 4.19 ^{1}H NMR spectra of enantiomeric pure fraction **1** and fraction **2**.

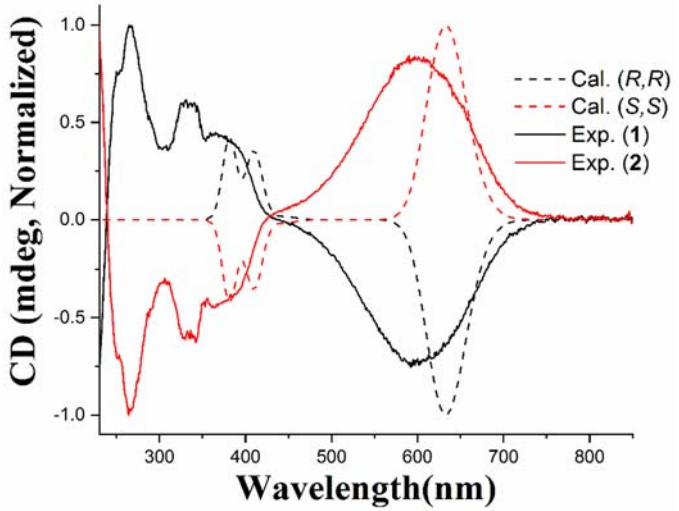

Figure 4.20 a) Calculated CD spectra of (*R, R*) and (*S, S*) closed form ligand enantiomers and measured CD spectra of closed ligand enantiomers from chiral HPLC resolved fraction 1 and 2 (0.1 mM, CH_3CN);. Both of the calculated CD spectrum of *c*-**L**[a] (*R, R*) and fraction **1** give negative cotton effect from 500 nm to 800 nm (this area shows the characteristic peak of closed form DTE derives), which means fraction 1 has *R, R* configuration, in contrast, fraction 2 is *S, S* configuration.

4.6.5 Temperature-dependent photocyclization

The samples *o*-**B**-**L**^{1P}(*c*-*o*)/*o*-**B**-**L**^{1M}(*c*-*o*) (1.0 mM,) were prepared in quartz NMR tubes with 617 nm irradiation to colorless from as-synthesized *c*-**B**-**L**^{1P}/*c*-**B**-**L**^{1M}. Later, *o*-**B**-**L**^{1P}(*c*-*o*)/*o*-**B**-**L**^{1M}(*c*-*o*) were immersed in cooling baths of different temperatures (see below) in a fully transparent quartz dewar, and irradiated back with 313 nm UV light to conformational closed form *c*-**B**-**L**^{1P}(*c*-*o*-*c*)/*c*-**B**-**L**^{1M}(*c*-*o*-*c*). Irradiation time for 298 K, 273 K and 231 K are all 1.5 h, while for both 195 K and 77 K, irradiation takes 50 h due to the freezing of the samples in these temperature. Subsequently, the samples were allowed to warm to room temperature under exclusion of light, the cages were disassembled by addition of Bu_4NOH (around 1.0 eq.) and EDTA, then separated by extraction with DCM. The enantiomeric excess of the photocyclization was determined by chiral HPLC (Daicel CHIRALPAK IC columns 250 x 4.6 mm).

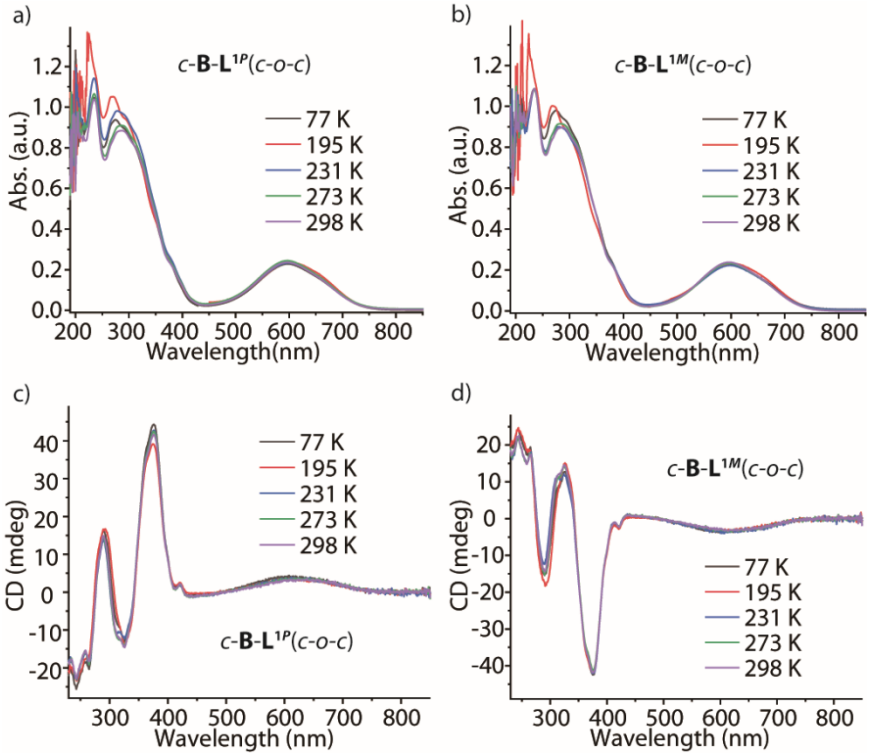

Figure 4.21 a) UV-Vis and c) CD spectra of heteroleptic cage *c*-**B**-**L**^{1P}(*c*-*o*-*c*) (0.05 mM, CH_3CN, 298 K) after irradiation with 313 nm light at temperatures from 298 K to 77 K (irradiation 1.5 h for 298 K, 273 K and 231 K, 50 h for 195 K & 77 K due to the freezing of the samples). For the same experiment of b) UV-Vis and d) CD spectra of *c*-**B**-**L**^{1M}(*c*-*o*-*c*).

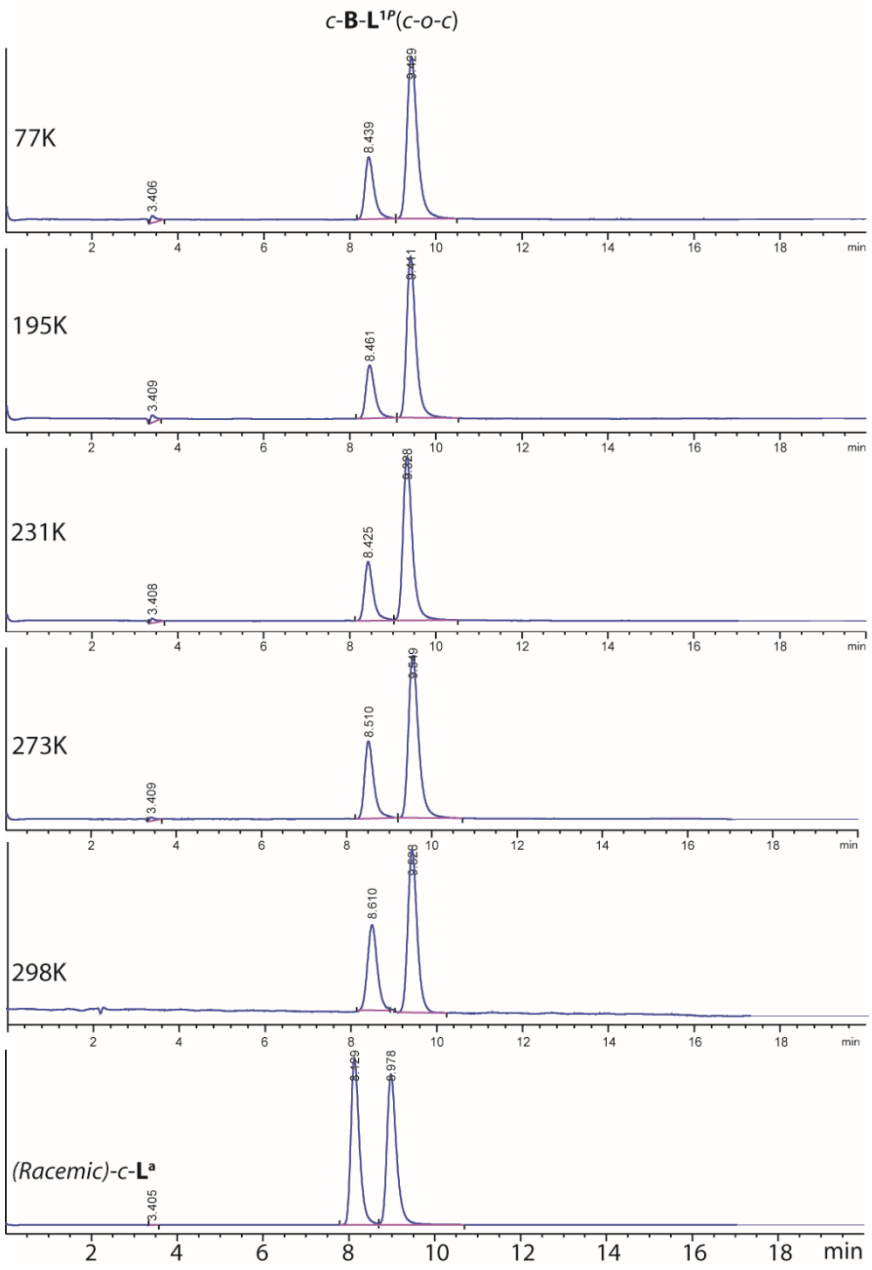

Figure 4.22 Chiral HPLC traces of c-**L**[a] from the breakdown of *c*-**B**-**L**[1P](*c*-*o*-*c*) (1 mM) after irradiation at varied temperatures ranging from 298 K to 77 K. (Chromatographic column: Daicel IC. Mobile phase: Hexane/CH_2Cl_2/Methanol = 60:39:1. Run time: 20 min. Flow rate: 1.0 mL/min).

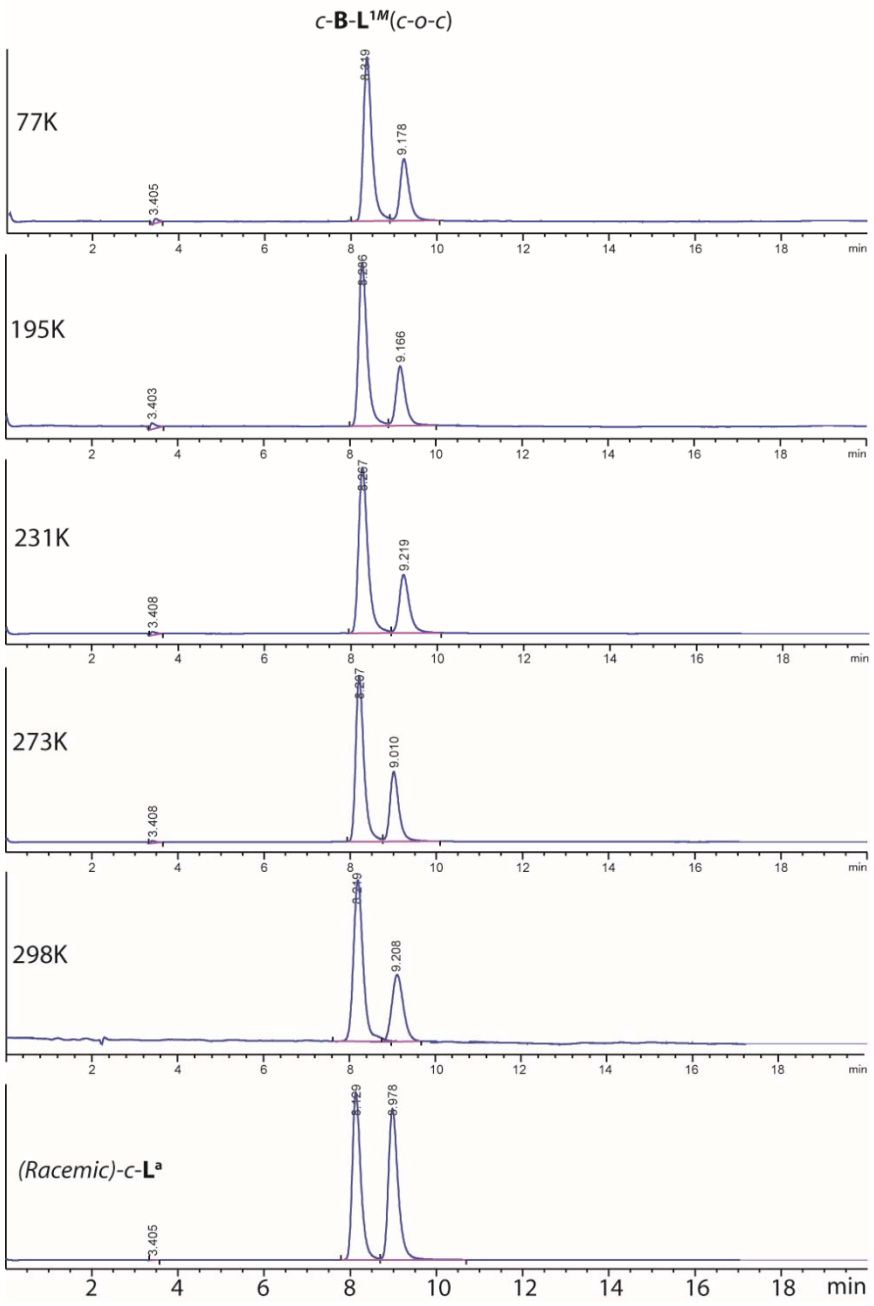

Figure 4.23 Chiral HPLC traces of c-$\mathbf{L^a}$ from the breakdown of *c*-**B**-$\mathbf{L^{1M}}$(*c*-*o*-*c*) (1 mM) after irradiation at varied temperatures ranging from 298 K to 77 K. (Chromatographic column: Daicel IC. Mobile phase: Hexane/CH_2Cl_2/Methanol = 60:39:1. Run time: 20 min. Flow rate: 1.0 mL/min).

4.7 References

[1] (a) H. Yamamoto, E. M. Carreira, (Eds.), *Comprehensive Chirality*, 1st ed., *Elsevier*, Amsterdam, **2012**. (b) B. L. Feringa, R. A. van Delden, *Angew. Chem. Int. Ed.* **1999**, *38*, 3418-3438. (c) A. R. Palmans, E. W. Meijer, *Angew. Chem., Int. Ed.* **2007**, *46*, 8948-8968. (d) M. Yoon, R. Srirambalaji, K. Kim, *Chem. Rev.* **2012**, *112*, 1196-1231; (e) G. Seeber, B. E. F. Tiedemann, K. N. Raymond, *Top. Curr. Chem*. **2006**, *265*, 147. (f) M. Liu, L. Zhang, T. Wang, *Chem. Rev.* **2015**, *115*, 7304-7397. (g) M. Raynal,

P. Ballester, A. Vidal-Ferran, P. W. van Leeuwen, *Chem. Soc. Rev.* **2014**, *43*, 1660-1733. (h) L. J. Chen, H. B. Yang, M. Shionoya, *Chem. Soc. Rev.* **2017**, *46*, 2555-2576. (i) K. Yan, R. Dubey, T. Arai, Y. Inokuma, M. Fujita, *J. Am. Chem. Soc.* **2017**, *139*, 11341-11344. (j) L. J. Prins, P. Timmerman, D. N. Reinhoudt, *J. Am. Chem. Soc.* **2001**, *123*, 10153-10163.

[2] (a) Y. Nishioka, T. Yamaguchi, M. Kawano, M. Fujita, *J. Am. Chem. Soc.* **2008**, *130*, 8160-8161. (b) W. Xuan, M. Zhang, Y. Liu, Z. Chen, Y. Cui, *J. Am. Chem. Soc.* **2012**, *134*, 6904-6907. (c) C. Gutz, R. Hovorka, C. Klein, Q. Q. Jiang, C. Bannwarth, M. Engeser, C. Schmuck, W. Assenmacher, W. Mader, F. Topic, K. Rissanen, S. Grimme, A. Lutzen, *Angew. Chem. Int. Ed.* **2014**, *53*, 1693-1698. (d) X. Wang, Y. Wang, H. Yang, H. Fang, R. Chen, Y. Sun, N. Zheng, K. Tan, X. Lu, Z. Tian, X. Cao, *Nat. Commun.* **2016**, *7*, 12469; (e) J. Sun, J. L. Bennett, T. J. Emge, R. Warmuth, *J. Am. Chem. Soc.* **2011**, *133*, 3268-3271; (f) A. M. Castilla, N. Ousaka, R. A. Bilbeisi, E. Valeri, T. K. Ronson, J. R. Nitschke, *J. Am. Chem. Soc.* **2013**, *135*, 17999-18006; (g) J. M. Rivera, T. Martín, J. Rebek, *Science* **1998**, *279*, 1021; (h) A. J. Terpin, M. Ziegler, D. W. Johnson, K. N. Raymond, *Angew. Chem., Int. Ed.* **2001**, *40*, 157-160; (i) A. V. Davis, D. Fiedler, M. Ziegler, A. Terpin, K. N. Raymond, *J. Am. Chem. Soc.* **2007**, *129*, 15354-15363.

[3] (a) W. M. Bloch, G. H. Clever, *Chem. Commun.* **2017**, *53*, 8506-8516.

[4] (a) (a) F. J. Rizzuto, M. Kieffer, J. R. Nitschke, *Chem. Sci.* **2018**, *9*, 1925-1930; (b) M. Frank, J. Ahrens, I. Bejenke, M. Krick, D. Schwarzer, G. H. Clever, *J. Am. Chem. Soc.* **2016**, *138*, 8279-8287; (c) M. Frank, L. Krause, R. Herbst-Irmer, D. Stalke, G. H. Clever, *Dalton Trans.* **2014**, *43*, 4587-4592.

[5] (a) R. Zhu, W. M. Bloch, J. J. Holstein, S. Mandal, L. V. Schafer, G. H. Clever, *Chem. Eur. J.* **2018**, *24*, 12976-12982; (b) W. M. Bloch, J. J. Holstein, W. Hiller, G. H. Clever, *Angew. Chem., Int. Ed.* **2017**, *56*, 8285-8289; (c) W. M. Bloch, Y. Abe, J. J. Holstein, C. M. Wandtke, B. Dittrich, G. H. Clever, *J. Am. Chem. Soc.* **2016**, *138*, 13750-13755; (d) D. Preston, J. E. Barnsley, K. C. Gordon, J. D. Crowley, *J. Am. Chem. Soc.* **2016**, *138*, 10578-10585; (e) M. Yamashina, T. Yuki, Y. Sei, M. Akita, M. Yoshizawa, *Chem. Eur. J.* **2015**, *21*, 4200-4204; (f) A. M. Johnson, R. J. Hooley, *Inorg. Chem.* **2011**, *50*, 4671-4673.

[6] (a) M. Irie, T. Fukaminato, K. Matsuda, S. Kobatake, *Chem. Rev*. **2014**, *114*, 12174-12277. (b) J. Zhang, H. Tian, *Adv. Optical Mater.* **2018**, 1701278.

[7] (a) D. J. van Dijken, J. M. Beierle, M. C. Stuart, W. Szymanski, W. R. Browne, B. L. Feringa, *Angew. Chem., Int. Ed.* **2014**, *53*, 5073-5077; (b) M. Fukagawa, I. Kawamura, T. Ubukata, Y. Yokoyama, *Chem. Eur. J.* **2013**, *19*, 9434-9437; (c) A. Mammana, G. T. Carroll, J. Areephong, B. L. Feringa, *J. Phy. Chem. B* **2011**, *115*,

11581-11587; (d) T. Shiozawa, M. K. Hossain, T. Ubukata, Y. Yokoyama, *Chem. Commun.* **2010**, *46*, 4785-4787; (e) M. Morimoto, S. Kobatake, M. Irie, *Chem. Commun.* **2008**, 335-337; (f) S. Yamamoto, K. Matsuda, M. Irie, *Angew. Chem., Int. Ed.* **2003**, *42*, 1636-1639; (g) E. Murguly, T. B. Norsten, N. R. Branda, *Angew. Int. Ed.* **2001**, *40*, 1752-1755; (h) K. Kawamura, K. Osawa, Y. Watanobe, Y. Saeki, N. Maruyama, Y. Yokoyama, *Chem. Commun*. **2017**, *53*, 3181-3184.

[8] J. J. D. de Jong, L. N. Lucas, R. M. Kellogg, J. H. van Esch, B. L. Feringa, *Science* **2004**, *304*, 278.

[9] T. C. Pace, V. Muller, S. Li, P. Lincoln, J. Andreasson, *Angew. Chem., Int. Ed.* **2013**, *52*, 4393-4396.

[10] (a) M. Han, R. Michel, B. He, Y. S. Chen, D. Stalke, M. John, G. H. Clever, *Angew. Chem., Int. Ed.* **2013**, *52*, 1319-1323. (b) M. Han, Y. Luo, B. Damaschke, L. Gomez, X. Ribas, A. Jose, P. Peretzki, M. Seibt, G. H. Clever, *Angew. Chem., Int. Ed.* **2016**, *55*, 445-449.

[11] (a) A. J. McConnell, C. S. Wood, P. P. Neelakandan, J. R. Nitschke *Chem. Rev.* **2015**, *115*, 7729-7793. (b) D. H. Qu, Q. C. Wang, Q. W. Zhang, X. Ma, H. Tian *Chem. Rev.* **2015**, *115*, 7543-7588.

[12] (a) S. Wiedbrauk, T. Bartelmann, S. Thumser, P. Mayer, H. Dube, *Nat. Commun.* **2018**, *9*, 1456. (b) Y. Hua, A. H. Flood, *J. Am. Chem. Soc.* **2010**, *132*, 12838-12840. (c) A. Diaz-Moscoso, F. A. Arroyave, P. Ballester, *Chem. Commun.* **2016**, *52*, 3046.

[13] R. Li, J. J. Holstein, W. G. Hiller, J. Andréasson, G. H. Clever, *J. Am. Chem. Soc.* **2019**, DOI: 10.1021/jacs.8b1187.

[14] (a) S. Fraysse, C. Coudret, J. P. Launay, *Eur. J. Inorg. Chem.* **2000**, 1581–1590; b) B. He, O. S. Wenger, *J. Am. Chem. Soc.* **2011**, *133*, 17027.

[15] T. R. Schulte, J. J. Holstein, G. H. Clever, *Angew. Chem. Int. Ed.* **2019**, DOI: 10.1002/anie.201812926.

[16] Spartan 08 Software, Wavefunction Inc., Irvine CA, **2008**.

[17] Gaussian 09, M. J. Frisch, G. W. Trucks, H. B. Schlegel, G. E. Scuseria, M. A. Robb, J. R. Cheeseman, G. Scalmani, V. Barone, B. Mennucci, G. A. Petersson, H. Nakatsuji, M. Caricato, X. Li, H. P. Hratchian, A. F. Izmaylov, J. Bloino, G. Zheng, J. L. Sonnenberg, M. Hada, M. Ehara, K. Toyota, R. Fukuda, J. Hasegawa, M. Ishida, T. Nakajima, Y. Honda, O. Kitao, H. Nakai, T. Vreven, J. A. Montgomery, Jr., J. E. Peralta, F. Ogliaro, M. Bearpark, J. J. Heyd, E. Brothers, K. N. Kudin, V. N. Staroverov, R. Kobayashi, J. Normand, K. Raghavachari, A. Rendell, J. C. Burant, S. S. Iyengar, J. Tomasi, M. Cossi, N. Rega, J. M. Millam, M. Klene, J. E. Knox, J. B. Cross, V. Bakken, C. Adamo, J. Jaramillo, R. Gomperts, R. E. Stratmann, O. Yazyev, A. J. Austin, R. Cammi, C. Pomelli, J. W. Ochterski, R. L. Martin, K.

Morokuma, V. G. Zakrzewski, G. A. Voth, P. Salvador, J. J. Dannenberg, S. Dapprich, A. D. Daniels, O. Farkas, J. B. Foresman, J. V. Ortiz, J. Cioslowski and D. J. Fox, Gaussian, Inc., Wallingford CT, **2009**.

5 Light-Controlled Transformation of Heteroleptic Cage

5.1 Introduction

Coordination-driven self-assembly cages[1] have received an increasing interest in the past decades due to their fascinating and designable structures[2] and promising functions such as catalysis,[3] recognition[4] and drug releasing,[5] etc. However, in most cases, the cages are composed only one type of ligands which limited their overall functions. Therefore, the focus is gradually shifting to assembly heteroleptic cages with multiple ligands these years in order to expand their degree of functionalities.[6] To date, much effort has been made to design supramolecular assemblies with multiple building blocks. For example, in 2011, Hooley constructed a $Pd_2L^A{}_3L^B$ type of heteroleptic cage in a 3:1 mixture of $Pd_2L^A{}_3L^B$ and $Pd_2L^A{}_4$ through endohedrally functionalized ligands (Figure 5.1).[7] In 2015, Yoshizawa reported a $Pd_2L^A{}_2L^B{}_2$ cage using fullerene as guest template.[8] Later, Crowly group formed $Pd_2L^A{}_2L^B{}_2$ cage by the donor-acceptor hydrogen bonds.[9] Clever and coworker built $Pd_2L^A{}_2L^B{}_2$ cage as well with shape complementary approach, not only assembling from ligands directly, but also obtained through homoleptic cage to heteroleptic cage transformation.[10]

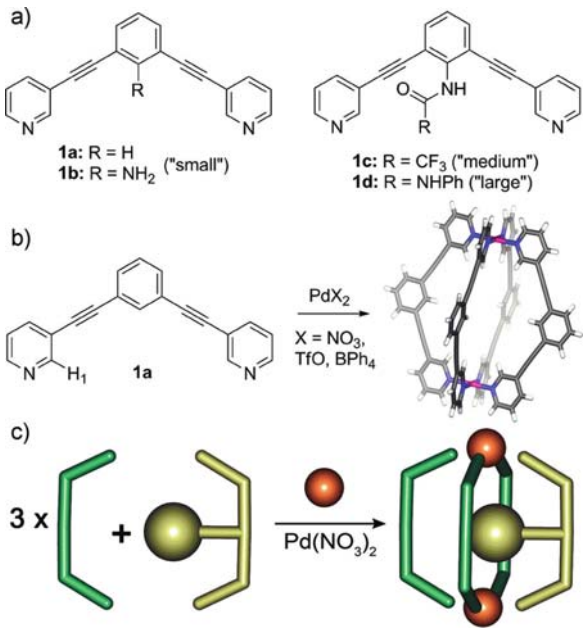

Figure 5.1 a) Ligands. b) Self-assembly of M_2L_4 cage (c) Self-sorting through steric effects.[7] Copyright © 2011 The American Chemical Society.

However, because of relatively weak and more diverse coordination bonds compared with covalent bonds, subtle changes such as ligand angle, solvents as well as external stimuli *etc.*, will result in unpredictable architectures. Thus, controlled synthesis of

heteroleptic cages, desired cage to cage transformation are still challenging. Clever and coworker managed reversible interconversion between a self-assembled triangle and a rhombicuboctahedral sphere[11] and Johnson even achieved their topology switching in polymer network[12] due to the property difference between the photoisomers of dithienylethene (DTE) backbone.

In this chapter, a $Pd_2L^A{}_3L^B$ type of cage $[Pd_2\mathbf{L^a}_3\mathbf{L^g}](BF_4)_4$ (*o*/*c*-**B**-$\mathbf{L^g}$), similar way to those in chapter 2, was synthesized. Due to its thermal instability, *o*/*c*-**B**-$\mathbf{L^g}$ gradually transferred to thermodynamic product $[Pd_2\mathbf{L^a}_2\mathbf{L^g}_2](BF_4)_4$ ($[Pd_2\mathbf{L^a}_2\mathbf{L^g}_2]$). As mentioned above, the property of the photoisomers is different. Open form ligands are flexible, while closed form ligands are relatively rigid. Thus, the transformation between open heteroleptic cages are much faster than closed ones (Figure 5.2).

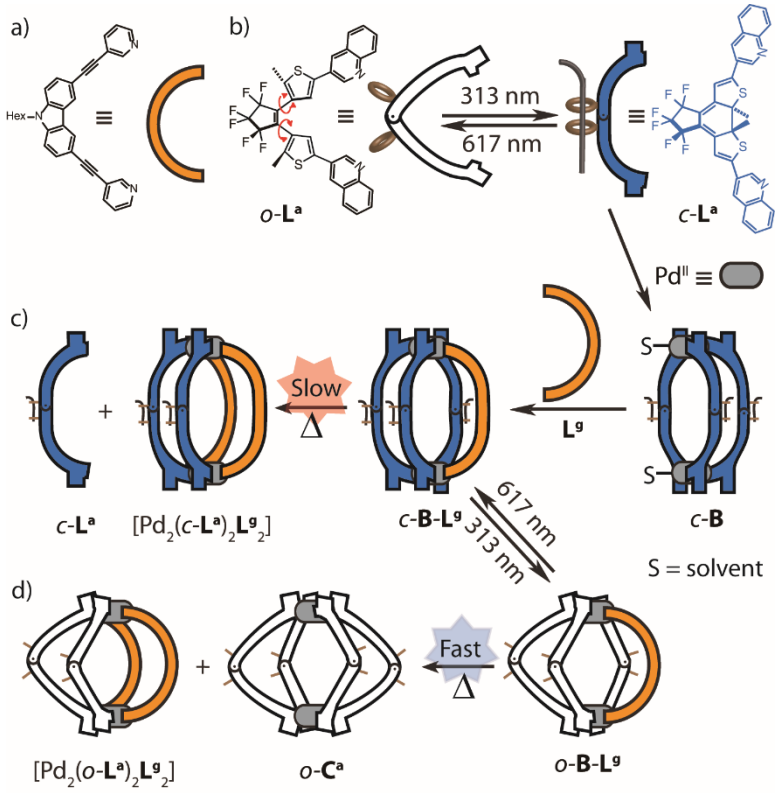

Figure 5.2 (a) Ligand $\mathbf{L^g}$; b) Reversible photo-switching of DTE based ligand between their conformational open form *o*-$\mathbf{L^a}$ and closed form *c*-$\mathbf{L^a}$; c) Formation of heteroleptic cages *c*-**B**-$\mathbf{L^g}$ and transformation to $[Pd_2(c\text{-}\mathbf{L^a})_2\mathbf{L^g}_2]$ d) Formation of heteroleptic cages *o*-**B**-$\mathbf{L^g}$ and their transformation to $[Pd_2(c\text{-}\mathbf{L^a})_2\mathbf{L^g}_2]$ and *o*-$\mathbf{C^a}$.

5.2 Synthesis of heteroleptic cage

Following the same synthesis methods in Chapter 2, *c*-**B** was synthesized by heating a mixture of 3.0 eq. *c*-$\mathbf{L^a}$ and 2.0 eq. of $[Pd(CH_3CN)_4](BF_4)_2$ in CD_3CN. $\mathbf{L^g}$ was synthesized according to the literature procedure.[13] Stirring 1 : 1 mixture of *c*-**B** and $\mathbf{L^g}$ in CD_3CN at room temperature for 2 h (same method in Chapter 2 as well), heteroleptic cage

$[Pd_2(c\text{-}\mathbf{L^a})_3\mathbf{L^g}](BF_4)_4$ (*c*-**B**-$\mathbf{L^g}$) was successfully obtained quantitatively, as confirmed through NMR spectroscopy and high resolution ESI-MS spectrometry (Figure 5.3). Since the convoluted NMR spectra in synthesizing *c*-**B**-$\mathbf{L^g}$ with racemic *c*-**B** due to numerous of diastereomers (mentioned in previous chapters), an enantiopure (*R/S*)-*c*-**B** was used instead. ^{1}H NMR spectrum shows all clear signals (Figure 5.3a), which could be fully analyzed through COSY and NOESY NMR spectra (Figure 5.9 & Figure 5.10). Moreover, all these signals exhibit same diffusion coefficient in DOSY spectrum (Figure 5.13), confirmed its purity of *c*-**B**-$\mathbf{L^g}$. However, besides the signals of *c*-**B**-$\mathbf{L^g}$, there are series of signals belonging to $[Pd_2(c\text{-}\mathbf{L^a})_2\mathbf{L^g}_2]$ displayed together in ESI mass spectrum (Figure 5.3b), even though measured the sample through CSI mass (-30 °C, Figure 5.12).

Open form heteroleptic cage $[Pd_2(o\text{-}\mathbf{L^a})_3\mathbf{L^g}](BF_4)_4$ (*o*-**B**-$\mathbf{L^g}$) could be assembled in the same way as closed form heteroleptic cage by mixing 1:1 mixture of *o*-**B** and $\mathbf{L^g}$ in CD_3CN at room temperature, or obtained directly by irradiation *c*-**B**-$\mathbf{L^g}$ under 617 nm. As confirmed by NMR (Figure 5.3a) and ESI mass (Figure 5.14). In the meanwhile, *o*-**B**-$\mathbf{L^g}$ could reversibly switch back to *c*-**B**-$\mathbf{L^g}$ with 313 nm irradiation (Figure 5.3a). Interestingly, the mass spectrum of *o*-**B**-$\mathbf{L^g}$ together displayed signals of $[Pd_2(o\text{-}\mathbf{L^a})_2\mathbf{L^g}_2]$ as well, and their relative intensity was higher than *o*-**B**-$\mathbf{L^g}$ both in ESI and CSI (-30 °C) mass spectra (Figure 5.15).

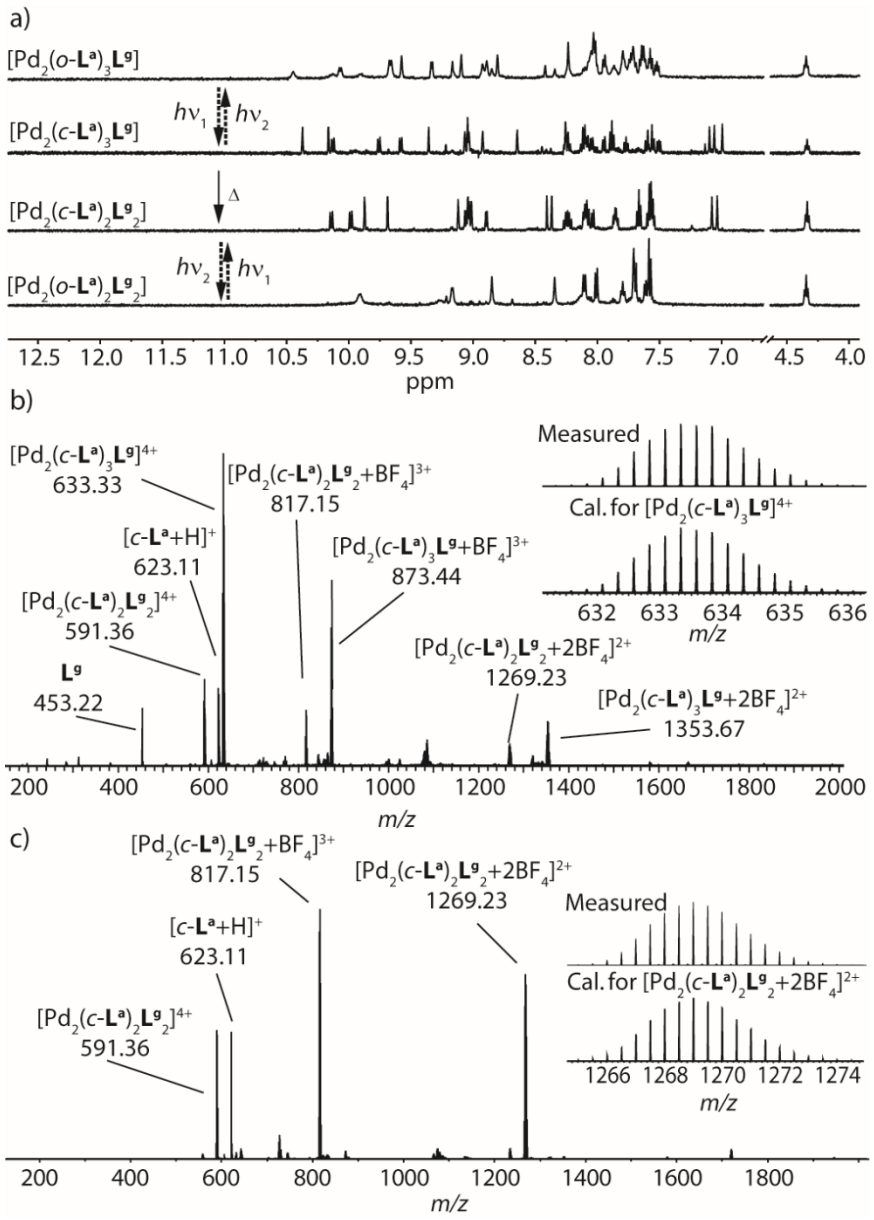

Figure 5.3 a) ^{1}H NMR spectra (500 MHz, CD_3CN, 298 K) of heteroleptic cages [Pd$_2$(*o*/*c*-**L**$^{\mathbf{a}}$)$_3$**L**$^{\mathbf{g}}$] (*o*/*c*-**B**-**L**$^{\mathbf{g}}$) and [Pd$_2$(*o*/*c*-**L**$^{\mathbf{a}}$)$_2$**L**$^{\mathbf{g}}_2$]; ESI-MS spectra of b) *c*-**B**-**L**$^{\mathbf{g}}$ and c) [Pd$_2$(*c*-**L**$^{\mathbf{a}}$)$_2$**L**$^{\mathbf{g}}_2$] with the measured and calculated isotope pattern shown in the inset.

[Pd$_2$(*o*/*c*-**L**$^{\mathbf{a}}$)$_2$**L**$^{\mathbf{g}}_2$] always came out from *o*/*c*-**B**-**L**$^{\mathbf{g}}$ sample in mass spectrum. Therefore, under ESI (or CSI) mass measurement condition, part of *o*/*c*-**B**-**L**$^{\mathbf{g}}$ could be transferred to the product of [Pd$_2$(*o*/*c*-**L**$^{\mathbf{a}}$)$_2$**L**$^{\mathbf{g}}_2$]. Heating a 1:1:1 mixture of *S, S*-*c*-**L**$^{\mathbf{a}}$, **L**$^{\mathbf{g}}$ and [Pd(CH$_3$CN)$_4$](BF$_4$)$_2$ in CD_3CN at 70 °C for 5 h, a clear and clean ^{1}H NMR was obtained (Figure 5.3a), which was different to *c*-**B**-**L**$^{\mathbf{g}}$. High resolution ESI mass spectrometry unambiguously confirms the [Pd$_2$(*c*-**L**$^{\mathbf{a}}$)$_2$**L**$^{\mathbf{g}}_2$] forming (Figure 5.3c) without any other peaks. It is worth to speculate that [Pd$_2$(*c*-**L**$^{\mathbf{a}}$)$_2$**L**$^{\mathbf{g}}_2$], as a thermodynamic product, is more stable than *c*-**B**-**L**$^{\mathbf{g}}$. Similarly, open formed heteroleptic cage [Pd$_2$(*o*-**L**$^{\mathbf{a}}$)$_2$**L**$^{\mathbf{g}}_2$] was synthesized as the same methods but *o*-**L**$^{\mathbf{a}}$ instead. Likewise, [Pd$_2$(*o*-**L**$^{\mathbf{a}}$)$_2$**L**$^{\mathbf{g}}_2$] could be directly obtained from [Pd$_2$(*c*-**L**$^{\mathbf{a}}$)$_2$**L**$^{\mathbf{g}}_2$] under 617 nm irradiation. Both heteroleptic cages

[Pd_2(*o*/*c*-$\mathbf{L^a}$)$_2$$\mathbf{L^g}_2$] were unambiguously confirmed by NMR spectroscopy (Figure 5.3a) and ESI mass spectrometry (Chapter 5.6.2.2). Moreover, the reversible interconversion between open form [Pd_2(*o*-$\mathbf{L^a}$)$_2$$\mathbf{L^g}_2$] and closed form [$Pd_2$(*c*-$\mathbf{L^a}$)$_2$$\mathbf{L^g}_2$] could be controlled under UV (313 nm) and visible light (617 nm) (Figure 5.3a).

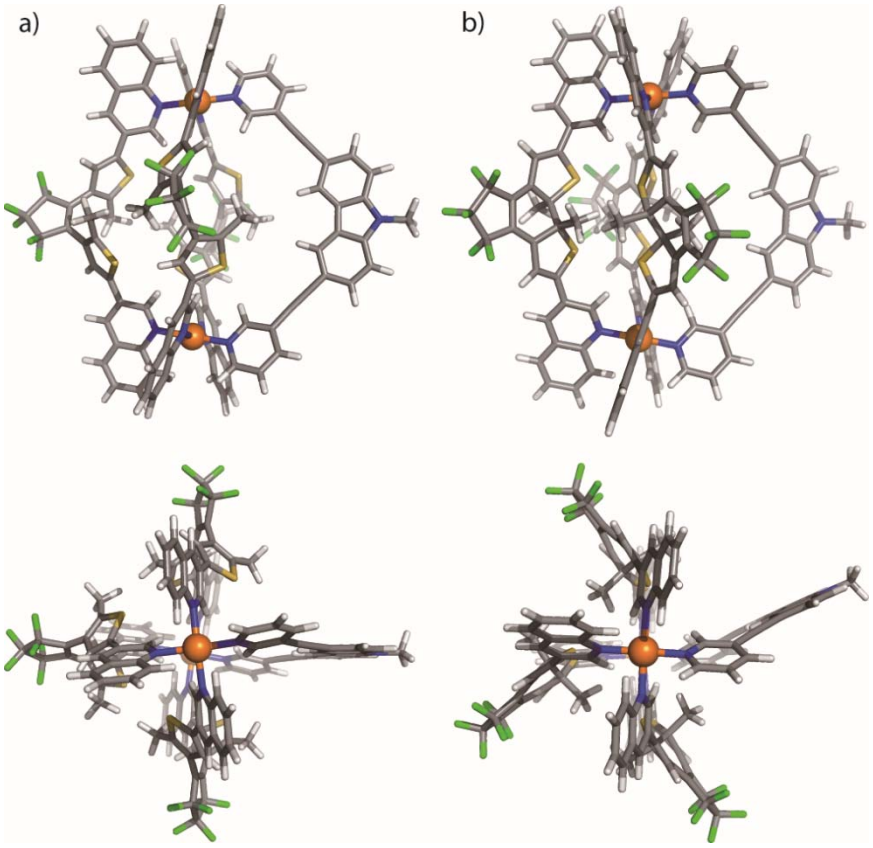

Figure 5.4 DFT optimized structures of heteroleptic cage a) *o*-$\mathbf{B}$-$\mathbf{L^g}$ and b) *c*-$\mathbf{B}$-$\mathbf{L^g}$ (side and top view). All solvent molecules, counter anions and long hexyl chain of $\mathbf{L^g}$ have been omitted, (here only one diastereomer *R*-*c*-$\mathbf{B}$-$\mathbf{L^g}$ is calculated and shown; C gray, N blue, F green, S yellow, Pd orange, H white).

5.3 Computational study

Despite numerous attempts, unfortunately, a single crystal suitable for X-ray analysis could not be obtained. Thus, a molecule modelling for all heteroleptic cages *o*/*c*-$\mathbf{B}$-$\mathbf{L^g}$ (Figure 5.4) and [Pd_2(*o*/*c*-$\mathbf{L^a}$)$_2$$\mathbf{L^g}_2$] (Figure 5.5) were carried out. The models were first built up using SPARTAN and then optimized on a PM6 level of theory without constrains. The obtained resulting structures were further refined by DFT calculations (B3LYP/LANL2DZ) using GUASSAIN software[15]. Meanwhile, the energy profiles for both *trans* and *cis* [Pd_2(*o*/*c*-$\mathbf{L^a}$)$_2$$\mathbf{L^g}_2$] were calculated to obtain further information of preferable isomers (*trans* or *cis*) in both open form and closed form. In Figure 5.5, the calculations showed that the *cis*-[Pd_2(*c*-$\mathbf{L^a}$)$_2$$\mathbf{L^g}_2$] was 8.62 kJ mol^{-1} lower than *trans*-[Pd_2(*c*-$\mathbf{L^a}$)$_2$$\mathbf{L^g}_2$]. Whereas, in open form heteroleptic cage, the *cis* isomer was 9.58 kJ mol^{-1} lower than

trans isomer. All the calculation results showed that the heteroleptic cages were more stable in their *cis* isomers, indicating *cis*-[Pd_2(*o*/*c*-$\mathbf{L^a}$)$_2\mathbf{L^g}_2$] formation.

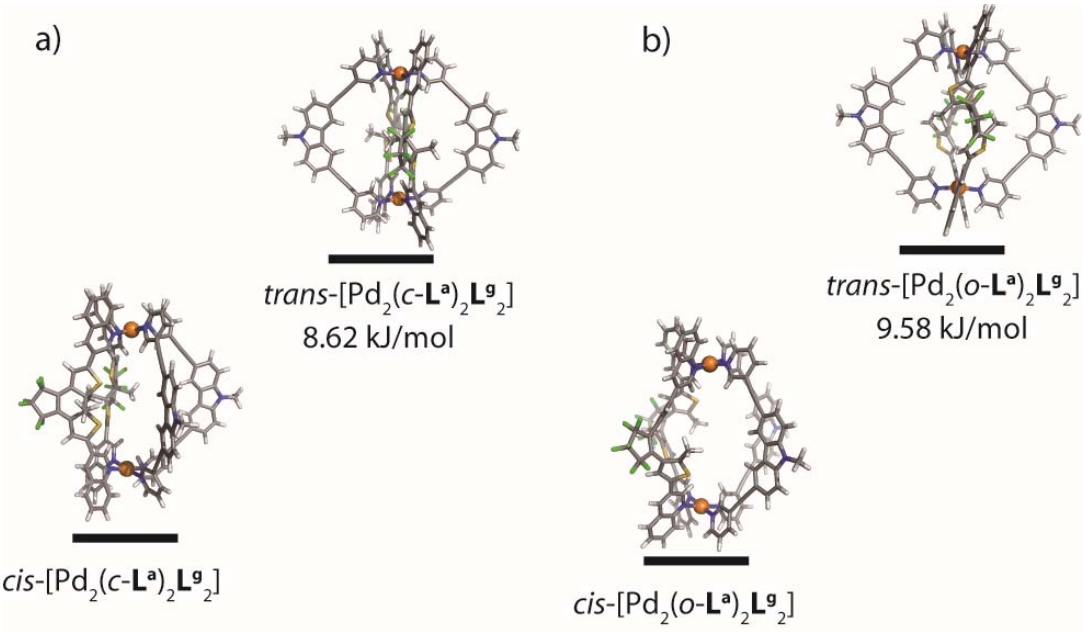

Figure 5.5 Energy diagram with DFT calculated structures of *trans*-[Pd_2(*c*-$\mathbf{L^a}$)$_2\mathbf{L^g}_2$], *cis*-[Pd_2(*c*-$\mathbf{L^a}$)$_2\mathbf{L^g}_2$], *trans*-[Pd_2(*o*-$\mathbf{L^a}$)$_2\mathbf{L^g}_2$] and *cis*-[Pd_2(*o*-$\mathbf{L^a}$)$_2\mathbf{L^g}_2$], (C gray, N blue, F green, S yellow, Pd orange, H white).

5.4 Cage to cage transformation

With the transformation of [Pd_2(*c*-$\mathbf{L^a}$)$_2\mathbf{L^g}_2$] from kinetic product *o*/*c*-**B**-$\mathbf{L^g}$ and rapid assembling from *c*-$\mathbf{L^a}$, $\mathbf{L^g}$ and Pd^{II}, we further investigate whether [Pd_2(*c*-$\mathbf{L^a}$)$_2\mathbf{L^g}_2$] is a thermodynamic minimum product in a mixture of bowl *c*-**B** and cage $\mathbf{C^g}$ (assembled from $\mathbf{L^g}$). Therefore, heating a 4:3 mixture of *S*-*c*-**B** and cage $\mathbf{C^g}$ in CD_3CN at 70 °C, fortunately, new set ^{1}H NMR spectrum as same as [Pd_2(*c*-$\mathbf{L^a}$)$_2\mathbf{L^g}_2$] was observed (Figure 5.26). In contrast to the assembled from individual ligands, the transformation from bowl *c*-**B** and cage $\mathbf{C^g}$ to [Pd_2(*c*-$\mathbf{L^a}$)$_2\mathbf{L^g}_2$] resulted in rather slow conversion, taking around 24 h, which presumably due to the requirement of disassembly the bowl and cage and reassembly of new species of [Pd_2(*c*-$\mathbf{L^a}$)$_2\mathbf{L^g}_2$] afterwards. Similarly, open form [Pd_2(*o*-$\mathbf{L^a}$)$_2\mathbf{L^g}_2$] could also be obtained in the same way.

As mentioned above, part of *o*/*c*-**B**-$\mathbf{L^g}$ could be transformed to [Pd_2(*o*/*c*-$\mathbf{L^a}$)$_2\mathbf{L^g}_2$] in ESI mass measurement. Here, the transformation kinetic experiment was investigated through ^{1}H NMR spectroscopy. Freshly prepared samples *o*/*c*-**B**-$\mathbf{L^g}$ (for closed form, enantiopure *R*-*c*-**B**-$\mathbf{L^g}$ is used for better NMR analysis) in NMR tube were heated in an oven at 70 °C, followed by ^{1}H NMR monitoring of [Pd_2(*o*/*c*-$\mathbf{L^a}$)$_2\mathbf{L^g}_2$] amount. In the sample of *R*-*c*-**B**-$\mathbf{L^g}$, free ligand signals, new species of [Pd_2(*c*-$\mathbf{L^a}$)$_2\mathbf{L^g}_2$] as well as *R*-*c*-**B** signals were observed (Figure 5.30), indicating the disassembly of *R*-*c*-**B**-$\mathbf{L^g}$ and new

coordination bond forming. The amount of [Pd_2(*c*-$\mathbf{L^a}$)$_2\mathbf{L^g}_2$] dramatic increased in 5 h, and slowly climbed up subsequently. After around 10 days heating under 70 °C, *R*-*c*-**B**-$\mathbf{L^g}$ was completely transferred to [Pd_2(*R*-*c*-$\mathbf{L^a}$)$_2\mathbf{L^g}_2$] (Figure 5.6). For *o*-**B**-$\mathbf{L^g}$, although suffering from disassembling coordination bonds, formation of new species of [Pd_2(*o*-$\mathbf{L^a}$)$_2\mathbf{L^g}_2$] together with *o*-$\mathbf{C^a}$ were extremely faster. Compared with closed form transformation, it reaches its balance in 24 h (Figure 5.6), due to the forming *o*-$\mathbf{C^a}$ and completely consuming of *o*-**B**-$\mathbf{L^g}$.

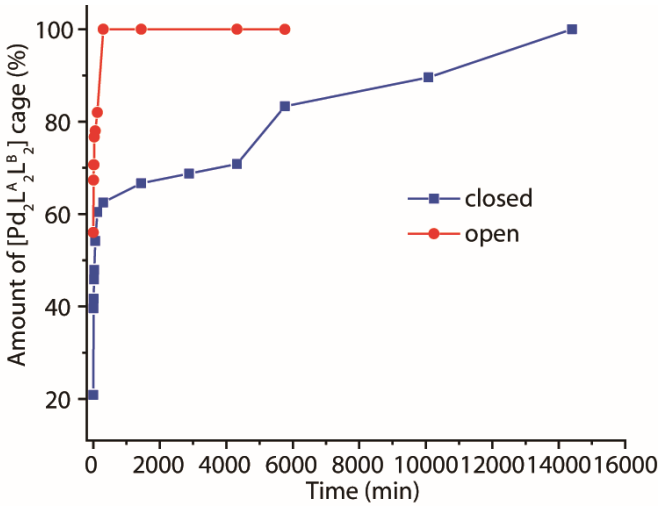

Figure 5.6 Kinetic experiment of heteroleptic cage transformation, showing amount of [Pd_2(*o/c*-$\mathbf{L^a}$)$_2\mathbf{L^g}_2$] transferred with time at 70 °C. Red: open form transformation; Blue: closed form transformation.

5.5 Conclusion

In conclusion, we successfully synthesized DTE based mixed-ligand $Pd_2L^A{}_3L^B$ type *o*/*c*-**B**-$\mathbf{L^g}$ and $Pd_2L^A{}_2L^B{}_2$ type [Pd_2(*o/c*-$\mathbf{L^a}$)$_2\mathbf{L^g}_2$] heteroleptic cages in both their open form and closed form. These cages were fully characterized by ^{1}H, COSY, NOESY, DOSY NMR spectroscopies and high resolution ESI mass spectrometry. DFT calculation suggests that both [Pd_2(*o*-$\mathbf{L^a}$)$_2\mathbf{L^g}_2$] and [Pd_2(*c*-$\mathbf{L^a}$)$_2\mathbf{L^g}_2$] exist as *cis* isomers. Besides self-assembly through direct combination of the ligands with Pd^{II}, we further demonstrated the formation of [Pd_2(*o/c*-$\mathbf{L^a}$)$_2\mathbf{L^g}_2$] from cage to cage transformations. Moreover, the kinetic heteroleptic cages *o*/*c*-**B**-$\mathbf{L^g}$ were found to be transferred to thermodynamic [Pd_2(*o/c*-$\mathbf{L^a}$)$_2\mathbf{L^g}_2$]. Further experiments revealed that the transformation balance from *o*-**B**-$\mathbf{L^g}$ was faster than that from closed *c*-**B**-$\mathbf{L^g}$, which showing light controlled cage to cage transformation rate.

5.6 Experimental section

5.6.1 General procedures

All chemicals, except otherwise specified, were obtained from commercial sources and used without further purification. Perfluoro-1,2-bis(2-iodo-5-methylthien-4-yl)cyclopentene[14], **L^{g}** were prepared according to a literature procedure.[13] Recycling gel permeation chromatography was performed on a JAI LC-9210 II NEXT GPC system equipped with Jaigel 1H and 2H columns in series using chloroform as the eluent (HPLC grade). NMR measurements were all conducted at 298 K on Avance-500 and Avance-600 instruments from Bruker and INOVA 500 MHz machine from Varian. High-resolution ESI mass spectrometric measurements were carried out on maXis ESI-TOF MS and ESI-timsTOF machines from Bruker. The irradiations were performed with a 500 W Hg Arc lamp from LOT-Quantum Design. Chiral HPLC was performed on an Agilent Technologies 1260 infinity HPLC system equipped with Daicel CHIRALPAK IC columns (250 x 4.6 mm and 250 x 10 mm) using a dichloromethane/hexane/methanol (39%/60%/1%) mixture as eluent for the separation of *c*-**L^{a}**. UV-vis spectra were recorded on an Agilent 8453 UV-Vis spectrophotometer. Heteroleptic cage models were constructed using SPARTAN[15] and were first optimized on a PM6 level of theory (no counter ions were included) without constrains. The resulting structures were then further refined by DFT calculations (B3LYP/LANL2DZ) using Gaussain 09 software.[16]

5.6.2 Synthesis

5.6.2.1 Synthesis of $[Pd_2(c\text{-}L^a)_3L^g]$

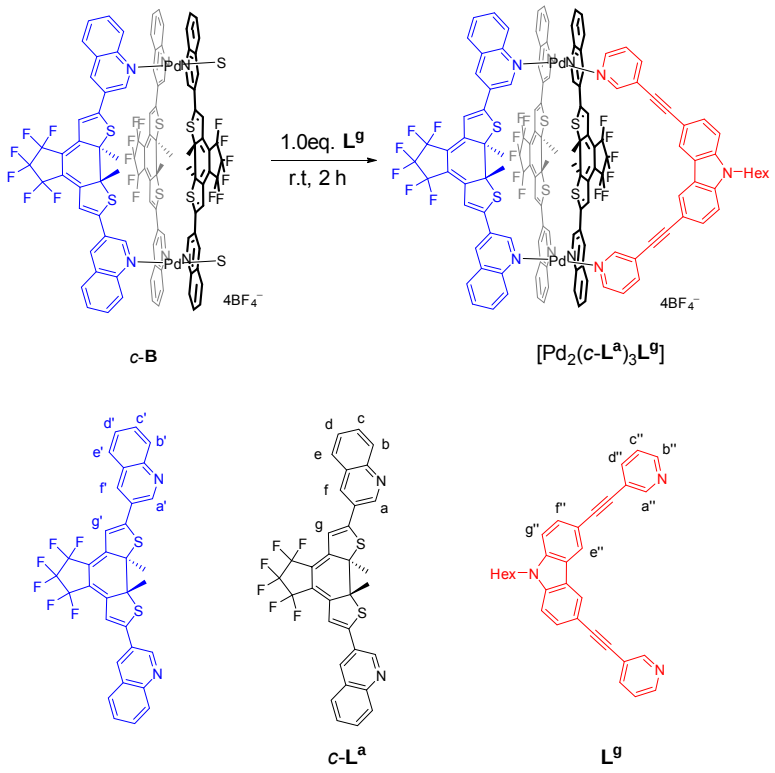

Scheme 4.1. Synthesis of $[Pd_2(c\text{-}\mathbf{L^a})_3\mathbf{L^g}](BF_4)_4$.

The $Pd_2L^A{}_3L^B$ type of heteroleptic cage compound $[Pd_2(c\text{-}\mathbf{L^a})_3\mathbf{L^g}](BF_4)_4$ (*c*-**B**-$\mathbf{L^g}$) was synthesized in quantitative yield by stiring a mixture of the $[Pd_2(c\text{-}\mathbf{L^a})_3(Solvent)_2](BF_4)_4$ (*c*-**B**) in CD_3CN (0.7 µmol, 976.67 µL) and $\mathbf{L^g}$ (0.7 µmol, 23.33 µL of a 4 mM stock solution in CD_3CN) at room temperature for 2 h in a closed vial to yield 1000 µl of a 0.7 mM solution of *c*-**B**-$\mathbf{L^g}$. For better analysis, only one enantiomer pure (*R*-*c*-**B**-$\mathbf{L^g}$) NMR spectra here are given. ^{1}H NMR (600 MHz, CD_3CN) δ 10.40 (d, *J* = 2.0 Hz, 2H), 10.18 (d, *J* = 2.0 Hz, 2H), 10.14 (dd, *J* = 8.7, 4.0 Hz, 2H), 9.77 (d, *J* = 8.6 Hz, 2H), 9.58 (d, *J* = 8.6 Hz, 2H), 9.37 (d, *J* = 2.0 Hz, 2H), 9.07 (t, *J* = 1.2 Hz, 2H), 9.05 (d, *J* = 1.0 Hz, 2H), 9.04 (s, 2H), 8.92 (d, *J* = 2.0 Hz, 1H), 8.66 (d, *J* = 1.8 Hz, 2H), 8.28 – 8.21 (m, 4H), 8.17 – 8.06 (m, 6H), 8.04 (dt, *J* = 8.1, 1.5 Hz, 2H), 7.97 – 7.93 (m, 6H), 7.88 (t, *J* = 7.6 Hz, 4H), 7.79 – 7.75 (m, 2H), 7.60 – 7.54 (m, 6H), 7.53 – 7.47 (m, 2H), 7.09 (s, 2H), 7.05 (s, 2H), 6.99 (s, 2H), 4.37 – 4.29 (m, 2H), 2.49 (s, 6H), 2.44 (s, 6H), 2.38 (s, 6H), 1.78 (p, *J* = 7.3 Hz, 2H), 1.35 – 1.13 (m, 6H), 0.78 (t, *J* = 7.0 Hz, 3H). ESI-HRMS calculated for $Pd_2C_{131}H_{87}F_{22}N_9S_6B$ (*c*-**B**-$\mathbf{L^g}$ $-3BF_4]^{3+}$) *m/z* = 873.4414, found *m/z* = 873.4374.

Similarly, open form heteroleptic cage $[Pd_2(o\text{-}\mathbf{L^a})_3\mathbf{L^g}](BF_4)_4$ (*o*-**B**-$\mathbf{L^g}$) can be synthesized from combining of *o*-**B** and $\mathbf{L^g}$. And it could also be obtained by switching of *o*-**B**-$\mathbf{L^g}$ under 617 nm.

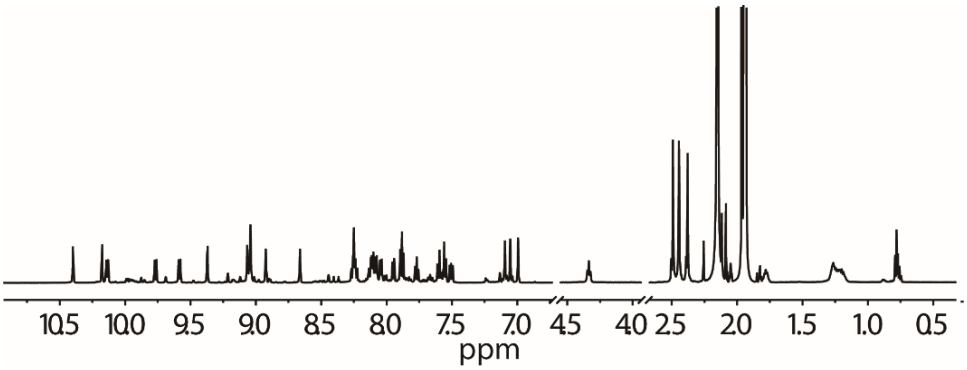

Figure 5.7 ^{1}H NMR spectrum (600 MHz, CD_3CN) of *R*-*c*-**B**-**L^{g}**.

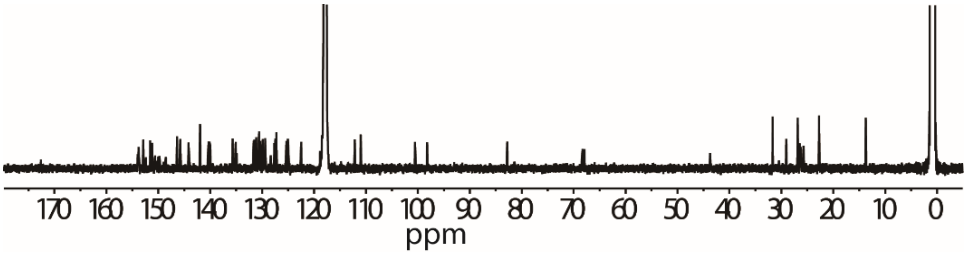

Figure 5.8 ^{13}C NMR spectrum (600 MHz, CD_3CN) of *R*-*c*-**B**-**L^{g}**.

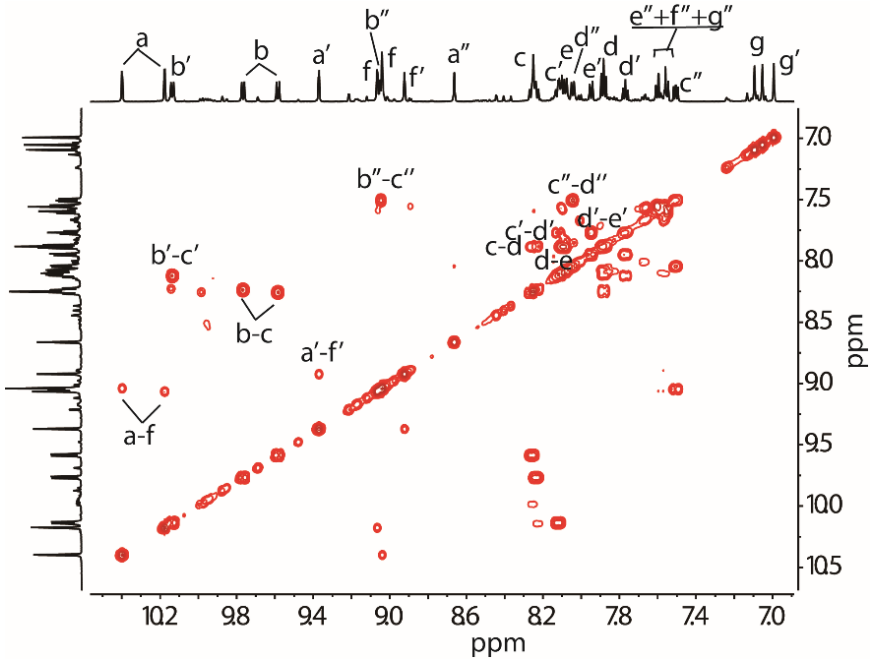

Figure 5.9 ^{1}H-^{1}H COSY spectrum (600 MHz, CD_3CN) of R-*c*-**B**-**L^{g}** (only showing aromatic region).

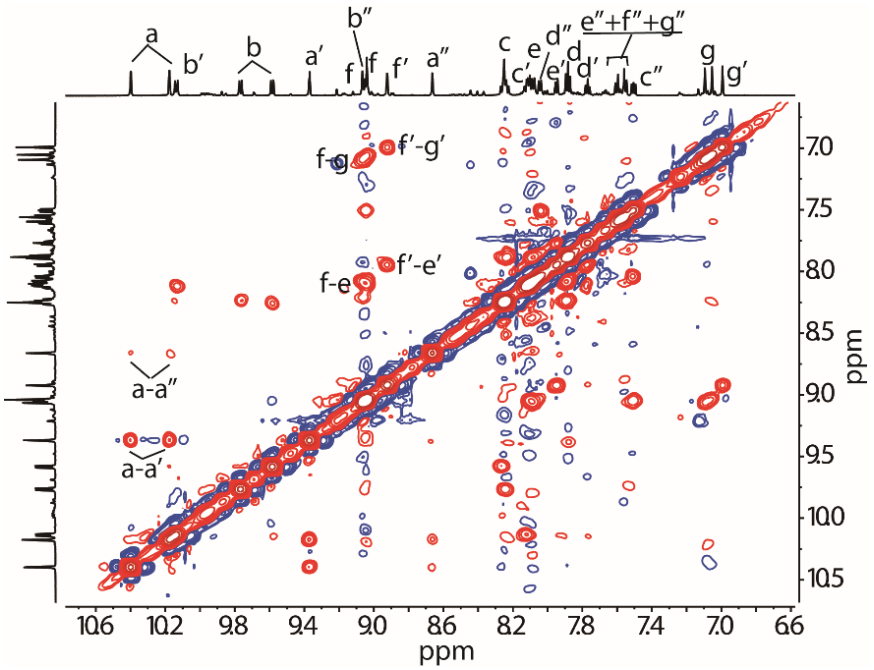

Figure 5.10 ^{1}H-^{1}H NOESY spectrum (600 MHz, CD_3CN) of *R*-*c*-**B**-**L**^{g} (only showing aromatic region).

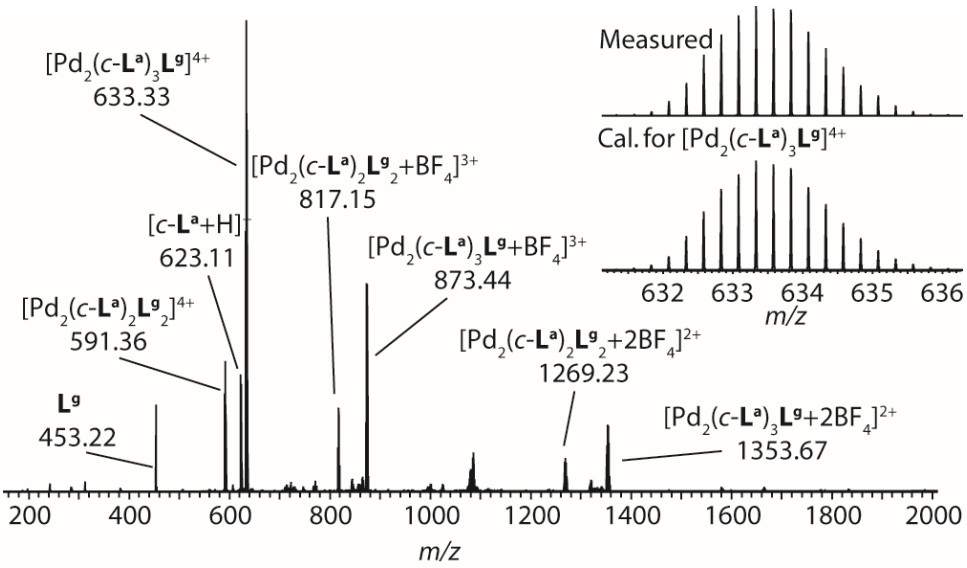

Figure 5.11 ESI-HRMS spectrum of *c*-**B**-**L**^{g}.

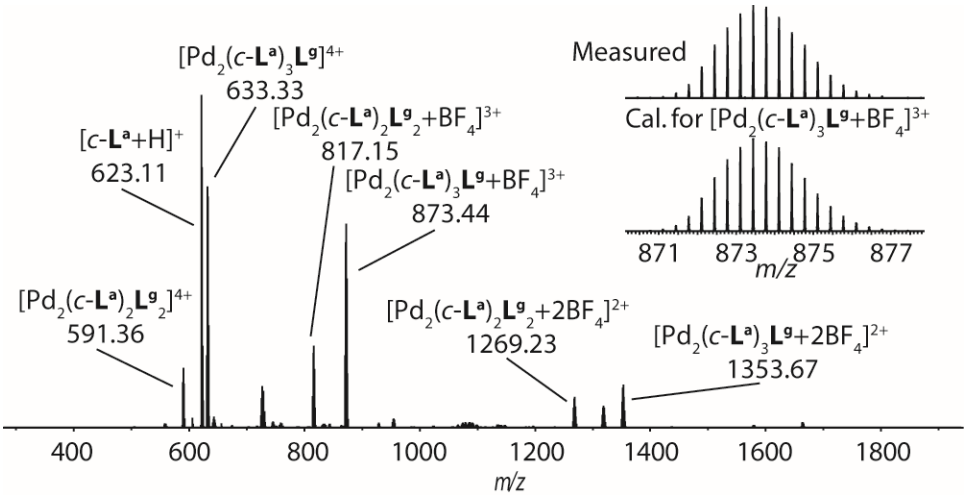

Figure 5.12 CSI-HRMS (–30 °C) spectrum of *c*-**B**-**L**^{g}.

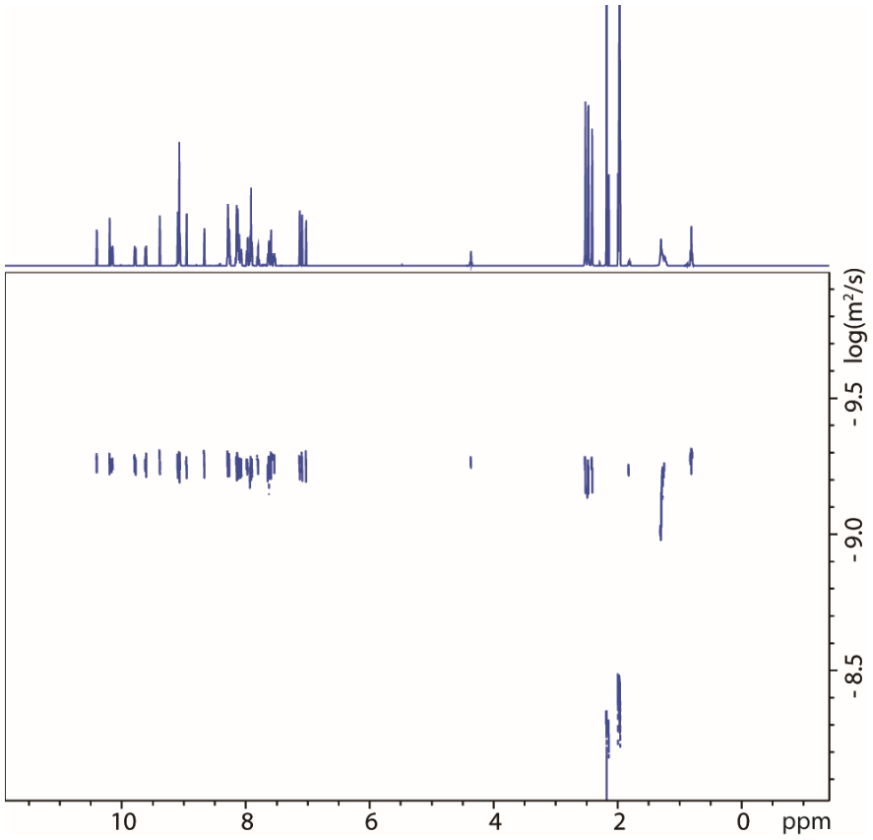

Figure 5.13 DOSY NMR spectrum (600 MHz, CD_3CN) of *R*-*c*-**B**-**L**^{g}**.**

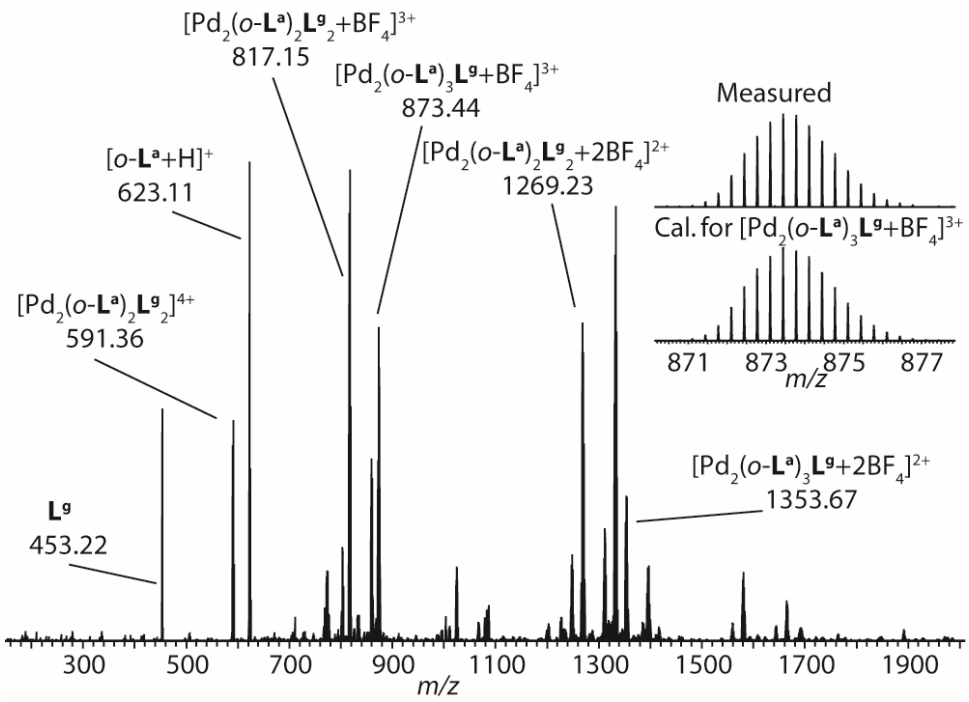

Figure 5.14 ESI-HRMS spectrum of *o*-**B**-**L**^{g}.

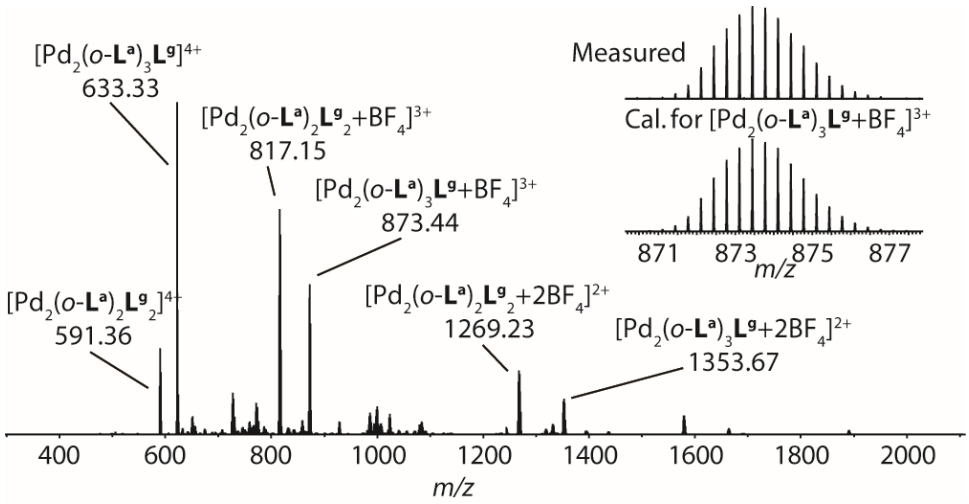

Figure 5.15 CSI-HRMS (–30 °C) spectrum of *o*-**B**-**L**^{g}.

5.6.2.2 Synthesis of [Pd$_2$(*c*-L^{a})$_2$L$^{g}_2$]

Path I:

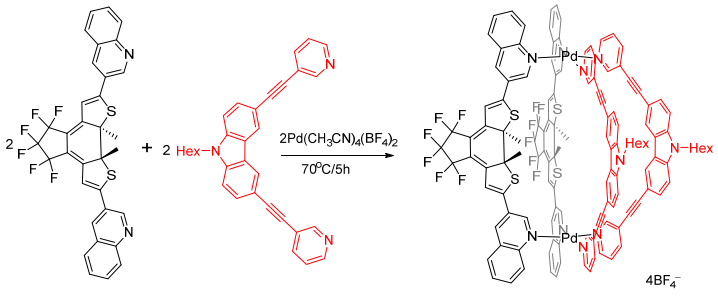

Path II:

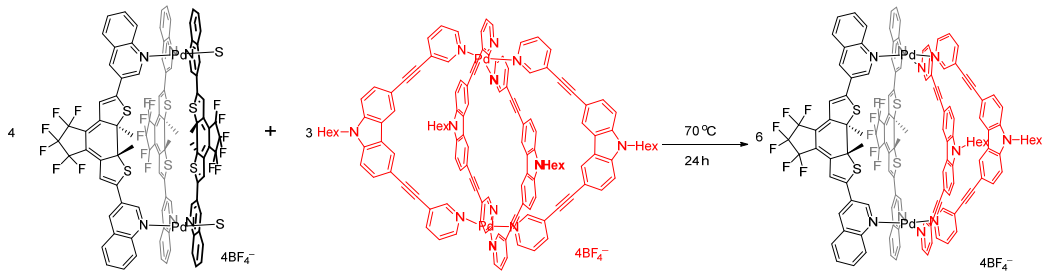

Scheme 4.2 Synthesis of $[Pd_2(c\text{-}\mathbf{L^a})_2\mathbf{L^g}_2]$.

The $Pd_2L^A{}_2L^B{}_2$ type of heteroleptic cage compound $[Pd_2(c\text{-}\mathbf{L^a})_2\mathbf{L^g}_2](BF_4)_4$ {$[Pd_2(c\text{-}\mathbf{L^a})_2\mathbf{L^g}_2]$} could be synthesized through two path. Path I: it was synthesized in quantitative yield by heating a 1:1:1 mixture of the *c*-$\mathbf{L^a}$, $\mathbf{L^g}$ and $Pd(CH_3CN)_4(BF_4)_2$ in CD_3CN at 70 °C for 5 h. Path II: By heating $[Pd_2(c\text{-}\mathbf{L^a})_3(Solvent)_2](BF_4)_4$ (*c*-**B**) (1.0 mM, 400 μL CD_3CN solution) and $[Pd_2\mathbf{L^g}_4](BF_4)_4$ ($\mathbf{C^g}$) (1.0 mM, 300 μL CD_3CN solution) at 70 °C for 24 h in a closed vial yield 700 μl of a 0.86 mM solution of $[Pd_2(c\text{-}\mathbf{L^a})_2\mathbf{L^g}_2]$. For better analysis, only one enantiomer pure ($[Pd_2(R,\ R\text{-}c\text{-}\mathbf{L^a})_2\mathbf{L^g}_2]$) NMR spectra here are given. ^{1}H NMR (600 MHz, CD_3CN) δ 10.14 (d, *J* = 8.6 Hz, 2H), 9.98 (d, *J* = 8.7 Hz, 2H), 9.87 (d, *J* = 2.0 Hz, 2H), 9.69 (d, *J* = 2.0 Hz, 2H), 9.12 (d, *J* = 1.8 Hz, 2H), 9.06 (d, *J* = 6.0 Hz, 2H), 9.04 (dd, *J* = 6.0, 1.9 Hz, 4H), 9.01 (d, *J* = 2.0 Hz, 2H), 8.89 (d, *J* = 6.0 Hz, 2H), 8.39 (dd, *J* = 22.8, 1.6 Hz, 4H), 8.24 (dddd, *J* = 17.2, 8.6, 7.1, 1.4 Hz, 4H), 8.13 – 8.08 (m, 4H), 8.08-8.02 (m, 4H), 7.89 – 7.82 (m, 4H), 7.67 (td, *J* = 8.5, 1.6 Hz, 4H), 7.61 – 7.52 (m, 8H), 7.08 (s, 2H), 7.04 (s, 2H), 4.34 (t, *J* = 7.1 Hz, 4H), 2.51 (s, 6H), 2.39 (s, 6H), 1.78 (p, *J* = 7.3 Hz, 4H), 1.31 – 1.13 (m, 12H), 0.76 (t, *J* = 7.1 Hz, 6H). ESI-HRMS calculated for $Pd_2C_{130}H_{94}F_{16}N_{10}S_4B$ ($[Pd_2(c\text{-}\mathbf{L^a})_2\mathbf{L^g}_2 - 3BF_4]^{3+}$) *m/z* = 817.1492, found *m/z* = 817.1457. Besides the synthesis from heating a 1:1:1 mixture of the *o*-$\mathbf{L^a}$, $\mathbf{L^g}$ and $Pd(CH_3CN)_4(BF_4)_2$ in CD_3CN at 70 °C, open form heteroleptic cage compound $[Pd_2(o\text{-}\mathbf{L^a})_2\mathbf{L^g}_2](BF_4)_4$ {$[Pd_2(o\text{-}\mathbf{L^a})_2\mathbf{L^g}_2]$} could be obtained through transformation of o-$\mathbf{C^a}$ and $\mathbf{C^g}$ in 1:1 ratio under heating at 70 °C as well as light switching from closed form $[Pd_2(o\text{-}\mathbf{L^a})_2\mathbf{L^g}_2]$ under 617 nm irradiation.

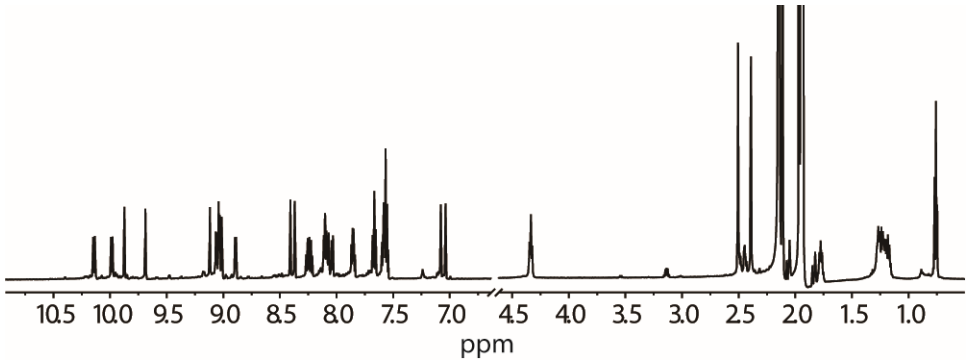

Figure 5.16 ^{1}H NMR spectrum (600 MHz, CD_3CN) of $[Pd_2(R,\ R\text{-}c\text{-}\mathbf{L^a})_2\mathbf{L^g}_2]$.

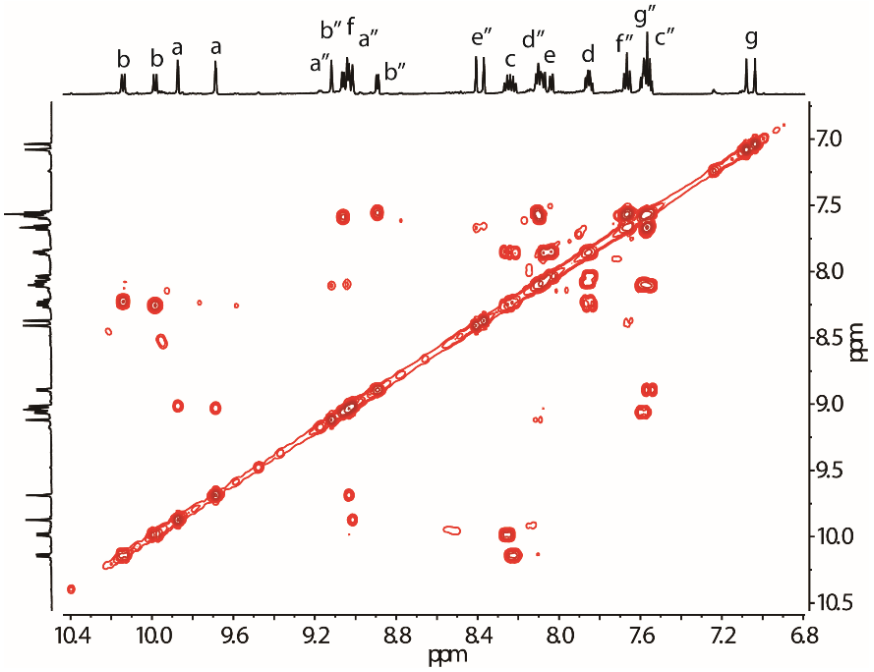

Figure 5.17 ^{1}H-^{1}H COSY spectrum (600 MHz, CD_3CN) of $[Pd_2(R, R\text{-}c\text{-}\mathbf{L^a})_2\mathbf{L^g}_2]$ (only showing aromatic region).

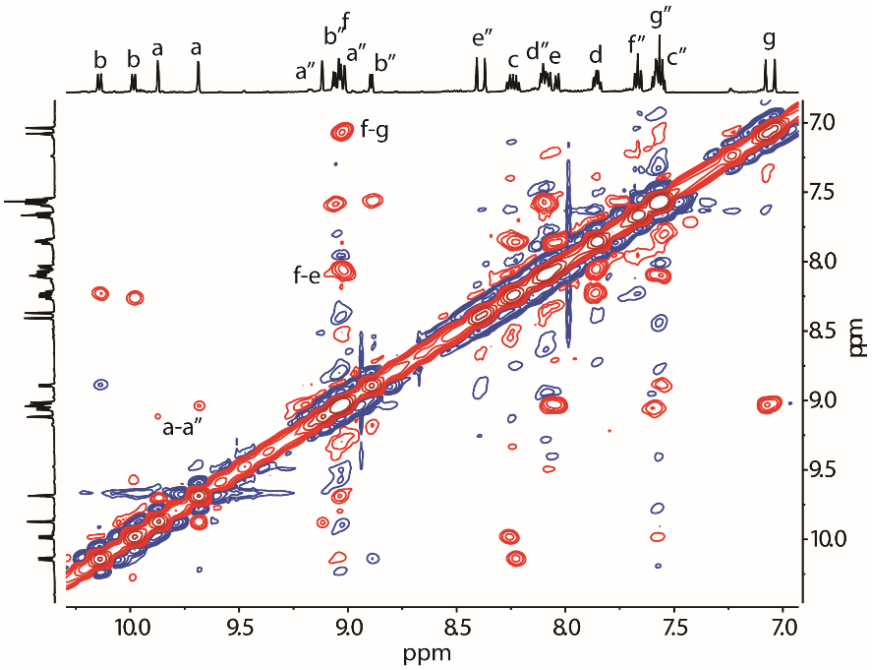

Figure 5.18 ^{1}H-^{1}H NOESY spectrum (600 MHz, CD_3CN) of $[Pd_2(R, R\text{-}c\text{-}\mathbf{L^a})_2\mathbf{L^g}_2]$ (only showing aromatic region).

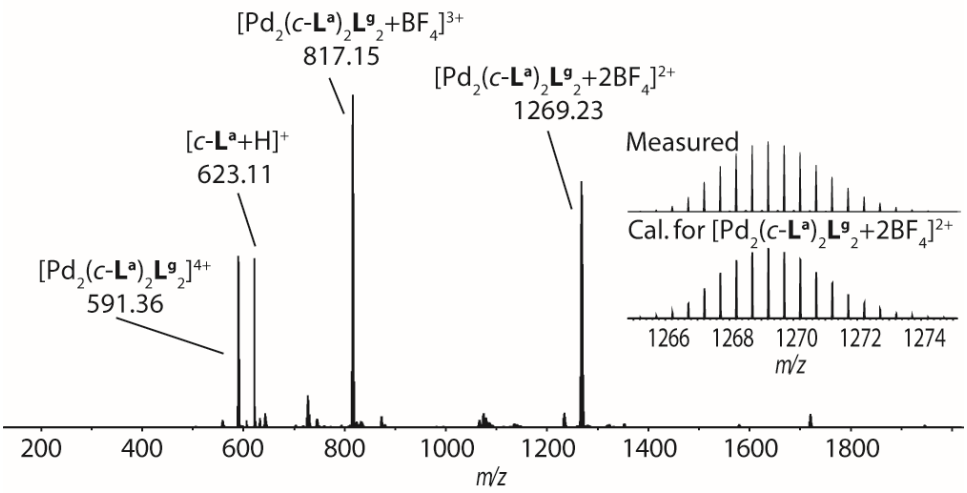

Figure 5.19 ESI-HRMS spectrum of [Pd_2(*c*-**L**^{a})$_2$**L**^{g}$_2$].

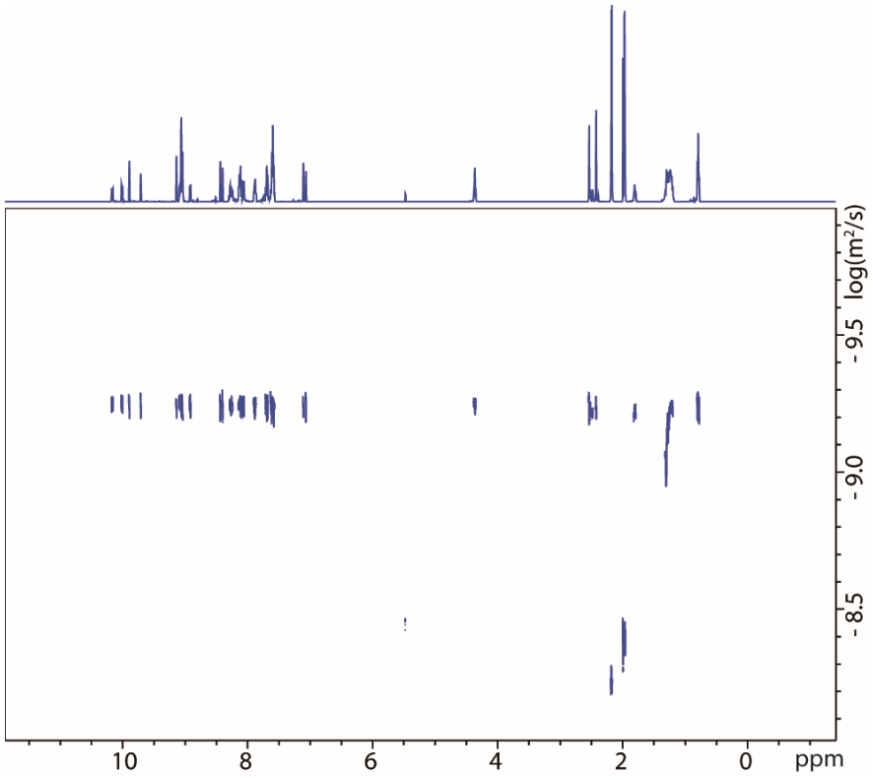

Figure 5.20 DOSY NMR spectrum (600 MHz, CD_3CN) of [Pd_2(*R, R*-*c*-**L**^{a})$_2$**L**^{g}$_2$**]**.

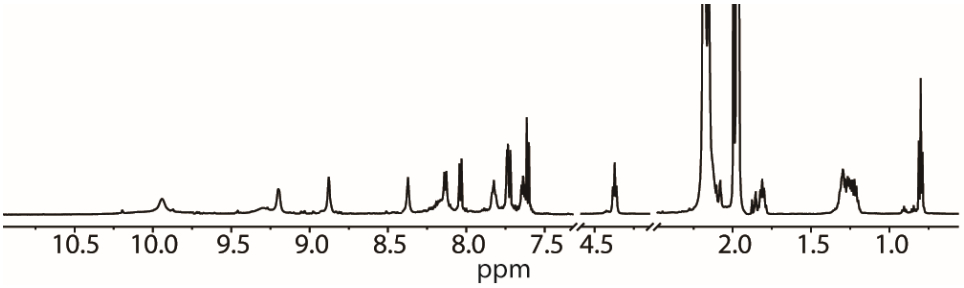

Figure 5.21 ^{1}H NMR spectrum (600 MHz, CD_3CN) of [Pd_2(*o*-**L**^{a})$_2$**L**^{g}$_2$].

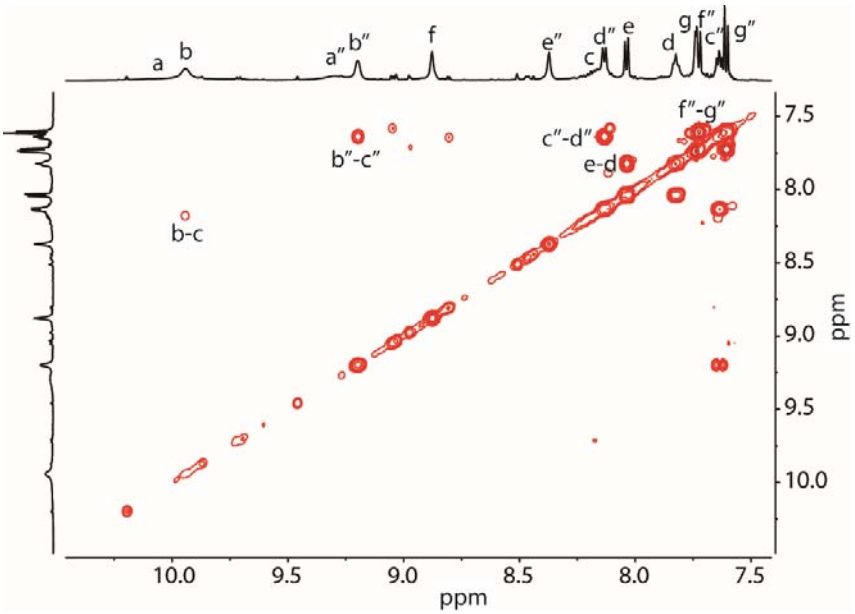

Figure 5.22 ^{1}H-^{1}H COSY spectrum (600 MHz, CD_3CN) of $[Pd_2(o\text{-}\mathbf{L^a})_2\mathbf{L^g}_2]$ (only showing aromatic region).

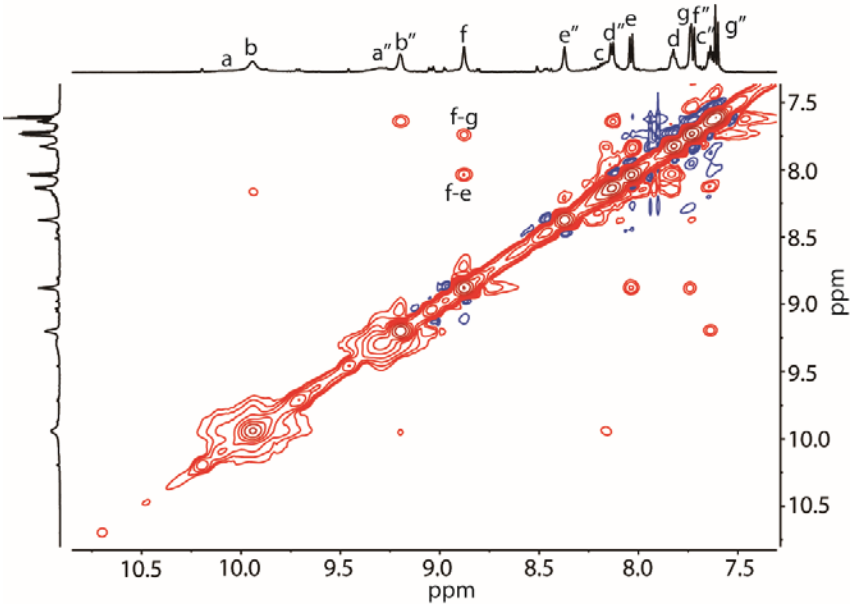

Figure 5.23 ^{1}H-^{1}H NOESY spectrum (600 MHz, CD_3CN) of $[Pd_2(o\text{-}\mathbf{L^a})_2\mathbf{L^g}_2]$ (only showing aromatic region).

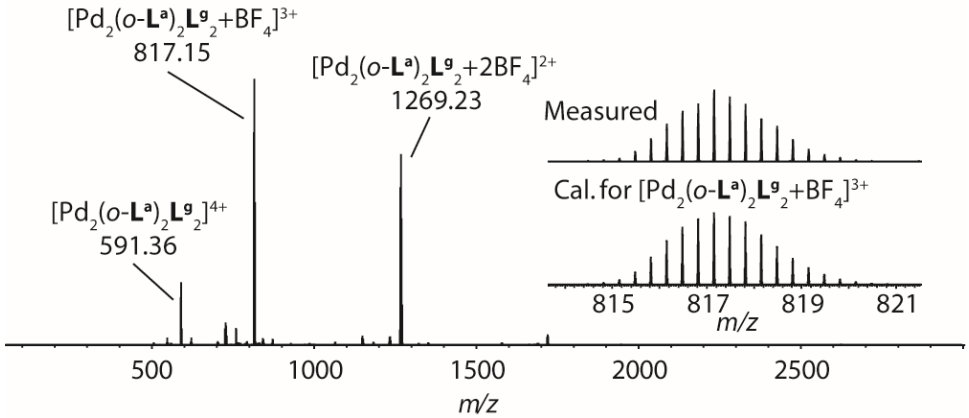

Figure 5.24 ESI-HRMS spectrum of $[Pd_2(o\text{-}\mathbf{L^a})_2\mathbf{L^g}_2]$.

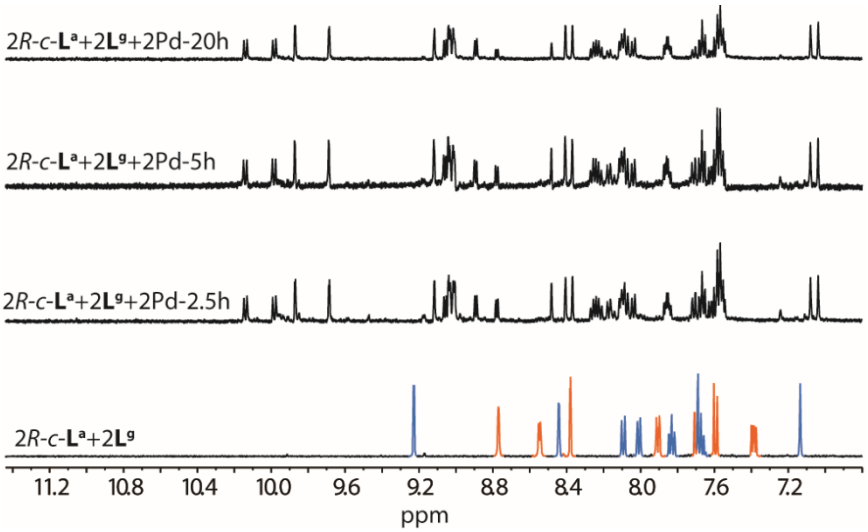

Figure 5.25 ^{1}H NMR spectra (500 MHz, CD_3CN) monitoring of [Pd_2(*R, R*-*c*-**L**^{a})$_2$**L**$^{g}_2$] synthesizing from *R, R*-*c*-**L**^{a}, Pd^{II} and **L**^{g} in 1:1:1 ratio at 70 °C (Blue *R*-*c*-**L**^{a}, orange **L**^{g})**.**

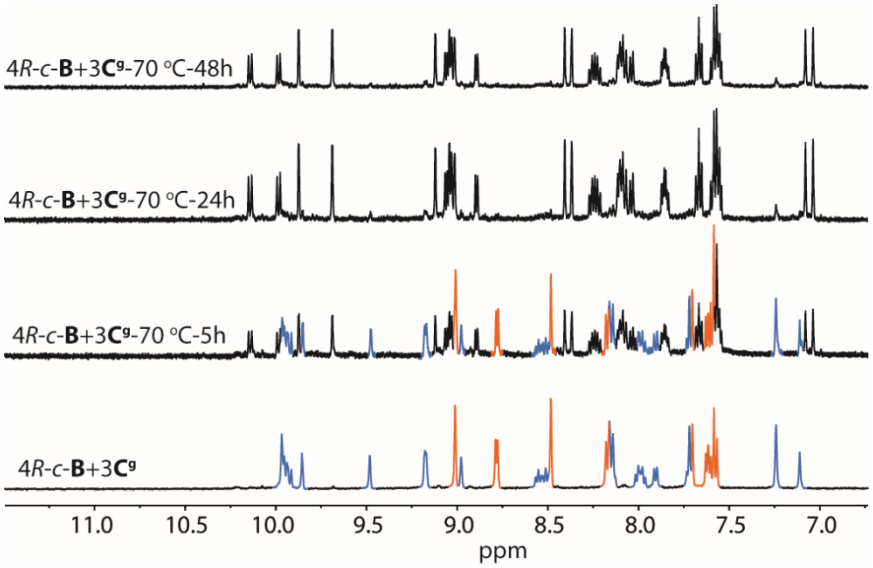

Figure 5.26 ^{1}H NMR spectra (500 MHz, CD_3CN) monitoring of [Pd_2(*R, R*-*c*-**L**^{a})$_2$**L**$^{g}_2$] synthesizing from *R*-*c*-**B**, and **C**^{g} in 4:3 ratio at 70 °C (Blue *R*-*c*-**B**, orange **C**^{g})**.**

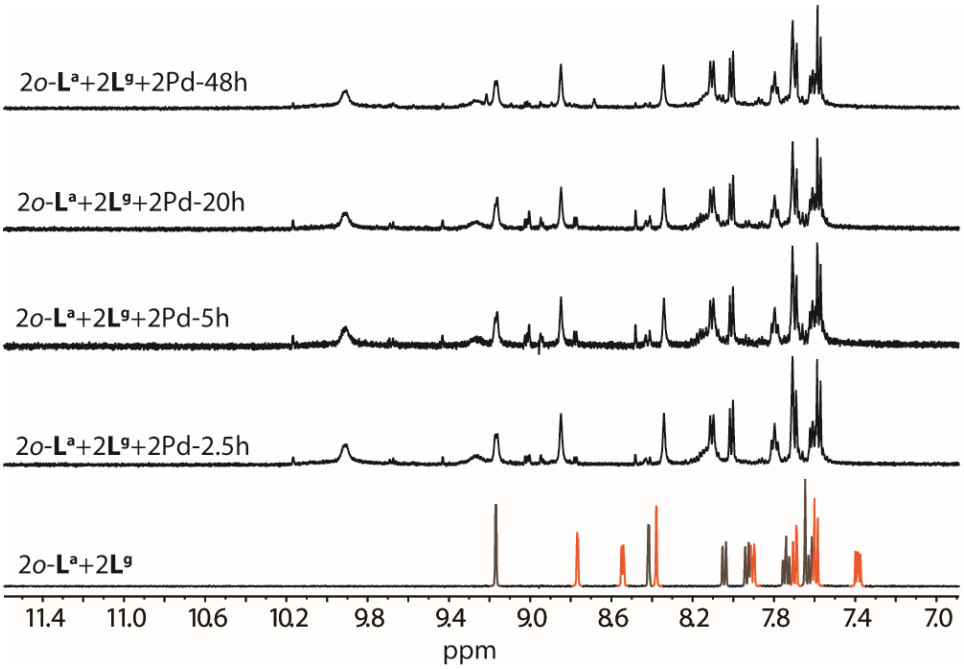

Figure 5.27 ^{1}H NMR spectra (500 MHz, CD_3CN) monitoring of $[Pd_2(o\text{-}\mathbf{L}^a)_2\mathbf{L}^g_2]$ synthesizing from *o*-$\mathbf{L}^a$, Pd^{II} and $\mathbf{L}^g$ in 1:1:1 ratio at 70 °C (Gray *o*-$\mathbf{L}^a$, orange $\mathbf{L}^g$).

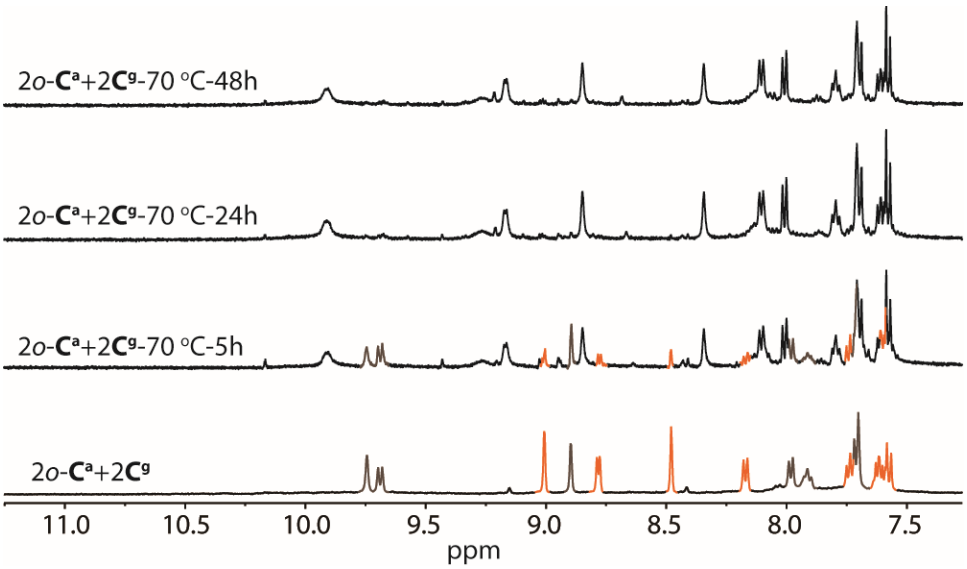

Figure 5.28 ^{1}H NMR spectra (500 MHz, CD_3CN) monitoring of $[Pd_2(o\text{-}\mathbf{L}^a)_2\mathbf{L}^g_2]$ synthesizing from *o*-$\mathbf{C}^a$, and $\mathbf{C}^g$ in 1:1 ratio at 70 °C (Gray *o*-$\mathbf{C}^a$, orange $\mathbf{C}^g$).

5.6.3 Kinetic experiment of heteroleptic cage tranformation

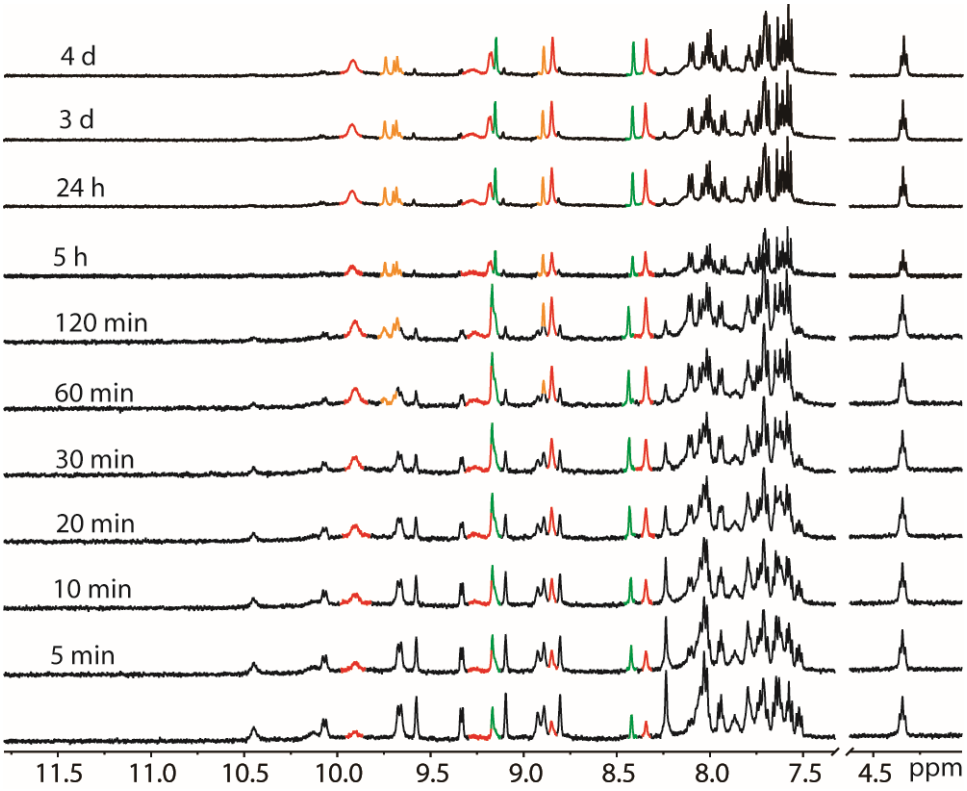

Figure 5.29 ^{1}H NMR spectra (500 MHz, CD_3CN) monitoring of *o*-**B-L^{g}** to [Pd_2(*o*-**L^{a}**)$_2$**L^{g}**$_2$] transfer at 70 °C (Red [Pd_2(*o*-**L^{a}**)$_2$**L^{g}**$_2$], orange *o*-**C^{a}**, green **o**-**L^{a}**).

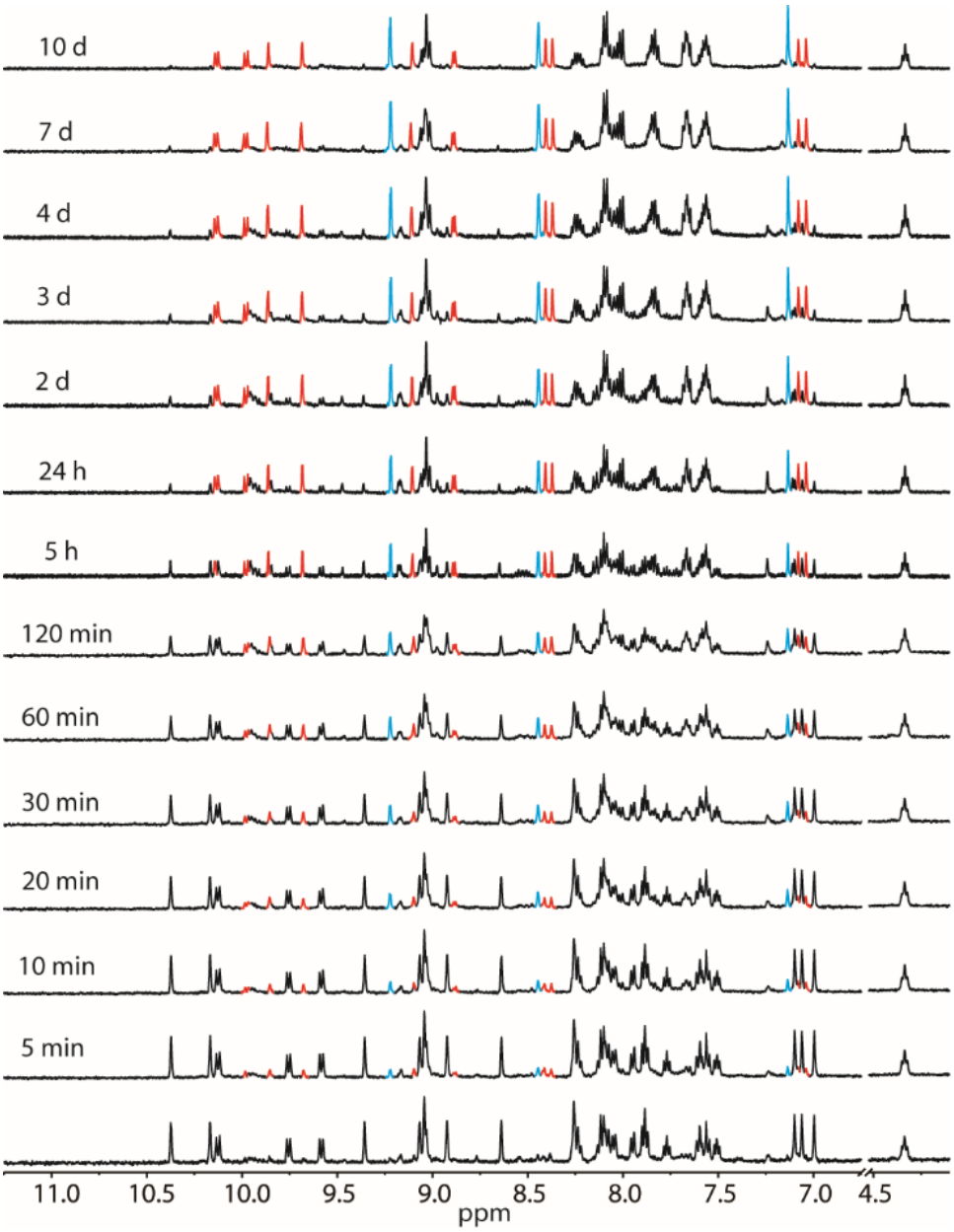

Figure 5.30 ^{1}H NMR spectra (500 MHz, CD_3CN) monitoring of *c*-**B**-**L^{g}** to [Pd_2(*c*-**L^{a}**)$_2$**L^{g}**$_2$] transfer at 70 °C (Red [Pd_2(*c*-**L^{a}**)$_2$**L^{g}**$_2$], blue **c**-**L^{a}**).

5.7 References

[1] (a) M. Fujita, *Chem. Soc. Rev.* **1998**, *27*, 417-425; (b) S. R. Seidel, P. J. Stang, *Acc. Chem. Res.* **2002**, *35*, 972-983; (c) M. Fujita, M. Tominaga, A. Hori, B. Therrien, *Acc. Chem. Res.* **2005**, *38*, 369-378; (d) M. Yoshizawa, J. K. Klosterman, M. Fujita, *Angew. Chem. Int. Ed.* **2009**, *48*, 3418-3438; (e) R. Chakrabarty, P. S. Mukherjee, P. J. Stang, *Chem. Rev.* **2011**, *111*, 6810-6918; (f) M. Han, D. M. Engelhard, G. H. Clever, *Chem. Soc. Rev.* **2014**, *43*, 1848-1860; (g) D. Rota Martir, E. Zysman-Colman, *Chem. Commun.* **2018**, *55*, 139-158.

[2] (a) Q.-F. Sun, J. Iwasa, D. Ogawa, Y. Ishido, S. Sato, T. Ozeki, Y. Sei, K. Yamaguchi, M. Fujita, *Science* **2010**, *328*, 1144; (b) D. Fujita, Y. Ueda, S. Sato, N. Mizuno, T. Kumasaka, M. Fujita, *Nature* **2016**, *540*, 563-566.

[3] (a) M. D. Pluth, R. G. Bergman, K. N. Raymond, *Acc. Chem. Res.* **2009**, *42*, 1650-1659; (b) D. Fiedler, D. H. Leung, R. G. Bergman, K. N. Raymond, *Acc. Chem. Res.* **2005**, *38*, 349-358.

[4] D. Zhang, T. K. Ronson, J. R. Nitschke, *Acc. Chem. Res.* **2018**, *51*, 2423-2436.

[5] (a) J. E. M. Lewis, E. L. Gavey, S. A. Cameron, J. D. Crowley, *Chem. Sci.* **2012**, *3*, 778-784; (b) S. M. Jansze, G. Cecot, K. Severin, *Chem. Sci.* **2018**, *9*, 4253-4257.

[6] (a) S. Pullen, G. H. Clever, *Acc. Chem. Res.* **2018**, *51*, 3052-3064; (b) W. M. Bloch, G. H. Clever, *Chem. Commun.* **2017**, *53*, 8506-8516.

[7] A. M. Johnson, R. J. Hooley, *Inorg. Chem.* **2011**, *50*, 4671-4673.

[8] M. Yamashina, T. Yuki, Y. Sei, M. Akita, M. Yoshizawa, *Chem. Eur. J.* **2015**, *21*, 4200-4204.

[9] D. Preston, J. E. Barnsley, K. C. Gordon, J. D. Crowley, *J. Am. Chem. Soc.* **2016**, *138*, 10578-10585.

[10] (a) W. M. Bloch, Y. Abe, J. J. Holstein, C. M. Wandtke, B. Dittrich, G. H. Clever, *J. Am. Chem. Soc.* **2016**, *138*, 13750-13755; (b) W. M. Bloch, J. J. Holstein, W. Hiller, G. H. Clever, *Angew. Chem. Int. Ed.* **2017**, *56*, 8285-8289; (c) R. Zhu, W. M. Bloch, J. J. Holstein, S. Mandal, L. V. Schafer, G. H. Clever, *Chem. Eur. J.* **2018**, *24*, 12976-12982.

[11] M. Han, Y. Luo, B. Damaschke, L. Gomez, X. Ribas, A. Jose, P. Peretzki, M. Seibt, G. H. Clever, *Angew. Chem. Int. Ed.* **2016**, *55*, 445-449.

[12] Y. Gu, E. A. Alt, H. Wang, X. Li, A. P. Willard, J. A. Johnson, *Nature* **2018**, *560*, 65-69.

[13] R. Zhu, J. Lubben, B. Dittrich, G. H. Clever, *Angew. Chem. Int. Ed.* **2015**, *54*, 2796-2800.

[14] (a) S. Fraysse, C. Coudret, J. P. Launay, *Eur. J. Inorg. Chem.* **2000**, 1581–1590; (b) B. He, O. S. Wenger, *J. Am. Chem. Soc.* **2011**, *133*, 17027-17036.

[15] Spartan 08 Software, Wavefunction Inc., Irvine CA, **2008**.

[16] Gaussian 09, M. J. Frisch, G. W. Trucks, H. B. Schlegel, G. E. Scuseria, M. A. Robb, J. R. Cheeseman, G. Scalmani, V. Barone, B. Mennucci, G. A. Petersson, H. Nakatsuji, M. Caricato, X. Li, H. P. Hratchian, A. F. Izmaylov, J. Bloino, G. Zheng, J. L. Sonnenberg, M. Hada, M. Ehara, K. Toyota, R. Fukuda, J. M. Ishida, T. Nakajima, Y. Honda, O. Kitao, H. Nakai, T. Vreven, J. A. Montgomery, Jr., J. E. Peralta, F. Ogliaro, M. Bearpark, J. J. Heyd, E. Brothers,

K. N. Kudin, V. N. Staroverov, R. Kobayashi, J. Normand, K. Raghavachari, A. Rendell, J. C. Burant, S. S. Iyengar, J. Tomasi, M. Cossi, N. Rega, J. M. Millam, M. Klene, J. E. Knox, J. B. Cross, V. Bakken, C. Adamo, J. Jaramillo, R. Gomperts, R. E. Stratmann, O. Yazyev, A. J. Austin, R. Cammi, C. Pomelli, J. W. Ochterski, R. L. Martin, K. Morokuma, V. G. Zakrzewski, G. A. Voth, P. Salvador, J. J. Dannenberg, S. Dapprich, A. D. Daniels, O. Farkas, J. B. Foresman, J. V. Ortiz, J. Cioslowski and D. J. Fox, Gaussian, Inc., Wallingford CT, **2009**.

6 Construction of Supramolecular Ferris-wheel and Light-Controlled Singlet Oxygen Generation

6.1 Introduction

Singlet oxygen $^1O_2$ is a highly reactive oxygen species, that is involved in photodegradation,[1] photochemical synthesis[2] as well as photodynamic therapy (PDT).[3] Many examples for the $^1O_2$ production were in recent years shown, however, the reversible control over $^1O_2$ generation is still at an early stage and attracts increasing attention recently. For example, Zhou and his coworkers developed a photochromic metal-organic framework (MOF) SO-PCN and demonstrated reversible control of $^1O_2$ generation.[4] Feringa achieved reversible noninvasive control over the generation of $^1O_2$ in a system comprising of a diarylethene (DAE) photochromic switch and a porphyrin photosensitizer by light irradiation (Figure 6.1).[5]

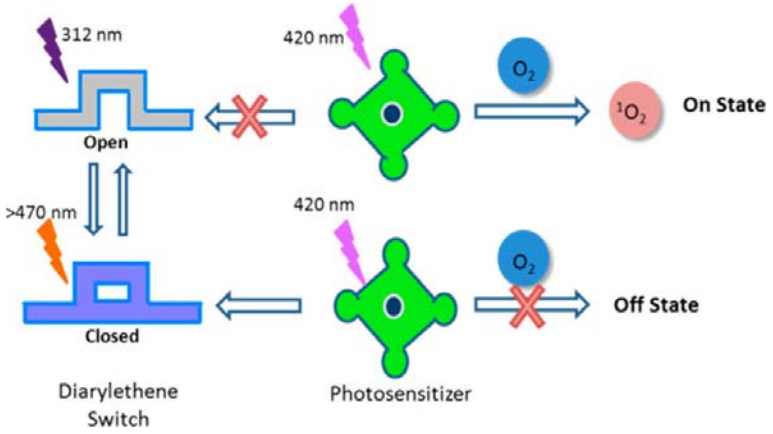

Figure 6.1 Photochemical control of the generation of $^1O_2$ by a photosensitizer using diarylethene switches[5] Copyright © 2014 The American Chemical Society.

Coordination-driven discrete supramolecular assemblies such as metallacages,[6] macrocycles[7] *etc*. have aroused extensive attention in the past few decades because of their fascinating structures,[8] designable and efficient synthesis and various applications.[9] Although well developed, the construction of supramolecular assemblies of multicomponent architectures remains challenging. Stang and coworkers constructed a series of metallacages and metallacycles utilizing carboxylate donors and Pt^{II} or Pd^{II} based acceptors.[7a] Ribas *et al*. synthesized tetragonal prismatic molecule cages by self-assembly of Pd^{II} based macrocyclic synthons and tetracarboxylate Zinc-porphyrin (Figure 6.2).[10]

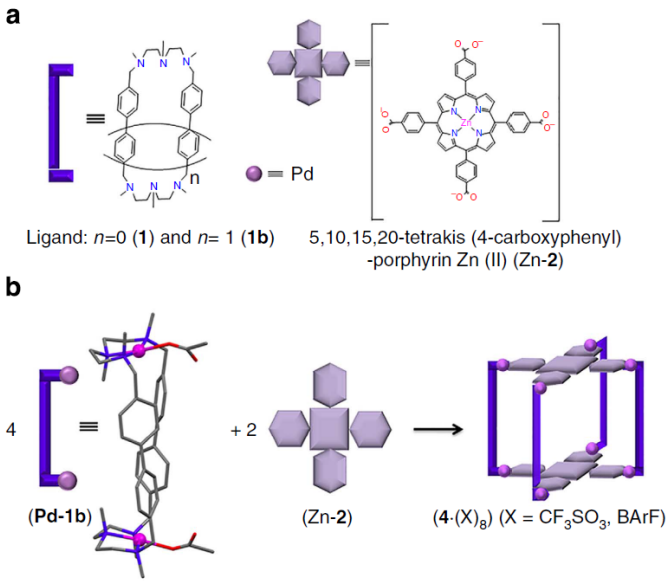

Figure 6.2 Building blocks (a) used for the self-assembly of (b) supramolecular nanocages **4**·$(X)_8$ ($X=CF_3SO_3$, BArF).[10c] Copyright © 2014 Nature Publishing Group.

As mentioned in Chapter 2, the the open and closed form of bowl *o*/*c*-**B** contains two activated metal sites. In this chapter, a series of di, tri and tetratopic carboxylate linkers are combined with the bowl *o*/*c*-**B** assembling into two, three and four- fold ferris wheel like capsules. The dithienylethene (DTE) units can be reversible interconverted between their colorless open form and colored closed formunder UV (313 nm) and visible (617 nm) light. On account of the different triplet energies between the open and closed state, the generation of $^1O_2$ with zinc-tetra(4-carboxylatophenyl)porphyrin acting as photosensitizer could be reversibly controlled.

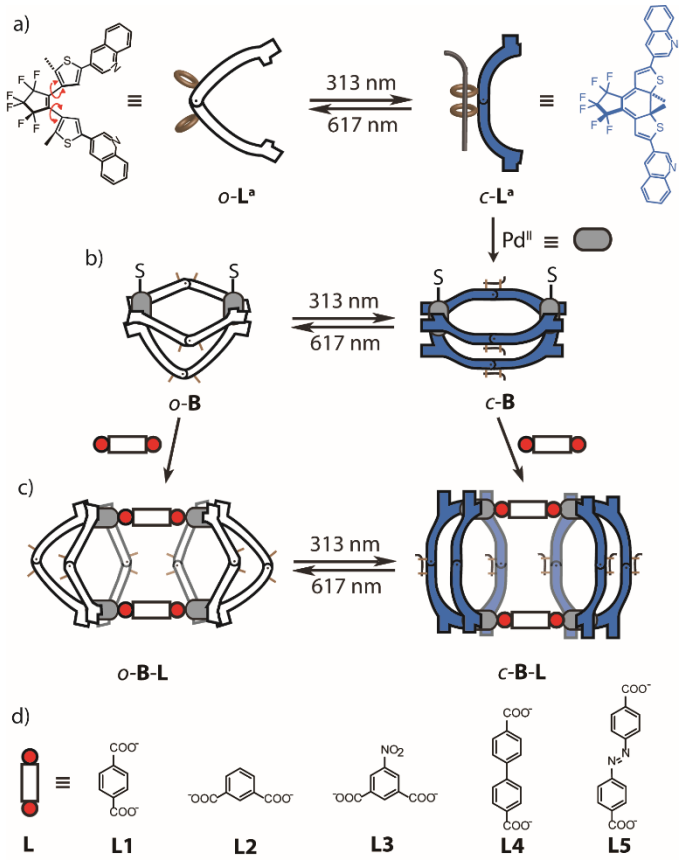

Figure 6.3 a) Reversible photo-switching of the DTE based ligand between the conformational open form *o*-**L[a]** and closed form *c*-**L[a]**; b) Formation of *c*-**B** and reversible conversion between *o*-**B** and *c*-**B**; c) Construction of the dimer *o/c*-**B**-**L** and reversible switching; d) di-carboxylate linkers.

6.2 Synthesis of dumbbell-like cage

As previously described in chapter 2, *c*-**B** was synthesized by heating a mixture of 3 eq. *c*-**L[a]** and 2.0 eq. of $[Pd(CH_3CN)_4](BF_4)_2$ in CD_3CN. Terephthalic acid was neutralized with NH_3/Et_4NOH/Bu_4NOH to give **L1** (Figure 6.3). Mixing of *c*-**B** and **L1** in a 1:1 ratio in CD_3CN under ambient conditions, resulted in a new set of ^1H NMR signals compared to *c*-**B.** And in high resolution ESI mass spectrometry, signals consistent with the formation of a dumbbell like dimer was observed. Even though we could not assign all of the broad signals in the ^1H NMR spectrum (Figure 6.4) due to numerous diastereomers, apparent shifts were observed, being consistent with the formation of supramolecular assembly from *c*-**B** and **L1**. As mentioned in chapter 2, the broad NMR signals were mainly derived from numerous of diastereomers. Thus, the enantiopure precursor *R/S*-*c*-**B** (only the enantiopure synthesis and NMR characters are shown in the following experiment as well for clarity) was used instead. Since no diastereomers could form from the enantiopure precursors, much sharper ^1H NMR spectra (Figure 6.4) were obtained, in which all signals could unambiguously be assigned by COSY and NOESY NMR spectra (Chapter 6.6.2.2.1), to confirm the formation of the capsule from *c*-**B** and **L1**. In the ESI-

MS spectrum (Figure 6.5a), the main signals ($[2Pd_2(\textit{c}\text{-}\mathbf{L^a})_3+2\mathbf{L1}]^{4+}$ and $[2Pd_2(\textit{c}\text{-}\mathbf{L^a})_3+2\mathbf{L1}+BF_4]^{3+}$) were corresponding to $[2Pd_2(\textit{c}\text{-}\mathbf{L^a})_3+2\mathbf{L1}](BF_4)_4$ (*c*-**B**-**L1**) with variable numbers of BF_4^- counter ions, supporting the proposed structure of *c*-**B**-**L1**. Both of the peaks were isotopically resolved and agreed very well with their calculated theoretical distribution.

The ability to reversibly switch between two ligand isomers (*o*-$\mathbf{L^a}$ and *c*-$\mathbf{L^a}$) promoted us to study the interconversion of *o*-**B**-**L1** and *c*-**B**-**L1**. When *c*-**B**-**L1** was irradiated with light at 617 nm until the deep blue solution of *c*-**B**-**L1** turned colorless, indicating the full conversion to the open form, the dumbbell dimer (now shown as $[2Pd_2(\textit{o}\text{-}\mathbf{L^a})_3+2\mathbf{L1}](BF_4)_4$, *o*-**B**-**L1**) was still observed, supported by ^{1}H NMR (Figure 6.4) and ESI-MS (Figure 6.50). In contrast, when *o*-**B**-**L1** was irradiated at 313 nm, the solution became deep blue again and the ^{1}H NMR showed the fromation of *c*-**B**-**L1**, proving thereversible light-controlled switching between *o*-**B**-**L1** and *c*-**B**-**L1** isomers under UV (313 nm) and visible (617 nm) light.

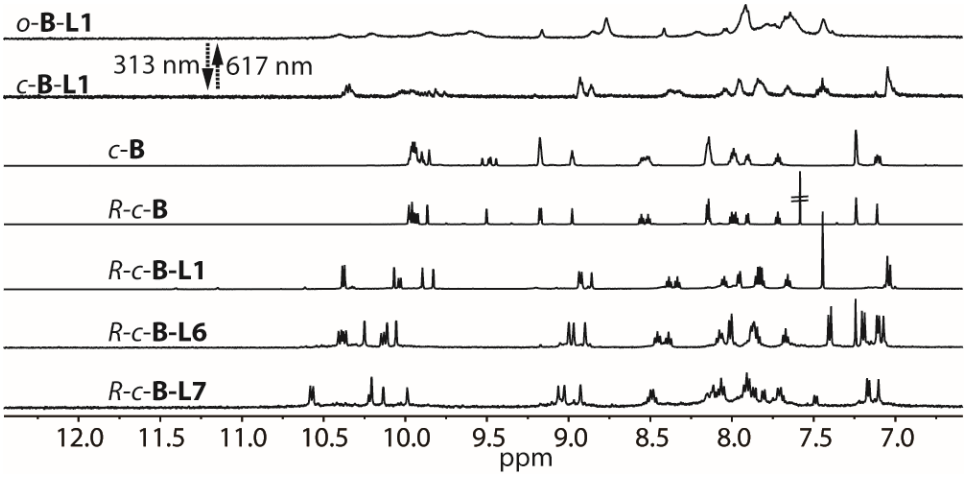

Figure 6.4 ^{1}H NMR spectra (500 MHz, CD_3CN, 298 K) of *o*-**B**-**L1**, *c*-**B**-**L1**, *c*-**B**, *R*-*c*-**B**, *R*-*c*-**B**-**L1**, *R*-*c*-**B**-**L6**, *R*-*c*-**B**-**L7**; and the photo-switching between *o*-**B**-**L1** and *c*-**B**-**L1**.

Since **L1** had two donor sites with a bite angle of 180° it was leading to the formation of dimerized capsule from *c*-**B**. Therefore, 120° **L2** and **L3** (Figure 6.3) were chose, anticipating to form multimer ($[nPd_2(\textit{c}\text{-}\mathbf{L^a})_3+n\mathbf{L}](BF_4)_{2n}$). Unfortunately, both of them preferred to form dimers, as confirmed through ^{1}H NMR and ESI-MS spectra (Chapter 6.6.2.2.2 & 6.6.2.2.3), even though with different angle of donors. Next, the length of the carboxylate linkers was extended while retaining the 180° bite angle in **L4** and **L5** (Figure 6.3). After mixing with *c*-**B**, similarly, they assembled into the respective dimers $[2Pd_2(\textit{o}\text{-}\mathbf{L^a})_3+2\mathbf{L4}](BF_4)_4$ (*c*-**B**-**L4**) and $[2Pd_2(\textit{o}\text{-}\mathbf{L^a})_3+2\mathbf{L5}](BF_4)_4$ (*c*-**B**-**L5**). NMR spectroscopy and ESI mass spectrometry (Chapter 6.6.2.2.4 & 6.6.2.2.5) supported the formation of these dimers structures.

6.3 Synthesis of supramolecular ferris-wheel

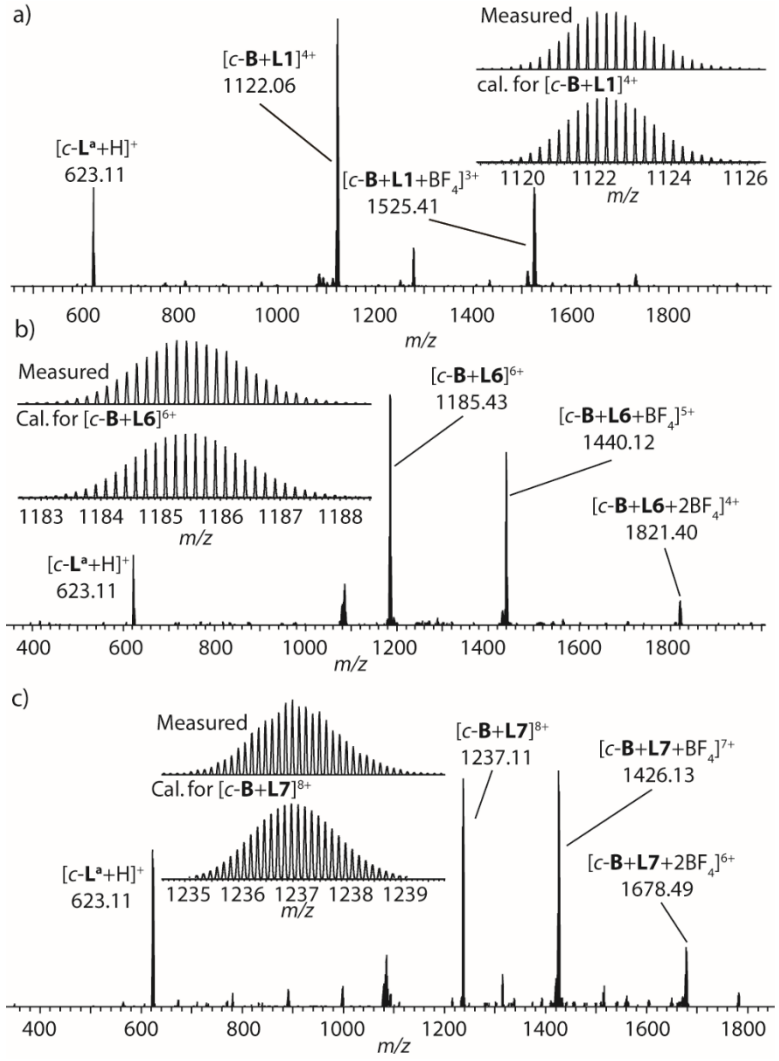

Figure 6.5 ESI-MS spectra of *c*-**B**-**L1**, *c*-**B**-**L6**, *c*-**B**-**L7**.

After a series of di-carboxylate donors was investigated and only a dimerization of two bowls was observed regardless of bite angle and length, a new set of bridging ligands with multiple carboxylate donors was investigated to construct hierarchical supramolecular structures. Firstly, 0.67 eq. of tritopic 1,3,5-tri(4-carboxylatophenyl)benzene (**L6**, Figure 6.6) was titrated into *c*-**B** CD_3CN solution, yielding in the formation of a trimer $[3Pd_2(c\text{-}\mathbf{L^a})_3{+}2\mathbf{L6}](BF_4)_6$ (*c*-**B**-**L6**). When using the enantiomeric pure precursor, clear NMR spectra were recorded (Figure 6.4), which could be completely assigned. The ESI mass spectrum showed a series of signals corresponding to $[3Pd_2(c\text{-}\mathbf{L^a})_3{+}3\mathbf{L6}]^{6+}$, $[3Pd_2(c\text{-}\mathbf{L^a})_3{+}3\mathbf{L6}{+}BF_4]^{5+}$ and $[3Pd_2(c\text{-}\mathbf{L^a})_3{+}3\mathbf{L6}{+}2BF_4]^{4+}$ (Figure 6.5b), consistent for the formation of the trimer *c*-**B**-**L6** structure assignment. Later, the tetratopic carboxylate 5,10,15,20-Tetra(4-carboxylatophenyl)porphyrin (**L7**, Figure 6.6) was used, applying the same synthetic procedure, to obtain a small ferris-wheel like tetramer $[4Pd_2(c\text{-}\mathbf{L^a})_3{+}2\mathbf{L7}](BF_4)_8$ (*c*-**B**-**L7**),

as supported by NMR spectroscopy (Figure 6.4) and ESI mass spectrometry (Figure 6.5c). Identically, the tetramer supramolecular ferris-wheel could also be reversibly switched between the open form ([4Pd$_2$(*o*-**L^a**)$_3$+2**L7**](BF$_4$)$_8$, *o*-**B**-**L7**) and closed form *c*-**B**-**L7** as well, which was monitored by ^{1}H NMR and ESI-MS spectra (Figure 6.51 & Figure 6.52).

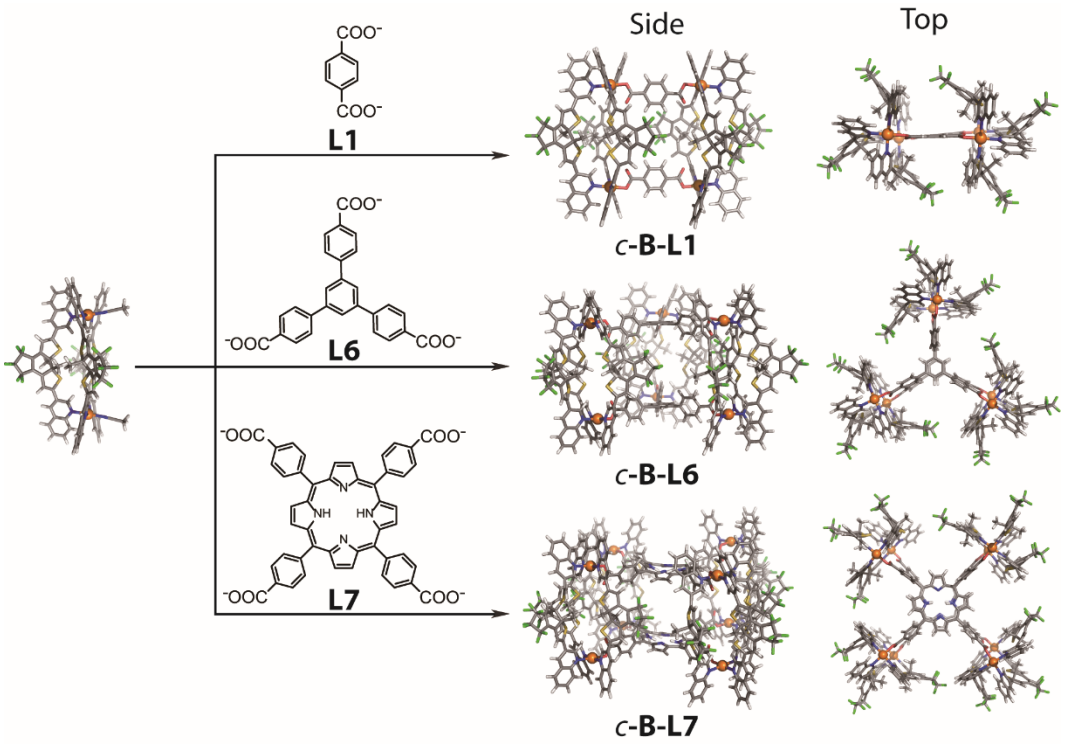

Figure 6.6 Scheme of formation *c*-**B**-**L1**, *c*-**B**-**L6**, *c*-**B**-**L7**, and their optimized (PM6) structures displayed from a side and top view.

Unfortunately, despite numerous attempts, we could not obtain a single crystal suitable for X-ray analysis. Thus we undertook a molecule modelling for all the supramolecular ferris-wheel cages (Figure 6.6). The models were first built up using SPARTAN and then geometry optimized on a PM6 level of theory without constrains.

6.4 Singlet oxygen generation

Zinc metalized porphyrin has been widely used as photosensitizers because of its high quantum yield (Φ = 0.84) towards $^1O_2$ generation and well-studied photochemistry. Diethienylethene (DTE) derivatives, as previously explained, can be interconverted between their open form and closed form. The structural and electronic differences result in a large difference in their properties such as electronic energy levels, colour and polarizability etc (Chapter 1). Since we could successfully prepare *o*/*c*-**B**-**L7** combining porphyrin and DTE units in both open and closed form. In the same way, the supramolecular ferris-wheel like tetramer [4Pd$_2$(*o*/*c*-**L^a**)$_3$+2**L8**](BF$_4$)$_8$ (*o*/*c*-**B**-**L8**) but with

zinc porphyrin derivative zinc-5,10,15,20-Tetra(4-carboxylatophenyl)porphyrin (**L8**) was synthesized, which was confirmed by NMR spectroscopy and ESI-MS spectrometry (Chapter 6.6.2.2.8). Irradiation of the sample of *c*-**B**-**L8** at 617 nm, resulted in a broadened ^{1}H NMR of *o*-**B**-**L8** (Figure 6.7b), similar to that of *o*-**B**-**L7** (Figure 6.51). Also the absorbance at 600 nm completely vanished (Figure 6.7c). When the same sample was then irradiated at 313 nm, the closed form *c*-**B**-**L8** as shown by the ^{1}H NMR and also absorbance intensity at~ 600 nm recovered almost to the original level (Figure 6.7b & c). This cycle was repeated 14 times with a decline of only 10%, with respect to the absorption at 600 nm (Figure 6.7c & d).

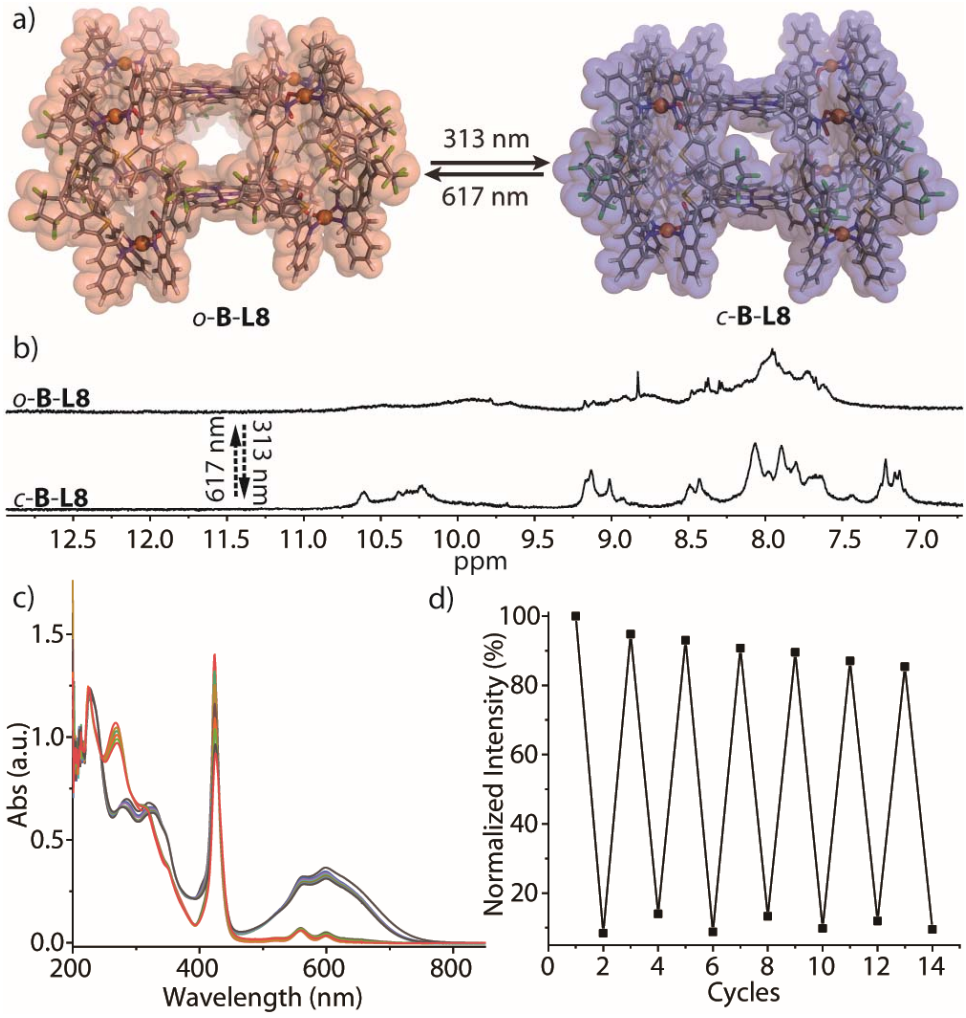

Figure 6.7 a) the reversible of photo-switching between *o*-**B**-**L8** and *c*-**B**-**L8** shown through a) reaction scheme; monitored by b) ^{1}H NMR spectra and c) UV-vis spectra at 600 nm for 14 cycles.

Since the photoisomerization of catalysts between *o*/*c*-**B**-**L8** could be controlled by light, $^{1}O_2$ generation capacities of the open form *o*-**B**-**L8** and closed form *c*-**B**-**L8** were investigated respectively. 1,3-diphenylisobenzofuran (DPBF) was used to detect the produced singlet oxygen by observing an absorbance decrease at 410 nm upon oxidative degradation by $^{1}O_2$ (Figure 6.8a). DPBF in acetonitrile was mixed with 5% of

catalyst (open form *o*-**B**-**L8** or closed form *o*-**B**-**L8**) and was irradiated at 617 nm while the evolution of $^1O_2$ was monitored by UV-vis spectroscopy (Figure 6.8c & d). From the spectra, a clear decrease of the absorbance from DPBF at 410 nm was observed for both *o*-**B**-**L8** and *c*-**B**-**L8** (Figure 6.8c & d). Over 300 seconds, a decrease of 78% of DPBF was observed when using *o*-**B**-**L8**, whereas the closed form catalyst of *c*-**B**-**L8** showed ~ 47% degradation (Figure 6.8b). The reason why *o*-**B**-**L8** showed a higher $^1O_2$ production than the closed form *c*-**B**-**L8**, according to literature, are followed by a quenching mechanism between the porphyrin and the closed DTE ligand, therefore resulting less efficient of $^1O_2$ generation. Upon irradiation under 420 nm (Soret band), **L8** was excited to **L8***. In *o*-**B**-**L8**, because of the higher triplet energy level of *o*-**L**^{a}, the energy of **L8*** cannot be transferred to the DTE ligand but to $^3O_2$, thus generating $^1O_2$, while in *c*-**B**-**L8**, the energy transfer of **L8*** to the closed form DTE ligands is possible because of the lower energy states, resulting in quenching of the $^1O_2$ generation. Thus as a benefit from the reversible switching between *o*-**B**-**L8** and *c*-**B**-**L8**, we could control the singlet oxygen generation by UV and visible light with a supramolecular ferris-wheel like capsule.

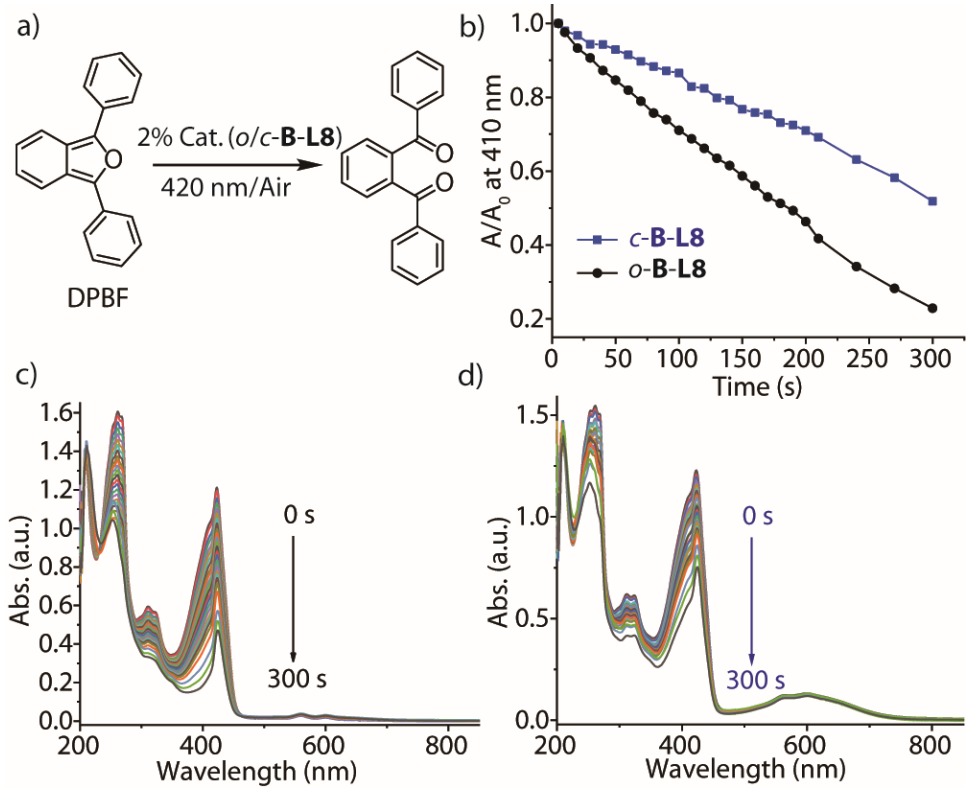

Figure 6.8 a) photo oxidation of DPBF catalyzed by *o*/*c*-**B**-**L8** in presence of 420 nm light and air; b) time-dependent UV-vis absorption decay at 410 nm and their corresponding spectra catalyzed by c) *o*-**B**-**L8** and d) *c*-**B**-**L8**.

6.5 Conclusion

In conclusion, a series di-, tri- and tetra-fold ferris-wheel like capsules were built up by constructing Pd-based supramolecular bowls *o*/*c*-**B** with di-, tri-, and tetratopic carboxylate linkers. Moreover, the photochromic properties for these ferris-wheel compounds are retained. In particular, combining a photochromic switch with a photosensitizer together in *o*/*c*-**B**-**L8**, led to the reversible control of singlet oxygen generation.

6.6 Experimental section

6.6.1 General

The conformational closed form bowl compound $[Pd_2(C_{33}H_{20}F_6N_2S_2)_3](BF_4)_4$ (*c*-**B**) was prepared according to previous protocols. NMR measurements were all conducted at 298 K on Avance-500 and Avance-600 instruments from Bruker and INOVA 500 MHz machine from Varian. High-resolution ESI mass spectrometric measurements were carried out on maXis ESI-TOF MS and ESI-timsTOF machines from Bruker. The 313 nm irradiations were performed with a 500 W Hg Arc lamp from LOT-Quantum Design equipped with a dichroitic mirror and a 313 nm bandpass filter. 617 nm irradiations were performed with a power LED irradiation apparatus (3x 1.4 W 617 nm Power LED, 25 nm FWHM) from Sahlmann photonics, Kiel. Chiral HPLC was performed on an Agilent Technologies 1260 infinity HPLC system equipped with Daicel CHIRALPAK IC columns (250 x 4.6 mm and 250 x 10 mm) using a dichloromethane/hexane/methanol (39%/60%/1%) mixture as eluent for the separation of *c*-**L**^{1}. UV-Vis spectra were recorded on an Agilent 8453 UV-Visible spectrophotometer. All cage models were constructed using SPARTAN and then geometry optimized on a PM6 level of theory (no counter ions were included) without applying constrains.

6.6.2 Synthesis

6.6.2.1 Synthesis of carboxylic linkers

All carboxylic acids were purchased from commercial sources and used without further purification. The zinc-tetrakis(4-carboxyphenyl)-porphyrin was prepared following the reported procedure.[10c]

To suspend carboxylic acids in CH_3CN, 2.0 eq. / 3.0 eq. / 4.0 eq. of tetraethylammonium hydroxide (25% w/w in methanol) or tetrabutylammonium hydroxide (10% w/w in

methanol) were added to neutralize these acid and the pH was adjusted to 7. After removing the solvent, the carboxylate linkers were quantitively obtained as the tetraethylammonium salts.

The terephthalic and Zn-TCPP acid was neutralized with triethylamine. To suspend terephthalic acid in CD_3CN or Zn-TCPP in d_6-DMSO, excess amounts of trimethylamine (around 20 eq.) were added separately. The neutralized deuterated solutions were used directly for the following reaction.

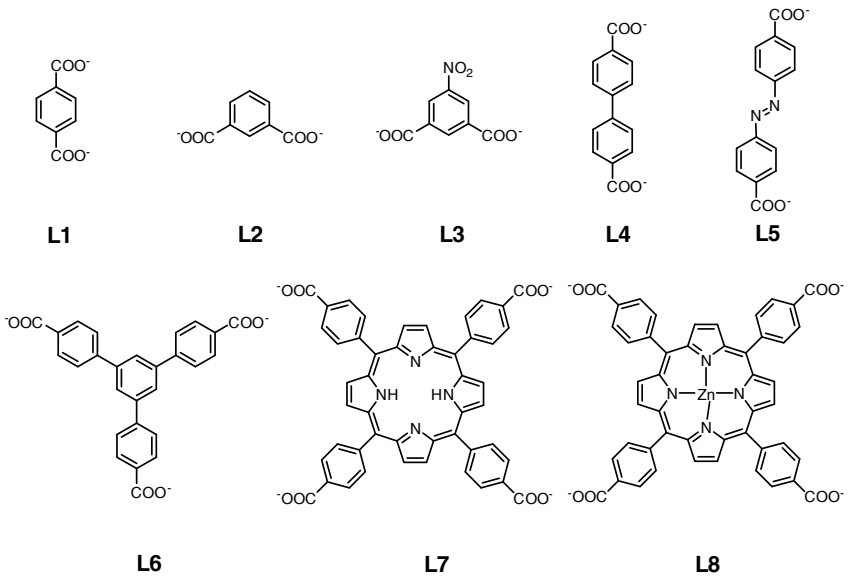

Scheme 5.1 Schematic structures of the carboxylate linkers.

6.6.2.2 Synthesis of prisms

*6.6.2.2.1 Synthesis of c-**B**-**L1***

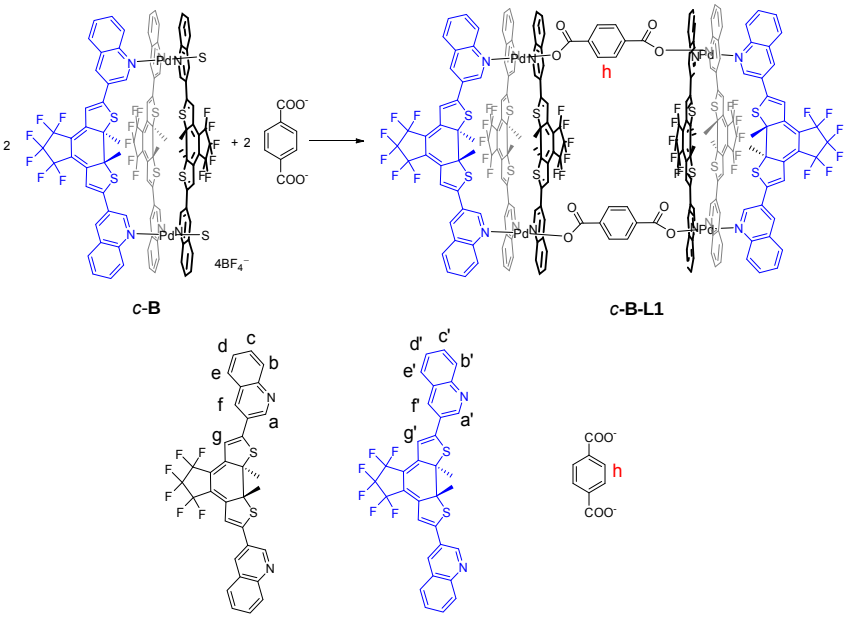

Scheme 5.2 Synthesis of c-**B**-**L1**

c-**B**-**L1** was quantitatively formed by titrating 1.0 eq. of the with triethylamine neutralized **L1** (10 mM, 25 µL, CD_3CN) to a solution of *c*-**B** (0.5 mM, 500 µL, CD_3CN) at room temperature. To ease analysis, only the enantiomeric pure (*R*-*c*-**B**-**L1**, which was synthesized from enantiomer pure *R*-*c*-**B**) NMR spectra are shown. ^{1}H NMR (600 MHz, CD_3CN) δ 10.41 – 10.36 (m, 8H), 10.07 (d, *J* = 2.0 Hz, 4H), 10.03 (d, *J* = 8.6 Hz, 4H), 9.89 (d, *J* = 2.1 Hz, 4H), 9.83 (d, *J* = 2.1 Hz, 4H), 8.93 (dd, *J* = 9.9, 2.0 Hz, 8H), 8.87 – 8.85 (m, 4H), 8.36 (dddd, *J* = 30.8, 8.5, 7.1, 1.4 Hz, 8H), 8.05 (ddd, *J* = 8.8, 7.4, 1.5 Hz, 4H), 7.97 – 7.94 (m, 8H), 7.87 – 7.79 (m, 12H), 7.69 – 7.63 (m, 4H), 7.44 (s, 8H), 7.05 (s, 8H), 7.03 (s, 4H), 2.43 (s, 12H), 2.37 (s, 12H), 2.26 (s, 12H). ESI-HRMS calculated for $[Pd_4C_{214}H_{128}F_{36}N_{12}S_{12}O_8]^{4+}$ $\{[Pd_2(c\text{-}\mathbf{L}^{\mathbf{a}})_3]_2(\mathbf{L1})_2\}^{4+}$ *m/z* = 1122.0564, found *m/z* = 1122.0629.

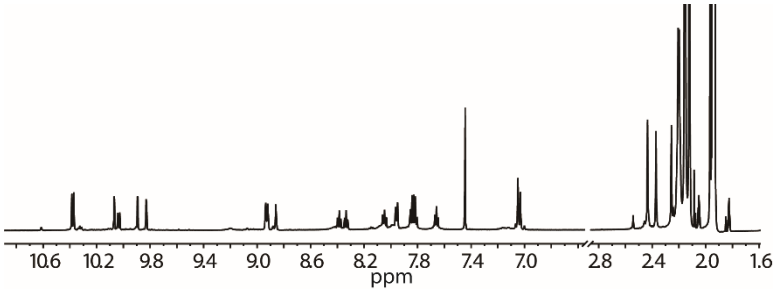

Figure 6.9 ^{1}H NMR spectrum (600 MHz, CD_3CN) of *R*-*c*-**B**-**L1**.

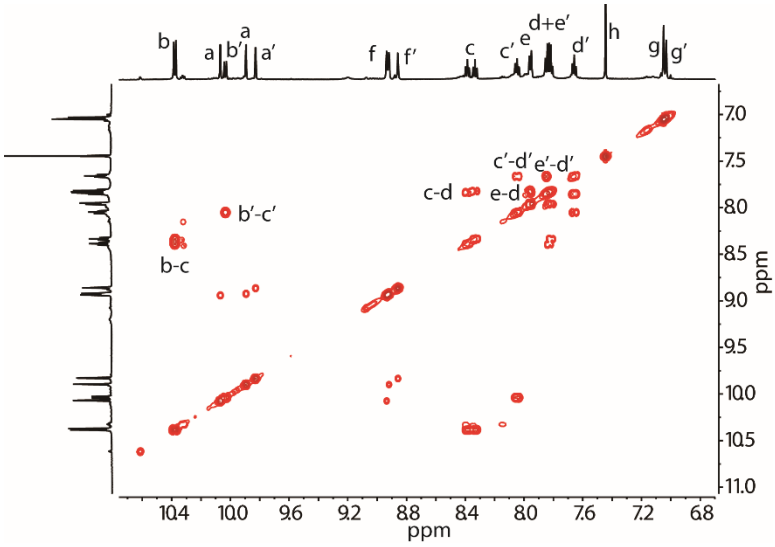

Figure 6.10 ^{1}H-^{1}H COSY NMR spectrum (600 MHz, CD_3CN) of *R*-*c*-**B**-**L1** (only showing aromatic region).

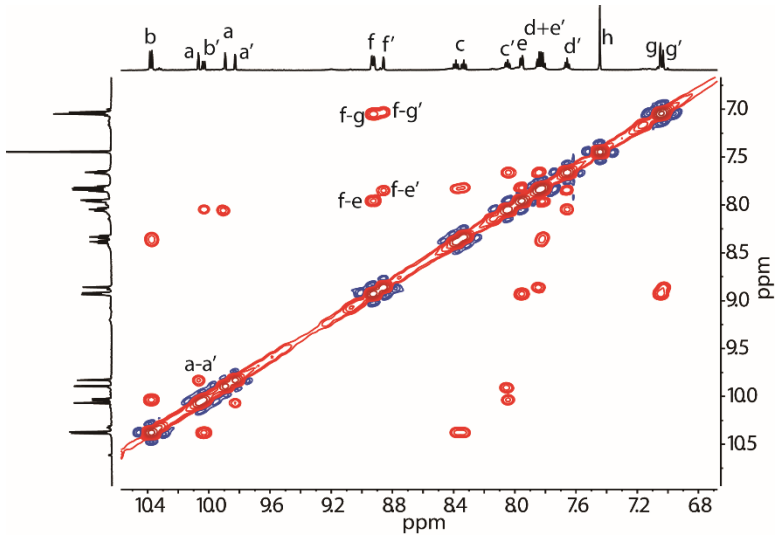

Figure 6.11 ^{1}H-^{1}H NOESY NMR spectrum (600 MHz, CD_3CN) of *R*-*c*-**B**-**L1** (only showing aromatic region).

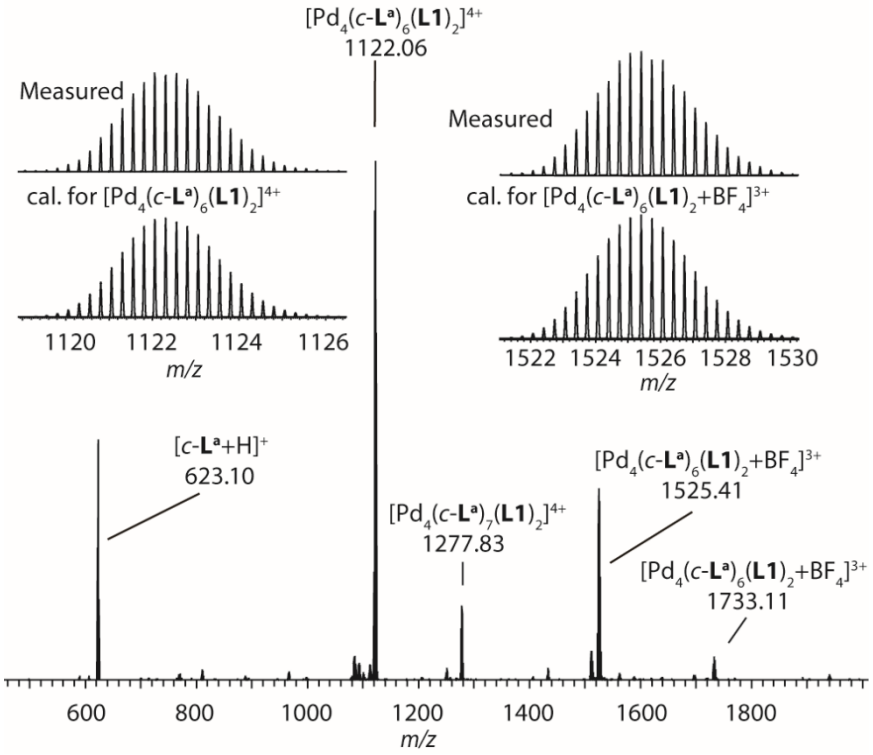

Figure 6.12 ESI-HRMS spectrum of *c*-**B**-**L1**.

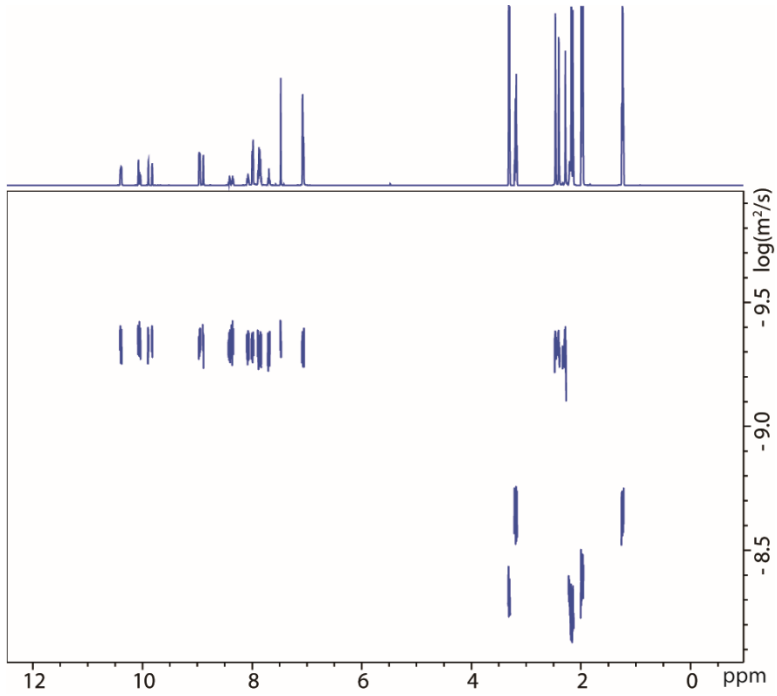

Figure 6.13 DOSY NMR spectrum (600 MHz, CD_3CN) of *R*-*c*-**B**-**L1**.

6.6.2.2.2 *Synthesis of c-B-L2*

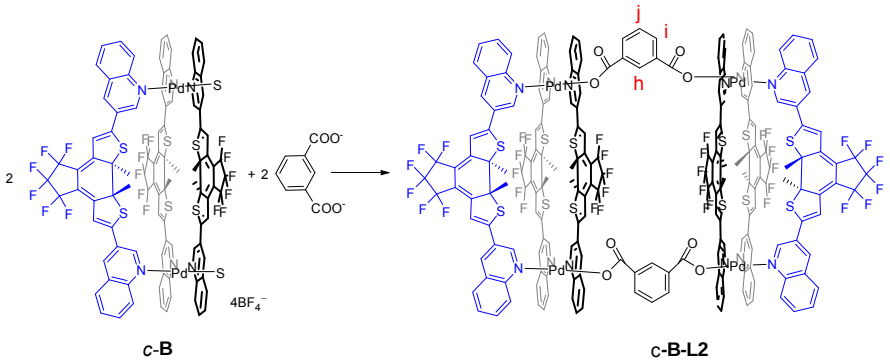

Scheme 5.3 Synthesis of *c*-**B**-**L2**.

c-**B**-**L2** was synthesized with the same procedure as *c*-**B**-**L1**.1.0 eq. of **L2** (10 mM, 25 µL, CD_3CN, tetraethylamounium as counter cation) was titrated to a *c*-**B** solution (0.5 mM, 500 µL, CD_3CN) at room temperature. To ease the analysis, only the enantiomeric pure (*R*-*c*-**B**-**L2**, which was synthesized from enantiomer pure *R*-*c*-**B**) NMR spectra are shown. ^{1}H NMR (600 MHz, CD_3CN) δ 10.51 (d, *J* = 8.7 Hz, 4H), 10.38 (d, *J* = 2.0 Hz, 4H), 10.23 (d, *J* = 8.6 Hz, 4H), 10.20 (s, 4H), 10.13 (d, *J* = 8.7 Hz, 4H), 9.98 (s, 4H), 8.93 (dd, *J* = 11.7, 1.8 Hz, 8H), 8.90 (s, 4H), 8.41 – 8.32 (m, 8H), 8.11 (t, *J* = 8.1 Hz, 4H), 7.95 (t, *J* = 7.1 Hz, 8H), 7.90 – 7.83 (m, 4H), 7.81 (d, *J* = 7.5 Hz, 8H), 7.68 (t, *J* = 7.7 Hz, 4H), 7.59 (dd, *J* = 7.9, 1.7 Hz, 4H), 7.37 (s, 2H), 7.10 – 7.07 (m, 8H), 7.06 (s, 4H), 7.03 (d, *J* = 7.8 Hz, 2H), 2.44 (s, 12H), 2.38 (s, 12H), 2.24 (s, 12H). ESI-HRMS calculated for

$[Pd_4C_{214}H_{128}F_{36}N_{12}S_{12}O_8]^{4+}$ $\{[Pd_2(c\text{-}\mathbf{L}^{a})_3]_2(\mathbf{L2})_2\}^{4+}$ *m/z* = 1122.5665, found *m/z* = 1122.5745.

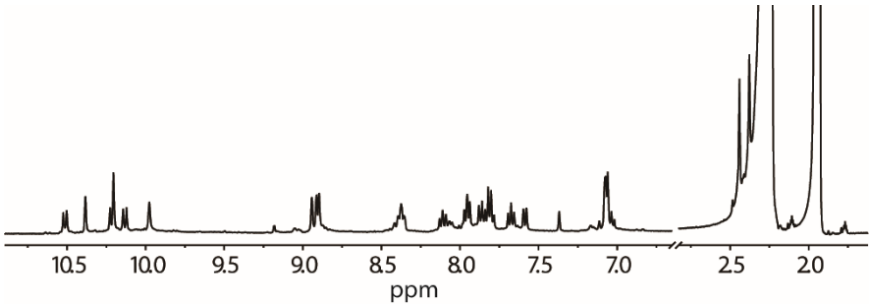

Figure 6.14 ^{1}H NMR spectrum (600 MHz, CD_3CN) of *R*-*c*-**B**-**L2**.

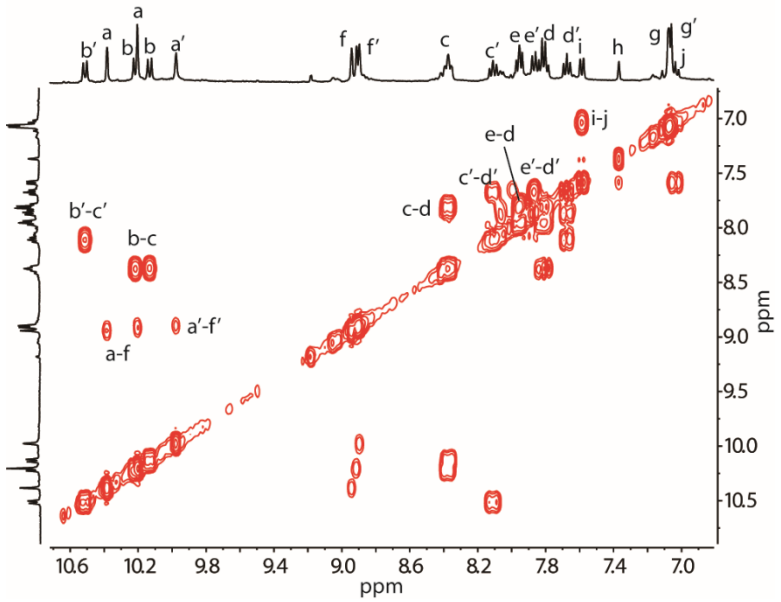

Figure 6.15 ^{1}H-^{1}H COSY NMR spectrum (600 MHz, CD_3CN) of *R*-*c*-**B**-**L2** (only showing aromatic region).

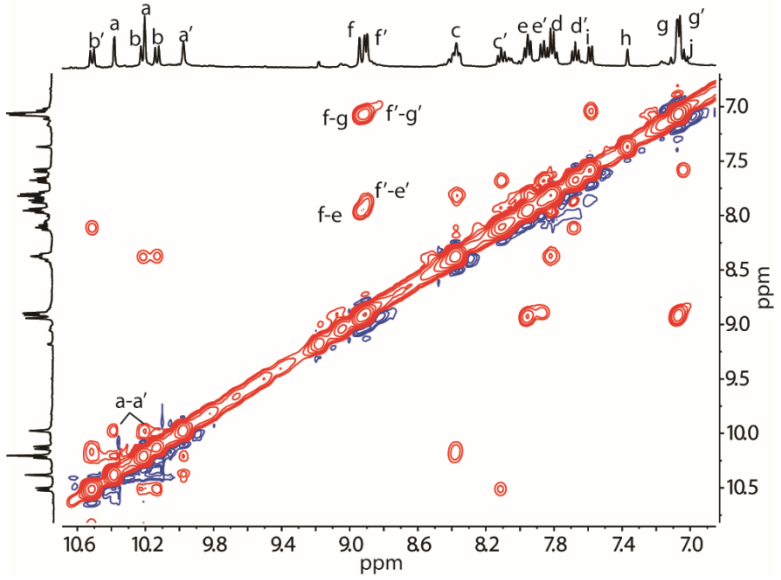

Figure 6.16 ^{1}H-^{1}H NOESY NMR spectrum (600 MHz, CD_3CN) of *R*-*c*-**B**-**L2** (only showing aromatic region).

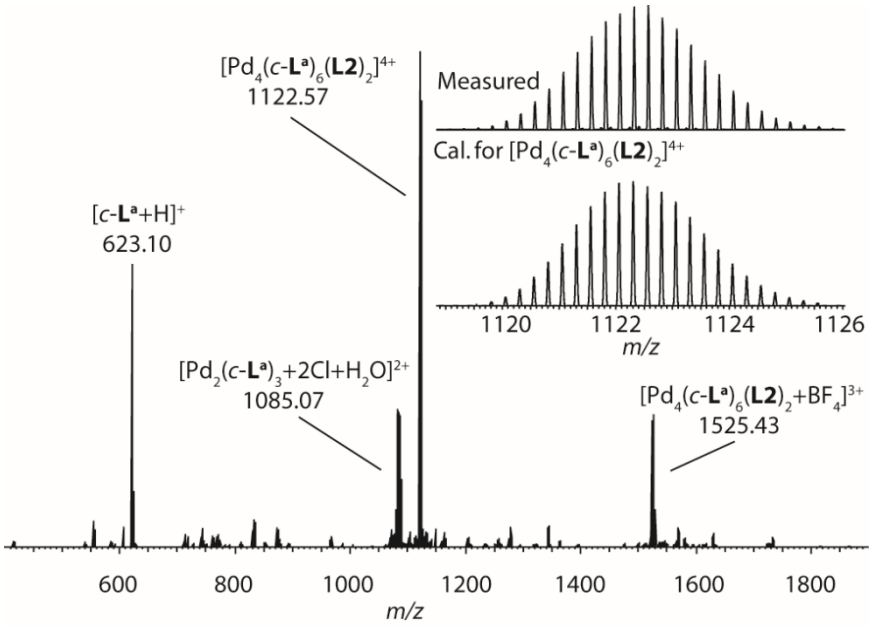

Figure 6.17 ESI-MS spectrum of *c*-**B**-**L2**.

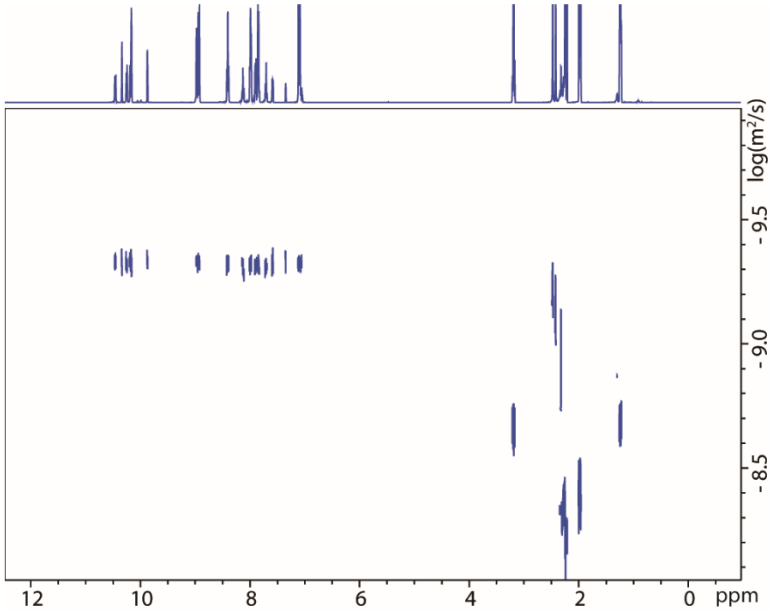

Figure 6.18 DOSY NMR spectrum (600 MHz, CD_3CN) of *R*-*c*-**B**-**L2**.

6.6.2.2.3 Synthesis of c-B-L3

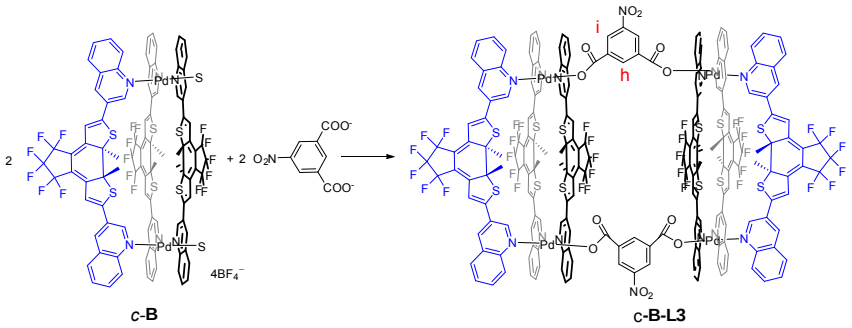

Scheme 5.4 Synthesis of *c*-**B**-**L3**.

c-**B**-**L3** was synthesized with the same procedure as *c*-**B**-**L2**. 1.0 eq. of **L3** (10 mM, 25 μL, CD_3CN, tetraethylamounium as counter cation) was titrated to a *c*-**B** solution (0.5 mM, 500 μL, CD_3CN) at room temperature. For better analysis, only one enantiomer pure (R-*c*-**B**-**L3**, which was synthesized from enantiomer pure *R*-*c*-**B**) NMR spectra here are given. ^{1}H NMR (600 MHz, CD_3CN) δ 10.43 (d, *J* = 8.7 Hz, 4H), 10.27 (d, *J* = 8.7 Hz, 4H), 10.24 (d, *J* = 2.0 Hz, 4H), 10.21 (d, *J* = 8.6 Hz, 4H), 10.08 (d, *J* = 2.0 Hz, 4H), 9.95 (s, 4H), 8.94 (d, *J* = 13.5 Hz, 8H), 8.91 (s, 4H), 8.40 (dd, *J* = 12.0, 7.8 Hz, 8H), 8.36 (d, *J* = 1.4 Hz, 2H), 8.14 – 8.08 (m, 4H), 7.96 (t, *J* = 8.5 Hz, 8H), 7.90 – 7.78 (m, 12H), 7.72 – 7.65 (m, 8H), 7.08 (d, *J* = 4.1 Hz, 12H), 2.45 (s, 12H), 2.38 (s, 12H), 2.23 (s, 12H). ESI-HRMS calculated for $[Pd_4C_{214}H_{126}F_{36}N_{14}S_{12}O_{12}]^{4+}$ $\{[Pd_2(c\text{-}L^a)_3]_2(\mathbf{L3})_2\}^{4+}$ *m/z* = 1144.7990, found *m/z* = 1144.8171.

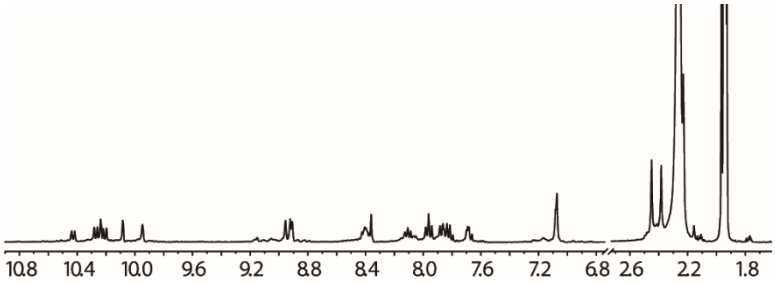

Figure 6.19 ^{1}H NMR spectrum (600 MHz, CD_3CN) of *R*-*c*-**B**-**L3**.

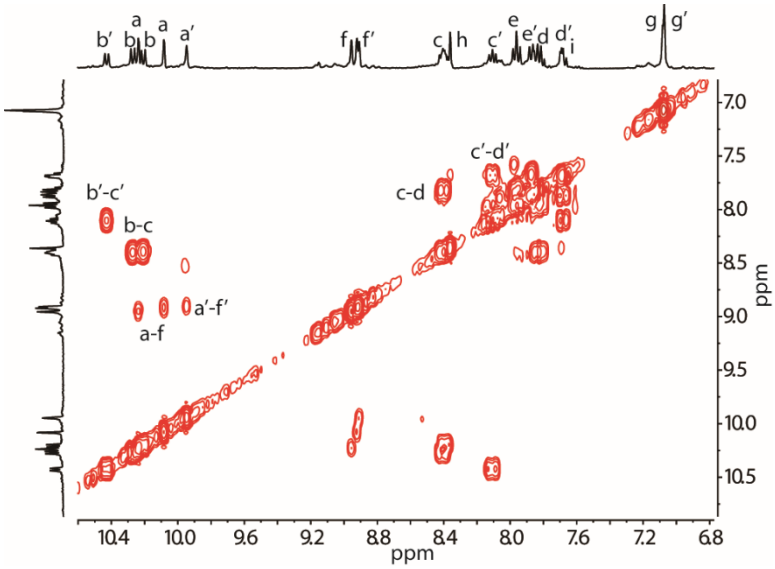

Figure 6.20 ^{1}H-^{1}H COSY NMR spectrum (600 MHz, CD_3CN) of *R*-*c*-**B**-**L3** (only showing aromatic region).

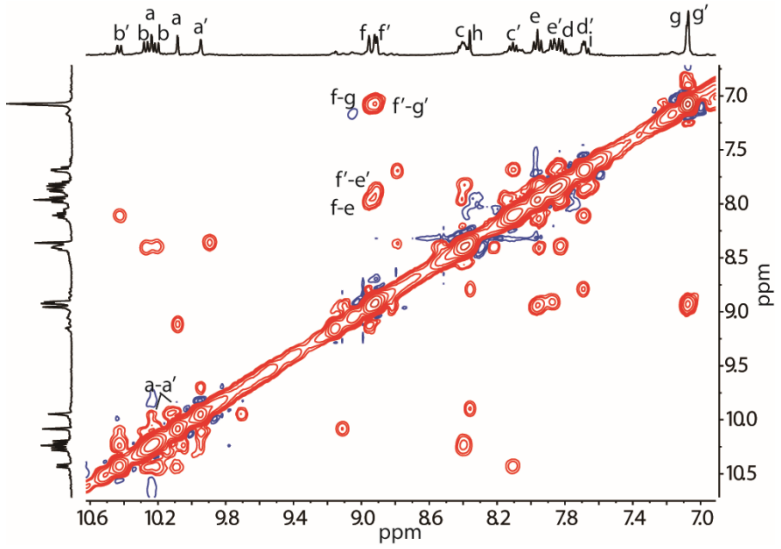

Figure 6.21 ^{1}H-^{1}H NOESY NMR spectrum (600 MHz, CD_3CN) of *R*-*c*-**B**-**L3** (only showing aromatic region).

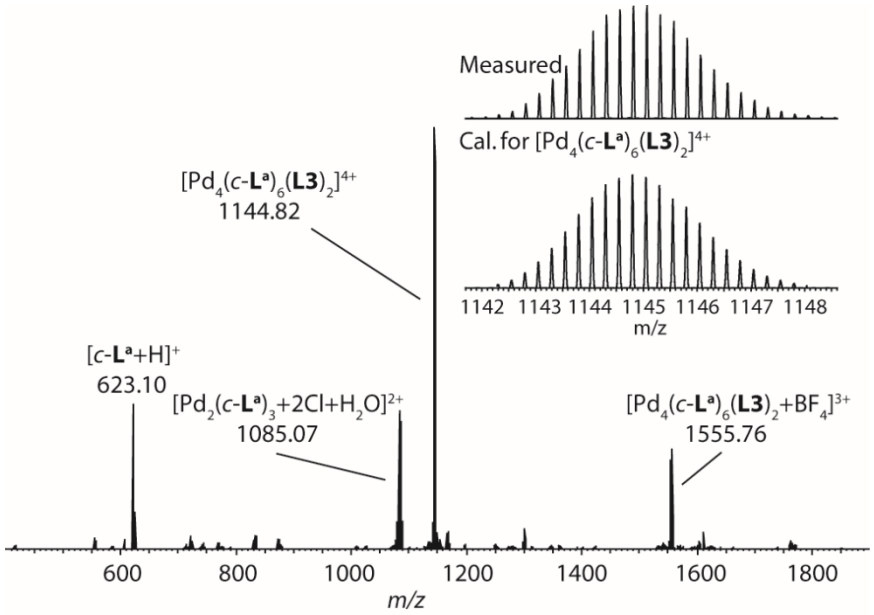

Figure 6.22 ESI-MS spectrum of *c*-**B**-**L3**.

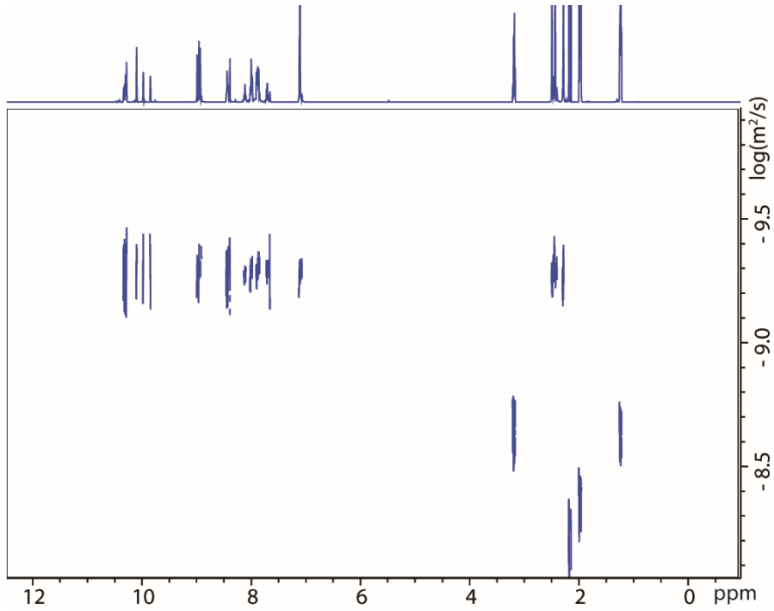

Figure 6.23 DOSY NMR spectrum (600 MHz, CD_3CN) of *R*-*c*-**B**-**L3**.

6.6.2.2.4 Synthesis of c-B-L4

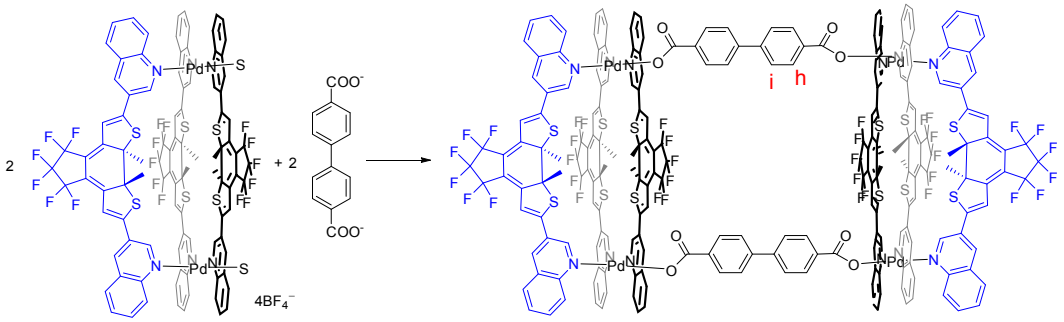

Scheme 5.5 Synthesis of *c*-**B**-**L4**.

c-**B**-**L4** was synthesized as the same procedure as *c*-**B**-**L1**. Titrate 1.0 eq. of **L4** (10 mM, 25 μL, CD_3CN, trimethylamine neutralized) to a *c*-**B** solution (0.5 mM, 500 μL, CD_3CN) at room temperature. For better analysis, only one enantiomer pure (*R*-*c*-**B**-**L4**, which was synthesized from enantiomer pure *R*-*c*-**B**) NMR spectra here are given. ^{1}H NMR (600 MHz, CD_3CN) δ 10.46 (dd, *J* = 16.1, 8.5 Hz, 8H), 10.14 (d, *J* = 2.1 Hz, 4H), 10.07 (d, *J* = 8.6 Hz, 4H), 9.93 (d, *J* = 2.0 Hz, 4H), 9.82 (d, *J* = 2.0 Hz, 4H), 8.97 (d, *J* = 10.6 Hz, 8H), 8.88 (s, 4H), 8.40 (dt, *J* = 37.5, 7.2 Hz, 8H), 8.07 (t, *J* = 8.5 Hz, 4H), 8.00 (d, *J* = 8.0 Hz, 8H), 7.91 – 7.80 (m, 12H), 7.68 (t, *J* = 7.6 Hz, 4H), 7.61 (d, *J* = 8.7 Hz, 4H), 7.34 (d, *J* = 8.6 Hz, 4H), 7.09 (d, *J* = 4.9 Hz, 8H), 7.05 (s, 4H), 2.46 (s, 12H), 2.41 (s, 12H), 2.35 (s, 12H). ESI-HRMS calculated for $[Pd_4C_{226}H_{136}F_{36}N_{12}S_{12}O_8]^{4+}$ $\{[Pd_2(c\text{-}\mathbf{L}^{a})_3]_2(\mathbf{L4})_2\}^{4+}$ *m/z* = 1160.3222, found *m/z* = 1160.3243.

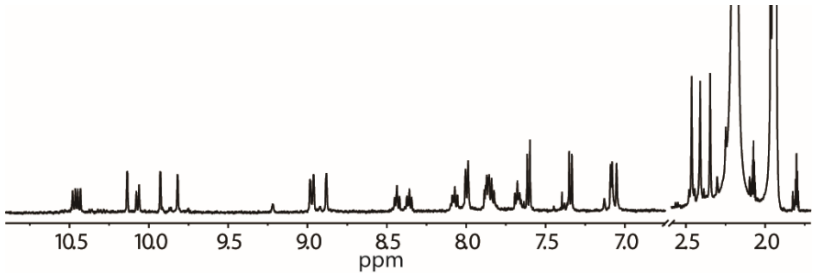

Figure 6.24 ^{1}H NMR spectrum (600 MHz, CD_3CN) of *R*-*c*-**B**-**L4**.

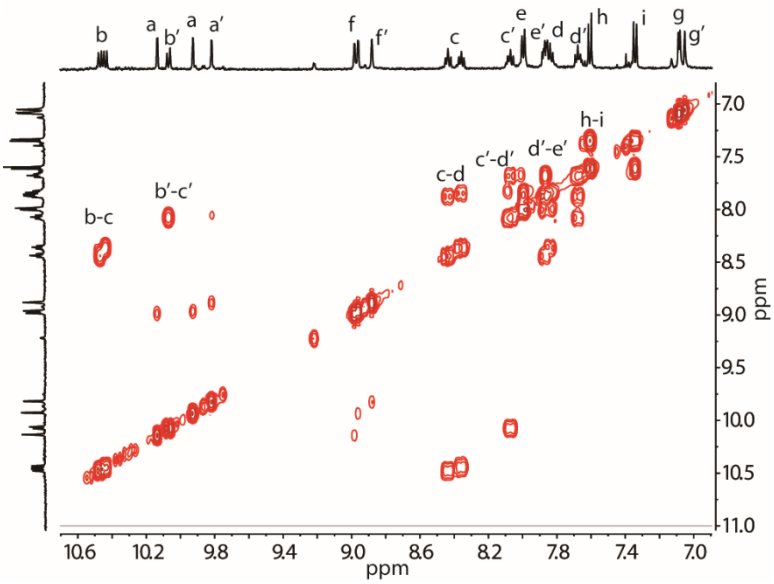

Figure 6.25 ^{1}H-^{1}H COSY NMR spectrum (600 MHz, CD_3CN) of *R*-*c*-**B**-**L4** (only showing aromatic region).

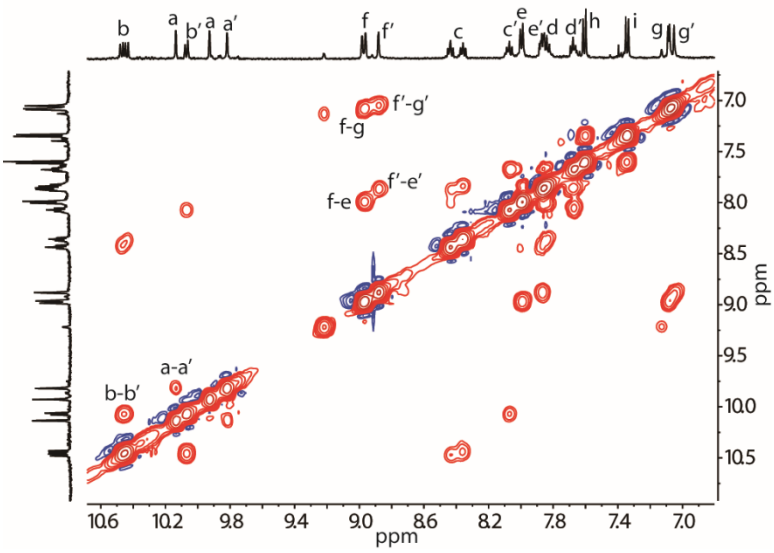

Figure 6.26 ^{1}H-^{1}H NOESY NMR spectrum (600 MHz, CD_3CN) of *R*-*c*-**B**-**L4** (only showing aromatic region).

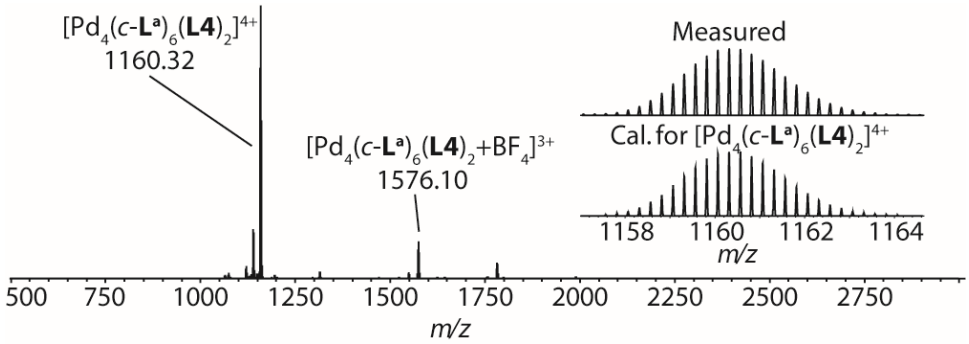

Figure 6.27 ESI-MS spectrum of *c*-**B**-**L4**.

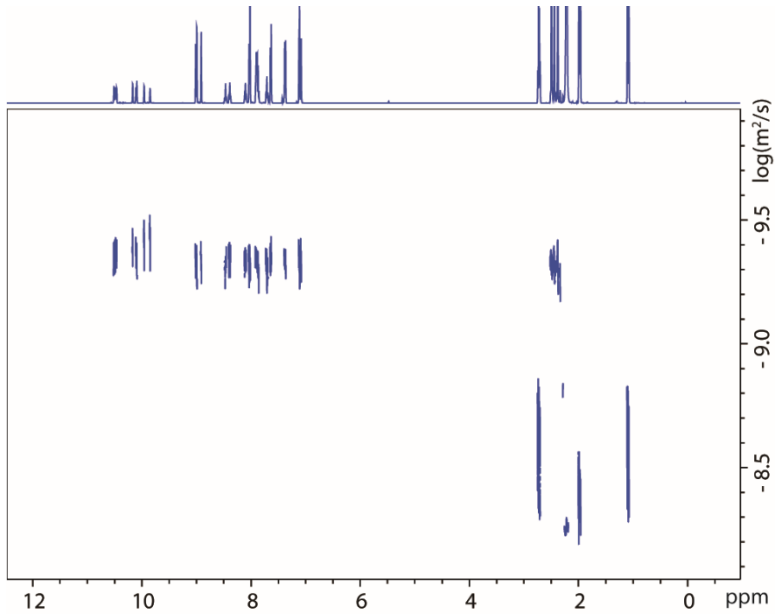

Figure 6.28 DOSY NMR spectrum (600 MHz, CD_3CN) of *R*-*c*-**B**-**L4**.

6.6.2.2.5 Synthesis of c-B-L5

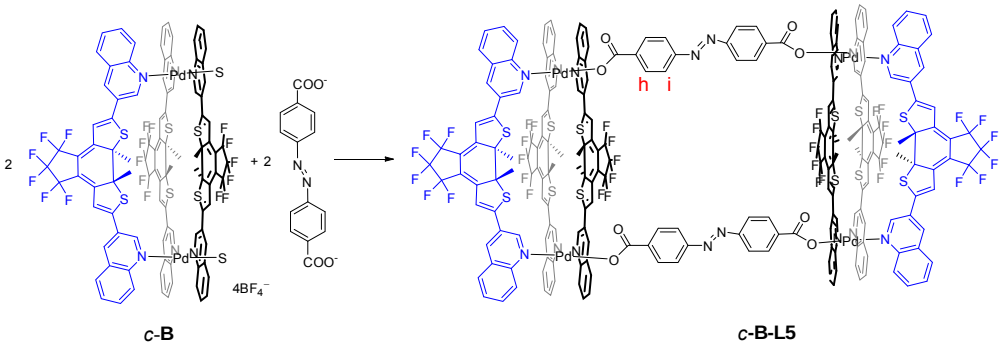

Scheme 5.6 Synthesis of *c*-**B**-**L5**.

c-**B**-**L5** was synthesized as the same procedure as *c*-**B**-**L2**. Titrate 1.0 eq. of **L5** (10 mM, 25 μL, CD_3CN, tetraethylamounium as counter cation) to a *c*-**B** solution (0.5 mM, 500 μL, CD_3CN) at room temperature. For better analysis, only one enantiomer pure (*R*-*c*-**B**-**L5**, which was synthesized from enantiomer pure *R*-*c*-**B**) NMR spectra here are given. ^{1}H NMR (600 MHz, CD_3CN) δ 10.55 – 10.45 (m, 8H), 10.16 (d, *J* = 2.1 Hz, 4H), 10.16 –

10.10 (m, 4H), 9.98 (d, *J* = 2.1 Hz, 4H), 9.87 (d, *J* = 2.1 Hz, 4H), 9.05 – 8.97 (m, 8H), 8.93 – 8.87 (m, 4H), 8.42 (dddd, *J* = 36.0, 8.5, 7.1, 1.4 Hz, 8H), 8.09 (ddd, *J* = 8.7, 7.4, 1.5 Hz, 4H), 8.04 – 7.98 (m, 8H), 7.92 – 7.82 (m, 12H), 7.78 – 7.73 (m, 4H), 7.70 – 7.66 (m, 4H), 7.64 – 7.61 (m, 4H), 7.11 (d, *J* = 4.7 Hz, 8H), 7.06 (s, 4H), 2.47 (s, 12H), 2.42 (s, 12H), 2.37 (s, 12H). ESI-HRMS calculated for $[Pd_4C_{214}H_{128}F_{36}N_{12}S_{12}O_8]^{4+}$ {$[Pd_2(c\text{-}\mathbf{L}^{a})_3]_2(\mathbf{L5})_2\}^{4+}$ *m/z* = 1174.3252, found *m/z* = 1174.3443.

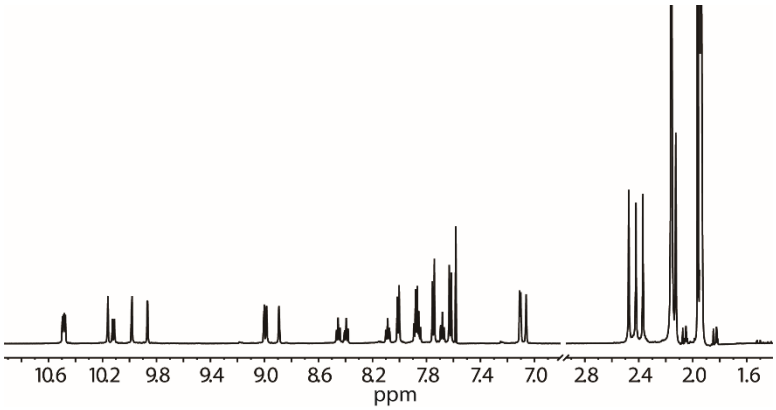

Figure 6.29 ^{1}H NMR spectrum (600 MHz, CD_3CN) of *R-c*-**B**-**L5**.

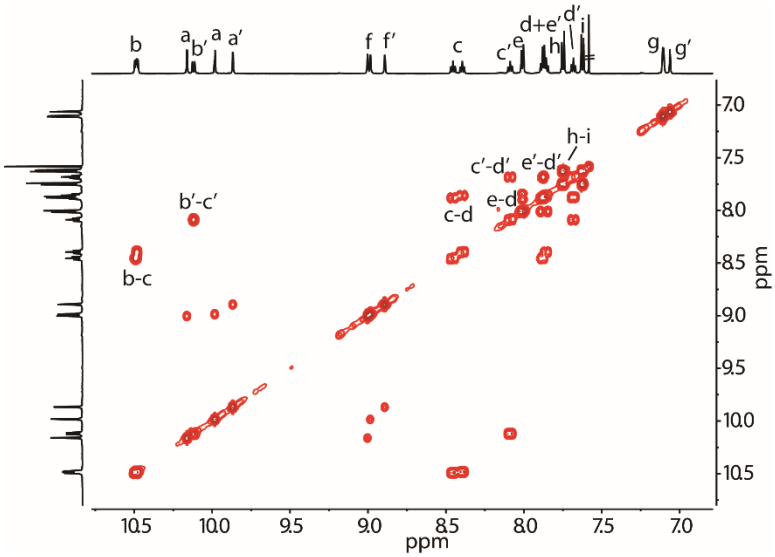

Figure 6.30 ^{1}H-^{1}H COSY NMR spectrum (600 MHz, CD_3CN) of *R-c*-**B**-**L5** (only showing aromatic region).

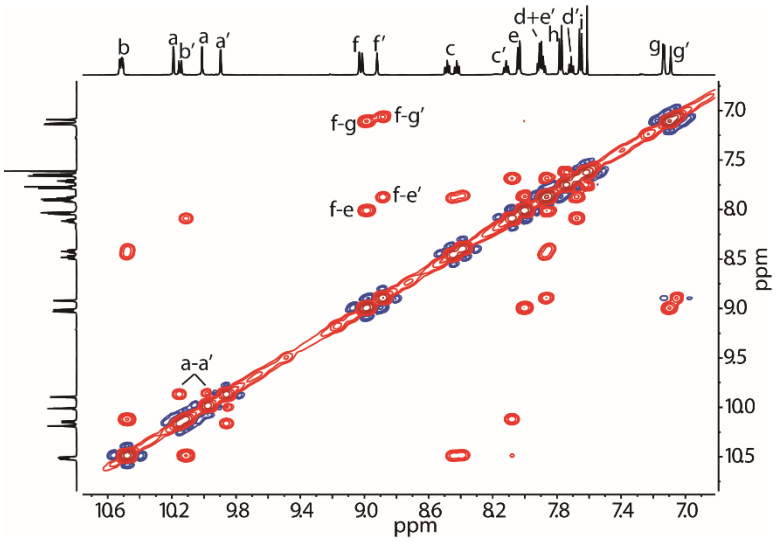

Figure 6.31 ^{1}H-^{1}H NOESY NMR spectrum (600 MHz, CD_3CN) of *R*-*c*-**B**-**L5** (only showing aromatic region).

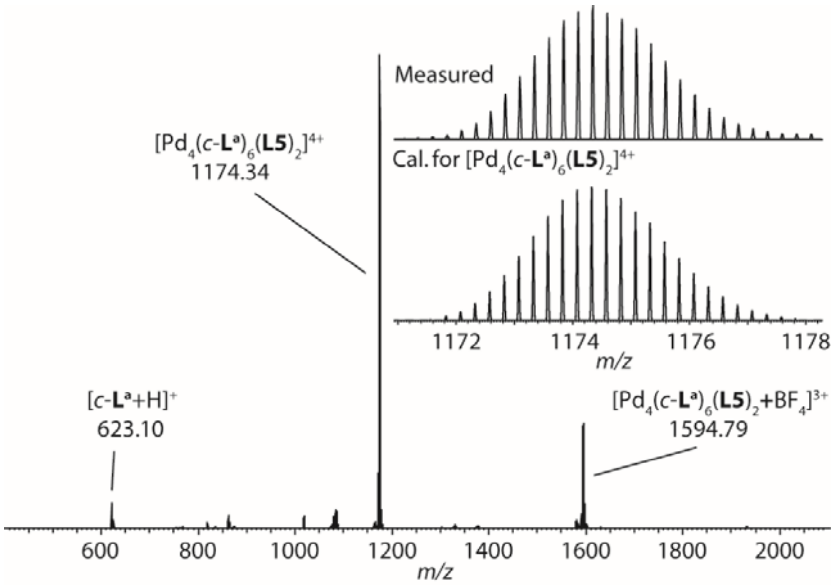

Figure 6.32 ESI-MS spectrum of *c*-**B**-**L5**.

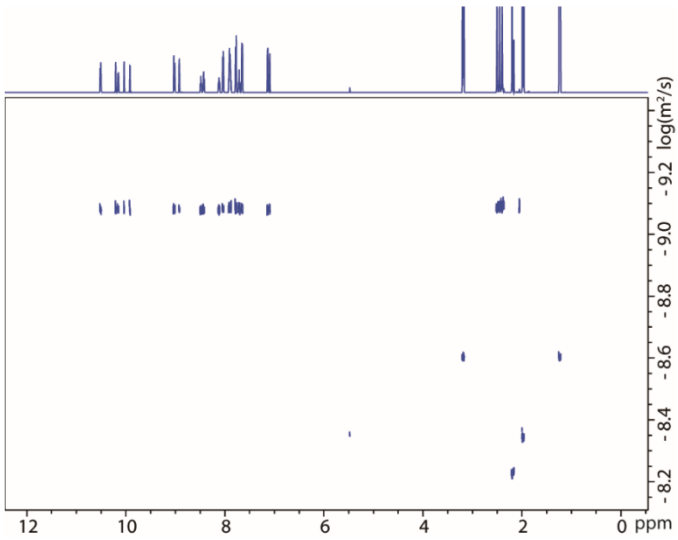

Figure 6.33 DOSY NMR spectrum (600 MHz, CD_3CN) of *R*-*c*-**B**-**L5**.

*6.6.2.2.6 Synthesis of c-**B**-**L6***

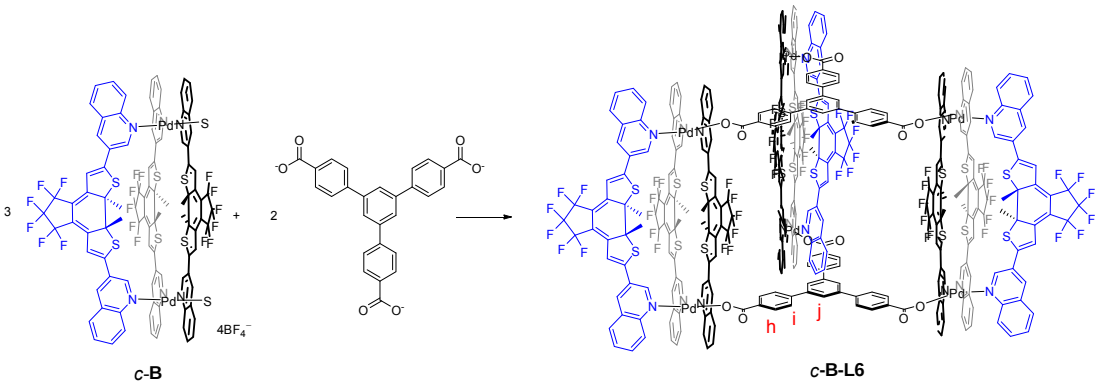

c-**B** *c*-**B**-**L6**

Scheme 5.7 Synthesis of *c*-**B**-**L6**.

c-**B**-**L6** was synthesized as the same procedure as *c*-**B**-**L2**. Titrate 0.67 eq. of **L6** (10 mM, 16.7 μL, CD_3CN, tetraethylamounium as counter cation) to a *c*-**B** solution (0.5 mM, 500 μL, CD_3CN) at room temperature. For better analysis, only one enantiomer pure (*R*-*c*-**B**-**L6**, which was synthesized from enantiomer pure *R*-*c*-**B**) NMR spectra here are given. ^{1}H NMR (600 MHz, CD_3CN) δ 10.39 (dd, *J* = 11.5, 8.6 Hz, 12H), 10.25 (d, *J* = 2.0 Hz, 6H), 10.14 (d, *J* = 8.8 Hz, 6H), 10.12 (d, *J* = 1.9 Hz, 6H), 10.06 (d, *J* = 2.0 Hz, 6H), 8.98 (d, *J* = 11.8 Hz, 12H), 8.90 (d, *J* = 1.8 Hz, 6H), 8.42 (dt, *J* = 27.0, 7.8 Hz, 12H), 8.08 (t, *J* = 8.2 Hz, 6H), 8.01 (d, *J* = 8.2 Hz, 12H), 7.91 – 7.80 (m, 18H), 7.67 (t, *J* = 7.7 Hz, 6H), 7.40 (d, *J* = 8.2 Hz, 12H), 7.24 (s, 6H), 7.20 (d, *J* = 8.3 Hz, 12H), 7.11 (d, *J* = 5.6 Hz, 12H), 7.07 (s, 6H), 2.47 (s, 18H), 2.40 (s, 18H), 2.29 (s, 18H). ESI-HRMS calculated for $[Pd_6C_{351}H_{210}F_{54}N_{18}S_{18}O_{12}]^{6+}$ $\{[Pd_2(c\text{-}L^a)_3]_3(\mathbf{L6})_2\}^{6+}$ *m/z* = 1185.4358, found *m/z* = 1185.4333.

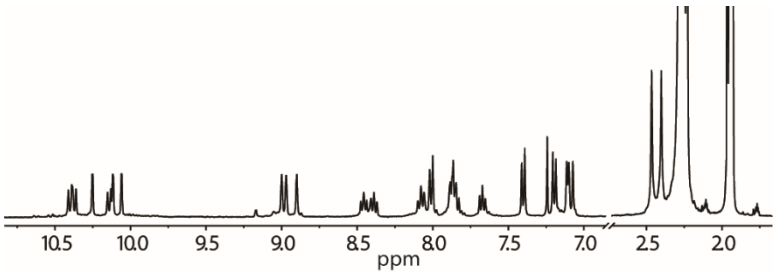

Figure 6.34 ^{1}H NMR spectrum (600 MHz, CD_3CN) of *R*-*c*-**B**-**L6**.

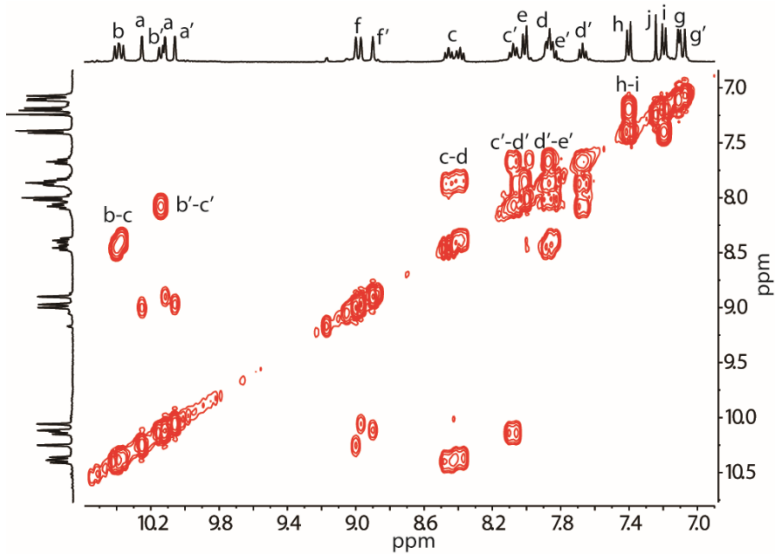

Figure 6.35 ^{1}H-^{1}H COSY NMR spectrum (600 MHz, CD_3CN) of *R*-*c*-**B**-**L6** (only showing aromatic region).

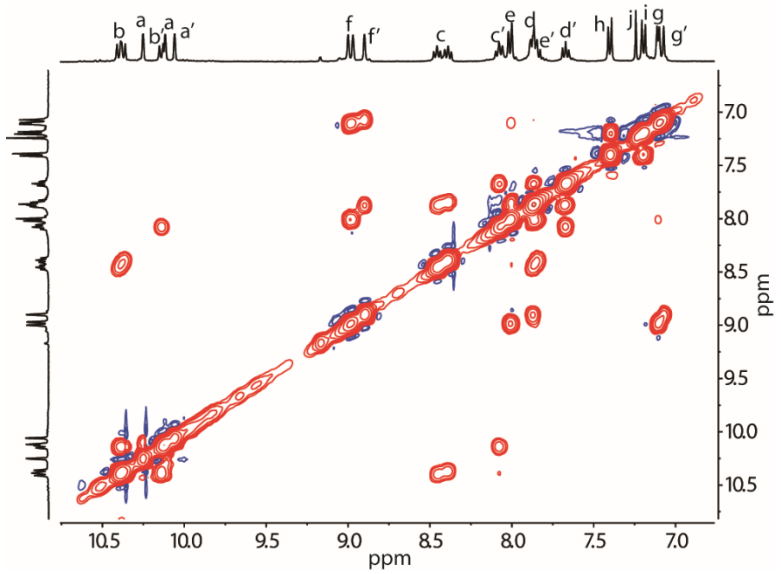

Figure 6.36 ^{1}H-^{1}H NOESY NMR spectrum (600 MHz, CD_3CN) of *R*-*c*-**B**-**L6** (only showing aromatic region).

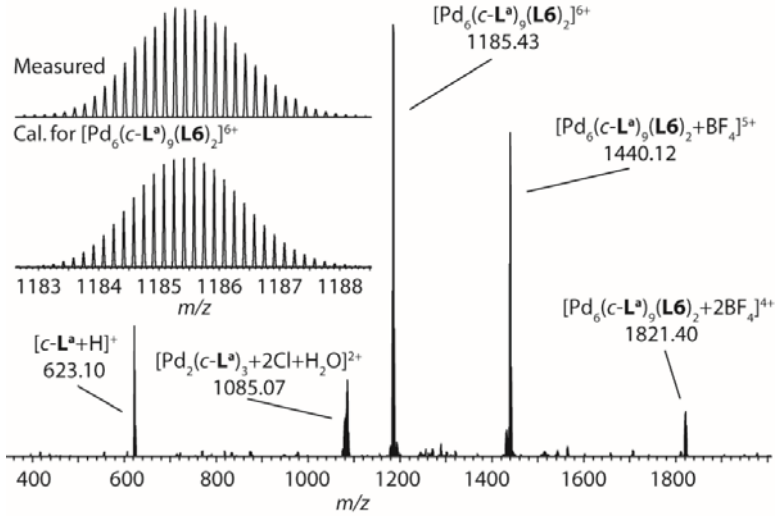

Figure 6.37 ESI-MS spectrum of *c*-**B**-**L6**.

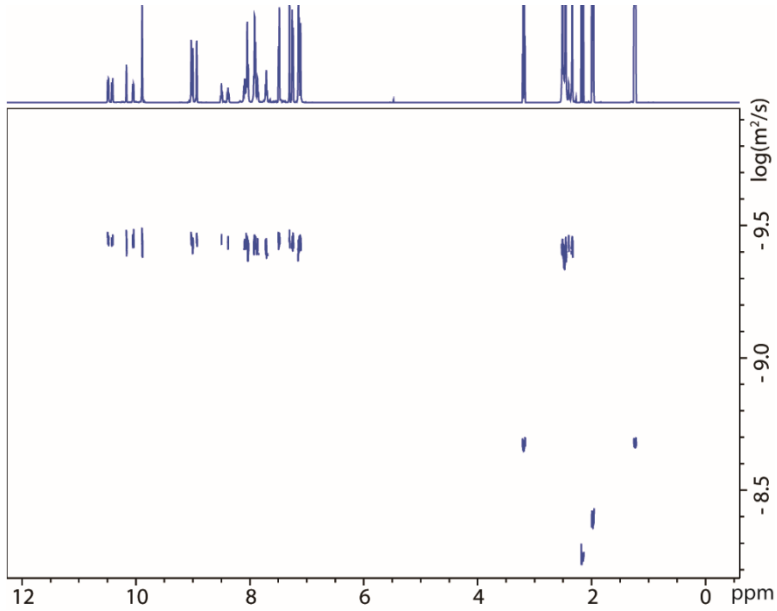

Figure 6.38 DOSY NMR spectrum (600 MHz, CD_3CN) of *R*-*c*-**B**-**L6**.

6.6.2.2.7 Synthesis of c-B-L7

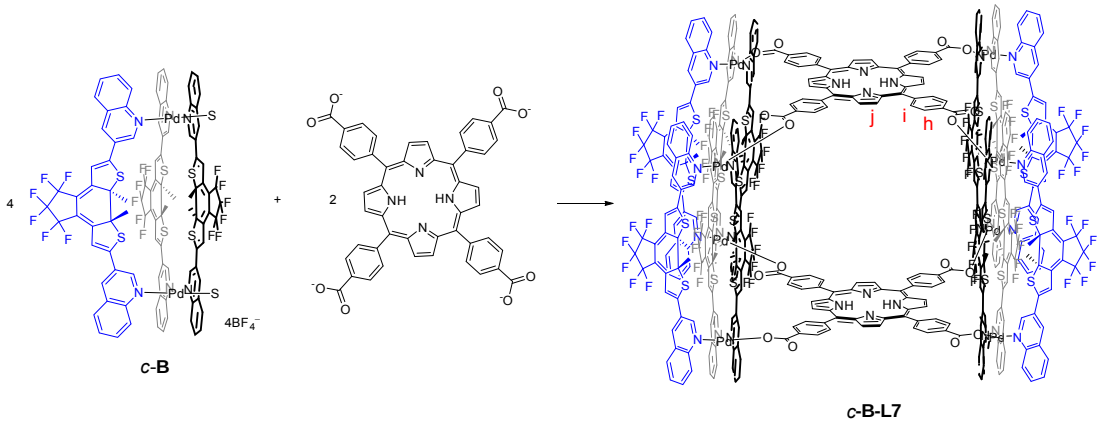

Scheme 5.8 Synthesis of *c*-**B**-**L7**.

c-**B**-**L7** was synthesized as the same procedure as *c*-**B**-**L2**. Titrate 0.5 eq. of **L7** (10 mM, 12.5 μL, CD_3CN, tetraethylamounium as counter cation) to a *c*-**B** solution (0.5 mM, 500 μL, CD_3CN) at room temperature. For better analysis, only one enantiomer pure (*R*-*c*-**B**-**L7**, which was synthesized from enantiomer pure *R*-*c*-**B**) NMR spectra here are given. ^{1}H NMR (600 MHz, CD_3CN) δ 10.58 (d, *J* = 8.6 Hz, 16H), δ 10.21 (d, *J* = 8.9 Hz, 8H), 10.19 (s, 8H), 10.12 (d, *J* = 1.9 Hz, 8H), 9.95 (s, 8H), 9.06 (s, 8H), 9.02 (s, 8H), 8.93 (s, 8H), 8.49 (dt, *J* = 13.2, 7.8 Hz, 16H), δ 8.11 (t, *J* = 7.8 Hz, 8H), 8.06 (dd, *J* = 11.9, 8.1 Hz, 16H), 7.91 (dd, *J* = 11.5, 7.7 Hz, 24H), 7.87 (d, *J* = 8.1 Hz, 16H), 7.83 – 7.78 (m, 16H), 7.70 (t, *J* = 7.4 Hz, 8H), 7.50 (d, *J* = 8.1 Hz, 8H), 7.17 (d, *J* = 9.0 Hz, 16H), 7.10 (s, 8H), 2.53 (s, 24H), 2.50 (s, 24H), 2.38 (s, 24H). ESI-HRMS calculated for $[Pd_8C_{492}H_{292}F_{72}N_{32}S_{24}O_{16}]^{8+}$ $\{[Pd_2(c\text{-}\mathbf{L}^{\mathbf{a}})_3]_4(\mathbf{L7})_2\}^{8+}$ *m/z* = 1237.1158, found *m/z* = 1237.1147.

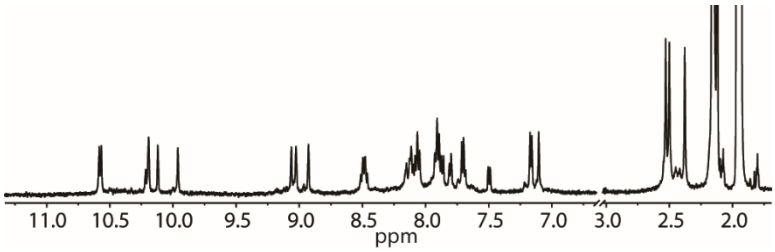

Figure 6.39 ^{1}H NMR spectrum (600 MHz, CD_3CN) of *R*-*c*-**B**-**L7**.

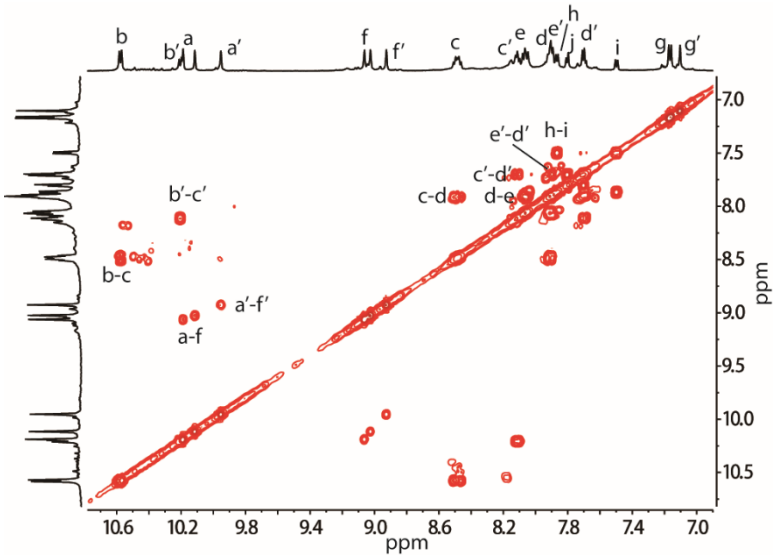

Figure 6.40 ^{1}H-^{1}H COSY NMR spectrum (600 MHz, CD_3CN) of *R*-*c*-**B**-**L7** (only showing aromatic region).

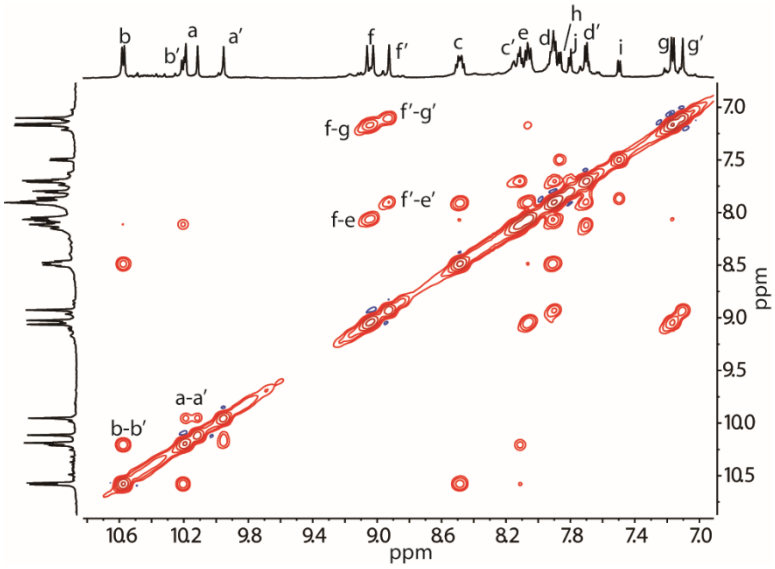

Figure 6.41 ^{1}H-^{1}H NOESY NMR spectrum (600 MHz, CD_3CN) of *R*-*c*-**B**-**L7** (only showing aromatic region).

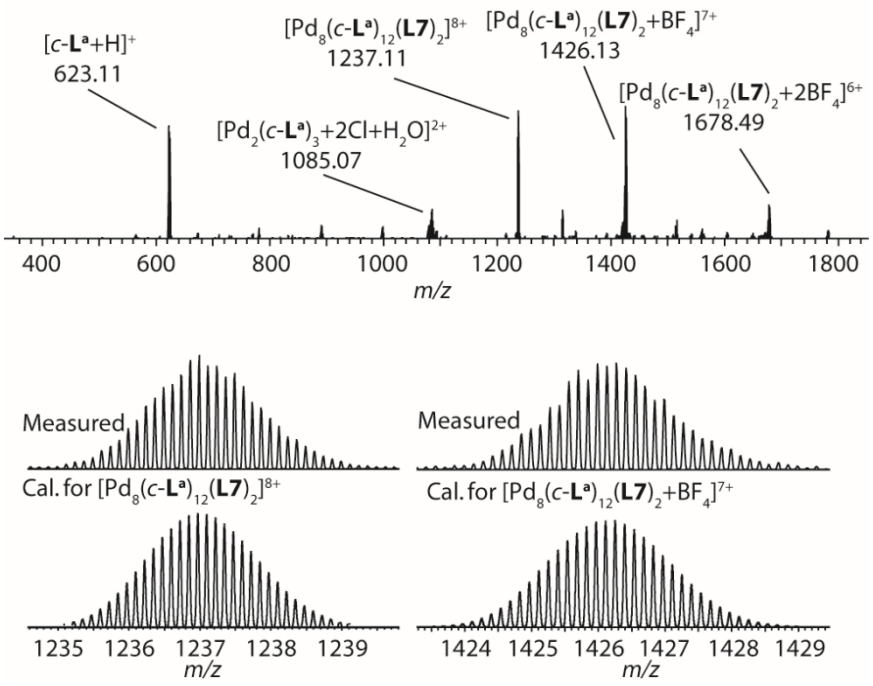

Figure 6.42 ESI-MS spectrum of *c*-**B**-**L7**.

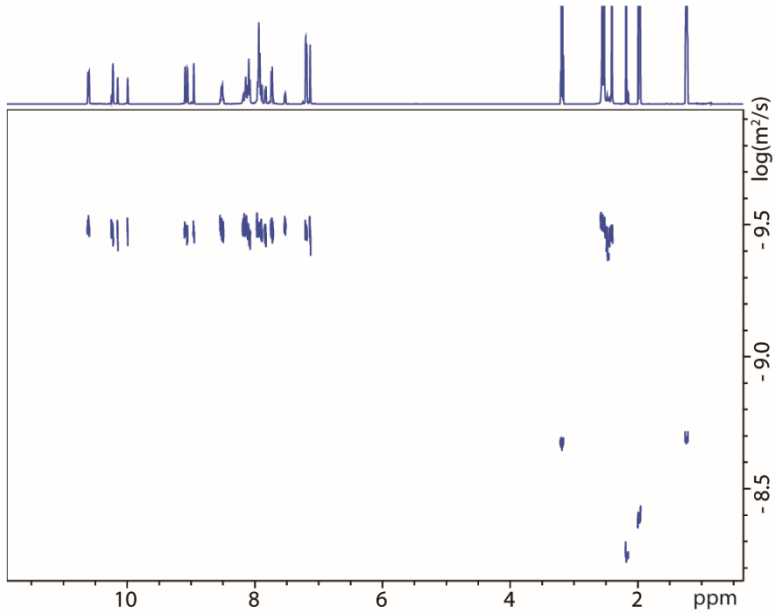

Figure 6.43 DOSY NMR spectrum (600 MHz, CD_3CN) of *R*-*c*-**B**-**L7**.

*6.6.2.2.8 Synthesis of c-**B**-**L8***

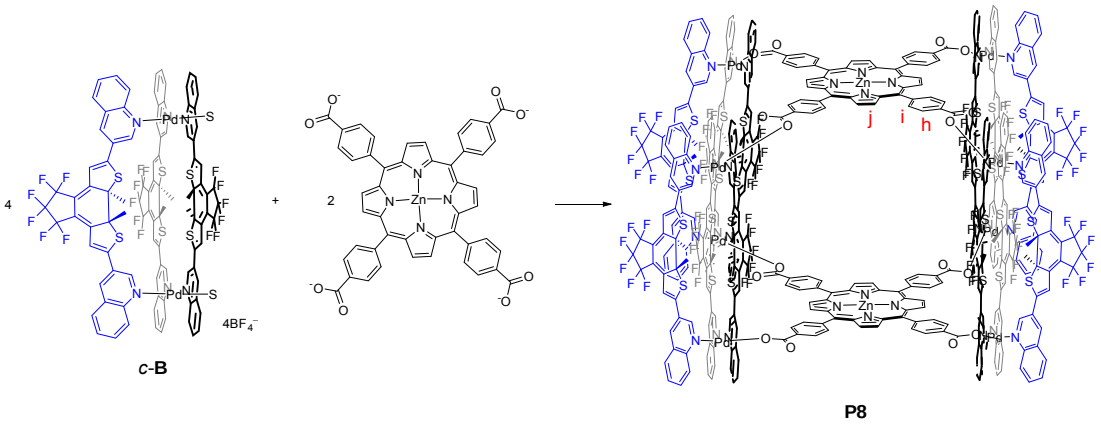

Scheme 5.9 Synthesis of *c*-**B**-**L8**.

c-**B**-**L8** was synthesized as the same procedure as *c*-**B**-**L1**. Titrate 0.5 eq. of **L8** (10 mM, 37.5 μL, d_6-DMSO, excess amount of trimethylamine neutralized) to a *c*-**B** solution (1.5 mM, 500 μL, CD_3CN) at room temperature. For better analysis, only one enantiomer pure (*R*-*c*-**B**-**L8**, which was synthesized from enantiomer pure *R*-*c*-**B**) NMR spectra here are given. ^{1}H NMR (600 MHz, CD_3CN) δ 10.61 (s, 16H), 10.38 (s, 8H), 10.30 (s, 8H), 10.24 (d, *J* = 8.9 Hz, 8H), 10.21 (s, 8H), 9.11 (d, *J* = 16.8 Hz, 16H), 8.99 (s, 8H), 8.49 (d, *J* = 8.4 Hz, 16H), 8.17 – 8.01 (m, 24H), 7.89 (d, *J* = 8.4 Hz, 24H), 7.80 (s, 16H), 7.72 (d, *J* = 7.6 Hz, 16H), 7.69 (d, *J* = 7.7 Hz, 8H), 7.44 (d, *J* = 8.3 Hz, 16H), 7.21 (d, *J* = 5.8 Hz, 16H), 7.14 (s, 8H), 2.53 (s, 24H), 2.36 (s, 24H), 2.22 (s, 24H). ESI-HRMS calculated for $[Pd_8Zn_2C_{492}H_{288}F_{72}N_{32}S_{24}O_{16}]^{8+}$ $\{[Pd_2(c\text{-}\mathbf{L}^{\mathbf{a}})_3]_4(\mathbf{L8})_2\}^{8+}$ *m/z* = 1252.9488, found *m/z* = 1252.9453.

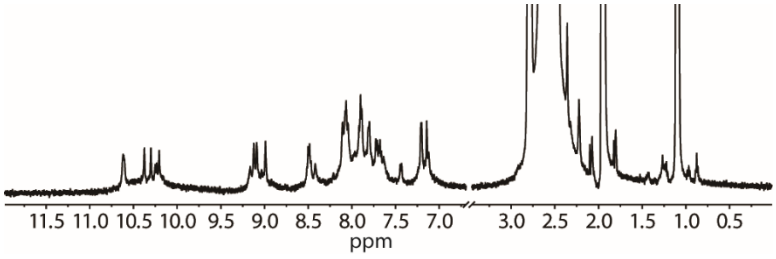

Figure 6.44 ^{1}H NMR spectrum (600 MHz, CD_3CN) of *R*-*c*-**B**-**L8**.

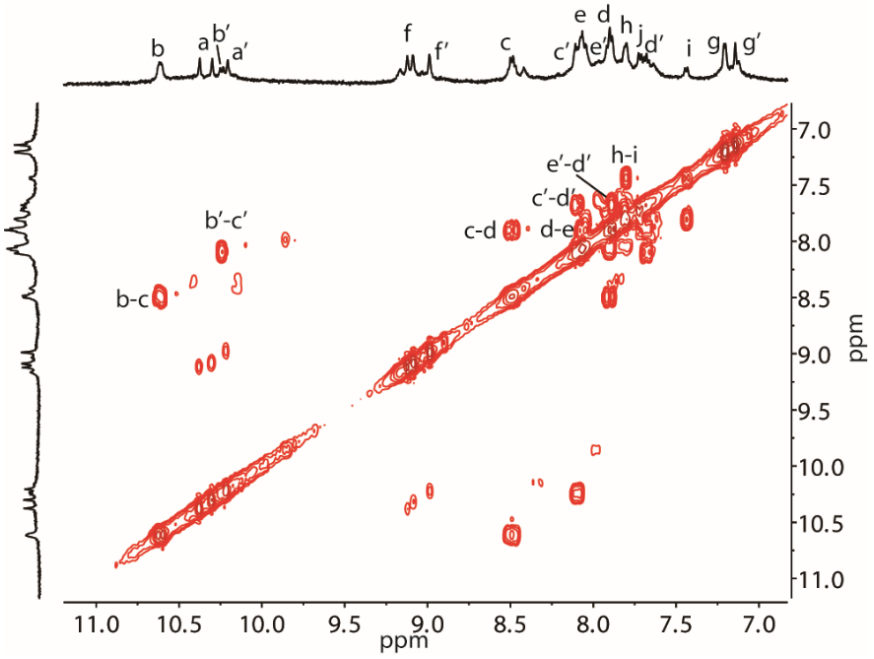

Figure 6.45 ^{1}H-^{1}H COSY NMR spectrum (600 MHz, CD_3CN) of *R*-*c*-**B**-**L8** (only showing aromatic region).

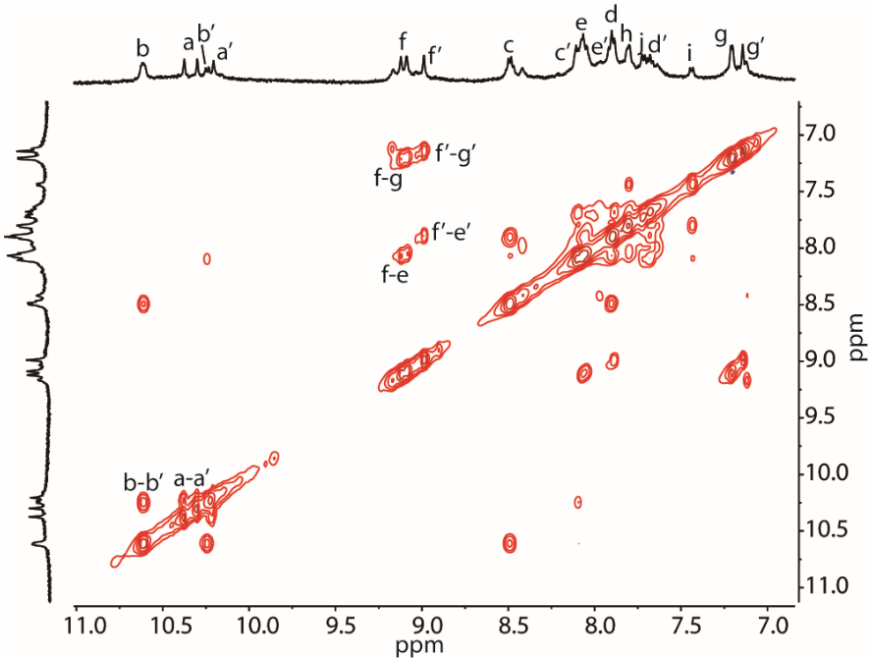

Figure 6.46 ^{1}H-^{1}H NOESY NMR spectrum (600 MHz, CD_3CN) of *R*-*c*-**B**-**L8** (only showing aromatic region).

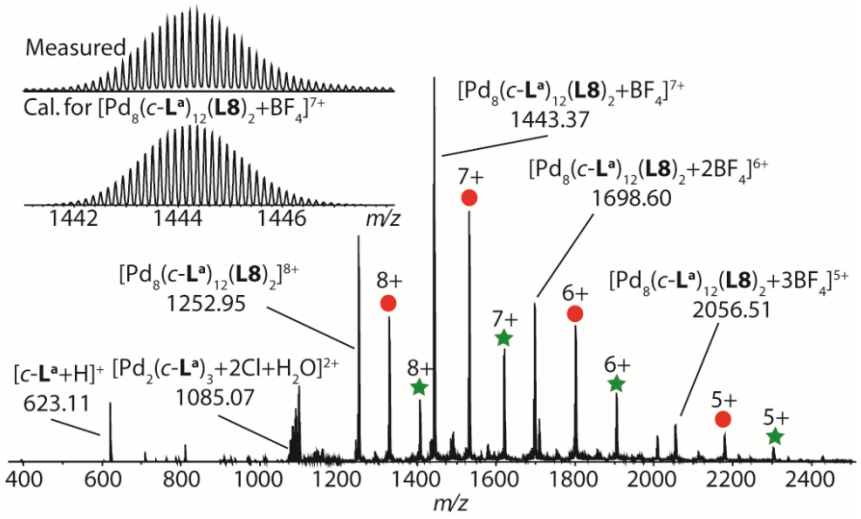

Figure 6.47 ESI-MS spectrum of *c*-**B**-**L8** (●: $[Pd_8(c\text{-}L^a)_{13}(L8)_2{+}nBF_4]^{8-n}$; ★: $[Pd_8(c\text{-}L^a)_{14}(L8)_2{+}nBF_4]^{8-n}$; n = 0, 1, 2, 3).

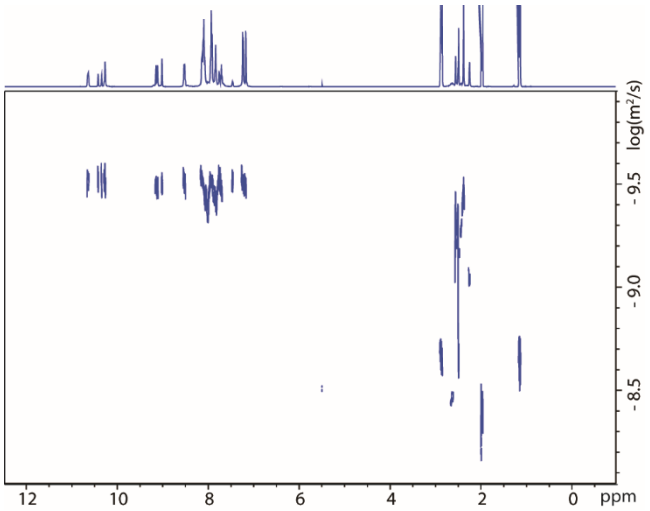

Figure 6.48 DOSY NMR spectrum (600 MHz, CD_3CN) of *R*-*c*-**B**-**L8**.

6.6.3 Photo-Switching

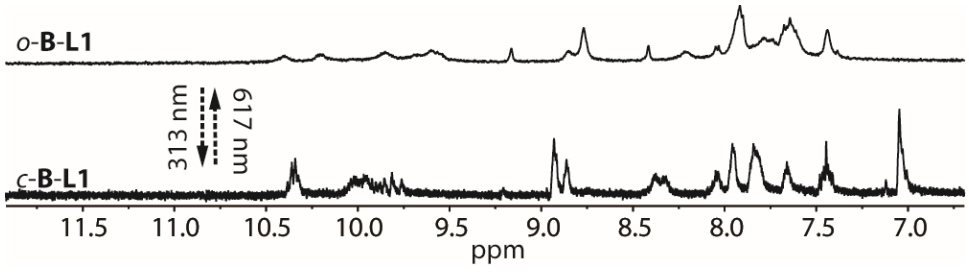

Figure 6.49 ^1H NMR spectrum (500 MHz, CD_3CN) of *c*-**B**-**L1** and *o*-**B**-**L1** showing the reversible interconversion under UV (313 nm) and visible (617 nm) light.

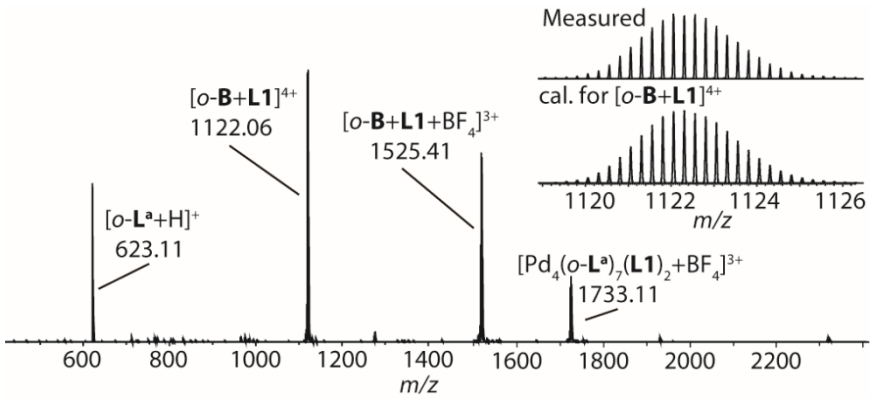

Figure 6.50 ESI-MS spectrum of *o*-**B**-**L1**.

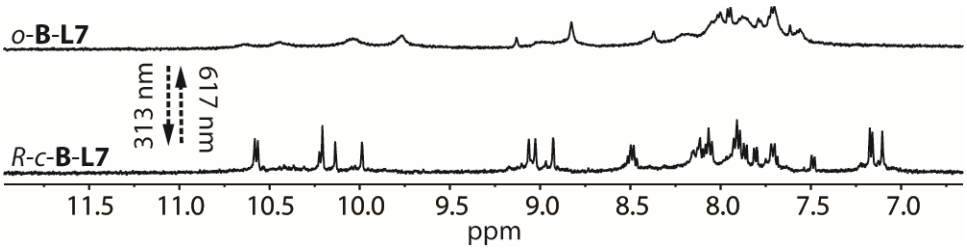

Figure 6.51 ^{1}H NMR spectrum (500 MHz, CD_3CN) of *R*-*c*-**B**-**L7** and *o*-**B**-**L7** showing the reversible interconversion under UV (313 nm) and visible (617 nm) light.

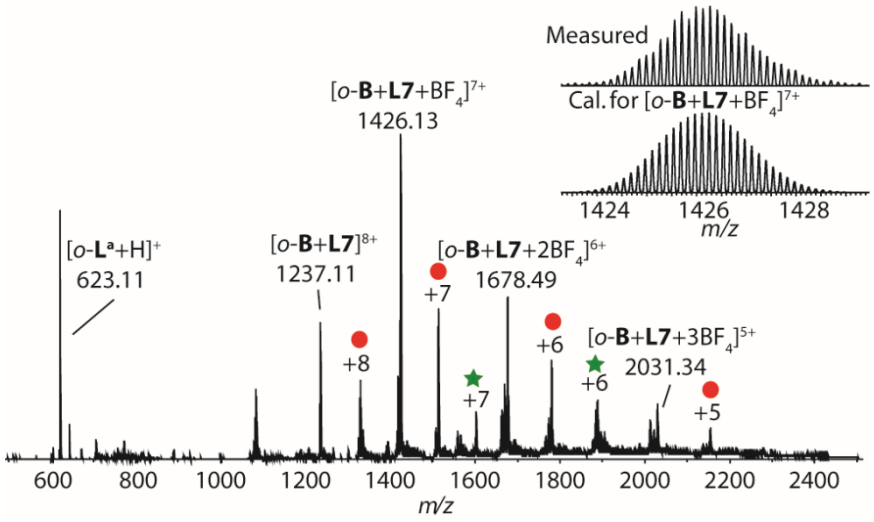

Figure 6.52 ESI-MS spectrum of *o*-**B**-**L7** (●: $[Pd_8(o\text{-}L^a)_{13}(L7)_2{+}nBF_4]^{8-n}$; ★: $[Pd_8(o\text{-}L^a)_{14}(L7)_2{+}nBF_4]^{8-n}$; n = 0, 1, 2, 3).

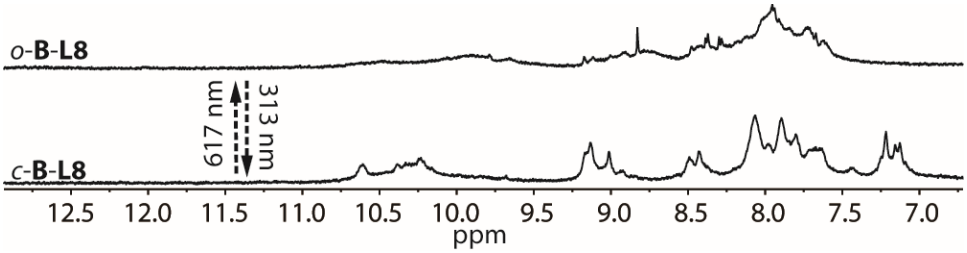

Figure 6.53 ^{1}H NMR spectrum (500 MHz, CD_3CN) of *c*-**B**-**L8** and *o*-**B**-**L8** showing the reversible interconversion under UV (313 nm) and visible (617 nm) light.

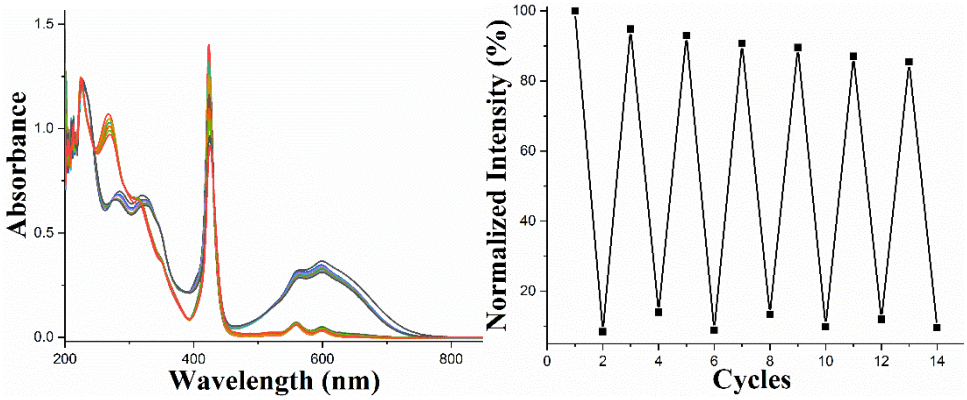

Figure 6.54 The reversibility of photoswitching between *c*-**B**-**L8** and *o*-**B**-**L8** (0.025 mM) as monitored by UV-vis spectroscopy at 600 nm.

6.6.4 Singlet oxygen generation

Singlet oxygen generation at 420 nm was performed by placing a quartz cuvette 65 cm in front a power LED irradiation apparatus (3x 1.4 W 617 nm Power LED, 25 nm FWHM) from Sahlmann photonics, Kiel, followed by monitoring the intensity at 410 nm via UV-vis spectroscopy.

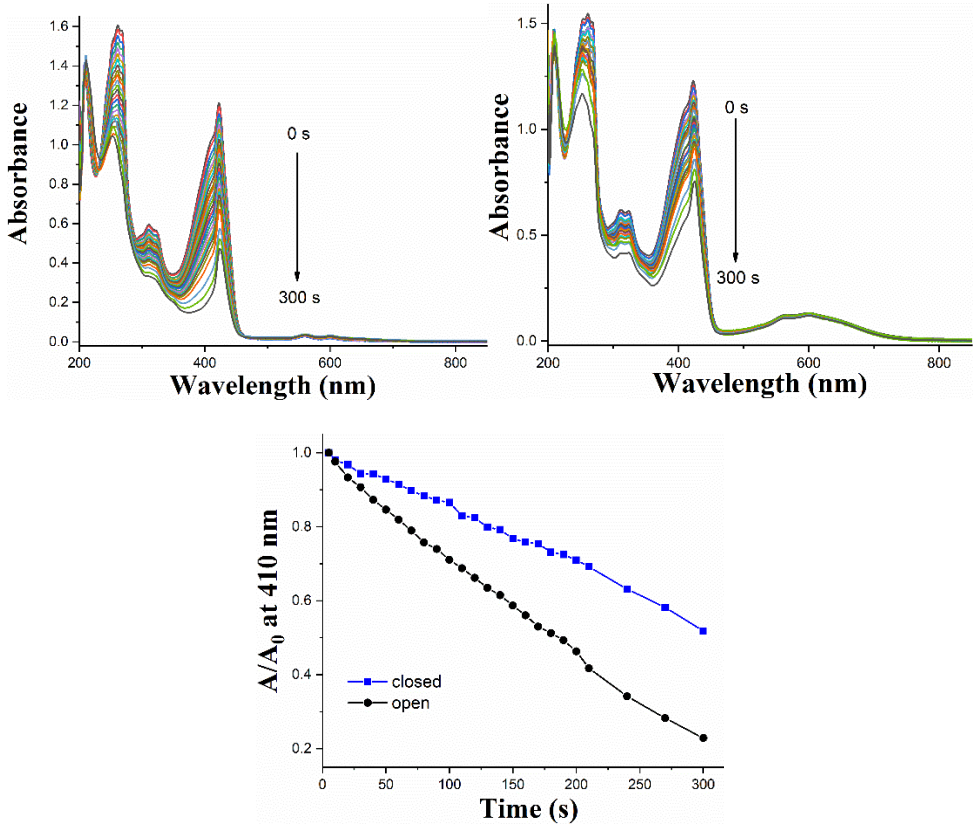

Figure 6.55 UV-vis spectra monitoring the decay rate of DPBF at 410 nm for *c*-**B**-**L8** and *o*-**B**-**L8**.

6.7 References

[1] R. D. Scurlock, B. Wang, P. R. Ogilby, J. R. Sheats, R. L. Clough, *J. Am. Chem. Soc.* **1995**, *117*, 10194-10202.

[2] (a) E. L. Clennan, A. Pace, *Tetrahedron* **2005**, *61*, 6665-6691; (b) M. Prein, W. Adam, *Angew. Chem. Int. Ed.* **1996**, *35*, 477-494.

[3] (a) A. P. Castano, P. Mroz, M. R. Hamblin, *Nat. Rev. Cancer* **2006**, *6*, 535-545; (b) M. C. DeRosa, R. J. Crutchley, *Coord. Chem. Rev.* **2002**, *233-234*, 351-371.

[4] J. Park, D. Feng, S. Yuan, H. C. Zhou, *Angew. Chem. Int. Ed.* **2015**, *54*, 430-435.

[5] L. Hou, X. Zhang, T. C. Pijper, W. R. Browne, B. L. Feringa, *J. Am. Chem. Soc.* **2014**, *136*, 910-913.

[6] (a) S. J. Dalgarno, N. P. Power, J. L. Atwood, *Coord. Chem. Rev.* **2008**, *252*, 825-841; (b) M. Han, D. M. Engelhard, G. H. Clever, *Chem. Soc. Rev.* **2014**, *43*, 1848-1860; (c) R. Chakrabarty, P. S. Mukherjee, P. J. Stang, *Chem. Rev.* **2011**, *111*, 6810-6918; (d) S. R. Seidel, P. J. Stang, *Acc. Chem. Res.* **2002**, *35*, 972-983; (e) M. Fujita, M. Tominaga, A. Hori, B. Therrien, *Acc. Chem. Res.* **2005**, *38*, 369-378.

[7] (a) Y. Ye, T. R. Cook, S. P. Wang, J. Wu, S. Li, P. J. Stang, *J. Am. Chem. Soc.* **2015**, *137*, 11896-11899; (b) X. Chang, Z. Zhou, C. Shang, G. Wang, Z. Wang, Y. Qi, Z. Y. Li, H. Wang, L. Cao, X. Li, Y. Fang, P. J. Stang, *J. Am. Chem. Soc.* **2019**; (c) N. C. Gianneschi, M. S. Masar, C. A. Mirkin, *Acc. Chem. Res.* **2005**, *38*, 825-837; (d) Y. K. Kryschenko, S. R. Seidel, A. M. Arif, P. J. Stang, *J. Am. Chem. Soc.* **2003**, *125*, 5193-5198.

[8] (a) D. Fujita, Y. Ueda, S. Sato, N. Mizuno, T. Kumasaka, M. Fujita, *Nature* **2016**, *540*, 563-566; (b) Q.-F. Sun, J. Iwasa, D. Ogawa, Y. Ishido, S. Sato, T. Ozeki, Y. Sei, K. Yamaguchi, M. Fujita, *Science* **2010**, *328*, 1144.

[9] (a) J. E. M. Lewis, E. L. Gavey, S. A. Cameron, J. D. Crowley, *Chem. Sci.* **2012**, *3*, 778-784; (b) S. M. Jansze, G. Cecot, K. Severin, *Chem. Sci.* **2018**, *9*, 4253-4257; (c) D. Fiedler, D. H. Leung, R. G. Bergman, K. N. Raymond, *Acc. Chem. Res.* **2005**, *38*, 349-358; (d) M. D. Pluth, R. G. Bergman, K. N. Raymond, *Acc. Chem. Res.* **2009**, *42*, 1650-1659; (e) D. Zhang, T. K. Ronson, J. R. Nitschke, *Acc. Chem. Res.* **2018**, *51*, 2423-2436.

[10] (a) C. Garcia-Simon, M. Costas, X. Ribas, *Chem. Soc. Rev.* **2016**, *45*, 40-62; (b) C. Colomban, C. Fuertes-Espinosa, S. Goeb, M. Salle, M. Costas, L. Blancafort, X. Ribas, *Chem. Eur. J.* **2018**, *24*, 4371-4381; (c) C. Garcia-Simon, M. Garcia-Borras, L. Gomez, T. Parella, S. Osuna, J. Juanhuix, I. Imaz, D. Maspoch, M. Costas, X. Ribas, *Nat. Commun.* **2014**, *5*, 5557.

7 Guest-to-Host Chirality Transfer in Photo-Switchable Pd_2L_4 Cages

7.1 Introduction

The propagation of chirality is a central feature both in the biosynthesis of natural products as well as in man-made homogeneous catalysis and recent developments in polymer sciences.[1] Besides the direct influence of covalently bound chiral substructures or auxiliaries, the transfer of stereochemical information through non-covalent contacts is a major pathway.[2]

In supramolecular chemistry, chirality has been introduced into self-assembled cavities via chiral backbones, metal centers, covalently bound moieties and emerging from topological effects.[3] In certain cases, systems were even found to keep a stereochemical memory after the chiral building block has been replaced.[4] Also non-covalent implementation of chiral information has been realized over the past decades, including the template-directed formation of dissymmetric, hydrogen-bonded capsules reported by Rebek[5] and the complete resolution of chiral M_4L_6 tetrahedra assembled in the presence of a chiral guest as shown by Raymond *et. al.* (Figure 7.1).[6]

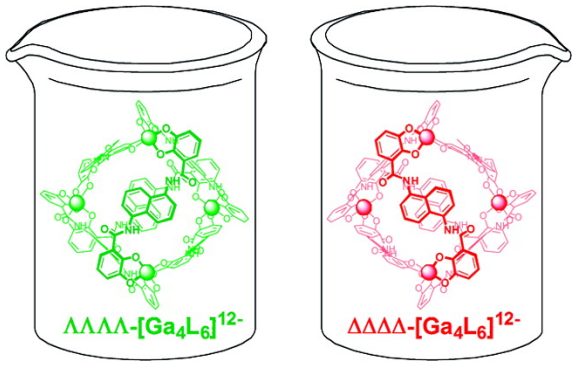

Figure 7.1 Resolution of Chiral, Tetrahedral M_4L_6 Metal-Ligand Hosts. Copyright © 2007 American Chemical Society.

Recently, intrinsically chiral DTE chromophores[7] were recognized to be attractive reporter groups for the quantification of non-covalent chirality transfer.[8] For example, van Esch and Feringa used DTE-based gels to demonstrate optical transcription of supramolecular into molecule chirality.[9] Andréasson achieved non-covalent binding of cationic DTE derivatives to DNA, followed by enantioselective photoswitching.[10]

In this chapter, we demonstrate that chiral guest-to-host induction can be achieved within the framework of a lantern-shaped [Pd_2**L**$_4$] coordination cage,[11,12] being a new member of our recently introduced family of photochromic DTE cages[13] with a stimuli-responsive host-guest chemistry.[14,15] In contrast to previously reported host-guest systems showing

chirality-transfer, chiral guests are not required as templates for cage formation, thus allowing a comparative study of hosts in presence and absence of guests. The post-assembly chiral induction using homochiral *R*-CSA and *S*-CSA was found to proceed under amplification of chiral information. A combination of CD results, DFT-calculated Cotton effects and chiral HPLC allowed us to relate the absolute configurations of guest and host and calculate the enantiomeric excess of isolated closed DTE backbones as a function of temperature during the photochemical fixation process. Resulting values, together with DOSY NMR and trapped ion mobility mass spectrometry reveal that the first photoisomerization event triggers guest release in this system (Figure 7.2).

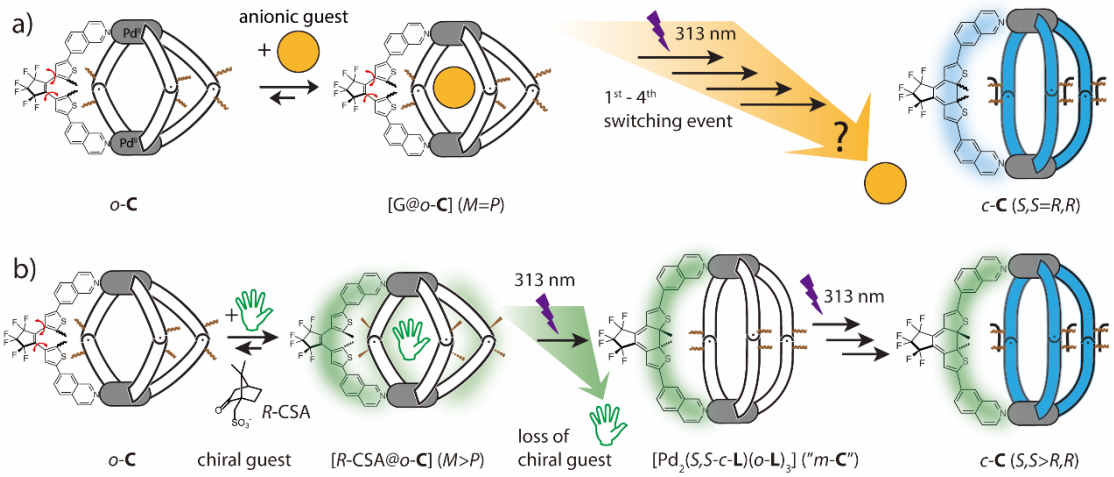

Figure 7.2 a) Open cage *o*-**C**^{b} based on four DTE photoswitches, is able to bind anionic guests and can be transformed into a diastereomeric mixture of closed cages *c*-**C**^{b} by irradiation with UV light (313 nm; back reaction at 617 nm).[15a] This leads to excretion of the encapsulated guest molecule, but it was previously not known when this occurs during the step-wise photoconversion. b) Encapsulation of a chiral guest (*R*-CSA, *S*-CSA or *S*-CSA-Br) into *o*-**C**^{b} induces *P* or *M* helical chirality of the DTE chromophores. Irradiation at 313 nm locks the induced chirality onto the structure of the first cyclized ligand, followed by a change of overall cage shape and ejection of the guest. The remaining three ligands are then photoswitched to give cage *c*-**C**^{b} without further induced stereoselectivity. Copyright © 2019 American Chemical Society.

7.2 Photo-isomer cages assembly

Following our previously protocols in Chapter 2, ligand *o*-**L**^{b} was synthesized by a Suzuki cross-coupling reaction of perfluoro-1,2-bis(2-iodo-5-methylthien-4-yl)cyclopentene and 2 eq. of isoquinolin-7-yl-boronic acid. By combining a 2 : 1 mixture of *o*-**L**^{b} with $[Pd(CH_3CN)_4](BF_4)_2$ in CD_3CN at 70 °C for 3 h, the light yellow cage $[Pd_2(o\text{-}\mathbf{L}^{b})_4](BF_4)_4$ (*o*-**C**^{b}) was formed quantitatively, as confirmed by ^{1}H NMR spectroscopy, high-resolution ESI mass spectrometry (Figure 7.3) as well as single crystal X-ray diffraction analysis (Figure 7.4a). Upon conversion of ligand into cage, the ^{1}H NMR signals of the isoquinolines, in particular protons H_a ($\Delta\delta$ = 0.56 ppm) and H_b ($\Delta\delta$ = 0.20 ppm), sitting close to the coordinating nitrogen atoms, undergo significant downfield shifts (Figure 7.3a). The ESI mass spectrum displayed a series of species supporting the expected

composition with a variable number of BF_4^- counter ions ([*o*-**C^b**]$^{4+}$, [*o*-**C^b**+BF_4]$^{3+}$ and [*o*-**C^b**+2BF_4]$^{2+}$). In all cases, experimental isotope patterns were found to be in very good agreement with the calculated distributions (Figure 7.3b).

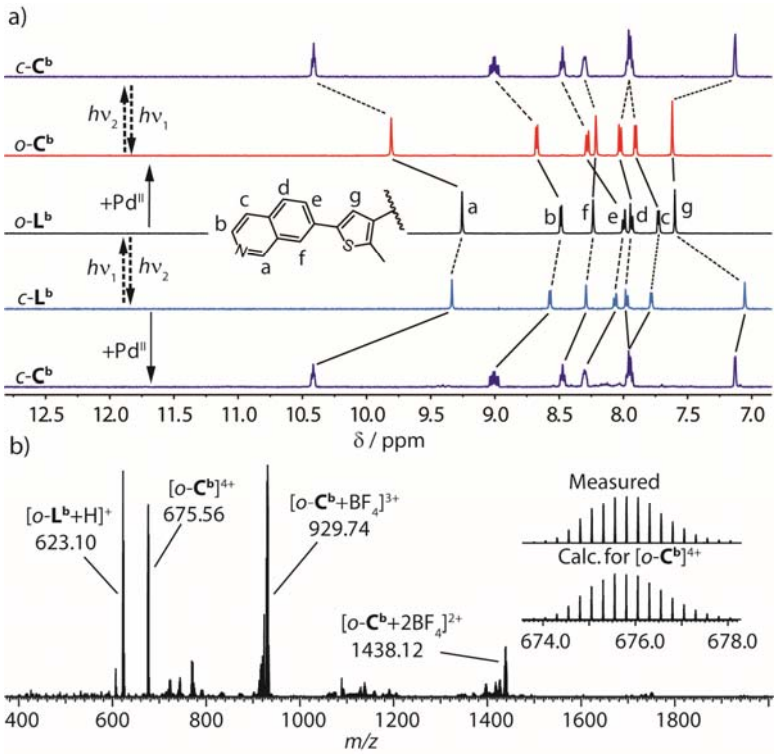

Figure 7.3 a) ^{1}H NMR spectra (500 MHz, CD_3CN, 298 K) of ligands *o*-**L^b**, *c*-**L^b** and cages *o*-**C^b**, *c*-**C^b**; b) ESI-MS spectrum of *o*-**C^b** with isotope pattern of [*o*-**C^b**]$^{4+}$ shown in the inset. Copyright © 2019 American Chemical Society.

The structure of cage *o*-**C^b**, possessing all four DTE switches in their open photoisomeric form, was finally proven by X-ray analysis. Therefore, single crystals were obtained by slow vapor diffusion of ethyl ether into an acetonitrile solution of *o*-**C^b** (Figure 7.4a). Cage *o*-**C^b** crystallized with low crystallographic symmetry in the triclinic space group *P-1* and features a *cis-PPMM* arrangement of both helical conformers (*M* and *P*) of the DTE backbone within each single cage. As a result, the molecule structure has a mirror plane (containing the Pd_2 axis with Pd–Pd distance = 15.06 Å), leading to a *meso*-arrangement with C_{2h}-symmetry. It has to be noted, however, that in ambient tempered solution, we expect the system to exist as an inseparable and rapidly interconverting mixture of all possible diastereomers, as indicated by the observation of strikingly sharp signals in the ^{1}H NMR spectrum of *o*-**C^b** (in full accordance with a related DTE cage derivative).[13a]

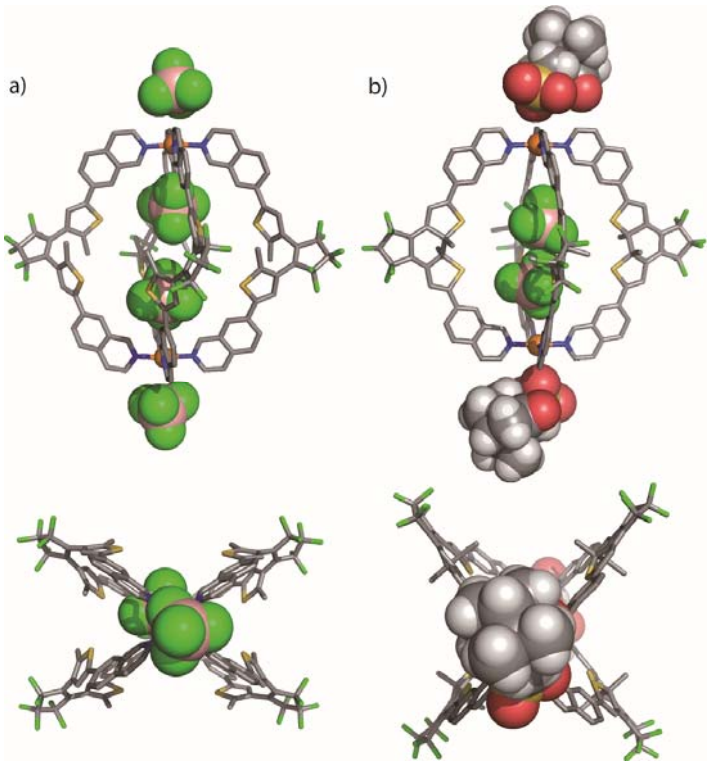

Figure 7.4 X-ray structures of a) cage *o*-**C^{b}** and b) *c*-**C^{b}** co-crystallized with *R*-CSA (side and top view) showing counter anions/guests inside and outside the cavities. All hydrogen atoms, solvent molecules, and minor disordered components have been omitted (details see Experimental section). In *c*-**C^{b}**, all backbone methyl groups are disordered over both possible positions with approximately 50% occupancy (here only one diastereomer is shown; B pink, C gray, N blue, O red, F green, S yellow, Pd orange). Copyright © 2019 American Chemical Society.

7.3 Photoswitching

Ligand **L^{b}** can be reversibly interconverted between its open and photoisomeric closed-form by irradiation with UV light (313 nm) and longer wavelength light (617 nm), respectively. Closed-form cage $[Pd_2(c\text{-}\mathbf{L^b})_4](BF_4)_4$ (*c*-**C^{b}**) could be obtained from self-assembly of *c*-**L^{b}** and Pd^{II} or directly from open-form cage *o*-**C^{b}** by irradiating a CD_3CN solution of the latter compound under 313 nm UV light (Figure 7.3a). Unlike conformationally flexible ligand *o*-**L^{b}**, closed-form isomer *c*-**L^{b}** comes in two separable enantiomers. As a result, a maximum of 6 possible cage stereoisomers of *c*-**C^{b}** can form from a racemic mixture of ligand *c*-**L^{b}**.[13a] Indeed, both the ^{1}H NMR (Figure 7.3) and ^{13}C NMR spectra (Figure 7.5) show a splitting and broadening for all proton and carbon NMR signals due to the diversity of the contained diastereomers. Under strict exclusion of light, we were able to obtain a crystal of cage *c*-**C^{b}** suitable for X-ray structure determination (formed in the course of a ^{1}H NMR titration with *S*-CSA). As observed for *o*-**C^{b}**, cage *c*-**C^{b}** was found to crystallize in the triclinic space group *P1*, however, showing a slightly shorter Pd···Pd distance of 14.67 Å (Figure 7.4b). Most strikingly, the cage co-

crystallized with an *R*-CSA guest molecule situated outside the cage's cavity, in full agreement with the solution results concerning guest binding (Figure 7.4b, below).

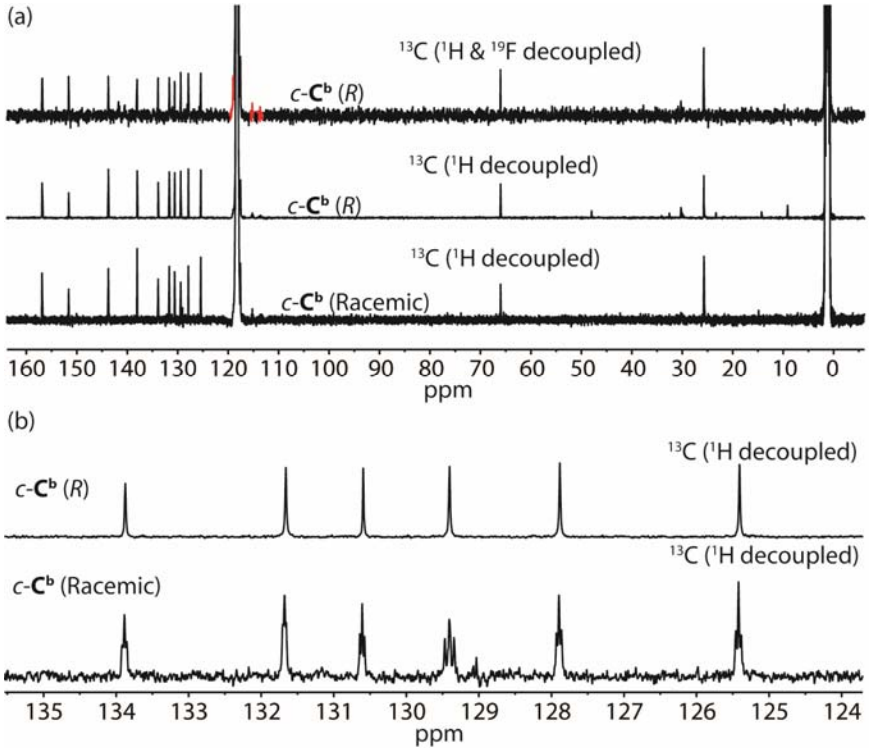

Figure 7.5 a) Full and b) part of expanded ^{13}C NMR spectra (CD_3CN, 298 K) of ***c*-C^{b}** (signals of perfluorocyclopentene ring could be detected in ^{19}F- & ^{1}H-decoupled ^{13}C spectra, marked in red). Copyright © 2019 American Chemical Society.

7.4 Guest Binding and Chiral Induction

With both open and closed cages in hand, we set out to test whether encapsulation of chiral guests can induce a transfer of chiral information onto the surrounding cage structure. Via ^{1}H NMR titration experiments, we first checked both cage photoisomers for encapsulation of the anionic *R*-CSA *or S*-CSA, respectively. Upon stepwise addition of *R*-CSA into a solution of ***o*-C^{b}**, the ^{1}H NMR signal of inward pointing proton H_a was found to broaden and gradually shift downfield until about 1.0 eq. of *R*-CSA had been added. The signal of outward pointing proton H_b, however, did not show any significant shift in this concentration range but started to move after more than 1.0 eq. of guest had been added, thereby indicating encapsulation of one equivalent of chiral guest followed by external association after saturation of the cage interior (Figure 7.6a). Since titration beyond 1.0 equivalent was accompanied by the onset of aggregation (solution turning turbid and formation of precipitates), we were not able to determine binding constants. In contrast, the titration of closed cage ***c*-C^{b}** with *R*-CSA only resulted in shifting of outward pointing proton H_b. Inward-pointing signal H_a, however, was observed to undergo almost no shifting but broadening, indicative of external association instead of

uptake inside the cavity (Figure 7.6a). This assumption was also backed by the obtained X-ray structure, showing co-crystallized guest exclusively outside the cage; (Figure 7.4b). In addition, ion mobility mass spectrometry experiments further confirmed the external interaction of CSA with *c*-**C^{b}** (Figure 7.9).

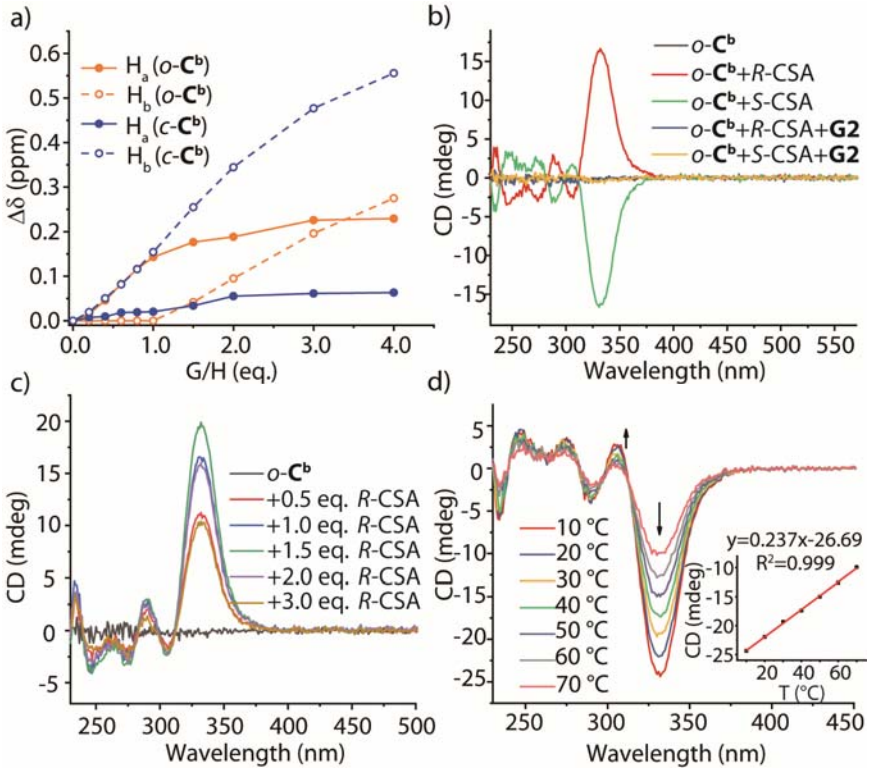

Figure 7.6 a) ^{1}H NMR titration plot of *o*-**C^{b}** and *c*-**C^{b}** (1.0 mM, CD_3CN) with *R*-CSA (15 mM, CD_3CN) showing the relative signal shifts of inward pointing proton H_a and outward pointing proton H_b; b) CD spectra of *o*-**C^{b}** (0.05 mM, CH_3CN) with and without 1.0 eq. *R*-CSA or *S*-CSA, and after addition 1.0 eq. of competitor **G2** (as NBu_4 salts in CD_3CN, 15 mM); c) CD spectra of *o*-**C^{b}** with increasing amounts of *R*-CSA; d) CD spectra of *o*-**C^{b}** (0.05 mM, CH_3CN) with 1.5 eq. *S*-CSA between 10 °C and 70 °C and CD_{330nm} over T plot showing a linear relationship (inset). Copyright © 2019 American Chemical Society.

Next, CD spectra were measured to examine the degree of chirality transfer. As expected, no CD signal was detected for open-form cage *o*-**C^{b}**. Addition 1.0 eq. of *R*- or *S*-CSA, however, lead to the occurrence of strong Cotton effects assigned to the ligand chromophore, indicative of a transfer of chiral information from guest to host (Figure 7.6b). Interestingly, this effect could be reversed by addition of 1.0 eq. of the non-chiral guest benzene-1,4-disulfonate (**G2**) which binds stronger inside the cavity and is able to completely replace monoanionic camphor sulfonate (Figure 7.6b). The latter was further confirmed by a ^{1}H NMR experiment (Figure 7.46). Variation of relative guest concentration between 0 and 3.0 eq. reveals that the CD signals pass through a maximum around 1.5 eq. with larger guest amounts leading to aggregation effects that reduce the signal intensity (Figure 7.6c). We further monitored the CD signal intensity of *o*-**C^{b}** containing 1.5 eq. *S*-CSA as a function of temperature, revealing that increasing

temperature leads to decreasing ellipticity, most probably caused by a decreased binding affinity at higher temperatures (Figure 7.6d).

7.5 Enantiomeric Excess Determination

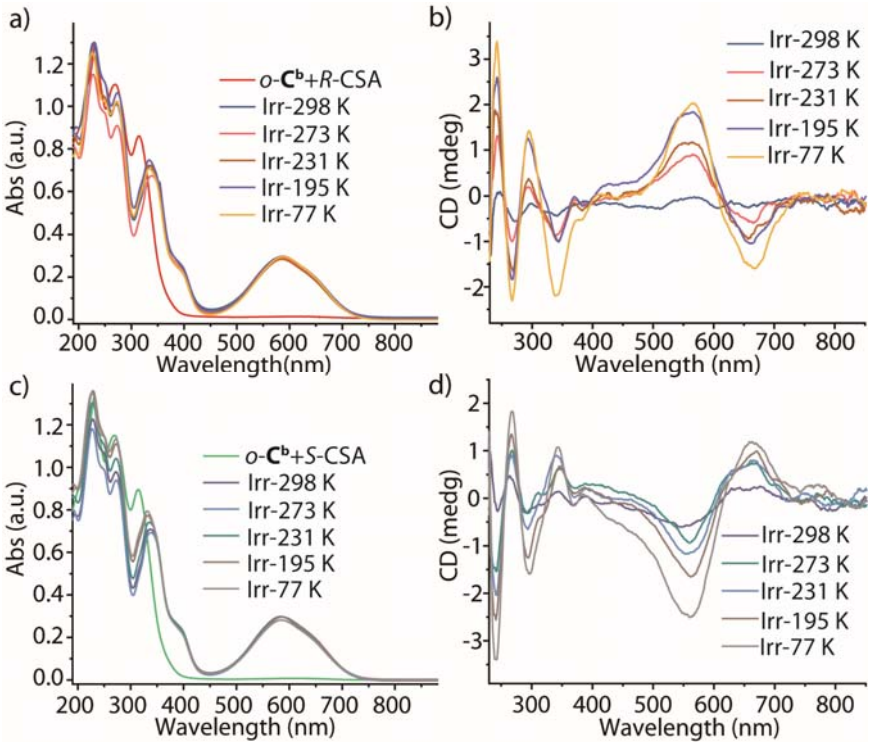

Figure 7.7 a) & c) UV-vis and b) & d) CD spectra of *o*-**C^{b}** (0.05 mM, CH_3CN) containing 1.5 eq. *R*-CSA or *S*-CSA, respectively, after irradiation with 313 nm light at temperatures from 298 K to 77 K (irradiation interval until complete conversion). Copyright © 2019 American Chemical Society.

Subsequently, we examined whether the induced chirality of the open-form host-guest complexes [*R*-CSA@*o*-**C^{b}**] and [*S*-CSA@*o*-**C^{b}**] can be locked within the cage's DTE backbones upon irradiation with 313 nm light. First, we irradiated a CD_3CN solution of cage *o*-**C^{b}** containing 1.5 eq. of *R*-CSA or *S*-CSA at room temperature. The colorless [*R/S*-CSA@*o*-**C^{b}**] solution turned deep blue and a new UV absorption band was observed around 585 nm (Figure 7.7a & c). Completion of the photoreaction was monitored by ^{1}H NMR spectroscopy. The CD spectra showed a negative Cotton effect corresponding to the closed-form DTE chromophore for the sample containing *R*-CSA and a positive for *S*-CSA, albeit of low intensity (Figure 7.7b & d). We explain this observation with a photochemical fixation of an enantiomeric excess in the configurationally stable closed-form DTE isomers, induced by the presence of the chiral guest. Since we observed that the degree of chiral transfer within [*R/S*-CSA@*o*-**C^{b}**] apparently increases with decreasing temperature (Figure 7.6d), we tested the same procedure at several lower temperatures down to 77 K. Therefore, a quartz NMR tube containing the acetonitrile solution of [*R/S*-CSA@*o*-**C^{b}**] was immersed in different cooling

baths in a transparent quartz Dewar and irradiated with 313 nm light until full conversion of the photoreaction was achieved. Interestingly, the final ^{1}H NMR spectra of the fully photoisomerized cages revealed that the proton signals became sharper as the bath temperature decreased, indicating a reduction of the number of major diastereomeric components (Figure 7.49). In addition, the CD spectra showed increasing signal intensities with decreasing bath temperatures, indicating enrichment of one ligand enantiomer over the other (Figure 7.7b & d). We then disassembled the closed-form cages by adding aqueous NBu_4OH and EDTA, followed by extraction with DCM under strict exclusion of light. The solution containing enriched ligands *R*, *R*-*c*-**L^b** and *S*, *S*-*c*-**L^b** was examined for enantiomeric excess (*ee*) by chiral HPLC. Table 6.1 summarizes the results, showing that the enrichment improves at lower temperatures. Intriguingly, the maximum obtained *ee* values were around 25 % for both guest enantiomers, thus indicating that the encapsulated guest transmits its chiral information onto one out of the four ligands.

Table 6.1 Enantiomeric excess (*ee*) of ligands *S*, *S*-*c*-**L^b** and *R*, *R*-*c*-**L^b** after irradiation of [*R/S*-CSA@o-**C^b**] with 313 nm light at various temperatures (*R*-CSA induces enrichment of *S*, *S*-*c*-**L^b**).

ee (%)[a]	298 K	273 K[b]	231 K[c]	195 K[d]	77 K[e]
R-CSA	7	8	13	21	28
S-CSA	10	13	14	24	31

[a] values determined by HPLC (monitored at 600 nm, estimated error ±5%, see SI) with a Chiralpak IA column; [b] ice-water; [c] dry ice-acetonitrile; [d] dry ice-acetone; [e] liquid nitrogen.

7.6 Evaluation of Guest Ejection Mechanism

Based on these observations, we assumed that the guest is ejected from the host early on, *i.e*. after the first DTE switch has been closed, during the stepwise ligand isomerization sequence (Figure 1b). Following this hypothesis, photoisomerization of the first ligand in *o*-**C^b** already results in a significant change of the structure and dynamics of the resulting cage $[Pd_2(o\text{-}\mathbf{L^b})_3(c\text{-}\mathbf{L^b})_1](BF_4)_4$ (="*m*-**C^b**"), bringing it close in shape to the fully switched isomer *c*-**C^b**. Likewise to *c*-**C^b**, partially switched $[Pd_2(o\text{-}\mathbf{L^b})_3(c\text{-}\mathbf{L^b})_1](BF_4)_4$ would then be an inapt host for the CSA guest, leading to its ejection. Consequently, assuming a potent chirality transfer at the lowest studied temperatures, the guest's stereochemical information remains only locked within the first switched DTE ligand while the other three ligands are then unselectively photoisomerized in absence of the chiral guest inside the cavity.

To test this hypothesis, we prepared cages from a 3:1 mixture of *o*-**L^b** and *c*-**L^b**. ^{1}H NMR and Ion Mobility ESI mass spectra indicate the formation of a mixture of cage isomers

containing the desired [Pd_2(*o*-**L**^{b})$_3$(*c*-**L**^{b})$_1$](BF_4)$_4$] (*m*-**C**^{b}) as dominant species (~42%) for statistical reasons (besides ~32% *o*-**C**^{b}, see Chapter 7.9.12). A first indication supporting that *m*-**C**^{b} closely resembles *c*-**C**^{b} came from a comparison of their DOSY NMR spectra, showing that the hydrodynamic radius of *m*-**C**^{b} is much closer to that of *c*-**C**^{b} than that of *o*-**C**^{b} (Figure 7.68). Furthermore, PM6- and DFT-calculated energy potentials obtained by squeezing *o*-**C**^{b}**,** *m*-**C**^{b} and *c*-**C**^{b} along their Pd-Pd axes indicated a major impact on cage conformational dynamics already induced by one closed ligand (Figure 7.8).

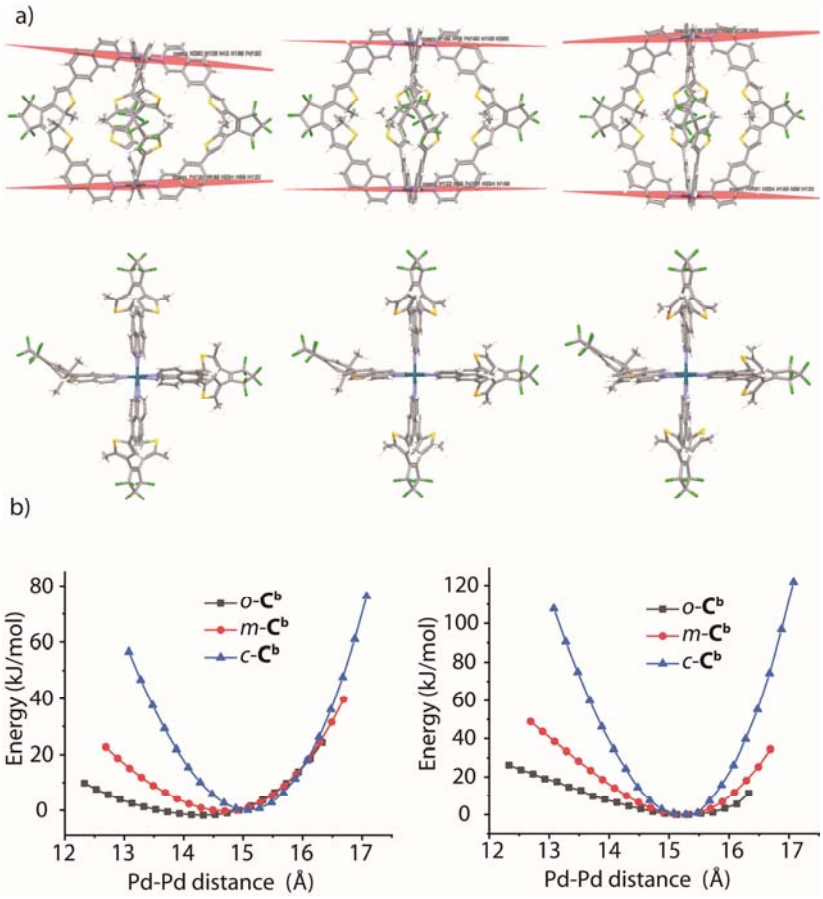

Figure 7.8 a) Side and top views of DFT (B3LYP/LANL2DZ) optimized [Pd_2(*o*-**L**^{b})$_3$(*c*-**L**^{b})] structures under constraining the Pd-Pd distance with shortest examined distance (12.69 Å, left), optimized Pd-Pd distance (15.29 Å, middle) and longest Pd-Pd distance (16.69 Å, right). b) PM6 (left) and DFT (B3LYP/LANL2DZ; right) calculated energies (scaled to a common value at 15 Å) under performing a relaxed scan of the Pd-Pd distance. Results show that the all-open cage o-**C**^{b} can be squeezed most easily (black), while the closure of only one photoswitch in *m*-**C**^{b} (3:1, red) already raises the slope of the energy-over-compression branch of the curve to an extent about half-way through towards the situation when all photoisomeric ligands are in their closed form (blue).

Next, we turned to chiral induction experiments using *m*-**C**^{b}: First, we examined the degree of chiral induction caused by addition of *R/S*-CSA to the mixed *m*-**C**^{b} sample on the *o*-**L**^{b} chromophores, showing that only the fraction of contained *o*-**C**^{b} (~32%) contributes to the characteristic CD signal at 330 nm, while the major species *m*-**C**^{b} does not (Figure 7.70 & Figure 7.71). Second, we irradiated *m*-**C**^{b}(*R/S*) (synthesized with one eq. of enantiomerically pure *R, R*- or *S, S*-c-**L**^{b}) under 313 nm at 231 K and found that

the *ee* value remains around 25% after cage disassembly, showing that interligand chirality transfer does not play any significant role (Figure 7.72 & Table 6.6). Third, irradiation of *m*-**C**$^{\mathbf{b}}$ (with racemic *c*-**L**$^{\mathbf{b}}$) in presence of 1.5 eq. of *R*-CSA or *S*-CSA only gave *ee* values lower than 7.8%, assumed to be caused by the contained share of *o*-**C**$^{\mathbf{b}}$ alone (Table 6.6). All results detailed above agree with our hypothesis that only the first switching ligand effectively experiences the encapsulated guest's chirality, followed by guest ejection and photocyclization of the residual three ligands without stereocontrol.

7.7 Trapped Ion Mobility Mass Spectrometry

As a further orthogonal technique aimed at supporting above stated mechanism, we employed trapped ion mobility spectroscopy (TIMS) coupled to ESI MS to obtain further insights into the structure of the host-guest aggregates (Figure 7.9). Results show that the drift time (correlating with the collisional cross section; see Chapter 7.9.13) of *o*-**C**$^{\mathbf{b}}$ (Figure 7.9a) is shorter than that of *c*-**C**$^{\mathbf{b}}$ (Figure 7.9c) and *m*-**C**$^{\mathbf{b}}$ (Figure 7.9e), while that of *c*-**C**$^{\mathbf{b}}$ and *m*-**C**$^{\mathbf{b}}$ are very close (all in accordance with the DOSY NMR results). After adding 1.5 eq. of *R*- or S-CSA, the mobilogram of *o*-**C**$^{\mathbf{b}}$, shows two extra signals (Figure 7.9b, fragment $[Pd(o\text{-}\mathbf{L})_2]^{2+}$ not counted in), one with shorter drift time (smaller size) and a shoulder with longer drift time (larger size). Both signals correspond to the mass of cage plus CSA, as seen in the mobility-filtered mass spectra. We assign the former signal to the host-guest complex CSA@*o*-**C**$^{\mathbf{b}}$ since encapsulation of the organic guest is expected to lead to a dispersion-driven compaction in the gas phase. In contrast, the signal with longer drift time is most likely attributed to an adduct with externally associated guest (*o*-**C**$^{\mathbf{b}}$+CSA), leading to an overall size increase. When CSA is added to *c*-**C**$^{\mathbf{b}}$, only one signal corresponding to the mass of cage plus CSA is observed, possessing a larger size than *c*-**C**$^{\mathbf{b}}$, thus representing outside adduct *c*-**C**$^{\mathbf{b}}$+CSA (Figure 7.9d), in full accordance with the above described observation that *c*-**C**$^{\mathbf{b}}$ is not able to encapsulate the guest. For *m*-**C**$^{\mathbf{b}}$, similarly to *c*-**C**$^{\mathbf{b}}$, only a slight drift time shift was observed after adding guest (Figure 7.9f), indicating that *m*-**C**$^{\mathbf{b}}$ and *c*-**C**$^{\mathbf{b}}$ are close in size.

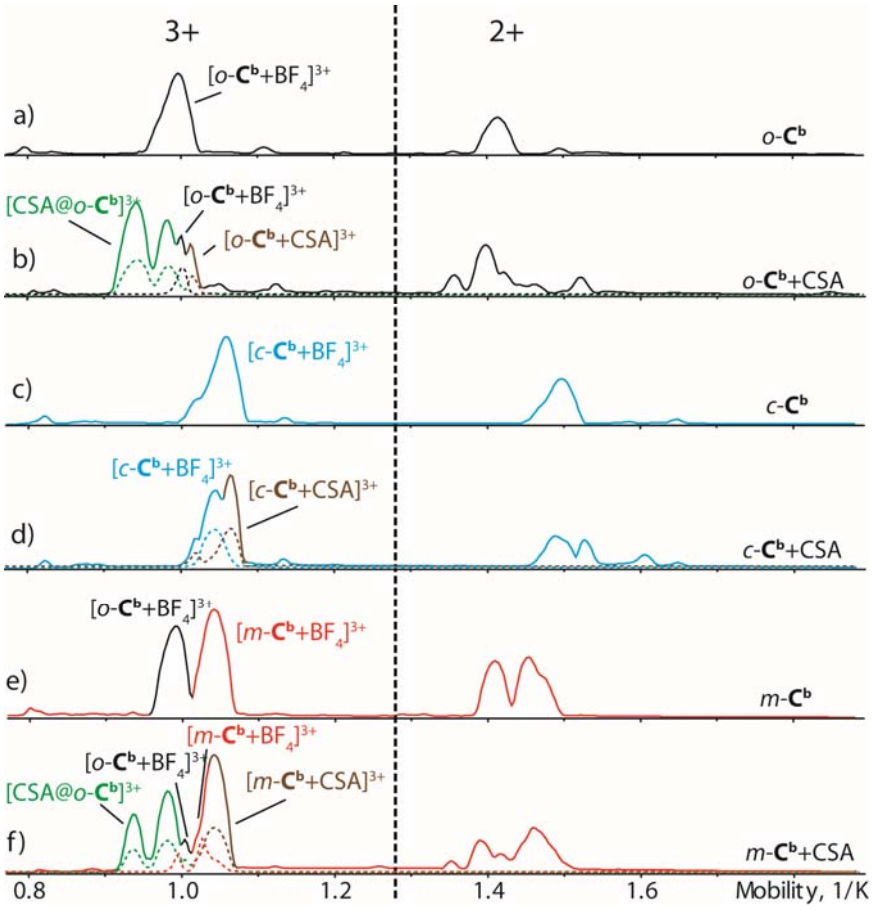

Figure 7.9 Ion mobility spectra of hosts a) *o*-**C^b**; c) *c*-**C^b** and e) *m*-**C^b**; and corresponding samples containing 1.5 eq *R*-CSA: b) *o*-**C^b**+*R*-CSA; d) *c*-**C^b**+*R*-CSA and f) *m*-**C^b**+*R*-CSA. Copyright © 2017 American Chemical Society.

7.8 Conclusion

In conclusion, our study revealed the temporal relationship between the stepwise photocyclization events and guest ejection of a light-triggered host composed of four DTE photoswitches. We showed that encapsulation of a chiral guest inside the non-chiral, photochromic coordination cage *o*-**C^b** results in strong induced CD effects. Chiral information could be locked into the configurationally stable photoisomer *c*-**C^b** by UV irradiation. The degree of non-covalent propagation of chiral information was found to be dependent on temperature, guest amount and absence of competing guests, but never exceeded about 25%. The latter observation, backed by a canon of NMR and CD experiments, X-ray and ion mobility mass spectrometric studies, shows that already the closure of the first photoswitch triggered the key structural conversion that leads to ejection of the guest. The herein introduced methodology, based on chirality reporters lining the walls of a self-assembled confinement, allows to serve as a basis for the examination of further host-to-guest size/shape relationships, including the role of solvent effects. Furthermore, progress in the fundamental understanding as well as

application of chirality transfer will spur developments in the fields of enantioselective homogeneous catalysis, supramolecular recognition and information processing on a molecule scale.

7.9 Experimental section

7.9.1 General procedures

All chemicals, except otherwise specified, were obtained from commercial sources and used without further purification. Perfluoro-1,2-bis(2-iodo-5-methylthien-4-yl)cyclopentene[16] was prepared according to a literature procedure. The tetrabutyl ammonium salts of the guests (*R/S*-CSA, **G2**, and *S*-CSA-Br) were prepared according to a previously reported procedure.[17] Corresponding starting materials were obtained commercially as sodium salt (**G2**) or free sulfonic acids (*R/S*-CSA and *S*-CSA-Br) in the highest available purity. Recycling gel permeation chromatography was performed on a JAI LC-9210 II NEXT GPC system equipped with Jaigel 1H and 2H columns in series using chloroform as the eluent (HPLC grade). NMR measurements were all conducted at 298 K on Avance-500 and Avance-600 instruments from Bruker and INOVA 500 MHz machine from Varian. High-resolution ESI mass spectrometric measurements were carried out on maXis ESI-TOF MS and ESI-timsTOF machines from Bruker. The irradiations were performed with a 500 W Hg Arc lamp from LOT-Quantum Design, equipped with a dichroic mirror (to remove IR wavelengths) using a custom-made transparent quartz glass Dewar vessel to host the sample tubes for applying the low temperatures using appropriate cooling bath mixtures as described below. Chiral HPLC was performed on an Agilent Technologies 1260 infinity HPLC system equipped with Daicel CHIRALPAK IA columns (250 x 4.6 mm and 250 x 10 mm) using a dichloromethane/hexane/methanol (3%/89%/8%) mixture as eluent for the separation of *c*-**L**. UV-vis spectra were recorded on an Agilent 8453 UV-Vis spectrophotometer. CD spectra were measured on an Applied Photophysics Chirascan circular dichroism spectrometer.

7.9.2 Synthesis of the ligand and cages

7.9.2.1 Synthesis of the ligand

*7.9.2.1.1 Synthesis of open ligand (o-**L**^{b})*

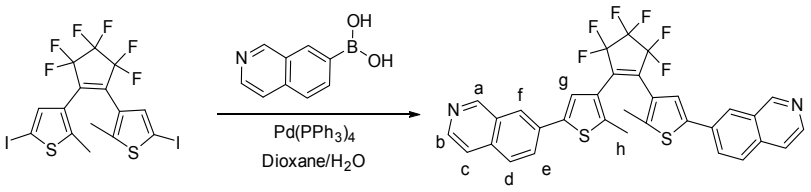

Scheme 6.1 Synthesis of *o*-**L**^{b}.

A mixture of perfluoro-1,2-bis(2-iodo-5-methylthien-4-yl)cyclopentene[16] (310 mg, 0.50 mmol), isoquinolin-7-ylboronic acid (259.6 mg, 1.50 mmol), $Pd(PPh_3)_4$ (34.7 mg, 0.03 mmol), K_3PO_4 (1.73 g, 7.5 mmol) and degassed dioxane/H_2O (30 mL V/V = 1:1) were combined in an oven-dried Schlenk tube and stirred at 90 °C overnight. After cooling down to room temperature, CH_2Cl_2 was added, and the solution was washed with water and brine, dried over anhydrous $MgSO_4$ and concentrated *in vacuo*. The crude product was purified by column chromatography (silica) using CH_2Cl_2/MeOH (50:1) as eluents and further purified by gel permeation chromatography (GPC) to give *o*-**L**^{b} (230.4 mg, 0.37 mmol) as a gray solid in 74% yield. ^{1}H NMR (600 MHz, CD_3CN) δ 9.25 (s, 2H), 8.48 (d, *J* = 5.7 Hz, 2H), 8.23 (s, 2H), 7.99 (dd, *J* = 8.6, 1.9 Hz, 2H), 7.93 (d, *J* = 8.6 Hz, 2H), 7.75 – 7.69 (m, 2H), 7.60 (s, 2H), 2.09 (s, 6H). ^{13}C NMR (151 MHz, CD_3CN) δ 153.51, 144.31, 143.75, 142.38, 137.66, 135.98, 132.85, 129.79, 129.00, 128.45, 126.66, 124.82, 124.35, 121.08, 117.22 (CF_2), 112.25 (CF_2), 14.83. ^{19}F NMR (565 MHz, CD_3CN) δ -110.71 (t, ^{3}J = 5.0 Hz, 4F) δ -132.48 (p, ^{3}J = 5.2 Hz, 2F). ESI-HRMS calculated for $C_{33}H_{21}F_6N_2S_2$ ([M+H]$^{+}$) *m/z* = 623.1050, found *m/z* = 623.1026.

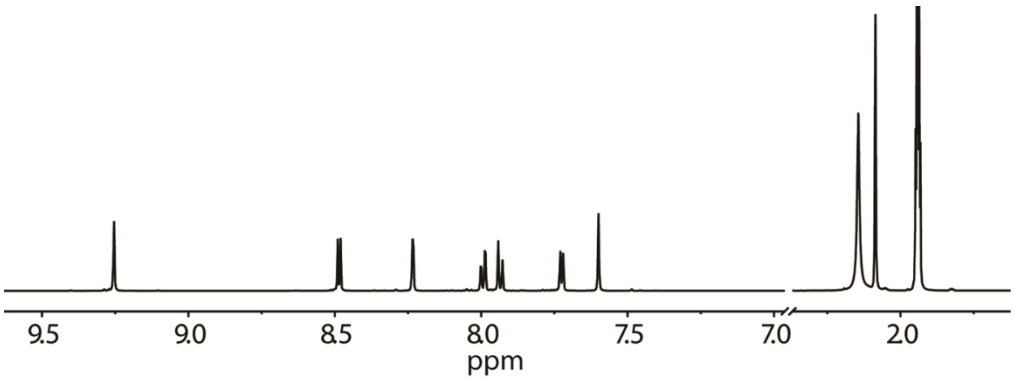

Figure 7.10 ^{1}H NMR spectrum (600 MHz, CD_3CN, 298 K) of *o*-**L**^{b}.

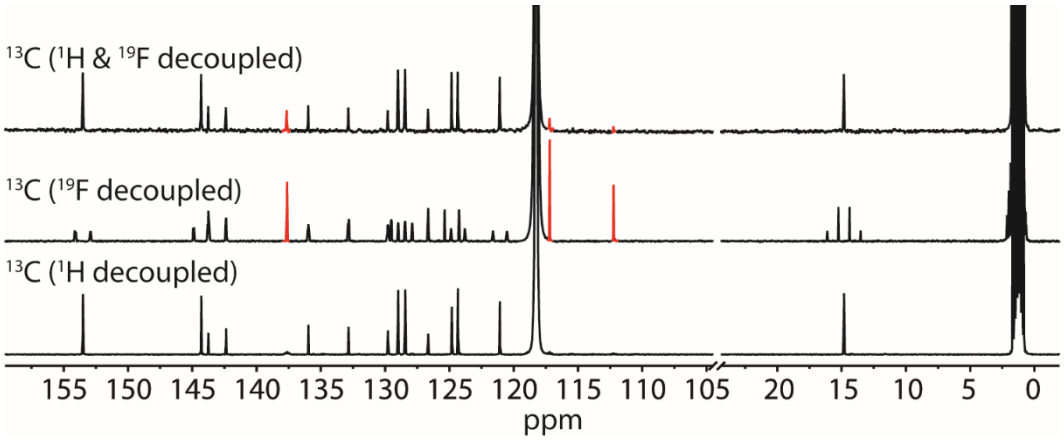

Figure 7.11 ^{13}C NMR spectra (CD_3CN, 298 K) of ***o*-L^{b}** (signals of perfluorocyclopentene ring could be detected in ^{19}F-decoupled and ^{19}F- & ^{1}H-decoupled ^{13}C spectra, marked in red).

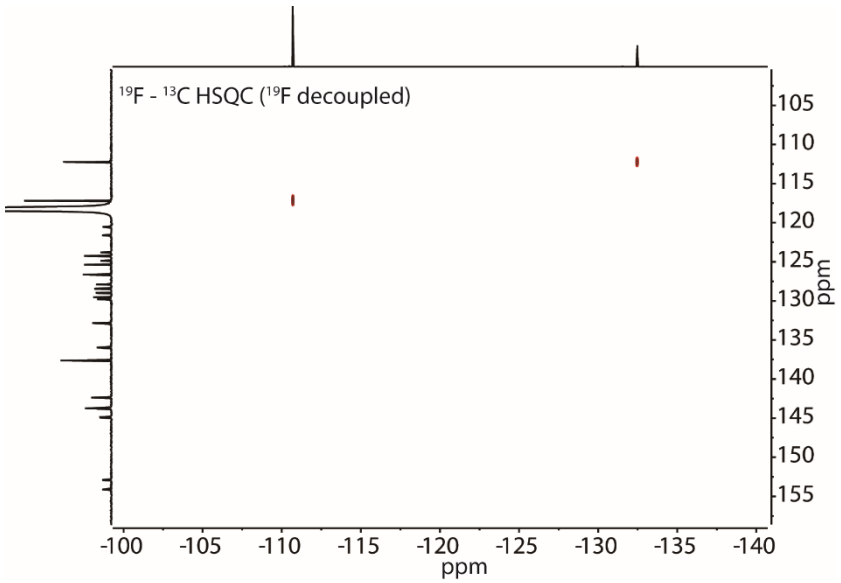

Figure 7.12 ^{19}F-^{13}C HSQC spectrum (600 MHz, CD_3CN, 298 K) of ***o*-L^{b}**.

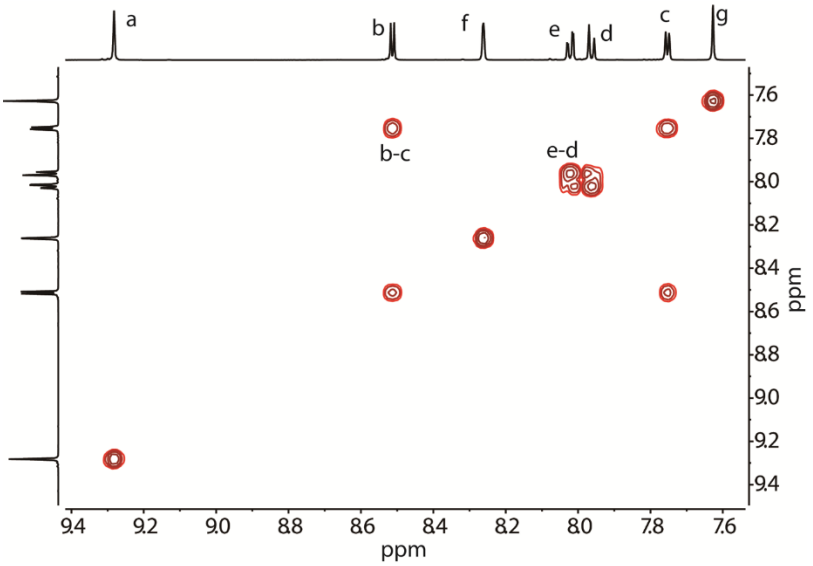

Figure 7.13 ^{1}H-^{1}H COSY spectrum (600 MHz, CD_3CN, 298 K) of ***o*-L^{b}** (only showing aromatic region).

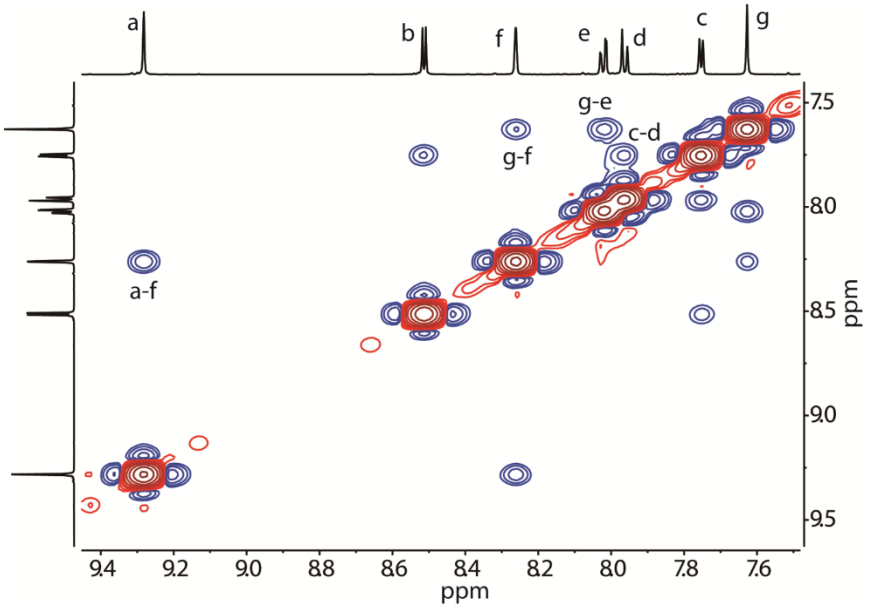

Figure 7.14 ^{1}H-^{1}H NOESY spectrum (600 MHz, CD_3CN, 298 K) of *o*-**L^{b}** (only showing aromatic region).

7.9.2.1.2 Synthesis of open ligand (c-L^{b})

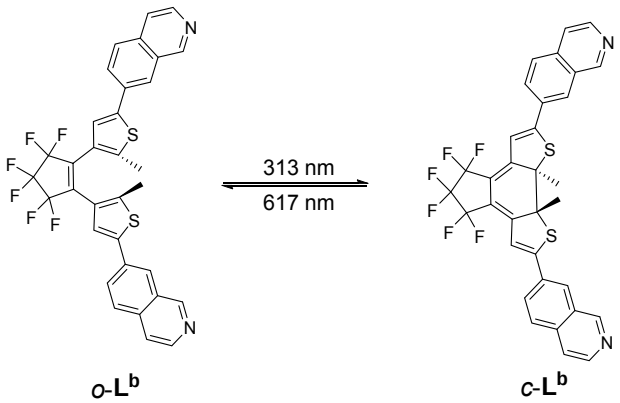

Scheme 6.2 Synthesis of *c*-**L^{b}**.

Closed form ligand *c*-**L^{b}** was obtained directly from open form ligand *o*-**L^{b}** by irradiation under 313 nm in a yield > 99%.(as determined by NMR and UV-Vis spectroscopy) ^{1}H NMR (500 MHz, CD_3CN) δ 9.33 (s, 1H), 8.57 (d, *J* = 5.7 Hz, 1H), 8.29 (d, *J* = 2.0 Hz, 1H), 8.06 (dd, *J* = 8.7, 2.0 Hz, 1H), 7.97 (d, *J* = 8.7 Hz, 1H), 7.78 (d, *J* = 5.7 Hz, 1H), 7.05 (s, 1H), 2.26 (s, 3H). ^{13}C NMR (126 MHz, $CDCl_3$) δ 156.75, 153.07, 149.35, 144.56, 136.51, 131.82, 128.40, 127.92, 127.23, 126.82, 120.37, 117.79, 115.11, 114.41 (CF_2), 112.87 (CF_2), 66.23, 25.33. ^{19}F NMR (565 MHz, $CDCl_3$) δ –111.36 – –114.23 (m), –133.32 (p, *J* = 5.8 Hz). ^{19}F NMR (565 MHz, $CDCl_3$) δ –111.22 – –114.15 (m), –133.32 (p, *J* = 5.8 Hz). ESI-HRMS calculated for $C_{33}H_{21}F_6N_2S_2$ ([M+H]$^{+}$) *m/z* = 623.1050, found *m/z* = 623.1028.

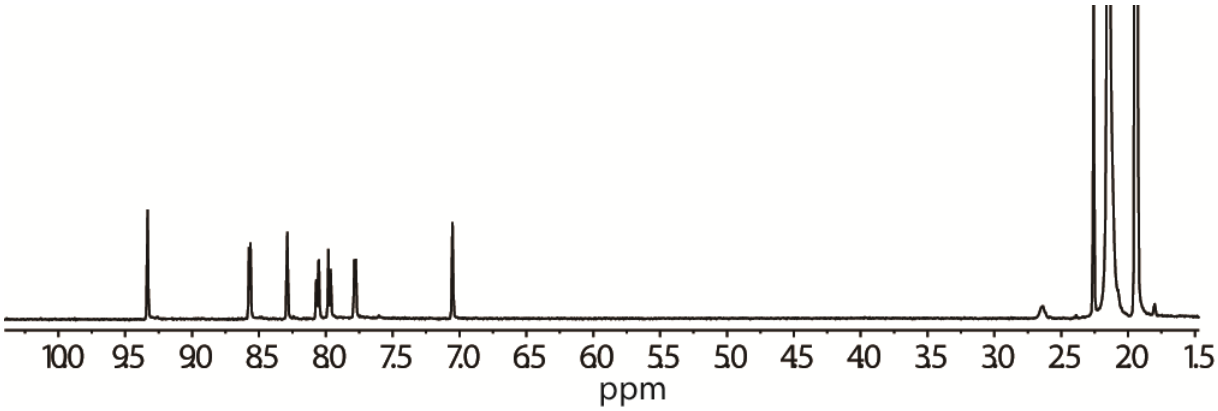

Figure 7.15 ^{1}H NMR spectrum (500 MHz, CD_3CN, 298 K) of ***c*-L^{b}**.

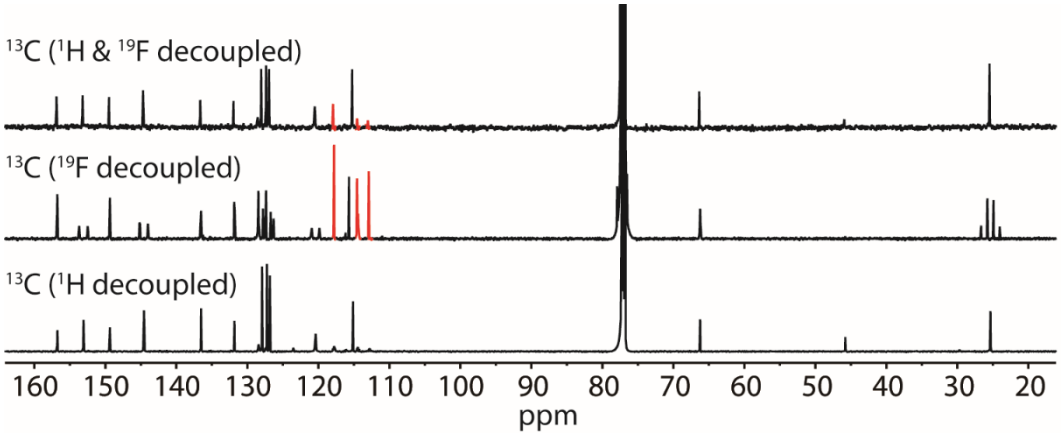

Figure 7.16 ^{13}C NMR spectra ($CDCl_3$, 298 K) of ***c*-L^{b}** (signals of perfluorocyclopentene ring could be detected in ^{19}F-decoupled and ^{19}F- & ^{1}H-decoupled ^{13}C spectra, marked in red).

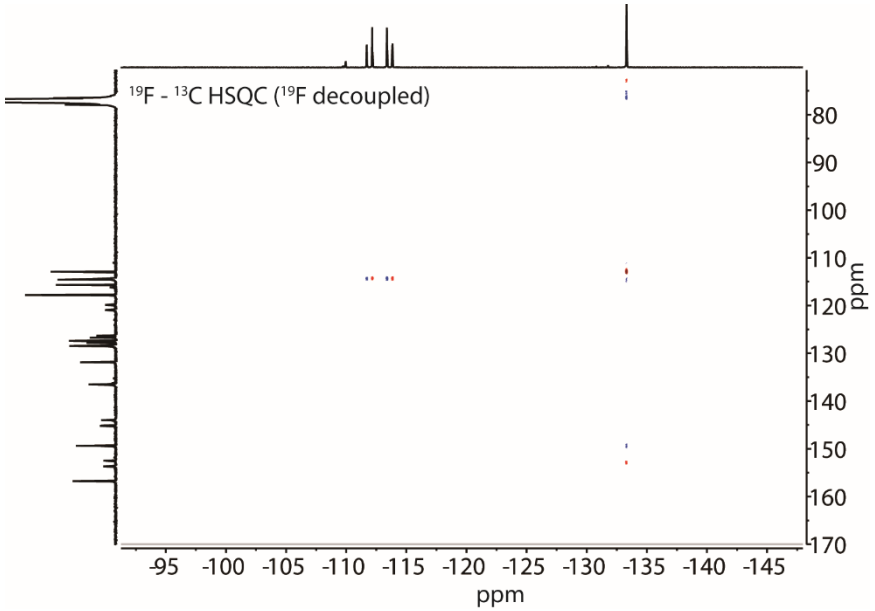

Figure 7.17 ^{19}F-^{13}C HSQC spectrum (600 MHz, $CDCl_3$, 298 K) of ***c*-L^{b}**.

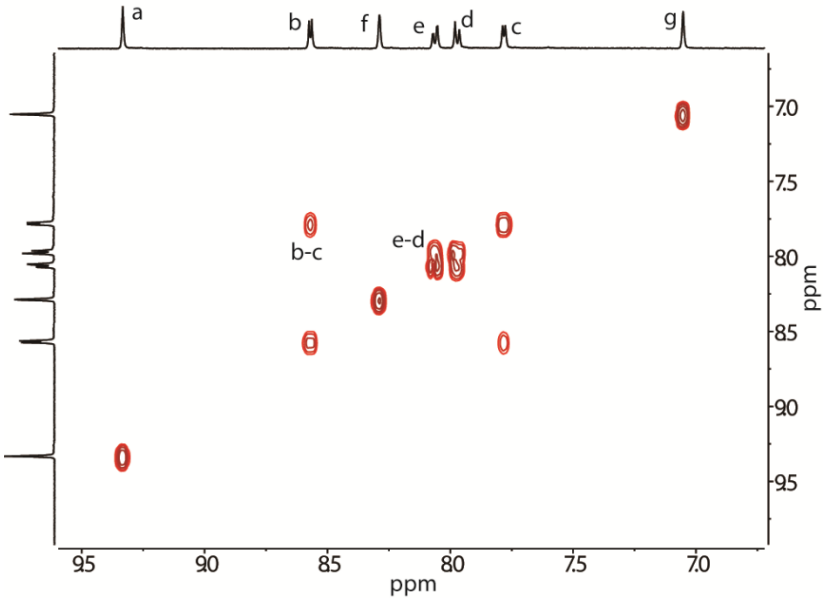

Figure 7.18 ^{1}H-^{1}H COSY spectrum (500 MHz, CD_3CN, 298 K) of *c*-**L^{b}** (only showing aromatic region).

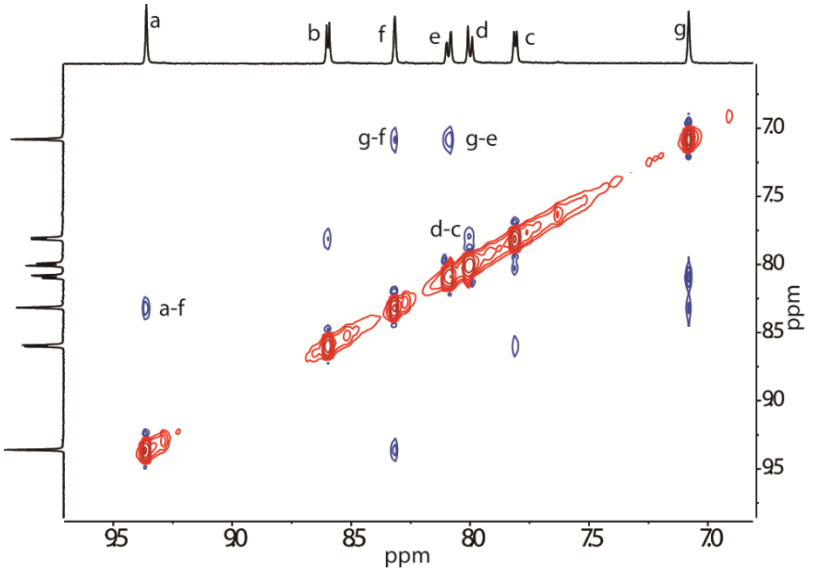

Figure 7.19 ^{1}H-^{1}H NOESY spectrum (500 MHz, CD_3CN, 298 K) of *c*-**L^{b}** (only showing aromatic region).

7.9.2.2 Synthesis of the cages

7.9.2.2.1 Synthesis of $[Pd_2(o\text{-}L^b)_4](BF_4)_4$ (o-C^b)

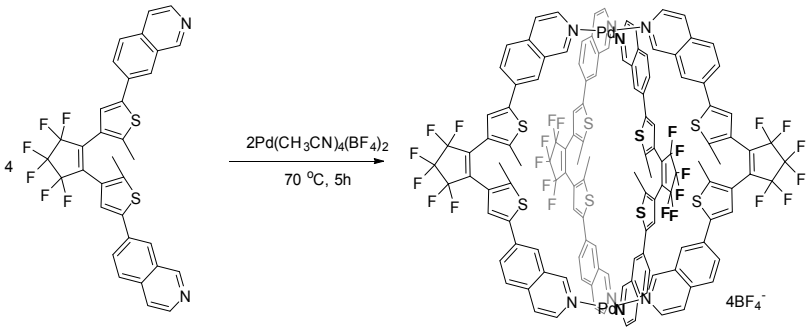

Scheme 6.3 Synthesis of *o*-**C^{b}**.

The open cage compound $[Pd_2(o\text{-}\mathbf{L^b})_4](BF_4)_4$ (*o*-$\mathbf{C^b}$) was synthesized in quantitative yield by heating a mixture of ligand *o*-$\mathbf{L^b}$ in CD_3CN (4 µmol, 2.49 mg, 866.7 µL) and $Pd(CH_3CN)_4(BF_4)_2$ (2 µmol, 133.3 µL of a 15 mM stock solution in CD_3CN) at 70 °C for 5 h to give 1000 µl of a 1 mM solution of *o*-$\mathbf{C^b}$. ^{1}H NMR (500 MHz, CD_3CN) δ 9.81 (s, 8H), 8.67 (d, *J* = 6.6 Hz, 8H), 8.28 (dd, *J* = 8.6, 1.9 Hz, 8H), 8.21 (d, *J* = 1.9 Hz, 8H), 8.03 (d, *J* = 8.6 Hz, 8H), 7.91 (d, *J* = 6.6 Hz, 8H), 7.62 (s, 8H), 1.97 (s, 24H). ^{13}C NMR (151 MHz, CD_3CN) δ 156.82, 144.69, 143.02, 141.48, 138.93, 136.73, 134.94, 132.19, 130.68, 128.55, 126.76, 126.29, 125.44, 125.29, 116.90 (CF_2), 112.28 (CF_2), 14.85. ^{19}F NMR (565 MHz, CD_3CN) δ –108.78 – –114.86 (m), –131.92 (t, *J* = 4.9 Hz), –150.61 (d, *J* = 30.5 Hz). ESI-HRMS calculated for $Pd_2C_{132}H_{80}F_{24}N_8S_8$ ([*o*-$\mathbf{C^b}$]$^{4+}$). *m/z*: calcd. = 675.0493, found = 675.0496.

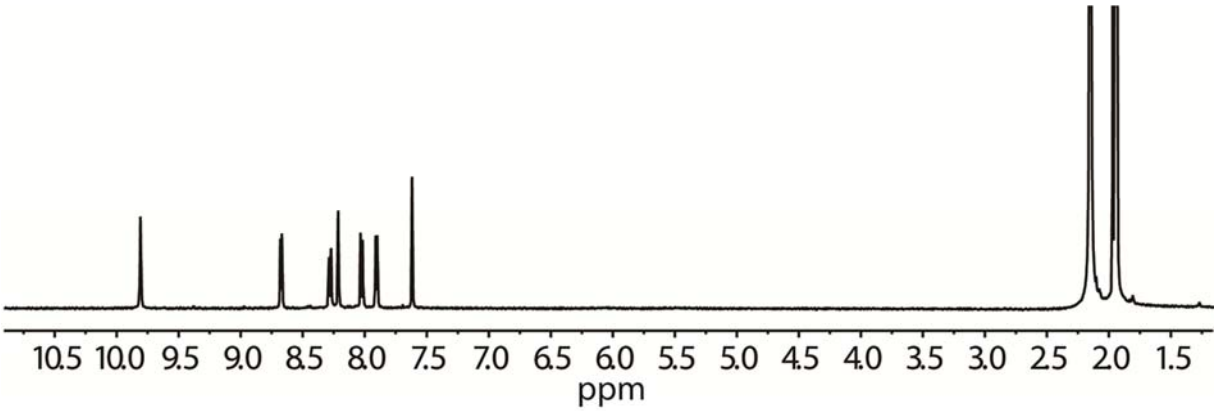

Figure 7.20 ^{1}H NMR spectrum (500 MHz, CD_3CN, 298 K) of *o*-$\mathbf{C^b}$.

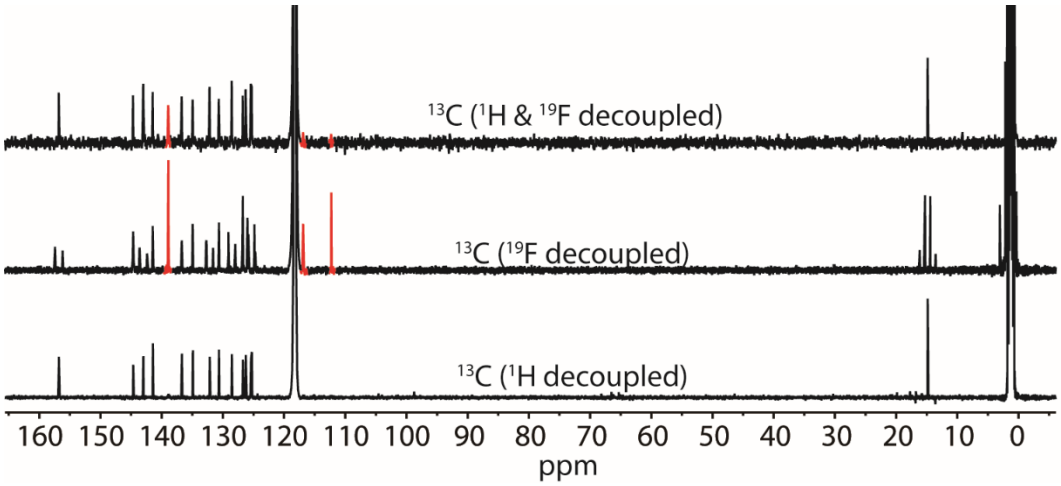

Figure 7.21 ^{13}C NMR spectra ($CDCl_3$, 298 K) of *o*-$\mathbf{C^b}$ (signals of perfluorocyclopentene ring could be detected in ^{19}F-decoupled and ^{19}F- & ^{1}H-decoupled ^{13}C spectra, marked in red).

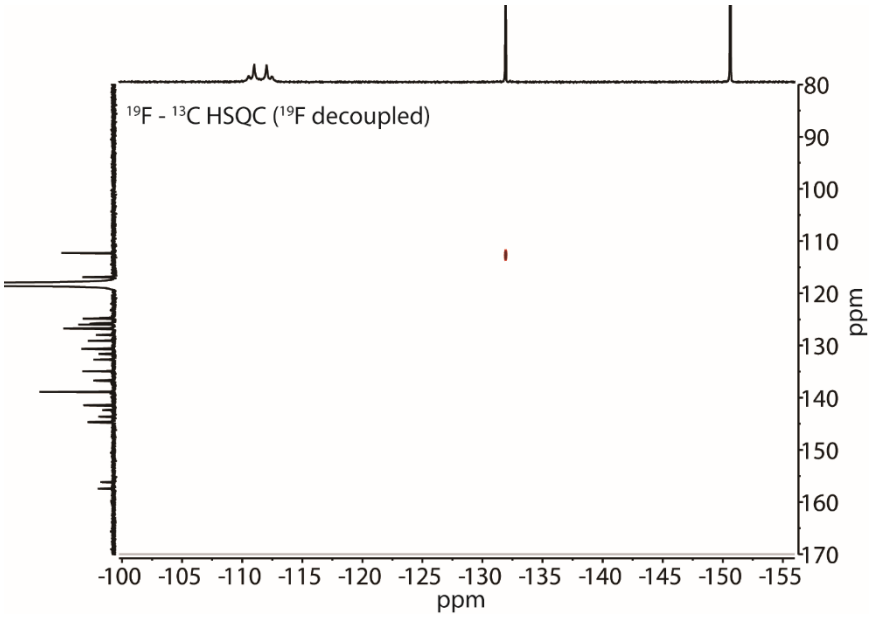

Figure 7.22 ^{19}F-^{13}C HSQC spectrum (600 MHz, CD_3CN, 298 K) of *o*-**C^{b}**.

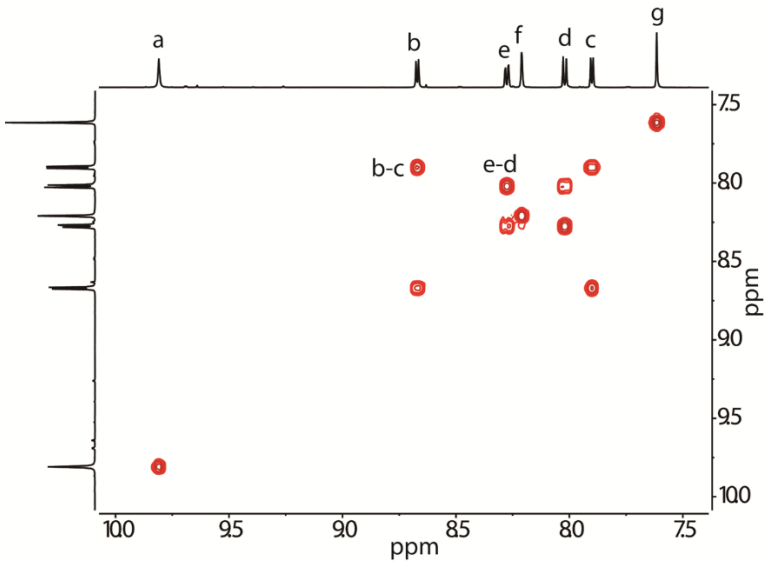

Figure 7.23 ^{1}H-^{1}H COSY spectrum (600 MHz, CD_3CN, 298 K) of *o*-**C^{b}** (only showing aromatic region)**.**

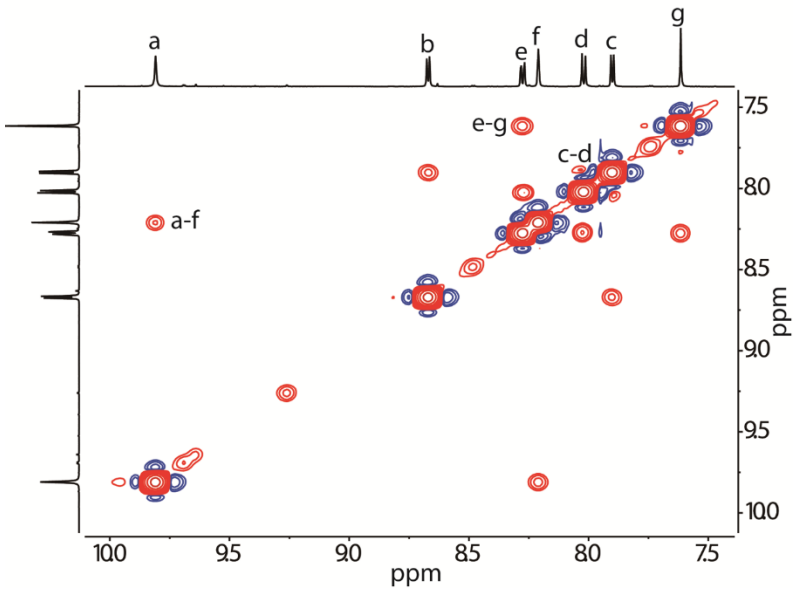

Figure 7.24 ^{1}H-^{1}H NOESY spectrum (600 MHz, CD_3CN, 298 K) of *o*-**C^{b}** (only showing aromatic region)**.**

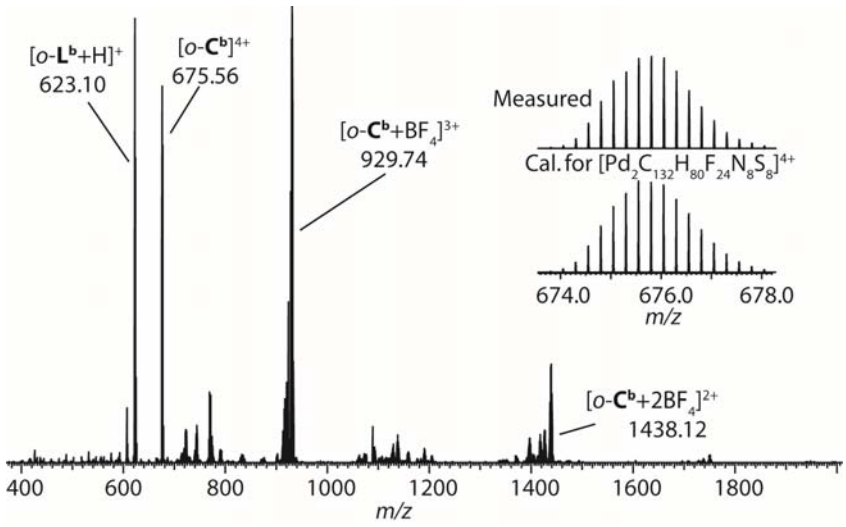

Figure 7.25 ESI-HRMS spectrum of *o*-**C^{b}.**

7.9.2.2.2 Synthesis of $[Pd_2(c\text{-}L^b)_4](BF_4)_4$ (c-C^b)

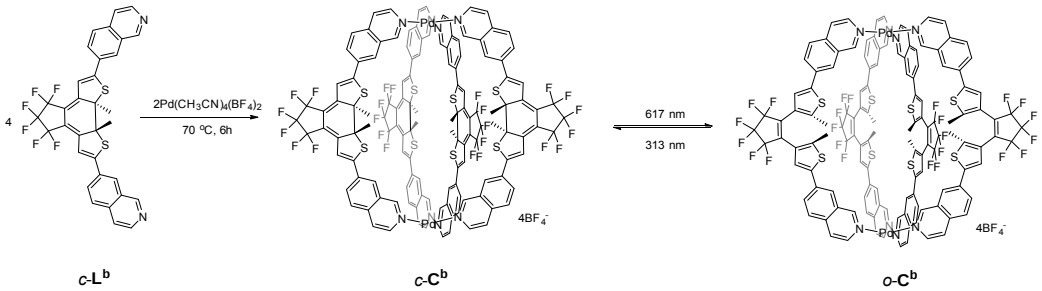

c-**L^{b}** *c*-**C^{b}** *o*-**C^{b}**

Scheme 6.4 Synthesis of *c*-**C^{b}** and light-controlled interconversion between *o*-**C^{b}** and *c*-**C^{b}**.

The closed cage compound $[Pd_2(c\text{-}L^b)_4](BF_4)_4$ (*c*-**C^{b}**) was synthesized in quantitative yield by heating a mixture of ligand *c*-**L^{b}** in CD_3CN (4 µmol, 2.49 mg, 866.7 µL) and $Pd(CH_3CN)_4(BF_4)_2$ (2 µmol, 133.3 µL of a 15 mM stock solution in CD_3CN) at 70 °C for 5 h to give 1000 µl of a 1 mM solution of *c*-**C^{b}**. Alternatively, it could be directly obtained

by irradiation of a CD_3CN solution of the open cage *o*-**C^b** with light of 313 nm wavelength. ^{1}H NMR (600 MHz, CD_3CN) δ 10.44 (8H), 9.03 (8H), 8.53 – 8.46 (8H), 8.33 (8H), 8.03 – 7.93 (16H), 7.16 (8H), 2.32 (24H). ^{13}C NMR (151 MHz, CD_3CN) δ 156.90, 156.81, 151.62, 143.76, 138.05, 133.89, 131.68, 130.61, 129.42, 127.90, 125.42, 119.04, 117.58, 115.19 (CF_2), 113.68 (CF_2), 66.03, 25.75. ^{19}F NMR (565 MHz, CD_3CN, *c*-**C^b**(*R*)) δ –112.28 – –115.41 (m), –134.44 (p, *J* = 5.9 Hz), –150.62 (d, *J* = 30.2 Hz). ESI-HRMS calculated for $Pd_2C_{132}H_{80}F_{28}N_8S_8B$ ([*c*-**C^b**+BF_4]$^{3+}$). *m/z*: calcd. = 929.7341, found = 929.7325.

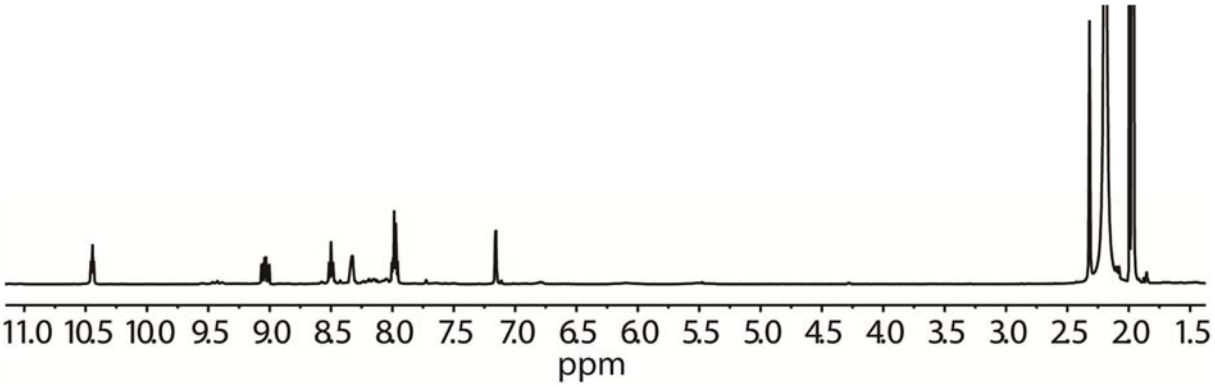

Figure 7.26 ^{1}H NMR spectrum (600 MHz, CD_3CN, 298 K) of *c*-**C^b**.

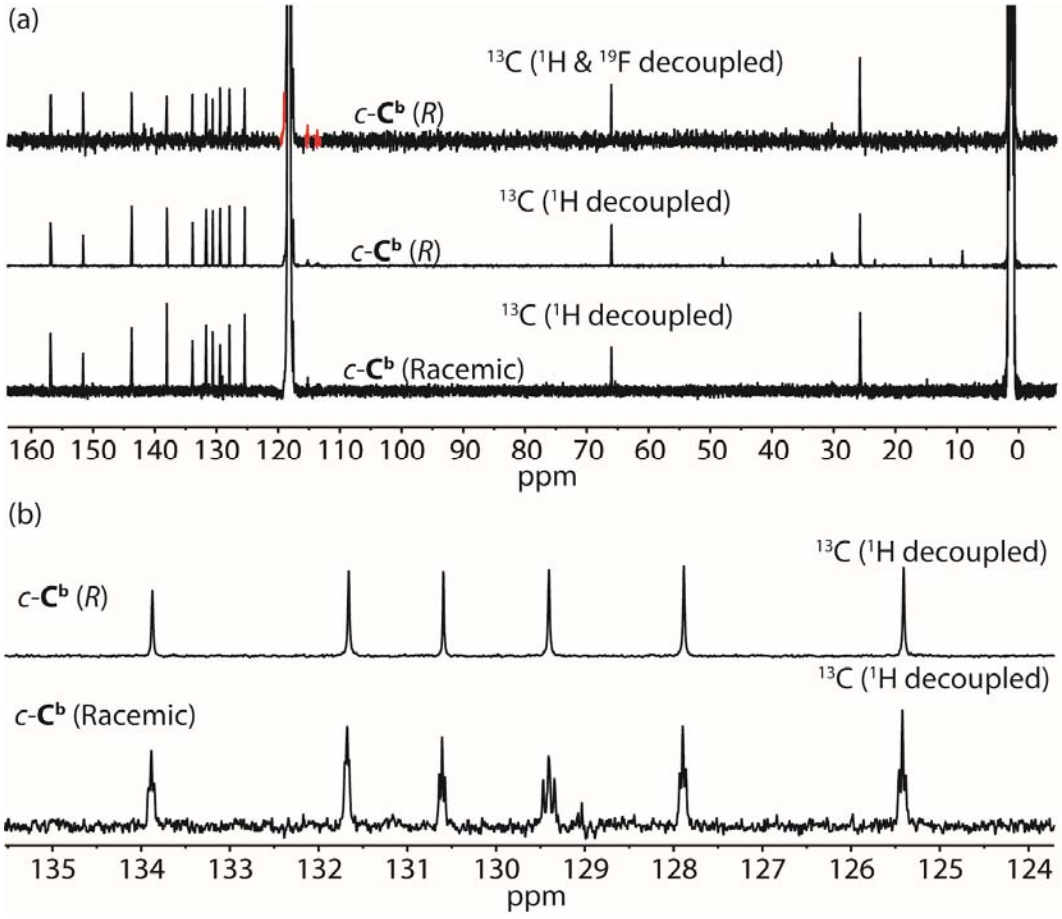

Figure 7.27 (a) Full and (b) part of expanded ^{13}C NMR spectra (CD_3CN, 298 K) of *c*-**C^b** (signals of perfluorocyclopentene ring could be detected in ^{19}F- & ^{1}H-decoupled ^{13}C spectra, marked in red).

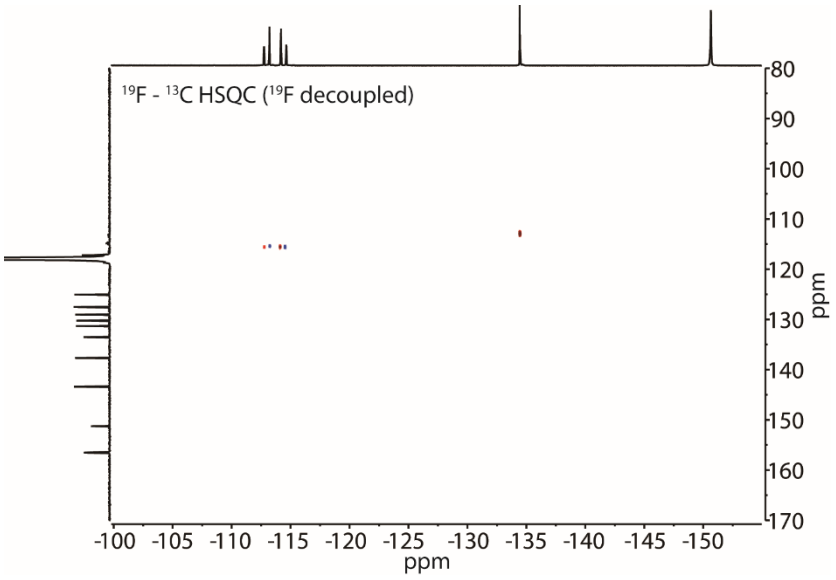

Figure 7.28 ^{19}F-^{13}C HSQC spectrum (600 MHz, CD_3CN, 298 K) of *c*-**C^{b}**.

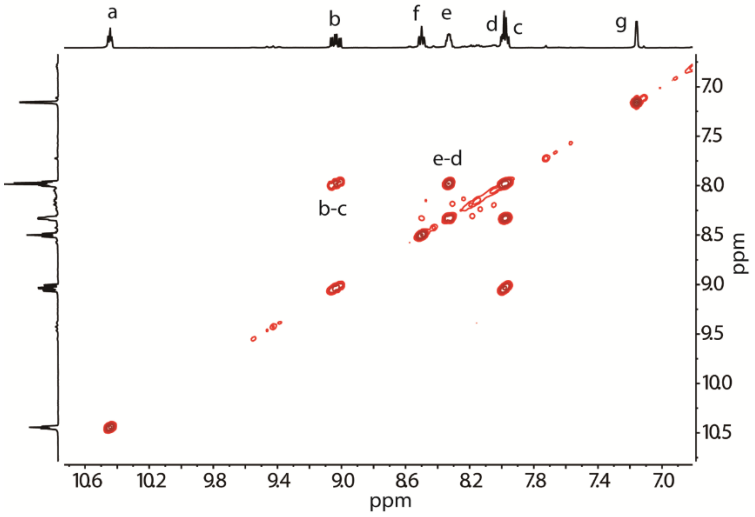

Figure 7.29 ^{1}H-^{1}H COSY spectrum (600 MHz, CD_3CN, 298 K) of *c*-**C^{b}** (only showing aromatic region).

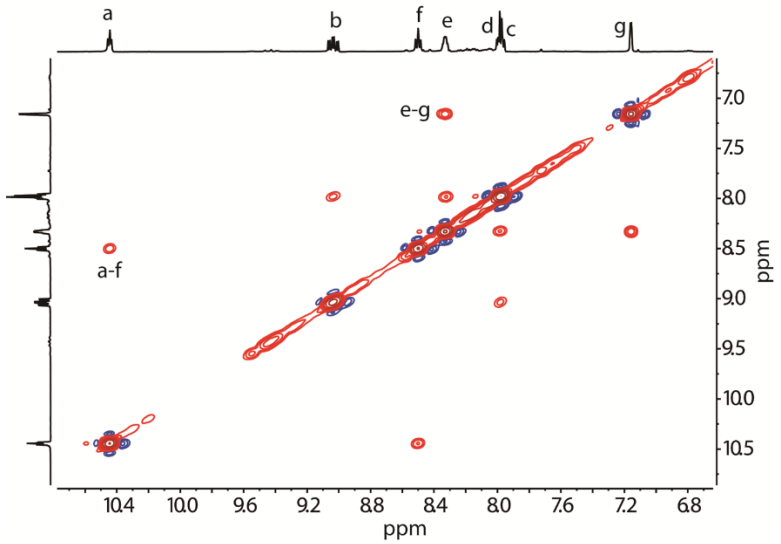

Figure 7.30 ^{1}H-^{1}H NOESY spectrum (600 MHz, CD_3CN, 298 K) of *c*-**C^{b}** (only showing aromatic region).

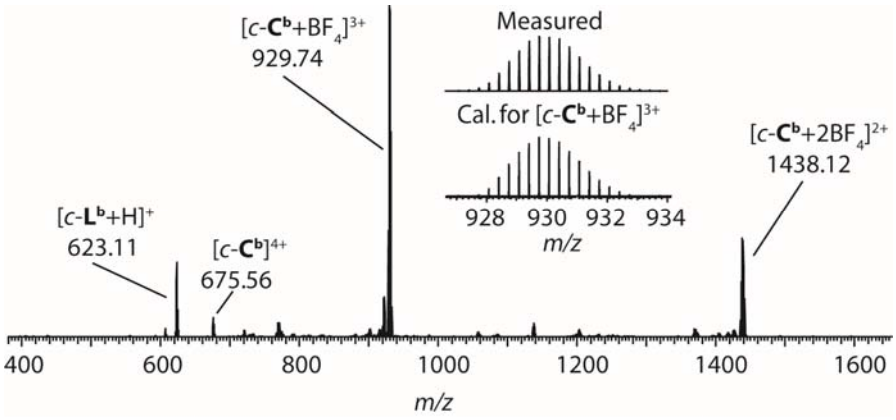

Figure 7.31 ESI-HRMS spectrum of *c*-**C^b**.

7.9.3 Photoswitching between the cage isomers

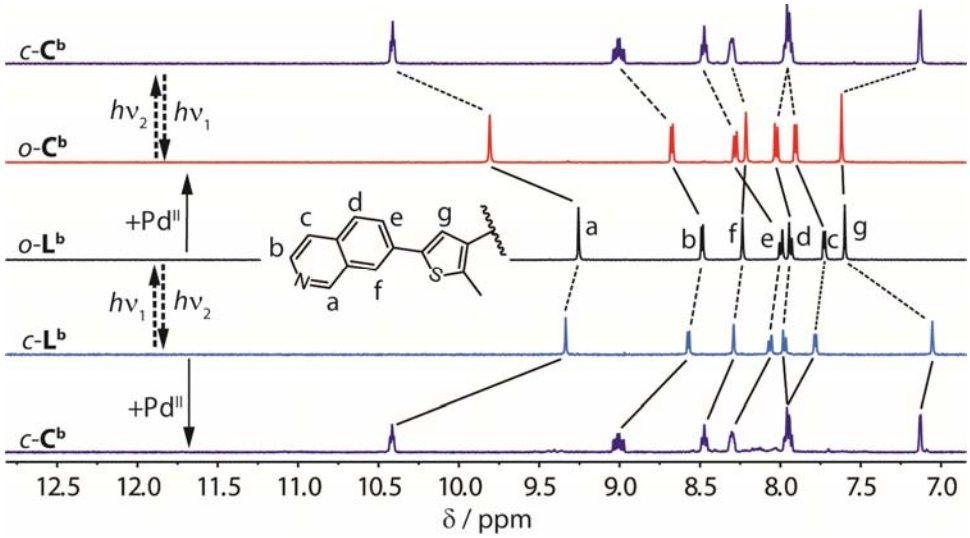

Figure 7.32 ^{1}H NMR spectra (500 MHz, CD_3CN, 298 K) of *c*-**L^b**, *c*-**L^b**, *o*-**C^b**, and *c*-**C^b**, indicating the changes upon assembly and photoswitching of the cage isomers.

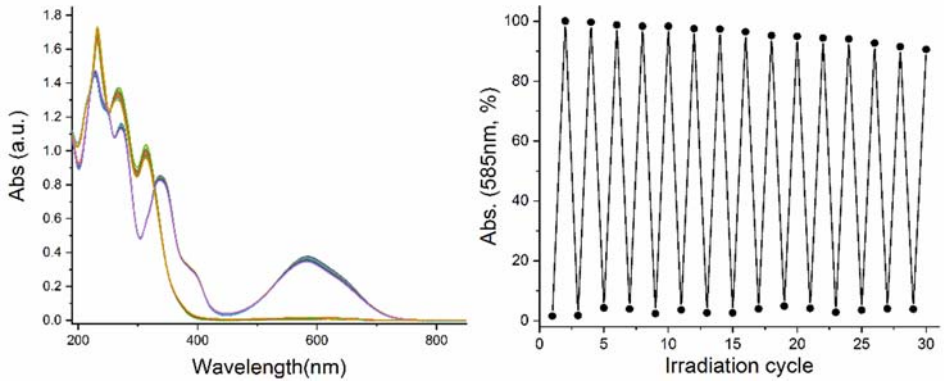

Figure 7.33 The reversibility of photoswitching between *o*-**C^b** and *c*-**C^b** (0.075 mM) was monitored by UV-vis spectroscopy at 585 nm (~5% loss in signal intensity of *c*-**C^b** after 15 cycles).

7.9.4 Titration experiments

Host-guest titrations were done by stepwise addition of aliquots from stock solutions of the guests *R/S*-camphor sulfonate (*R/S*-CSA, as their tetrabutyl ammonium salts in CD_3CN, 15.0 mM) or benzene-1,4-disulfonate (**G2**, as their tetrabutyl ammonium salts in CD_3CN, 15.0 mM) to 500 µL of a 1.0 mM solution of *o*-**C^b**/*c*-**C^b** in CD_3CN in an NMR tube. The ^{1}H NMR spectra were recoded immediately after briefly shaking the solution. All titration of *c*-**C^b** were conducted in the dark.

7.9.4.1 Titration of *R*-CSA to *o*-C^b & *c*-C^b

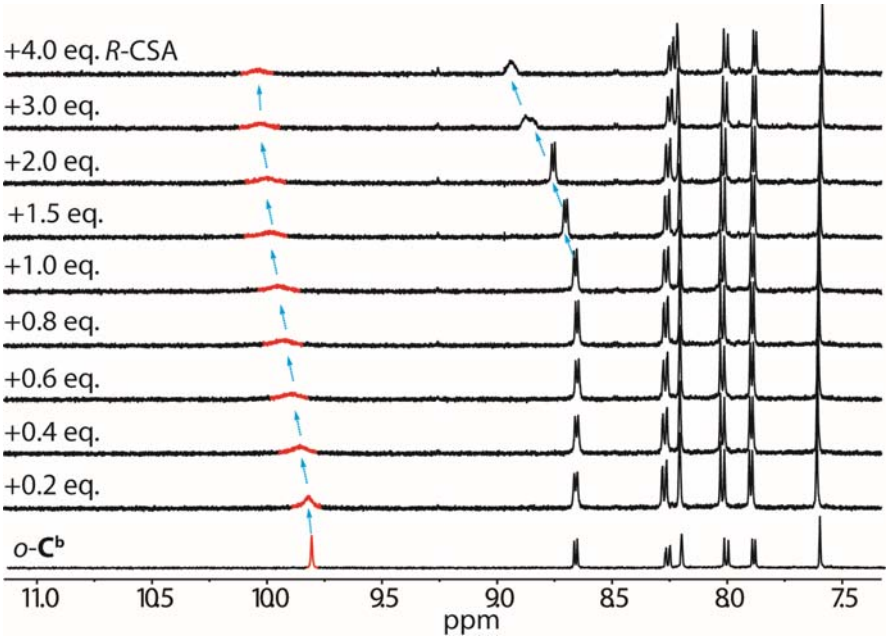

Figure 7.34 ^{1}H NMR spectra (500 MHz, CD_3CN, 298 K) of the titration of *o*-**C^b** (1 mM) with *R*-CSA.

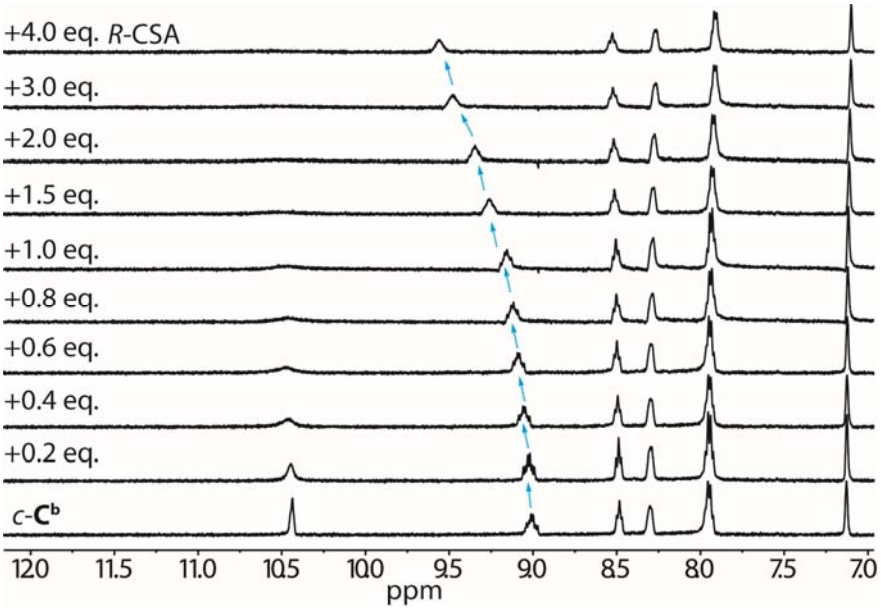

Figure 7.35 ^{1}H NMR spectra (500 MHz, CD_3CN, 298 K) of the titration of *c*-**C^b** (1 mM) with *R*-CSA.

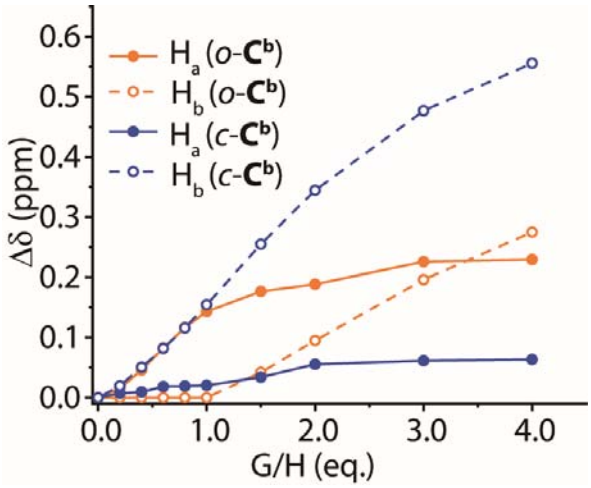

Figure 7.36 Binding isotherms of *o*-**C^{b}** and *c*-**C^{b}** with *R*-CSA for inward-pointing proton Ha and outward-pointing proton H_b at 298 K. As can be seen, for cage *o*-**C^{b}** the shift of the inward-pointing proton starts right away whereas the signal for the outward-pointing proton only starts to shift after about one equivalent guest has been added, speaking for a preferential binding of the guest inside the cavity until saturation is reached. For cage *c*-**C^{b}**, however, both inward- and outward-pointing proton signals shift from the beginning of the titration experiment, indicating no noteworthy preference for guest uptake in this case.

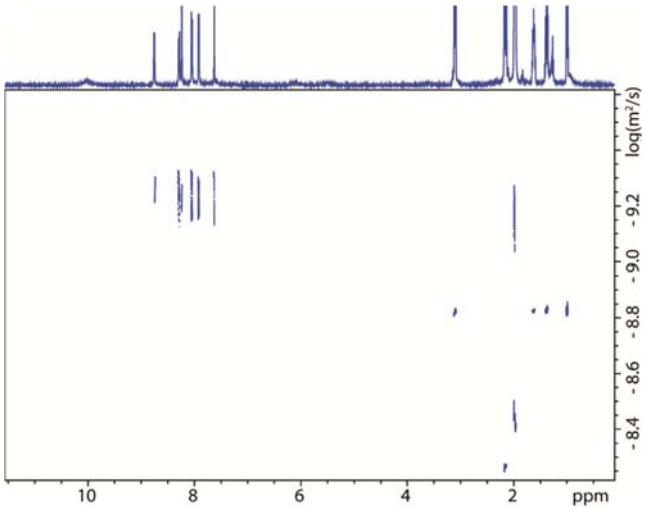

Figure 7.37 DOSY NMR spectrum (500 MHz, CD_3CN, 298 K, 1 mM) of *R*-CSA@*o*-**C^{b}** at room temperature.

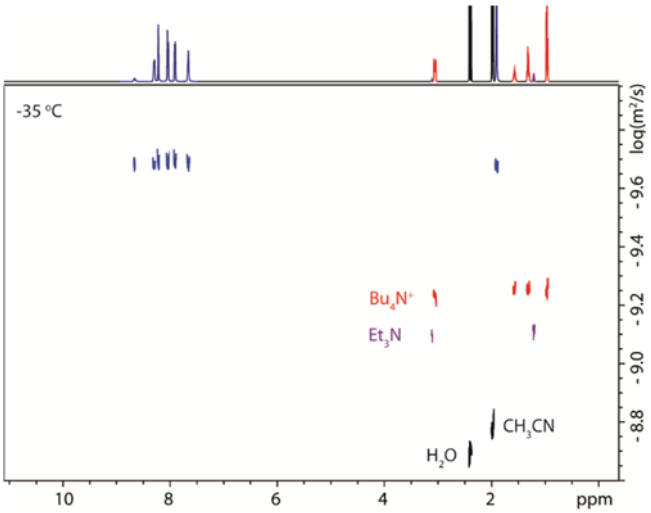

Figure 7.38 DOSY NMR spectrum (500 MHz, CD_3CN, 238 K, 1 mM) of *R*-CSA@*o*-**C^{b}** at 238 K.

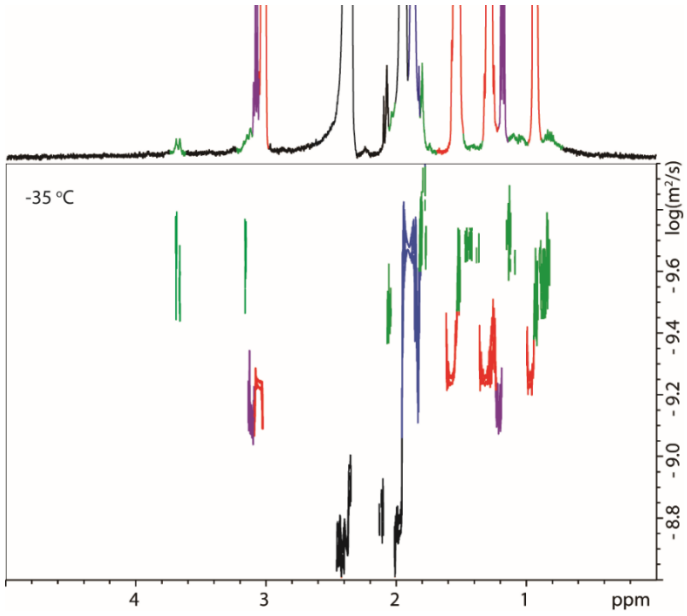

Figure 7.39 Zoom into aliphatic area of DOSY NMR spectrum (500 MHz, CD_3CN, 238 K, 1 mM, 1 eq. guest) of *R*-CSA@*o*-**C**^{b}, showing guest signals (green) sharing about the same diffusion constant (logD ~ –9.7) as the aliphatic host peak (blue; CH_3-group at 1.9 ppm), thus indicating encapsulation inside the cage (red: NBu^{4+}, purple: NEt_3, black: solvents).

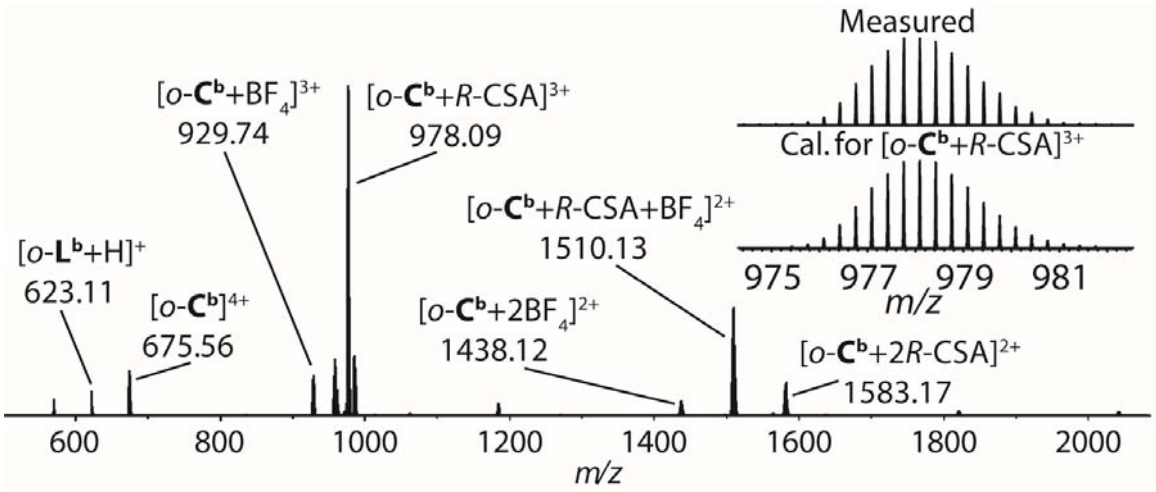

Figure 7.40 ESI-HRMS of *R*-CSA@*o*-**C**^{b}.

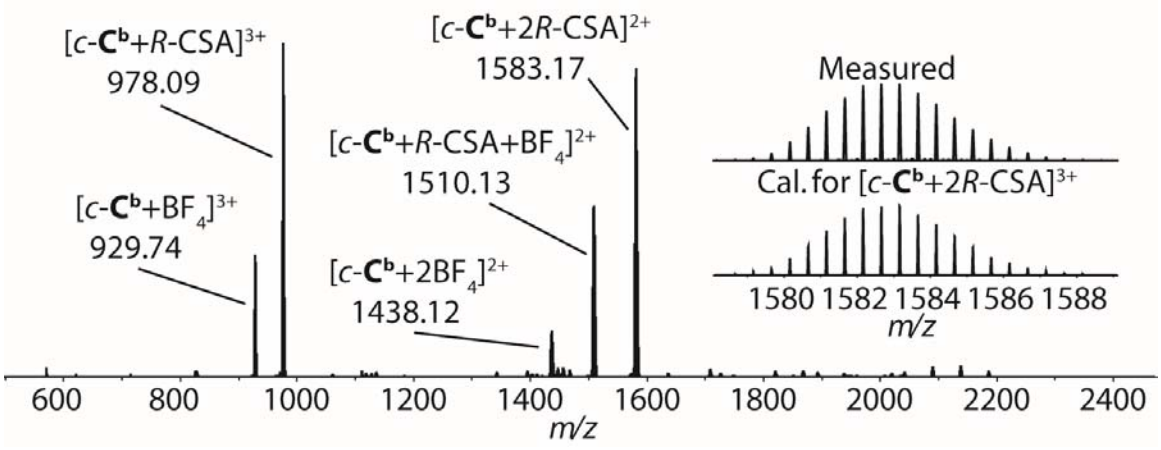

Figure 7.41 ESI-HRMS of *R*-CSA@*c*-**C**^{b}.

7.9.4.2 Titration of *S*-CSA to *o*-C^{b} & *c*-C^{b}

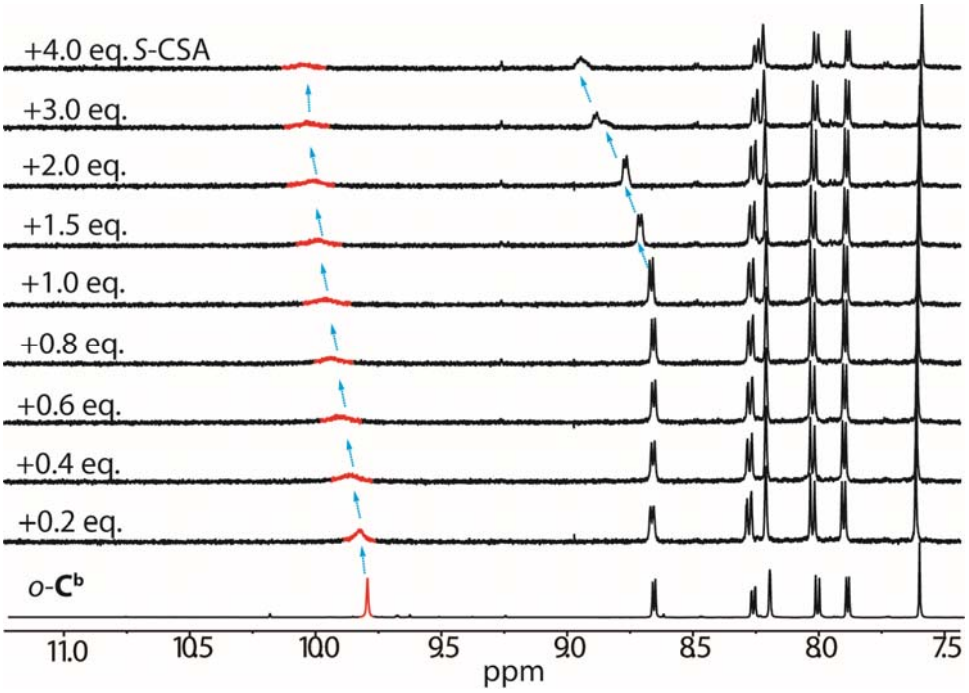

Figure 7.42 ^{1}H NMR spectra (500 MHz, CD_3CN, 298 K) of the titration of *o*-**C^{b}** (1 mM) with *S*-CSA.

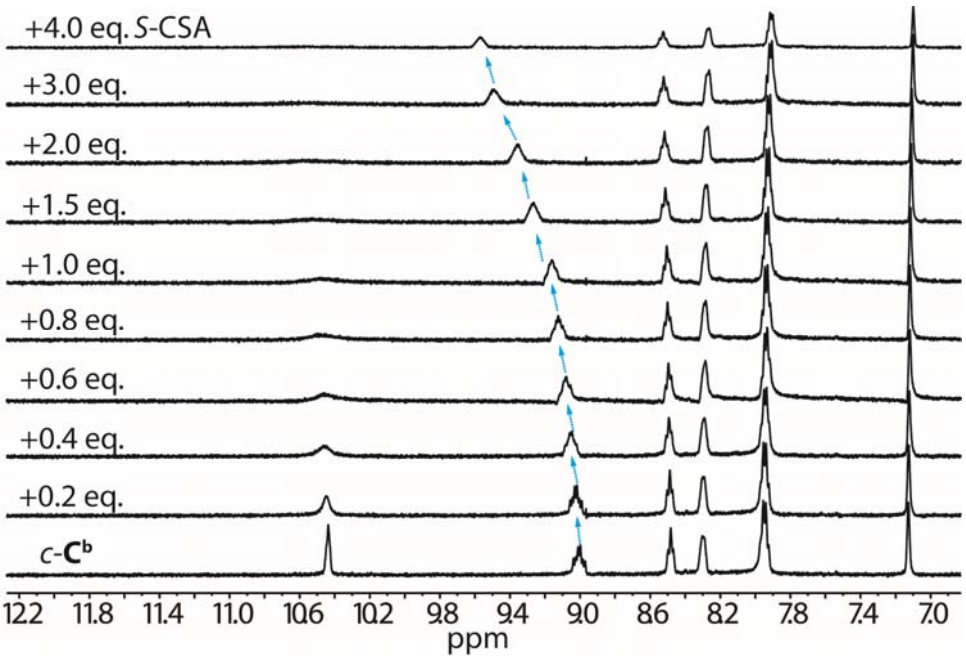

Figure 7.43 ^{1}H NMR spectra (500 MHz, CD_3CN, 298 K) of the titration of *c*-**C^{b}** (1 mM) with *S*-CSA.

7.9.4.3 Titration of G2 to *o*-C^b

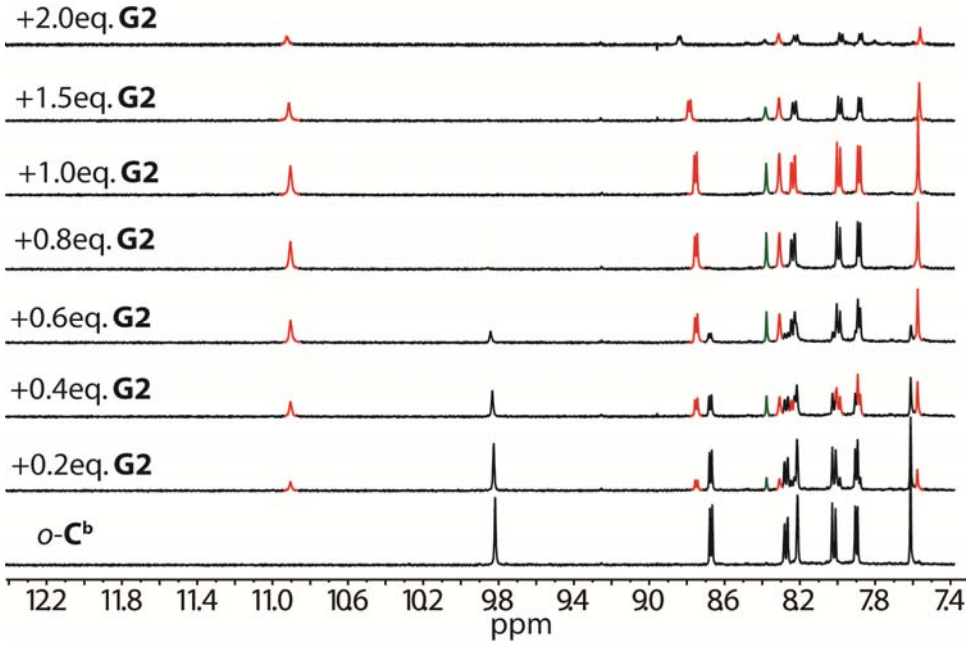

Figure 7.44 ^{1}H NMR spectra (500 MHz, CD_3CN, 298 K) of the titration of *o*-$\mathbf{C^b}$ (1 mM) with benzene-1,4-disulfonate (**G2**, as their tetrabutyl ammonium salts in CD_3CN, 15.0 mM).

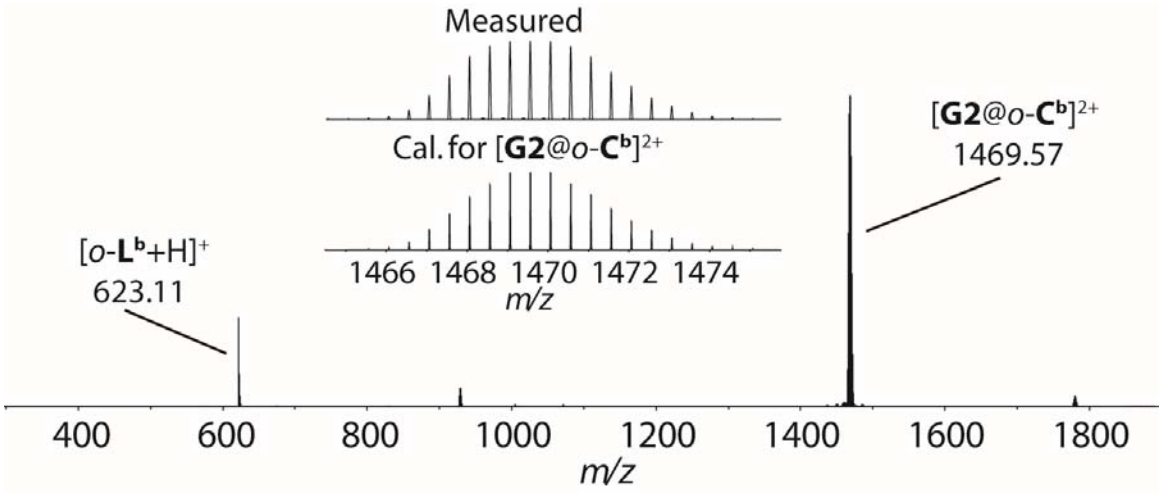

Figure 7.45 ESI-HRMS of *R*-CSA@*c*-$\mathbf{C^b}$.

7.9.5 Guest exchange experiment

A guest exchange experiment was carried out by adding 1.0 eq. of achiral guest **G2** (15 mM, CD_3CN) into an *R*-CSA@*o*-$\mathbf{C^b}$ (1.0 mM, CD_3CN) solution. NMR shows that the encapsulated *R*-CSA was completely replaced by **G2**. In contrast, titration of *R*-CSA (15 mM, CD_3CN) into **G2**@*o*-$\mathbf{C^b}$ (1.0 mM, CD_3CN) solution did not lead to replacement of **G2**.

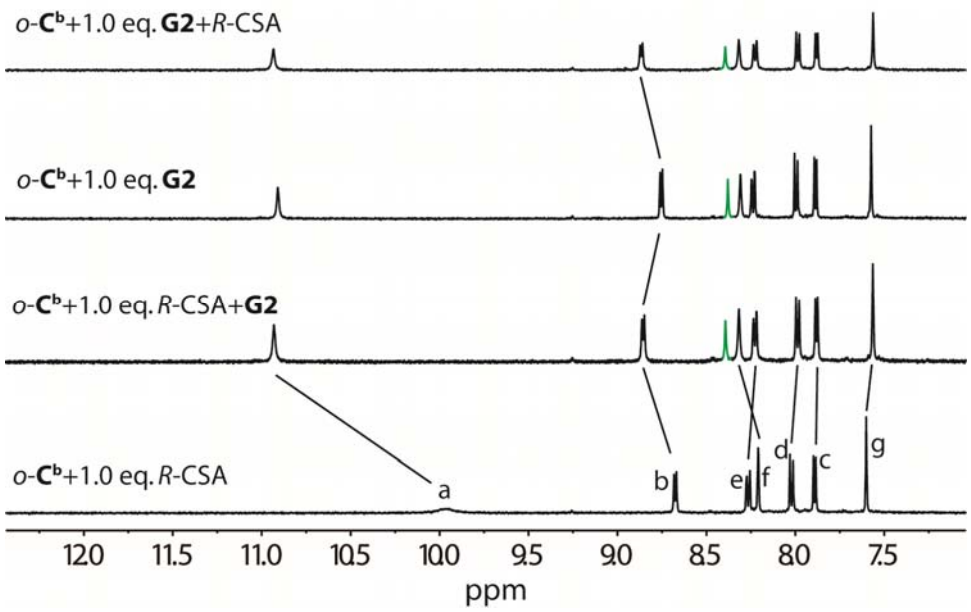

Figure 7.46 ^{1}H NMR spectra (500 MHz, 298 K, CD_3CN) of *R*-CSA@*o*-**C^{b}** (1 eq. *R*-CSA in 1 mM *o*-**C^{b}**, CD_3CN solution), *R*-CSA@*o*-**C^{b}**+**G2** (add 1 eq. of **G2** to *R*-CSA@*o*-**C^{b}**), **G2**@*o*-**C^{b}** (1 eq. **G2** in 1 mM *o*-**C^{b}** CD_3CN solution) and **G2**@*o*-**C^{b}**+*R*-CSA (add 1 eq. of *R*-CSA to **G2**@*o*-**C^{b}**). After adding 1 eq. **G2** to *R*-CSA@*o*-**C^{b}**, ^{1}H NMR shows that *R*-CSA was completely replaced by **G2**. All proton signals are then assignable to **G2**@*o*-**C^{b}**, except for downfield shifted H_b (outward pointing proton that experiences increased amount of anionic species in the solution). In contrast, after adding 1 eq. *R*-CSA to **G2**@*o*-**C^{b}**, no change is visible, except for downfield shifting of H_b. This unambiguously shows that **G2** binds stronger to *o*-**C^{b}** than *R*-CSA.

7.9.6 CD spectra of *R/S*-CSA and *c*-C^{b}+*R/S*-CSA

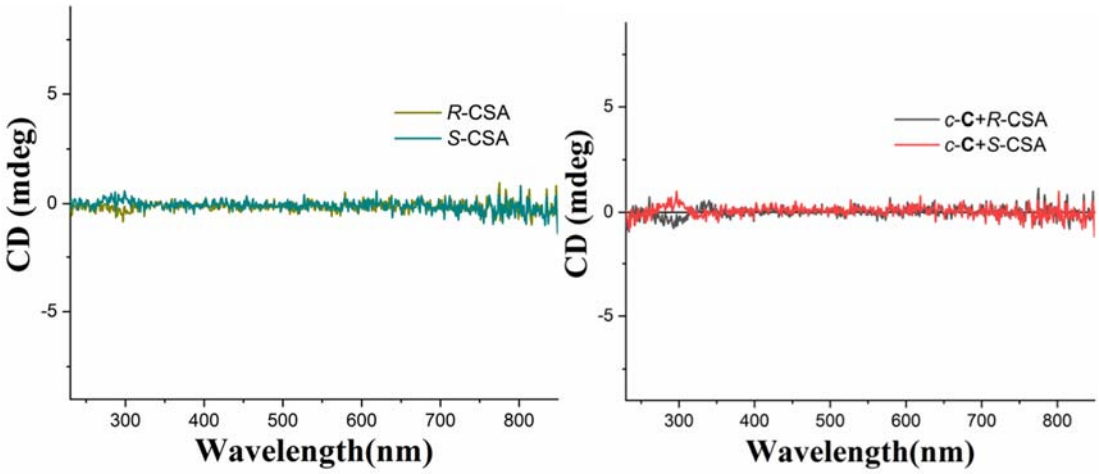

Figure 7.47 CD spectra (298 K) of *R/S*-CSA (left, 0.05 mM, CH_3CN) and *c*-**C^{b}**+*R/S*-CSA (right, 0.05 mM, CH_3CN). Chiral guests *R/S*-CSA show very weak CD signals at 300 nm. The racemic mixture of all possible *c*-**C^{b}** diastereomers after addition of *R/S*-CSA do not show any induced chirality but the same weak signal at 300 nm as the guests alone.

7.9.7 Induced chirality as function of added amount of chiral guest

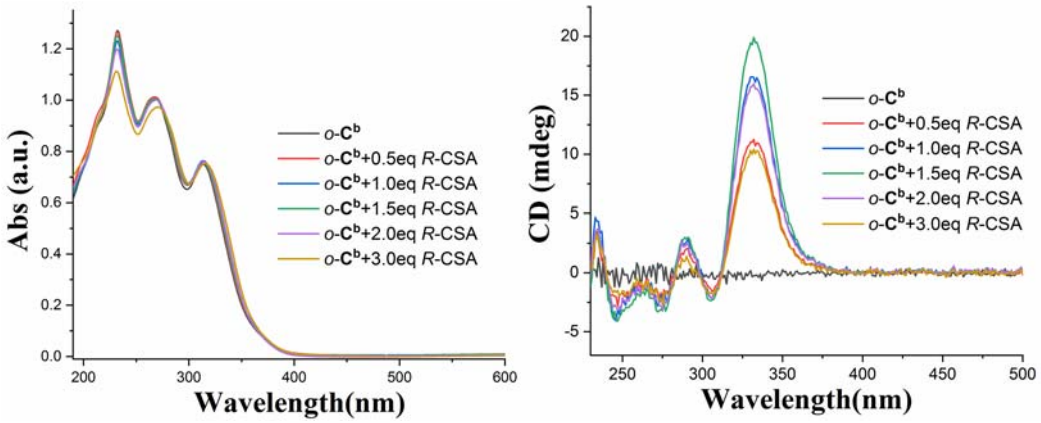

Figure 7.48 UV-Vis (left, 298 K) and CD (right, 298 K) spectra of *o*-**C^b** and *o*-**C^b** with increasing equivalents of added *R*-CSA (*o*-**C^b** concentration = 0.05 mM, cuvette path length for all UV-Vis and CD measurement is 1 mm).

7.9.8 Temperature-dependent photocyclization

Host-guest samples *R/S*-CSA@*o*-**C^b** (*o*-**C^b** concentration = 1 mM, host : ratio = 1 : 1.5) were prepared in quartz NMR tubes, immersed in cooling baths of different temperatures (see below) in a fully transparent quartz dewar vessel, and irradiated with 313 nm UV light. The completion of the irradiation was controlled by ^{1}H NMR spectroscopy. Subsequently, the solutions were allowed to warm to room temperature under exclusion of light, the cages were disassembled by addition of Bu_4NOH and EDTA, then separated by extraction with DCM. The enantiomeric excess of the photocyclization was determined by chiral HPLC (Daicel CHIRALPAK IA columns 250 x 4.6 mm).

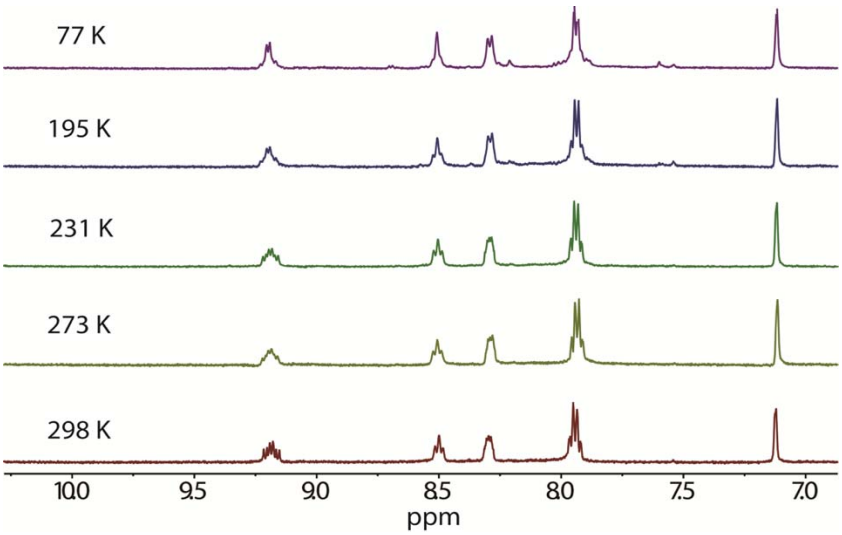

Figure 7.49 ^{1}H NMR spectra (298 K) of *c*-**C^b** (1 mM) with 1.5 eq. of *R*-CSA after irradiation under varied temperature ranging from 298 K to 77 K (cooling baths: 273 K: water ice mixture; 231 K: dry ice and acetonitrile mixture; 195 K: dry ice acetone mixture; 77 K: liquid N_2).

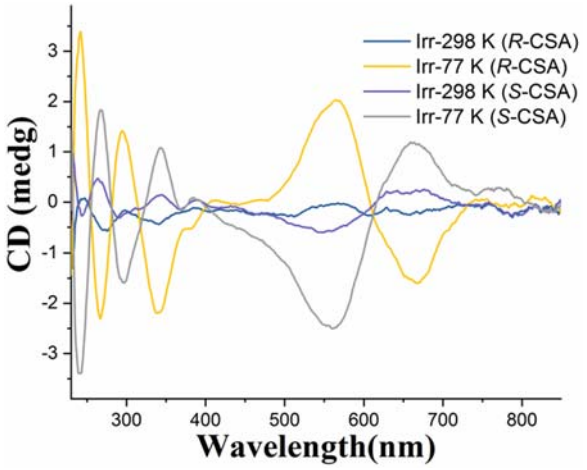

Figure 7.50 Exemplary CD spectra (298 K) of *c*-**C^{b}** (0.05 mM) with 1.5 eq. of *R/S*-CSA after irradiation with 313 nm UV light at 298 K and 77 K, respectively.

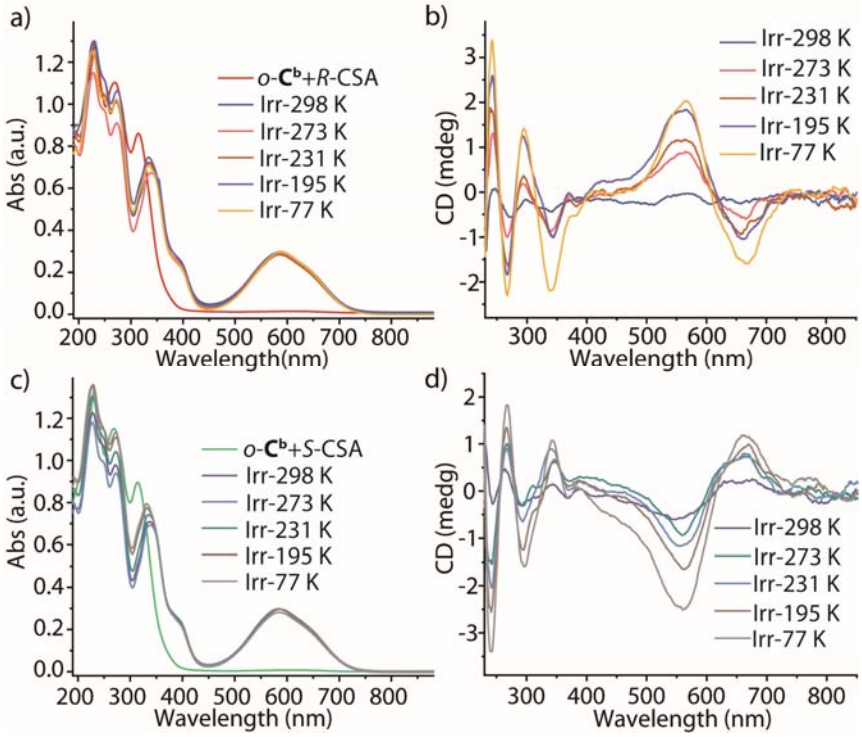

Figure 7.51 a) UV-Vis and b) CD spectra of *o*-**C^{b}** (0.05 mM, CH_3CN) containing 1.5 eq. *R*-CSA after irradiation with 313 nm light at temperatures from 298 K to 77 K (irradiation intervals were chosen until complete conversion was reached). For the same experiment of c) UV-Vis and d) CD spectra of *o*-**C^{b}** containing 1.5 eq. *S*-CSA.

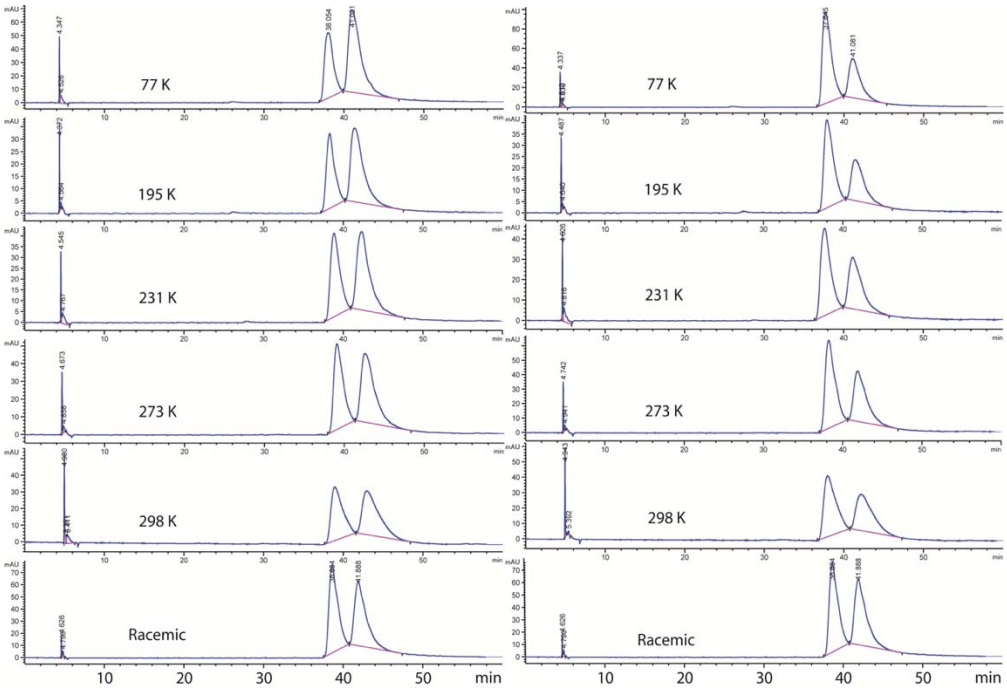

Figure 7.52 Chiral HPLC traces of *c*-**L**$^{\mathbf{b}}$ from the breakdown of *c*-**C**$^{\mathbf{b}}$ (1 mM) with 1.5 eq. of *R*-CSA (left) or *S*-CSA (right) after irradiation at varied temperatures ranging from 298 K to 77 K (Chromatography column: Daicel IA. Mobile phase: Hexane/Methanol/CH_2Cl_2 = 89:8:3. Run time: 60 min. Flow rate: 1.0 mL/min).

Table 6.2 *ee* values of isolated ligands *c*-**L**$^{\mathbf{b}}$ after irradiation of *o*-**C**$^{\mathbf{b}}$ containing 1.5eq. *R/S*-CSA at 313 nm at various temperatures (*R*-CSA induces enrichment of *S*, *S*-*c*-**L**$^{\mathbf{b}}$). HPLC trace integration suffered from signal overlap between *R, R* and *S, S* enantiomer of *c*-**L**$^{\mathbf{b}}$ as well as non-uniform peak widths and a drifting baselines. Based on comparing the results of two different integration methods for the racemic mixture (baseline projection vs. tangential skim) we estimate the integration error for the chosen method to about ±5% ee.

ee±5 (%)	298 K	273 K	231 K	195 K	77 K
R-CSA	7	8	13	21	28
S-CSA	10	13	14	24	31

7.9.9 Chirality transfer with guest *S*-CSA-Br

Similar to *R/S*-CSA, we tested chiral (1*S*)-(+)-3-bromocamphor-10-sulfonate for uptake and chirality transfer (*S*-CSA-Br, as its tetrabutyl ammonium salt in CD_3CN, 15.0 mM).

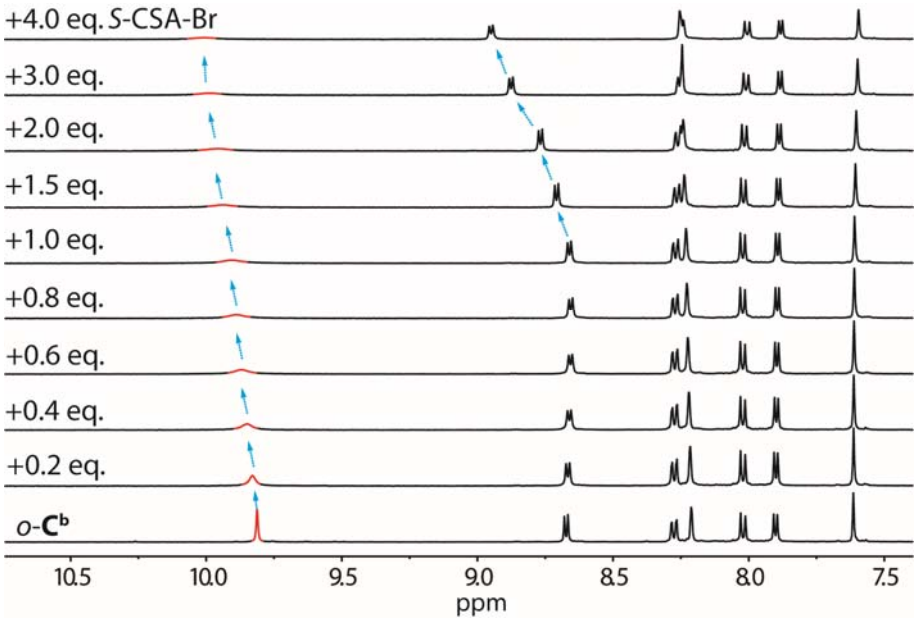

Figure 7.53 ^{1}H NMR spectra (500 MHz, CD_3CN, 298 K) of the titration of *o*-**C^{b}** (1.0 mM) with *S*-CSA-Br.

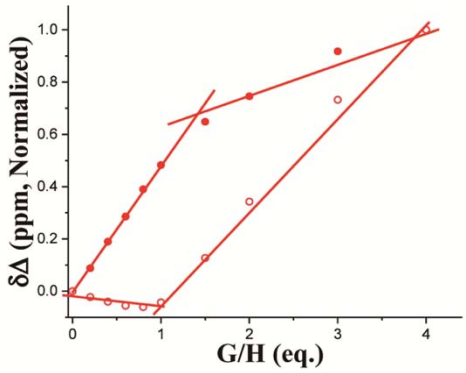

Figure 7.54 Binding isotherms of *o*-**C^{b}** with *S*-CSA-Br for inward proton H_a (filled circles) and outward proton H_b (empty circles) at 298 K.

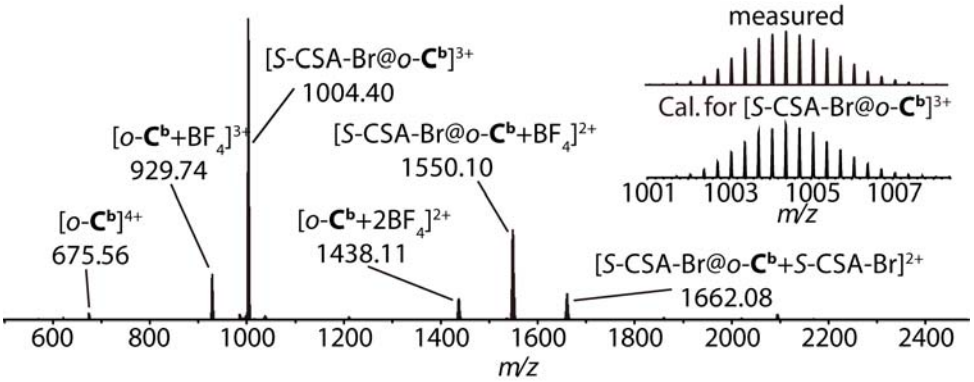

Figure 7.55 ESI-HRMS of [*S-CSA*-Br@*o*-**C^{b}**].

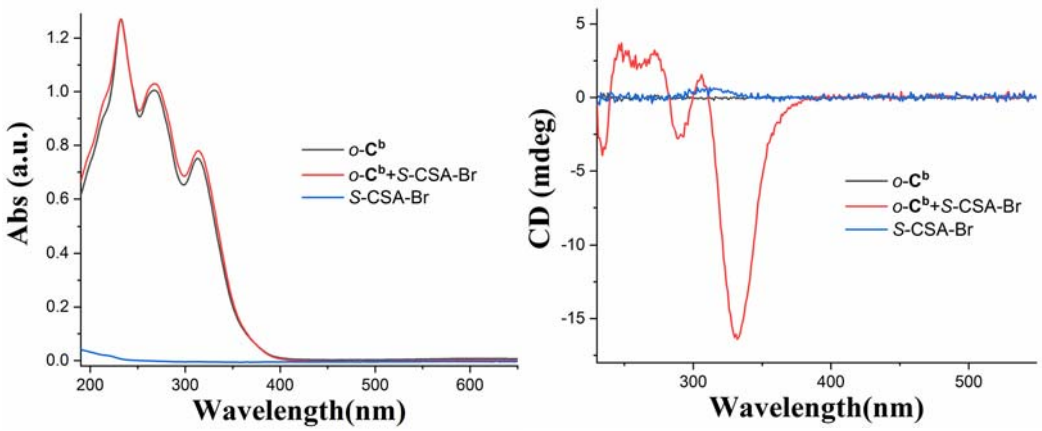

Figure 7.56 UV-Vis (left, 298 K) and CD (right, 298 K) spectra of *o*-**C^b**, *S*-CSA-Br and *o*-**C^b** with or without 1.5 eq. S-CSA-Br (*o*-**C^b** concentration = 0.05 mM).

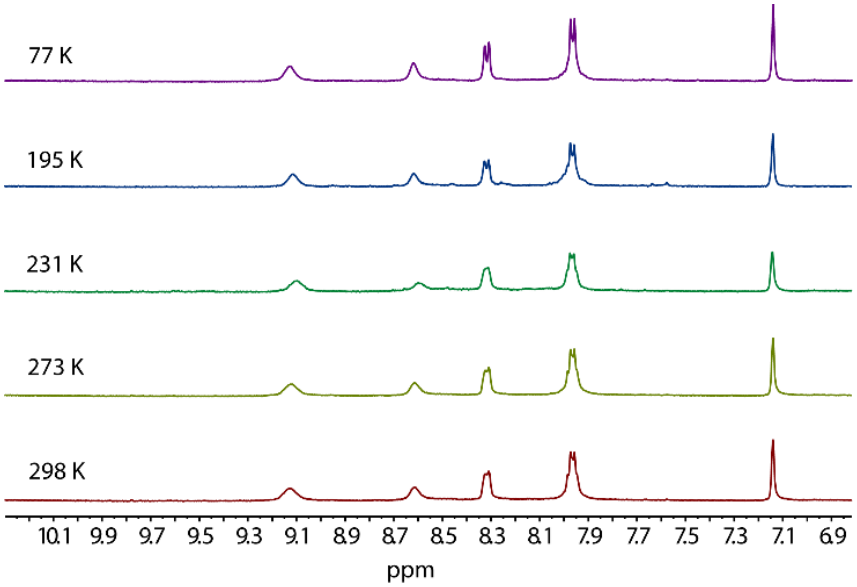

Figure 7.57 ^{1}H NMR spectra (298 K) of *c*-**C^b** (1 mM) with 1.5 eq. of *S*-CSA-Br after irradiation under various temperatures ranging from 298 K to 77 K.

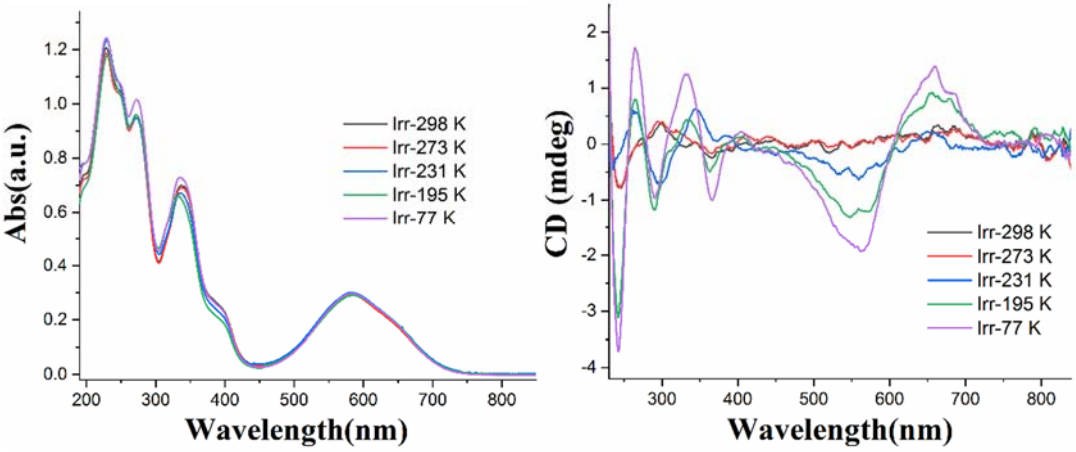

Figure 7.58 Exemplary CD spectra (298 K) of *c*-**C^b** (0.05 mM) with 1.5 eq. of *S*-CSA-Br after irradiation with 313 nm UV light between 298 K and 77 K.

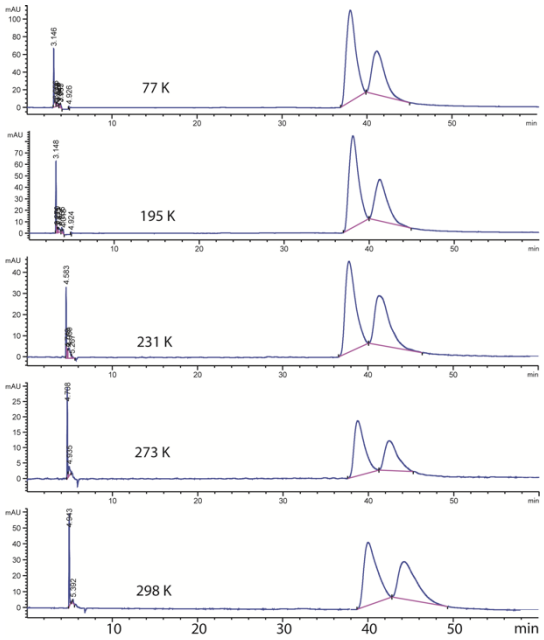

Figure 7.59 Chiral HPLC traces of the breakdown of *c*-**C^{b}** (1 mM) with 1.5 eq. of *S*-CSA-Br after irradiation under various temperatures ranging from 298 K to 77 K. (Chromatography column: Daicel IA. Mobile phase: Hexane/Methanol/CH_2Cl_2 = 89:8:3. Run time: 60 min. Flow rate: 1.0 mL/min).

Table 6.3 *ee* value of after irradiation at 313 nm of *o*-**C^{b}** with 1.5eq. *S*-CSA-Br at various temperatures. The results are very similar to what was observed for *R/S*-CSA (for error estimation see **Table 6.2**).

ee ±5 (%)	298 K	273 K	231 K	195 K	77 K
S-CSA-Br	10	12	14	23	26

7.9.10 Determination of absolute configuration

The open-form ligand *o*-**L^{b}** (10 mg) was dissolved in CD_2Cl_2 (1 mL) and then irradiated with 313 nm UV light. The pure (*R, R*) and (*S, S*) ligand enantiomers were separated by preparative chiral HPLC using a Daicel IA column (250 x 10 mm) under strict exclusion of daylight. The purity of separated **1** (the first fraction of HPLC) and **2** (the second fraction of HPLC) enantiomers were checked using analytical HPLC using a Daicel IA column (250 x 4.6 mm). In order to determine the absolute stereochemistry of the enantiomers, CD spectra were calculated by TD-DFT methods at the B3LYP/6-31G(d) level of theory in the Gaussian 09 software (using keyword iop(9/40=2)) and compared to experimental values.

7.9.10.1 Chiral resolution of *c*-L^{b}

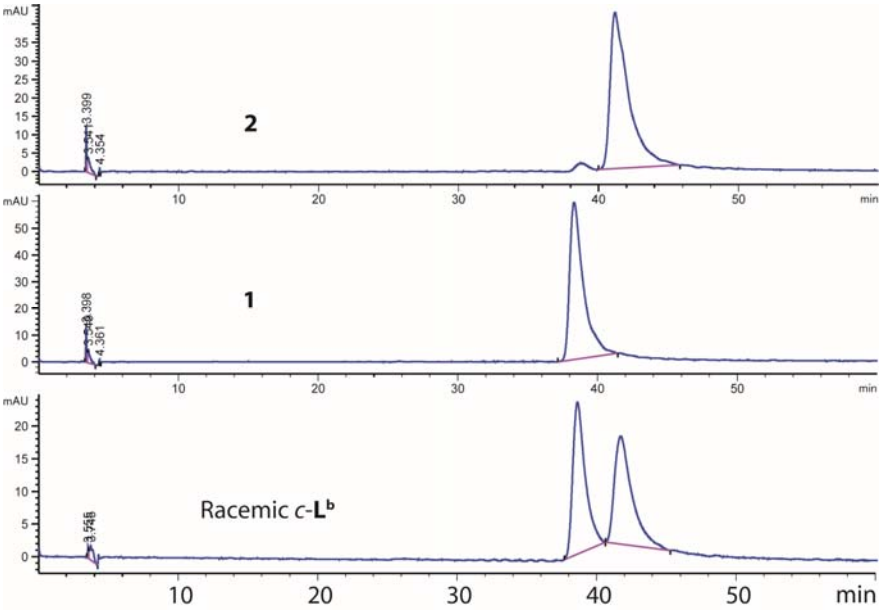

Figure 7.60 Chiral HPLC chromatograms of racemic and enantiomerically pure **1** and **2** compounds *c*-**L**^{b} before and after the chiral HPLC separation. (Chromatography column: Daicel IA. Mobile phase: Hexane/methanol/CH_2Cl_2 = 89:8:3. Run time: 60 min. Flow rate: 1.0 mL/min).

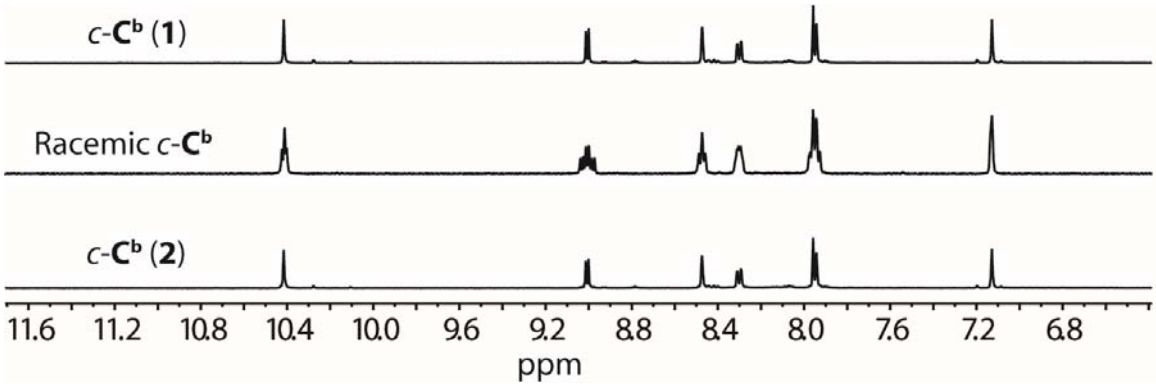

Figure 7.61 ^{1}H NMR spectra of racemic *c*-**C**^{b} and enantiomerically pure *c*-**C**^{b} (**1**) and *c*-**C**^{b} (**2**) made from enantiomerically pure ligands **1** and **2**, respectively. As can be seen, the signals of the enantiomerically pure cages *c*-**C**^{b} are much sharper than those of the racemic mixture of all possible *c*-**C**^{b} diastereomers.

7.9.10.2 Absolute configuration

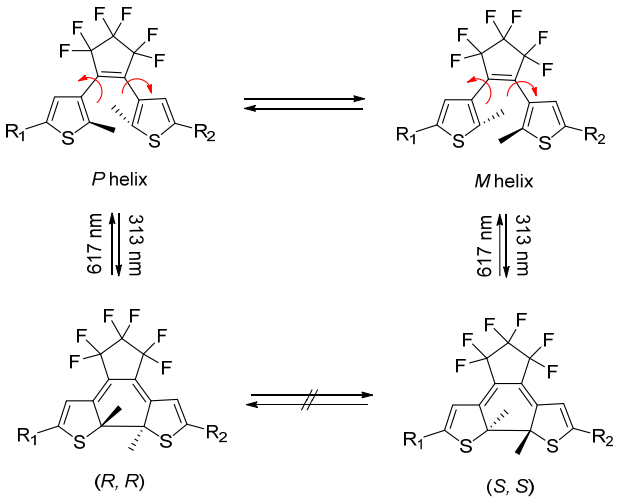

Scheme 6.5 Photoisomerization of a diarylethene (DTE). The photocyclization reactions from *P*- and *M*-helical conformers of the open-ring isomer produce (*R, R*) and (*S, S*) enantiomers of the closed-ring isomer, respectively.

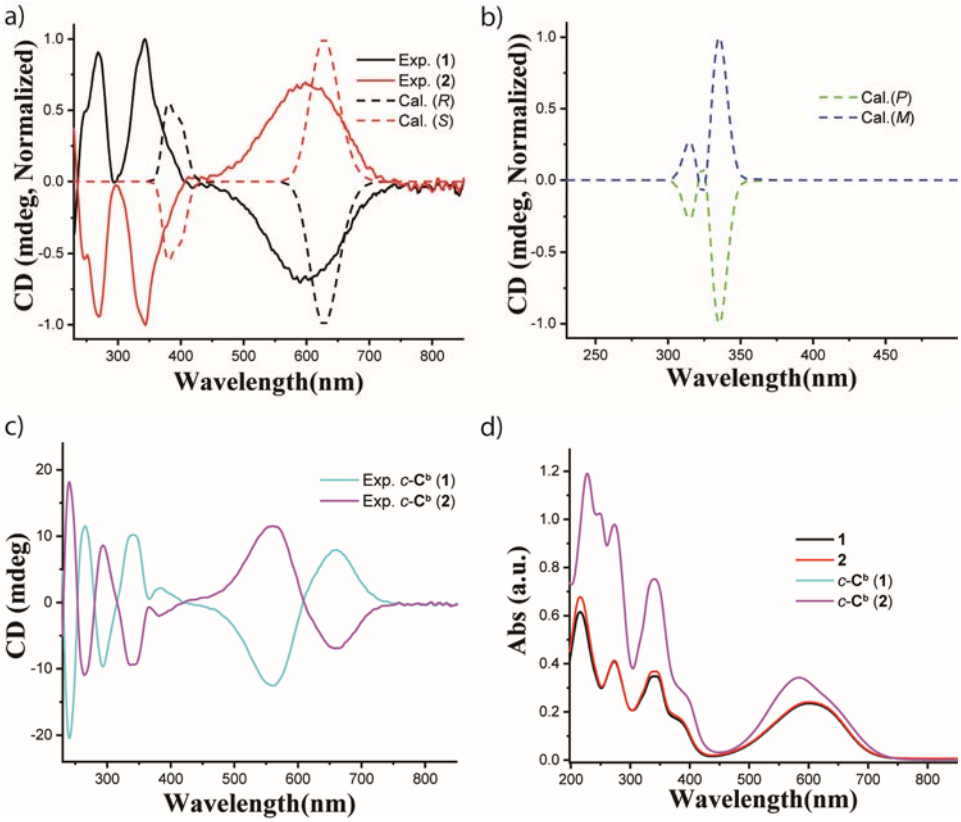

Figure 7.62 a) Calculated CD spectra of (*R, R*) and (*S, S*) closed form ligand enantiomers and measured CD spectra of closed ligand enantiomers from chiral HPLC resolved fraction **1** and **2** (0.1 mM); b) Calculated CD spectra of *P*- and *M*-helical conformers of open ligands; c) Measured CD spectra of closed cage enantiomers from **1** and **2** (0.05 mM); d) UV-Vis spectra of ligands **1** and **2** (0.1 mM) and *c*-**C^{b}** (**1**) (0.05 mM) and *c*-**C^{b}** (**2**) (0.05 mM). We can see from Figure 7.62a that the calculated CD spectrum of *c*-**L^{b}** (*R, R*) and experimental CD spectrum of fraction **1** both show a negative Cotton effect from 500 nm to 700 nm, indicating **1** has *R, R* configuration while fraction **2** exhibits *S, S* configuration. As a result, *R*-CSA was found to induce *M*-helical chirality of the ligand backbones in *o*-**C^{b}**, giving *S, S* enriched *c*-**L^{b}** ligands after ring closure under 313 nm irradiation. In contrast, *S*-CSA induces *P*-helical chirality in *o*-**C^{b}**, giving *R, R* enriched ligand *c*-**L^{b}**.

7.9.11 X-ray data

7.9.11.1 X-ray data of *o*-C^{b}

Crystals were obtained after 10 days by slow vapor diffusion of ethyl ether into a 1.0 mM *o*-**C^{b}** solution in CD_3CN in the dark.

Suitable single crystals for X–ray structural analysis of [*o*-**C^{b}**] were mounted at room temperature in NVH oil. Crystals were stored at cryogenic temperature in dry shippers, in which they were safely transported to macromolecular beamline P11[18] at the Petra III synchrotron, DESY, Germany. X-ray diffraction data was collected at 80(2) K on a single axis goniometer, equipped with an Oxford Cryostream 800 low temperature device and a Pilatus 6M fast detector. The data integration and reduction were taken with XDS[19]. The structure was solved by direct methods[20]. The structure model was refined against all data by full-matrix least-squares methods on F^2 with the program SHELXL2014[21]. The SQUEEZE[22] method provided by the program Platon[23] was used to improve the contrast of the electron density map the structure.

Table 6.4 Crystallographic data on [*o*-**C^{b}**].

CCDC number	1841263
Empirical formula	C150 H111 B4 F40 N15 O1 Pd2 S8
Formula weight	3412.06
Temperature	80(2) K
Wavelength	0.5636 Å
Crystal system	Triclinic
Space group	*P*-1
Unit cell dimensions	a = 15.475(3) Å; b = 17.268(3) Å; c = 19.388(4) Å. = 63.67(3)°; = 70.32(3)°; = 86.65(3)°.
Volume	4346(2) Å^3
Z	1
Density (calculated)	1.304 mg/m^3
Absorption coefficient	0.213 mm^{-1}
F(000)	1724
Crystal size	0.15 x 0.1 x 0.05 mm^3
Theta range for data collection	0.991 to 18.247°.

Index ranges	-17<=h<=17, -19<=k<=19, -21<=l<=21
Reflections collected	41851
Independent reflections	11982 [R(int) = 0.1049]
Completeness to theta = 18.161°	95.9 %
Refinement method	Full-matrix least-squares on F^2
Data / restraints / parameters	11982 / 2528 / 1158
Goodness-of-fit on F2	1.272
Final R indices [I>2sigma(I)]	R1 = 0.1172, wR2 = 0.3222
R indices (all data)	R1 = 0.1622, wR2 = 0.3580
Largest diff. peak and hole	2.195 and -0.632 e.$Å^{-3}$

7.9.11.2 X-ray data of *c*-C^{b}

After titrating 4.0 eq. of *S*-CSA solution (15mM, CD_3CN) to *c*-**C^{b}** (1.0mM, CD_3CN), crystals were found to grow in the NMR tube after several days in the dark.

Suitable single crystals of [*c*-**C^{b}**] were mounted in NVH oil on a nylon loop. X-ray diffraction data were collected on Bruker d8 venture systems based on a kappa goniometers with Incoatec microfocus X-ray sources (IμS 2.0), Incoatec QUAZAR mirror optics and a Photon 100 detector. The data were collected at 100 K crystal temperature (Oxford Cryosystems CRYOSTREAM 700), 50 kV and 600 μA and an appropriate 0.5° omega scan strategy. Data reduction was performed with SAINT v8.30C (Bruker, 2009a) out of the APEX II v2.2012.2 0 (Bruker, 2009b) program package. SADABS[24] (version 2014/4) was employed for the incident beam scaling, determination of the spherical harmonic coefficients, outlier rejection and determination of the error model parameters. All the structures were solved by direct methods with SHELXT[25]. They were refined by full-matrix least-squares against F^2 using SHELXL2014[21] with the help of the SHELXle[S11] graphical user interface. The SQUEEZE[22] method provided by the program Platon[23] was used to improve the contrast of the electron density map the structure.

In the structure, the *S*-CSA guest is not encapsulated inside the inner cavity, but positioned with the anionic sulfate group close to the outer face of the Pd centre. The purity of the titrated *S*-CSA guest was given as 99% by the manufacturer (Sigma Aldrich). Additionally, we have unambiguously confirmed the absolute configuration of this guest alone crystallographically using the enantiopure distinguishing parameter. As this enantiopure chiral *S*-CSA guest was titrated to the cage solution, the symmetry of the suggested centrosymmetric triclinic space group *P*-1 was lowered to triclinic space group

*P*1. In the host-guest complex, the anomalous signal of the *S*-CSA guest is insufficient to reliably determine the absolute structure using the enantiopure distinguishing parameter, because major parts of the asymmetric unit obey the pseudo symmetry (inversion center). Thus, the absolute structure was assigned based on the confirmed configuration of the *S*-CSA guest.

Table 6.5 Crystal data and structure refinement for [*c*-**C**[b]].

CCDC number	1841264
Empirical formula	C160 H122 B2 F32 N12 O8 Pd2 S10
Formula weight	3503.71
Temperature	100(2) K
Wavelength	1.54178 Å
Crystal system	Triclinic
Space group	*P*1
Unit cell dimensions	a = 16.2723(7) Å; b = 18.2308(7) Å; c = 19.8269(8) Å. = 106.559(2)°; = 90.9442(2)°; = 108.396(2)°.
Volume	5313.0(4) Å^3
Z	1
Density (calculated)	1.095 mg/m^3
Absorption coefficient	2.919 mm^{-1}
F(000)	1780
Crystal size	0.3 x 0.2 x 0.1 mm^3
Theta range for data collection	2.341 to 75.359°
Index range	-20<=h<=20, -22<=k<=22, -24<=l<=24
Reflections collected	158638
Independent reflections	39778 [R(int) = 0.0456]
Completeness to theta = 67.679°	98.1 %
Refinement method	Semi-empirical from equivalents
Data / restraints / parameters	Full-matrix least-squares on F^2
Goodness-of-fit on F2	1.042
Final R indices [I>2sigma(I)]	R1 = 0.0563, wR2 = 0.1612
R indices (all data)	R1 = 0.0728, wR2 = 0.1749
Largest diff. peak and hole	1.566 and -0.460 e.Å^{-3}

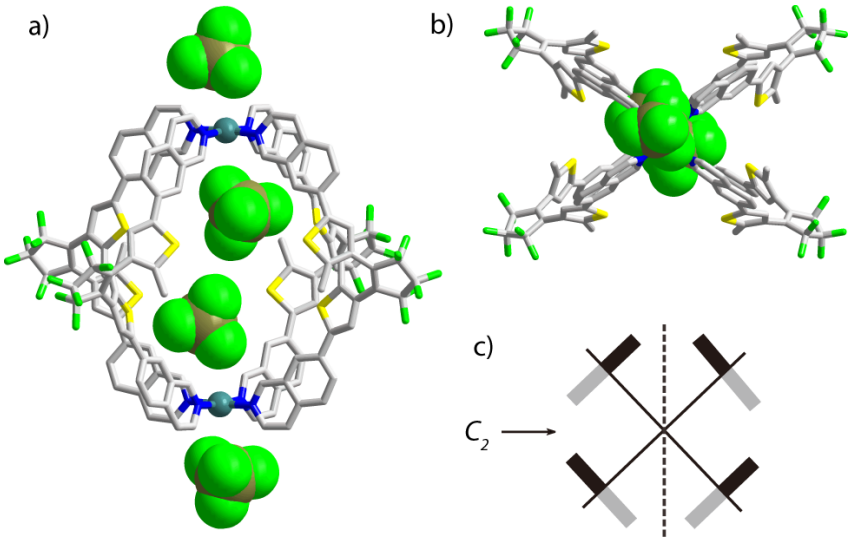

Figure 7.63 X-ray structure of cage *o*-**C**$^{\mathbf{b}}$ shown a) in side view and b) top view. c) Depiction of the stereochemical relationships between the four ligands viewed from the top (black/gray bars: close/remote methyl groups).

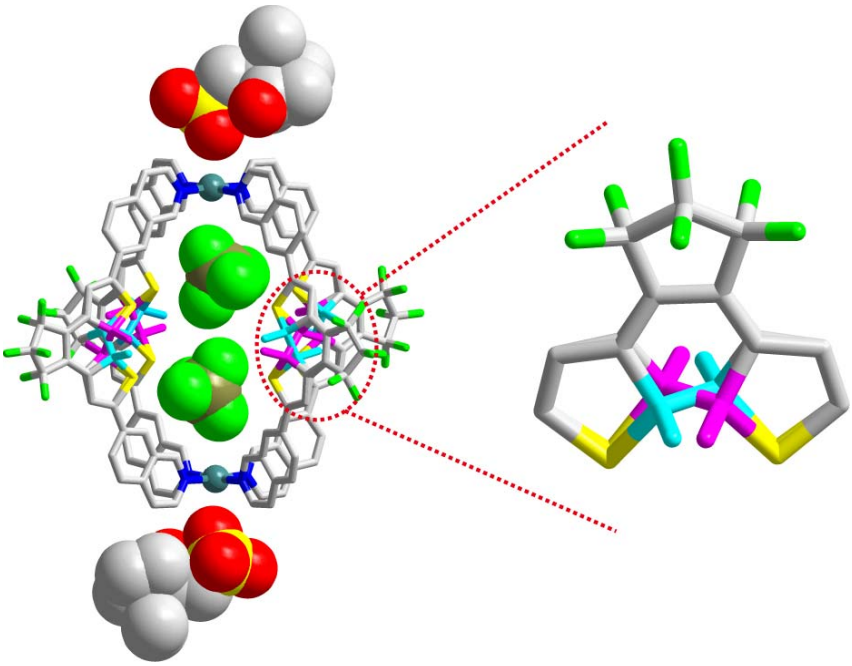

Figure 7.64 X-ray structure of cage *c*-**C**$^{\mathbf{b}}$ shown from side view (left). The *S*-CSA guests were found to be positioned outside the cage cavity. From the crystal structure, we can clearly see the disorder of the methyl group positions at the bond bridging the two thiophene rings, meaning that the cage crystallized as a mixture of diastereomers (highlight with color of cyan and purple, shown in the expand picture on the right).

7.9.12 Experiments with mixed open/closed-ligand cages *m*-**C**$^{\mathbf{b}}$

The statistical mixtures of mixed-ligand cages, containing both open and closed DTE photoisomers, were synthesized by reacting a mixture of the corresponding amounts of *o*-**L**$^{\mathbf{b}}$ and *c*-**L**$^{\mathbf{b}}$ with Pd^{II}. Exemplary procedure: "*m*-**C**$^{3:1}$" = $[Pd_2(o\text{-}\mathbf{L}^{\mathbf{b}})_x(c\text{-}\mathbf{L}^{\mathbf{b}})_{4-x}](BF_4)_4$ (x = 4: *o*-**C**$^{\mathbf{b}}$ [32%]; x = 3: [42%]; x = 2 [21%]; x = 1 [5%]; x = 0: *c*-**C**$^{\mathbf{b}}$ [<1%]; statistically expected composition given in square brackets), synonymously with its major component

[Pd_2(*o*-$\mathbf{L^b}$)$_3$(*c*-$\mathbf{L^b}$)$_1$] (whose behavior should be of main interest here), was synthesized by heating a mixture of ligands *o*-$\mathbf{L^b}$ and *c*-$\mathbf{L^b}$ (3:1 ratio) in CD_3CN (total 4 µmol; 1.87mg of *o*-$\mathbf{L^b}$ and 0.62 mg of *c*-$\mathbf{L^b}$, 866.7 µL) and [$Pd(CH_3CN)_4$](BF_4)$_2$ (2 µmol, 133.3 µL of a 15 mM stock solution in CD_3CN) at 70 °C for 5 h. The ^{1}H NMR spectra depicted in Figure S56 show a convoluted set of signals assigned to the *m*-$\mathbf{C}^{3:1}$ species, along with sharp signals for the contained *o*-$\mathbf{C^b}$ (marked red). Signal integration, while hampered by severe overlaps, indicated formation of the major species in approximate relative quantities as statistically expected. The experiment was carried out with racemic *c*-$\mathbf{L^b}$ as well as enantiopure *R*, *R*-*c*-$\mathbf{L^b}$ & *S*, *S*-*c*-$\mathbf{L^b}$, respectively.

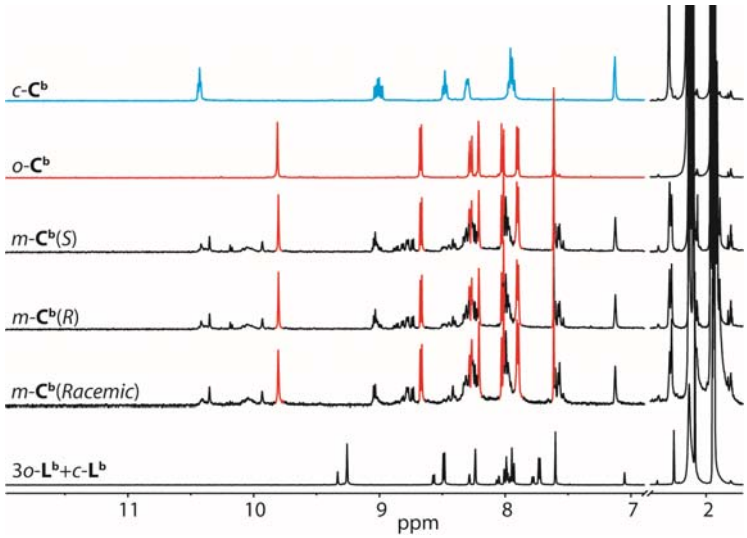

Figure 7.65 ^{1}H NMR spectra (500 MHz, CD_3CN, 298 K) of a mixture of *o*-$\mathbf{L^b}$ and *c*-$\mathbf{L^b}$ (3:1), the mixed-ligand cage samples "*m*-$\mathbf{C}^{3:1}$" resulting from the Pd-mediated assembly of the 3:1 mixture of *o*-$\mathbf{L^b}$ with racemic, *R, R*- or *S, S*-configured, *c*-$\mathbf{L^b}$ and the pure cages *o*-$\mathbf{C^b}$ (red) and *c*-$\mathbf{C^b}$ (blue).

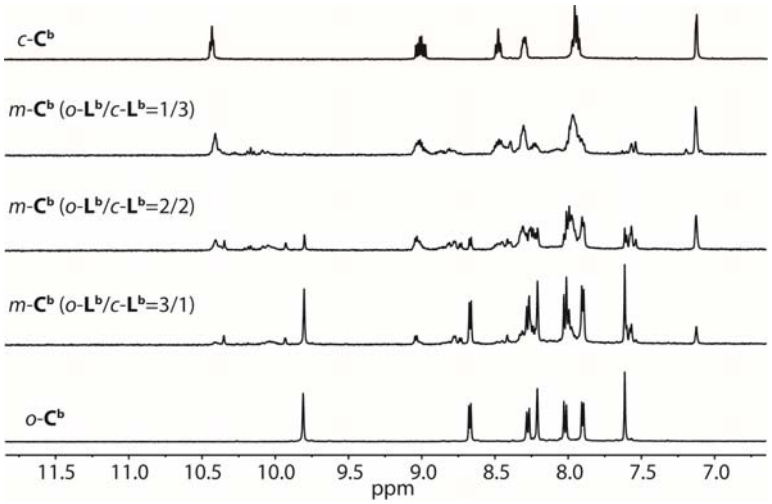

Figure 7.66 ^{1}H NMR spectra (500 MHz, CD3CN, 298 K) of *o*-$\mathbf{C^b}$, *m*-$\mathbf{C}^{3:1}$, *m*-$\mathbf{C}^{2:2}$, *m*-$\mathbf{C}^{1:3}$ and *c*-$\mathbf{C^b}$ (mixtures of isomers synthesized from 3:1, 2:2 and 1:3 *o*-$\mathbf{L^b}$/*c*-$\mathbf{L^b}$ ratios). The *m*-$\mathbf{C}^{3:1}$ (*o*-$\mathbf{L^b}$/*c*-$\mathbf{L^b}$ = 3:1) contains about 32% of o-$\mathbf{C^b}$, 42% of [Pd_2(*o*-$\mathbf{L^b}$)$_3$(*c*-$\mathbf{L^b}$)$_1$], 21% of [Pd_2(*o*-$\mathbf{L^b}$)$_2$(*c*-$\mathbf{L^b}$)$_2$], 5% of [Pd_2(*o*-$\mathbf{L^b}$)$_1$(*c*-$\mathbf{L^b}$)$_3$] and 0.4% of *c*-$\mathbf{C^b}$; The *m*-$\mathbf{C}^{2:2}$ (*o*-$\mathbf{L^b}$/*c*-$\mathbf{L^b}$ = 2:2) contains about 6% of *o*-$\mathbf{C^b}$, 25% of [Pd_2(*o*-$\mathbf{L^b}$)$_3$(*c*-$\mathbf{L^b}$)$_1$], 38% of [Pd_2(*o*-$\mathbf{L^b}$)$_2$(*c*-$\mathbf{L^b}$)$_2$], 25% of [Pd_2(*o*-$\mathbf{L^b}$)$_1$(*c*-$\mathbf{L^b}$)$_3$]] and 6 % of *c*-$\mathbf{C^b}$; The *m*-$\mathbf{C}^{1:3}$ (*o*-$\mathbf{L^b}$/*c*-$\mathbf{L^b}$ = 1:3) contains about 0.4% of *o*-$\mathbf{C^b}$, 5% of [Pd_2(*o*-$\mathbf{L^b}$)$_3$(*c*-$\mathbf{L^b}$)$_1$], 21% of [Pd_2(*o*-$\mathbf{L^b}$)$_2$(*c*-$\mathbf{L^b}$)$_2$], 42% of [Pd_2(*o*-$\mathbf{L^b}$)$_1$(*c*-$\mathbf{L^b}$)$_3$] and 32% of *c*-$\mathbf{C^b}$.

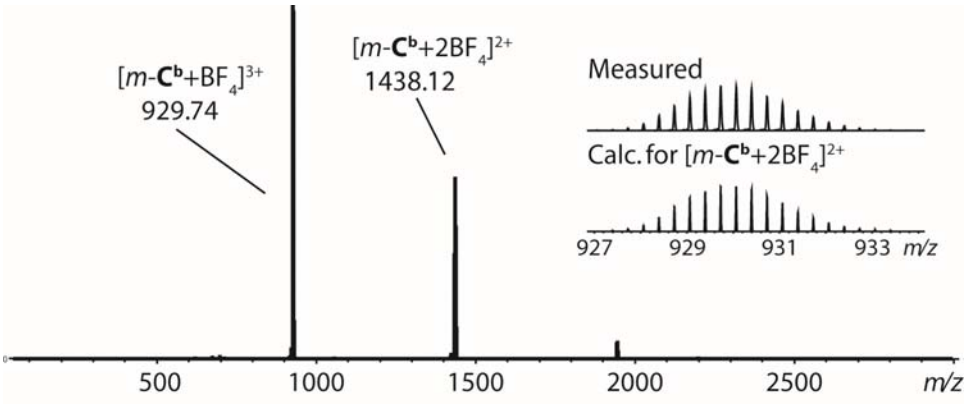

Figure 7.67 ESI-HRMS of the 3:1 mixed-ligand cages $[Pd_2(o\text{-}\mathbf{L^b})_x(c\text{-}\mathbf{L^b})_{4-x}](BF_4)_4$ (x = 0, 1, 2, 3, 4; see further description above), showing that all contained species are $[Pd_2\mathbf{L^b}_4]$ cages.

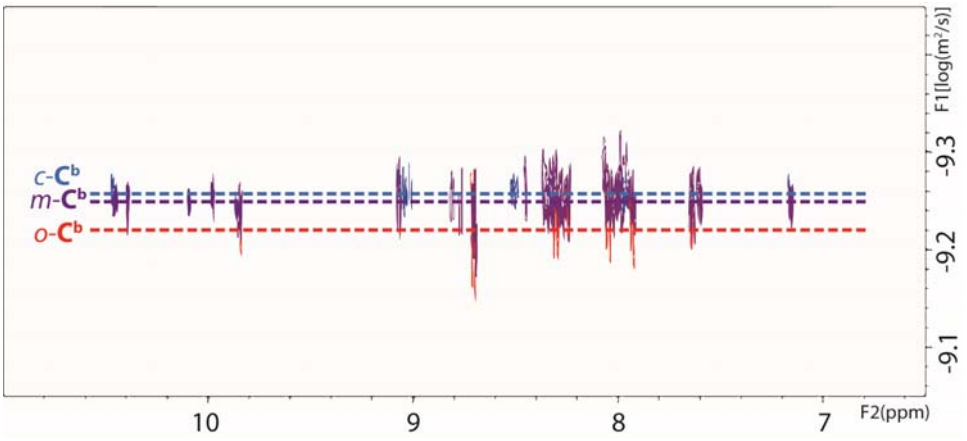

Figure 7.68 Overlay of DOSY NMR spectra (500 MHz, CD3CN, 298 K) of *o*-$\mathbf{C^b}$, *c*-$\mathbf{C^b}$, and the mixture *m*-$\mathbf{C}^{3:1}$ (dominated by *o*-$\mathbf{C^b}$ [32%] and $[Pd_2(o\text{-}\mathbf{L^b})_3(c\text{-}\mathbf{L^b})_1]$ [42%]). It can be seen that the major species in *m*-$\mathbf{C}^{3:1}$ (=$[Pd_2(o\text{-}\mathbf{L^b})_3(c\text{-}\mathbf{L^b})_1]$) and *c*-$\mathbf{C^b}$ have almost the same diffusion coefficient, much lower than the value of *o*-$\mathbf{C^b}$, further confirming that the sizes of *m*-$\mathbf{C^b}$ and *c*-$\mathbf{C^b}$ are similar, and larger than the size of *o*-$\mathbf{C^b}$.

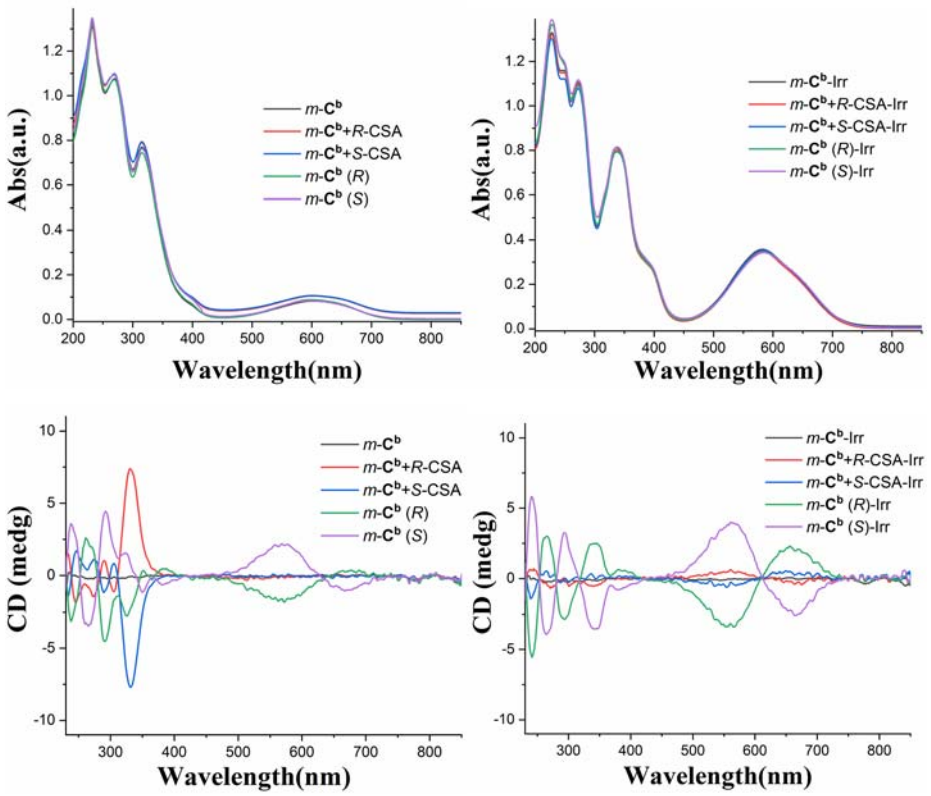

Figure 7.69 UV-vis and CD spectra of *m*-$\mathbf{C}^{3:1}$, *m*-$\mathbf{C}^{3:1}$+*R*-CSA, *m*-$\mathbf{C}^{3:1}$+*S*-CSA, *m*-$\mathbf{C}^{3:1}$(*R*) and *m*-$\mathbf{C}^{3:1}$(*S*) (0.05 mM based on cage) and corresponding UV-vis and CD spectra *after* irradiation with 313 nm light at 231 K. Most interestingly, the degree of chiral induction in the *m*-$\mathbf{C}^{3:1}$ sample (containing about 32% of *o*-$\mathbf{C}^{\mathbf{b}}$ and 42% of $[Pd_2(o\text{-}\mathbf{L}^{\mathbf{b}})_3(c\text{-}\mathbf{L}^{\mathbf{b}})_1]$ plus 1.5 eq. of one of the CSA enantiomers) as indicated by the total ellipticity of the band at 330 nm (7.3 mdeg) that is assigned to the open-form DTE chromophore was significantly lower than in case of a sample of pure *o*-$\mathbf{C}^{\mathbf{b}}$ at the same concentration (19.9 mdeg). Thus, the signal intensity in the *m*-$\mathbf{C}^{3:1}$ mixture amounts to only 36% of the one in *o*-$\mathbf{C}^{\mathbf{b}}$, in well accordance with the approximated fraction of *o*-$\mathbf{C}^{\mathbf{b}}$ in *m*-$\mathbf{C}^{3:1}$ (32%) and the assumption, that the major component $[Pd_2(o\text{-}\mathbf{L}^{\mathbf{b}})_3(c\text{-}\mathbf{L}^{\mathbf{b}})_1]$ is not able to bind the guest.

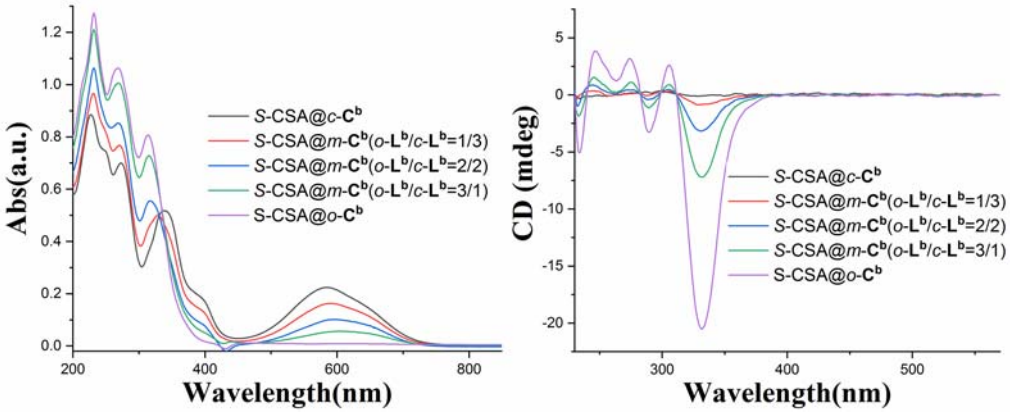

Figure 7.70 UV-vis (left) and CD (right) spectra of *S*-CSA@*o*-$\mathbf{C}^{\mathbf{b}}$, *S*-CSA@*c*-$\mathbf{C}^{\mathbf{b}}$, and *S*-CSA@*m*-$\mathbf{C}^{\mathbf{b}}$, (0.05 mM based on cage with 1.5 eq. of *S*-CSA). The *m*-$\mathbf{C}^{\mathbf{b}}$ samples were synthesized from 3:1, 2:2 and 1:3 *o*-$\mathbf{L}^{\mathbf{b}}$/*c*-$\mathbf{L}^{\mathbf{b}}$ ratios, composition.

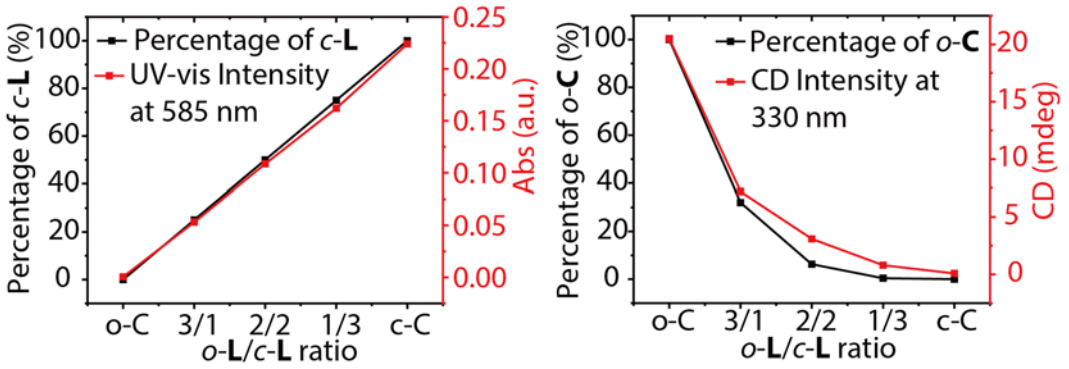

Figure 7.71 (left) The plot of UV absorbance 585 nm (red; absorption maximum of *c*-$\mathbf{L^b}$) of equally concentrated samples of *S*-CSA@*o*-$\mathbf{C^b}$, *S*-CSA@*m*-$\mathbf{C^b}$ (with 3:1, 2:2 and 1:3 *o*-$\mathbf{L^b}$/*c*-$\mathbf{L^b}$) and *S*-CSA@*c*-$\mathbf{C^b}$ against the *o*-$\mathbf{L^b}$/*c*-$\mathbf{L^b}$ ratio superimposes with the contained percentage of *c*-$\mathbf{L^b}$ (black), showing the expected linear relationship; (right) in contrast, the plot of the observed *S*-CSA guest-induced CD intensities in the same samples monitored at 330 nm (red; ellipticity maximum of *o*-$\mathbf{L^b}$) against the *o*-$\mathbf{L^b}$/*c*-$\mathbf{L^b}$ ratio non-linearly follows the statistical content of *o*-$\mathbf{C^b}$ (black) in the corresponding samples. Thus, chiral induction is only expressed in the contained fraction of *o*-$\mathbf{C^b}$ in all samples, neither in [Pd_2(*o*-$\mathbf{L^b}$)$_3$(*c*-$\mathbf{L^b}$)$_1$], [Pd_2(*o*-$\mathbf{L^b}$)$_2$(*c*-$\mathbf{L^b}$)$_2$], [Pd_2(*o*-$\mathbf{L^b}$)$_1$(*c*-$\mathbf{L^b}$)$_3$] or *c*-$\mathbf{C^b}$, indicating that the guest cannot bind when at least one photoswitch is closed.

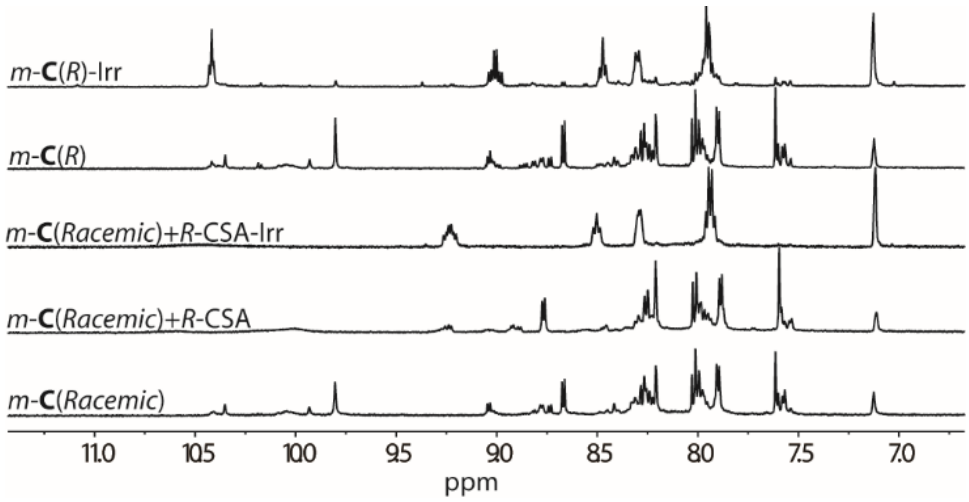

Figure 7.72 ^{1}H NMR spectra (500 MHz, CD_3CN, 298 K) of *m*-$\mathbf{C^{3:1}}$(Racemic), *m*-$\mathbf{C^{3:1}}$(Racemic)+*R*-CSA, *m*-$\mathbf{C^{3:1}}$(Racemic)+*R*-CSA-Irr, *m*-$\mathbf{C^{3:1}}$(R) and *m*-$\mathbf{C^{3:1}}$(*R*)-Irr. After irradiation with 313 nm light at 231 K, *m*-$\mathbf{C^{3:1}}$ was completely converted into *c*-$\mathbf{C^b}$.

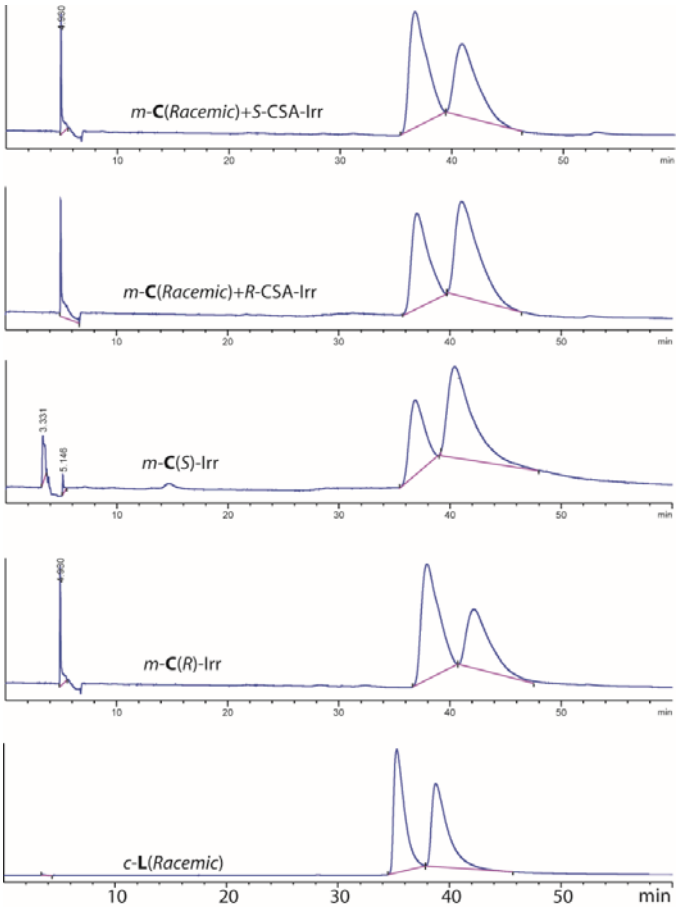

Figure 7.73 Chiral HPLC traces of isolated *c*-**L**^{b} from the disassembly of samples *m*-**C**$^{3:1}$(*R*), *m*-**C**$^{3:1}$(*S*) and *m*-**C**$^{3:1}$(Racemic) with 1.5 eq. of *R*-CSA or *S*-CSA after irradiation at 231 K. (Chromatography column: Daicel IA. Mobile phase: Hexane/Methanol/CH_2Cl_2 = 89:8:3. Run time: 60 min. Flow rate: 1.0 mL/min).

Table 6.6 Ligand *c*-**L**^{b} enantiomeric excesses obtained after 313 nm irradiation of *m*-C$^{3:1}$(*R/S*) or *m*-**C**$^{3:1}$ with 1.5eq. *R/S*-CSA at 231 K, followed by disassembly and release of free ligands (for error estimation see **Table 6.2**).

sample	*m*-**C**^{b}(R)-Irr	*m*-**C**^{b}(S)-Irr	*m*-**C**^{b}+R-CSA-Irr	*m*-**C**^{b}+S-CSA-Irr
ee ±5 (%)	29	29	7	8

7.9.13 Trapped Ion Mobility Mass Spectrometry

Ion mobility measurements were performed on a Bruker timsTOF instrument combining a trapped ion mobility (TIMS) with a time-of-flight (TOF) mass spectrometer in one instrument. In contrast to the conventional drift tube method to determine mobility data, where ions are carried by an electric field through a stationary drift gas, the TIMS method is based on an electric field ramp to hold ions in place against a carrier gas pushing them in the direction of the analyzer. Consequently, larger sized ions that experience more carrier gas impacts leave the TIMS units first and smaller ions elute later. This method offers a much higher mobility resolution despite a smaller device size.

Measurement: After the generation of ions by electrospray ionisation (ESI, analyte concentration: C = 0.1 mM, solvent: CH_3CN, capillary voltage: 3600V, end plate offset voltage: 500 V, nebulizer gas pressure: 0.3 bar, dry gas flow rate: 3.0 l/min, dry temperature: 200 °C) the desired ions were orthogonally deflected into the TIMS cell consisting of an entrance funnel and the TIMS analyser (carrier gas: N_2, temperature: 305 K, entrance pressure: 2,55 mbar, exit pressure: 0,89 mbar, IMS imeX ramp end: 1.88 1/K0, IMS imeX ramp start: 0.77 1/K0). As a result, the ions are stationary trapped. After accumulation (accumulation time: 5 ms), a stepwise reduction of the electric field strength leads to a release of ion packages separated by their mobility. After a subsequent focussing, the separated ions are transferred to the TOF-analyser.[27-29]

For calibration of both the TIMS and TOF analysers, commercially available Agilent ESI tuning mix was used. The instrument was calibrated before each measurement, including each change in the ion mobility resolution mode ("imeX" settings: survey, detect or ultra).

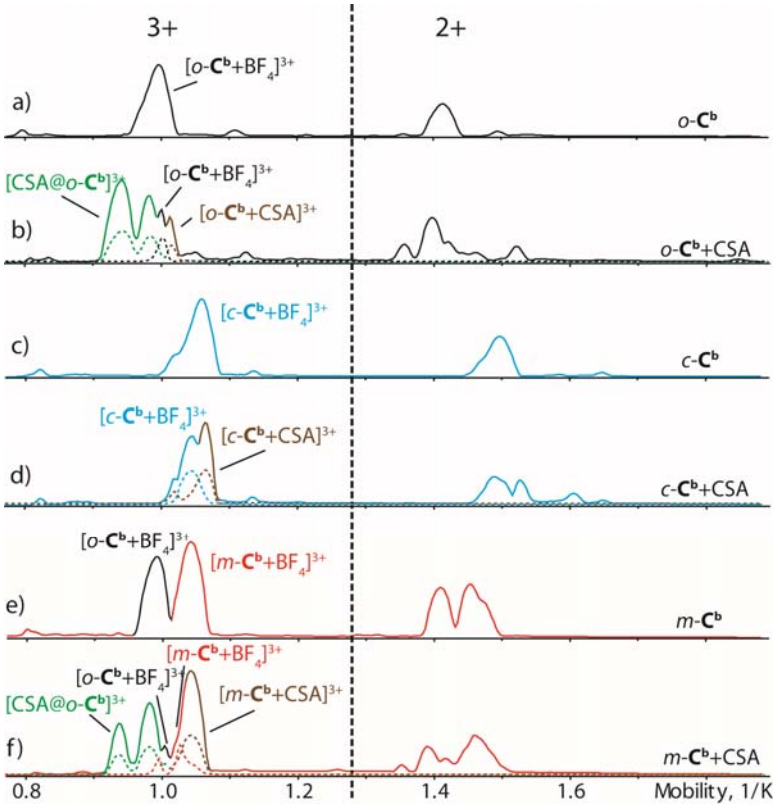

Figure 7.74 Trapped ion mobility spectra of a) ***o*-C^b,** b) ***o*-C^b+*R*-CSA**, c) ***c*-C^b**, d) ***c*-C^b+*R*-CSA**, e) ***m*-C$^{3:1}$** and f) ***m*-C$^{3:1}$+*R*-CSA** ("***m*-C$^{3:1}$**" stands for the statistical mixture, dominated by $[Pd_2(o\text{-}L^b)_3(c\text{-}L^b)_1]$, as described above).

The spectra on the left side of the dotted line are for 3+ charged cages (containing one BF_4^- counter anion or anionic guest, respectively), on the right side for 2+ charged cages (incl. two anions). The spectra show that the gas-phase mobility of ***o*-C^b** is significantly smaller than the mobilities of ***c*-C^b** & ***m*-C$^{3:1}$**, while the values of ***c*-C^b** and ***m*-C$^{3:1}$** are very close, indicating that ***m*-C$^{3:1}$** and ***c*-C^b** have similar sizes, but ***o*-C^b** is smaller (in full

accordance with the DOSY NMR results, see below). Addition of *R*-CSA to *o*-**C**$^{\mathbf{b}}$ produces further signals, two with smaller mobilities than [BF_4@*o*-**C**$^{\mathbf{b}}$] and mass signatures clearly pointing to 1:1 CSA host species. Under the assumption that dispersive host-guest interactions with encapsulated CSA mono-anion allow the flexible cage structure to shrink slightly more in the gas phase than in case of the parental species including the small, loosely bound BF_4^- anion, these signals were assigned to different arrangements of the encapsulation complex "[CSA@*o*-**C**$^{\mathbf{b}}$]". In addition, a small signal with a larger mobility than that for [BF_4@*o*-**C**$^{\mathbf{b}}$] was observed, again identified as CSA-containing species and thus assigned to the cage carrying an externally associated CSA anion, "[*o*-**C**$^{\mathbf{b}}$+CSA]". For *c*-**C**$^{\mathbf{b}}$, only one additional peak arises from the association with CSA and it has a larger mobility than the peak assigned to [BF_4@*c*-**C**$^{\mathbf{b}}$], pointing to the inability of *c*-**C**$^{\mathbf{b}}$ to encapsulate the guest in its interior. For the mixed-ligand *m*-**C**$^{3:1}$ sample, without CSA guest, two major mobilities are observed, one assignable to the contained [BF_4@*o*-**C**$^{\mathbf{b}}$], the other to the major mixed-ligand species [BF_4@Pd_2(*o*-**L**$^{\mathbf{b}}$)$_3$(*c*-**L**$^{\mathbf{b}}$)$_1$]. After addition of CSA, the mobilogram reveals a combination of signals, where the left part is comparable to the situation of [CSA@*o*-**C**$^{\mathbf{b}}$]/[*o*-**C**$^{\mathbf{b}}$+CSA] and the right part shares similarity to the [*c*-**C**$^{\mathbf{b}}$+CSA] sample, i.e. a smaller peak assigned to [BF_4@*m*-**C**$^{3:1}$], partially overlapped by a large signal with a larger mobility carrying the mass signature of a CSA-containing cage ([*m*-**C**$^{3:1}$+CSA]), indicating that *m*-**C**$^{3:1}$ is also not able to encapsulate the guest. Peak assignment in the mobilograms is based on drift time comparisons amongst the measurements (all individually calibrated) and coupled HRMS detection in the Bruker tims-TOF instrument.

7.9.14 Molecular Modeling

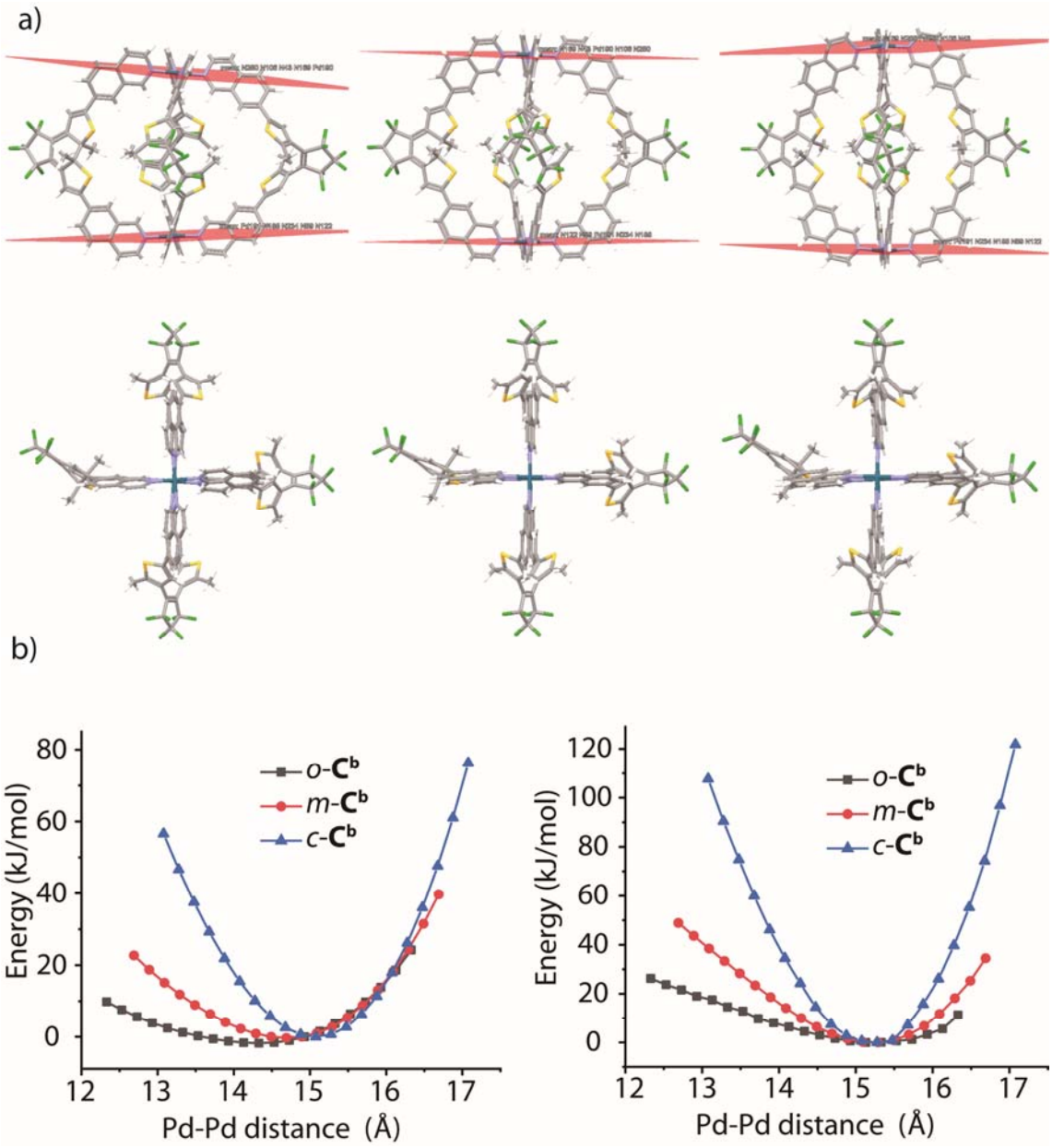

Figure 7.75 a) Side and top views of DFT (B3LYP/LANL2DZ) optimized $[Pd_2(o\text{-}\mathbf{L^b})_3(c\text{-}\mathbf{L^b})_1]$ structures under constraining the Pd-Pd distance with shortest examined distance (12.69 Å, left), optimized Pd-Pd distance (15.29 Å, middle) and longest Pd-Pd distance (16.69 Å, right). b) PM6 (left) and DFT (B3LYP/LANL2DZ; right) calculated energies (scaled to a common value at 15 Å) under performing a relaxed scan of the Pd-Pd distance. Results show that the all-open cage *o*-$\mathbf{C^b}$ can be squeezed most easily (black), while the closure of only one photoswitch in *m*-$\mathbf{C}^{3:1}$ (red) already raises the slope of the energy-over-compression branch of the curve to an extent about half-way through towards the situation when all photoisomeric ligands are in their closed form (blue).

7.10 References

[1] (a) H. Yamamoto, E. M. Carreira, (Eds.), *Comprehensive Chirality*, 1st ed., *Elsevier*, Amsterdam, **2012**. (b) B. L. Feringa, R. A. van Delden, *Angew. Chem. Int. Ed.* **1999**,

38, 3418-3438. (c) A. R. Palmans, E. W. Meijer, *Angew. Chem., Int. Ed.* **2007**, *46*, 8948-8968. (d) M. Yoon, R. Srirambalaji, K. Kim, *Chem. Rev.* **2012**, *112*, 1196-1231.

[2] (a) G. Seeber, B. E. F. Tiedemann, K. N. Raymond, *Top. Curr. Chem*. **2006**, *265*, 147. (b) M. Liu, L. Zhang, T. Wang, *Chem. Rev.* **2015**, *115*, 7304-7397. (c) M. Raynal, P. Ballester, A. Vidal-Ferran, P. W. van Leeuwen, *Chem. Soc. Rev.* **2014**, *43*, 1660-1733. (d) L. J. Chen, H. B. Yang, M. Shionoya, *Chem. Soc. Rev.* **2017**, *46*, 2555-2576. (e) K. Yan, R. Dubey, T. Arai, Y. Inokuma, M. Fujita, *J. Am. Chem. Soc.* **2017**, *139*, 11341-11344. (f) L. J. Prins, P. Timmerman, D. N. Reinhoudt, *J. Am. Chem. Soc.* **2001**, *123*, 10153-10163.

[3] (a) Y. Nishioka, T. Yamaguchi, M. Kawano, M. Fujita, *J. Am. Chem. Soc.* **2008**, *130*, 8160-8161. (b) W. Xuan, M. Zhang, Y. Liu, Z. Chen, Y. Cui, *J. Am. Chem. Soc.* **2012**, *134*, 6904-6907. (c) C. Gutz, R. Hovorka, C. Klein, Q. Q. Jiang, C. Bannwarth, M. Engeser, C. Schmuck, W. Assenmacher, W. Mader, F. Topic, K. Rissanen, S. Grimme, A. Lutzen, *Angew. Chem. Int. Ed.* **2014**, *53*, 1693-1698. (d) X. Wang, Y. Wang, H. Yang, H. Fang, R. Chen, Y. Sun, N. Zheng, K. Tan, X. Lu, Z. Tian, X. Cao, *Nat. Commun.* **2016**, *7*, 12469. (e) J. Sun, J. L. Bennett, T. J. Emge, R. Warmuth, *J. Am. Chem. Soc.* **2011**, *133*, 3268-3271.

[4] A. M. Castilla, N. Ousaka, R. A. Bilbeisi, E. Valeri, T. K. Ronson, J. R. Nitschke, *J. Am. Chem. Soc.* **2013**, *135*, 17999-18006.

[5] J. M. Rivera, T. Martín, J. Rebek, *Science* **1998**, *279*, 1021.

[6] (a) A. J. Terpin, M. Ziegler, D. W. Johnson, K. N. Raymond, *Angew. Chem., Int. Ed.* **2001**, *40*, 157-160. (b) A. V. Davis, D. Fiedler, M. Ziegler, A. Terpin, K. N. Raymond, *J. Am. Chem. Soc.* **2007**, *129*, 15354-15363.

[7] (a) M. Irie, T. Fukaminato, K. Matsuda, S. Kobatake, *Chem. Rev*. **2014**, *114*, 12174-12277. (b) J. Zhang, H. Tian, *Adv. Optical Mater.* **2018**, 1701278.

[8] (a) M. Morimoto, S. Kobatake, M. Irie, *Chem. Commun.* **2008**, 335-337. (b) K. Kawamura, K. Osawa, Y. Watanobe, Y. Saeki, N. Maruyama, Y. Yokoyama, *Chem. Commun*. **2017**, *53*, 3181-3184.

[9] J. J. D. de Jong, L. N. Lucas, R. M. Kellogg, J. H. van Esch, B. L. Feringa, *Science* **2004**, *304*, 278.

[10] T. C. Pace, V. Muller, S. Li, P. Lincoln, J. Andreasson, *Angew. Chem., Int. Ed.* **2013**, *52*, 4393-4396.

[11] (a) S. R. Seidel, P. J. Stang, *Acc. Chem. Res.* **2002**, *35*, 972-983. (b) T. R. Cook, Y. R. Zheng, P. J. Stang, *Chem. Rev.* **2013**, *113*, 734-777. (c) M. M. Smulders, I. A. Riddell, C. Browne, J. R. Nitschke, *Chem. Soc. Rev.* **2013**, *42*, 1728-1754.

[12] (a) M. Han, D. M. Engelhard, G. H. Clever, *Chem. Soc. Rev*. **2014**, *43*, 1848-1860. (b) G. H. Clever, P. Punt, *Acc. Chem. Res.* **2017**, *50*, 2233-2243.

[13] (a) M. Han, R. Michel, B. He, Y. S. Chen, D. Stalke, M. John, G. H. Clever, *Angew. Chem., Int. Ed.* **2013**, *52*, 1319-1323. (b) M. Han, Y. Luo, B. Damaschke, L. Gomez, X. Ribas, A. Jose, P. Peretzki, M. Seibt, G. H. Clever, *Angew. Chem., Int. Ed.* **2016**, *55*, 445-449.

[14] (a) A. J. McConnell, C. S. Wood, P. P. Neelakandan, J. R. Nitschke *Chem. Rev.* **2015**, *115*, 7729-7793. (b) D. H. Qu, Q. C. Wang, Q. W. Zhang, X. Ma, H. Tian *Chem. Rev.* **2015**, *115*, 7543-7588.

[15] (a) S. Wiedbrauk, T. Bartelmann, S. Thumser, P. Mayer, H. Dube, *Nat. Commun.* **2018**, *9*, 1456. (b) Y. Hua, A. H. Flood, *J. Am. Chem. Soc.* **2010**, *132*, 12838-12840. (c) A. Diaz-Moscoso, F. A. Arroyave, P. Ballester, *Chem. Commun.* **2016**, *52*, 3046-3049.

[16] (a) S. Fraysse, C. Coudret, J. P. Launay, *Eur. J. Inorg. Chem.* **2000**, 1581–1590; b) B. He, O. S. Wenger, *J. Am. Chem. Soc.* **2011**, *133*, 17027-17036.

[17] (a) G. H. Clever; W. Kawamura; M. Shionoya, *Inorg. Chem*. **2011**, *50*, 4689-4691. (b) G. H. Clever; S. Tashiro; M. Shionoya, *Angew. Chem. Int. Ed*. **2009**, *48*, 7010-7012. (c) G. H. Clever; S. Tashiro; M. Shionoya, *J. Am. Chem. Soc*. **2010**, *132*, 9973-9975. (d) S. Loffler, J. Lubben, A. Wuttke, R. A. Mata, M. John, B. Dittrich, G. H. Clever, *Chem. Sci.* **2016**, *7*, 4676-4684.

[18] A. Burkhardt; T. Pakendorf; B. Reime; J. Meyer; P. Fischer; N. Stübe; S. Panneerselvam; O. Lorbeer; K. Stachnik; M. Warmer; P. Rödig; D. Göries; A. Meents, *Eur. Phys. J. Plus.*, **2016**, *131*, 56.

[19] W. Kabsch, *Acta Crystallogr. Sect. D*, **2010**, *66*, 125.

[20] T. R. Schneider; G. M. Sheldrick, *Acta Cryst*. **2002**, *D58*, 1772.

[21] G. M. Sheldrick, *Acta Crystallogr. Sect. A*, **2008**, *64*, 112.

[22] A. Spek, *Acta Crystallogr. Sect. C*, **2015**, *71*, 9.

[23] A. Spek, *Acta Crystallogr. Sect. D*, **2009**, *65*, 148.

[24] G. M. Sheldrick, *SADABS*, Universität Göttingen, Germany, **2000**.

[25] G. M. Sheldrick, *Acta Crystallogr. Sect. A*, **2015**, *71*, 3.

[26] C. B. Hubschle; G. M. Sheldrick; B. J. Dittrich, *Appl. Crystallogr.*, **2011**, *44*, 1281.

[27] F. A. Fernandez-Lima, D. A. Kaplan, M. A. Park, *Rev. Sci. Instrum.* **2011**, *82*,

[28] D26R06Hernandez, J. D. DeBord, M. E. Ridgeway, D. A. Kaplan, M. A. Park, F. Fernandez-Lima, *Analyst* **2014**, *139*, 1913.

[29] J.-F. Greisch, J. Chmela, M. E. Harding, D. Wunderlich, B. Schäfer, M. Ruben, W. Klopper, D. Schooss, M. M. Kappes, *Phys. Chem. Chem. Phys.* **2017**, *19*, 6105.

8 Abbreviations

Å	Ångström
°C	Celcius (centigrad)
BF_4^-	tetrafluoroborate anion
$CDCl_3$	Deuterated Chloroform
CD_3CN	Deuterated Acetonitrile
COSY	correlated spectroscopy
CSI	cryospray ionization
DMSO	dimethylsulfoxid
DOSY	Diffusion-ordered spectroscopy
DAE	Diarylethene
DTE	Dithienylethene
DFT	Density functional theory
eq.	equivalent
ESI	electrospray ionization
ee	Enantiomeric excess
h	hour
HR-MS	High resolution mass spectrometry
HSQC	Heteronuclear single quantum correlation
HMBC	Heteronuclear multiple bond correlation
Hz	Hertz
J	coupling constant
K	Kelvin
L	Ligand
M	Metal
m/z	Mass-to-charge ratio
MHz	Megahertz
mM	mmol L^{-1}
MOF	Metal-organic framework
NMR	nuclear magnetic resonance
NOESY	nuclear overhauser effect spectroscopy
ppm	parts per million
r.t.	room temperature

9 Acknowledgements

I would like to thank all the people who help me in the journey of my PhD.

First of all, huge thanks goes to my supervisor Prof. Dr. Guido H. Clever for offering me a great chance to conduct my PhD study in his working group. I appreciate all his help both in life and research. He gave me complete freedom and useful advices to my PhD research. And I am very grateful for his personal help and support, especially the beginning time when I leave my home country to Germany.

I would like to thank Prof. Dr. Guido H. Clever, Prof. Dr. Andreas Steffen and Prof Dr. Martin Hiersemann for being in my PhD examination board.

I would like to thank SFB (B05) project and TU Dortmund. SFB project supported with a scholarship at my first year in Göttingen University and TU Dortmund funded the rest years of my PhD.

I would like to thank my collaboration partner Prof. Dr. Joakim Andréasson (Chalmers University of Technology, Sweden). With the gifts of series DAE ligands he sent, I had chance and could obtained nice results to be shown in this thesis that either produced already or will lead to fruitful publications.

I would like to thank all the collaborators for their experimental and technical support. In particularly, Prof Dr. Lars Schäfer and his working group (Ruhr-Universität Bochum) for molecule dynamic simulation; Prof. Dr. Patrick Nürnberger and Kevin Artmann (Ruhr-Universität Bochum) for time-resolved UV-vis spectra measurement; Dr. Michael John (Göttingen University) and Prof Dr. Wolf Hiller for helping with NMR spectroscopy; Laura Schneider, Dr. Holm Frauendorf (Göttingen University) & his team and Mrs Christiane Heitbrink (MPI Dortmund) for measuring mass spectra; Dr. Julian Holstein and Dr. Haeri Lee for the X-ray measurement and structures refinement.

I thank Dr. Gabi Trötscher-Kaus, Birgit Thormann, Kristian Surich, Laura Schneider and Alexandra Klauke for their help over the past years in Dortmund. I thanks Birgit and Gabi for helping me translate and prepare tons of documents; Kristian, Alex and Laura for chemicals ordering and Kristian for some special technical support such as home-made quartz Dewar and so on.

I also would like to thank Dr. Susanne Löffler, Dr. Thorben Schulte, Bo Zhang, Philip Punt, Dr. Subhadeep Saha and Dr. Jacopo Tessarolo for their proofreading of my thesis. I thank André Platzek for his translation of the abstract chapter to German. And I thank all my students for their contribution to the work.

Special thank goes to all the member in Clever research group from past and present: Muxin, David, Marina, Fernenda, Susanne, Rongmei, Thorben, Marcel, Yoko, Mark, Witold, Julia, Soham, Subhadeep, Shin, Hiro, Bin, Bo, Irene, Lucas, Robin, Philip, André, Kristina, Qianqian, Sonja, Jacopo, Sudhakar, Haeri and Kai, Eri. Hopefully I did not forget anyone. Thank you for sharing the happy hours together and thank you for your help and advices in my tough time in the past years.

Last but not the least, I thanks my family for their unconditional support and understanding.

Eidesstattliche Versicherung (Affidavit)

Name, Vorname
(Surname, first name)

Matrikel-Nr.
(Enrolment number)

Belehrung:

Wer vorsätzlich gegen eine die Täuschung über Prü- fungsleistungen betreffende Reg(Surname, first name)(Enrolment number)elung einer Hochschul- prüfungsordnung verstößt, handelt ordnungswidrig. Die Ordnungswidrigkeit kann mit einer Geldbuße von bis zu 50.000,00 € geahndet werden. Zuständige Verwaltungs- behörde für die Verfolgung und Ahndung von Ordnungs- widrigkeiten ist der Kanzler/die Kanzlerin der Techni- schen Universität Dortmund. Im Falle eines mehrfachen oder sonstigen schwerwiegenden Täuschungsversu- ches kann der Prüfling zudem exmatrikuliert werden, § 63 Abs. 5 Hochschulgesetz NRW.
Die Abgabe einer falschen Versicherung an Eides statt ist strafbar.
Wer vorsätzlich eine falsche Versicherung an Eides statt abgibt, kann mit einer Freiheitsstrafe bis zu drei Jahren oder mit Geldstrafe bestraft werden, § 156 StGB. Die fahrlässige Abgabe einer falschen Versicherung an Eides statt kann mit einer Freiheitsstrafe bis zu einem Jahr oder Geldstrafe bestraft werden, § 161 StGB.
Die oben stehende Belehrung habe ich zur Kenntnis genommen:

Official notification:

Any person who intentionally breaches any regulation of university examination regulations relating to deception in examination performance is acting improperly. This offence can be punished with a fine of up to EUR 50,000.00. The competent administrative authority for the pursuit and prosecution of offences of this type is the chancellor of the TU Dortmund University. In the case of multiple or other serious attempts at deception, the candidate can also be unenrolled, Section 63, paragraph 5 of the Universities Act of North Rhine-Westphalia.

The submission of a false affidavit is punishable. Any person who intentionally submits a false affidavit can be punished with a prison sentence of up to three years or a fine, Section 156 of the Criminal Code. The negligent submission of a false affidavit can be punished with a prison sentence of up to one year or a fine, Section 161 of the Criminal Code.

I have taken note of the above official notification.

Ort, Datum
(Place, date)

Unterschrift
(Signature)

Titel der Dissertation:

(Title of the thesis):

Ich versichere hiermit an Eides statt, dass ich die vorlie- gende Dissertation mit dem Titel selbstständig und ohne unzulässige fremde Hilfe angefertigt habe. Ich habe keine anderen als die angegebenen Quellen und Hilfs- mittel benutzt sowie wörtliche und sinngemäße Zitate kenntlich gemacht.
Die Arbeit hat in gegenwärtiger oder in einer anderen Fassung weder der TU Dortmund noch einer anderen Hochschule im Zusammenhang mit einer staatlichen oder akademischen Prüfung vorgelegen.

I hereby swear that I have completed the present dissertation independently and without inadmissible external support. I have not used any sources or tools other than those indicated and have identified literal and analogous quotations.
The thesis in its current version or another version has not been presented to the TU Dortmund University or another university in connection with a state or academic examination.*

*Please be aware that solely the German version of the affidavit ("Eidesstattliche Versicherung") for the PhD thesis is the official and legally binding version.

Ort, Datum
(Place, date)

Unterschrift
(Signature)